QUANTIFICATION OF FLOW IMPAIRMENT IN FAULTED SANDSTONE RESERVOIRS

by

Thomas H. P. Manzocchi B.Sc.

Thesis submitted for the Degree of Doctor of Philosophy

Department of Petroleum Engineering
Heriot-Watt University
Edinburgh

March 1997

TABLE OF CONTENTS

LIST OF FIGURES

LIST OF TABLES

LIST OF SYMBOLS

Notes:
1 The appearance of the subscript x in this list signifies that a term is never used without one. Unless specified otherwise, x is the dimension (1, 2 or 3) of a sample.
2 The term S represents a measure of fault size which may be D, L, or T.

Term	Units	Meaning
UPPERCASE ROMAN LETTERS		
A	m^2	The area WJ
B	m^{1-n}	Constant linking D and L
$CUMFD$	m^{-1}	Cumulative fault density
Cv	dimensionless	Coefficient of variation
D	m	Fault displacement
D_0	m	Displacement of the largest fault in a population
D'	m	Maximum displacement on a fault trace
F	m^{1-r}	Constant linking D and T
H	dimensionless	Fault heterogeneity
H	m	Distance parallel to ε_2
J	m	Distance parallel to ε_3
L	m	Fault length
M	dimensionless	Cluster mass
N	dimensionless	Number of faults
N_x	dimensionless	Number of nodes ($x = I$, Y, X or N)
$N_x(S)$	dimensionless	Number of faults of size $\geq S$ in a sample
$N_x(S_{pq})$	dimensionless	Number of faults in the size range $S_p < S \leq S_q$ in a sample
P	dimensionless	Proportion
S	m	Fault spacing
S_L	m	Average streamline length over the distance W.
S_p	m^{-1}	Surface area / pore volume
$\overline{S}_{pq}$	m	Average size of faults in the displacement range $D_p < D < D_q$
T	m	Fault thickness
T	mPa	Tensile strength
W	m	Distance parallel to ε_1
LOWERCASE ROMAN LETTERS		
a	dimensionless	Constant linking H and d_L, to k_e / k_m
a_x	$m^{c_x - x}$	Constant linking $N_x(D)$ and D
a_{Lx}	$m^{c_{Lx} - x}$	Constant linking $N_x(L)$ and L
a_{Tx}	$m^{c_{Tx} - x}$	Constant linking $N_x(T)$ and T
c	dimensionless	Constant linking H and d_L, to k_e / k_m

Term	Units	Meaning
c_x	dimensionless	Power-law exponent linking $N_x(D)$ and D
c_{Lx}	dimensionless	Power-law exponent linking $N_x(L)$ and L
c_{Tx}	dimensionless	Power-law exponent linking $N_x(T)$ and T
d	dimensionless	Constant linking H and d_L, to k_e / k_m
d_G	dimensionless	Gouge density
d_L	dimensionless	Line density
d_S	m^{-1}	Scan-line density
e	m	Component of h parallel to ε_1
h	m	Fault heave
k	mD	Permeability
k_o	dimensionless	Shape factor
k_z	dimensionless	Kozeny Constant
n	dimensionless	Power-law exponent linking D and L.
p	dimensionless	Probability
p	mPa	Pore pressure
r	dimensionless	Power-law exponent linking D and T
t	dimensionless	Tortuosity factor

GREEK LETTERS

α	dimensionless	Angle between the population strike and ε_1
β	dimensionless	Stretching factor
γ	dimensionless	Shear strain
γ	dimensionless	semivariance
δ	°	Population average dip
ε	dimensionless	Brittle strain
ζ	dimensionless	Connectivity term for an IX system
η	dimensionless	Connectivity term for an IY system
θ	°	Angle between a fracture and σ_3
σ	mPa	Normal stress
σ'	mPa	Effective stress
τ	dimensionless	Tortuosity factor
τ	mPa	Shear stress
ϕ	dimensionless	Porosity

SUBSCRIPTS

Term	Meaning
1,2,3	Sample dimension
1,2,3	Maximum, intermediate and minimum diagonal terms for tensor properties
45	Equivalent orthogonal
a	Arithmetic average
c	Critical
e	Effective
eo	normalised effective
f	Fault

Term	Meaning
h	Harmonic average
I	I-nodes
m	Matrix
N	Nodes
max	Maximum
min	Minimum
p, q	Any particular value
X	X-nodes
Y	Y-nodes

ACKNOWLEDGEMENTS

Foremost I thank Philip Ringrose for his patient and insightful supervision. I'm sure he knew in advance which alleyways would prove blind, but by allowing me to find out for myself he left me in no doubt what direction the research should take.

Silke Schallenburger, Margaret Forrester and Dan Carruthers between them programmed the code described in Chapter 4. Without their contribution of time and skill, my infamous triangles would have remained lifeless abstractions.

Vigorous (sometimes even violent) technical debate in the pub over the last three years with Brian Crawford, and more recently with Pascale Royer and Richard Jackson, has taught me much more than I thought I wanted to know about topics I never knew existed. This is greatly appreciated.

Less esoteric discussion with Dan Carruthers, Jerry Jensen, Gillian Pickup and Ross Garden from Heriot-Watt University; John Underhill, Patience Cowie, Zoë Shipton and Peter Leary from Edinburgh University; Andrew Foxford and John Walsh from the Liverpool Fault Analysis Group and Mark Manzocchi from Imperial College has also contributed greatly to my thinking.

Warm thanks to those friends I coerced into proof-reading / collating duties: Natalya Hunter Williams, Pascale Royer, Simon Thomas, Caroline Hern, Julian Clark, Brian Crawford and Richard Jackson. The latter I praise deeply, for he has just brought me a half-bottle of wine. Thanks also to Andrea Massey for running a flexible and friendly library.

The research was funded by Amerada Hess, Bow Valley, British Gas, Chevron, Conoco, Deminex, Elf, Esso, Mobil, Shell and the Department of Trade and Industry as part of the second phase of the Reservoir Heterogeneity Project.

ABSTRACT

This thesis establishes a method for calculating effective permeability in faulted sandstone reservoirs. No specific reservoir is at issue, the work is aimed towards developing a general technique to predict the significance of sub-seismic faulting for reservoir simulation and risk management programs. A 2D analytical solution is derived, requiring as input a quantitative geological description of sub-seismic faulting. The method is a significant advance, as it is more robust and widely applicable than existing ones, and incorporates a more complete fault system model.

A new criterion is developed to characterise and quantify geological connectivity. The influence of fault splays on connectivity is addressed using methods from percolation theory. The critical connectivity of systems incorporating splays is determined analytically. Network modelling is used to confirm this result, and also shows that the critical density of systems incorporating geological connectivity is less than half the value for the random continuum networks which are often used in flow modelling.

Numerical flow simulation is used to derive empirical relationships between a transmissibility term, a tortuosity term and effective permeability for orthogonal fault systems. Geometrical techniques are developed to generalise these solutions for anisotropic systems. This new method allows determination of effective permeability at a single length-scale for systems of any fault density, orientations, length, thickness and permeability. These results are incorporated into a simple upscaling routine which represents the four orders of magnitude of sub-seismic faulting as a discrete hierarchy. Application to published sub-surface datasets confirms that high fault densities are needed to reduce the permeability of a reservoir significantly. Deformation bands are not particularly significant as flow baffles, as larger scales of sub-seismic faulting generally have a greater influence on effective permeability than smaller ones.

INTRODUCTION

" The model will be a simplification and an idealisation, and consequently a falsification. It is to be hoped that the features retained for discussion are those of greatest importance in the present state of knowledge."

Alan Turing, 1952

I contend that a paradigm shift is occurring in structural geology. Many quantitative predictions can be made about small-scale fault and fracture systems in reservoirs where only qualitative conjectures were possible a decade ago. The shift will be completed when the spatial characteristics of fault systems are incorporated in the same coherent mathematical scheme which already describes their scaling frequencies.

Reservoir engineering practice is at odds with this improved understanding of fault populations. Models of fault and fracture systems for engineering applications need to reproduce the flow behaviour observed in the reservoir. Therefore, fracture-flow "sugar-cube" models are generally used, and these have served engineering applications adequately. These models can be used in flow simulation provided they can be calibrated against field-specific flow information. They cannot be used to predict flow performance without calibration, as the models are based on geometrical, not geological criteria. Geologists and engineers alike recognised that these models were not accurate representations of the fracturing in the reservoir. Without a firm quantitative basis from which to start, however, there was no way for predictive geological models to be built. This platform now exists.

This thesis combines engineering and geological approaches to develop a technique to predict flow in faulted sandstone reservoirs. The first part comprises Chapters 1 to 3. This reviews the state of current geological understanding of small-scale fault systems, and identifies the aspects which can already be quantified from seismic data. Studies of

outcrop analogues allows other parameters to be estimated. A simple hierarchical model is developed to describe sub-seismic fault systems, incorporating the features of faults which are most important for single phase flow.

The second part of the thesis (Chapter 4) focuses on connectivity. Fault or fracture connectivity is a crucial control on flow in a system, and a new method to quantify it is developed in Chapter 3. Connectivity analysis shows that available modelling approaches fail to reproduce the connectivity of natural systems. Therefore a new modelling approach is introduced in Chapter 4. With this approach, realistic fault connectivity and clustering characteristics can be reproduced in numerical models. Percolation theory is used at a more theoretical level to explore the connectivity characteristics of geological systems, and several new results and conclusions are determined.

The third part (Chapters 5 to 7) relate specifically to predicting effective permeability in reservoirs containing low permeability faults. Methods are developed for calculating the permeability of a fault system at a single scale. This technique is incorporated into the mathematical and procedural model which is gradually developed throughout the thesis, culminating in an illustration using published sub-surface data in Chapter 7.

CHAPTER 1

MODELLING FLOW IN FAULT SYSTEMS

1.1 Introduction

This study concerns the analysis of fluid flow in porous clastic hydrocarbon reservoirs containing pervasive partially sealing faults. In traditional "fractured reservoirs", the fracturing is beneficial to field development, which often would not be viable without the fractures to act as flow conduits. Fractured reservoirs have therefore received much attention from reservoir engineers, and dual-porosity models of varying complexity are commonly used in flow simulation of fracture reservoirs (e.g., Golf-Racht, 1982). In contrast, porous clastic reservoirs may also be extensively faulted, but the engineering implications of such small scale faulting have received scant attention. This is despite the considerable volume of geological work describing their detrimental petrophysical properties; particularly in high porosity sandstones. This work is concerned with modelling flow through fault systems in porous sandstones with the aim of developing a method for routinely managing sub-seismic faulting in reservoir simulation. The study integrates field observations of faults and fault systems, the analysis of their geometrical and scaling characteristics, and numerical flow simulation.

Small-scale faulting in porous sandstone is of potential consequence for reservoir management for the following reasons.

A) Porous sandstones often have high fault densities, with a disproportionate quantity of faults with low displacements.

B) Fault with displacements as low as a fraction of a millimetre are characterised by significant petrophysical alteration over a narrow gouge zone.

Because the strength of a sandstone is proportional to its porosity (Dunn *et al.*, 1973), and because high porosity favours fault work-hardening (Underhill and Woodcock, 1987), faulting will tend to be most prevalent in the best quality sandstone reservoirs, and this faulting will be predominantly small-scale.

In a study investigating the changes in reserve estimates from appraisal to development of UKCS fields, Corrigan (1993) concluded that structural complexity is the most significant factor in common for fields in which estimated recovery had diminished severely as the field life progressed. Another study, discussed by Bu and Damsleth (1996), ascribes three quarters of the total uncertainty in reserves in the Veslefrikk field (Norwegian Sector, North Sea) to structural parameters. An early recognition of possible compartmentalisation and flow impairment owing to partially sealing sub-seismic faults is critical if development strategies in structurally complex fields are to be optimised (e.g., Smalley and Hale, 1996).

Although there is agreement that small scale faults in porous sandstone may be permeability baffles, and therefore have an influence on flow calculations, there is no consensus as to their significance, nor is there a method in place to adequately assess this. The goals of this work are two-fold:

A) To determine the circumstances under which small scale faulting in porous sandstones are of significance to reservoir management, and

B) To derive a method for incorporating the effects of small-scale faulting in reservoir simulation of sandstone reservoirs.

1.1.1 Small-scale faulting in porous sandstone reservoirs

Small-scale faulting in porous sandstones has received considerable geological attention. Engelder (1974) presented the first comprehensive description of such faults, summarising their texture and stressing the role of cataclasis in reducing porosity and grain size within the narrow faults. A few years later Aydin and co-workers made a study of small scale faulting in porous sandstone in Utah, and established a three-tier progression of fault style with increased displacement (*deformation bands*, *zones of deformation bands* and *slip surfaces* : Aydin, 1978; Aydin and Johnson, 1978, 1983; Aydin and Reches, 1982). Apart from many (usually inappropriate) semantic embellishments, this useful mechanical subdivision is still widely used.

Aydin's work was a geo-mechanical treatment, and the main issue discussed was the temporal evolution of the faults. The theory of *work-hardening* of brittle shear fractures (e.g., Rudnicki and Rice, 1975) was applied to explain the field characteristics of the faulting. Field characteristics in different settings were also described by Jamison and Stearns (1982) and Underhill and Woodcock (1987). Jamison and Stearns studied the small-scale faulting associated with larger faults, with an emphasis on fault density distribution. Underhill and Woodcock studied small-scale faulting in relation to a pluton intrusion, with emphasis on the orientation of the small-scale faults. Both pairs of workers related work-hardening to quantitative analyses of the porosity reduction within the faults. The mechanical development of the faults has recently been discussed by Antonellini *et al.* (1994). While confirming that a significant proportion of faults in porous sandstone are of the work-hardening type described by earlier workers, a more detailed analysis determined that faults are not always formed through cataclasis. Some faults in pure sandstones are non-cataclastic, and in less pure sandstones shear displacement is often accommodated by shale-smearing with subordinate cataclasis.

The petrophysical characteristics of cataclastic faults have been studied specifically by Pittman (1981), Antonellini and Aydin (1994) and Fowles and Burley (1994). The petrophysical properties of the faults are found to be governed closely by the petrology of the sandstone. Generally, cataclastic faults are flow baffles. Petrophysical properties vary with provenance, and porosity can be reduced by up to 80%, permeability is frequently two to three orders of magnitude less than that of the unfaulted sandstone matrix, and capillary pressures across faults are much higher than in matrix samples. In addition to alteration of the petrophysical properties due to the cataclastic formation of the faults, they can also be altered due to diagenetic effects. Edwards *et al.* (1993) studied faults in the Hopeman sandstone (Scotland) and found that at different periods in the basin history, the faults had acted both as conduits and baffles. This resulted in cementation adjacent to the faults, accompanied by a further reduction in permeability.

Faulting affects flow in different ways at different scales. At the pore scale, the flow through the fault is controlled by the petrophysical properties of the faults. Figure 1.1 shows maps of faults in porous sandstones at a variety of scales. The smallest scale image (Figure 1.1a) is a computerised tomograph (CT) scan of a 1 cm thick fault gouge zone from a sample recovered from core from the North Sea. The image has a pixel resolution of 0.2 x 0.2 mm, and has been processed to display only CT numbers above an arbitrary threshold. CT number correlates directly with density, therefore a high CT number indicates low porosity in monomineralic rock. This is the scale at which the fault petrophysical properties are determined. The gouge zone is composed of several anastomosing strands of low porosity material, with higher porosity material between them. Each low porosity fault strand is a deformation band, and the entire structure is a zone of deformation bands. The bands within the zone show porosity variation along their traces. This is indicated on the figure by white patches with a higher porosity along the lower porosity black fault traces. Permeability, as well as porosity, is also likely to vary considerably over relatively small distances along faults.

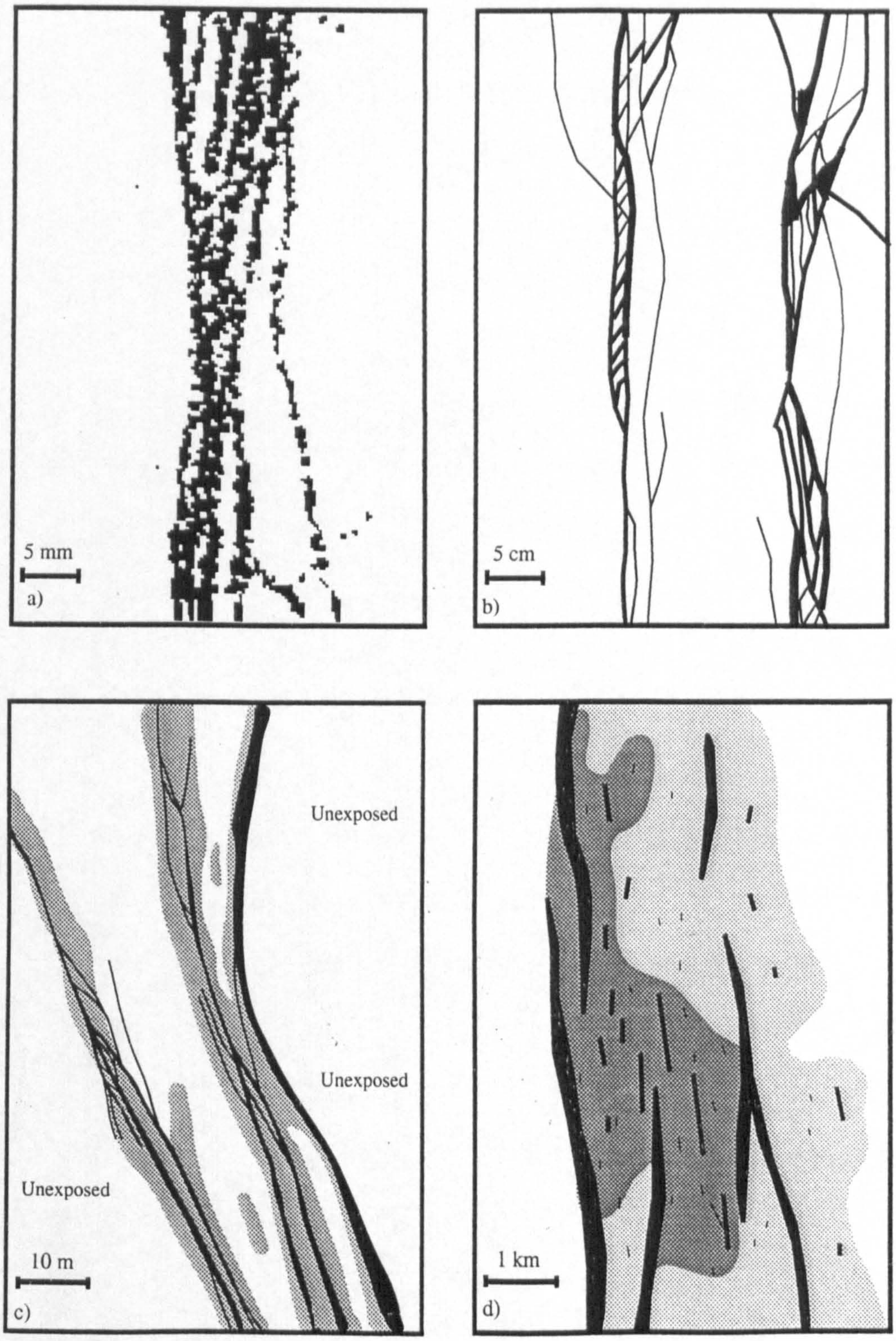

Figure 1.1. Faulting in high porosity sandstone at four scales. a) Millimetre scale CT image of a narrow zone of deformation bands from core from the North Sea. Pixel resolution in 0.2 x 0.2 mm. Image courtesy of Leslie Ball. b) Centimetre-scale field map from the Penrith Sandstone, N.E. England. c) Tens of metres scale field map from Navajo sandstone, SE Utah. Resolution for discrete faults is 10 cm thickness. The shaded regions have been inferred from 1D scan-lines, and represent areas with fault density > 5 faults / m. d) Hypothetical kilometre scale reservoir structure map.

The second fault map is one order of magnitude larger, and comes from the Penrith Sandstone at George Gill in the North of England (Figure 1.1b). Two zones of deformation bands are shown, each with a variable and complex internal morphology. Again a high frequency of splays and anastomosing strands within the zones is evident. Because of this, the overall connectivity of deformation band systems is often very high. However, both at this and the previous scale, many of the splay faults also have isolated terminations. At this larger scale, it is possible to make slightly different inferences regarding the flow through the zones. The grain scale structure is not resolved by this field map, so the petrophysical heterogeneity observed at the smaller scale is undetected, however the variable thickness of the zones is important too. If all the faults are assumed to have the same petrophysical properties, then fluid will flow preferentially through the zones where they are thinnest, as this requires less of a pressure drop across the fault.

Figure 1.1c is a fault map from the Navajo sandstone on the Moab anticline in Arches National Park, SE Utah. The 50 m x 80 m area is two orders of magnitude larger than the previous map, and contains faults ranging in width from 1 mm to 1 m. This range is too great to allow a construction of a completely scaled map, and only faults thicker than 10 cm are shown. A series of 13 scan lines perpendicular to strike have been averaged to infer the shaded regions which represent areas with over 5 bands per metre. This average (based on the number of faults) is only one of several possible representations and others are feasible: a fault density average is proportional to gouge thickness, and a strain average is proportional to fault displacements. Thus density and displacement information, as well as data appertaining to connectivity, is not represented by the average selected.

Figure 1.1d shows a hypothetical reservoir map. Such a map is drawn based on seismic interpretation, and therefore does not contain any information about sub-seismic faulting. In order to make inferences about the flow performance in this reservoir due

to faulting, faults at all scales down to Figure 1.1a need to be considered. The seismic map provides the basic framework of the reservoir faulting, and therefore must to be the initial source of sub-seismic fault modelling in reservoirs.

1.1.2 Reservoir fault data acquisition

Data availability is a vital consideration for any application designed to model faulting in reservoirs. The smallest faults which have a significance on flow may have displacements less than 1 mm. The resolution of good quality 3D seismic is in the order of 20-40 m displacement for normal or reverse faults. Faults are interpreted on seismic from the vertical displacement of strata and the faults themselves are seldom imaged. In strike-slip faults, the displacement is horizontal, not vertical, so strike-slip faults may have significantly greater displacements yet may remain undetected by seismic interpretation. Seismic is of no value in determining the petrophysical properties of faults. There are at least 4 orders of magnitude of sub-seismic fault displacement which may affect the flow behaviour of a reservoir (Figure 1.2).

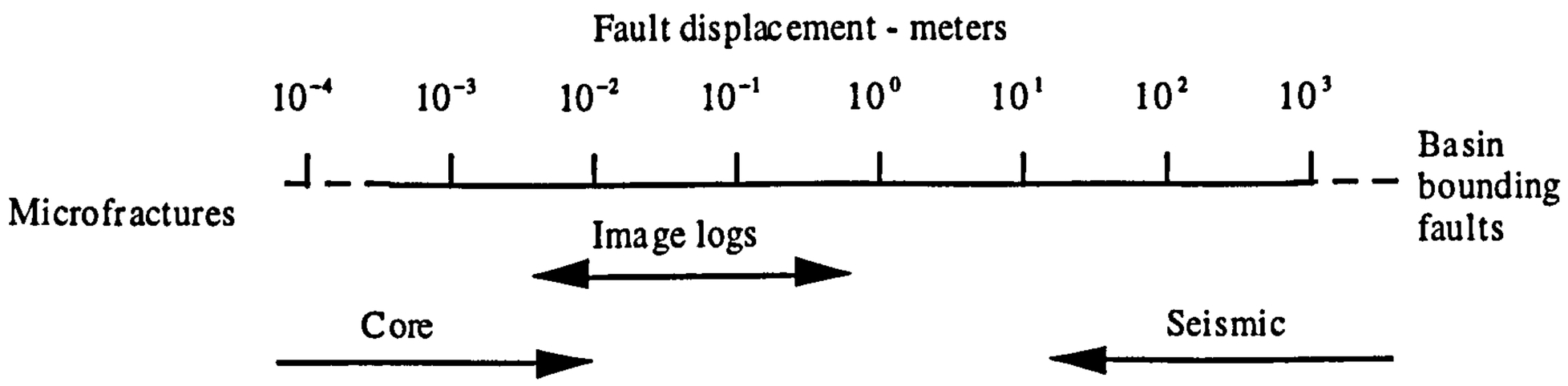

Figure 1.2. Fault displacement resolution in reservoirs.

Information about sub-seismic faulting in the reservoirs can only come from wells. Core is arguably the most important source of information, as is the only one which can yield the petrophysical properties of the faults. Core can only resolve faults with displacements less than about 1 cm. Recovery of core from fault zones with displacements larger than these is generally poor (Kulander *et al.*, 1990). Scales larger than this may be may be resolved by acoustic and electrical well-bore image logs. These may reveal information about fault density and clustering, but their use for

determining the petrophysical properties of faults is the subject of debate (e.g., Homann and Gauthier, 1995). Any petrophysical inferences are based on correlations between the character of the sonic or resistivity response and are probably only able to distinguish between conductive and non-conductive fractures. These tools may be of use for qualitative assessment of fracture types, but not for specific petrophysical determination. Each of these data sources (seismic, core, logs) gives some information about the faulting, but none present a complete picture, even at the scale at which they resolve. Therefore the use of analogue or conceptual models of fault systems is vital at all scales.

1.2 Modelling sub-seismic faulting in reservoirs

This Section considers modelling sub-seismic faulting in reservoirs. Section 1.2.1 reviews briefly geological approaches which have been used for this purpose. Section 1.2.2 discusses the incorporation of faults in reservoir flow simulation models, and shows that sub-seismic faults, which are often modelled discretely in geological models, cannot be incorporated discretely in flow models.

1.2.1 Geological approaches

Attempts to model sub-seismic faulting in reservoirs have usually had the aim of producing a more detailed map of the reservoir faulting. This map is then used for whatever application the modelling was performed for. The methods rely on stochastic placement of sub-seismic faults, although innovative methods for trying to predict the locations of seismically irresolvable faults from the curvature of structure maps (e.g., Lisle, 1994) are potentially valuable.

The stochastic methods described by Belfield (1992) and Gauthier and Lake (1993) are similar. A power-law cumulative length frequency relationship is derived from the seismic map of the reservoir. The relationship is extrapolated to a threshold length substantially smaller than seismic resolution, and this extrapolation is used to determine

the number of faults with lengths between this cut-off and seismic resolution which must be added to the map. The length and orientation of each fault is selected using a Monte Carlo process, so the final fault map (incorporating interpreted and simulated faults) forms the same length-frequency relationship down to cut-off length, and the system has an orientation rose diagram similar to the seismic faulting.

There are slight differences in the way these workers place the generated faults. Belfield (1992) splits his reservoir into four regions, predicts the number of faults in each, and then places them at random in each region. Gauthier and Lake (1993) predict the number of faults in the whole reservoir, and place them according to a probability map which is determined from a seismic fault density map. Both these methods result in placement of more sub-seismic faults in areas of higher seismic fault density.

These methods generate stochastic sub-seismic fault maps based primarily on the scaling systematics of the seismically-resolved faults. Spatial clustering of the faults is incorporated only very crudely with the two different approaches discussed in the previous paragraph. Spatial connectivity is not considered at all by Belfield, and Gauthier and Lake include a routine in their automated method which does not allow faults to intersect. As will be shown in Section 1.4.2, the spatial arrangements these methods generate are unrealistic, and the geometrical features they lack are potentially those of greatest significance for flow. Many of these features are incorporated into the modelling described by Munthe *et al.* (1994). Their method is similar to those discussed above, but specifically incorporates fault system connectivity and clustering systematics, and the resultant fault maps appear much more realistic.

The result of such modelling is a series of realisations of fault maps (2D treatments) or faulted volumes (3D treatments). These methods seldom attempt to model the entire scale-range of sub-seismic faults (over four orders of magnitude), primarily due to

doubts that the scaling relationships which describe the seismically resolved faulting may be validly extrapolated far beyond seismic resolution.

1.2.2 Incorporation of faulting into reservoir simulation models

Typical full-field reservoir simulation models are generally composed of orthogonal grid blocks of dimensions about 100 x 100 x 10 m. Faults interpreted from seismic are mapped as lines or heave polygons, in orientations which do not necessarily match the orientation of the grid-model (Figure 1.3a). Large, deterministic faults are input into reservoir simulation models at the boundaries of grid-blocks. These grid-blocks may be displaced by the faults, and the transmissibility between the grid-blocks can be modified to reflect the petrophysical properties of the fault. If the faults are large (many kilometres long), it is relatively simple to maintain the fault system geometry using the edges of the orthogonal grid-blocks (Figure 1.3b). If the faults are only a few grid-blocks long, then representing them at grid-block edges is more problematic.

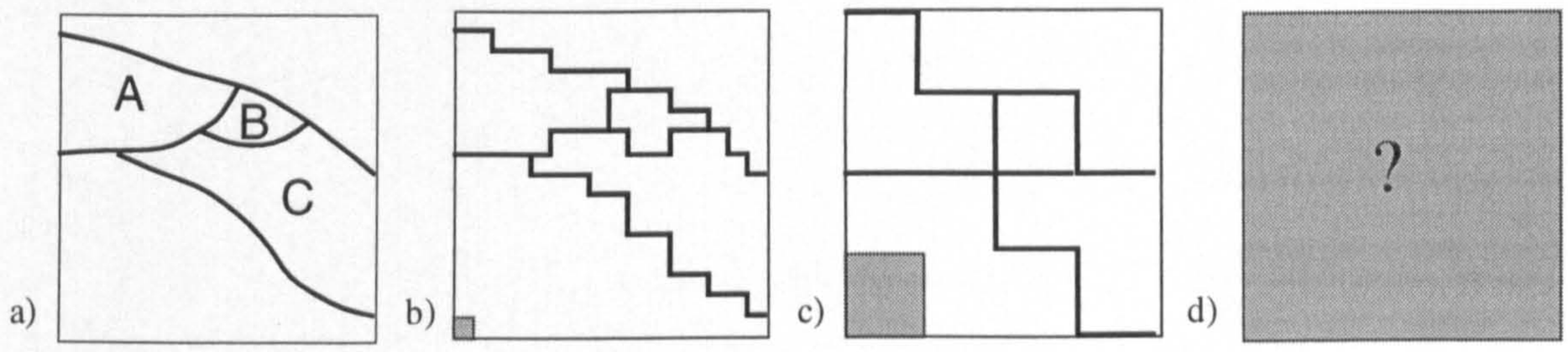

Figure 1.3. a) A portion of an hypothetical fault map applied to different levels of discretisation. b) The map is discretised to 256 grid-block, and the fault geometry may be fully reproduced. c) When discretised to 16 grid-blocks, aspects of the system geometry are lost. d) No faulting contained in a single grid-block can be represented discretely.

Consider Figure 1.3c. The smallest fault considered is about 100m long. The system drawn is the closest estimate which can be made of the fault system, using only the boundaries of the grid-blocks, however it gives a distorted picture of the reservoir. Reservoir compartments A and C no longer abut one another, and compartment B is much larger than it should be. The model at this degree of discretisation is not

representative of the faulting mapped. Either the areas of the compartments, or the topology of the system can be as close to reality as possible, but neither can be perfect and improving one is at the expense of the other. As the scale of the fault system tends towards the size of the grid-blocks, discretisation is increasingly problematic. On Figure 1.3d, the entire area is the size of a grid-block. Clearly faulting at this scale (which is approximately the scale of Figure 1.1c) cannot be represented discretely at grid-block boundaries.

The smallest seismically resolvable faults have lengths in the order of 1 km, and therefore, unless they are spaced extremely closely (< 100 m), may be incorporated at grid-block boundaries. Faults smaller than this cannot. It is fortuitous that seismic resolution and the limit for discretisation approximately coincide. It is possible, using local grid refinements, to increase the discretisation of the simulator model to incorporate faults which are modelled, but cannot be represented at grid-block boundaries. This might be desirable close to wells, where a deterministic system of sub-seismic faulting could be interpreted from core, but to attempt to manage stochastic realisations of sub-seismic faulting throughout the reservoir in this way is intractable. Instead, the faulting must be managed by modifying the grid-block properties in simulation models to incorporate the effects of sub-seismic faulting as effective flow properties, eliminating the need to actually produce sub-seismic fault maps. Determination of the effective flow properties in faulted systems is discussed in the following section.

1.3 Modelling flow through sub-seismic fault systems

Flow through a fault system is a function of the permeability structure of the system. Much of the work in this thesis is concerned with establishing models of the permeability structure of a generic system of small-scale faults in a high porosity sandstone reservoir. The permeability structure is a sum of scaling and geometrical characteristics of the fault system, as well as fault density and the fault and matrix

petrophysical properties. In Section 1.3.1, details are given of the three disparate causes for permeability impairment due to low permeability faults. In the following sections, three studies aimed at modelling flow through sealing and partially sealing faults systems are reviewed. In the first analysis (Omre *et al.*, 1994), an over-simplistic geological model limits the general applicability of the flow results. In the second analysis (Heath *et al.*, 1994), the geological model discussed is too sophisticated to be included in the simplistic flow method used. The third analysis Walsh *et al.* (in press) overcomes, to some extent, the limitations of the other two. All these studies consider single-phase flow.

1.3.1 Flow retardation mechanisms

In this thesis, two kinds of faults are discussed. If a fault is described as a *barrier*, it has zero permeability and fluid cannot flow through it. If it is a *baffle*, then it has a permeability which is lower than that of the unfaulted sandstone, but flow through the fault is possible.

In a faulted 3D volume, three distinct flow retardation mechanisms can be recognised (Figure 1.4). These are discussed with reference to the length of time it takes a tracer to travel from one edge of the model to the other, given a constant pressure drop across the system. The greater this retardation, the lower the overall permeability of the system (see Darcy's law, Section 5.1.1).

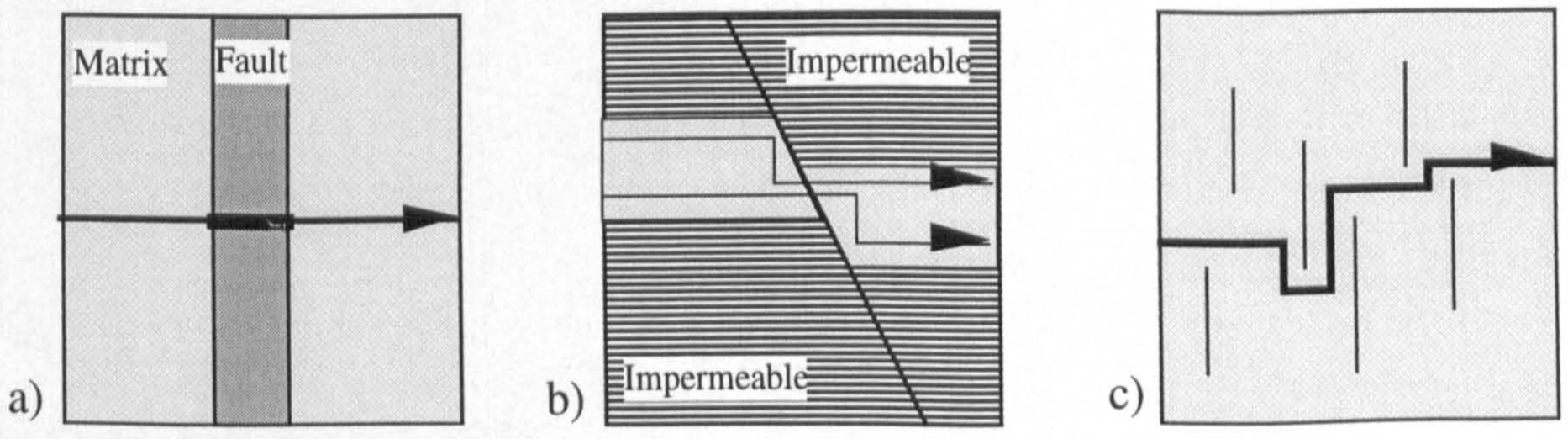

Figure 1.4. Cartoon of the three flow retardation mechanisms. a) The transmissibility effect (plan view) b) The juxtaposition effect (cross-sectional view). c) The tortuosity effect (plan view).

The *transmissibility effect* (Figure 1.4a) occurs when the tracer travels through a baffle. As the baffle has a low permeability, the tracer takes longer to pass through it than it would to travel the same distance in the unfaulted matrix. Therefore the overall travel time is longer than it would be in a completely unfaulted system. If a fault is a barrier, transmissible flow is impossible.

The *juxtaposition effect* (Figure 1.4b) also concerns flow through a baffle, but occurs due to changes in the geometry of the flow unit. If a sandstone is sandwiched between impermeable layers, then the displacement of a fault causes a narrowing of the conduit, creating a bottle-neck, and hence flow retardation. The juxtaposition effect operates even if the faults have the same permeability as the matrix.

The *tortuosity effect* (Figure 1.4c) is caused by flow around faults. In this case, the distance which the tracer travels is extended, and therefore the tracer spends longer in the system. If the faults are barriers, then the only flow mechanism possible through the system is tortuous flow.

In the following Sections, previous work in determining the flow impairment of a faulted volume is discussed with reference to these three flow mechanisms, and the influence of geometrical properties of the models.

1.3.2 Flow across a fault zone

Omre *et al.* (1994) were essentially concerned with assigning effective properties to relatively large (10-100m displacement) fault zones in a reservoir layered on a comparable scale. Their models are based on the recognition that faults which might be resolved by seismic as discrete structures are often composed of distinct fault strands forming a fault zone (Figure 1.5). The effective permeability of the zone is calculated as a function of three parameters which are deemed to be of critical significance;

A) the total displacement of the zone,

B) the total number of faults in the zone, and

C) the permeability of the individual faults.

All three retardation mechanisms identified above are active in these models. As either the total displacement, or the number of faults in the zone increases, juxtaposition of high permeability reservoir against impermeable layers increases, with a corresponding decrease in effective permeability. Similarly, as the number of faults in the zone decreases, or the permeability of them increases, so does the overall transmissibility of the system. As fault permeabilities decrease, the tortuosity effect becomes more important.

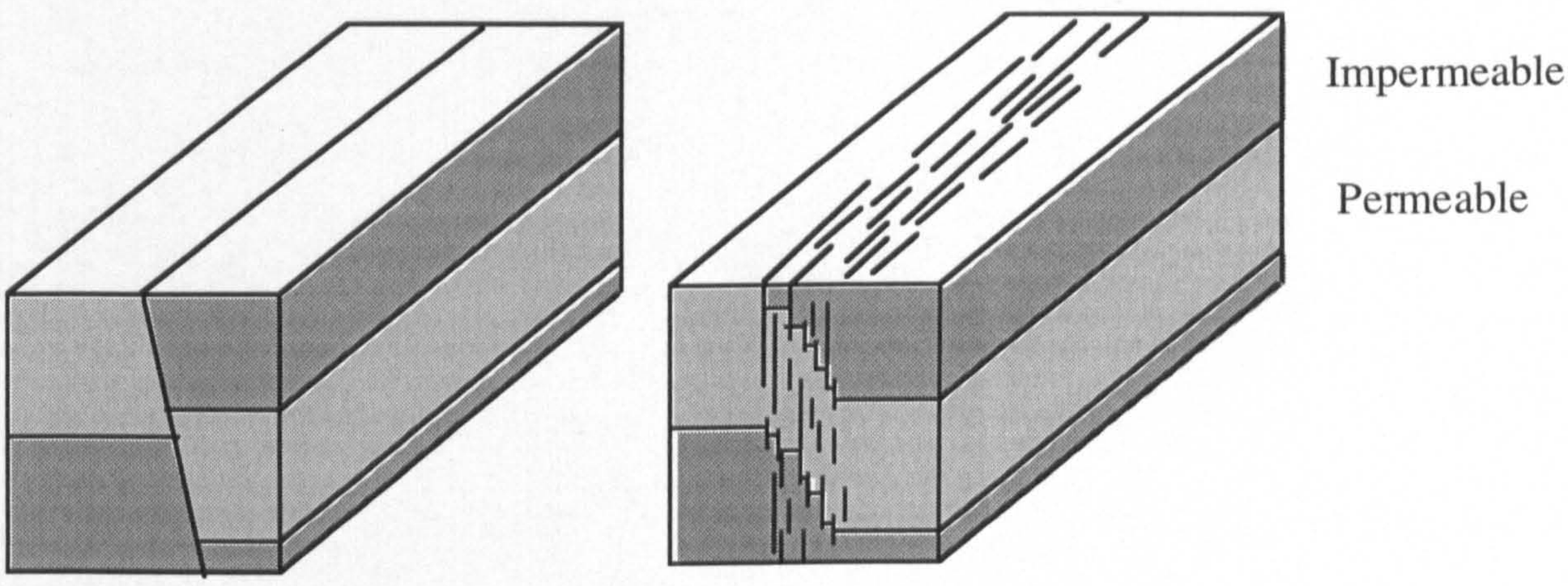

Figure 1.5. The system considered by Omre *et al.* (1994). a) A fault resolved by seismic as a single structure displacing a layered reservoir / non reservoir sequence. b) Model of the system. The displacement is represented by a variable number of individual faults in a zone, whose cumulative displacement is that of the seismically-resolvable fault. The fault zone and all the faults contained in it are modelled vertically.

Omre *et al.* (1994) recognise that varying the orientations of individual faults results in the potential for faults to become connected and the reservoir more compartmentalised, but consider that connectivity and compartmentalisation are only significant for zero-transmissibility faults (barriers). They consider that the effect of connectivity in 2D is low, but do not explain why they reach this conclusion. In models of this kind, fault connectivity is a function of the width of the fault zone as well as the number, sizes and orientations of the faults in the zone, but the width of the zone is held constant in all

their models, as is the fault size. Omre *et al.* consider that the probability of connectivity in 3D is lower than in 2D. This is correct for random systems of planes, but might not be correct for real fault zones, which are often connected in both plan and cross-section (e.g., Arboleya and Engelder, 1995; Antonellini and Aydin, 1995; Cartwright *et al.*, 1996).

The work of Omre *et al.* (1994) is a contribution towards estimation of the effective permeability of a fault zone. It is only of relevance to a single fault zone, and although faults are assigned discrete permeabilities, fault connectivity is given only cursory attention. The models are therefore of most value in determining the significance of the juxtaposition effect. The models are built based on the conjecture that only three parameters are critical, and as a consequence are not sufficiently flexible to rigorously determine the sensitivity of other parameters.

1.3.3 Flow around a system of parallel barriers

The flow modelling performed by Heath *et al.* (1994) is much less complex that of Omre *et al.*, and is mainly concerned with applying a simulation method. The models contain impermeable barriers which are all parallel and vertical, and effective permeability is calculated perpendicular to the faulting. The only effect which is modelled is the effect of tortuosity around sealing faults, varying as a function of fault density and fault length distribution.

Faults are modelled with a variety of length-distributions over one order of magnitude length. The longer faults in any system are found to have a disproportionately greater effect than the shorter ones, and analytical solutions for effective permeability based on fault density and lengths are presented. This variability is one which Omre *et al.* deemed insignificant, and indeed Heath *et al.* consider it subordinate to other parameters. The effects of fault connectivity and orientation are not considered, as the simulation technique (the statistical streamline method, discussed further in Section 5.3)

is not sufficiently flexible to determine the permeability of non-parallel systems or systems with non-zero fault permeabilities. Therefore, although Heath *et al.* discuss more realistic fault systems than Omre *et al.*, less complexity is actually included in their flow analysis.

1.3.4 Flow through a system of baffles

The conceptual models discussed by Heath *et al.* (1994) are applied to flow simulation rather more successfully by Walsh *et al.* (in press). This work uses a more conventional finite difference flow simulator, and incorporates effects of juxtaposition, transmissibility and tortuosity. Faults are modelled in a layer-cake 3D volume based on the Brent sequence with realistic elliptical displacement geometries with maximum displacements between 2 and 20 m. Like Omre *et al.*, most of the modelling is done with parallel faults. Fault density and the fault / matrix permeability contrast are found to be the most important variables and fault clustering is shown to be insignificant. The juxtaposition effect can be isolated by assigning the same permeability to both the faults and the matrix. This shows that the juxtaposition effect is relatively insignificant, compared to the other two mechanisms.

Although most of the modelling is done with parallel faults, some of *Walsh et al.*'s models have faults with variable orientations (Figure 1.6). The effect of fault orientation itself is not significant to the flow results. However, allowing orientation variability increases the connectivity of the system. The models in Figure 1.6b and 1.6c were generated from the same system of parallel faults perpendicular to flow direction, but the greater orientation variability in Figures 1.6c produces a continuous fault baffle, which is not present in the more parallel system in Figure 1.6b. Walsh *et al.* recognise that fault connectivity is likely to be significant, especially at low fault permeability.

The flow results presented for these fault orientation cases do not vary significantly

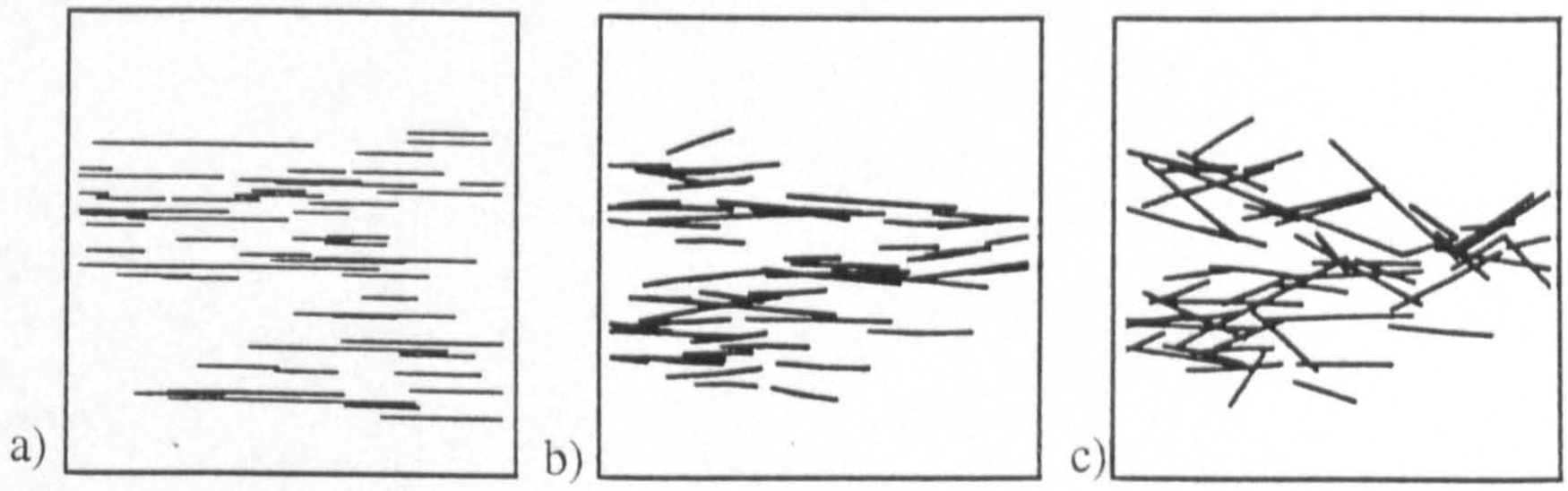

Figure 1.6. Three of the systems from Walsh *et al.* (In press). All have moderate fault density and moderate clustering. a) Parallel faults. Fault strikes dispersed from parallel by up to b) 5°, and c) 20°.

from the parallel cases, but this may be an effect of modelling limitations, specifically an effect of representing the faults as transmissibility factors rather than as discrete thicknesses of a particular permeability. If a fault is represented as a transmissibility factor between two grid-blocks, this has the effect of assigning the low permeability to the entire up-stream grid-block. For the parallel fault systems, this is overcome by decreasing the transmissibility factor by a scaling factor in order to reduce the effective fault thickness. This works for parallel faults as the system geometry can be represented by orthogonal grid-blocks. Non-parallel systems cannot be represented by orthogonal grid-blocks, and it is unclear how this thickness scaling was modified for these systems in which grid-blocks are of different sizes and shapes. A single transmissibility factor is inappropriate, as the downstream block thickness must vary throughout the model (Figure 1.7).

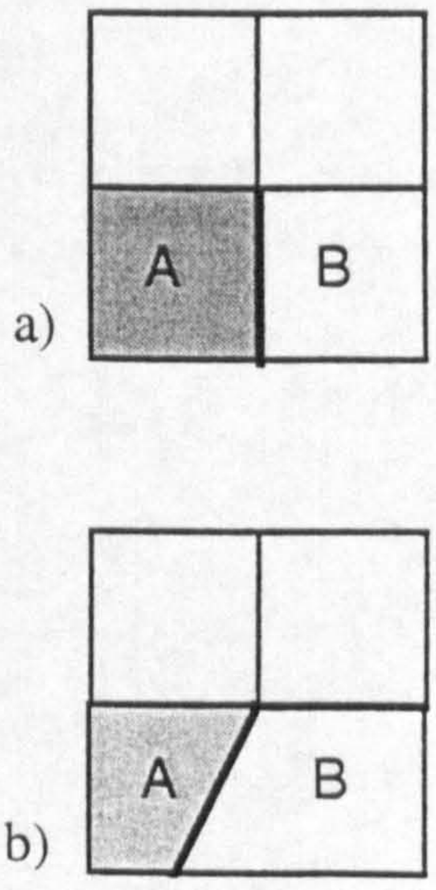

Figure 1.7 A transmissibility factor assigned to the fault (bold line) is effectively assigned to the whole downstream grid-block (flow direction is left to right). In an orthogonal system (a), the thickness of the fault is modelled by modifying the transmissibility factor. This is impossible in non-orthogonal systems (b) as a single transmissibility factor results in variable fault thickness. A transmissibility factor assigned to the fault in (b) results in different fault thickness if flow direction is right to left, as the mean thickness of blocks A and B block is different.

1.3.5 Discussion

Unsurprisingly, all three teams found that the variables which had the greatest impact on the system permeability are the number, and permeability, of the faults. Walsh *et al.* (in press) studied the effect of clustering, and found it to be insignificant. This is because it affects none of the three retardation mechanisms. Consider Figure 1.8. The systems in Figure 1.8a and b have the same number of faults, but faults are clustered in 1.8b. The two continuous lines on these figures represent the flow paths of particles for which retardation is caused entirely via either the transmissibility or the tortuosity effect. The number of baffles encountered during the former mechanism is the same in both models, as is the length of the flow path for tortuous flow. Therefore the permeability of each model is the same.

Omre *et al.* (1994) and Walsh *et al.* (in press) made only a cursory study of varying fault orientation. Fault orientation has a much more complicated effect on transmissibility and tortuosity than is immediately obvious. Consider Figure 1.8c.

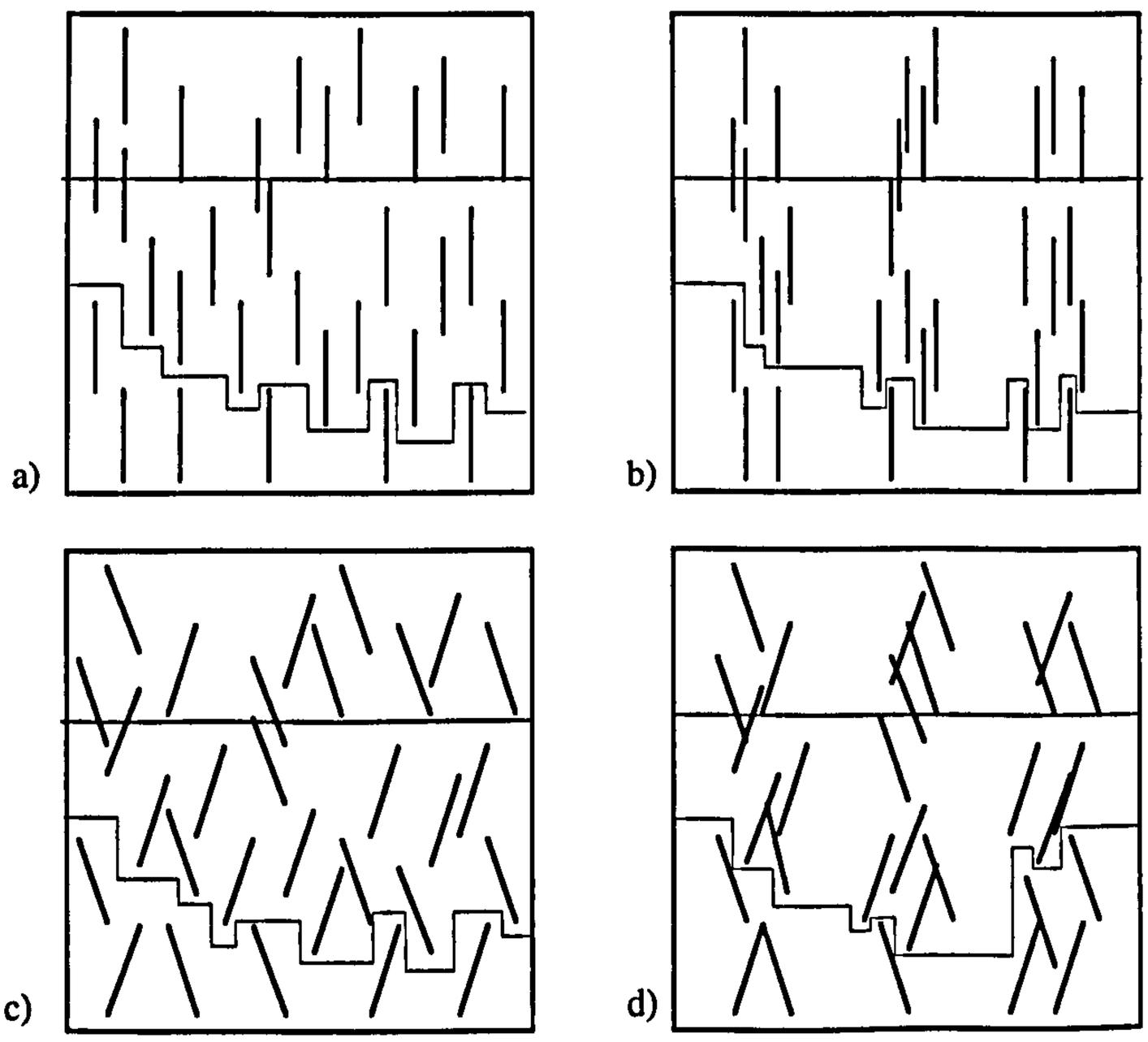

Figure 1.8. Cartoon demonstrating the effect of fault clustering, orientation and connectivity on the transmissibility (upper line) and tortuosity (lower line) effects. a) Parallel, unclustered faults. b) Parallel clustered faults. c) Non-parallel, unclustered faults. d) Non-parallel, clustered faults.

This system is the same as Figure 1.8a, except that each fault is now assigned to one of two orientation populations. This transformation allows the potential for faults to become connected, although in this example they are not. Nonetheless, both the transmissibility and the tortuosity of the system are modified with respect to Figure 1.8a. The transmissibility effect is decreased because any random flow path will encounter fewer faults, yet flow through each fault will still be perpendicular to fault strike. The tortuosity effect is decreased, as the flow path is extended by a slightly shorter amount on encountering each fault. Therefore the overall permeability of this system is greater.

The same transformation on the clustered model (Figure 1.8b) produces Figure 1.8d. In this case, many faults are connected. Owing to this, the tortuosity effect in this system is greater than in any other illustrated. The transmissibility effect is the same as in Figure 1.8c. Figure 1.8d, therefore, has a lower transmissibility effect, but a higher tortuosity effect , than Figure 1.8a.

It is clear from these simple examples that changes in the spatial distributions of the faults can affect the flow response of a system in a complex manner. No geological considerations have been made in the construction of Figure 1.8, and discussion has been based upon purely geometrical effects. In Chapter 3, the geometrical arrangements of fault systems are considered, and a new method to deal with fault connectivity in a quantitative manner is developed. This allows the inclusion of connectivity as a parameter in the flow simulation modelling (Chapter 5). In previous modelling, connectivity has entered the models as a consequence of orientation and clustering variability, in an unpredictable and unrealistic way. By modelling as a function of orientation and connectivity, rather than as a function of orientation and clustering, the flow models presented herein have a much more realistic geometrical arrangement. Connectivity, not clustering, is a control of effective permeability. For parallel faults, clustering has no effect at all (Figure 1.8a and b). If the faults have

variable orientation, clustering affects the flow response, but only as a consequence of changing the connectivity of the system (Figures 1.8c and d). Orientation, however, does have an effect in its own right (Figure 1.8a and c).

Determining the permeability of 2D systems of the kind illustrated on Figure 1.8 is the subject of Chapter 5. The discussion above has considered the transmissibility and tortuosity effects as quite distinct processes; in reality, both mechanisms operate simultaneously. The relative significance of each, in any model, depends on details of the system geometry, and on the permeability of the faults. Consideration of both separately, however, allows great insight in the flow responses of systems. In Chapter 5, analytical manipulations of geometrical properties are coupled with flow simulation results to characterise flow impairment as a function of terms representing transmissibility, tortuosity and orientation. This allows the determination of the effective permeability of systems as a function of fault density, the matrix permeability, and the length, thickness, permeability and orientation of the faults. The systems have connectivities representative of the fault density considered. Clustering is not considered to be a control on effective permeability in its own right, although it is possible to imagine extreme cases of clustering causing bottle neck effects for tortuous flow. It will be shown in Chapter 7 that clustering is an important variable in two phase flow.

1.3.6 Section Summary

There are three flow mechanisms which combine to reduce the permeability of a faulted volume. These are transmissibility, juxtaposition, and tortuosity effects. The relative contribution to flow impairment of each in any volume depends on details of the geometries and permeabilities present in the volume. The only three public domain studies (of which I'm aware) which try to determine the effective flow properties of sealing or partially sealing fault systems have been discussed.

The main conclusions drawn from these studies are:

A) The most important fault system variables modelled are the number, and permeability, of the faults.

B) The juxtaposition effect is insignificant relative to the other two.

C) Fault clustering is not an important geometrical variable.

D) Realistic fault densities may have a significant effect on system permeability reduction if the faults have permeabilities at least two orders of magnitude lower than the sandstone.

The main limitation of these studies are:

A) Faulting is only considered at a single length-scale (Omre *et al.*, 1994) or a single order of magnitude length-scale (Heath *et al.*, 1994; Walsh *et al.*, in press). At least four orders of magnitude of sub-seismic faults are likely to be significant to flow.

B) Fault connectivity is given only cursory attention, yet both high and low connectivity is a feature of real fault systems. Connectivity has been shown to be of great significant in the flow performance of other systems (e.g., low permeability shale connectivity; Deutsch, 1989), and is therefore likely to be more significant in fault systems than these studies have intimated.

C) All flow modelling has considered only single phase effective permeability determination.

The relative interactions of orientation, clustering and connectivity have been discussed with reference to the tortuosity and transmissibility effects. Reasons have been given for the dismissal of clustering from models in favour of connectivity. This is discussed further in Chapter 3. The approach to determining effective permeability as a function of quantitative fault system variables adopted in Chapter 5 has been introduced. Like previous workers, only single phase flow is considered.

1.4 Integrating fault modelling and flow modelling

The previous section highlighted the difficulties in reconciling complex geological models of sub-seismic fault systems with flow simulation. A compromise is required between modelling fault systems as realistically as possible, and the practical application for which the models are designed. Two problems in particular dog advances in this field: how to honour the geometrical arrangements of fault systems, and how to incorporate multiple scales of faulting. The overall scheme developed in this thesis is discussed below. This involves consideration of four inter-related aspects of fault systems: strain, scaling, geometry and petrophysical properties.

1.4.1 The geopseudo method

The petroleum industry relies on finite difference flow simulators in which permeability structure is incorporated as a discrete grid (in this work, the commercial Eclipse 100 simulator is used). It is impossible to represent any great degree of geometrical complexity in a single simulation run, as the number of grid-blocks is limited by computational capacity. For the same reason, it is impossible to treat faulting at a variety of length-scales simultaneously. Nonetheless, in any faulted reservoir, over four orders of magnitude of sub-seismic faulting exist, and these faults have complex geometrical characteristics.

The approach adopted in the present work is to produce simple models at a single scale which include the salient geometrical features of the fault system at that scale, and to

determine the effect on flow of this system. The effects of the faulting at smaller scales define the properties of the unfaulted regions at this scale, and the combined properties at this scale define the unfaulted regions at the larger scale. Eventually, the effects of all sub-seismic scales are represented as a single set of effective flow properties, which may then be incorporated in a full-field reservoir simulation model.

This approach, termed the *geopseudo method* (Corbett, 1993), has been used to determine the effective flow properties of clastic reservoirs (e.g., Corbett, 1993; Ciammetti *et al.*, 1995; Sylvester *et al.*, 1996). Such work has used the natural scale transitions widely believed to occur in sedimentary sequences as the scales at which the flow models are calculated. These scale transitions are the stratal elements of the system: laminae, laminasets, beds, bedsets and parasequences (e.g., Van Wagoner *et al.*, 1990). If a system exhibits natural scale separations, it can be described as a *discrete hierarchy* (Cushman, 1990). In a fault system, there appear to be no natural separations of scales (e.g., Scholz, 1990), and so fault systems form *continuous hierarchies*. In order to determine the flow characteristics of a fault system it must be transformed analytically into a discrete hierarchy. The robustness of this transformation is of great importance if the flow results are to adequately represent the fault model, and relies on the scaling characteristics of the fault population.

In addition to the type of hierarchy the systems form, there is another important issue in which modelling faulted or sedimentary media for flow analysis differ. At any position in a reservoir, a particular lithofacies is always present. The non-trivial problem of the sedimentological modeller is to determine which lithofacies are present where. Faulting is not uniformly distributed throughout reservoirs, and there may be large portions of reservoirs which are unfaulted. The fault modeller must determine how much faulting, if any, is present in any portion of the reservoir. This requires a model of fault density, or strain, distribution throughout the reservoir.

Based on knowledge of the scaling characteristics of the system, and on the fault density at any portion of the reservoir, fault system parameters at each scale within the discrete hierarchy may be determined. These parameters are then combined to determine the effective permeability of the system at each scale in the hierarchy, as discussed in Section 1.3.5.

These various aspects of modelling faulting and flow in fault systems are illustrated on Figure 1.9. The conceptual geological model comprises four inter-related aspects, each of which must be considered in a determination of the flow in a sub-seismic fault system.

A) *Strain* determines the quantity of faulting within any portion of the reservoir.

B) *Geometry* describes the spatial arrangement of the faulting at all scales.

C) *Scaling* describes the distribution of strain between faults of various length-scales.

D) *Petrophysics* determine the relevant properties of the faults at each scale.

1.4.2 Fault clustering and connectivity

Fault clusters contain spatially related faults of various sizes. That small faults cluster around larger ones is a well documented but poorly understood geological paradigm (e.g., Jamison and Stearns, 1982; Gillespie *et al.*, 1993). Clustering involves many aspect of fault systems which are usually considered independently; strain, scaling and geometry, and this is why it is such a problematic aspect of a fault system to characterise.

Gauthier and Lake (1993) recognised that although their fault placement rules produced fault clusters, these clusters formed only around seismically resolved faults, and no independent clusters of sub-seismic faults were produced. As Westaway (1992) remarked, there is no reason why most of the faulting in a reservoir should not comprise of sub-seismic clusters, especially when strain is low. A certain proportion of the smaller faults will not be spatially associated with a large faults, as they will form

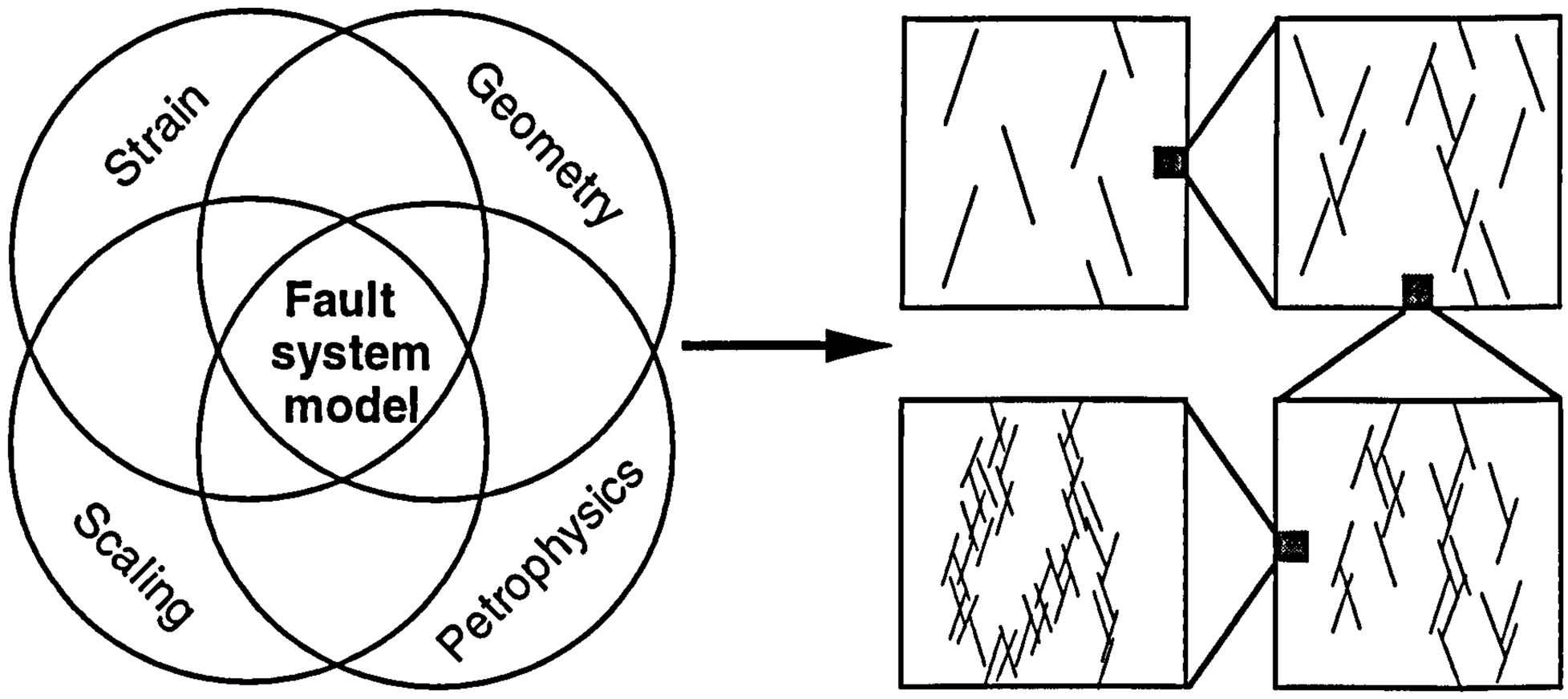

Figure 1.9 Transformation of the conceptual to the mathematical fault model. The conceptual model is a function of four interrelated aspects. For the determination of the effective flow properties, the system is represented as a discrete hierarchy, and representative systems constructed at each scaling in the hierarchy. Note that in this cartoon, as the length-scale decreases, the number of faults in an area increases and the faults become relatively smaller. This is controlled by the scaling characteristics of the mathematical model. Also the faults become more clustered and connected. This is governed by the geometrical characteristics.

clusters at their own length-scale. Determining the proportion of faults at any length-scale which are clustered around the faults at the larger length-scale is an unresolved problem. Attempts must be made to deal with it, however, otherwise areas which contain no large faults will be modelled as containing no small faults either. Understanding rock deformation processes in terms of self-organised chaotic processes (e.g., Bak and Tang, 1989; Sornette *et al.*, 1990; Hobbs, 1993) must eventually make it possible to formalise mathematically, based on geophysical theory, the assumptions needed to produce both seismic and sub-seismic fault clusters. To date, however, clustering can only be incorporated in reservoir fault models based on geometrical, rather than geophysical modelling criteria (e.g., Munthe *et al.*, 1994).

The second problem with the modelling of Belfield (1992) and Gauthier and Lake (1994) is specifically a geometrical one. If faults are placed randomly, the resultant fault patterns will not be realistic, either in terms of clustering or connectivity. Fault

system geometry at a single length-scale is summarised conceptually on Figure 1.10. No particular scale is implied in these cartoons, as self-similarity is assumed. The four maps have an identical number of faults of all lengths, and the only differences are the relative positions of the faults. Using the terminology of La Pointe and Hudson (1985), clustering is considered in terms of fault system heterogeneity. A heterogeneous system is highly clustered, while in an homogeneous system the faults are distributed evenly throughout the area.

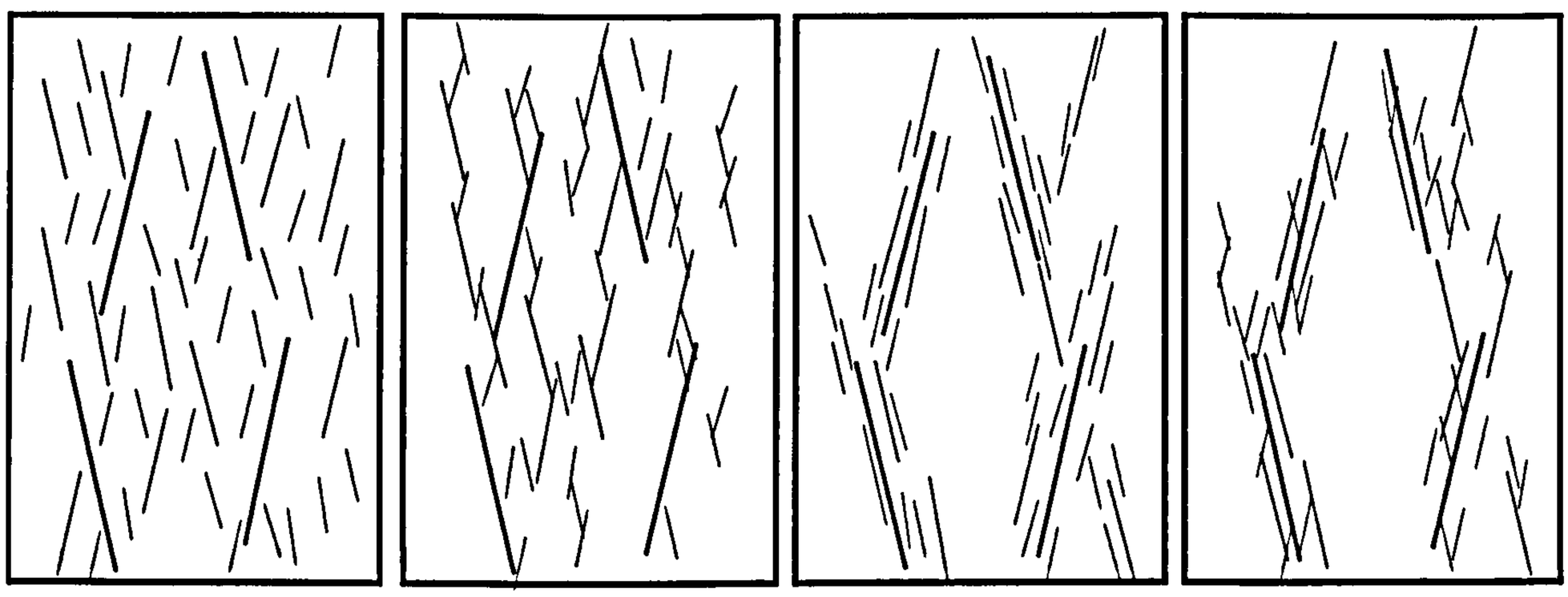

a) Disconnected, Homogeneous

b) Connected, Homogeneous

c) Disconnected, Heterogeneous

d) Connected, Heterogeneous

Figure 1.10 Conceptual end-member maps of fault clustering and connectivity.

This is the issue where the modelling of Munthe *et al.* (1994) is much more realistic than that of Belfield (1992) and Gauthier and Lake (1993). The modelling method of Munthe *et al.* specifically incorporates clustering and connectivity characteristics, and the systems produced are connected, heterogeneous ones (Figure 1.10d). The systems produced by Belfield are homogeneously clustered, and the random fault placement tends to produce a disconnected case. Belfield's systems are therefore similar to Figure 1.10a. Gauthier and Lake incorporate clustering rather more pragmatically than Belfield, but their systems are entirely disconnected by design, lying somewhere between those in Figure 1.10a and 1.10c. As a qualitative judgement, faults systems in porous sandstones appear to be well connected, but of varying heterogeneity (i.e., they lie between 1.8b and 1.8d).

Clustering and connectivity are intrinsic properties of fault systems which are poorly understood and seldom incorporated in fault system models applied to flow. Both are potentially significant to flow calculations and therefore their incorporation is important. As discussed in Section 1.3.5, fault clustering is omitted from the general discussion in this thesis. This is partly because there is no method available to quantitatively model it, and party because it need not necessarily have an influence on single phase flow, *provided that the indirect effects of clustering are captured in some other way* (Figure 1.8). These effects are incorporated via a quantitative fault connectivity term.

Fault connectivity is much more significant to flow than previous workers have intimated. The connectivity of a fault system is considered in terms of fault terminations and intersections. A fault can terminate as either an isolated fault tip (an I node) or as a splay off, or termination against, another fault (Y nodes). Additionally, faults can intersect one another (X nodes). The proportions of these node types present in any fault system can be expressed by a point on a ternary diagram (Figure 1.11). Depending on the fault termination proportions present, and irrespective of the fault density, flow in a system can be characterised as a tortuosity problem (flow around faults) or a transmissibility problem (flow must pass through faults). As the permeability of the faults relative to the matrix decreases, the flow response becomes

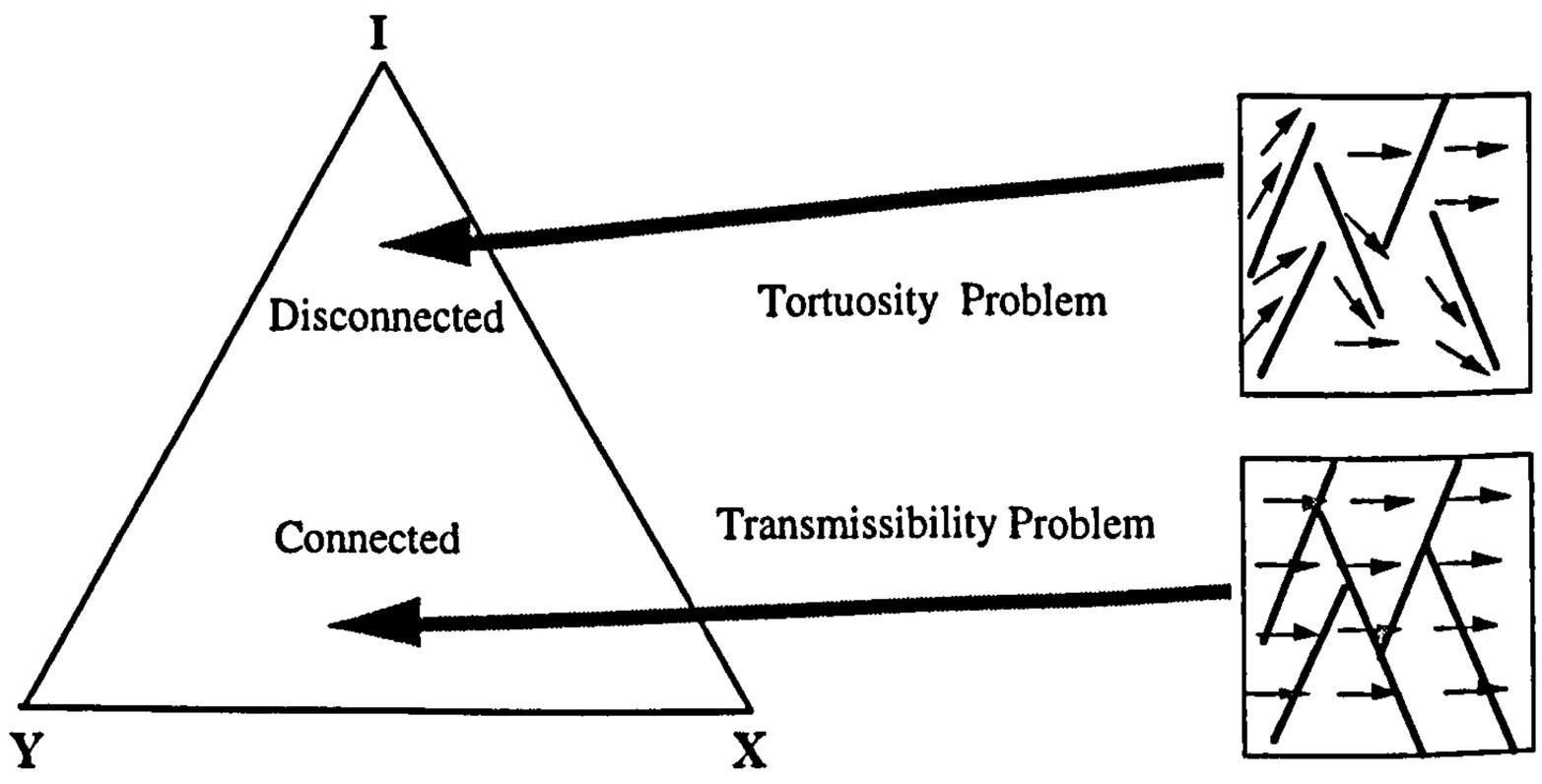

Figure 1.11. Fault connectivity is a critical determinant on the paths that may be exploited by flow.

increasingly sensitive to these mechanisms. The modelling reviewed in Section 1.2.3. is only applicable to disconnected systems and is not representative of compartmentalised reservoirs.

1.4.3 Fault system analysis using fractal methods

The basic model of normal faulting in sedimentary basins currently in vogue is the *soft-domino model*, conceptualised by Walsh and Watterson (1991). This model derives from the recognition that strain in a rock-mass is accommodated by brittle fracturing (faulting) and by strain which can be considered ductile at the scale under consideration. At successively smaller scales of investigation, much of this ductile strain is accommodated as discrete faults; however, these faults are too small to be regarded discretely at the larger scale. This model implicitly assumes that some aspects of fault systems are geometrically self-similar over some length-scales. In systems recognised to contain faults spanning several orders of magnitude length-scale, the relationships between fault system scaling and fault system geometry are intimately linked. Recently, attempts to reproduce fault system characteristics based on fractal methods have been proposed (e.g., Hewett, 1994).

Fractal systems may form either discrete or continuous hierarchies. Among the most cited numerical fractals, examples of both are easily found. The von Koch snowflake and Cantor dust are both discrete hierarchies, while Julia sets or the Mandelbrot set are continuous hierarchies (e.g. Barnsley, 1988). Gillespie *et al.* (1993) have suggested that while fault systems form continuous hierarchies, joint system often show characteristics of discrete hierarchies. Fractals may be both self-similar or self-affine. A formal definition of these two types of fractals in 2D space is given by Turcotte (1992) as follows: If $f(rx, ry)$ is statistically similar to $f(x, y)$ (where r is a scaling factor), then the fractal is self-similar , and if $f(rx, r^H y)$ is statistically similar to $f(x, y)$, then the fractal is self-affine. H is known as the Hausdorff measure. More simply,

self-affine fractals experience a co-ordinate transformation at different scales, and must be characterised by both a fractal dimension and a Hausdorff measure.

The recognition that fault systems may be, in the loosest sense, fractal, is not a new idea (e.g., Tchalenko, 1970), but it is only recently that attempts have been made to formalise this analytically. Kakimi (1980) presented the first plots of frequency vs. displacement for 2D samples of faults in Japan, and related these to the Guttenberg-Richter formula of magnitude / frequency of earthquakes (Guttenberg and Richter, 1944). Later, 1D versions of this relationship were taken to imply that fault systems are self-similar (e.g., Childs *et al.*, 1990; Heffer and Bevan, 1990), and the power-law gradient of the relationship was widely reported as the fractal dimension of the fault system. A fault system is composed of many relationships which may show power-law scaling: displacement frequency, length frequency, thickness frequency, each with their own power-law gradient. Unless these relationships have identical power-law gradients, none of them is the fractal dimension of the system, and the system must be characterised as a function of each scaling relationship. Some of these relationships are examined for fault systems at outcrop in Section 2.4.

While considerable work has shown that 1D or 2D samples of fault systems obey frequency power-law scaling relationships, determination of a fractal spatial distribution of faults has been less successful. Box-counting has been used widely to argue that systems are fractal (e.g., Barton and Larsen, 1985; Hirata, 1989), however there may be problems with these analyses. Walsh and Watterson (1993) revisited one of the most cited examples of 2D fractal fault distributions (Barton and Larsen, 1985). Through rigorous box counting of this dataset they show it to be either non-fractal, or that box counting is not a sufficiently robust technique for fractal analysis of fault patterns. Gillespie *et al.* (1993) synthesised fracture systems in both one and two dimensions according to fractal rules. Upon conventional analysis of the 2D system (the Sierpinski carpet), they found it to barely conform to the very rules which had been

used to generate it. This system must be fractal, but the techniques available to analyse it are not sufficiently sensitive to reflect this. It is easy to imagine fault systems as fractals, which involves a degree of conceptualisation (conscious or subconscious), but it is harder to analyse, and harder still to parameterise them.

Voss and Wyatt (1993) combined analytical techniques with cognitive science approaches in a multifractal analysis of the character of ancient Chinese landscape paintings. They reached the conclusion that:

> *"The human perceptual system evolved over millions of years in a natural fractal environment. Only recently, by evolutionary time scales, have we found ourselves in a primarily Euclidean environment of straight lines and few spatial variables. Our visual system shows a particular response to random fractals. Nevertheless, it has proven extremely difficult to quantitatively mimic with fractal analysis the classification and feature detection that the eye performs with ease."*

Therefore, while recognising that fault systems are fractal in the loosest sense, it is unlikely that their spatial distribution can be sufficiently-well characterised for fractal approaches to their modelling to be successful. This also implies that the best method for determining whether a numerically generated fault map is realistic might be to see if it looks right, rather than by numerical analysis.

Fractal analysis of scaling information is relatively robust, and is a useful method of modelling the scaling characteristics of fault systems. Fractal analysis of the spatial distributions of faults in a fault system is not. Even if box-counting methods were to unequivocally show a good relationship for a particular fault pattern, there is no consensus as to what the derived "fractal dimension" refers to. Less pragmatic methods are probably more useful in characterising the spatial distributions of faults.

If a single fractal dimension is determined for a fault system, the only thing this dimension relates to is the amount of space the fractal object (in this case a fault system)

occupies. A fractal dimension contains no information about the spatial arrangement of the individual faults within the fractal system. Two fractal objects with identical fractal dimensions may have different clustering and connectivity characteristics. Therefore any method used to generate fault systems using fractal methods must contain conceptualisations about the geometrical arrangements of the faults, as these criteria are not, in any way, incorporated in the fractal description of the system *per se*. The geometrical characteristics of any fault map, whether it is fractal or not, need to be validated against the properties of the system which is being reproduced. The fact that the system is fractal simply makes this harder to do, as the system contains faults over a range of length-scales, all of which cannot be represented on the same map (e.g., Yielding *et al.*, 1996). This is discussed in the following Section. Many of the issues which have been discussed in general terms in this Section, are readdressed with reference to a single, well characterised fault outcrop map in Chapter 3.

1.4.4 Geometrical fault system generation and analysis

The significance of modelling fractal systems is important to the concept of *representative elementary volume* (REV). In a fractal system, there is no REV (e.g., de Marsily, 1985), however the transformation of fault systems to a discrete hierarchy allows scale-specific REVs to be inferred, and these are what the methods used in this work rely on. By considering each length-scale in isolation, an area containing sufficient faults to approximate the REV can be determined. The size of the REV changes at each length-scale, and it also changes at a single length-scale as a function of fault clustering. Different modelling implications of assuming REVs are discussed in Sections 4.1.2 and 5.1.2.

Because the REV changes at each length-scale, it is impossible to construct a single map which adequately represents more than a small range of fault length-scales. Therefore a conceptual model of fault system scaling must be implicitly assumed when a map such as Figure 1.1c is used as a basis for either interpretation of fault system geometry or for

flow analysis. Geometrical analysis can be rigorously undertaken, from a single map, only between certain length-scales. Faults which are too big cannot be treated, as they are either too few to be representative, or they are longer than the map, and only a portion of them is shown. Only faults in a central scaling region are adequately represented by any scale of map, and inferences about fault system geometry are only relevant to structures of this scale. This is true of any map, and is possibly a reason why box-counting of mapped faults has proved unsuccessful. Consider the fault maps in Figure 1.1. Only a few of the bands on Figure 1.1a terminate in the map. Therefore the map is only of value for analysing the pore scale. Figure 1.1b contains two zones of bands, both which pass entirely through the map. This map is therefore only of use in assessing the internal morphology of the zones. Both pore scale structure, and structure at the scale of the zones is unresolved.

Consider Figure 1.12. This shows a cartoon fault map similar to those in Figure 1.1. Figure 1.12a shows the whole map, with areas of high density of faults which are below the resolution of the map shaded. Figure 1.12b shows only the faults which are explicitly and entirely mapped. The map no longer looks like a realistic fault map, because it only contains faults of a single length-scale. Notwithstanding this, it highlights the only faults which are adequately sampled for geometrical analysis of the map to be meaningful. Figure 1.12c shows only the faults which are too large to have been included on Figure 1.12b, and all smaller faulting is represented by the shaded area. While it is possible to infer the shaded regions on Figure 1.12c from the large faults, it is impossible to predict the exact locations of the faults in Figure 1.12b. Therefore sub-seismic fault modelling must be intrinsically stochastic, but must also honour the geometrical characteristics of the fault system (connectivity and clustering) at the smaller scale.

Fault connectivity is considered in terms of the numbers of intersections and splays present in the system at any scale. The fault model will give an accurate representation

of the true faulting only if the connectivity characteristics shown by the faults in Figure 1.12a are reproduced by the mathematical model which stochastically generates irresolvable faults from Figure 1.12c. The faults in Figure 1.12a are clearly more connected than those in Figure 1.12b, and this is because most of the smaller faults splay off the larger ones. Therefore, there are two connectivity issues which need to be honoured. First, is the proportion of faults in a cluster which intersect or splay off the faults of the larger length-scale. Second is the number of faults which intersect or splay from faults of the length-scale being modelled.

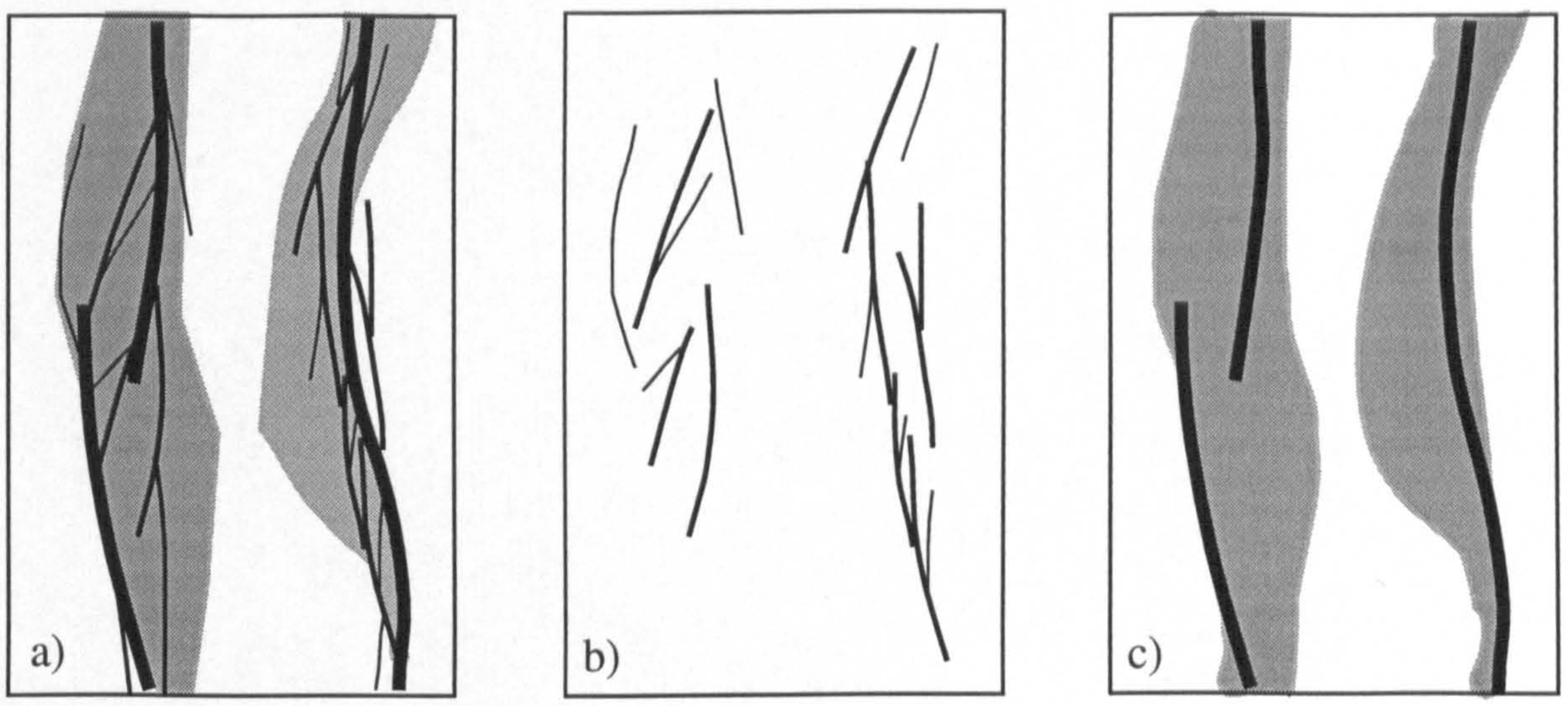

Figure 1.12 a) Cartoon of a fault map (no scale implied) Faults below map resolution in shaded regions. b) Faulting for which the map is representative. c) "Large" faults, with all smaller faults in shaded regions.

1.4.5 The mathematical model for sub-seismic fault systems

Much geological and geophysical fault system modelling is directed towards a very specific aspect of a fault system. Consider the two examples below. Ma and Kusznir (1992, 1993) used computer modelling to calculate 3D displacements at any point in a volume of rock containing a fault of a particular geometry. This modelling conceptualised faults as ellipses with displacement ranging from a maximum at the centre to zero at the fault tip, according to a precise geometrical relationship. Rules from elastic dislocation theory were incorporated in the mathematical model, and the resultant displacement geometries were calculated for a number of cases.

A second example is the work of Cowie and Scholz (1992b). This work concerns a geometrical relationship assumed in Ma and Kusznir's work, namely the variation in displacement on a fault surface. This work uses mathematical modelling with the aim of reconciling field observations of faults (geological and conceptual models) with theory (mechanical models) in order to determine fault scaling relationships. The mechanical model applied is the Dugdale model of cohesion at crack tips, which has its roots in the discipline of fracture mechanics. Assumptions made by Ma and Kusznir were addressed specifically by Cowie and Scholz. In each case, however, assumptions were necessary, as no model can incorporate every aspect of a system, no matter how well-understood that aspect of the system may be.

The work cited above is basic scientific research, investigating very specific aspects of fault systems. Its purpose is to broaden understanding of faulting. Both pieces of work have relevance to the present research: the former might be used to help predict the locations of small faults around large ones, and the latter to predict the distribution of strain at different lengthscales in different media. However they are merely two of many potentially relevant studies, all of which cannot possibly be explicitly incorporated in mathematical models for the application of analysing flow through fault systems. The conceptual model is perforce a distillation of the most relevant research and observation. What to include and what to leave out of the mathematical model is an important consideration. If important features are not retained, the mathematical model is inappropriate for the application, and the results are of little value. If too much is included, the model is too cumbersome to be of any use. In this thesis, importance is judged in terms of the significance to flow. Below is a summary of the main aspects of the model. Systems are two dimensional and only single phase flow is considered.

A) The extensional strain in the reservoir is considered to be taken up by dip-slip normal faults with a lower fault displacement cut-off of 1 mm.

B) The scaling in the fault system is expressed by a cumulative displacement frequency power-law relationship, and by two power-law relationships linking displacement to thickness and length.

C) The continuous hierarchy is transformed into a discrete hierarchy in which the geometrical arrangement of the faults is assumed to be independent of the arrangement at any other scale. Effective permeability is calculated at each scale in the hierarchy.

D) Fault orientation is simplified to two orientation populations. The proportion of faults in each population is equal. Faults are assumed to have the same orientations at each length-scale.

E) Any fault model has a particular connectivity which is a function of the fault density at each length-scale. These connectivities are representative of the proportions of splays and intersections observed in faulted sandstone outcrops.

F) All faults at each length-scale have identical lengths, thicknesses and permeabilities.

Limiting the treatment to 2D is a large simplification. A plan-view 2D treatment is a reasonable approximation provided the vertical distribution of the faulting is not variable. A 2D treatment also means that the juxtaposition effect is ignored. The flow modelling of Omre *et al.* (1994) and Walsh *et al.* (in press) show that, for the net/gross ratios which exist in high porosity (aeolian) reservoirs in which deformation bands are likely to be present, the juxtaposition effect is likely to be negligible. Limitations to 2D are less significant for single phase flow than for two phase flow, in which gravity effects have an influence on the flow behaviour.

1.5 Summary and thesis structure

This Chapter has introduced the issues pertinent to calculating the effective flow properties of faulted sandstone reservoirs. Modelling flow through fault systems requires first a model of the fault system itself, which must include petrophysical, geometrical and scaling characteristics. The second requirement is for a method for incorporating the flow effects of the faulting as effective properties in the final reservoir simulation grid-blocks. Only faults with displacements greater than about 20 m can be resolved by 3D seismic and these may be incorporated discretely in reservoir models. Faults in porous sandstones with displacements as low as 1 mm have permeabilities significantly lower than the unfaulted matrix, and these faults must be modelled statistically. There are four orders of magnitude of fault size between these limits, and the eventual effective flow properties included in the large scale reservoir grid-block (typically 10 x 100 x 100 m) must incorporate the properties of the faulting at all these scales.

Scale-up and pseudoisation methods allow inclusion of the effects of small-scale sedimentary structure in field-scale reservoir simulation, and are finding increasing use in industry. This work applies a similar approach to fault systems, and incorporates the effects of the faulting at one scale as effective properties in a model of the faulting at a larger scale, eventually arriving at the scale of the seismic faulting. The density of faulting at each length-scale is determined using established fault scaling methods.

At any length-scale, the effective flow behaviour is calculated through numerical simulation, as a function of the fault density, the petrophysical properties of the faults and matrix, and of the geometrical architecture of the fault system. Any geometrical model is an idealisation, requiring simplifications and assumptions that are partially determined by the final use for which the model is designed. Different aspects of the fault system geometry are significant to different flow processes. Fault clustering, for example, will be shown to be irrelevant in single phase effective permeability

calculations, as clustering affects none of the three flow impairment mechanisms In waterflood situations, clustering is highly important, as recovery is a function of the sizes of fault enclosed compartments.

Quantitative treatments of the soft domino model allow determination of a mathematical model comprising two of the four aspects on Figure 1.9 - strain and scaling. These treatments are the topic of Chapter 2. This scaling model determines the input into the geometrical model, with which flow impairment at each length-scale is calculated.

Fault system geometry is much less well understood than fault scaling, and is the topic of Chapter 3. Geometrical descriptions are seldom quantitative, and are therefore not readily amenable to incorporation into mathematical models. As discussed in Section 1.3.5, the key geometrical variables which are incorporated into the geometrical model are fault orientation and connectivity. Chapter 3 defines a novel method by which the connectivity of real fault systems may be defined quantitatively. This is done on the basis of the relative proportions of faults splays, intersections and tips present in the system.

The implications of fault connectivity as an independent fault system variable are examined in Chapter 4. This Chapter concerns the network properties of systems with variable proportions of intersections and splays. Numerical and analytical methods from percolation theory are applied to determine the characteristics of systems with connectivities representative of those observed in natural systems, as a function of fault density. Particular attention is placed on mapping the percolation threshold of the networks as a function of the proportions of intersections and splays present in a system. (The network code used in this analysis was written by Silke Schallenburger, on a six-month work placement on the project as part of an applied mathematics course at the Technical University of Flensburg.)

The fourth item in the conceptual model is petrophysics. Specifically, what are the absolute permeabilities (for single phase flow) or dynamic, saturation dependent relative permeability and capillary pressure characteristics of the fault gouge. Many workers believe that petrophysical properties of faults are the greatest source of uncertainty in determination of flow in faulted reservoirs (e.g., Heath *et al.*, 1994, Walsh *et al.*, in press). The only source of information about the petrophysical characteristics of reservoir faulting are cored samples of the faults. Therefore, if the small-scale faulting in a particular reservoir is considered to be a development issue, it is essential that samples of the faulting present be obtained. The permeabilities of deformation bands are extremely variable (Antonellini and Aydin, 1994) but, in general, deformation bands have permeabilities several orders of magnitude lower than the sandstone containing them. While it is correct to surmise that gouge permeabilities are a large uncertainty, there is still a need to develop better methods for incorporating their effects in full-field flow models. The petrophysical properties of fault gouges are not studied in this thesis, and a range of realistic fault and matrix permeabilities have been used for faults and matrix.

By the end of Chapter 4, all aspects of the conceptual fault model have been converted into a mathematical model of faulting at each length-scale in the hierarchy. In Chapter 5, methods are developed for calculating the effective permeability at each length-scale in the hierarchy, as a function of the input provided by the mathematical model. The philosophy used for these determinations has been described in Section 1.3.5. Equations and look-up charts are presented for determining effective permeability as a function of a transmissibility, a tortuosity and an orientation term.

In Chapter 6, fault system scaling and strain are revisited. Details of the algebra necessary for the determination of the transmissibility and tortuosity terms at each length-scale in the discontinuous hierarchy are presented.

In Chapter 7, the techniques developed throughout this thesis are combined. This allows rapid calculation of the effective permeability at any position in a reservoir, based on maps of the distribution of the individual input parameters. The sensitivity of effective permeability to uncertainties in the mathematical fault model is discussed, and methods for incorporating this uncertainty in flow simulations are recommended. Finally, conclusions arising from this study are presented in Chapter 8.

CHAPTER 2

QUANTITATIVE FAULT SYSTEM CHARACTERISATION
PART 1: FAULT SCALING

2.1 Introduction

Faulting was conceptualised in Chapter 1 as consisting of four interrelated aspects; strain, fault system scaling, fault system geometry, and fault petrophysical properties (Figure 1.9). A quantitative model is a prerequisite for engineering applications, but geological fault system descriptions, particularly details of the geometry, are often qualitative. This chapter and the next summarise and discuss the empirical and theoretical bases for the quantitative models of faulting which are used in this thesis, and emphasise in particular, the assumptions inherent in the model.

This Chapter predominantly concerns fault systems scaling, and Chapter 3 predominantly concerns fault system geometry, but there is inevitable over-lap. Techniques and assumptions necessary for deriving the key parameters contained in each aspect of the model are addressed. Although much of this discussion is valid for any sort of fracture system, the emphasis is always towards normal faults, and in particular, small-scale normal faults in high porosity sandstones.

2.1.1 Brittle strain

Strain is a dimensionless tensor which quantifies the macroscopic changes in shape and size which have occurred to a volume between two observation times. Brittle strain is considered the portion of this change caused by macroscopic fracturing. Strain is intimately linked to stress, which is defined as the force acting on a unit area at a

particular time. Macroscopic stress is also a tensor, with principal components $\sigma_1 > \sigma_2 > \sigma_3$.

The form of brittle fracturing that occurs in a rock-mass is governed by the principal stresses operating, and by the Griffith-Coulomb failure envelope of the rock, which is determined as a function of shear stress (τ) and effective stress (σ_n'). Effective stresses ($\sigma_1' > \sigma_2' > \sigma_3'$) are given by subtracting the fluid pressure from the normal stresses, and the stress-state in a rock can be represented as a Mohr circle centred on the effective stress axis on a plot of shear stress vs. effective stress (Figure 2.1). The position of the Mohr Circle is determined by the magnitudes of σ_1' and σ_3', and the size of the circle depends on the differential stress ($\sigma_1 - \sigma_3$). The type and orientation of fracture which occurs can be determined by where the Mohr circle touches the failure envelope (e.g. Engelder, 1987; Sibson, 1996). Pure extensional fractures form perpendicular to σ_3 (in the σ_1 and σ_2 plane) at low differential stress, and occur when the pore pressure exceeds the sum of the minimum principal stress (σ_3) and the tensile strength of the rock (T). Extensional fractures can only form at low differential stress. As differential stress and minimum effective stress increase, there is a continuum of fractures with both extensional and shear components, termed hybrid extensional-shear fractures. These are oriented parallel to σ_2, and at an angle θ to σ_1. This angle varies as a function of differential stress, up to a maximum $\theta \approx 30°$. At $\theta \approx 30°$, there is no longer any extensional component to the fracture, and shear fractures are formed (Figure 2.1).

The word *fault* is generally reserved for shear fractures with no extensional component. The term *fracture*, however, technically covers the entire continuum from extensional fractures (joints, veins, dykes etc.) to faults. In this thesis, the term fracture is generally used to mean an extensional fracture, following petroleum engineering conventions. Hence fracture-flow implies flow focused in the apertures of

extensional or extension-shear fractures. Fracture flow is not the principal objectives of this thesis, which concerns shear faults.

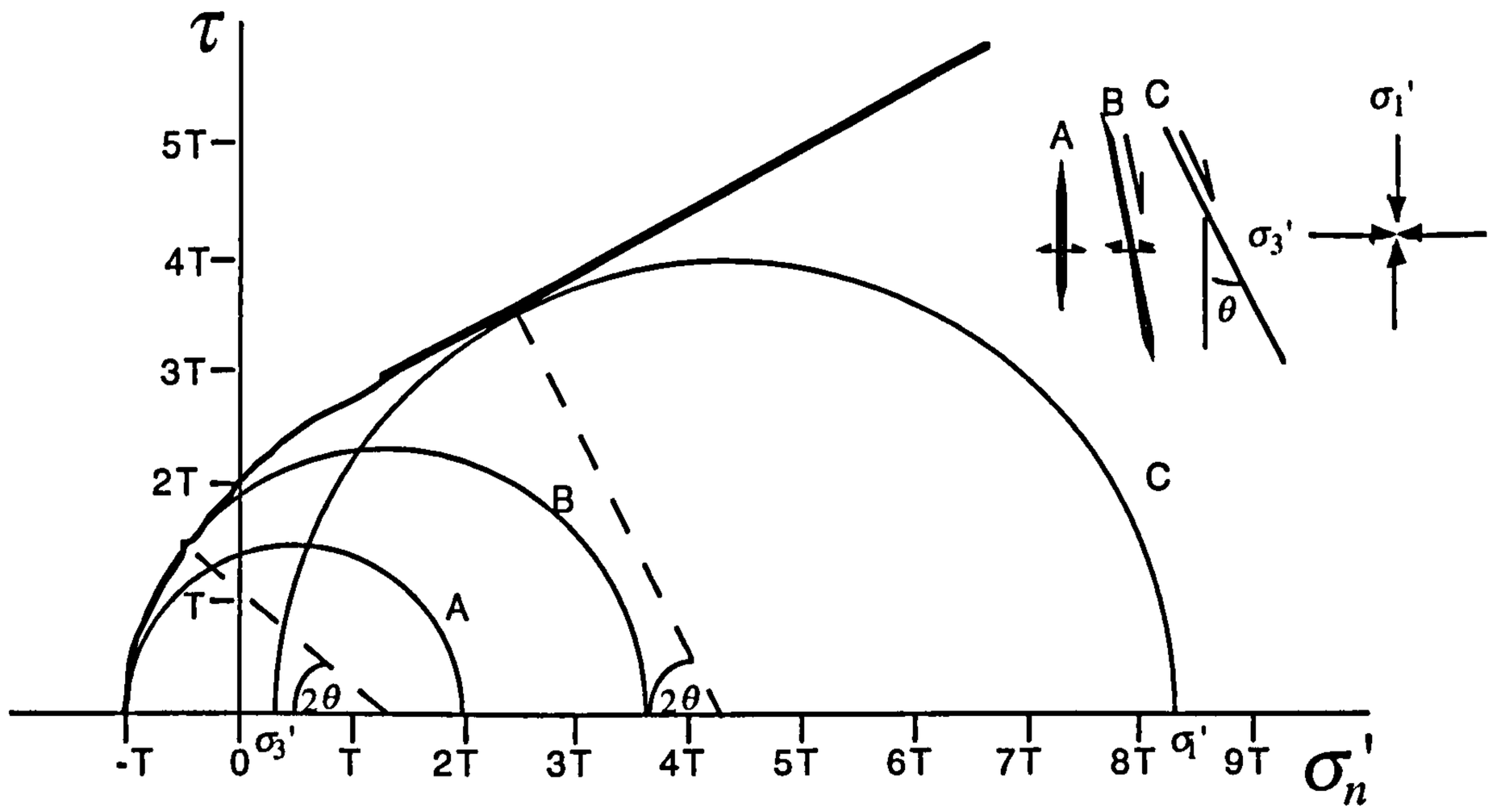

Figure 2.1. Shear stress (τ) vs. effective stress (σ_n') showing the Griffith-Coulomb failure envelope, and Mohr circles for cases of extensional fractures (A), hybrid extension-shear fractures (B) and shear fractures (C). See text for discussion.

Macroscopic stress regimes are determined by the relative orientations of the principal stresses. If σ_1 is vertical, then the regime is extensional, the faults formed in this regime are termed normal faults. In the classical model of normal Andersonian faulting (Anderson, 1951); two normal fault populations (a conjugate pair) dip at 60° and strike parallel to σ_2 (Figure 2.2a). Reches (1977, 1983) and Krantz (1988) have shown that this model is over-simplistic and a quadrimodal system is needed to accommodate triaxial stress (Figure 2.2b). Each fault in such a system has a shear direction which is slightly oblique to the dip of the fault (i.e. $\theta \neq 90 - \delta$), in contrast to classical normal faults, on which the displacement direction is parallel to the dip of the fault ($\theta = 90 - \delta$).

Brittle strain in a normal fault system is a product of the displacements and orientations of all the faults in the system, with extension components $\varepsilon_1 > \varepsilon_2 > \varepsilon_3$. Strain in such a system may be simplified to pure shear, in which a sphere of dimensions 1:1:1 is

converted into an ellipsoid of dimensions $1+\varepsilon_1:1+\varepsilon_2:1+\varepsilon_3$ (e.g. Ramsay and Huber, 1983). A positive ε signifies extension, and maximum extension (ε_1) occurs in direction of minimum stress. Strain in extensional regimes is often reported in terms of a vector stretching factor, β (e.g. Roberts *et al.*, 1993). β occurs in the ε_1 orientation, and is defined as $\beta = 1+\varepsilon_1$.

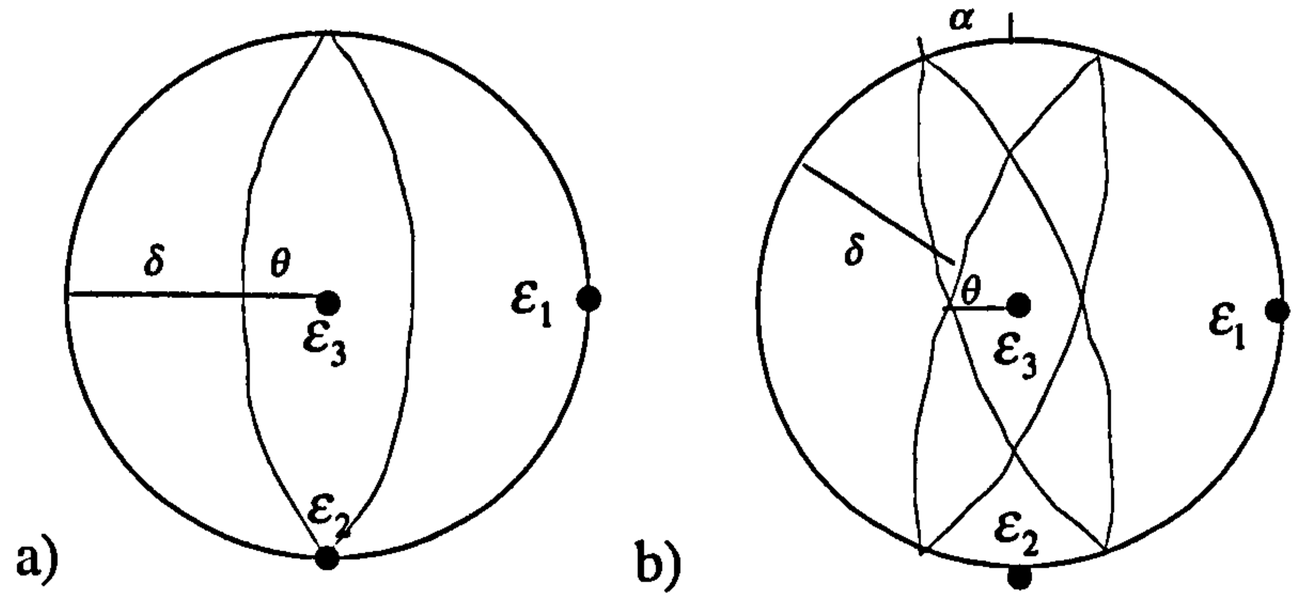

Figure 2.2. A comparison between classical bimodal normal faulting (a) and triaxial quadrimodal oblique faulting (b) on stereographic projections. The great circles represent the ideal fault planes, and the points represent the directions of the principle strain axes. In bimodal faulting, all faults are normal, strain is accommodated by two fault orientations, and $\varepsilon_2 = 0$. In quadrimodal faulting, four orientations of oblique-slip normal faults are necessary, and $\varepsilon_2 \neq 0$. The angle between the strike and ε_2 is denoted α.

Marrett (1996) describes brittle strain as an *aggregate property* of a fault system. Aggregate properties (synonymous with *effective* properties defined in Section 5.1.2) are single parameters used to describe some global aspect of the system. This thesis is primarily concerned with the aggregate permeability through partially sealing fault systems, and eventually a link is made between aggregate strain and aggregate permeability (Chapter 7). The formulation of aggregate strain as a function of the internal structure of the system has been treated most comprehensively to date by Westaway (1994), and a similar treatment is needed to determine aggregate permeability. Aggregate properties are macroscopic descriptions of the system, but the factors which determine these properties are contained within the system. While aggregate strain is relatively insensitive to any geometrical characteristic of the system

other than fault orientation, aggregate permeability is sensitive to both scaling and geometrical characteristics of the system, and both must be considered in detail.

2.2 The mathematical fault model

2.2.1 Fault scaling

A particular stress tensor active on an undeformed rockmass of particular mechanical properties (potentially anisotropic due to sedimentary layering) will produce a particular strain tensor. Temporal variations in the stress state may superimpose strain tensors, such that the later faulting events occur in a rockmass in which the mechanical properties are not only anisotropic, but also heterogeneous due to the presence of earlier faulting. The arrangement of all faulting in this rockmass is termed the *fault system*, and can be split into distinct *fault populations*.

A fault population is a coherent grouping of faults which all share particular geometrical properties. At the crudest sub-division, a fault population is the product of a single, invariant stress state. This population may be sub-divided further into two or four orientation populations, as discussed in the previous section. A useful sub-division of a fault population is often made according to size (e.g. Scholz and Cowie, 1990; Marrett and Allmendinger, 1991; Westaway, 1994). A population of small faults are those which do not span the brittle crust, and a population of large faults are those which do. This is an important sub-division when addressing crustal scale strain, as small and large faults scale differently. Knott *et al.* (1996) have argued, by analogy, that sedimentary layering is important in determining small-scale fault scaling systematics (see Section 2.3.1).

This work concerns populations of sub-seismic faults. This faulting is assumed to be the product of a single stress state, and all the faults in a sub-seismic system are assumed to belong to the same scaling population. This assumption is addressed with reference to faulting in porous sandstones in Section 2.4.

Strain in a single population is distributed between faults of different sizes according to power-law size-frequency distributions. Fault size parameters follow relationships of the form:

$$N \propto S^{-d}, \tag{2.1}$$

where N is the number of faults larger than a particular size S, and d is a constant which determines the relative proportions of small and large faults in the system. This constant is often called the fractal dimension of the system; more correctly it is the power-law exponent of the particular size parameter being considered. A power-law scaling relationship gives a straight line on a graph of $\log N$ vs. $\log S$, and the gradient of this line is $-d$. This graph is called a *cumulative size frequency plot*, according to modern fault populations parlance. The power-law exponent varies according to the size parameter being measured, the dimensions of the sample, and the nature of the particular fault system being analysed. The constant of proportionality varies as a function of all of these, and also as a function of the size of the sample, and the units of size. In this work, the unit of distance is always the metre.

Consider a volume WJH, containing a population which follows equation 2.1 (Figure 2.3). The largest fault in the volume is of area $> JH$, and therefore will be sampled by the 3D volume, by any 2D sample WJ, or by any 1D sample W. Smaller faults, which are contained entirely within the volume, might not be sampled by 2D slices or 1D lines. A 2D sample will not sample any faults which do not intersect the sample horizon. A 1D sample line will not sample any faults which do not intersect the sample line. The fraction of faults of any size in WJH which are sampled in 1D or 2D decreases as the faults become smaller. Therefore, in Equation 2.1, $d_1 < d_2 < d_3$, where the subscript relates to the dimensions of the sample.

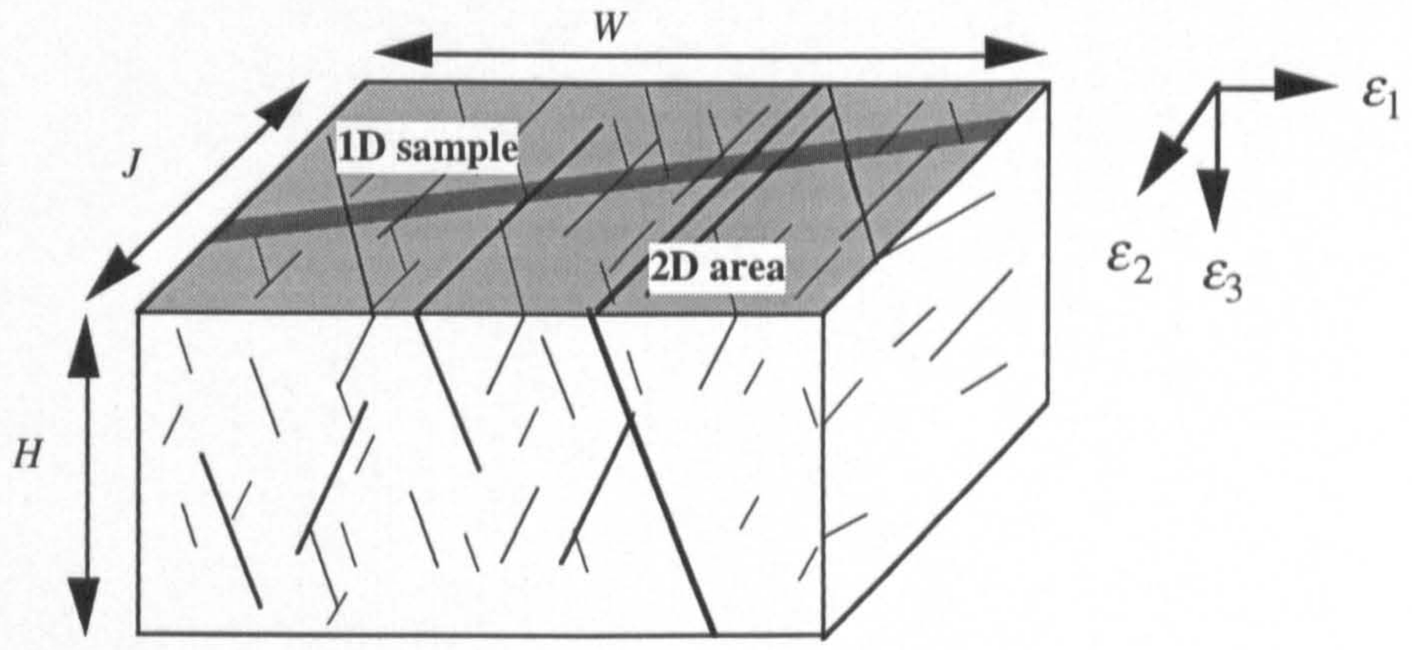

Figure 2.3. 1D and 2D samples of a 3D volume WJH.

Most workers prefer to analyse fault scaling data from samples of the smallest possible dimension, as this allows the most objective interpretation (e.g. Walsh *et al.*, 1994; Pickering *et al.*, 1996). Fault displacement is the most common measure of fault size, and the smallest dimension for which samples can be gathered is 1D. Three conventions, used by Westaway (1994), are adopted in this thesis. The first is to denote the size measure being considered in the term N. The second is to subscript all terms which vary as a function of sample dimension with the dimension to which they refer. The third is to explicitly include the size of the sample in the proportionality constant. Hence the 1D and 2D forms of the cumulative displacement frequency relationship are given by:

$$N_1(D) = a_1 W D^{-c_1}, \tag{2.2}$$

and

$$N_2(D) = a_2 W J D^{-c_2}, \tag{2.3}$$

where a_1 and a_2 are coefficients related to 1D and 2D fault density. The 1D form of the cumulative thickness frequency relationship is:

$$N_1(T) = a_{T1} W T^{-c_{T1}}. \tag{2.4}$$

The treatments given in this thesis are mainly two-dimensional, although some aspects require consideration of the third dimension. The plane considered contains the maximum and intermediate principle strain axes. For normal fault systems, this is a horizontal plane. The orientation convention taken, is that W is parallel to ε_1, and J is parallel to ε_2 (Figure 2.3).

The intersection of this plane with both orientation populations of a classic bimodal fault system will produce one orientation population, and quadrimodal faults will produce two orientation populations, each of which is oriented at an angle α to ε_2 (Figure 2.2). Any fault in WJ has a length L, a thickness T, and a permeability k_f, which are assumed to be constant along the length of the fault.

The scaling model used in this work takes displacement as the fundamental measure of fault size, and a 1D sample as the fundamental sample dimension (Equation 2.2). The thickness and length of a fault are given as a function of displacement according to the relationships:

$$D = BL^n, \tag{2.5}$$

and

$$D = FT^r, \tag{2.6}$$

where n and r are power-law exponents, and B and F are constants.

2.2.2 Fault sampling dimensions

An idealised normal fault in 3D is widely assumed to be an ellipse with maximum displacement (D_{max}) at it's centre, decreasing to $D=0$ at the fault tip, through concentric displacement ellipses (Watterson, 1986). Aspect ratios of fault ellipses are often between 2:1 and 3:1 (Davidson, 1994). Any 2D sample plane intersects the fault at an arbitrary level, and the maximum displacement of the fault at this level is D'. Any

1D sample line at this level intersects an arbitrary point of this trace, and therefore the displacement at this point could be anywhere in the range $0 < D < D'$ (Figure 2.4).

1D cumulative displacement frequency relationships are based on samples of D, rather than either D_{max} (which would require a 3D sample), or D' (which would require a 2D sample). The smallest possible sample dimension for L is 2D, and displacement / length relationships for fault populations are based on correlations between D' and L. In much fault modelling work it is conventional to assume that the displacement at an arbitrary point on the fault trace (D) does not vary significantly from D' (e.g. Marrett and Allmendinger, 1991; Westaway, 1994). Therefore Equation 2.5 can be assumed valid for a random sample of D although, strictly, the relationships should be between D' and L.

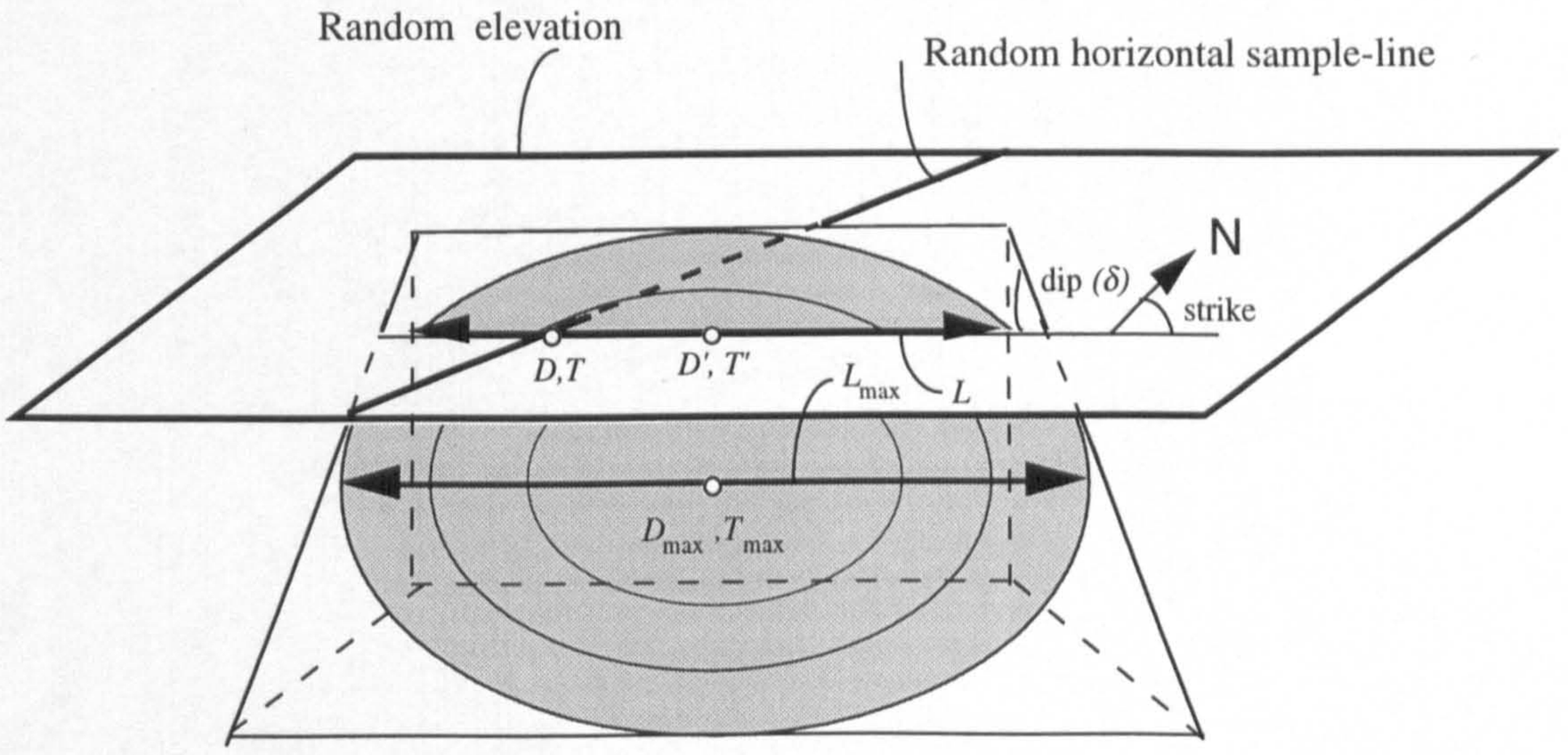

Figure 2.4. Geometrical relationships between the total dimensions of a normal fault and measurements made at a random point on the surface of the fault.

The validity of this assumption depends on the rate at which the displacement varies over the surface of the fault ellipse (the displacement gradient of the fault). Observational and theoretical studies (e.g. Muroka and Kamata, 1983; Walsh and Watterson, 1987, 1988; Cowie and Scholz, 1992a, 1992b) show that displacement gradients are generally steepest close to fault tips, particularly for faults with few slip events, such as deformation bands in sandstones. Therefore the assumption may be

generally valid, as few faults in any sample will have been intersected close to their tips. It is, perhaps, worth bearing in mind that this assumption means that fault lengths will be systematically underestimated.

A slightly contradictory assumption needs to be made regarding displacement / thickness scaling. Both displacement and thickness can be sampled in 1D, and the thickness of the fault is assumed to be constant along the fault trace. Systematic thickness variation along a fault surface has been studied less than the displacement variations, but it is reasonable to assume that the thickness gradient will take a similar form to the displacement gradient. If we now make the assumption that D does not differ significantly from the *average* displacement of the fault trace, we can assume that T is the average thickness of this trace. Therefore a fault trace of maximum displacement D' is taken to have a constant thickness T, where T is the thickness of the fault at the arbitrary sample point D. This pair of assumptions are summarised on Figure 2.5.

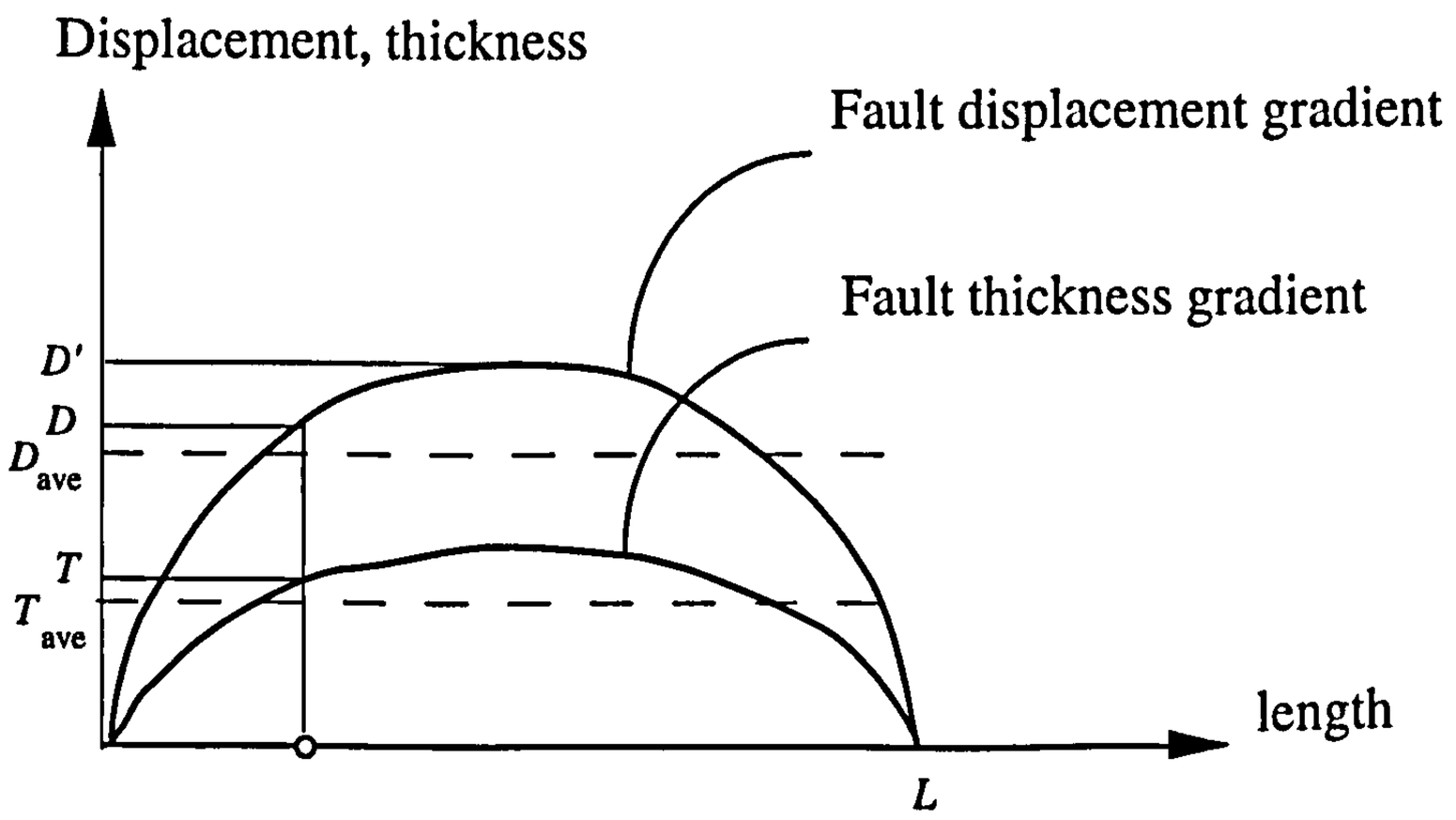

Figure 2.5. Schematic displacement and thickness gradients on a fault trace illustrating the assumptions necessary to make displacement / length and displacement / thickness correlations. Displacement (D) is measured at an arbitrary point. Displacement / length correlations are between L and D', so D must be assumed equal to D'. Displacement thickness relationships are based on arbitrary point samples of each, so T (and by implication D) must be assumed to be equal to the average thickness (and therefore average displacement) of the trace.

2.2.3 Transformation to a discrete hierarchy

The scaling model described in the previous section represents faulting as a *continuous hierarchy* (see Section 1.4.1). In a continuous hierarchy, individual faults can take any size in the interval $D_{min} \leq D \leq D_0$, where D_{min} is the smallest fault considered (though not necessarily the smallest fault present), and D_0 is the largest fault considered. In a *discrete hierarchy*, individual faults can only be particular sizes, $D_1, D_2 \ldots D_n$. The number of possible sizes in a discrete hierarchic approximation depends on the discretisation of the hierarchy, and, as $D_n \rightarrow D_\infty$, the discrete and continuous hierarchies become indistinguishable. In this work, thresholds are taken one order of magnitude apart. D_{min} is taken as 1 mm, D_0 is taken as 20 m (representing seismic resolution), and all faults in the model are of one of four possible sizes; $1\text{ mm} < D_1 < 1\text{ cm}$, $1\text{ cm} < D_2 < 1\text{ dm}$, $1\text{ dm} < D_3 < 1\text{ m}$, and $1\text{ m} < D_4 < 20\text{ m}$ (Figure 2.6). This conversion is performed as it allows the assumption of separation of scales to be made. This assumption is implicit in any attempt to assign effective flow properties (or indeed any other aggregate property) to a system. This topic is discussed further in Section 5.1.2.

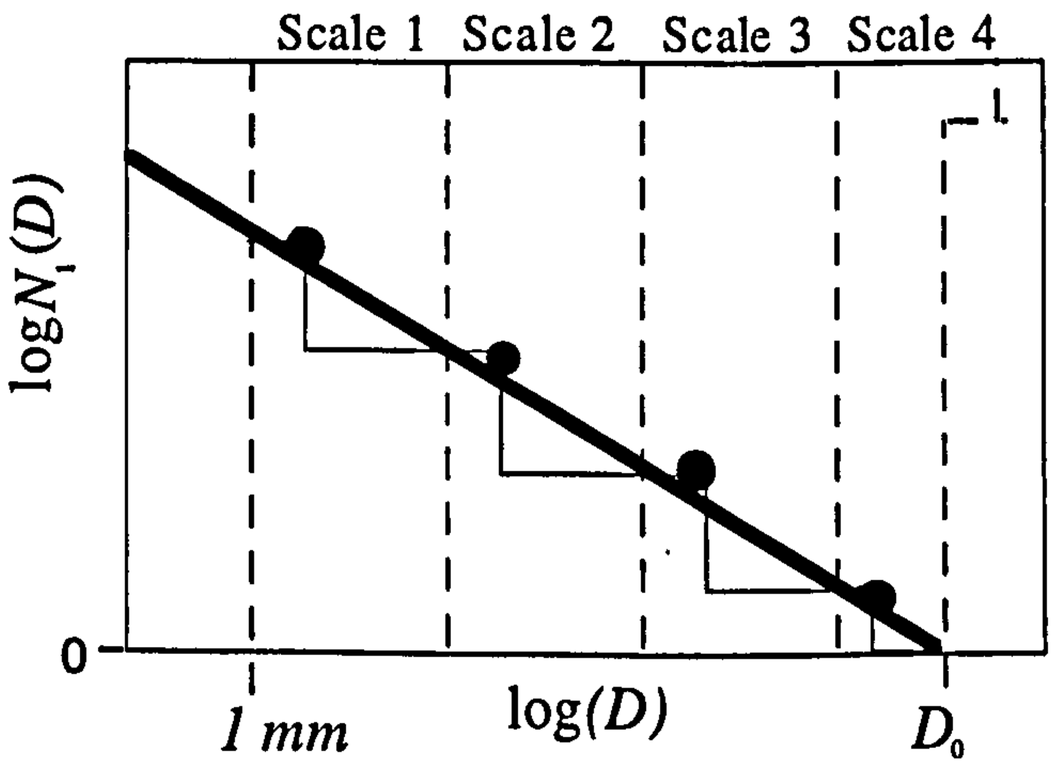

Figure 2.6. Conversion of a continuous to a discrete hierarchy, illustrated on a cumulative displacement frequency plot. The continuous hierarchic faulting (bold line) is converted into a discrete model at selected scale thresholds (dashed lines), in which the faults only exist at particular length-scales (dots).

2.2.4 Fault system geometry

The fault scaling model yields a description of the system as N faults of length L and thickness T contained in an area WJ at a series of length-scales. The faults at each length-scale are assumed to be split equally between two orientation populations at $\pm\alpha°$ to the J (σ_2) direction. A new numerical model based on percolation theory is used to

determine the spatial arrangements used, as a function of the fault orientation (α), and fault density (a function of N, L and WJ). These arrangements honour the connectivity characteristics of faults systems in porous sandstones. This model is the topic of Chapter 4. Geological aspects of fault system geometry are discussed further in Chapter 3.

2.2.5 Petrophysical properties

Antonellini *et al.* (1994) have presented the most comprehensive study so far of deformation band permeability, and stressed the role of fault texture in determining the permeability. Deformation bands have permeabilities between one and four orders of magnitude lower than the host sandstone, with the greater reductions observed in bands contained in more permeable host sandstones. Field measurements of the permeability of deformation bands has shown that huge ranges may be present even within a single fault system (e.g. Pittman, 1981; Kulander *et al.*, 1990; Antonellini *et al.*, 1994; Fowles and Burley 1994; Fisher and Knipe, 1996; Conybeare *et al.*, 1996). Most authors quote an average permeability reduction of about three orders of magnitude (e.g. Antonellini *et al.*, 1994; Fowles and Burley 1994). The highly polished walls of slip surfaces are often reported to have permeabilities in excess of seven orders of magnitude lower than the host sandstone (Antonellini *et al.*, 1994).

At each length-scale in the mathematical model developed in this study, all faults are assigned a constant permeability (k_f), and the undeformed sandstone matrix a constant permeability k_m. The method developed in Chapter 5 allows any values of k_f and k_m to be used, provided k_f is at least about one order of magnitude less than k_m. The flow behaviour of the system is calculated independently at each length-scale in the discrete hierarchic model, and effective flow properties calculated at one scale are input into the next scale as matrix flow properties. In this way the hierarchy is reconstructed to give the overall aggregate flow behaviour of the system.

2.2.6 Data sources for the fault model

Direct information about faulting in a reservoir can be gained from only two sources; seismic and wells. Seismic interpretation provides information about the displacements and lengths of faults within the resolved populations. Well data, and in particular cores, are the only source of information about the thickness scaling and petrophysical properties of the faults, however, cored sections of large faults are seldom available. In theory, core data can give displacement scaling information too, but it is often difficult to gain accurate, quantitative displacement scaling information from cores (Walsh *et al.*, 1994). Small-scale faulting can be characterised much better in outcrop than in core. Outcrop analogue data is therefore an important analogue source of information. Well test responses are a function of the permeability structure in the vicinity of the well, and so can also give information about the faulting in this volume.

In a specific reservoir, displacement scaling of sub-seismic faults must be extrapolated from seismic data, and, if possible, this extrapolation validated from core. Displacement / length scaling may also be extrapolated from seismic, but this extrapolation cannot be validated. Nor can displacement / thickness scaling, which can only be extrapolated from core in certain circumstances. Extrapolations, though necessary, introduce great uncertainty into the sub-seismic fault model.

2.2.7 Summary and discussion

This section has given an overview of the mathematical model of faulting which is used to determine the flow behaviour of the system. In particular, the assumptions in the model have been highlighted. The most important details of the model are as follows:

A) The brittle strain of the fault system is assumed to be a diagonal tensor ($\varepsilon_1 < \varepsilon_2 < \varepsilon_3$).

B) Cumulative displacement, thickness and length frequency are assumed to follow power-law scaling relationships over the size-range considered ($1\ mm < D < 20\ m$).

C) The fault system is converted into a discontinuous hierarchy, consisting of four length-scales at each of which all faults are assumed to be identical.

D) The geometrical arrangement of the faults at each length-scale is assumed to be independent of the arrangement at any other scale.

The remainder of this chapter deals with determining the scaling parameters needed for input into this model.

2.3 Assigning fault density parameters to reservoirs

The basis of the fault model is the cumulative displacement frequency relationship (Equation 2.2). The first unknown (a_1) governs the overall fault density of the system, and the second (c_1) the relative frequencies of small and large faults.

2.3.1 Displacement frequency

Childs *et al.* (1990) and Heffer and Bevin (1990) first suggested extrapolating seismically derived cumulative displacement frequency relationships to determine sub-seismic fault densities. Figure 2.7 shows an ideal cumulative displacement frequency plot constructed by amalgamating data from several seismic lines into a single dataset. Faults with displacements in the range $10m < D < 900m$ have been interpreted, and the data form a straight line plot in the range $20m < D < 400m$. This is the range over which the faults are adequately sampled. At the largest displacements, there is a steep sampling bias due to the largest fault in the system being sampled by several of the lines at a more or less equal displacement. This effect is not present if cumulative frequency plots are derived from a single sample line, but in this case the quality of the central

straight-line segment is usually degraded (e.g. Walsh *et al.*, 1994, Figure 2). For a multi-line sample, the $N_1(D)$ value at which the central segment starts is approximately the number of lines in the sample (*ibid.*). Although faults might be interpreted with displacements as low as 10m, many faults of this size have been missed in the interpretation, resulting in a flattening of the curve at low displacement. The onset of this resolution bias marks the true resolution of the data, in this case at $D = 20m$.

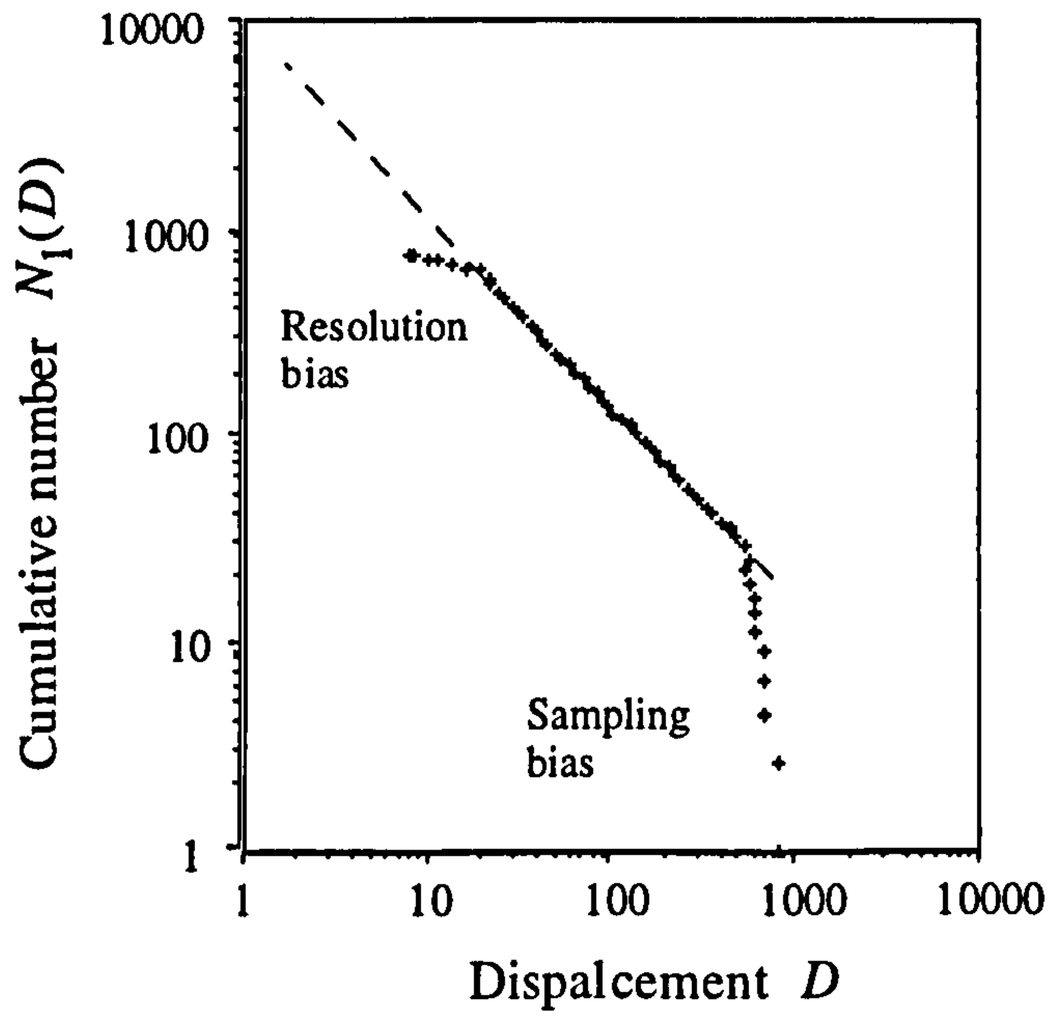

Figure 2.7 Ideal cumulative displacement frequency plot for a multi-line sample of seismic data. The plot gives a straight line on a log/log plot if displacement scaling is power-law. This may be extrapolated to sub-seismic scales to estimate cumulative fault frequency for any displacement threshold (dashed line).

If the sub-seismic fault system is believed to form part of the same population as the seismic faulting, then the straight line may be extrapolated to predict the sub-seismic fault density. Good correlations between seismic and sub-seismic cumulative frequency relationships are often reported (e.g. Yielding *et al.*, 1992; Pickering *et al.*, 1996), although many workers (e.g. Gauthier and Lake, 1993) are loath to extrapolate seismically derived power-law frequency distributions over more than about one order of magnitude. Discussion persists as to whether displacement population extrapolations over several orders of magnitude are valid. See, for example, the special issue of the Journal of Structural Geology devoted to fault and fracture scaling (1996, Volume 18, numbers 2/3). In this issue, Needham *et al.* (1996) find a consistent power-law relationship between core and seismic data, Nicol *et al.* (1996) observe a decrease in power-law gradient with decreasing scale, Watterson *et al.* (1996) gradually degrade a

well-defined dataset, and show that accurate predictions from the degraded datasets can only be made over one order of magnitude, and Knott *et al.* (1996) stress the significance of sedimentological layering on causing inflections from the ideal power-law gradient. Inflections in power-law gradient caused by the particular mechanical evolution of faults in porous sandstone are addressed in Section 2.4.

2.3.2 The spatial distribution of fault density

Yielding *et al.* (1992) and Walsh *et al.* (1994) have published pairs of maps of *cumulative fault density* and c_1, showing the spatial variation of scaling parameters in two North Sea reservoirs (Figure 2.8). Cumulative fault density (*CUMFD*) maps relate to a specific fault displacement , which is termed D_p (in this work). $CUMFD_{D_p}$ values represents the number of faults of displacement $\geq D_p$ likely to be intersected by a 1D sample of a particular length in a particular orientation, $CUMFD_{D_p}$ is given by:

$$CUMFD_{D_p} = N_1(D_p) / W \qquad (2.7)$$

Replacing this in Equation 2.2, gives:

$$CUMFD_{D_p} = a_1 D_p^{-c_1}. \qquad (2.8)$$

$D_p^{-c_1}$ is a constant, so $CUMFD_{D_p}$ is linearly proportional to a_1.

Such maps could be used to predict sub-seismic fault frequencies incorporating variations in fault density in different regions of the reservoir. Further refinement of sub-seismic fault density variation is impossible to predict from seismic data, and at this scale probabilistic placement methods must take over (see Chapter 3). Interdependence of c_1 and *CUMFD* is discussed in Section 6.2.3.

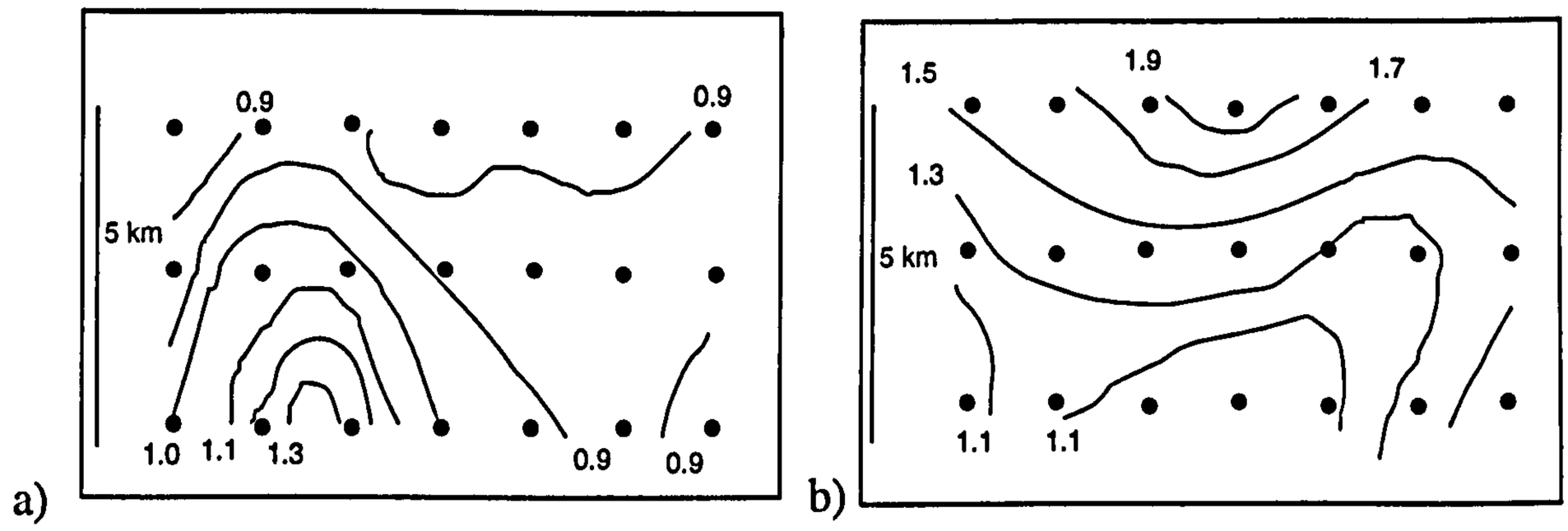

Figure 2.8. Maps of a) Cumulative displacement frequency power-law exponent (c_1), and b) cumulative fault density *CUMFD* for the same area (from Walsh *et al.*, 1994). The total area has been split into 21 sub-areas, each containing 11 lines. Population systematics have been averaged from these lines. *CUMFD* values in this case are the number of faults per kilometre with displacements $D \geq 10$ *ms* two-way travel time.

2.4 Assigning fault size parameters to faults in sandstone reservoirs

The assumption that faulting over all sub-seismic scales form a single scaling population (Section 2.2.1) is a potential source of error in the model, particularly in light of the variety of styles of faulting observed in high porosity sandstones (Section 1.1.1). Any natural system exhibiting power-law scaling must have upper and lower cut-offs outside which power-law scaling is no longer operative. The lower cut-off for fault systems is governed by grain size, and the upper cut-off by the thickness of the brittle crust (e.g. Scholz and Cowie, 1990). This section addresses the determination of optimum scaling relationships within these limits, and investigates the evidence for scaling transitions in the sub-seismic displacement range 1 mm < D < 20 m. A lower displacement cut-off of 1 mm is assumed for the modelling in this thesis.

2.4.1 Sub-seismic faulting in porous sandstones

Faults in porous sandstones occur in three styles; single deformation bands, zones of deformation bands and slip surfaces (e.g. Aydin and Johnson, 1978). A continuum of physical morphologies may exist between the first two styles as both represent strain hardening processes, but the development of slip surfaces involves a physical transition from shear displacement accommodated across a thickening fault zone to displacement

accommodated on a single plane. Slip surfaces strain-soften rather than strain-harden. It is, therefore, unlikely that fault systems would show constant scaling over length-scales spanning this mechanical transition.

There is a general agreement between Dunn *et al.* (1973), Aydin and Johnson (1983), Underhill and Woodcock (1987) and Antonellini *et al.* (1994) as to the way in which deformation bands form. Two mechanical processes are significant; granulation and cataclasis. Granulation is a process active at low confining pressure involving the sliding and rotation of grains past each other, which requires a local increase in volume. Little deformation of the grains themselves occurs during granulation. At higher confining pressure, a volume increase is no longer possible, and the sandstone must deform cataclastically. During cataclasis, the grain sliding associated with granulation is accompanied by grain fracture, which allows compaction. Scholz (1990) has formally distinguished between granulites and cataclasites as having less than, or more than, 10% of fractured grains respectively.

The stress / strain path during the formation of a deformation band is shown schematically on Figure 2.9, after Underhill and Woodcock (1987). Initially, a sandstone will deform through recoverable elastic strain. At point A, grain contact cements start to fracture, the grain framework to collapse, and strain localises into an initially strain hardening proto-deformation band. Granulation involves dilation of the band, and, because of this dilation, grain contact stresses are increased due to the reduction in grain contacts per unit volume. This grain contact stress peak aids the onset of fracture, however granulation within the zone is the dominant mechanism at this stage. During granulation, the grains in the band slide and rotate around each other into an optimally compacted state. After a while (at point C, Figure 2.9), no further porosity collapse is possible without considerable grain fracturing, and cataclasis becomes the dominant deformation mechanism. During cataclasis, the grain sliding

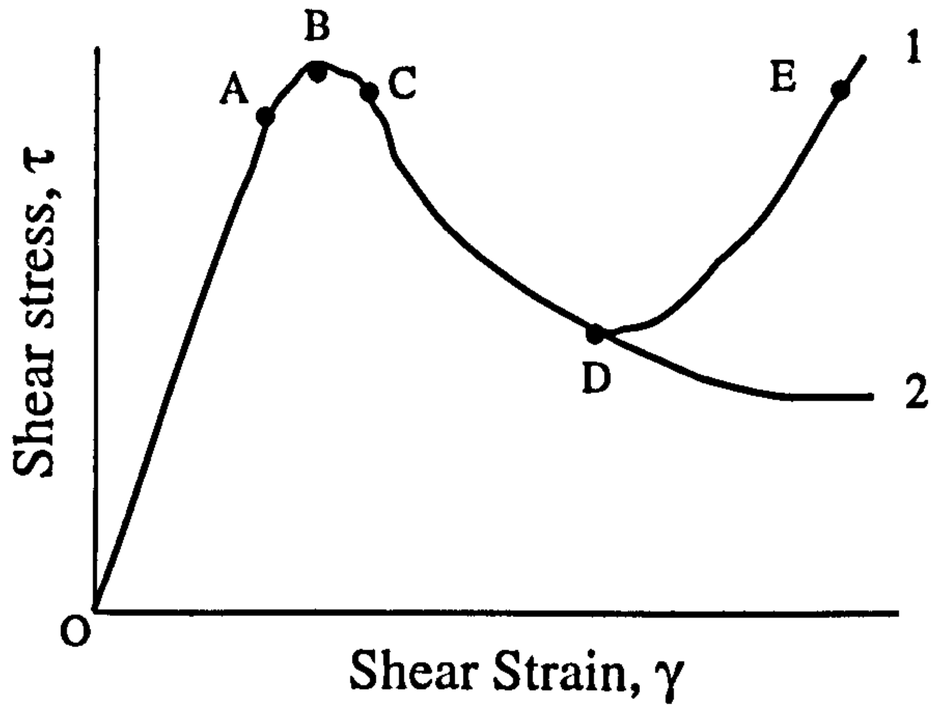

Figure 2.9. Conceptual stress / strain path during the formation of a deformation band (1) compared to a strain softeing fault (2). See text for discussion. After Underhill and Woodcock, (1987).

associated with granulation is accompanied by grain fracture, which allows the structure to compact further. As the gouge becomes progressively fractured, its strength increases due to an increase in grain contact friction (point D). It is at this point where the stress / strain path of a deformation band (Curve 1) and a strain-softening fault (Curve 2) diverge. Once the cohesive strength of a rock has been lost on a strain softening fault surface, slip (shear strain) can continue on the surface at low shear stresses, provided there is no increase in friction on this surface. In a deformation band, however, progressive grain fracture and band compaction produce an increase in friction. This, coupled with an increase in grain contacts, and thereby a decrease in grain contact stresses, makes it progressively harder to continue the cataclastic process unless the shear stress is increased. This strain-hardening effect causes an upwards increase in the stress-strain curve, until, at point E, the fault strength has surpassed the yield strength of the sandstone (Point B). Net strain hardening has occurred, and the deformation band will not grow further.

Deformation bands are the product of a single faulting event, usually have displacements less than a centimetre, and are rarely reactivated within the same gouge zone. Instead, reactivation produces zones of deformation bands. A zone of deformation bands consists of two or more adjacent deformation bands, each sharing the same orientation. Each band in a zone follows the cycle described above, and therefore a zone of deformation bands has undergone net strain hardening.

Aydin and Johnson (1983) studied the formation of slip surfaces based on a generalised theory of elasto-plastic materials (e.g. Rudnicki and Rice, 1975; Rudnicki, 1977). They argued that, because the gouge in deformation bands and zones is stiffer than the undeformed sandstone, it can support larger stresses than the sandstone which would deform elastically. These stress concentrations in the zones can be large enough to cause a "runaway instability" in the gouge, producing highly localised accommodation of large strains within the gouge. This localisation causes a slip surface, on which significant displacement is accommodated on a plane, in contrast to either deformation bands or zones, in which smaller displacements are accommodated across a gouge zone of discrete thickness. Slip surfaces are often highly polished, striated surfaces, and may be reactivated. The development of a slip surface is the point at which complete strain localisation has occurred, and their formation represents the transition from strain hardening deformation bands and zones, to strain softening faulting.

The mechanical transitions from deformation bands, to zones of deformation bands, to slip surfaces are likely to affect both displacement / length scaling relationships and displacement / thickness scaling relationships. These are discussed in the following two sections. Scaling relationships in porous sandstones have not been studied extensively, but mechanically induced scaling transitions have been reported from other fracture styles, for example extensional fractures in basalts by Hatton *et al.* (1994).

2.4.2 Displacement / length scaling

The relationship between maximum displacement D (Figure 2.4) and length (L) of populations of normal faults has received enormous attention in the last decade. There are two main thrusts to these studies; firstly those which use a particular geometrical or mechanical fault growth model to predict the power-law exponent, and secondly those which attempt to apply empirical correlations to field data. This section presents no more than a cursory review of this vast volume of literature, and no original

displacement / length data are presented in this thesis. The best source for recent developments in this area is the special issue of the Journal of Structural Geology mentioned above.

A recent modelling paper by Peacock and Sanderson (1996) includes a review section on the conclusions of previous modelling approaches. Depending on the fault growth model favoured by various authors, the power-law exponent (n, Equation 2.4) has taken values of $n = 2$ (Watterson, 1986; Walsh and Watterson, 1987, 1988); $n \approx 1.5$ (Gillespie *et al.*, 1992); $n = 1$ (Cowie and Scholz, 1992a); has varied according to mechanical properties (Burgmann *et al.*, 1994); or has varied according to propagation history (Peacock and Sanderson, 1996). The models that predict a constant value of n are based on the growth of single isolated faults. Peacock and Sanderson's model includes the possibility of fault linkage, which need not degrade power-law displacement / length relationships (Dawers and Anders, 1995), and which some theoreticians suggest is actually a pre-requisite for power-law scaling distributions in the first place (e.g. Cladouhos and Marrett, 1996).

Analysis of field data is also ambiguous. General correlations including data from a variety of sources (Figure 2.10) usually conclude that a "global" relationship exists with $n \approx 1.5$ (e.g. Marrett and Allmendinger, 1991; Gillespie *et al.*, 1992), though one team recently concluded that $n \approx 1$ from a compilation which included more small ($L < 100m$) faults (Schlische *et al.*, 1996). Analyses of data from single fault systems often give values of n close to unity (e.g. Scholz and Cowie, 1990; Cowie and Scholz, 1992a; Dawers *et al.*, 1993), though some individual datasets also give n as high as 1.65 (Gillespie *et al.*, 1992). The problem with individual datasets is that the distribution in fault sizes rarely span more than about 2 orders of magnitude, which, in view of the inevitable scatter in any dataset, is insufficient to allow incontrovertible correlations to be made (see Section 2.4.8).

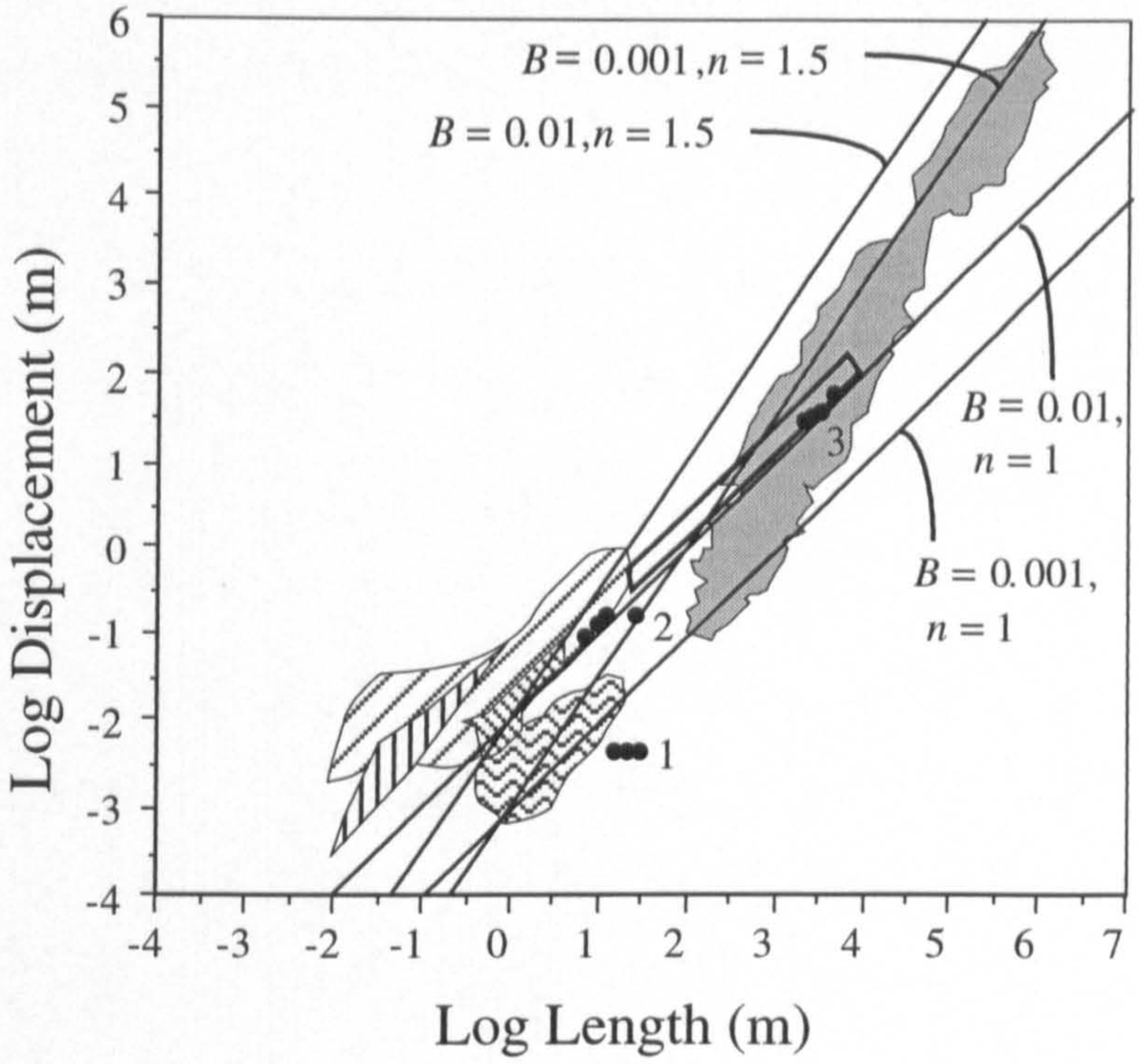

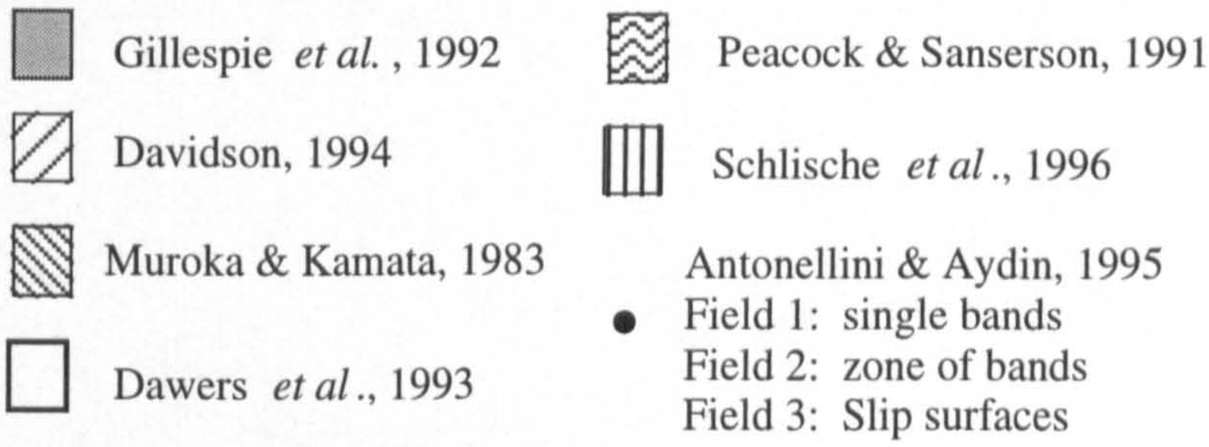

Figure 2.10. Compilation of displacement / length data from a variety of datasets. The datasets from Gillespie *et al.*, (1992) include datasets from earlier sources. Additional datasets from Muroka and Kamata (1983), Peacock and Sanderson (1991), Dawers *et al.*, (1993), Davidson (1994; after McGrath 1992), Antonellini and Aydin (1995), and Schlische *et al.*, (1996). The labelled relationships are those used for the effective permeability sensitivity cases (Chapter 7).

In summary, workers addressing displacement / length scaling of fault populations are in unanimous agreement that Equation 2.4 is mechanically valid for tectonic fault systems, but cannot reach a consensus on the value of the power-law exponent n. This exponent has received far more attention than the constant B, because n was believed to be a universal constant, but B was recognised to vary as a function of material properties (Watterson, 1986; Cowie and Scholz, 1992b). More recently, the belief in a universal value of n is evaporating in favour of defining system specific displacement /

length parameters, and the trend for defining n for individual datasets is moving away from an historically preferred value of $n \approx 1.5$, towards one of $n \approx 1$.

Theoretically derived displacement / length relationships are often based on models in which the size of events during fault reactivation influences the displacement gradients of the faults, which in turn influences the form of the displacement / length scaling relationship. High porosity sandstones are often massively bedded with few good marker laminations and it is notoriously difficult to measure deformation band displacement gradients. Data reported by Antonellini and Aydin (1995) show that although displacement / length relationships may be scale invariant between zones of deformation bands and slip surfaces, no such relationship seems to exist for populations of deformation bands (Figure 2.10).

Displacement / length scaling transitions are discussed no further, since no new data are presented. It is, however, worth noting that care is required in using a relationship for which $n \neq 1$. A relationship with $n > 1$ will eventually predict physically impossible faults with displacements larger than their lengths, and a relationship with $n < 1$ will predict very long faults with small displacements. This suggests that relationships with $n \neq 1$ are likely to be valid over only limited scale ranges. In the following sections, focus is shifted to displacement / thickness scaling.

2.4.3 Displacement / thickness scaling

The relationship between fault displacement and fault thickness has received significantly less attention than displacement / length relationships. This is particularly irksome, since the thickness of deformation bands is much more significant to the flow performance of a faulted sandstone than the length of the faults, as will be shown in Chapter 7. Compilations of displacement / thickness data (e.g. Robertson, 1983; Hull, 1988) suggest a power-law relationship between these two variables (Equation 2.6) with the scaling exponent r at unity, and the constant F varying as a function of

mechanical properties. For faulting in Nubian Sandstone in Western Sinai, Knott *et al.* (1996) suggest a relationship of $D \approx 10T$ for sandstone juxtaposed against sandstone, reducing in relative thickness to approximately $D \approx 100T$ for sandstone juxtaposed against shale.

Figure 2.11 shows a compilation of available displacement / thickness data, plotted in log / log space. This plot includes three new datasets which are discussed below. Evans (1990) pointed out that the considerable scatter in any dataset makes cross-plot correlations extremely problematic, and that attention should focus as much on the variability in any dataset, as on ideal relationships.

Faults at all scales have large variation in thickness along their traces. Foxford *et al.* (in review) studied the excellently exposed Moab fault (SE Utah, see Figure 2.12) over 40 km of its trace. They concluded that it is impossible to predict the structure, content or thickness of this large fault for distances along the fault trace as small as 10 m. Childs *et al.* (1996) described a process by which multiple active slip surfaces combine to cause mechanical erosion and accretion of non-planarities within the fault zones. This *asperity bifurcation* process may cause regions of almost zero thickness adjacent to area in which the thickness is doubled average. Nonetheless, Foxford *et al.*'s data does show a weak positive correlation between thickness and displacement (Figure 2.11).

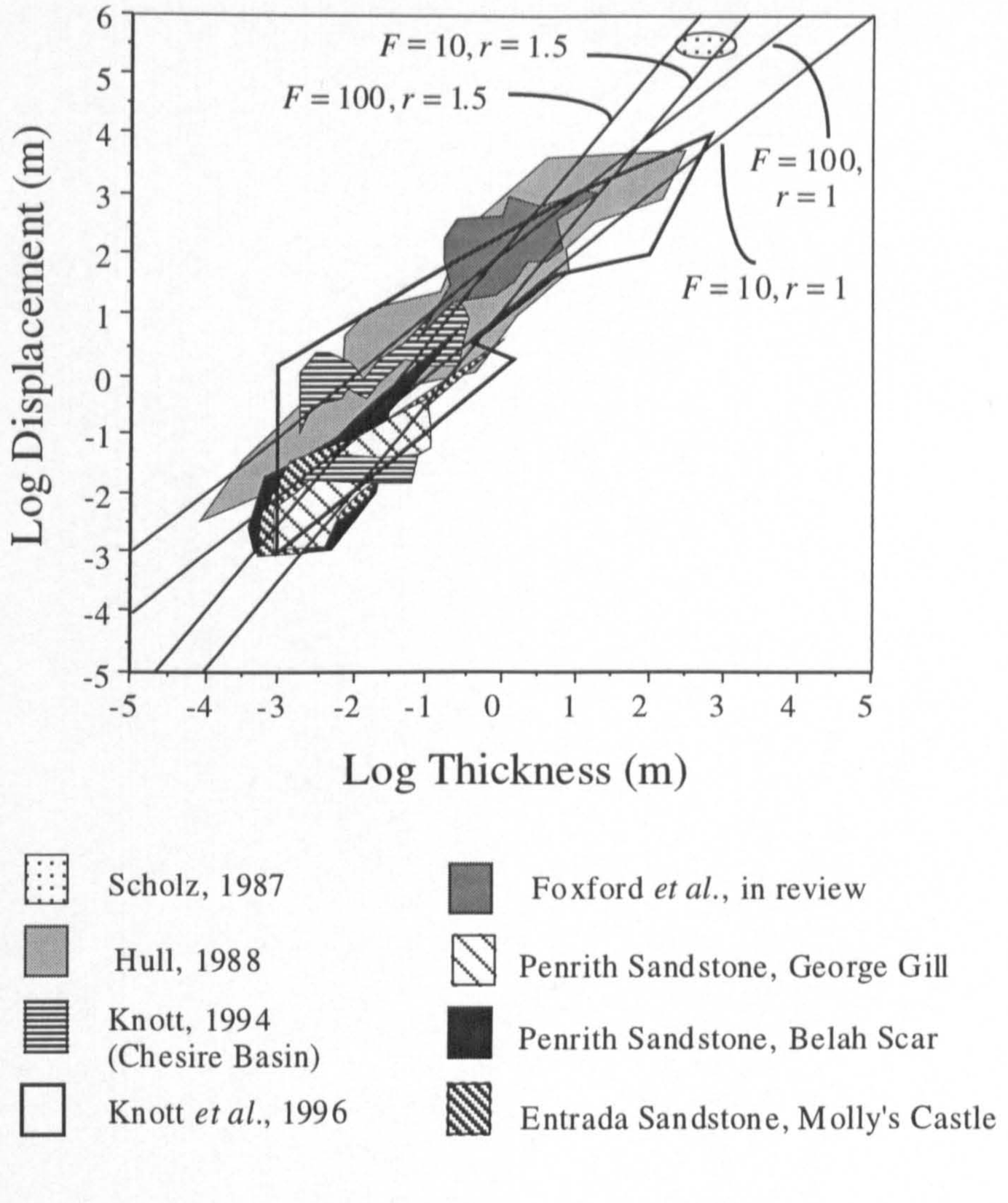

Figure 2.11. Compilation of displacement / thickness data from a variety of datasets. The data from Scholz (1987) is an estimate for the San Andreas Fault. Data from Hull (1988) are from a variety of earlier sources. The data from Knott (1994) is from the Cheshire Basin; his data from the Vale of Eden is not shown. Knott *et al*, (1996) data are from the Nubian Sandstone in Western Sinai, and data from Foxford et al. (in review) is from the Moab Fault (SE Utah). Original displacement / thickness data comprise two datasets from the Penrith Sandstone, and one dataset from Entrada Sandstone. The labelled relationships are those used for the effective permeability sensitivity cases (Chapter 7).

2.4.4 Displacement / thickness scaling - new datasets

In this section, three sets of displacement / thickness data are considered. Belah Scar and George Gill are both cliff outcrops of Penrith Sandstone in the Vale of Eden, Northern England. Aspects of faulting at these outcrops have previously been characterised by Gillespie *et al.* (1993) and Knott (1994). The third locality is Molly's

Castle in SE Utah, which is one of the classic deformation band outcrops studied by Aydin (1978). Location maps are shown on Figure 2.12

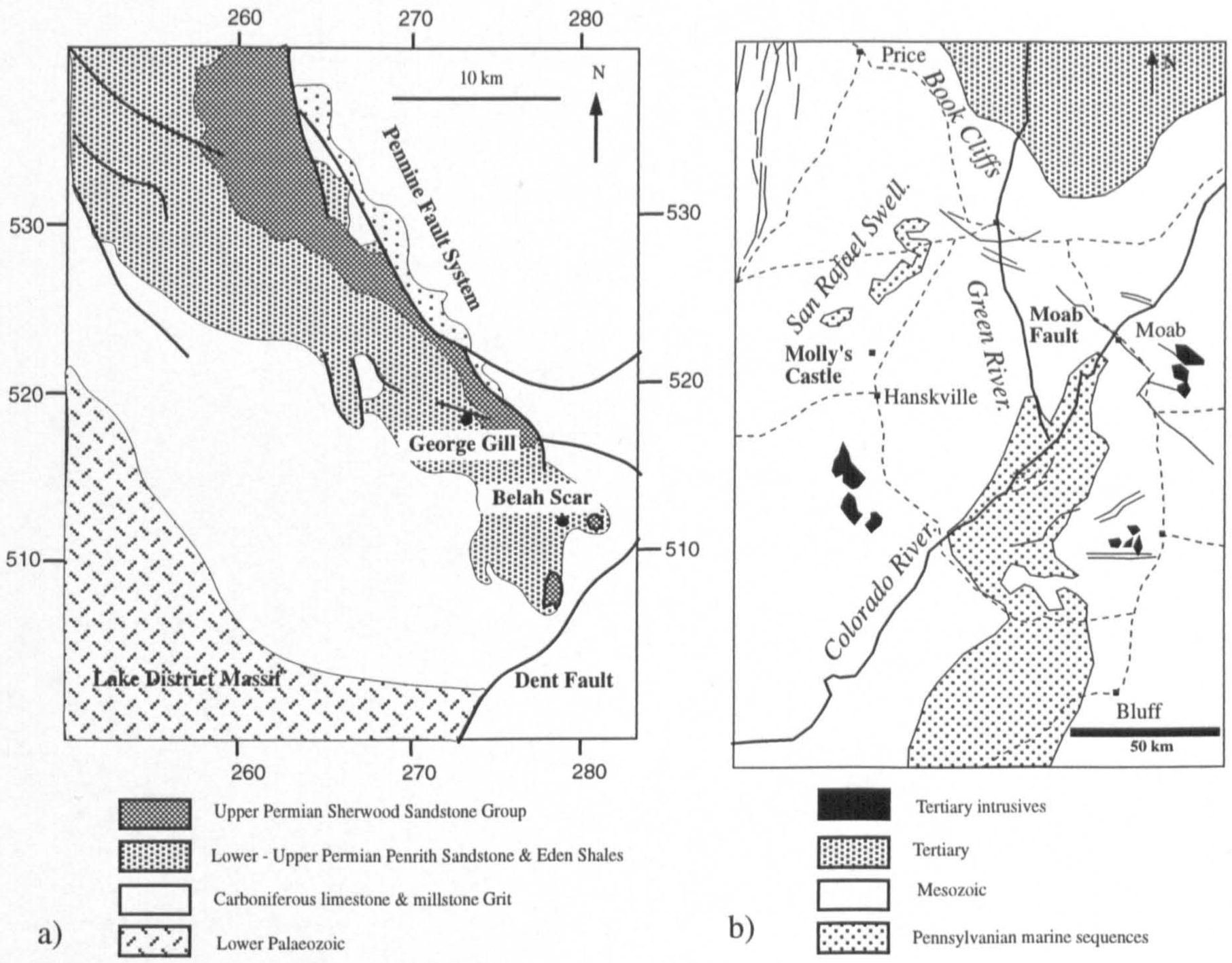

Figure 2.12. Location maps for a) the Vale of Eden (N. England) and b) Molly's Castle (S.E. Utah). (Map a is after British Geological Survey, 1982; and Map b after Stokes, 1986).

At each of these outcrops, oriented 1D transects were made, recording the position, orientation, displacement and thickness of each fault. The thickness of deformation bands or zone of deformation bands was measured over the width of gouge, recognisable as a pale zone of texturally altered sandstone. In the case of slip surfaces, the thickness of the bounding zone and the fault aperture were included in the thickness measurement. Where the sample lines intersected a zone of bands containing an unfaulted block of sandstone, each strand was measured separately. These thickness data have therefore been sampled according to the same criteria used by Knott *et al.* (1996). The data are tabulated in Appendix 1 (Tables A1.1 - A1.3).

Cumulative displacement and thickness frequency plots for the samples are shown on Figure 2.13. Each dataset spans about two orders of magnitude, and displacement power-law gradients (c_1) show greater variability than thickness ones (c_{T1}). From each dataset, a displacement / thickness relationship of the form $D = FT^r$ has been derived. As pointed out by Gillespie *et al.* (1992), a simple linear regression on a plot of log(D) vs. log(T) is inappropriate, as such a regression assumes that displacement is the independent variable. Gillespie *et al.* suggest that a reduced major axis regression method should be used when neither the ordinate nor the abscissa of a graph is the obvious independent variable. In this work, a new method is used to derive the relationship from the individual cumulative displacement and thickness plots. The method is validated with a synthetic dataset for which the constants F and r are known.

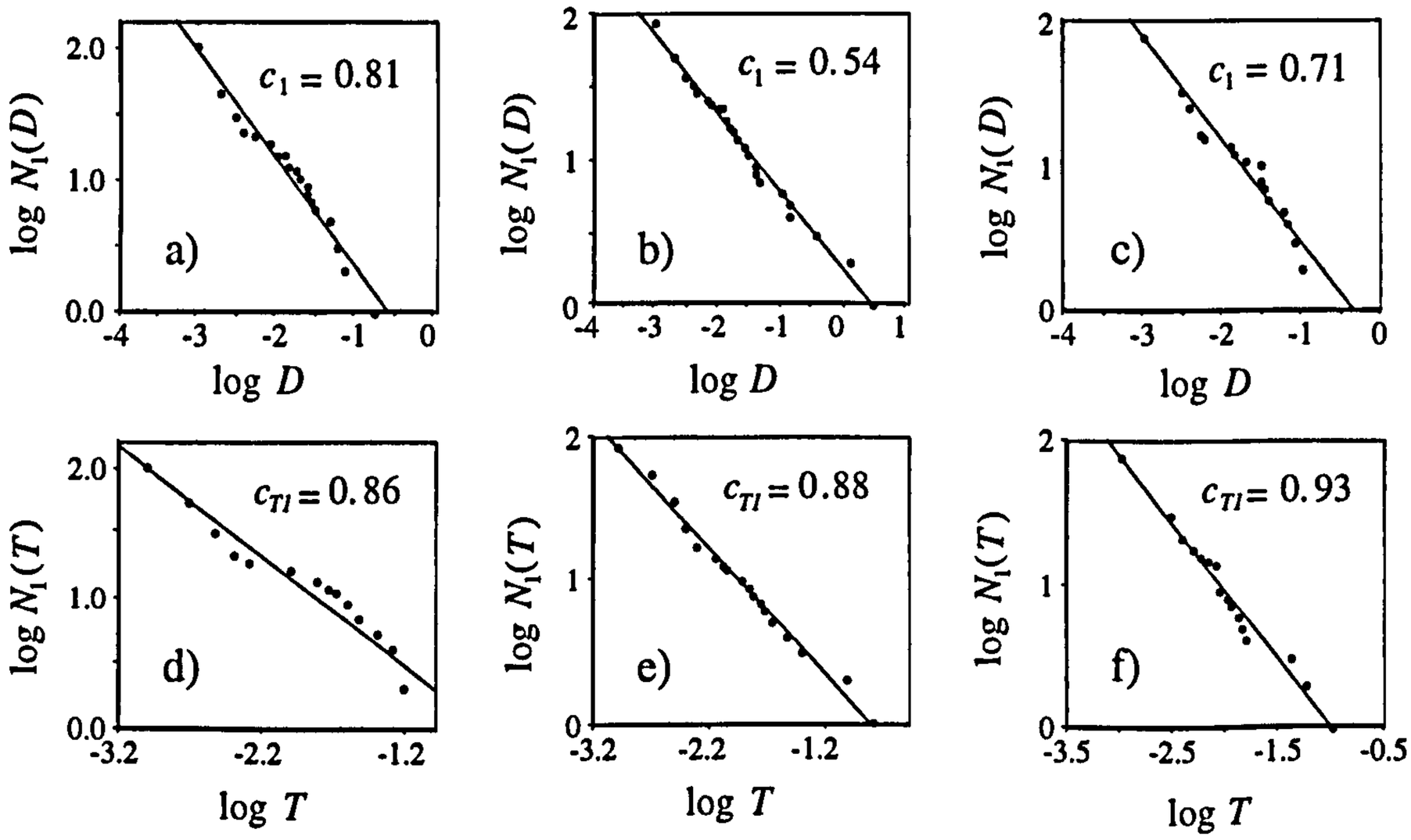

Figure 2.13. Cumulative displacement (a-c) and thickness (d-f) frequency plots from George Gill (a, d), Belah Scar (b, e) and Molly's Castle (c, f).

2.4.5 A mathematically coherent displacement / thickness relationship

The relationships for cumulative displacement and thickness frequency are given by Equations 2.2 and 2.4, respectively. If we assume that displacement and thickness are correlated, then $N_1(D)$ and $N_1(T)$ can be equated. If this assumption is made, then Equations 2.2 and 2.4 give:

$$D = (a_{T1} / a_1)^{-1/c_1} T^{c_{T1}/c_1}, \tag{2.9}$$

which equates with 2.6 to give:

$$F = (a_{T1} / a_1)^{-1/c_1}, \tag{2.10}$$

and

$$r = c_{T1} / c_1. \tag{2.11}$$

A reason for using this method to calculate the displacement / thickness correlation is that it automatically results in a coherent mathematical model. If Equations 2.2 and 2.4 are taken to define the displacement and thickness scaling in a fault system, then Equations 2.10 and 2.11 *must* define the displacement / thickness scaling. If constants F and r are not related to a_1, c_1, a_{T1} and c_{T1} according to these equations, then the model of the fault system contains mathematical contradictions, and is therefore incorrect. The method also ensures that the displacement / thickness correlation is based on the more stable cumulative frequency plots, rather that cross-plot correlations.

2.4.6 Validation with a synthetic dataset

The validity of this method is illustrated with synthetic displacement and thickness datasets (Figure 2.14), for which the displacement / thickness scaling is taken as $D = 10T$. Ideal cumulative frequency datasets (each containing 300 data) have been determined according to the relationships $N_1(D) = 6.3xD^{-0.8}$ and $N_1(T) = xT^{-0.8}$, where x is selected from a uniform rectangular distribution in the range $0 < x < 2$, to

add a random element to the data. Due to the random factor, the thickness / displacement relationship for these datasets, is slightly different from $D = 10T$.

The cumulative frequency plots (Figure 2.14a) show a marked bias at the left-hand side, reminiscent of resolution biases (Figure 2.7). In this case, however, these biases are due to inclusion of the random factor drawn from a uniform distribution. At any particular $N_1(D)$, D cannot be more than double its ideal value, but can be reduced to virtually zero. As the plot is on a logarithmic scale, linear decreases from the ideal value have a more profound effect than increases. A regression through the straight line portions of each graph gives the relationships $N_1(D) = 6.97D^{-0.76}$, and $N_1(T) = 1.01T^{-0.77}$, illustrating the deterioration in the input relationship by the random factor. Applying equations 2.10 and 2.11 to these, gives $D = 12.7T^{1.01}$, very close to the ideal relationship of $D = 10T$. The small increase in F is due to the decrease in c_1 from 0.8 to 0.76, caused by inclusion of the random factor. Regressions of $\log(D)$ derived from $\log(T)$ (Figure 2.14b, Curve 1) and $\log(T)$ derived from $\log(D)$ (Curve 2) give much poorer estimates, namely $D = 0.96T^{0.62}$ and $D = 191T^{1.46}$, respectively.

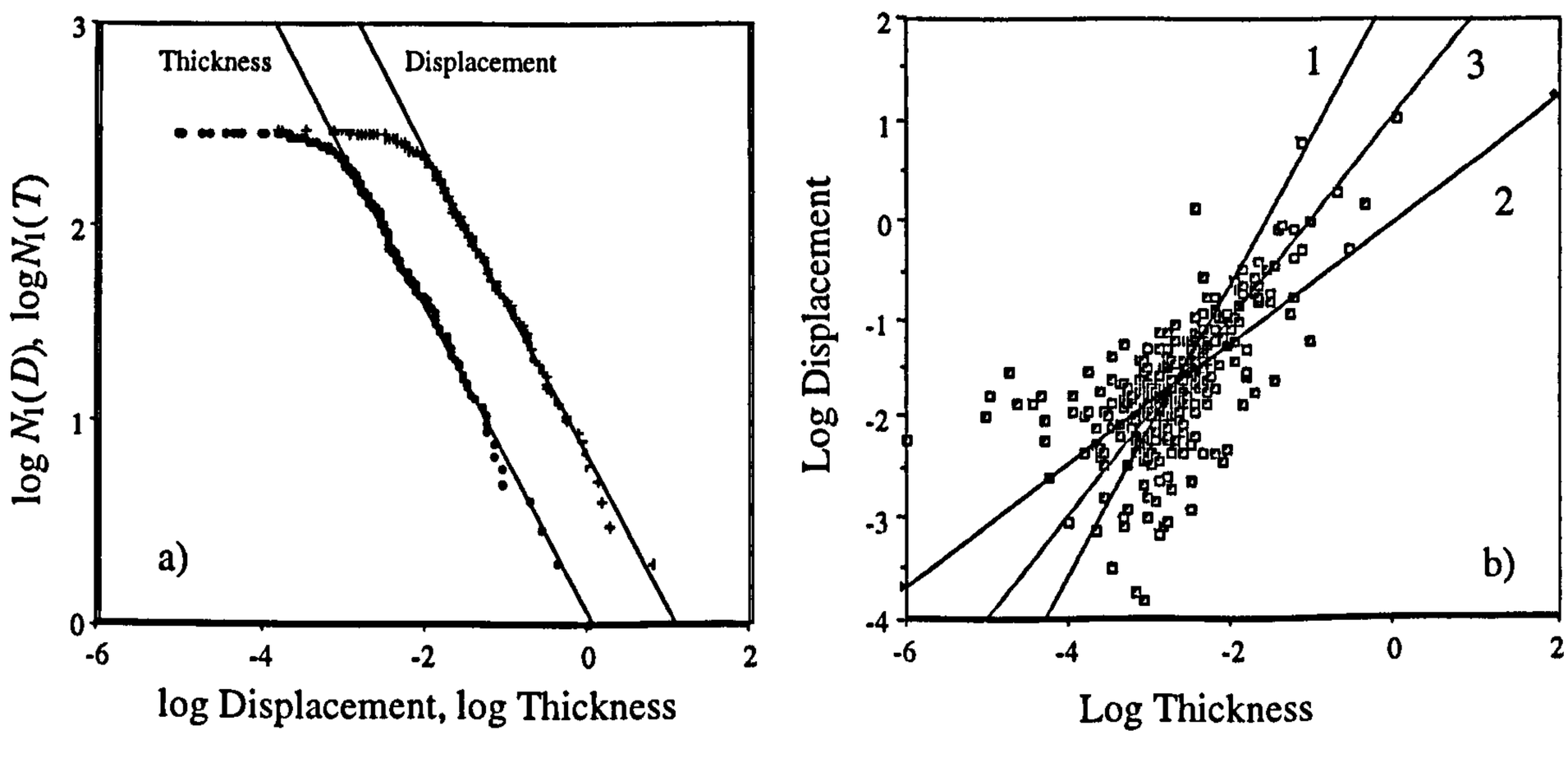

Figure 2.14. Displacement / thickness scaling of a synthetic dataset. a) Cumulative displacement and thickness frequency plots. b) Log displacement vs. log thickness. Curve 1: Regression of displacement with respect to thickness. Curve 2: Regression of thickness with respect to displacement. Curve 3: Relationship determined from the cumulative size frequency plots, using Equations 2.10. and 2.11.

Thus for simple regression, both F and r are significantly different from what they should be, whereas the proposed new method yields an accurate result (curve 3).

2.4.7 Controls on displacement / thickness scaling

Applying Equation 2.10 and 2.11 to the three field datasets (Figure 2.12) gives $D = 1.45T^{1.06}$ at George Gill, $D = 66T^{1.63}$ at Belah Scar, and $D = 8.8T^{1.31}$ at Molly's Castle. These relationship are plotted on Figure 2.15. Due to differences in cumulative displacement frequency (Figure 2.13a-c), the displacement / thickness scaling relationships are different. These differences appear to be related to the lithologies present.

Deformation bands form through cataclasis, which is pressure sensitive, and relatively strain rate independent (e.g. Rutter, 1986). The principal controls on cataclastic faulting are the mechanical properties of the rock and the pressure conditions. The outcrops of Lower Permian Penrith Sandstone at George Gill and Belah Scar differ significantly. George Gill consists of a well sorted, coarse grained aeolian sandstone, and the faults are characteristic deformation bands and zones, in which strain is accommodated across a discrete thickness of cataclastic gouge. At Belah Scar the succession is mixed fluvial / aeolian, and is generally finer grained. The field characteristics of many faults at Belah Scar show failure localised onto a single plane within a gouge zone. The faulting at both these locations occurs in similar orientations, tectonically linked to movement on the Pennine Fault System which bounds the Vale of Eden half-graben (Figure 2.12a). It is therefore reasonable to assume that the faulting at the two locations occurred at a similar time, under similar stress conditions, and that the differences in scaling systematics relate to differences in mechanical properties of the rock.

The faulting in the Middle Jurassic Entrada Sandstone at Molly's Castle on the San Rafael Swell (Figure 2.12b) has values of c_1 and r intermediate between those from

Belah Scar and George Gill. The Entrada Sandstone is composed of a climatically wet aeolian sequence of fine grained sandstones (from which the fault dataset was taken) and shaley interdune sequences (e.g. Doelling, 1985). The faults observed are deformation bands and zones, and throughout the field area, deformation zones in the aeolian facies can be traced into overlying shales where they form slip surfaces. No comparisons between pressure conditions during faulting can be made between the Vale of Eden and the San Rafael Swell, however a simple mechanical correlation between fault scaling systematics and sandstone petrology applies at each of the three outcrops. Increasingly porous, quartz rich sandstones are most prone to forming small faults (and therefore have a high displacement frequency power-law exponent c_1), and these faults show a linear relationship between thickness and displacement (i.e. the displacement / thickness exponent tends to one). A conceptual model of deformation band growth followed by cessation due to strain hardening (Section 2.4.1) is consistent with a high c_1 and low r for deformation band systems, and might be the characteristic fault system scaling in higher porosity (lower strength) regions of sandstone reservoirs.

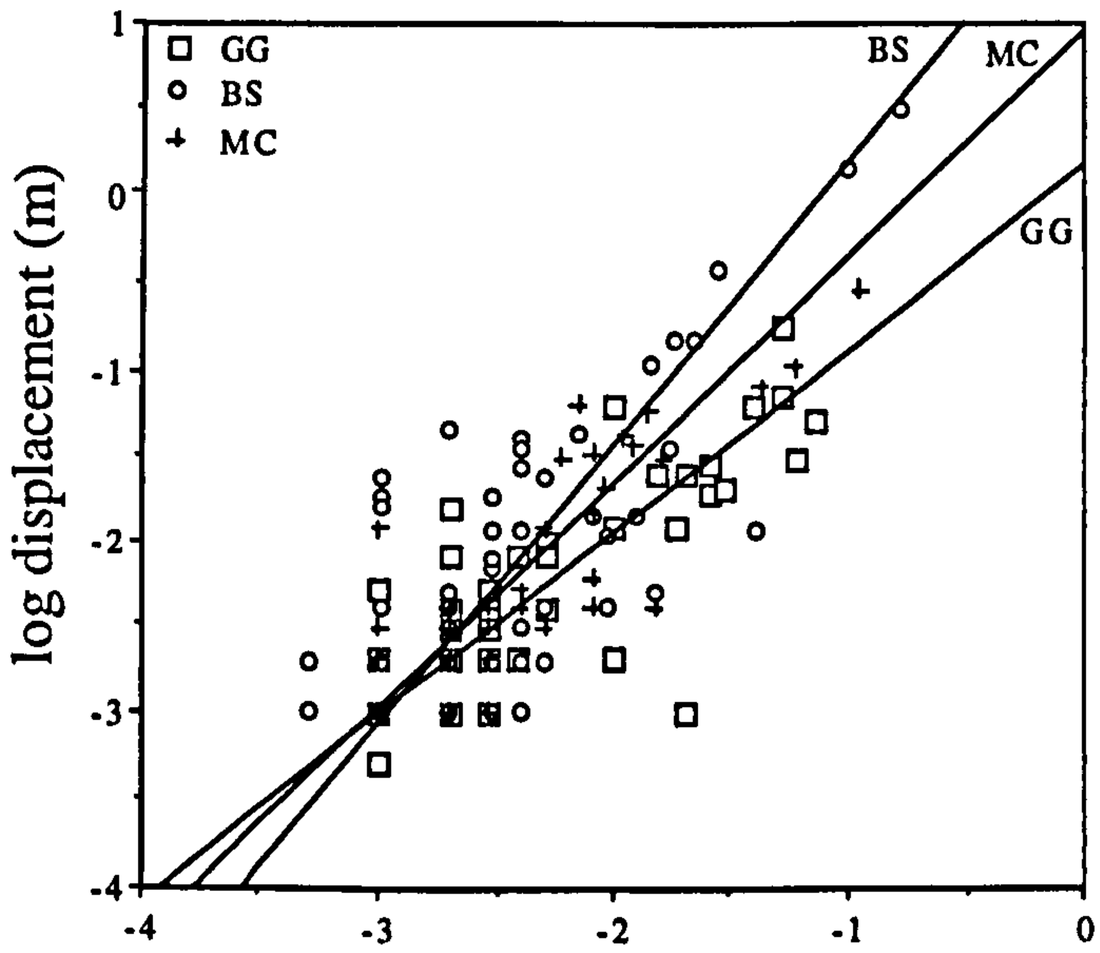

Figure 2.15. Log displacement vs. log thickness for faulting at George Gill (GG), Belah Scar (BS) and Molly's Castle (MC), including best fit relationships derived from the 1D cumulative displacement and thickness frequency plots (Figure 2.13).

Knott (1994) described a conceptual model of displacement / thickness scaling in high porosity sandstones in which a deformation bands grows into a geometrically similar zone of deformation bands (i.e. r=1) until, at a particular displacement, a slip surface is

formed. At this point, a large increase in displacement is accommodated with no additional increase in thickness. After a certain time, according to Knott's model, the slip surface becomes inactive, and subsequent growth is accompanied by further thickening of the fault, again with r=1, but now at a higher value of F. The displacement / thickness curve this growth model would produce is shown schematically on Figure 2.16a.

According to this model, an ideal fault system in a porous sandstone spanning the zone of bands / slip surface mechanical transition should contain two populations with different values of F, and both with $r = 1$. In reality, the displacement at which faults in a particular system form slip surfaces does not occur at a distinct threshold. This, coupled with the natural scatter of data in thickness populations means that the threshold itself cannot be resolved, and the entire system appears as a single population with a value of $r > 1$. The approximate positions of the three systems with respect to an idealised displacement /thickness growth path are sketched onto Figure 2.16a. Although all three samples contain approximately the same ranges in thickness and displacement (Figure 2.16b), the development of slip surfaces occurs at a lower

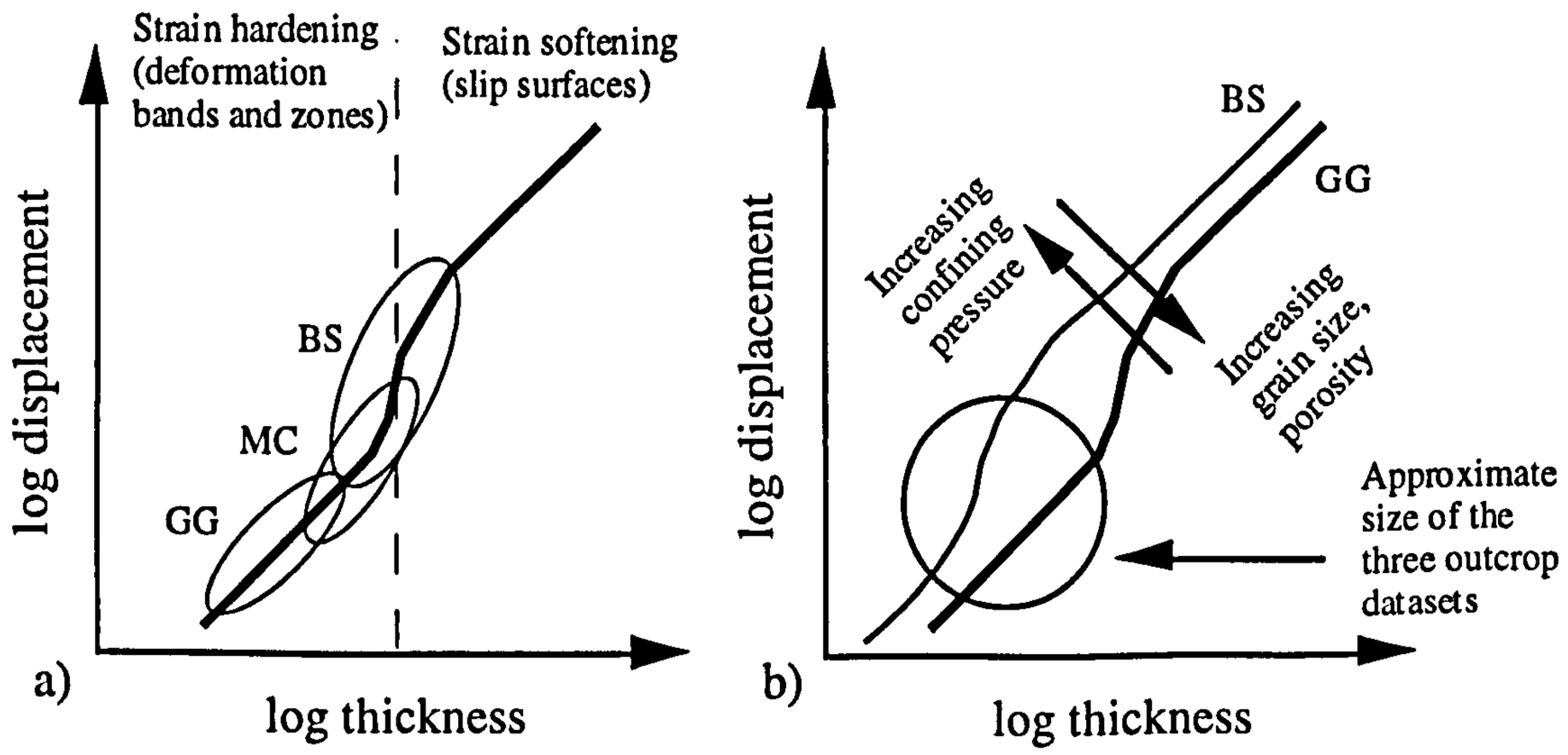

Figure 2.16. Schematic displacement / thickness scaling faulted porous sandstones. a) The location of the three field datasets according to the zone of bands / slip surface transitions. b) The relative influences on texture and pressure conditions on displacement / thickness scaling transitions. GG: George Gill, BS: Belah Scar, MC: Molly's Castle

thickness at Belah Scar, and at a greater thickness at George Gill. Figure 2.16b illustrates the influence of texture on likely ideal displacement / thickness scaling in sandstones. Although there is large scatter in the datasets, the comparisons in the best-fit scaling relationship conform with conceptual models of deformation band growth (Knott, 1994). As the sandstone becomes finer grained or less porous, localisation onto slip surfaces occurs at lower displacements and thicknesses. This is the factor distinguishing Belah Scar from George Gill. However the same effect may also be achieved by increasing the effective stress (the second control on cataclastic faulting), as discussed below.

Crawford (in press) produced fault gouges in well sorted, medium to coarse grained, high porosity Clashach Sandstone in a series of experiments at various confining pressures (representing depths in the range 600 m - 3000 m). The samples were subjected to a constant shear displacement of 1 mm, and the gouges formed at the lowest confining pressure had an average thickness of 1 mm, while those at the highest confining pressure was about 0.3 mm thick. A decrease in gouge thickness for a constant displacement implies an increase in angular shear strain of the gouge zone. This influences the permeabilities of the experimental gouges, which ranged between 2.5 orders of magnitude less than the unfaulted sandstone at lower confining pressure, to 3.5 at higher confining pressure. These values are comparable to the field measurements of deformation bands (Section 2.2.5). Faults with a higher angular shear strain have a greater degree of grain comminution resulting in thinner gouge zones but lower permeability. Assigning permeability values to faults is therefore intimately linked to assigning thicknesses.

2.4.8 Conditioning data to reflect transmissibility

In this study, all faults are assumed to be homogeneous, with a constant thickness and permeability along their length. This is certainly an oversimplification. A characteristic of deformation band systems is that they exhibit changes in thickness and texture over

short distances along fault traces, and both these influence the way in which thickness and permeability data should be conditioned prior to input into a flow calculation. The influence on flow of the natural data scatter on displacement / length cross-plots could also be significant.

The spread of data on a displacement / thickness cross-plot is often large (Figure 2.11), and a conventional fit to the data reflects the geometric average thickness at a particular displacement. As flow will occur disproportionately through the thinner sections of a trace of variable thickness (but constant permeability), a displacement / thickness correlation which reflects the geometric average thickness is inappropriate, and a relationship which reflects thickness weighted towards thinner sections of fault traces should be applied in flow analysis.

A potential solution is illustrated with a synthetic displacement / thickness dataset on Figure 2.17. This data has a spread of about 2 orders of magnitude displacement at any thickness, typical of field data (Figure 2.11). Curve 1 represents the best statistical fit to this data, calculated according to the method discussed in Section 2.3.5. The data has been separated into sized bins according to displacement. In each bin, the harmonic average thickness is plotted against the geometric average displacement to produce curve 2. This transformation therefore takes into account the inevitable scatter in the data with respect to the influence of this scatter on the transmissibility of individual faults. The best fit for this relationship (curve 2) has the same power-law gradient (r), but a higher value of F, than the untreated data.

A similar argument applies to permeability. Although the permeability of a population may be, on (geometric) average, 3 orders of magnitude lower than the host sandstone, data may be spread between one and four orders of magnitude lower. In this case, the most appropriate permeability value to assign to faults in a model in which all faults of a particular size are assumed to be identical is not the geometric average, but an average

weighted towards permeability highs, possibly using the arithmetic average. In natural fault systems, there may be mechanically induced spatial correlations between permeability and thickness. For instance, the asperity bifurcation model (Childs *et al.*, 1996) suggests a positive correlation between thickness and permeability. In such a case, it might be impossible to treat the variability in permeability and thickness independently, as the transmissibility of the fault at any point is a function of them both.

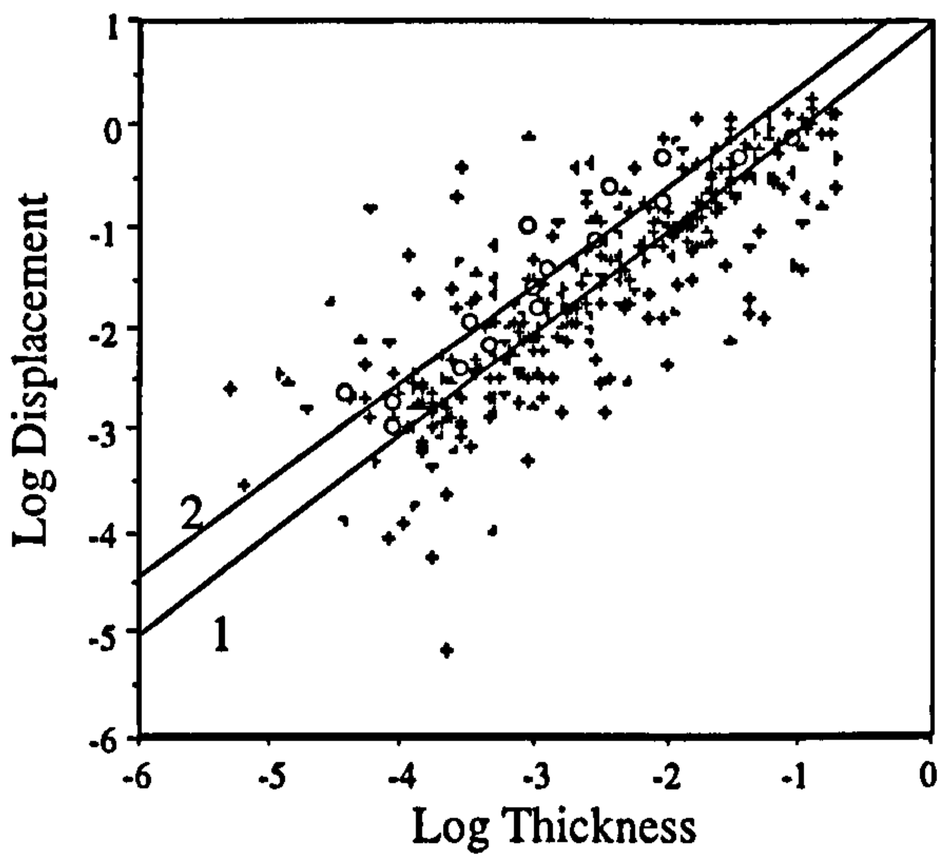

Figure 2.17. Conditioning displacement / thickness data for inclusion in flow analysis. Plot of log displacement vs. log thickness for a synthetic dataset (crosses), with the non-weighted correlation (Curve 1), and geometric average displacement vs. harmonic average thickness, according to different size bins (Curve 2).

2.5 Summary and discussion

The mathematical model of faulting is based primarily on a 1D cumulative displacement frequency relationship $N_1(D) = a_1 W D^{-c_1}$, which defines the number of faults larger than any displacement, likely to be encountered by a sample of length W in the ε_1 direction. The length and thickness of a fault of any displacement are determined by the relationships $D = BL^n$ and $D = FT^r$. This model therefore requires estimates of three system constants (a_1, B and F), and three power-law exponents c_1, n and r. The constant a_1 is the principal control on the overall fault density, and if not known can be determined as a function of brittle strain (ε_1, see Chapter 6).

Sub-seismic fault system properties in any particular reservoir, or portion of reservoir, must be extrapolated from available data. Seismic data give information about displacement and length scaling. A 1D displacement relationship ($N_1(D) = a_1 W D^{-c_1}$) is

determined from depth conversion of the interpreted seismic sections, and a 2D length relationship ($N_2(L) = a_{L2} W J L^{-c_{L2}}$) from analysis of the horizon fault trace maps. A 2D cumulative displacement frequency relationship ($N_2(D') = a_2 W J D'^{-c_2}$) must be determined from the seismic data, and then the method discussed in Section 2.4.5. may be used to determine the constants B and n. The conversion of cumulative size relationships between samples of different dimensions is discussed in Chapter 6.

Core data can give information about thickness and displacement scaling. The cumulative size frequency relationships obtainable from core are 1D, so may be used directly to give the constants F and r. The only relationship for which an extrapolation throughout sub-seismic scales may be validated is 1D displacement scaling, as this is the only relationship obtainable from both core and seismic. Considerably greater uncertainty is therefore attached to displacement / length and displacement / thickness scaling of sub-seismic faults.

Faults in porous sandstones occur in three distinct styles, with at least one mechanical threshold at a scale which cannot be resolved by either seismic or core. This threshold is the transition between zones of bands and slip surfaces, and the displacement at which it occurs is a function of rock properties and pressure conditions. In porous sandstones, it occurs in the displacement range 0.1 m < D < 2 m. The effect of this mechanical transition has been considered in terms of displacement / thickness scaling. In theory, a population of deformation bands and zones will have a lower value of F than a population of slip surfaces, but the same value of r (one). In practice, this effect is unlikely to be discernible in any single dataset, and the data which span the mechanical transition are most likely to form a single population with a larger value of r. Based on mechanical considerations, the scaling systematics observed at three outcrops may be explained in terms of the petrology of the sandstone at each. These are:

A) An increase in cumulative displacement frequency power-law exponent (c_1) as a function of increased sandstone porosity. This is believed to be a manifestation of the disinclination of small faults to be reactivated in more porous media (e.g. Underhill and Woodcock, 1987).

B) An increase in the displacement / thickness power-law exponent (r) for small-scale ($D < 1$ m) faults in less porous sandstones. This is considered a consequence of spanning the zone of deformation bands / slip surface threshold at a lower displacement in higher strength (less porous) sandstones (e.g. Knott, 1994).

Cumulative displacement, length and thickness frequency plots often display good power-law scaling distributions, but cross-plots between these parameters invariably contain tremendous scatter. This scatter is not due to measurement inaccuracies, it is a real property of fault systems, and therefore should be included in a fault system model. Typically, the length or thickness data for faults at a particular displacement covers a range between one to two orders of magnitude in a single system, or even when measured on a single fault trace (e.g. Foxford et al., in review). Individual datasets rarely span more than two orders of magnitude, so there is large uncertainty associated with determining the best statistical scaling relationships from cross-plots (e.g. Evans, 1990). A method for determining relationships between size parameters based on individual cumulative size frequency relationships is proposed, partly because size frequency relationships are easier to determine than cross-plot relationships, and partly because the method inevitably results in a coherent mathematical model. However the simple relationships $D = BL^n$ and $D = FT^r$, no matter how they are derived, contain no information about the variability in the system. Simple weighting methods have been suggested to account for the effects of this variability on flow, and sensitivity to this effect is investigated in Chapter 7.

The statistically most robust scaling relationships may not be the most appropriate for flow calculations. The displacement / thickness relationship used should be weighted towards thins. The displacement / length relationship should be weighted towards longer faults, as these have a disproportionate effect on permeability impairment (e.g. Heath et al., 1994). Ideally, therefore, the statistically most robust power-law relationships should be modified to ones with the same power-law exponents (n and r), but a lower displacement / length constant (B), and a higher displacement / thickness constant (F). Further work is needed to determine a rigorous method for making these modifications, which are necessary in order to incorporate the significance of the variability in any dataset.

Several facts emerge from the considerations in this Chapter.

A) There is large uncertainty in determining optimum scaling relationships from any dataset, even over the scale range at which the dataset was collected.

B) There is even greater uncertainty associated with extrapolating these relationships to different length-scales. Scaling systematics of small-scale faulting are controlled by the mechanical properties of the medium in which the faulting is contained. Scaling relationships derived from seismic include only large faults, which might span several mechanically distinct horizons of the reservoir. The use of lithology specific outcrop analogue information may reduce this uncertainty.

C) The best statistical relationship for geometrical scaling is not necessarily the most appropriate for flow estimation due to the natural variability in fault systems. There is no general method available to make the necessary modifications, and a simple scheme is proposed.

In the light of this uncertainty, attempting to assign a single set of scaling relationships to a sub-seismic fault system in a reservoir is naive. Several possible scaling models should be produced, and the flow impairment of each model calculated. These results can then be used to determine the most likely effect on flow, but can also be used to quantify the inherent uncertainty in this estimate. This is the approach taken in Chapter 7.

2.6 The fault scaling model

This chapter has defined the *input* to the fault scaling model used in this work. These input are the unknown terms in Equations 2.2, 2.5 and 2.6. The 1D cumulative displacement frequency relationship (Equation 2.2) contains a term which relates to the over-all fault density (a_1), and a term which defines the distribution of this density between faults of different length-scales (c_1). The displacement / length and displacement / thickness relationships (Equations 2.5 and 2.6) each contain two terms with which the sizes of faults of any displacement may be determined. Any set of these six variables is sufficient to characterise quantitatively the scaling aspects of fault systems which are used in the flow calculation.

The details of transforming this model from a continuous to a discrete hierarchy is the subject of Chapter 6. After this transformation, the fault system is defined by a specific number of faults of specific lengths and thickness, equally divided between two specific orientation populations, contained in an area of a particular size, all at four different length-scales. Chapters 3 and 4 concern modelling the spatial arrangement of these faults.

CHAPTER 3

QUANTITATIVE FAULT SYSTEM CHARACTERISATION PART 2: FAULT GEOMETRY

3.1 Geometrical fault system characterisation

Dershowitz and Einstein (1988) differentiate between two classes of fault system characterisation. *Primary characterisation* concerns properties of the system for which all faults may be considered independently. *Secondary characterisation* requires consideration of the system as a whole, and concerns aspects such as clustering and connectivity. A primary description of a fault system comprises rose diagrams or stereographic projections which define fault orientations, and cumulative displacement, length and thickness frequency distributions which define the fault size parameters. Whilst these distributions incorporate the scaling and orientation characteristics of the system, they contain no information about the spatial correlation of the faults. The chapter concerns secondary characteristics, and their effect on flow. Primary characteristics govern fault density, which determines the transmissibility of the systems (see Section 1.3). Secondary characteristics govern the tortuosity of flow through the system.

3.1.1 Sub-seismic fault modelling

From analysis of the seismic data in a field, a fault trace map can be produced which represents an interpretation of all seismically resolved faulting in the area. In addition, portions of the reservoir with different fault scaling and frequency systematics can be identified (e.g. Figure 2.8). From these, the absolute number and shape of sub-seismic faults present in any portion of the reservoir can be estimated (as discussed in Chapter 2), but their positions in space cannot. The principal method for populating sub-

seismic fault maps was discussed in Section 1.2.1. These methods usually incorporate secondary characteristics of the system crudely, if at all.

Consider the procedures necessary for producing a map which attempts to reproduce the secondary characteristics of sub-seismic fault system. This map must honour first the primary characteristics of the system, and therefore must contain N_1 faults of length L_1, N_2 faults of length L_2, etc. The map must also honour the orientations of the faults, which may be achieved by drawing the orientation of each fault from a probability distribution function (PDF). The faults must be placed probabilistically, within the deterministic framework of the seismically interpreted faults. The spatial arrangement with which the sub-seismic faults are placed must be governed by a set of rules. From a geometrical point of view, it may seem logical to place the largest faults first. These faults could be placed at random, or could be attracted to, or repelled from each other, or the seismic faults (e.g. Munthe *et al.*, 1994). Deciding the placement of faults requires a conceptual model of fault clustering, and *damage zones* could be invoked. A damage zone is conceptualised as a roughly elliptical aureole of smaller faulting around a larger fault (e.g. Koestler, 1994; Knott, 1996; Welbon *et al.*, 1996). Delegate discussion at a recent conference which included a session on damage zones (Faulting, Fault Seal and Fluid Flow in Hydrocarbon Reservoirs, Leeds, September 1996) highlighted that damage zones are far from ubiquitous and seem to depend very much on the structural history of the particular fault system, and even the particular fault being studied. In short, no one knows if, and why, any fault will have a damage zone. Our hypothetical algorithm, however, must contain rules governing the shape and size of the damage zone, and must decide on the proportion of faults of any size contained in the damage zone of each fault. A proportion of faults will not be contained in damage zones. Should these faults form clusters at their own length-scale, and if so, what proportion of them? Should these clusters form shear zones, and if so, what sort of shear zone?

It is evident that a plethora of rules need to be incorporated into a sub-seismic fault placement algorithm, but the geological understanding of the geometrical properties of fault systems is simply not sufficiently advanced for these rules to be deduced. It is impractical even to attempt to do so, as these rules are most probably not transferable between different fault systems. Cowie *et al.*, (1996) stress the necessity (and under-emphasise the difficulty) in reconciling site-specific observations and global scaling when predicting models of sub-seismic faulting.

Any numerical model of a fault or fracture system cannot contain all aspects of the system. Models must therefore be designed to incorporate aspects which are most pertinent to the application for which the modelling will be performed. As discussed in Section 1.3, integration of (geological) reality with (engineering) tractability, inevitably requires that idealisations and simplification be made to the system. In the modelling used in this thesis, fault system geometry is considered at a single length-scale, as the fault scaling is converted into a discrete hierarchy (Section 2.2.3). The fault model is discussed in the following Section.

3.1.2 The hierarchical fault model

In the discrete hierarchic approximation of the fault system, every level in the hierarchy considers the flow response to all faults in a scale-range $D_p < D < D_q$, where D_p and D_q are the sizes at which the continuous hierarchy is separated. These are generally taken at fault displacements one order of magnitude apart. Using Equation 2.3 (which relates fault density to length-scale), the total number of faults in this displacement range which are contained in a particular area is determined. Equations 2.5 and 2.6 (which link fault displacement to length and thickness) determine the total length and thickness of all faults in the scale-range, contained in this area. These totals are divided equally between the total number of faults present. Therefore the hierarchic model represents the continuous faulting over the length-scale interval, as a particular number

of faults of identical lengths and thicknesses, contained in a particular area. Algebraic details of these transformations are given in Chapter 6.

The hierarchic model honours all definitions of fault density: the number of faults in an area (of dimensions m^{-2}), the length of faults in an area (of dimensions m^{-1}) and area of fault gouge in an area (dimensionless) are identical in the continuous and discrete models. Therefore the approximation honours the transmissibility effect of the faulting (see Section 1.3). In order to honour the tortuosity effect of the faulting, the spatial arrangement of the faulting must be considered. The purpose of this Chapter is therefore:

A) To review methods for modelling the spatial distribution of faults and fractures (Section 3.2).

B) To investigate the spatial arrangement of fault in natural systems (Section 3.3).

C) To determine a method for honouring the geometrical effects of natural systems on flow, within the framework of the overall fault system model (Section 3.4).

This chapter concludes that, for single phase flow, all geometrical effects may be incorporated in a quantitative fault connectivity term. This term can be included as a parameter within Boolean network modelling methods, and represents a significant advance towards incorporating critical geological information in engineering flow models.

3.2 Numerical models of fault systems

This Section gives a review of the techniques available for modelling fault or fracture systems. Consideration of simple 1D fracture systems illustrates the various approaches (Section 3.2.1). 2D networks are discussed in more detail in the remainder of the Section. This discussion focuses on the forms of fault nodes which various methods produce. Three kinds of node are important in fault system characterisation (Figure 3.1), fault intersections (X-nodes), fault splays (Y-nodes) and isolated fault tips (I-nodes).

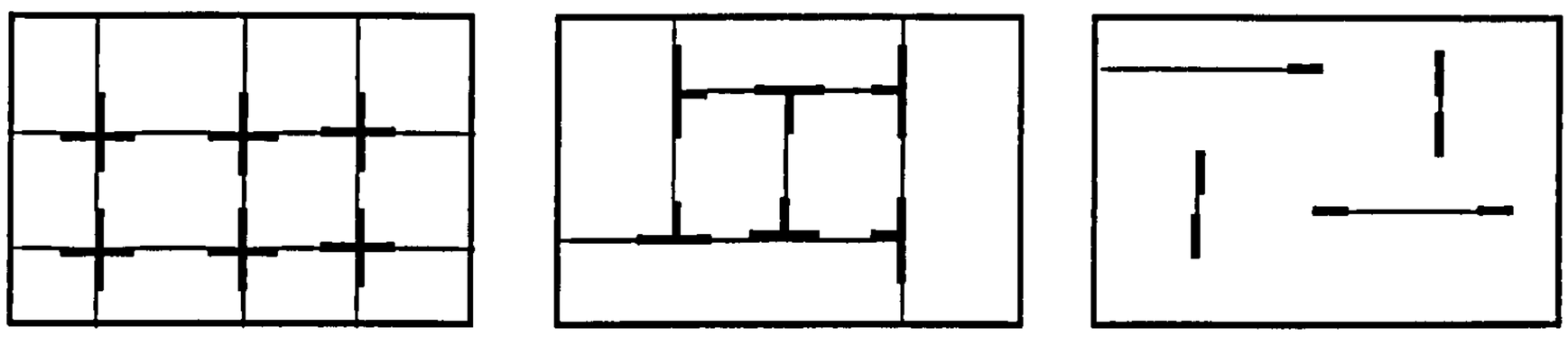

Figure 3.1. The three fault node types.

3.2.1 1D fracture networks

Approaches used to generate numerical fracture systems have included deterministic, stochastic, fractal or process modelling methods. These are discussed in turn. A *deterministic model* has a fixed set of rules which control the structure of the system. By knowing the rules, the exact details of the system can be determined. Figure 3.2a shows a simple 1D deterministic model in which all fractures are equally spaced and the system is completely characterised by the rule governing spacing. The two systems in Figure 3.2b have the same average spacing as the deterministic network, but these fractures are generated according to a *stochastic processes*, by random sampling from probability distribution functions (PDF). In a stochastic model, only the statistical characteristics of the system can be established if the rules used to generate the system are known. The most common stochastic process is a *Poisson process*, used in all the stochastic methods discussed here.

In a Poisson process, events (fractures, in this case) are distributed according to a uniform rectangular distribution, which is a continuous distribution over the interval $[a,b]$, with a probability distribution function $f(x)=1/(b-a)$. The number of fractures within any portion of the network depends only on the sample length being considered and the total number of fractures placed. Details of the statistics of 1D and some 2D systems generated by Poisson processes are given in Grady and Kipp (1987). Because Poisson processes use PDFs to determine aspects of the system, systems generated from the same rules are different. Each is a *realisation* of the system, and there is no way of determining the specific details of the system in any particular realisation. Statistically, however, all realisations generated by the same set of rules are similar, provided a large enough system is generated for it to be representative.

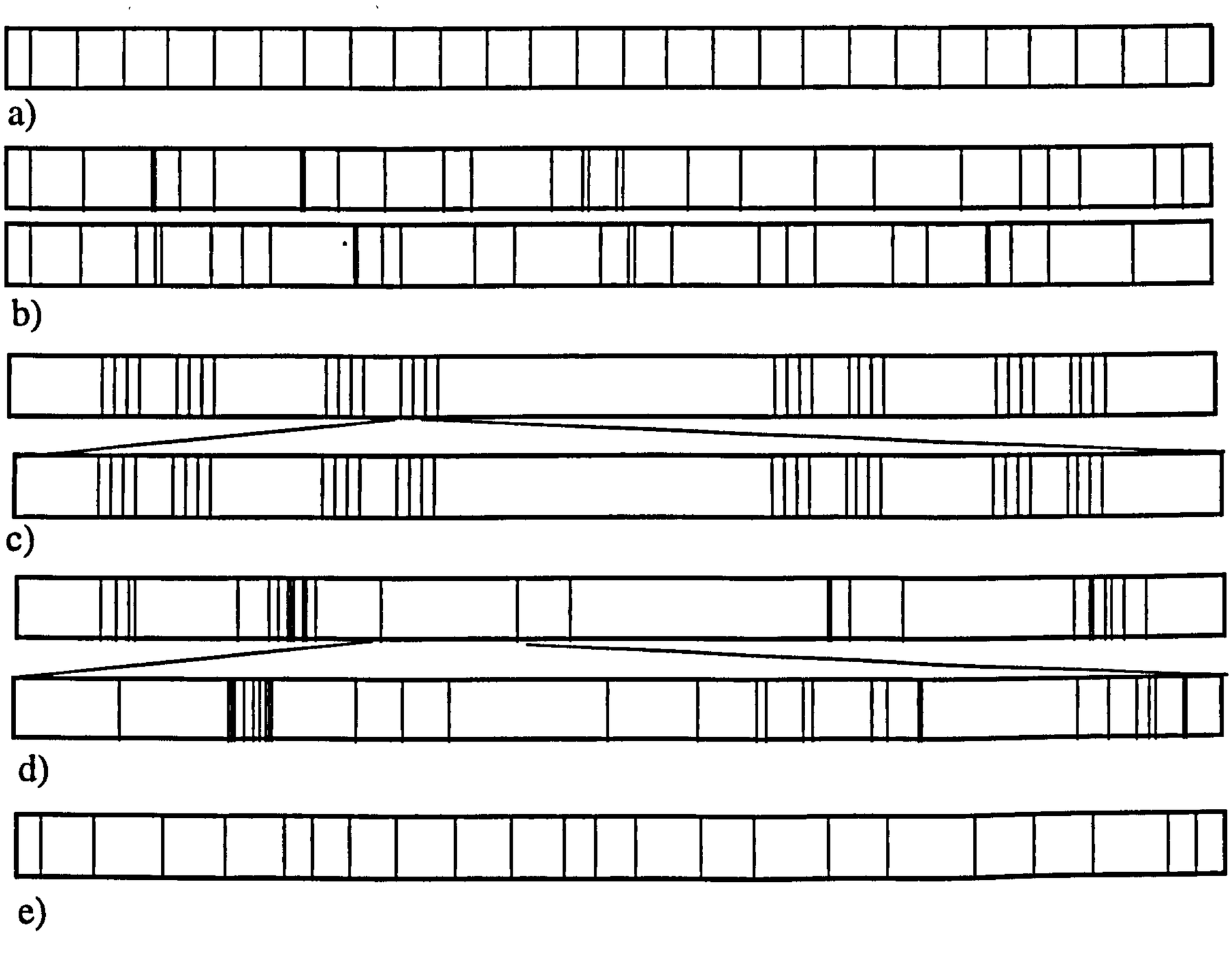

Figure 3.2. 1D fracture networks. a) Deterministic network. b) Two realisations of a network generated by the same stochastic process. c) Two scales of a deterministic fractal network. d) Two scales of a stochastic fractal network, generated with the same stochastic processes at each scale. e) An hypothetical realisation of a process model based on jointing in a single bed of uniform thickness.

Fractal networks may be generated with either deterministic or stochastic methods, and are designed to incorporate structure over several length-scales. Fractal systems are often defined qualitatively by saying that whatever scale the system is observed at, the same fracture density is apparent. It is important to note that this is only true of specific portions of the network. For instance, the central portion of Figure 3.2c will contain no fractures whatever the magnification, as the fractures in fractal networks are intrinsically clustered. Figure 3.2c shows the classical 1D fractal known as Cantor's dust. Fractures are placed every third-length of the model, the central portion is then ignored, and the process repeated on the other two portions. This is a completely deterministic fractal network. Figure 3.2d shows a stochastic fractal realisation based on Cantor dust. In this example, a Poisson sampling process is incorporated every time a distance is divided by three, resulting in a fracture network combining stochastic variations and fractal scaling.

Process models attempt to reproduce the spatial arrangement of fractures in response to mechanical, rather than geometrical controls, and the system evolves as a function of boundary and internal conditions through time. A simple 1D example is conceptualised briefly. Ladeira and Price (1981) suggested a mechanical basis for the empirical relationship between fracture spacing and bed thickness, including dependence on pore pressure (p) and rock tensile strength (T). These could be incorporated in a process model with pore pressure as the boundary condition. As p is gradually raised, the conditions necessary for fracture will occur (when $p > (\sigma_3 + T)$; see Section 2.1.1). At this point, a Poisson process is used to determine exactly where the fracture forms. Upon formation of this fracture, there is a lowering of p in the system as a whole, and, as the pore pressure is raised again, it is drained by the fracture. If the fracture is able to transmit fluid out of the system only at a particular rate, the fracture pore pressure cannot increase sufficiently to form another fracture within a particular distance from the existing one. Figure 3.2e shows a possible realisation of this process model, the

geometrical characteristics of which lie between the deterministic and stochastic networks (Figure 3.2a, and b).

3.2.2 Deterministic models

Fracture system models developed in petroleum engineering are geometrical conceptualisations. They have proven useful in flow simulation as multi-phase solutions exist with which the relative influences of matrix and fracture storage and flux can be represented numerically (e.g. Warren and Root, 1962; Kazemi, 1969). Geometrically, a few variables define the system, and look-up charts (e.g. Reiss, 1980) relate these to single phase absolute permeability and porosity. Nelson (1987) proposed using nested models incorporating hierarchical fracture systems with different spacing systematics, in an attempt to introduce more variability. Such systems, however, remain inherently unrealistic, and the geometrical parameters which define the systems have no geological meaning.

3.2.3 Stochastic Tessellation models

There are two distinct families of stochastic model; tessellation models (often called fragmentation models) and Boolean models. Discussion about the stochastic models is limited to 2D, but all these methods can been extended to 3D.

The fundamental feature of all tessellation models is that at some point during their derivation, a tessellation model consists of completely enclosed areas. The simplest tessellation models consist of infinite lines whose position and orientation are selected by independent Poisson processes (Figure 3.3a). The assumption of infinite fractures is clearly over-simplistic, and only X nodes are present.

Grady and Kipp (1987) discuss a method they call "fragmentation by construction", shown on Figure 3.3b. In this method, every line has an origin selected by a Poisson point process, and each line is censored beyond intersections with other lines already

placed. This network therefore contains a hierarchy of fracture lengths, and as more fractures are added to the system, they become progressively shorter. All fracture intersections are Y-nodes, and no I-nodes are present. Grady and Kipp were concerned with particle size distributions during catastrophic fragmentation, rather than gradual development of a fault or fracture system over geological time. Their tessellation models, therefore, though elegant are not exportable to petroleum applications.

Other modifications are shown on Figure 3.3c, and d. In a 2D Veneziano Model, Poisson points are produced on each Poisson line (at a lower density than the set of points defined by the intersections of the lines), and these points define a set of triangles. A third Poisson process marks each triangle as fractured or unfractured, and

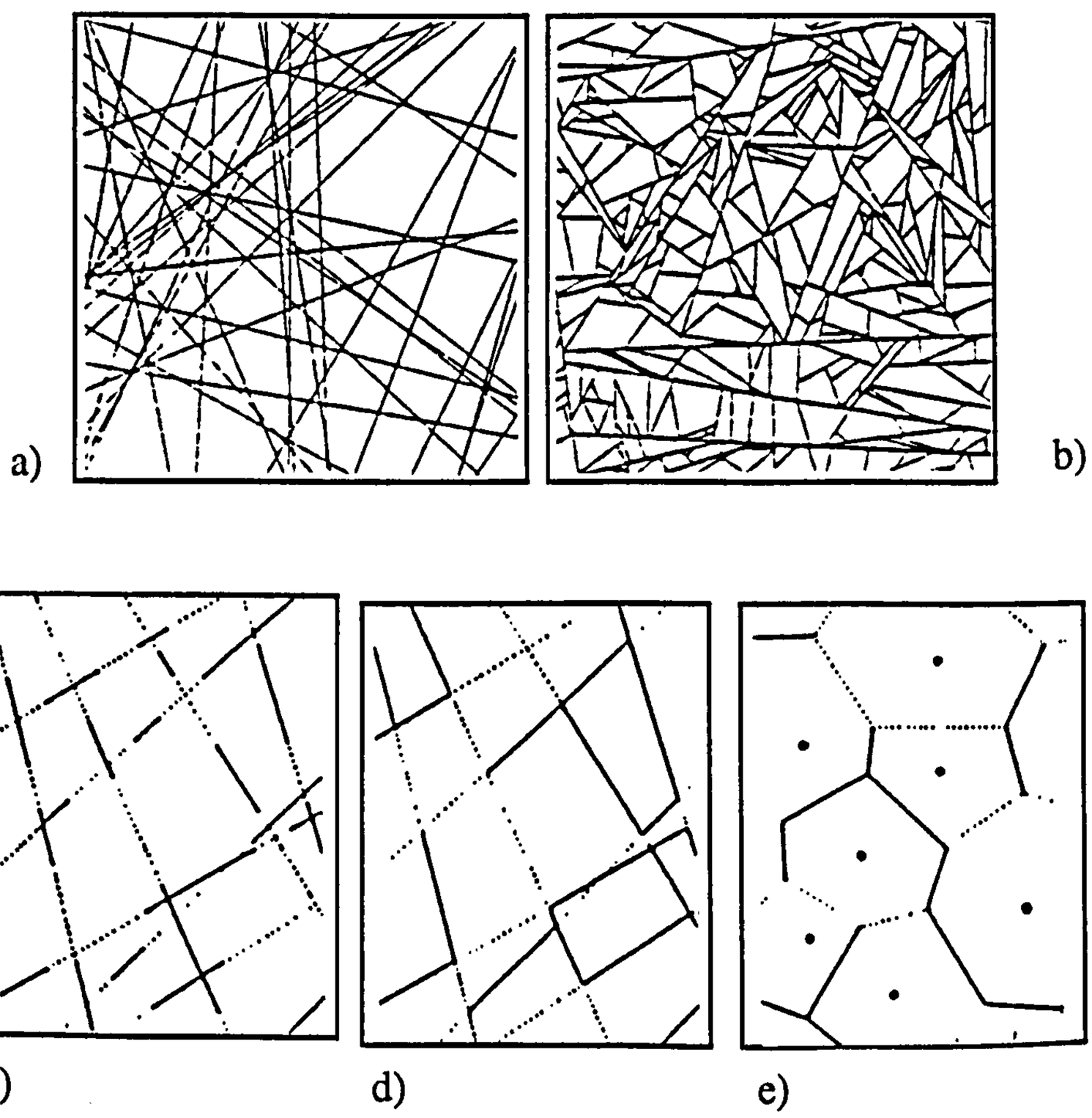

Figure 3.3. Stochastic tessellation models in 2D. a) Simple Poisson lines. b) Fragmentation by construction. c) The Veneziano model. d) The Dershowitz model. e) Voronoi network. (a, b from Grady and Kipp, 1987; c, d, e from Chiles and de Marsily, 1993).

fracture trace segments within each triangle are removed or retained accordingly. A Veneziano model therefore produces I and X nodes, in a proportion which depends on how many traces are removed. In a 2D Dershowitz model, the intersections of the Poisson lines defines a set of points, and each line is sub-divided into segments at these points. A second Poisson process removes or retains each of these segments. Therefore the Dershowitz model has significant advantage that all three node types are produced.

Another group of tessellation models involve Voronoi polyhedra (Figure 3.3e). The simplest construction involves generating a set of Poisson points, and "growing" grains from these points at a constant rate. When two grains come in contact, growth is stunted. Dershowitz and Einstein (1988) discuss the relative merits of combinations of deterministic and stochastic points and growth rates, however these networks are generally inappropriate for fault systems (with the exception of the polygonal fault systems recently described by Cartwright and Lonergan, 1996). As in the Dershowitz model, edges can be removed (Figure 3.3e), and in this case Voronoi models contain I and Y nodes.

A major disadvantage of tessellation models is that fault length distributions cannot be controlled, as the models are based upon segments of Poisson lines. Therefore, fault density can be honoured in terms of number of fractures per area, but not in terms of trace length per area. Descriptions of all these models in 3D are given by Dershowitz and Einstein (1988) and Chiles and de Marsily (1993).

3.2.4 Stochastic Boolean models

The fundamental difference between tessellation models and Boolean models is that tessellation models (with the exception of Voronoi models) rely on Poisson line processes (Poisson plane processes in 3D), while Boolean models rely on a Poisson point process irrespective of the dimensions considered.

A simple 2D Boolean model is shown on Figure 3.4a. A Poisson point process determines the centre of each fracture, and the length and orientation of the fractures are then chosen from PDFs. This technique results in a system which is the antithesis of those produced by the fragmentation by construction method (Figure 3.3b). Boolean systems contain only I and X nodes, and this is their main disadvantage. Considerable sophistication can be included in these models, particularly through incorporation of clustering systematics (e.g. La Pointe and Hudson, 1985; Long and Billaux, 1987). Figure 3.4b shows an example of a Boolean reconstruction of fracturing in a chalk

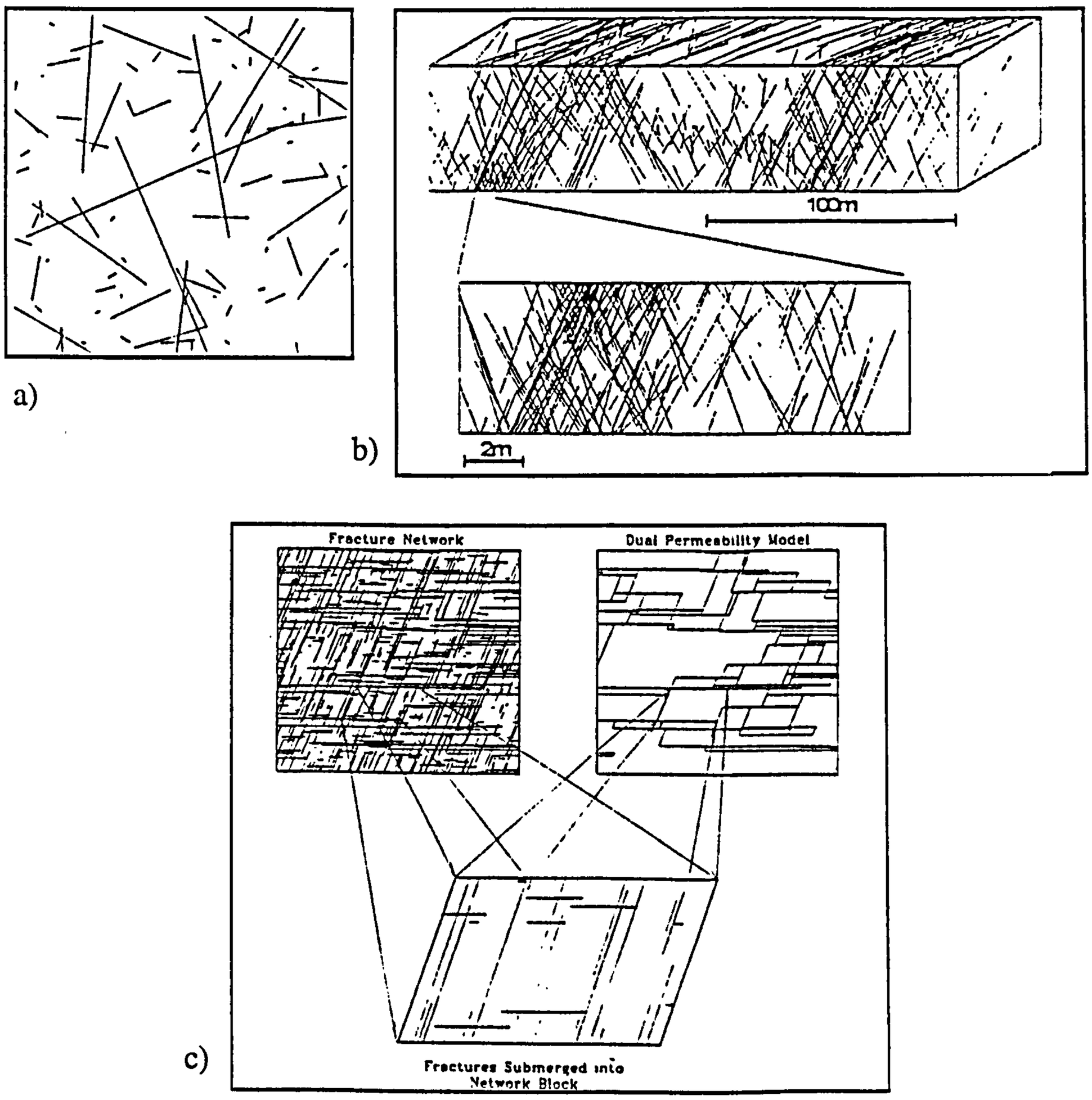

Figure 3.4. Boolean methods for generating fracture networks. a) Simple 2D system, from Balberg (1986). b) 3D system incorporating information from field characterisation. From Koestler *et al.* (1995). c) Nested dual permeability Boolean model. From Smith and Schwartz (1993).

quarry, based on an impressive 3D characterisation (Koestler *et al.*, 1995). This model includes length distributions, orientation distributions, 3D density distributions, lithological controls and damage zone concepts.

Many applications of Boolean modelling to fracture flow are reviewed by Smith and Schwartz (1993), who discuss the example shown in Figure 3.4c. In this nested model, the smaller fractures are too frequent to be modelled discretely, but they are, nevertheless, significant to the flow in the entire model. They are therefore incorporated as equivalent flow properties in network blocks in a dual-permeability model. The great advantage of Boolean models is their tremendous versatility, and the comparative simplicity of their construction. Their main disadvantage is their inability to reproduce the connectivity characteristics of real systems. This will be discussed further in Section 3.4.

3.2.5 Fractal models

Fractal models can be either deterministic or can involve stochastic processes. One deterministic method (Barnsley, 1988) involves using *iterative function systems* (IFS). Details of applying the method to generate fracture system are given by Hobbs (1993). A basic template is constructed, and undergoes a series of *affine transformations*, which are coded into the IFS. Transformations continue until the system approaches the desired attractor, which is a fractal object representing a fracture system. Figures 3.5a and b shows entirely deterministic systems generated by applying different IFS to the same template (Hobbs 1993).

A series of papers by Acuna and Yortsos (e.g., 1991, 1995) describe combining IFS methods with probabilistic processes, to generate stochastic fractal fracture systems in 2D and 3D, which are used to characterise fractal pressure transients. Modelled pressure transients are compared to oil-field well-tests to determine an optimum fracture generation routine. Figures 3.5c and d show two of these stochastic fractal systems,

which represent systems with different size frequency power-law exponents. Clearly IFS methods have a strong practical value and research using these techniques will doubtlessly grow.

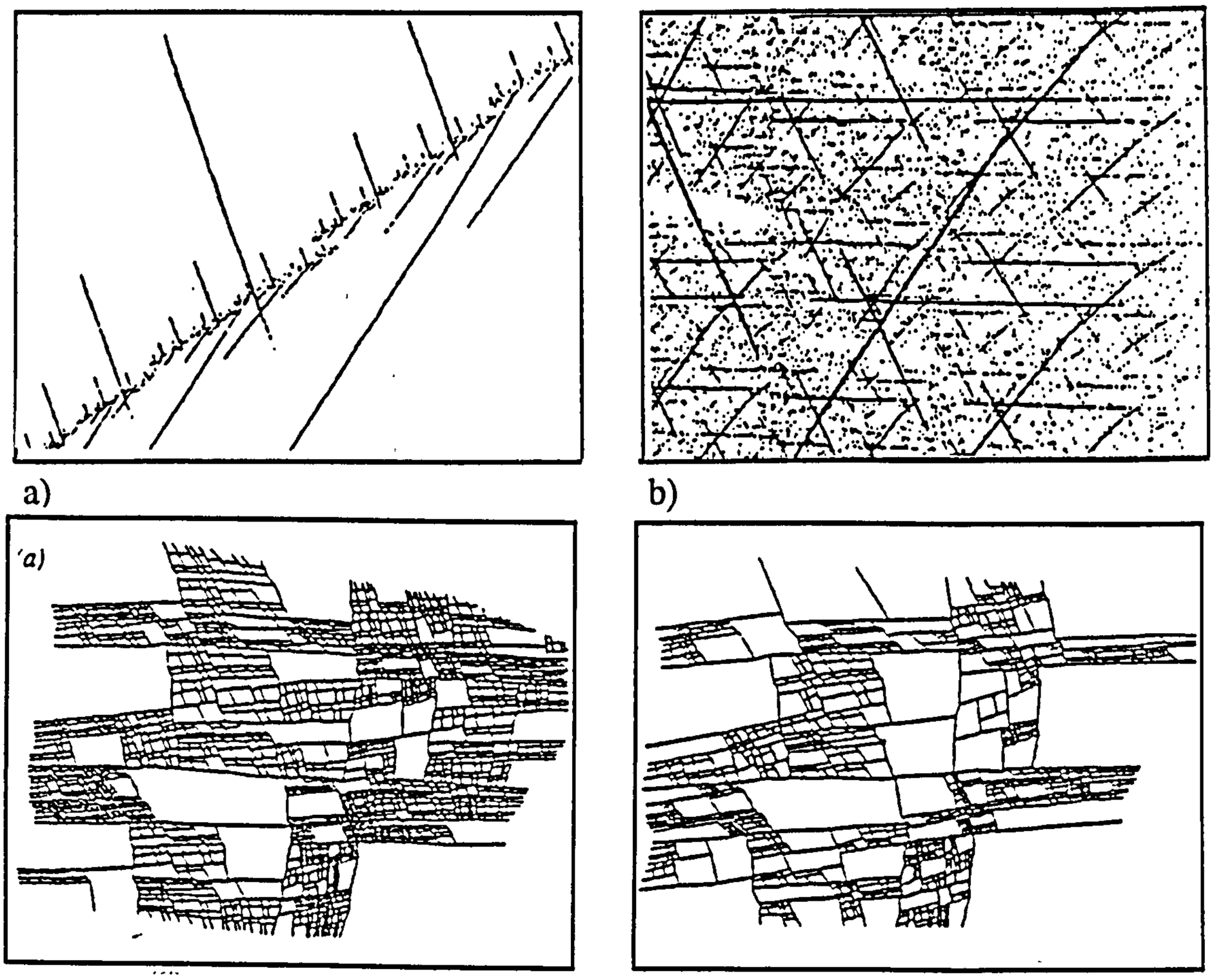

Figure 3.5. Fractal fracture networks generated with Iterated Function Systems (IFS). a), b) Two deterministic systems generated using different IFS on the same template. From Hobbs (1993). c), d). Two stochastic systems generated using the same IFS on the same template, but different PDF to determine size-specific density distributions. From Acuna and Yortsos (1995).

3.2.6 Process models

Process models of fault systems have been used primarily to test the conceptual understanding of the way in which fault systems grow (e.g. Sornette *et al.*, 1992; Cowie *et al.*, 1993, 1995). Figure 3.6 shows three stages in the evolution of the same realisation of a process model based on the development of normal fault systems (Cowie *et al.*, 1993). These models are based on *block-slider* models, in which coupled blocks interact under constant velocity boundary conditions. Interaction

between blocks is initially elastic. As the deformation in the volume increases, rupture and post rupture criteria control the development of numerical faults. Chaotic, self-organised interactions of blocks determines the eventual system structure. During the simulation run, initially random small flaws (Figure 3.6a) build up into complex fractal structures, which mimic the spatial characteristics of natural fault systems (Figure 3.6c).

These numerically generated systems are much more realistic than any of those figured above. To date, process models are only of qualitative use, and cannot be applied to any particular oil-field. The boundary conditions of real systems (through geological time) can never be defined with accuracy, therefore different realisations need to be made not only with the same boundary conditions, but also with a range of boundary conditions. Process modelling of fault systems is in its infancy, but the approach represents a significant step forward towards numerically generating realistic fault systems.

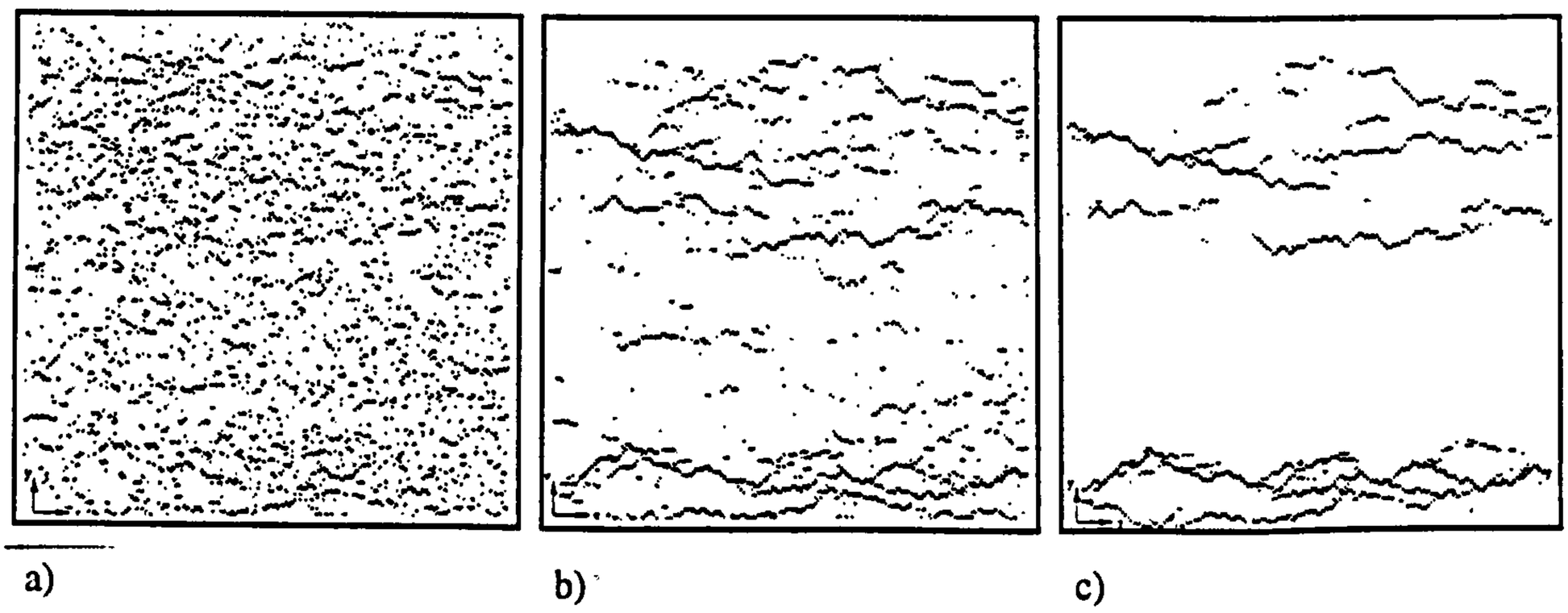

Figure 3.6. Three sequential maps of the evolution of a process model of a fault system. Grey-scale indicates accumulated displacement, and is normalised on each figure. From Cowie *et al.* (1993)

3.2.7 Summary and discussion

Several approaches to modelling fault and fracture systems exist. Stochastic approaches allow connectivity and orientation criteria to be incorporated in the models, and these approaches can be combined with fractal scaling methods to produce systems

combining scaling and geometrical parameters. All these methods rely on a detailed statistical description of the primary characteristics of the system which is being modelled. Secondary characteristics can only be incorporated in Boolean models if descriptions of these characteristics are available. The following Section discusses characterisation of a natural fault trace map, and discusses how such descriptions may be determined.

3.3 Geometrical characterisation of a fault map

In this Section, the geometrical characteristics of a fault trace map of from an exposed pavement are discussed. This discussion assumes that the primary characteristics (the number, lengths and thicknesses) of the faults are known. This discussion focus on:

A) Techniques available for the characterisation of spatial properties of fault systems.

B) Developing, conceptually, methods with which these spatial relationships might be modelled stochastically, such that their effects on flow may be captured in the model.

The mapped area is a pavement of Entrada Sandstone near Seven Mile Canyon in SE Utah. The area studied (Figure 3.7) lies about 500 m into the hanging-wall of the Moab fault (Figure 2.12b). The Moab fault has a displacement of about 700 m at this point (Foxford *et al.*, in review). The pavement is close to the tip of a synthetic fault with a trace length of around 4 km (Doelling, 1993). The fault trace map is shown on Figure 3.8. A fault map at any scale is not representative of the fault system (Section 1.4), and details of geometries observed at the scale considered can only be understood within the large-scale geological context of the area. Small-scale particulars of the system are better understood with reference to structures which are below the resolution of the map. Therefore both a large scale map containing the area of interest, and a small scale map of a single fault trace are included (Figures 3.9 and 3.10). Many aspects of fault

system geometry cannot be interpreted in 2D, so four 1D transects across the area have been taken (Data are in Appendix 1, Tables A1.4 - A1.7).

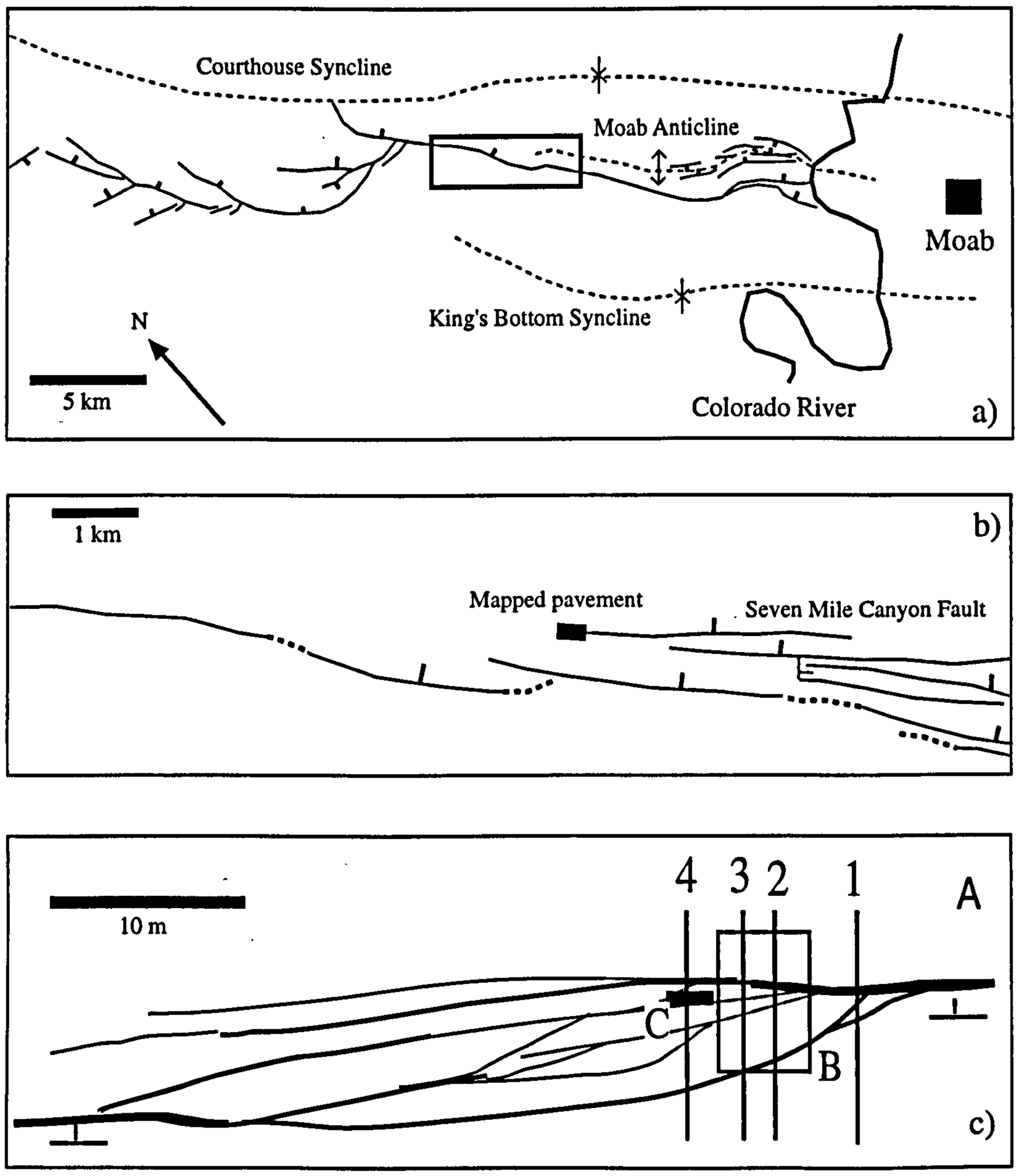

Figure 3.7. Seven Mile Canyon location and data synthesis. a) Semi-regional map of the Moab Fault, from Foxford *et al.*, 1996. b). Detail of the Moab fault in the Seven Mile Canyon area. From Doelling, 1993. c) Summary map of the pavement showing the Seven Mile Canyon dataset. Three maps: A. Large scale map of the entire pavement (50m x 15 m, Figure 3.9). B Detailed map of a portion of the pavement (6m x 4.5 m, Figure 3.8). C Map of a fault trace (1.3 m x 0.3 m, Figure 3.10). Four 10m 1D survey-lines (1-4).

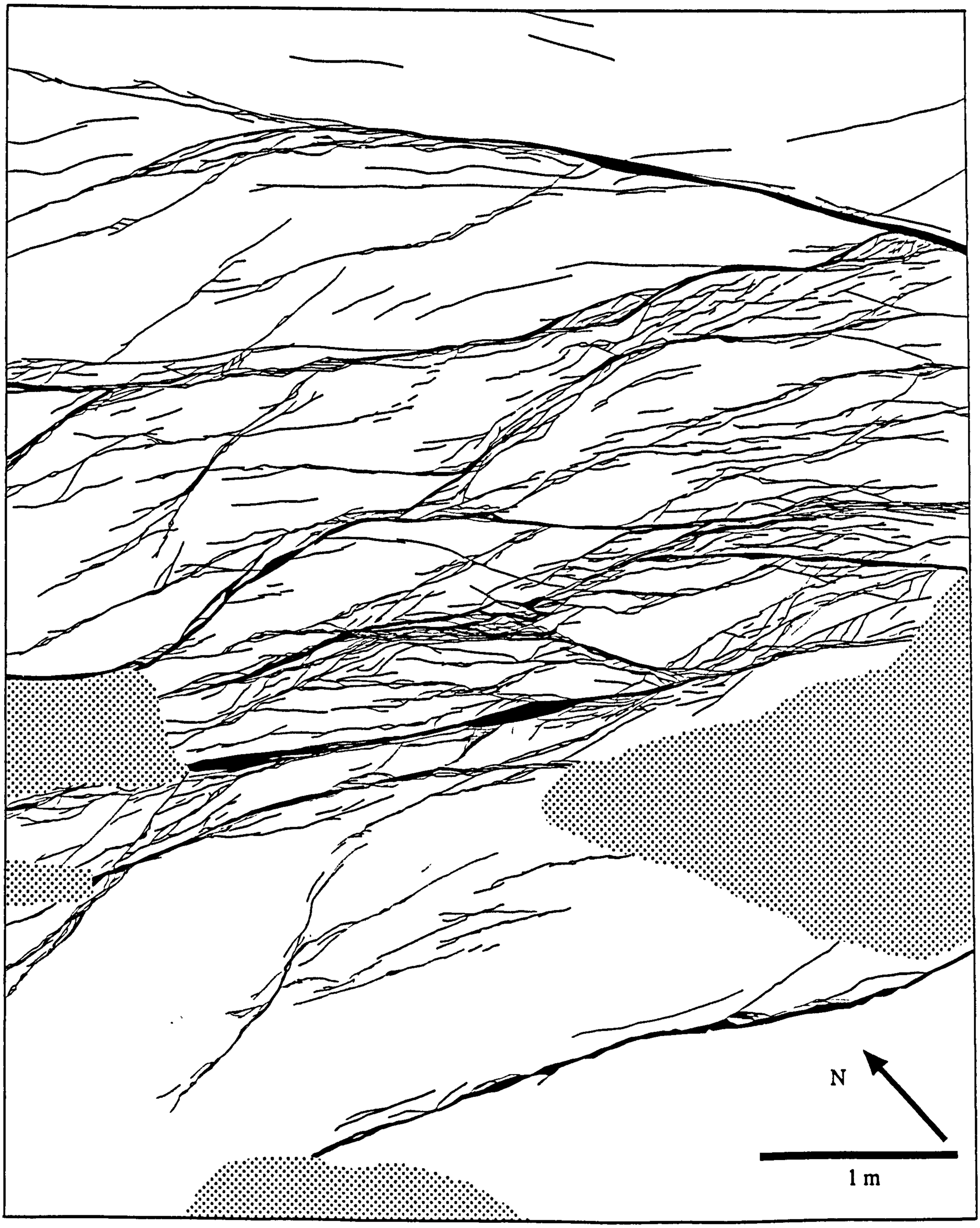

Figure 3.8. Fault trace map of a portion of the relay ramp at Seven Mile Canyon, S.E. Utah. See Figure 3.9 for location.

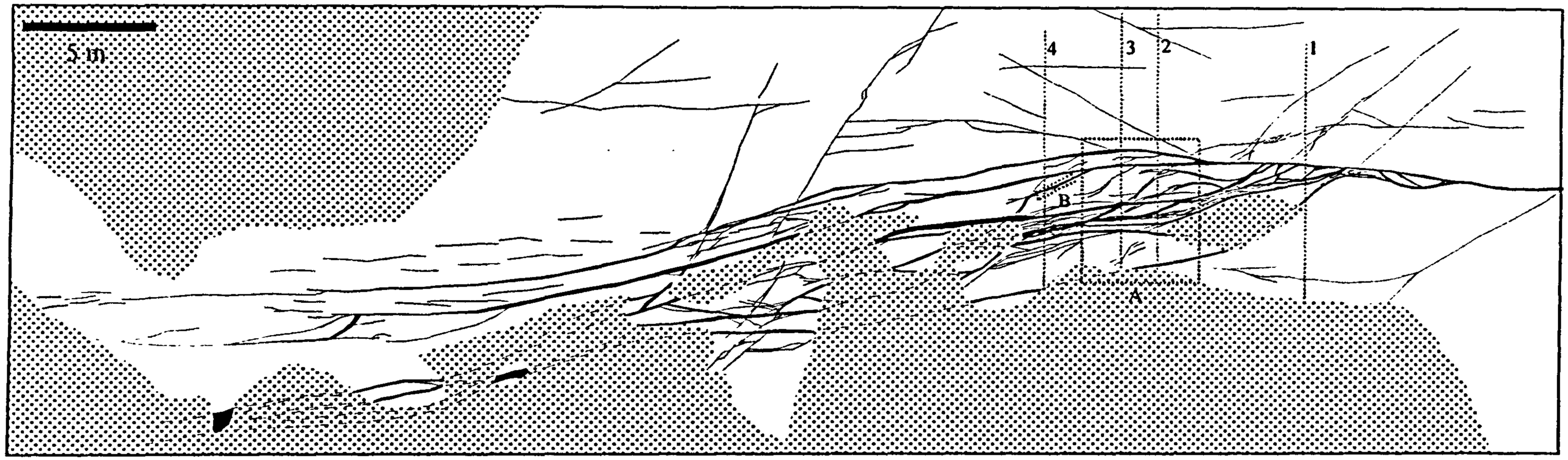

Figure 3.9. Fault trace map of the pavement at Seven Mile Canyon, showing the main structural elements of the relay. The inserts show the locations of Figure 3.8 (A) and 3.10 (B) and of the four scan-line surveys (1 - 4).

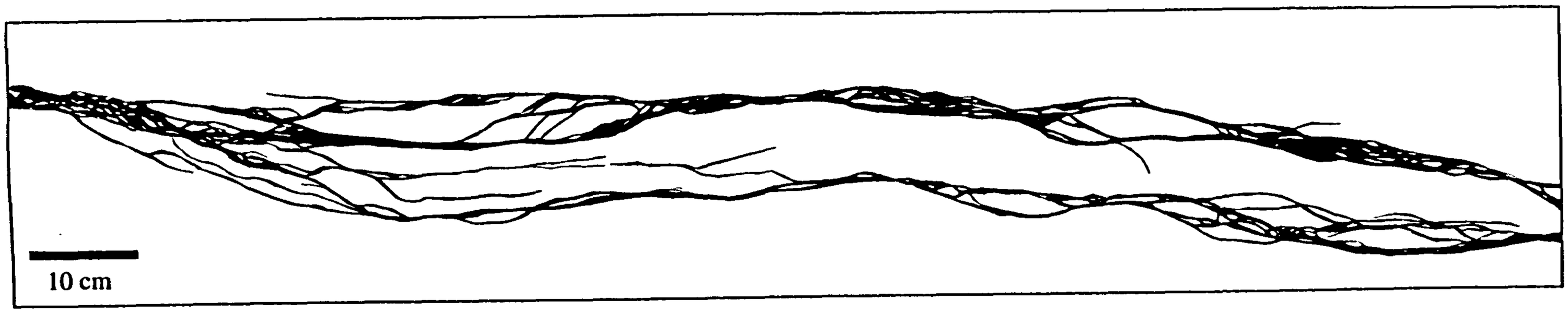

Figure 3.10. Detail of a fault trace, mapped at 1:1 in the field. See Figure 3.9 for location.

The displacement of the fault is approximately 4 m at the South-eastern edge of the pavement. Following the terminology of Peacock and Sanderson (1991), the system is a left-stepping relay structure. Structures of this kind are extremely common at all scales in this area, and have been called duplex-like structures by Cruikshank *et al.* (1991), and ramp structures by Antonellini and Aydin (1995). In a relay structure, displacement is transferred laterally from one dominant fault to another, resulting in a strained relay ramp between non-coplanar fault segments. The relay at Seven Mile Canyon steps approximately 10 m over a distance of 40 m. Most of the larger faults in this ramp are synthetic, a characteristic of structurally complex relay ramps (Peacock and Sanderson 1991). In the following Sections, various aspects of the spatial correlation of faults in the relay are addressed.

3.3.1 Fault clustering

Conceptual 1D end-member clustering models are shown in Figure 3.11. By comparing the spacing between pairs of adjacent faults, a first estimation of the clustering present in a system can be made. In a clustered system, a small spacing is most likely to be next to another small spacing, but in a random system there is no correlation between adjacent fault spacings. Figure 3.12 shows plots comparing the spacing of adjacent pairs of faults measured on the four 1D transects, of which three reveal spatial correlation of fault spacing. A positive correlation factor implies that the systems show some clustering, and the strength of this clustering may be qualitatively assessed as a function of the ellipticity of the confidence ellipses.

Spacing cross-plots are a useful method for determining if there is any clustering present in the system. If there is, semivariograms can be used to analyse this. While the cross-plots compared only adjacent fault spacings, semivariograms allow determination of correlation over large separations. A semivariogram is a plot of semivariance (γ), which is a measure of correlation, against lag, which is a measure of

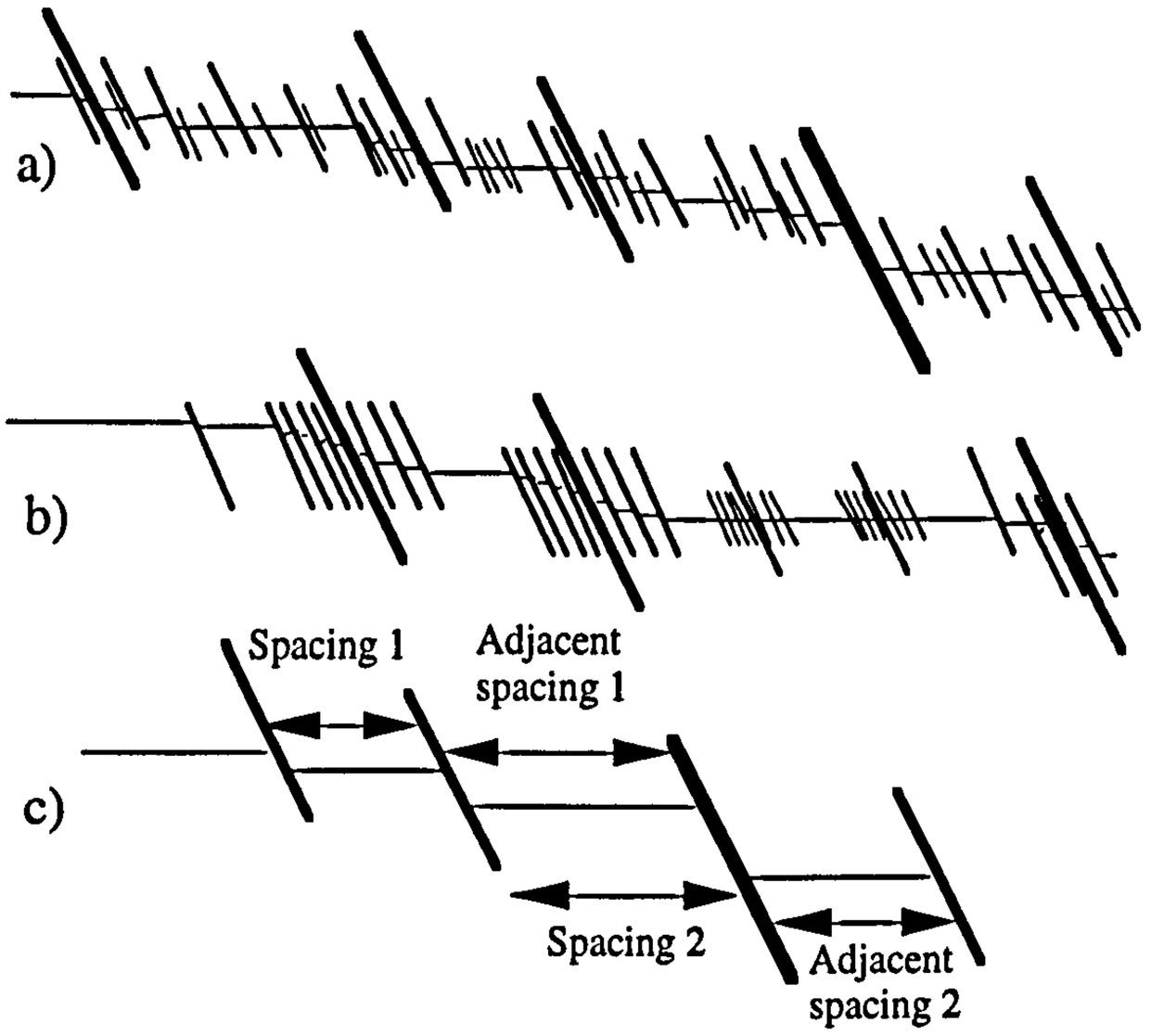

Figure 3.11. Characterising clustering from 1D surveys.

a) Unclustered system.

b) Clustered system.

c) Comparisons of separations between pairs of adjacent faults gives a quantitative indication of the clustering in the sample.

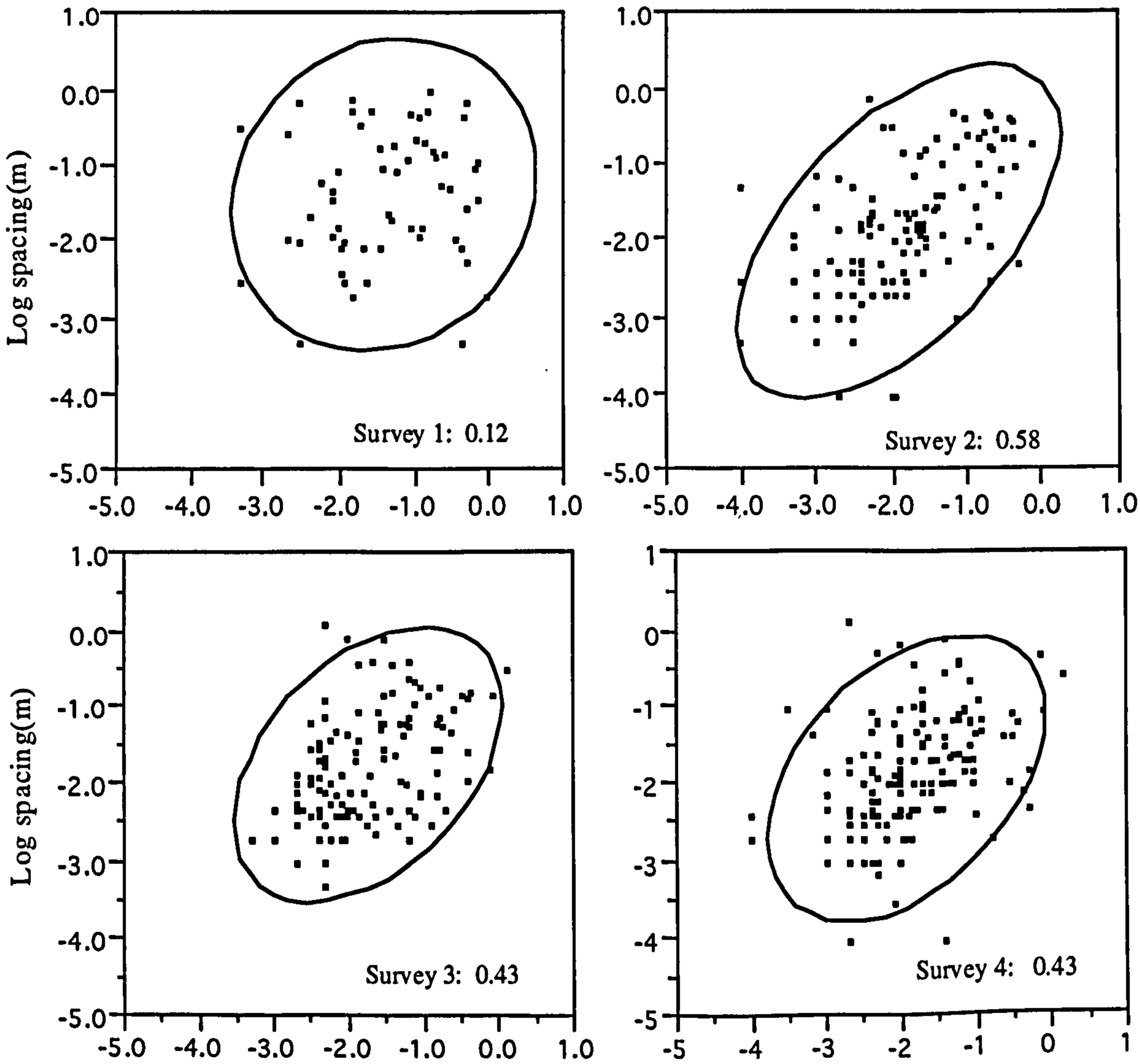

Figure 3.12. Log spacing vs. Log adjacent spacing for the four survey lines at Seven Mile Canyon. 95% confidence ellipses and correlation factor (*r*, the Pearson correlation coefficient) reported on each plot.

separation (e.g. Jensen *et al.*, 1997). The shape of the semivariogram reflects the strength and type of correlation present in the system.

The semivariance of a dataset consisting of n data of a particular property, z, is given by:

$$\gamma = \frac{1}{2n}\sum_{n=1}^{n}(z_p - z_q)^2, \qquad (3.1)$$

where $(p-q)$ is the lag. A low value of γ is achieved when $z_p - z_q$ is low, and is most likely when the lag is small. Features of semivariograms are shown on Figure 3.13. The value of γ at a lag of 1 is termed the *nugget*, and reflects the correlation between adjacent pairs of points. Various models can be fitted to semivariograms. In a spherical model, semivariance increases as the lag increases, until, at a certain lag (the *range* of the semivariogram), a plateau (termed the *sill*) is reached. Data are uncorrelated beyond the range of the semivariogram. If no range is present, then there is no correlation between adjacent points, and the semivariogram is said to exhibit a pure nugget effect. If semivariance increases with lag, but does not form a sill, then a fractal model could be applied, although the same effect might be obtained as a consequence of a systematic trend in fault density. In a fractal system there are no correlation-lengths, as the structure is correlated at all length-scales.

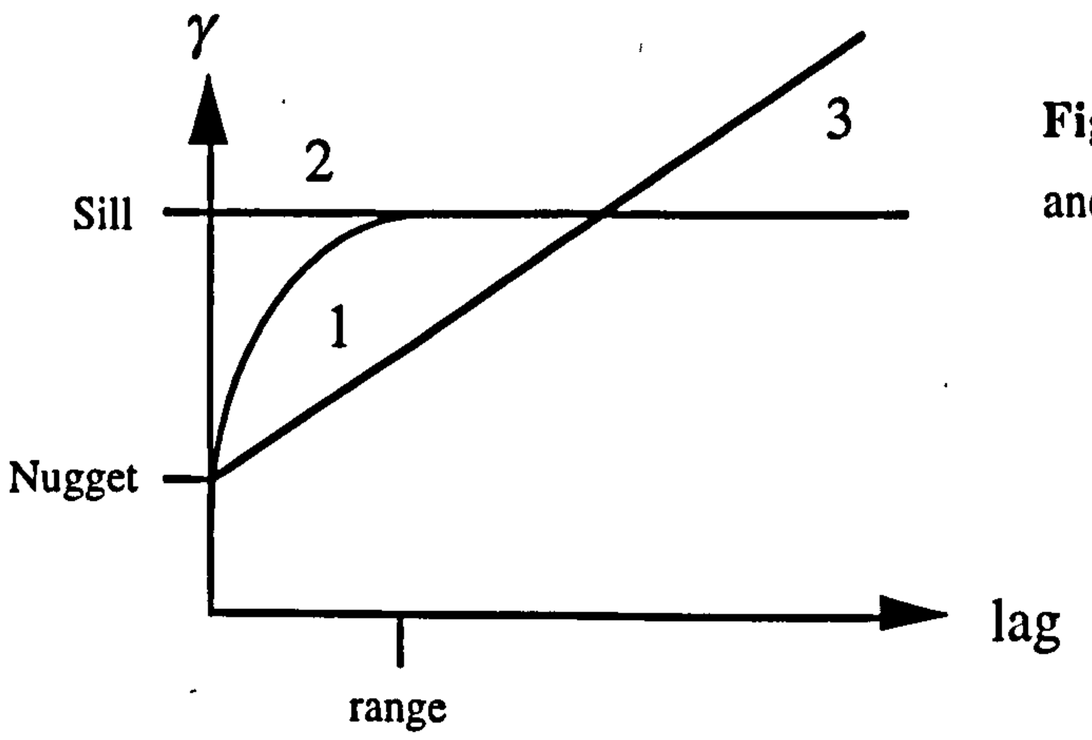

Figure 3.13. Semivariogram terminology and models.

1. Spherical model
2. Pure nugget effect.
3. Fractal model

Fault spacing semivariograms for the Seven Mile Canyon pavement are shown on Figure 3.14. Survey 1, for which there was little correlation at lag = 1, shows only a moderate decrease in correlation with an increase in lag. Survey 2 might be interpreted with a spherical model, reaching a sill at about 10 fault separations, and this is possibly supported by Survey 3. Survey 4, closest to the centre of the relay-ramp, does not have a sill and could be interpreted as showing a fractal, or even multi-fractal arrangement of fault spacings. There is some evidence for periodicity on Survey 2, occurring every 13 faults (increases in correlation highlighted by the vertical lines on Figure 3.14b). This effect could indicate the presence of damage zones around the larger faults in the ramp. Such an interpretation, however, is not corroborated on any other semivariogram.

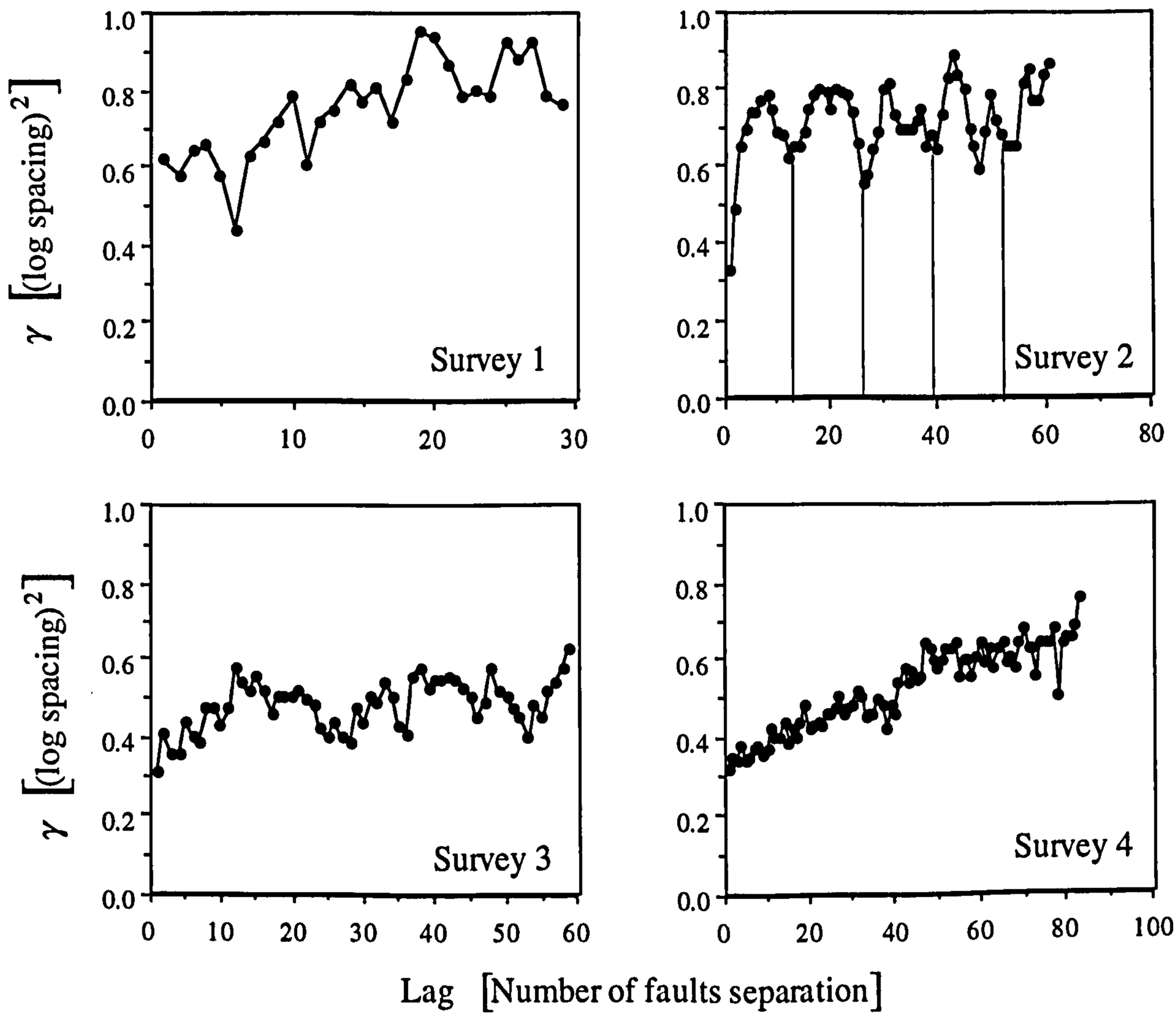

Figure 3.14. Semivariograms of the log of fault spacing (meters) for the four Seven Mile Canyon transects. Possible fault clusters at 13 faults intervals are indicated on the plot for Survey 2.

The characteristics of the semivariograms are different from one another, despite the survey lines being only a few meters apart. This could imply that the variability in faulting within the relay is occurring at a length-scale which is below the resolution of these plots. In Section 4.4.7, fault spacing semivariograms of numerically generated systems which are known to contain no spatial trends are studied.

Although three out of the four transects showed correlation between adjacent spacings (Figure 3.12), such clustering is not always present in fault systems. Figure 3.15 shows spacing cross-plots for the two datasets in the Penrith Sandstone and the one at Molly's Castle (see Chapter 2), and in these cases no clustering is apparent.

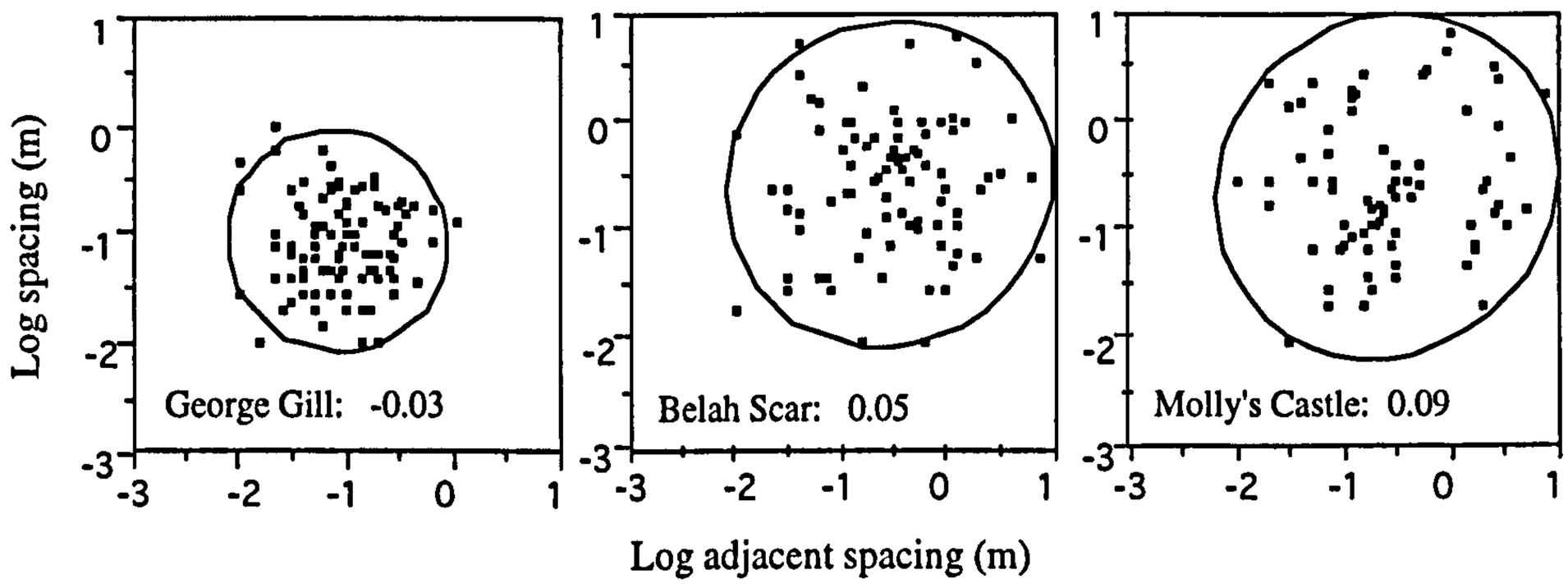

Figure 3.15. Log spacing vs. Log adjacent spacing for the scan-line surveys at George Gill, Belah Scar and Molly's Castle. 95% confidence ellipses and correlation factor reported on each plot.

3.3.2 Spatial correlation of fault size

The previous section concerned clustering, defined as correlation in fault density perpendicular to the over-all strike of the relay. A comparison of the scaling characteristics of the individual transects additionally reveals changes in fault density distribution perpendicular to the dip of the relay. The four parallel scan-line samples are located near the south-eastern edge of the relay (Figure 3.7), which increases in width from 75 cm (Survey 1) to the maximum relay width of about 5m (Surveys 3 and 4). This increase in relay width is related to an increase in the thickness frequency power-law exponent (Figure 3.16). A high exponent signifies a greater relative frequency of

small faults. This observation is consistent with displacement at the edges of relay ramps being dominated by a few, large faults, while in the middle the displacement is accommodated by a larger number of smaller faults. A similar systematic increase in population power-law has been observed by Walsh *et al.* (1994), on seismically derived cumulative displacement frequency plots in a region where a large fault divides into a number of splays.

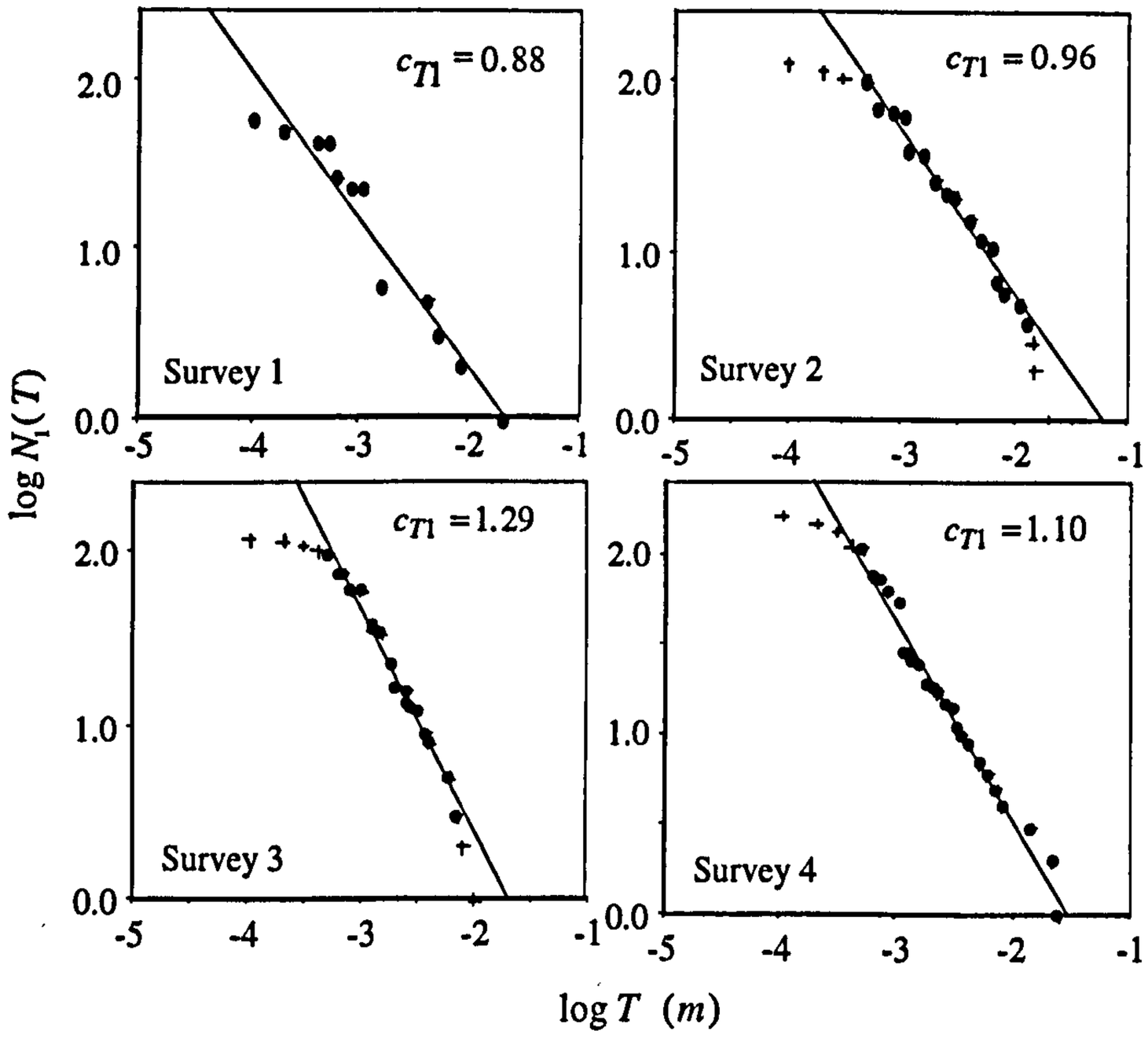

Figure 3.16. Cumulative thickness frequency plots for the four scan-line surveys at Seven Mile Canyon, with best fit relationships. The data shown as crosses have not been incorporated in the determination of the relationships.

3.3.3 Fault Linkage

Davidson (1994) defines a linked fault system as a "*network of broadly contemporaneous branching faults, which link up over a length-scale much greater than individual fault segments*". These faults may be *soft-linked* or *hard-linked* (Walsh and Watterson, 1991). An example of both is shown on Figure 3.17 (which is a portion of the map in Figure 3.8). Strand A is soft-linked, and although the segments are structurally related (they form part of the same shear zone) there is no physical

connection between them. Segment B is hard-linked, and there are physical connections between the different strands.

The linkage of structurally-related fault strands in any setting is a function of the displacement of the entire structure. Cox and Scholz (1982) showed that increasing displacement causes segments of micro-cracks to become hard-linked. Naylor *et al.* (1986) produced fault systems in sandbox experiments very similar to strands A and B as a function of displacement, and Foxford *et al.* (in review) relate linkage characteristics of strands of the Moab fault to changes in displacement along the trace. Structurally-related fault traces at Seven Mile canyon are generally hard-linked, but linkage is not distributed evenly across the map, as it relates to the displacement of the overall shear zone containing multiple segments.

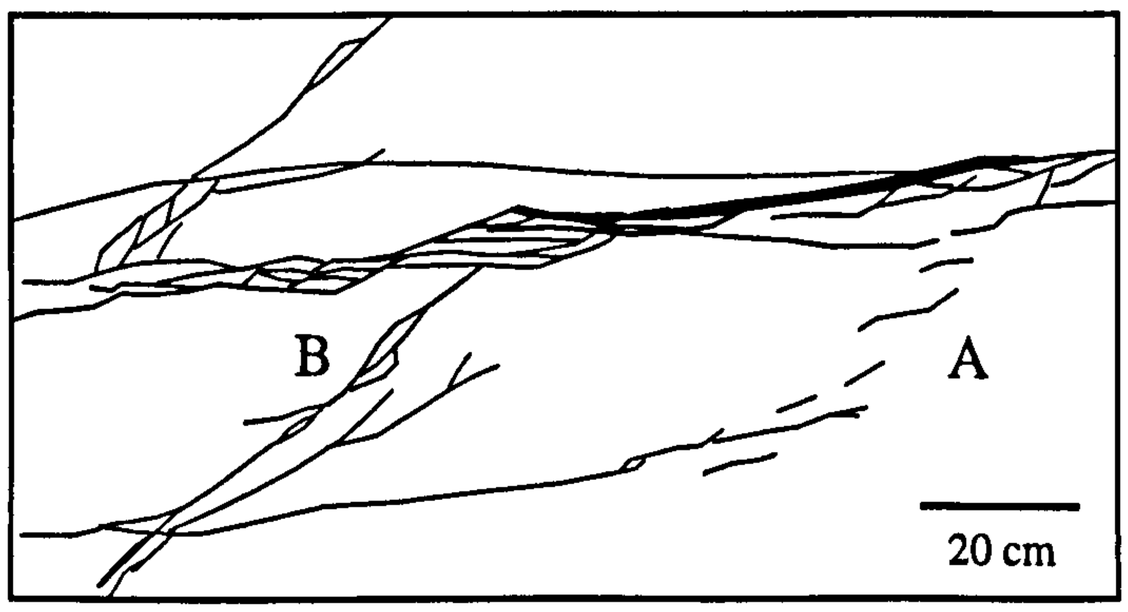

Figure 3.17. A detail of the map in Figure 3.8, showing soft-linked (A) and hard-linked (B) segments.

3.3.4 Summary and discussion

In the preceding Sections, details of the secondary characteristics of a 30 m^2 area of the faulting in a relay ramp at Seven Mile Canyon have been analysed. This analysis indicates that:

A) The faults are clustered. Fault clustering can be recognised either on spacing cross-plots, or on spacing semivariograms. The characteristics of the semivariograms measured on transects only a few meters apart are quite different.

B) There is a systematic increase in the relative proportion of small faults towards the centre of the relay ramp. This is recognised on the basis of changes in the cumulative thickness frequency plots measured on 1D transects.

C) The fault system is hard-linked. There is spatial correlation of fault linkage, as linkage is related to the degree of localisation of shear zones comprising many distinct fault segments.

Several conclusions may be drawn from these results.

A) Simple stochastic models based only on PDFs of primary system characteristics would not reproduce the secondary characteristics of the system.

B) No single set of parameters adequately describes the faulting in the area. Either the system is not geometrically representative over a large enough area for these parameters to be defined, or the map is not large enough to be representative.

Despite these conclusions, stochastic models could reproduce, at least in part, the secondary characteristics of the system. Instead of using a uniform rectangular distribution (see Section 3.2.1) to govern the spatial distribution of faulting, inclusion of scale-specific skews in the strike direction, and a spherical semivariogram of fault density in the dip direction, would allow incorporation of observations A and B. Incorporation of the linkage characteristics in a Boolean model is more problematic, as Boolean models only produce I and X nodes. Tessellation models allow greater flexibility for modelling linkage, but lack the versatility of Boolean methods in other respects.

In light of the problems associated with modelling, or even characterising, fault system geometry, is useful instead to step backwards and remember why the fault system is being modelled in the first place. How accurate a representation of the system must the geometrical model be, in order for it to give an acceptable approximation to the flow behaviour of the system? This is discussed below.

Odling (1992b) compared the fracture-flow permeability responses of two mapped fracture patterns with results from Boolean approximations of the systems (Figure 3.18). The systems were modelled with fracture permeabilities up to six orders of magnitude greater than matrix permeability. The models honour the orientations and orientation distributions, length and length distributions, and density of two different natural fracture systems. However, the permeabilities of the models did not match those of the natural systems, and therefore the models, though robust according to primary characteristics, are an inadequate representation of the system for flow analysis. Her comparison illustrates well the importance of secondary fracture system characteristics for flow, and reasons for the discrepancy in permeabilities in the models are discussed below.

In the first system (Figure 3.18a, b), the permeability of the natural pattern is greater than that of the models. This is due to the connectivity of the systems: the natural system has several connected pathways of fractures from bottom and top, but these are not reproduced by the realisations. This is due to clustering in the natural pattern, which results in a greater number of fracture connections in certain portions of the map, as the strands in these clusters are hard-linked. No clustering is incorporated in the realisation, and so fault connections are distributed evenly and nowhere is their density sufficiently high for a connected pathway to form. This effect is exacerbated by the nature of the connections: in the natural system there is a high proportion of Y nodes, but these are not present in the numerical approximations of the system.

In the second system modelled (Figure 3.18c, d), permeability differences are reversed. The realisations give a higher permeability than the natural pattern. This is again a function of clustering and orientation. In the natural pattern the fractures are rather regularly spaced, and the larger fractures are sub-parallel to each other. Many short strands are soft-linked with other fractures they are probably structurally related to. There is only one connected pathway from left to right, and this path is a single fracture connected to no others. In the realisations, the random placement has produced more intersections, as the fractures are not correlated in orientation with those they are close to, as they are in the natural pattern. Therefore the fractures are more likely to form intersections in this case. The results is two connected paths from left to right, and a greater proportion of the entire system is connected to these paths. Therefore the permeability of the realisation is higher.

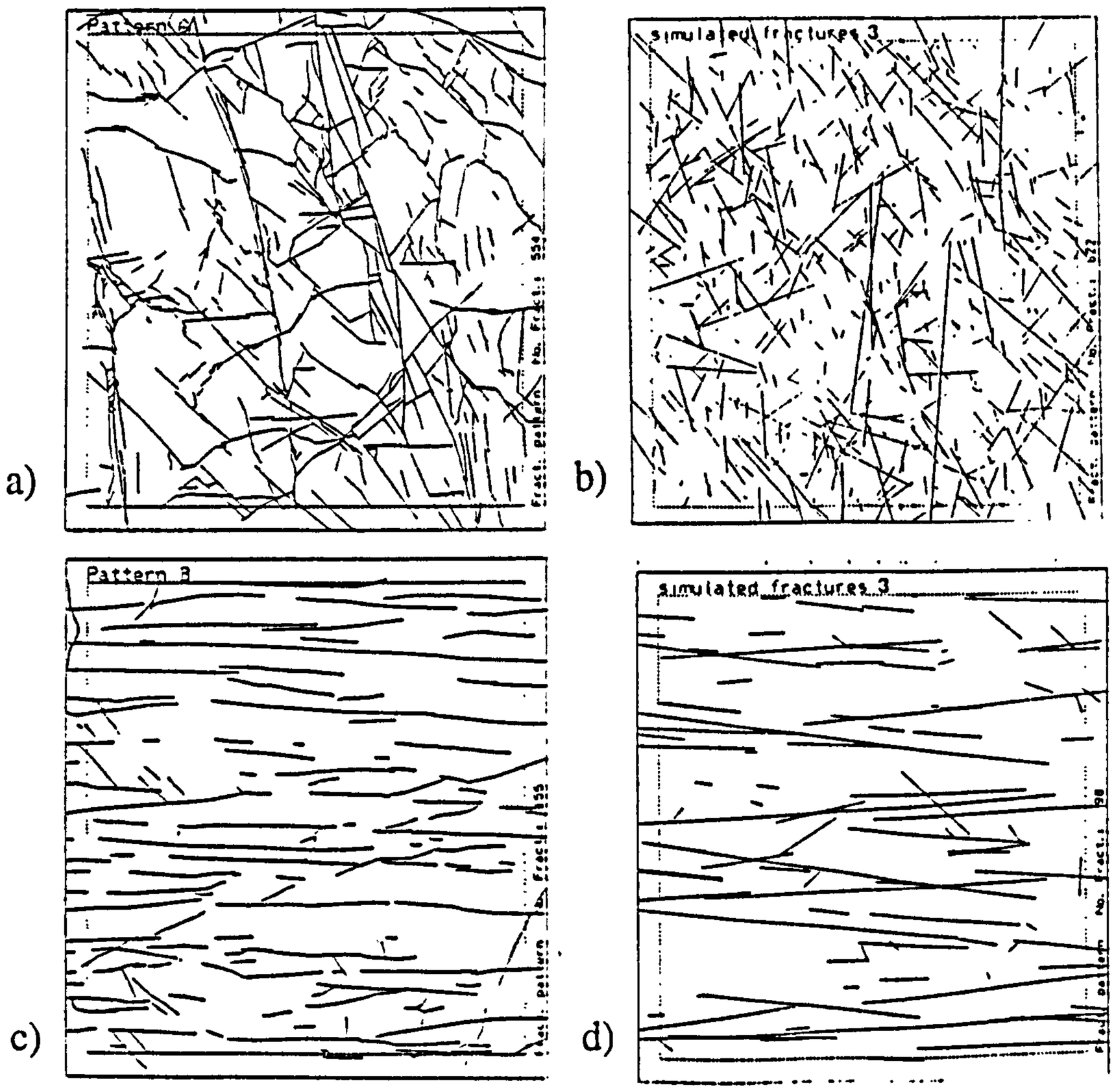

Figure 3.18. A comparison between the fracture permeability of mapped fracture systems with geostatistical models, from Odling 1992b. a), c) The natural fracture patterns. b), d) Models honouring the lengths and orientations of the natural patterns.

Odling recognised that the differences in permeability response were a function of the secondary characteristics of the systems, and in a related paper (Odling, 1992a; discussed in Section 4.5) investigated how the secondary characteristics of a natural fracture system and Boolean realisations based on primary characteristics differ. The following Section argues that spatial correlations of fault density and orientation are not significant in determining the permeabilities of these systems *per se*, but only inasmuch as they influence the connectivity of the systems. Connectivity is the critical parameter that governs flow in these systems. If system connectivity can be quantified as a variable in its own right, the independent geometrical factors which cause it to vary become of subordinate importance.

3.4 Quantifying connectivity

The connectivity of a system can be fully defined in terms of the quantity, and types, of fault nodes present. Two connection types are important: three-branch intersections (Y-nodes), and four branch intersections (X-nodes). Topologically, many more than four branches can meet at a point, but intersections involving more than four branches are extremely unlikely in fault systems. Both Y-nodes and X-nodes involve two faults. A Y-node is formed where a fault terminates against, or splays off, another fault, and X-nodes are formed by one fault crossing another. It is often problematic to distinguish between an X-node or two Y-nodes, particularly when significant shear displacement has occurred parallel to the plane of investigation. It is important to do so, however, as fault scaling models (Chapter 2) are based on the number and lengths of entire faults, not on fault segments.

Every fault trace has two ends, either Y-nodes or isolated fault tips, called I-nodes. The connectivity of the system can be characterised by the relative quantities of the three node types present. Odling's (1992b) results can be addressed in terms of this single issue: in one case (Figure 3.18a,b) the realisation contained a greater proportion of I nodes than the natural system, and therefore had a lower permeability, and in the other

case (Figure 3.18c,d) the realisation contained a lower proportion of I nodes than the natural system, and therefore had a higher permeability. Had the *I:Y:X* node proportions of the realisations matched those of the natural systems, the effective permeability results would have been more accurate, as the reasons for the discrepancies (discussed in the previous Section) would not have been present.

In the systems considered in this thesis, faulting with a variations of fault lengths and orientation are simplified to systems in which all faults have the same length and are equally divided between two orientation populations (see Section 3.1.2). That is, the primary characteristics of the system are simplified This simplification is formalised analytically in Section 6.5.2. The models do, however, incorporate connectivity systematics. Because of this, it is argued that they honour the flow behaviour of the system. Consider Figure 3.19. Figure 3.19a shows a "natural" system, within which faults have variable lengths and orientations, have particular spatial correlations of density and orientation characteristics, and contain both Y and X connections. Figure 3.19b shows a Boolean model of this system based only on the primary characteristics. As discussed above, such a system does not reproduce the effects on flow. Figure 3.19c shows a Boolean realisation based on the simplified primary characteristics - due to these simplifications, this system would produce flow results no more accurate than Figure 3.19b

Figure 3.19d incorporates the same simplifications to the primary characteristics, but in this case the connectivity characteristics of Figure 3.19a are reproduced: the system contains exactly the same number of I, Y and X nodes as 3.19a. As Figures 3.19a and 3.19d contain the same total length of faults, the transmissibility effect (see Figure 1.8) is the same in each. As they also contain the same number of faults, and the same proportions of fault nodes, then the tortuosity effect is also the same. Discussion in Section 1.3 showed that clustering without connectivity had no effect on single phase flow. Altering the clustering characteristics of models can influence flow response, but

only because it affects connectivity. By inference, therefore, if the connectivity of a system is honoured, the flow response will be the same irrespective of the clustering.

Fault orientation has a dual influence on modelling flow in fracture systems. Firstly, altering the orientation characteristics can influence the connectivity characteristics, and hence the permeability of a system (e.g. Figure 1.7). Secondly, orientation has an influence on flow which is independent of any other geometrical characteristics (Figure 1.8). The first effect is implicitly incorporated in the proposed method, as connectivity is modelled independently. The second effect must be honoured within the framework of selecting the two orientation populations. It is no less logical to simplify a system containing a range of orientations to two populations, rather than one, and this simplification allows connectivity to be modelled. If all faults are parallel, no connectivity is possible.

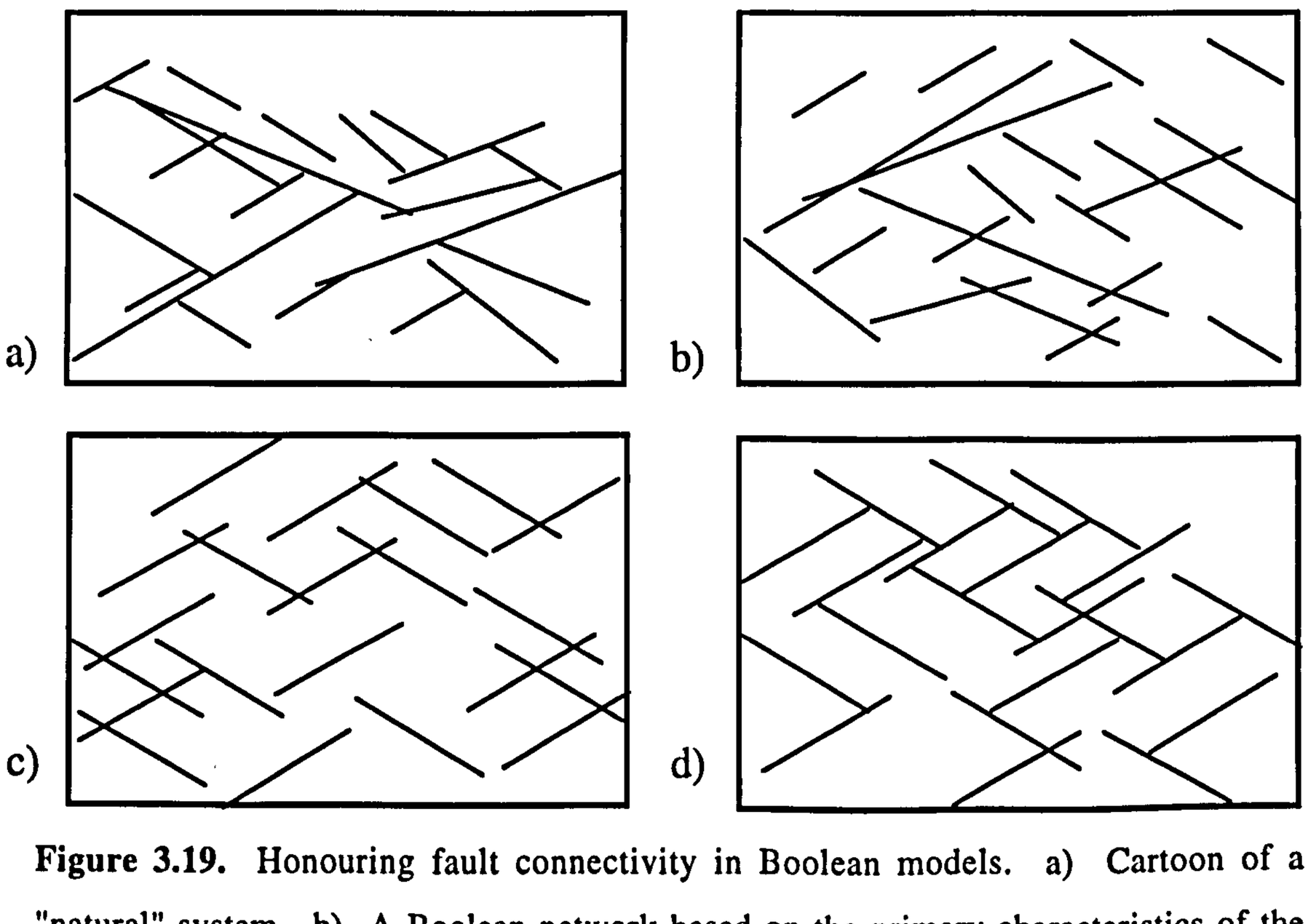

Figure 3.19. Honouring fault connectivity in Boolean models. a) Cartoon of a "natural" system. b) A Boolean network based on the primary characteristics of the system in a). c) A Boolean network based on the simplified primary characteristics of the natural system. d) The proposed model is based on the simplified primary characteristics, but reproduces the connectivity of the natural system.

3.4.1 Connectivity of natural fault and fracture systems

In addition to having more significant influence on single phase flow, connectivity is also easier than clustering to quantify, and therefore to model with. Quantification of fault clustering requires semivariograms which are often problematic to interpret (see Section 3.3.1). Connectivity, on the other hand, can be characterised by a simple point count of all three node types present on a fault trace map. The method for representing the connectivity of fracture systems as a point on a fault node ternary diagram (Figure 3.20) has previously been used by Barton and Hsieh (1989), and is a significant advance on node counts which only consider I and X nodes (e.g. Robinson, 1983), as it incorporates geologically common Y nodes. A different quantitative measure of network connectivity is used by Odling (1993, 1997), who uses the proportion of the total fracture length in the largest connected cluster as a connectivity measure. Often however, connectivity is only considered qualitatively (e.g. Pickering *et al.*, 1997).

Figure 3.20 shows the connectivity characteristics of a number of fault systems which are reproduced on Figure 3.21. The least connected is a normal faults system in the Timor Sea mapped at a Miocene seismic horizon (Nicol *et al.*, 1995). The system is the product of a simple, apparently bimodal, stress state (see Figure 2.2), which has resulted in sub-parallel fault traces. Both seismic maps from the North Sea (one from a pre-rift Jurassic horizon; Gillespie *et al.*, 1993, the other on a Rotliegend horizon; Oudmayer and Jager, 1993) contain a lower proportion of I-nodes. These systems are therefore more connected, although the overall fault density is not necessarily greater than the Timor Sea example. Greater connectivity is achieved through fault splays (Y nodes), a result of the increased structural complexity, which has produced a more hard-linked system with greater variation in fault orientations. The small-scale field maps of fault systems in porous sandstones (points 6 to 8, Figure 3.20) all contain a very high proportion of Y-nodes, indicating that splays are the characteristic node type for faults in this medium. Figure 3.20 also contains the characteristics of one joint system (Gillespie *et al.*, 1993) which contains high proportions of both Y and X nodes.

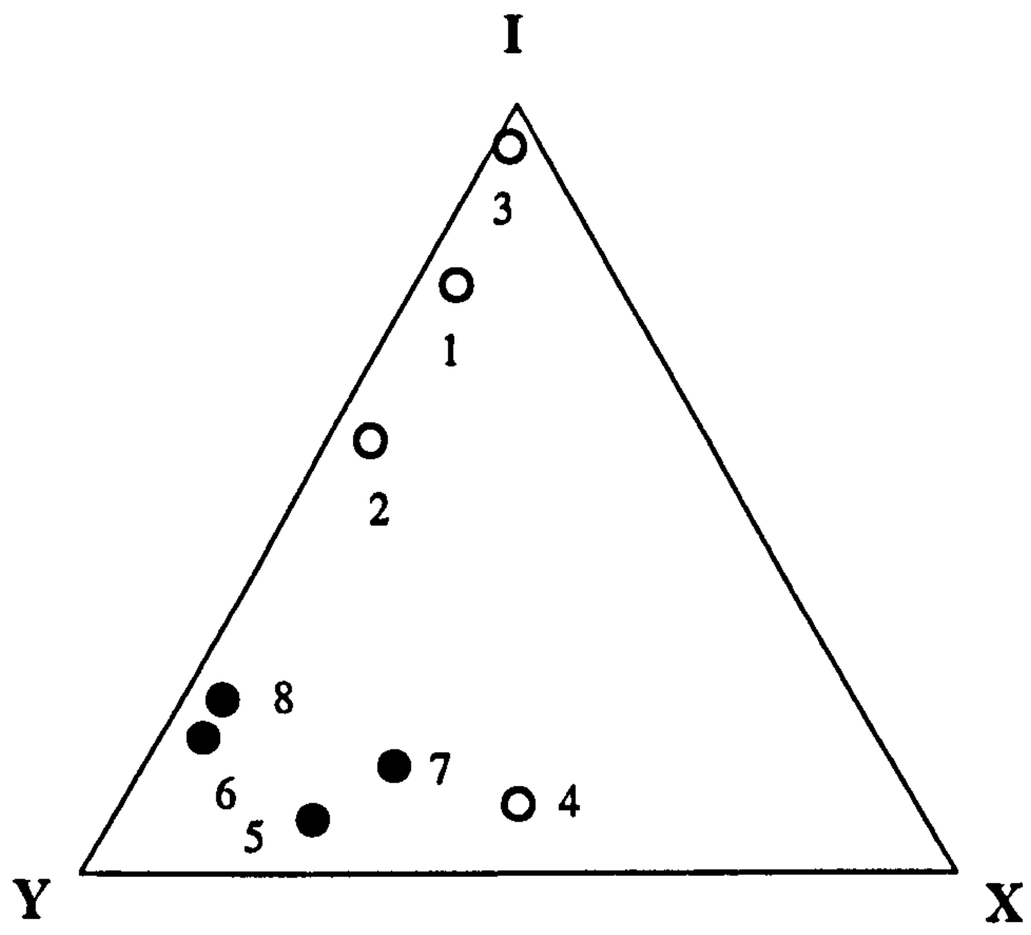

Figure 3.20. Connectivity of fault systems on a ternary diagram of the three node types: 1. Upper Jurassic faulting in the Northern North Sea (Gillespie *et al.*, 1993). 2. Rotligend fault map, Netherlands Quad K (Oudmayer and Jager, 1993). 3. Miocene fault map, Timor Sea (Nicol *et al.*, 1995). 4. Joints in Carboniferous sandstone, UK (Gillespie *et al.*, 1993). 5. Deformation bands in Penrith Sandstone UK (Manzocchi *et al.*, in press). These are all shown on Figure 3.21. 6 Zone of deformation bands from a North Sea Core (Figure 1.1a) 7. Fault system in Navajo Sandstone, Utah (Figure 1.1b). 8. Faulting at Seven Mile Canyon (Figure 3.8). The data with black circles are deformation band systems in porous sandstones, the open circles are seismic maps or fracture systems.

The distribution in fault length influences the overall connectivity of a system. Monte Carlo simulations have proven that as the distribution in fault lengths increases, the fault density necessary to connect the four edges of the model decreases (*e.g.*, Balberg and Binenbaum, 1983; Robinson, 1983). The proportion of I and X nodes at which the system becomes connected, however, is not tremendously sensitive to length distributions, provided that a largest line in the system is small relative to the model dimensions (*e.g.*, Robinson, 1983; Hestir and Long, 1990; Berkowitz, 1995). The orientation distribution also has an influence on connectivity, and randomly oriented lines require a greater proportion of X nodes to become macroscopically connected than a system with lines equally distributed between two populations (e.g. Hestir and Long, 1990). Hence both length and orientation distributions influence the node proportions at which systems become connected.

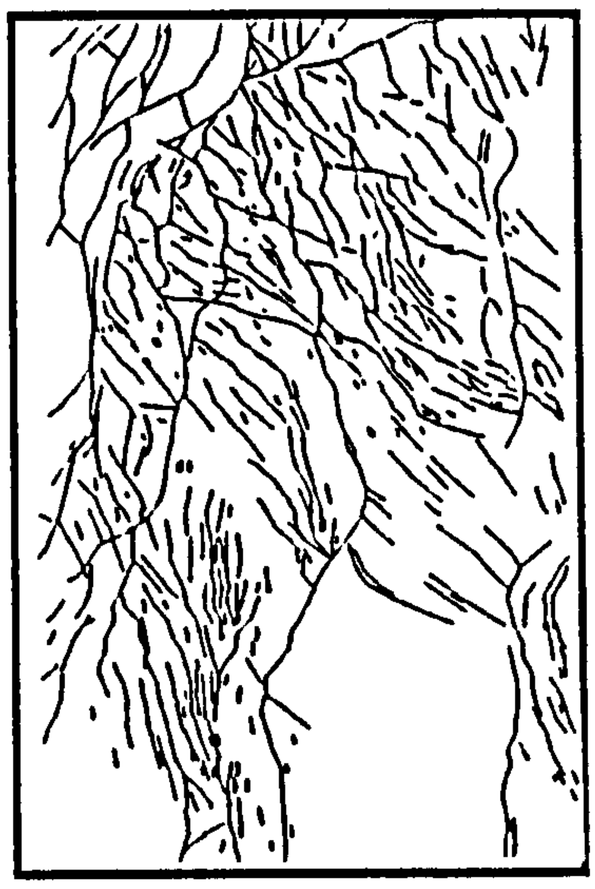

10 km

Upper Jurassic (pre-rift)
Northern North Sea

Gillespie et al 1993

20 km

Rotliegend faults,
Netherlands Quad K

Oudmayer & Jager 1993

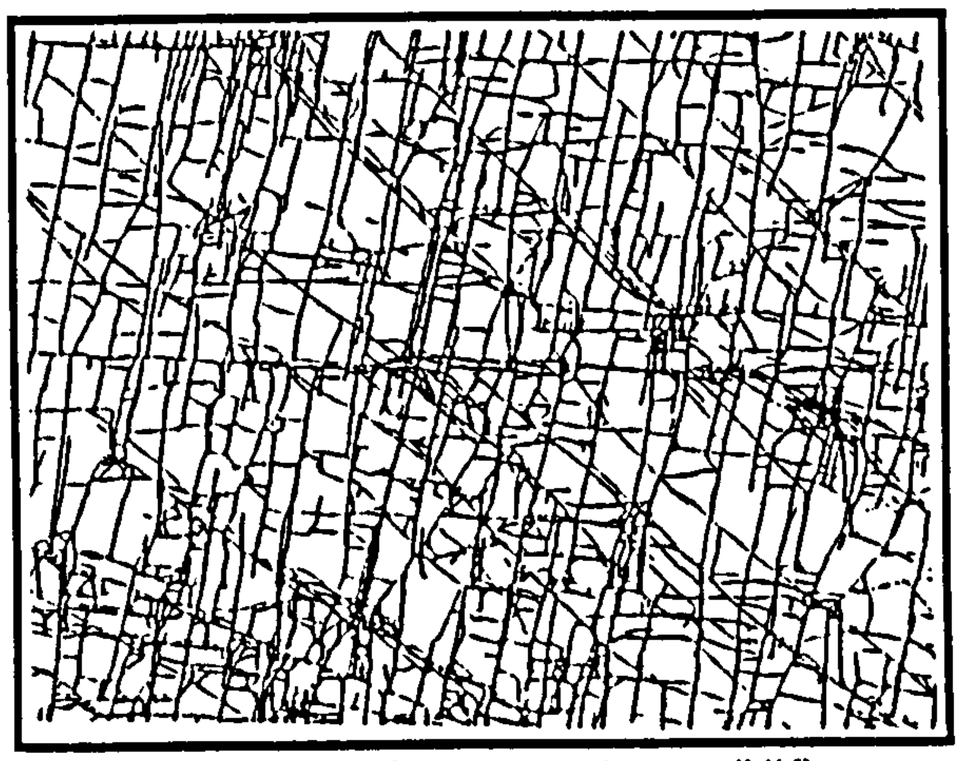

Joints in Carboniferous sandstone (UK)

5 m

Gillespie et al 1993

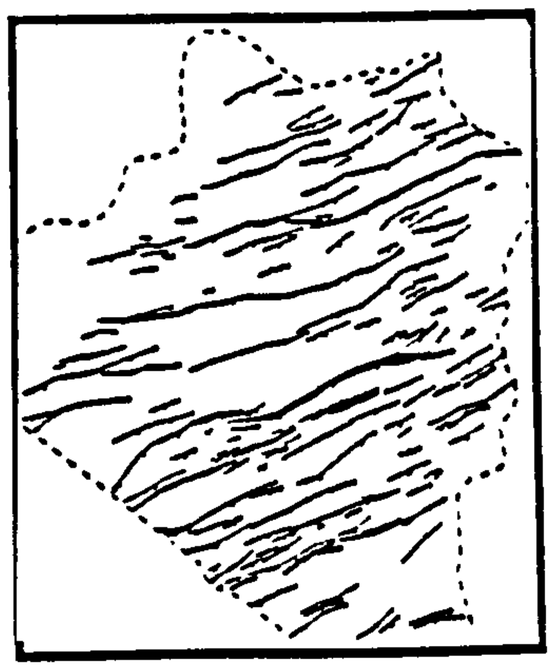

10 km

Miocene (post rift)
Timor Sea

Nicol et al 1995

20 cm

Deformation bands in Penrith Sandstone,
Vale of Eden, N England

Manzocchi et al In Press

Figure 3.21. Fault and fracture maps from a variety of geological settings at a variety of scales, for which the connectivity characteristics are plotted on Figure 3.20. From Gillespie *et al.* (1993), Oudmayer and Jager (1993), Nicol *et al.* (1995) and Manzocchi *et al.* (in press).

Of the systems plotted on Figure 3.20, only System 4 connects both left to right and top to bottom. Systems 2 and 3 do not connected either pair of edges, and Systems 1, 5, 6, 7 and 8 connect in one direction. These properties are partially a function of the size of the maps. As pointed out in Section 1.4.4, statistical analysis of maps is problematic owing to the fractal scaling of faults: no map will contain a representative sample of the largest faults. This is why System 2 is connected in one direction although it has low proportions of Y and X nodes. The longest faults have a disproportionate effect. Representivity is also the reason why Systems 5 and 6 do not connect in both directions. The maps are too small relative to the cluster spacing for all the clusters to have connections within the area of the maps.

Consideration of these natural systems shows that a point on a ternary diagram does not completely define the characteristics of a system. Length and orientation characteristics, and, importantly, system representivity also play a role. This thesis considers simplified representative systems in which all faults are of the same length, and are equally divided between two orientation populations. Even for such systems, a node count does not completely define the macroscopic connectivity, as is shown in Chapter 4.

3.4.2 Connectivity of network models

In this thesis, node proportions are taken as a key geometrical variable of a fault system, as connectivity is the most important geometrical control on flow in systems of either conductive fractures (e.g. Odling 1992b) or sealing and partially sealing faults. A feature of all the systems on Figure 3.20 is that they lie close to the IY axis. Any network model which can only produce I and X nodes is inappropriate as the fundamental characteristic of linked fault systems are not reproduced by such methods. The network models used for flow analysis must be able to honour the connectivity of a system.

Figure 3.22 shows the regions of the IYX ternary diagram in which networks generated with the various methods discussed in Section 3.2 lie. All Boolean models (except certain fragmentation models) fall on the IX axis. Tessellation models are more versatile, but the only one which can form all three node types in the same system is the Dershowitz model.

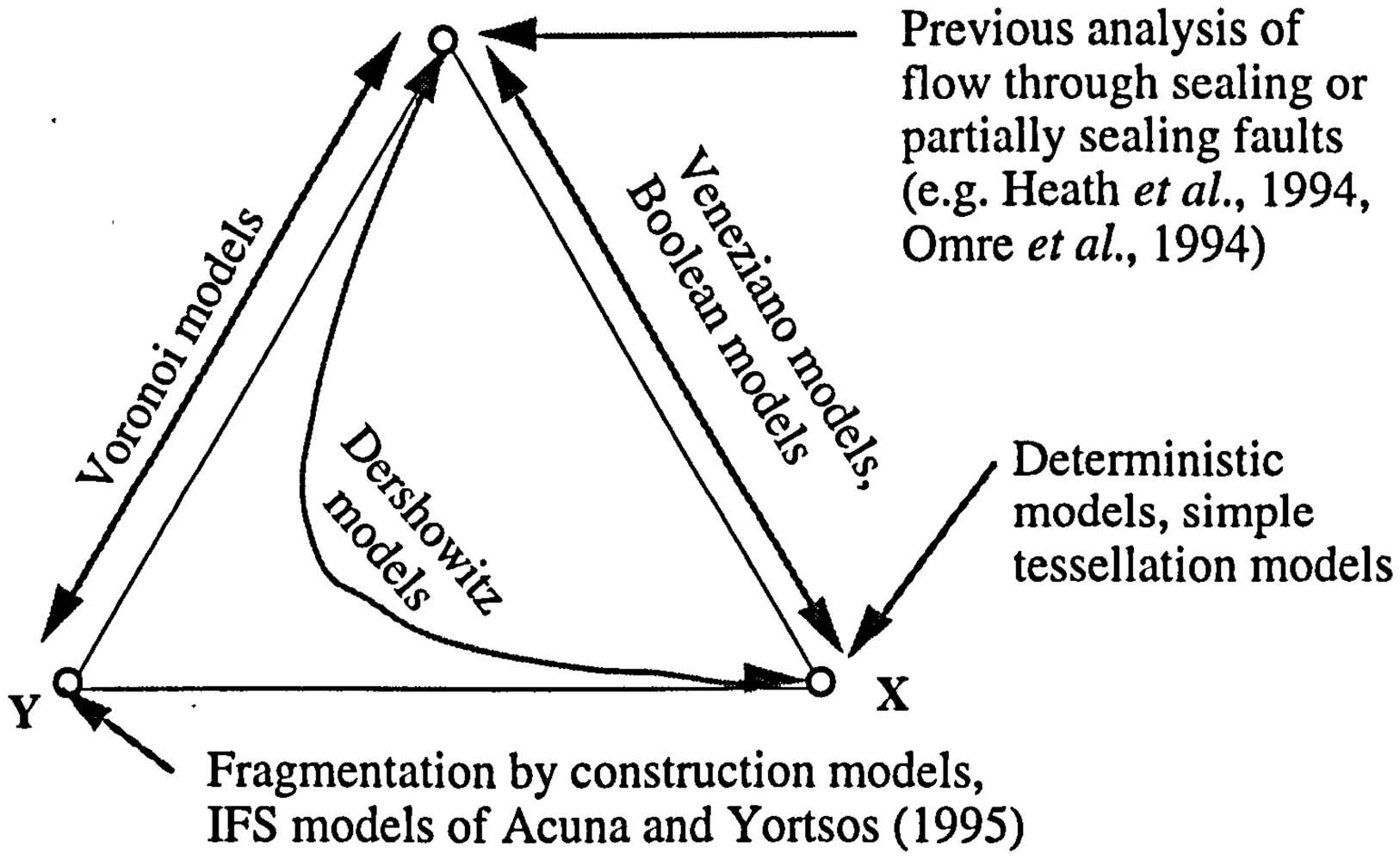

Figure 3.22. IYX ternary diagram showing the connectivity ranges possible with the various network modelling approaches. The position of the line for the Dershowitz model is represented schematically, as the precise location of this line has not been calculated.

There are, however, serious limitations to the Dershowitz model. Dershowitz models produce a fourth node type (L-nodes). An L-node forms where two lines in different orientations terminate at a point. Such a geometry, although rare, is geologically plausible in some fault and fracture systems (e.g. Pollard and Segal, 1987). Where present naturally, one of the fractures associated with an L-node is considerably smaller than the other, and therefore these nodes should be neglected from systems which consider faults of a constant length.

The Dershowitz model starts from a network of Poisson lines, and removal of the first few lines produce Y-nodes. Consider Figure 3.23, which simplifies the initial Poisson line process to an orthogonal system. The second Poison process in a Dershowitz

model removes line segments at random. A single line segment has been removed (Figure 3.23a), and the circled Y-node is formed. This node will change when segment A, B or C is removed, but will become an I-node only if two of these three segments are removed. If segment A is removed, the point is no longer a node of any sort, but removal of segments B or C will produce an L-node. Therefore L nodes are much more common that I-nodes in a high fault density Dershowitz model, and much more common than Y nodes as fault density is decreased. Additionally, the relative proportions of all four node types which are present in any system is simply a function of the proportion of segments that have been removed. All Dershowitz models lie one specific line in IYX space, and any one fault density is associated with a particular connectivity (Figure 3.22).

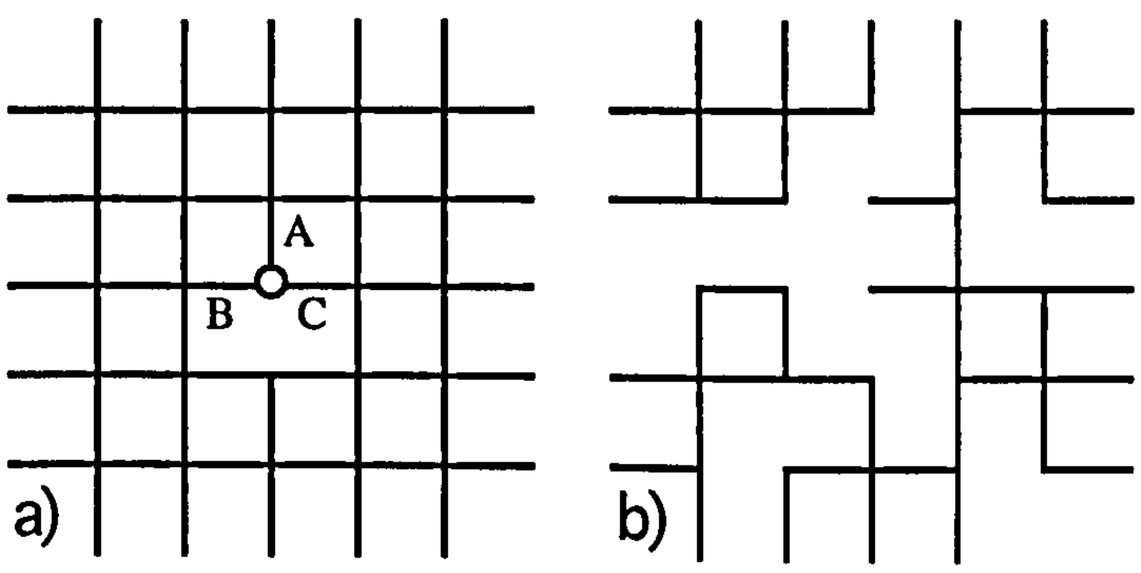

Figure 3.23. Representation of a Dershowitz model on an orthogonal grid. a) Removal of the first fault segment. b) The network after 25% of segments are removed.

If a system comprising a particular number of lines is generated with any stochastic method, it will lie at a particular point in the IYX ternary diagram. If different fault systems are believed to have different affinities for forming splays and intersections, then each of these systems, though containing the same fault density, will plot in a different position on the ternary diagram. Thus simple stochastic methods do not have sufficient versatility of connectivity with respect to fault density. A more general network model is needed to generate systems with different connectivities. An improved Boolean method capable of producing systems with specific connectivities is developed in Chapter 4.

3.5 Summary and conclusions.

This and the previous Chapter have given an quantitative overview of the faulting model which is considered in this thesis. Chapter 2 concerned the derivation of primary characteristics of fault systems based on the scaling and strain portions of the conceptual fault model (Figure 1.9). This Chapter has considered how best to incorporate the secondary fault system characteristics which are most important to flow. The two assumption in this work which are of most relevance to the geometrical arrangement of faults systems (see Section 3.1.2) are:

A) The continuous hierarchic fault scaling model is converted into a discrete hierarchy, and the arrangement of the faulting at each scale in this hierarchy is independent of the faulting at any other scale.

B) All the faults in any scale of the discrete hierarchy are of identical sizes, and are divided equally between two orientation populations.

Both these are simplifications of reality. This Chapter has argued that:

C) Simplifications must be made to the system in any case, as it is impossible to reproduce the true spatial arrangement of a fault system - there are neither the methods nor sufficient information about sub-seismic systems for realistic geometrical characterisation and modelling.

D) Provided that the most important aspects (with respect to flow) are incorporated in some simple quantitative manner, then the model, though a simplification, is adequate for the purpose for which it is designed.

E) The most important aspects of faults system geometry with respect to single phase flow can be captured by simple connectivity criteria. Other aspects of

fault system geometry which are grossly simplified in the geometrical scheme used (notably simplifications made to fault lengths, orientations and clustering) are not significant to the flow results.

The number of faults present in a system (N) determines the *sum* of I-nodes and Y-nodes present. Therefore, if the *proportions* of I-, Y- and X- nodes in a simplified model match the proportions in the real system, and N is equal in both, the total *numbers* of I-, Y- and X- nodes in the real system are honoured by the model. Hence the fact that the system is simplified to one in which there are only two possible fault orientations and no variability in fault length is of secondary importance. These factors can be a *cause* of connectivity, but connectivity and orientation, not clustering and orientation, are the fundamental controls on the flow through the system. By quantifying (rather than merely conceptualising) fault system connectivity, simplifications to other geometrical characteristics of the system may legitimately be made.

3.5.1 The geometrical model

The fault scaling model comprises three relationships which determine the density, length and thickness of faults of any size. These faults, which span the entire sub-seismic scale-range (1 mm < displacement < 20 m), are separated into discrete size-classes one order of magnitude apart. This approximation allows the assumption of scale-separation to be made, which means that flow in each size-class may be considered independently (see Section 5.1). Following this transformation (Chapter 6), the system is described as N faults of length L, thickness T and orientation $\pm\alpha$ contained in an area A, at each discrete length-scale. The spatial arrangement of these faults is governed by the geometrical model used.

The relative proximity of faults in an area is determined by the number and length of the faults present. The connectivity of the system is a function of this and of the orientation

of the faults. In the geometrical model used, a fault system is assumed to grow by forming Y-nodes in preference to X-nodes. In Chapter 4, the connectivity of systems with a high affinity for forming Y-nodes is determined as a function of N, L, A and α. Any system at a specific line density and fault orientation has a particular connectivity, which is achieved dominantly through Y-nodes. These connectivity characteristics are incorporated in the flow models described in Chapter 5, which therefore honour the connectivity behaviour of fault systems.

CHAPTER 4

ANALYTICAL AND NUMERICAL DETERMINATION OF NETWORK CONNECTIVITY

4.1 Introduction

This chapter considers the network characteristics of 2D systems of lines. It builds on previous continuum percolation results for random systems (e.g. Robinson, 1983, 84; Berkowitz, 1995), by including fault splaying systematics in the model. Analytical and numerical methods are combined to determine connectivity thresholds of random systems with different fault node proportions; an entirely novel treatment. Results indicate that previous estimates of the fracture density needed to form a connected system are far too high, and incorporation of fault splays in network models can have a significant influence on flow estimates in faulted and fractured systems.

4.1.1 Fracture systems and flow modelling

Bear and Berkowitz (1987) defined four approaches with which fracture flow can be modelled. These are summarised on Figure 4.1. The *very near field* concerns flow in a single, well defined fracture. In the *near field*, flow occurs in a small number of discrete, individually characterised fractures. In both these regimes, exchange between the fracture and the bounding porous medium may occur. In the *far field*, flow occurs simultaneously in two overlapping continua - the porous medium and the fracture system, and exchange occurs between these continua, which conceptually occupy the same space. For the *very far field*, flow is considered to occur in a single continuum, which reflects the behaviour of both the fracture system and the porous medium.

These distinctions relate to the scale of investigation, and the most important criterion to distinguish between the suitability of each model is system representivity. In the case of near field flow, a description of the flow in a region must involve a complete description of each fracture. As the volume being considered becomes larger, the number of fractures contained within it increases. It is impractical to define explicitly every fracture in a large system, so the far field method is preferable when considering large volumes. If the far field method is used, then the volume being considered must be sufficiently large that flow within the fracture system may be considered a continuum. In other words, the scale of investigation must be at least as large as the *representative elementary volume* (REV) of the system.

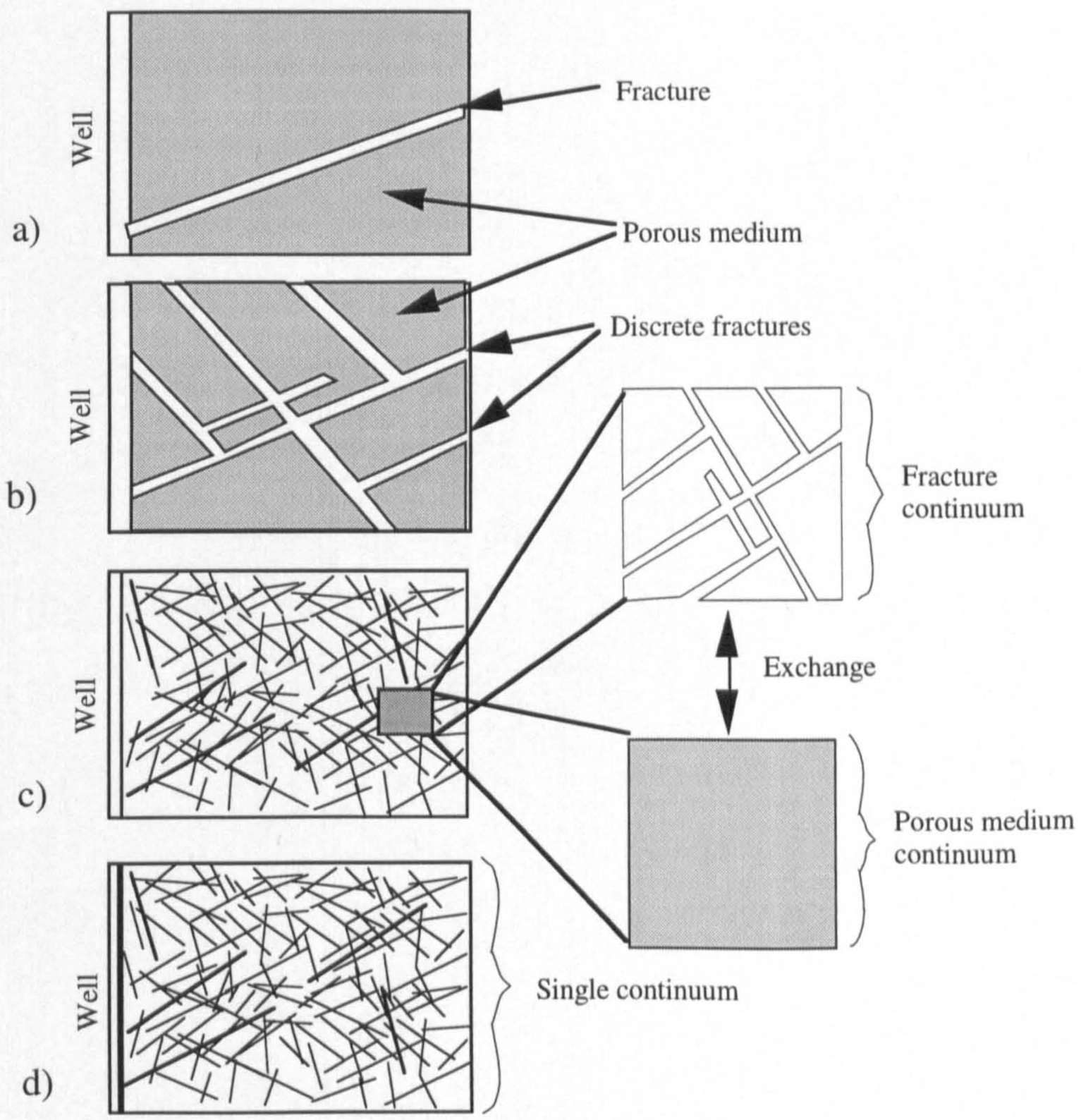

Figure 4.1. Cartoon of the four approaches to modelling flow in fractured media. a). The very near field. b) The near field. c) The far field. d) The very far field. After Bear and Berkowitz (1987).

The most widely used method to characterise fracture flow is the far-field approach, often with the dual porosity (two continua for fluid storage) / dual permeability (two continua for fluid flux) model. All far field methods implicitly assume that the fracture system is representative (Bear, 1993). If a volume contains a representative system, the exact location of fractures within the volume is not critical to the flow result obtained. Different numerical realisations will give the closely similar flow properties, and specific geometrical details of the system are irrelevant. If the volume being considered does not contain sufficient fractures such that different realisations of the system yield a unique flow solution, then the far field method is not suitable, and either a larger area must be considered, or the near field method must be used.

4.1.2 Fracture connectivity and the Representative Elementary Volume

This chapter concerns fault and fracture system representivity and connectivity. Connectivity is of critical importance to flow in fracture systems. If a fracture system in a reservoir is not connected, and recovery is via fracture flow, then production from the reservoir will be low. If the fracture system is connected, but a producer or injector well does not intersect fractures which are part of the connected fracture system, the well will be unproductive. If faults in a reservoir are sealing, flow between fault compartments is impossible if the system is connected, and recovery can only occur from compartments containing a producer well. Finally, in the case of partially sealing faults, connectivity is the key variable distinguishing between two flow mechanisms - tortuous flow around faults in the disconnected case, and flow through faults in a connected or compartmentalised case.

The representative elementary volume (REV) of a system depends on the application for which the REV is being defined. When considering fracture flow in dynamic systems, a static (geometrical) definition of an REV is not sufficient. Even though a geometrical REV might exist, if the system is disconnected, the behaviour of the fluid phase contained in the fractures cannot be treated as a continuum, and therefore the system

cannot be modelled using far field approaches. Because of this, a prerequisite in the definition of the REV for far-field fracture-flow models is that the system is connected (de Marsily, 1985; Bear, 1993).

The case is quite different for sealing faults. Following the reasoning given above, for flow to be possible in a volume of rock containing sealing faults, it is necessary that the matrix is connected. This is, therefore, a prerequisite for the definition of an REV for flow through sealing fault systems. Consider a 2D section containing a network of either conductive fractures or sealing faults. It is impossible for both the fractures and the matrix to be simultaneously connected in 2D - either one is or the other is. Defining an REV depends on both the flow process and on geometrical details of the system.

In 3D it is possible to have both the matrix and the fracture system connected. Madden (1983), and Gomez *et al.* (1995) have used a renormalisation-group method to determine the density at which a fracture system becomes connected, and the density at which the matrix becomes disconnected, for 3D fracture systems. In the case where the fracture density is equal in three orthogonal directions, the situation simplifies to a standard bond percolation problem on a cubic lattice; if over 25% of the fracture bonds are occupied, the fracture system is connected, and if less than 75% of the bonds are occupied, the matrix is connected (e.g. Stauffer, 1985). It would appear that only within these limits is it technically possible to have an REV for strongly dynamic flow in fracture systems.

The four modelling approaches (Section 4.1.1) apply specifically to fracture flow, in which the matrix contains the bulk of the reserves, but has low permeability, and the bulk of the flux occurs within the fractures, which occupy only a small proportion of the total volume. For partially sealing faults, the bulk of the reserves and the bulk of the flux both occur in the matrix, therefore there is no need to represent the system with two continua - one will suffice. Where only one continuum is necessary, there is no

difference between the far field method and the very far field method. If the system is approximated to only one continuum, then there is no need for the either fault system connectivity or matrix connectivity in the definition of the REV of the system, as a single continuum conceptually occupies the whole volume under consideration, and therefore cannot be disconnected. The geometrical REV is, however, important - the area being considered must be sufficiently large for details of individual faults to be insignificant.

4.1.3 Percolation theory applied to fault connectivity

Irrespective of whether or not a geometrical REV exists for any particular system, or whether connectivity is a control on defining a process REV, it is of critical importance to know if a fault or fracture system is connected or disconnected. Percolation theory has proven that, for any distribution of lines or planes in an area or volume, there is a critical density at which the system will become connected, and systems, when considered in a large enough volume, have very sharp connectivity thresholds.

Most network modelling work concerned with determination of the critical density of fault and fracture systems has considered 2D fracture systems as lines distributed with respect to well defined geometrical criteria, but have never included interdependence of any line on any other line. What all previous percolation modelling work applied to fracture systems has in common, therefore, is that it assumes that faults are spatially uncorrelated, either at large scales relative to the faults (i.e. there is no spatial clustering) or smaller scales (i.e. there are no fault splaying systematics).

This chapter considers these two assumptions, and contends that:

A) Published fault system network modelling results overestimate the critical fault density by a factor of between two and three.

B) Fault systems rarely form a geometrical REV, and any form of flow estimation must therefore include probabilistic connectivity criteria.

4.2 Applications of percolation theory to fault networks

Connectivity of systems is best studied with percolation theory. This section introduces the topic, and discusses its application to fault and fracture systems.

4.2.1 Site, bond and continuum percolation methods

The most appropriate network modelling method for fault networks is continuum percolation. Unlike either site or bond percolation, in which areas or lines are placed with respect to a fixed lattice, continuum percolation does not rely on a lattice. Site, bond and continuum percolation are summarised on Figure 4.2.

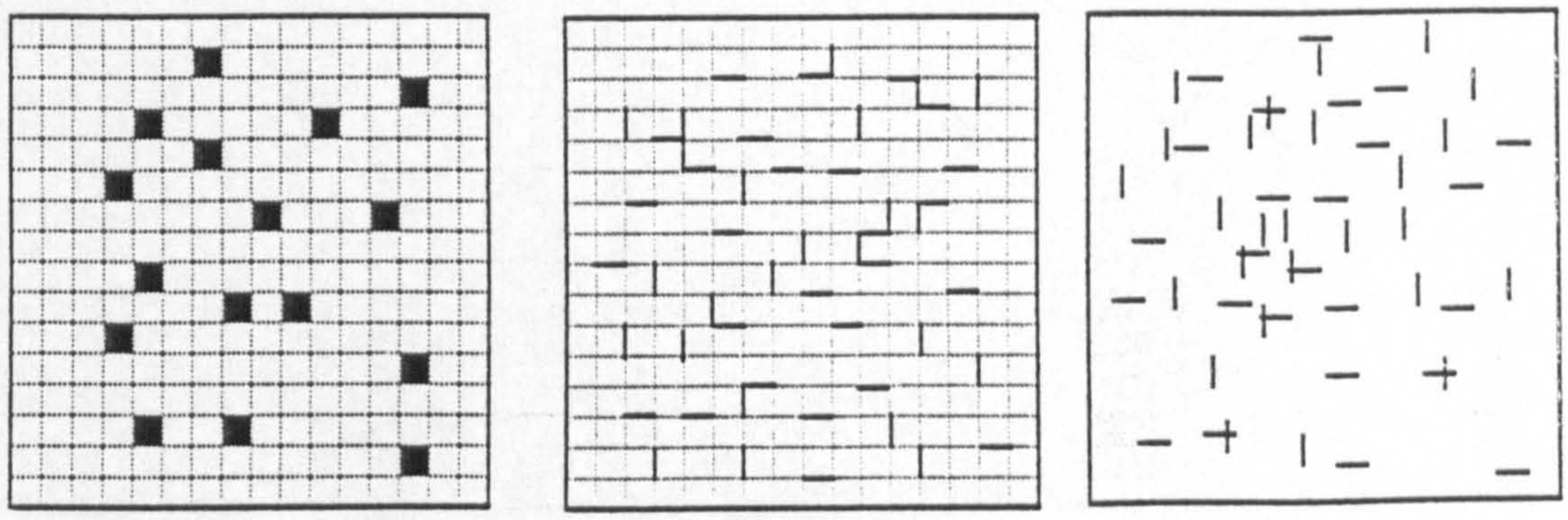

Figure 4.2. Percolation methods in 2D. a) Site percolation. Areas are placed in a fixed lattice. b) Bond percolation. Lines are placed on a fixed lattice. c) Continuum percolation. Lines are placed at random positions in an area.

Consider site percolation. An area is divided into equidimensional squares (Figure 4.2a). Squares are coloured black sequentially and randomly. After each square is coloured, the entire area is checked to see if a continuous path of black squares can be followed from one side of the area to the other. The proportion of black squares at which this occurs is recorded. The area is then divided into smaller squares, and the procedure repeated. It is found that as the squares are made smaller, the proportion needed to cause connectivity converges on a single value (P_c). This is termed the

critical density, and its value is the *percolation threshold* of the system. The connected path is called the *percolation cluster* (in percolation theory, a *cluster* is a group of connected objects). If we consider the area to be of infinite extent, then for $0 < P < P_c$, all clusters in the system are of finite size. At $P = P_c$, a cluster of infinite size appears.

In both site and bond percolation, the percolation threshold (P_c) of the lattice is defined as the proportion of occupied sites or bonds at which an infinite cluster forms. This definition is impossible in continuum percolation, because no lattice is used, and it is possible to have an infinite number of lines in a finite area. There are, effectively, an infinite number of bonds, so a measure of the percolation threshold as the proportion of occupied bonds is meaningless. To overcome this, Robinson (1983) introduced a dimensionless term which is used to describe the relative proximity of lines. Line density (d_L) is given by:

$$d_L = NL^2 / 4A, \tag{4.1}$$

where N is the number of lines of length L present in an area A. For a system of lines of length 2, d_L is the average number of line centres contained in a unit area. If lines are placed within an area using a continuum approach, the connectivity of the system is a function of the line density. If d_L is low, occasional lines may be connected, but, on the whole, the system is disconnected. As d_L increases, the system become gradually more connected until, at a critical line density (d_{Lc}), a continuous connected cluster forms. For lattice based models, $0 \leq P \leq 1$, but in a continuum system, d_L has the range $0 \leq d_L \leq \infty$. In this thesis, the terms connected or disconnected, when applied to an entire system, are taken to mean that the system has $d_L \geq d_{Lc}$, and $d_L < d_{Lc}$, respectively.

4.2.2 Continuum percolation fracture network models

The percolation properties of continuum systems are often studied using Boolean network models (see Section 3.2.4). A simple 2D system consists of lines of a constant length, distributed equally between two orthogonal populations and placed randomly in an area (Figure 4.3). For this system, Robinson (1983, 1984) determined analytically, and confirmed numerically, that $d_{Lc} \approx 1.556$. The characteristics of the system at percolation may also be expressed in terms of connectivity. The connectivity of these system is defined as the average number of intersections per line (Robinson, 1983). This is often termed zeta (ζ), e.g. Berkowitz (1995), and its critical value is ζ_c. Robinson (who called connectivity I) determined that $\zeta_c \approx 3.112$. Hence, either the line density or the connectivity of a system can be used to infer whether the system is below, or above, the percolation threshold.

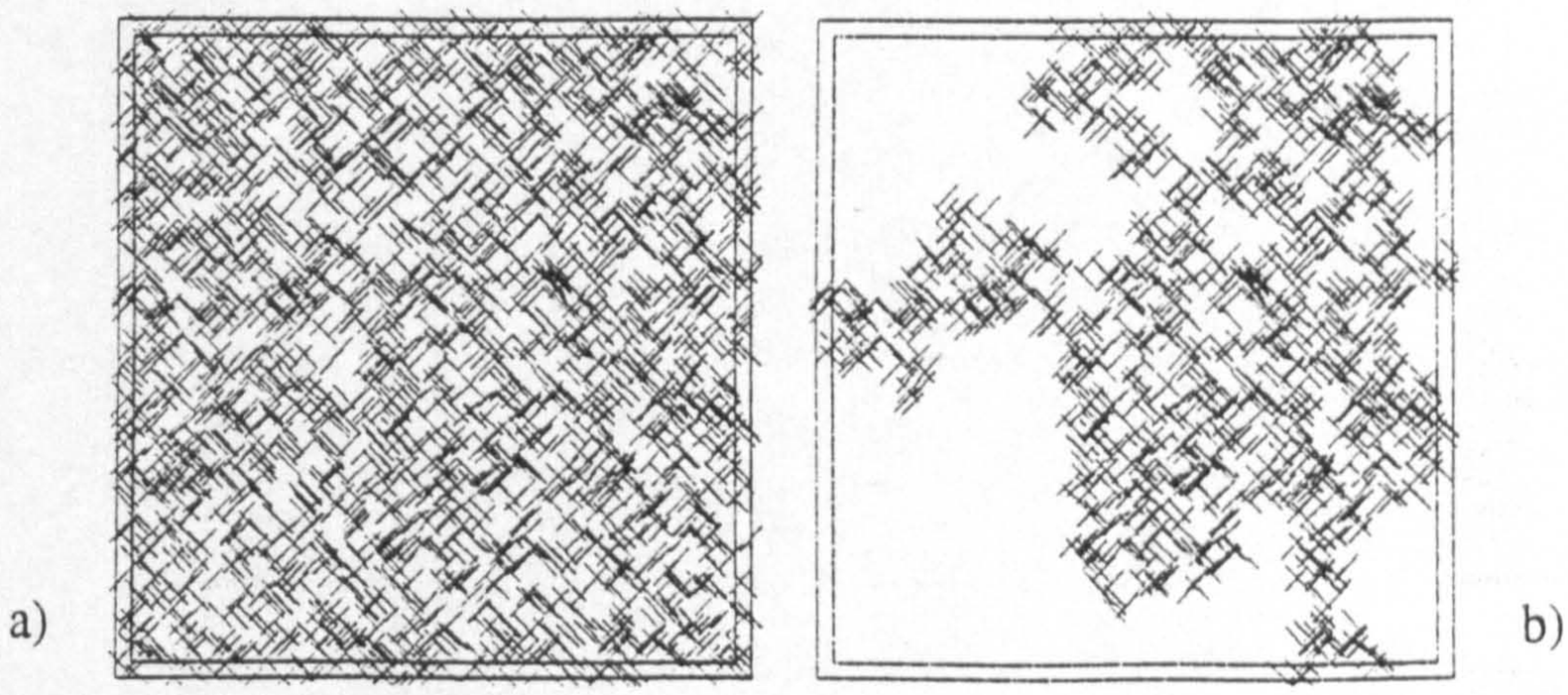

Figure 4.3. a) Network at percolation of the kind studied by Robinson (1983). The system contains 2405 lines equally distributed between two orthogonal populations and placed entirely randomly. b) Percolation cluster of the same network. This cluster contains 1268 lines.

Robinson, as well as several other workers, considered 3D systems and more complex 2D systems, and the percolation characteristics of systems incorporating criteria such as orientation and length distributions are reasonable well formulated. This work has recently been reviewed by Berkowitz and Balberg (1993). One aspect of fault system geometry which has not previously been included in network models is spatial

correlation of lines. This chapter describes network models which incorporate very small-scale spatial correlation, in the form of fault splays, or Y nodes. Real fault system show a high preponderance of fault splays, and network models which incorporate only I and X nodes cannot capture effects of this fundamental connectivity characteristic of fault systems (Section 3.2).

4.2.3 Incorporation of splays in network models

This Chapter considers 2D systems of lines of constant length, equally distributed between two orientation populations, incorporating fault splays. There are two aspects to this work.

A) Critical connectivity for random systems has previously been defined as a point on the IX axis of an IYX ternary diagram (Point A on Figure 4.4). This definition is expanded to a line in IYX space.

B) A Boolean modelling approach is developed, in which connectivity and fault density are independent parameters. This allows generation of geologically more reasonable systems that has previously been available (See Section 3.4).

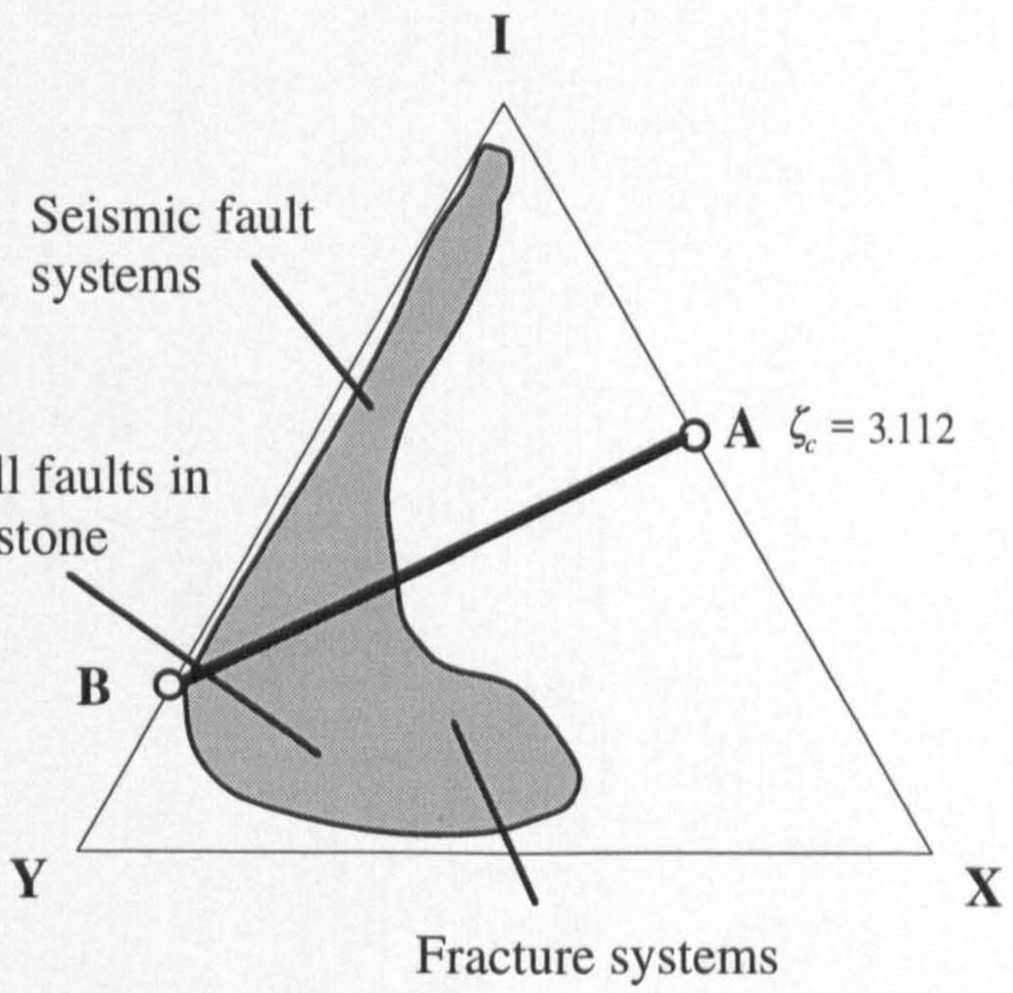

Figure 4.4. IYX ternary diagram showing the node characteristics of natural systems (*c.f.* Figure 3.20). The percolation threshold of a Boolean model is Point A. In IYX space, this must be represented as a line, AB

The structure of this Chapter is as follows. In Section 4.3, theoretical aspects of modelling systems incorporating fault splays are discussed. Analytical methods are used to discuss properties of non-random line systems, and to determine the percolation threshold of random systems in IYX space. Section 4.4, introduces the numerical code developed. This is used to verify the analytical solutions determined in Section 4.3. In Section 4.5, some of the implications of these results are discussed, with reference to the geological evolution of fault and fracture systems as well as to modelling flow through them. The techniques developed, and conclusions reached, in this Chapter is entirely new, as systems incorporating Y nodes have never been considered before.

4.3 Theoretical characterisation of the network properties of IYX systems

Before discussing the network modelling, it is useful to consider, theoretically, some of the implications involved with modelling systems of lines of a constant length incorporating fault splays. This section addresses several, perhaps apparently abstract, questions:

- With what IYX proportions can a system be connected?
- What are the characteristics of systems at the connectivity threshold?
- What makes a random system random?
- What degrees of freedom are involved in IYX systems?

In order to begin to answer these fundamental questions, it is necessary first to clarify the connectivity terminology and nomenclature which is used (Section 4.3.1), and then to make some differentiations between networks with different, overall, geometrical characteristics (Sections 4.3.2 - 4..3.3).

4.3.1 Connectivity parameterisation

In this Chapter, connectivity is usually described in terms of either node ratios (I:X, I:Y and Y:X), or in terms of the parameter favoured in the literature (ζ). Earlier workers were only concerned with IX systems, and so ζ has no meaning anywhere except on the IX axis of an IYX ternary diagram. An IY connectivity term, synonymous with ζ, is introduced. This is given the symbol eta (η). The axes of an IYX ternary diagram represent the proportions of I, Y and X nodes present in a system (P_I, P_Y, and P_X). Therefore, there are three sets of measures which describe connectivity; node ratios, connectivity parameters, and node proportions. Below, the conversion between these measures is clarified.

Connectivity on the IX axis

Consider first an IX system containing N_I I nodes and N_X X nodes. For this system:

$$I{:}X = N_I / N_X. \tag{4.2}$$

ζ represents the average number of intersections (X nodes) per line. Each X node involves two lines, therefore N_X in a system composed of N lines is $\zeta N/2$. The number of I nodes (N_I) present in the system is $2N$. Therefore:

$$I{:}X = 4 / \zeta. \tag{4.3}$$

For an IX system:

$$P_I = N_I / (N_I + N_X). \tag{4.4}$$

Combining equations 4.2 and 4.4 gives:

$$P_I = I{:}X \,/\, (1 + I{:}X). \tag{4.5}$$

Therefore, using equations 4.3 and 4.5; $\zeta_c = 3.112$, corresponds to $(I{:}X)_c = 1.285$, and $P_{Ic} = 0.562$.

For random IX systems, a useful relationship exists between ζ and d_L. Robinson (1983) showed that $\zeta_c = 2d_{Lc}$. Numerical results (see Section 4.4) show that this relationship is not specific to the percolation threshold (Figure 4.5), and, in general:

$$\zeta = 2d_L. \tag{4.6}$$

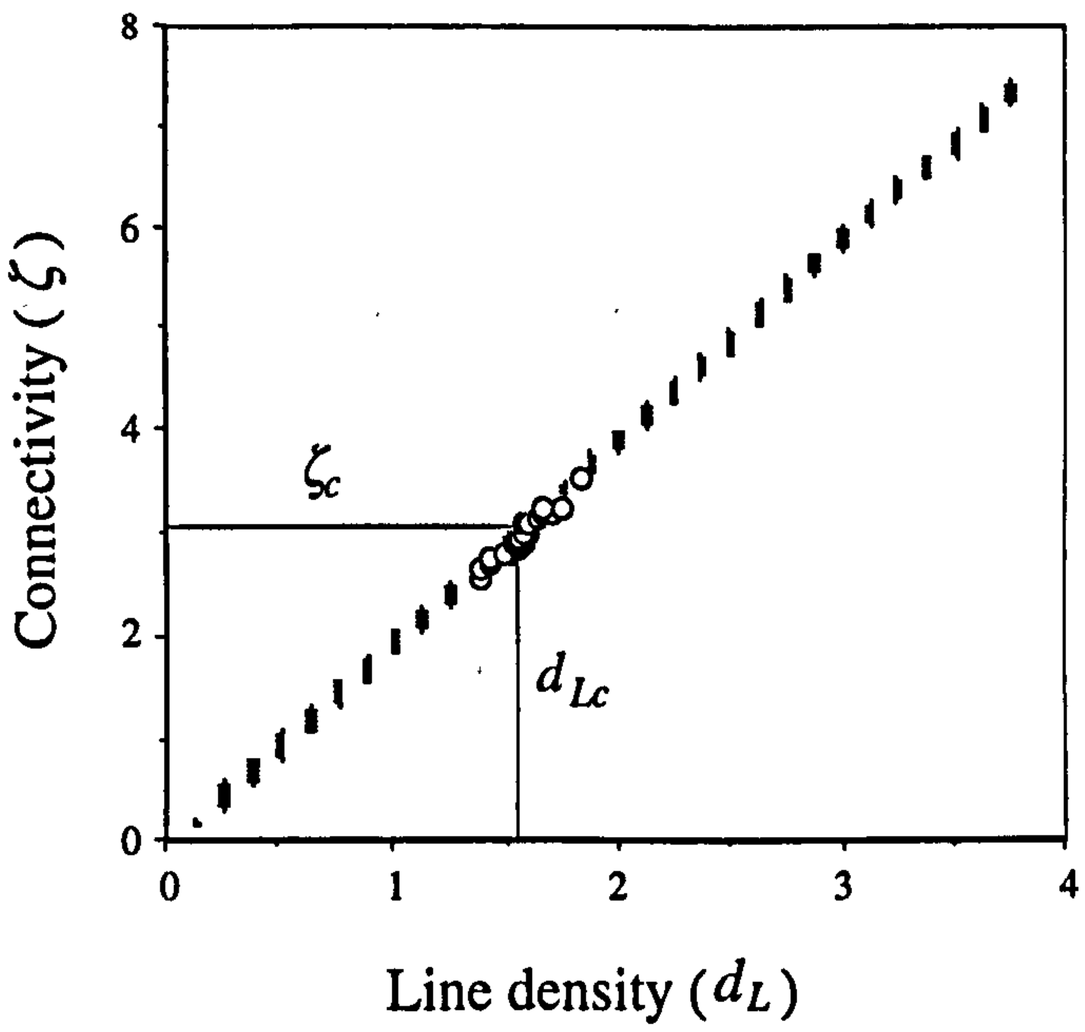

Figure 4.5. Connectivity vs. Line density results for 20 realisations of random system (crosses). The open circles are results at the percolation threshold for a further 28 realisations.

Connectivity on the IY axis

Consider an IY system containing N_I I-nodes and N_Y Y-nodes. For this system:

$$I{:}Y = N_I \,/\, N_Y. \tag{4.7}$$

η is the average number of Y-nodes per line. Because each Y node must involve two lines, $\eta = 2N_Y \,/\, N$, where N is the number of lines present. In an IY system, N is a direct function of N_I and N_Y. As every line has two ends;

$$N = (N_I + N_Y)/2 \tag{4.8}$$

Therefore, $$\eta = 4N_Y/(N_I + N_Y). \tag{4.9}$$

This can be manipulated to give:

$$I{:}Y = (4-\eta)/\eta \tag{4.10}$$

The proportion of I nodes present in an IY system is given by P_I, where

$$P_I = I{:}Y/(1+I{:}Y). \tag{4.11}$$

4.3.2 Random systems

In codes which have been developed to study the percolation properties of continuum line systems (e.g. Robinson, 1983), the centre-points of each line is determined by a Poisson point process (see Section 3.2.1). In a Poisson process, all events are independent of other events, so there is no spatial correlation of lines in these systems. The orientation and lengths of the lines are determined by independent Poisson sampling of specified PDFs. In the systems considered in this Chapter, all lines have the same length, and orientations are in one of two, mutually perpendicular directions.

The critical line density of such a system is $d_{Lc} = 1.556$, and the critical connectivity is $\zeta_c = 3.112$ (Robinson 1983). All networks generated by this stochastic process are statistically identical, and constitute the set of random IX networks.

In geological systems, there is spatial correlation of faults and fractures (see Section 3.3.). Two forms of spatial correlation have been identified; splaying and clustering. Clustering is discussed first. As there is no correlation in a random system, such a

system can be considered as completely unclustered. If there is correlation of line position, this may involve either self-repulsion, or self-attraction of the lines. In the former case this results in an anti-clustered system, and in the latter case, results in a clustered system. An anti-clustered system will tend to form fewer connections at the same line density than a random system. Therefore, d_{Lc} of an anti-clustered system is greater than in a random system, but ζ_c is lower.

In a clustered system, lines tend to form connections with other lines. Therefore ζ_c of a clustered system is greater than of a random system. A clustered system is composed of regions in which there is a high density of connected lines, and regions in which the density is sparse. In order for the entire system to become connected, it is necessary for the clusters to become connected. Intuitively, therefore, clustered systems should become connected at a higher line density than the unclustered systems.

All the systems discussed above contain only I and X nodes. Three sorts of systems have been defined, anti-clustered, random and clustered systems. Systems become increasingly heterogeneous in this order. $\zeta_c = 3.112$ for a random system, is lower for an anti-clustered system, and higher for a clustered system. $d_{Lc} = 1.556$ for a random system, and is higher for either anti-clustered or clustered systems.

In a system containing Y nodes, there *has* to be spatial correlation of lines, as a Y node can never form by chance in a continuum. However, we can still conceive of a random system which contains Y nodes, based on clustering. Consider a line on an IYX ternary diagram with a constant $Y{:}X$ node ratio (Figure 4.6). Systems can become connected over the entire length of this line (as will be shown in Section 4.3.4). Following the inferences made above about IX systems, if the fraction of I nodes at which a system becomes connected (P_{Ic}) is high, then the system is anti-clustered and has a high d_{Lc}. As P_{Ic} decreases, d_{Lc} reduces to a minimum, at which point the system is neither clustered nor anti-clustered. At a lower P_{Ic}, the system is clustered,

and d_{Lc} increases again. This d_{Lc} minimum defines the set of random systems at this particular $Y{:}X$. If all values of $Y{:}X$ ratio are considered, then the percolation threshold of a random systems plots as a line in IYX space (figure 4.6).

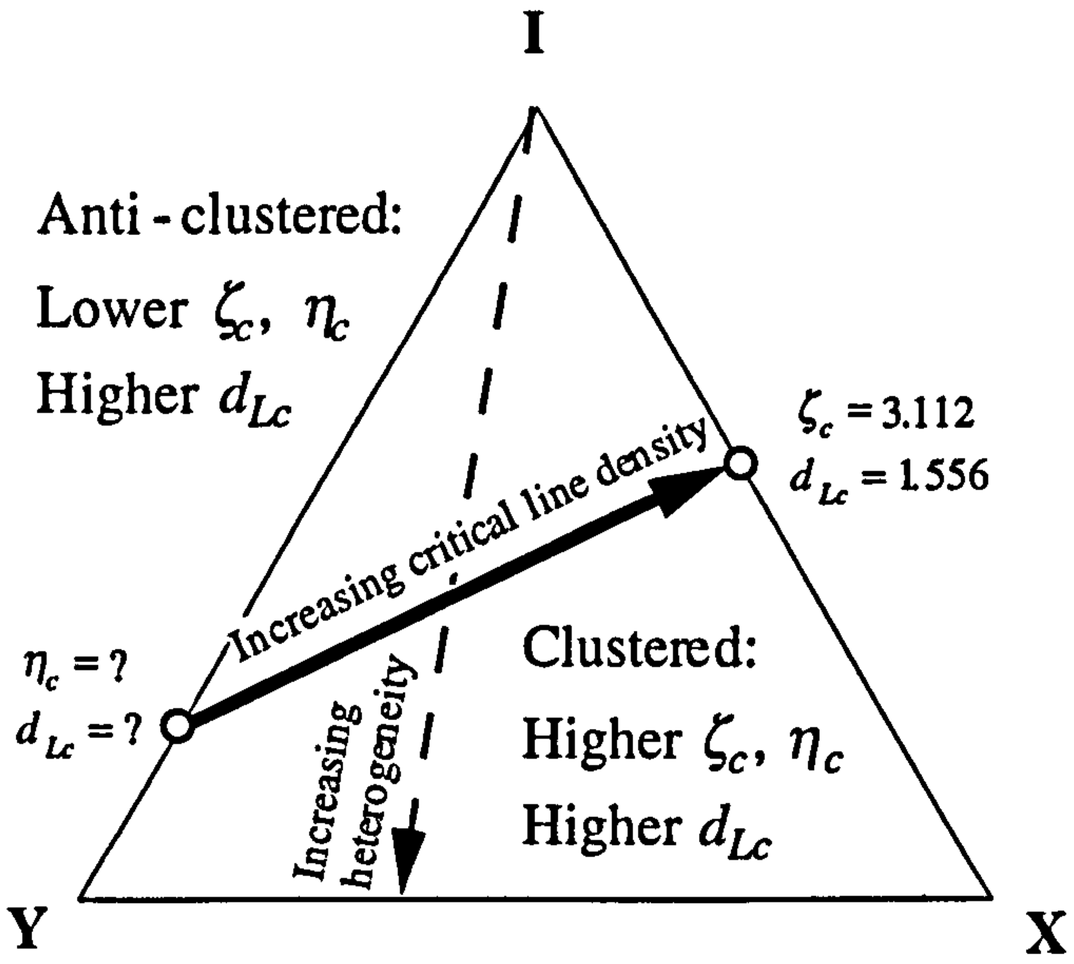

Figure 4.6. IYX ternary diagram showing the inferred characteristics of anti-clustered, random and clustered systems. A random system at any arbitrary Y:X node ratio (dashed line) will become connected when it intersects the percolation threshold for random systems (bold line). The critical line density at which this occurs decreases as Y:X increases.

A random system on the IX axis is generated if the system is allowed as many degrees of freedom as possible. If these degrees of freedom are curtailed (by incorporation of either clustering or connectivity systematics), non-random systems are produced. Consideration of systems with Y nodes inevitably necessitates a reduction in the degrees of freedom present. However, for a random system at a particular $Y{:}X$ ratio, honouring this ratio is the only reduction in freedom allowed. For the purposes of this Chapter, therefore, a random system is defined as one which has as many degrees of freedom as possible, *at a particular $Y{:}X$ ratio*.

4.3.3 Uniform systems

The network modelling code which is described in Section 4.4 allows generation of statistically distinct, non-random systems at different $Y{:}X$ ratios, through the incorporating of nine line placement rules in the code. Lines are placed according to predetermined proportions of each rule. For instance, 30% of lines could be forced to form a X node with an existing line, and the remaining 70% forced to form a Y node.

Spatial correlation of lines occurs in these models as a consequence of the line placement rules.

In the previous Section, random systems were defined based on clustering. The clustering in this discussion arose as a consequence of considering system with non-random connectivities, but was not explicit to the definition of random systems. Similarly, spatial clustering is not incorporated explicitly in the code. Because of this, a further distinction between systems is made. A *uniform* system is one which can be generated without incorporation of explicit clustering rules in a network code, while *non-uniform* systems would require incorporation of spatial clustering rules (with or without connectivity rules).

The implications of this distinction allows generalisation of the definition of a uniform system. A uniform system is one in which the connectivity characteristics of clusters of different sizes are similar. In a uniform system with $d_L \geq d_{Lc}$, the percolation cluster and all smaller clusters contain approximately the same proportions of the three node types. If this condition is not satisfied, then the system is *non-uniform*. Uniform systems can be generated stochastically with only connectivity rules, but non-uniform systems require greater deterministic input (clustering rules). At any particular $Y{:}X$ node ratio there are many possible, statistically distinct uniform systems, each with a particular d_{Lc}, but only one of these systems is random.

In the section that follows, geometrical analysis is used to derive the regions of the IYX ternary diagram in which I believe systems to have particular properties (Figure 4.6). In Section 4.3.4, any possible line geometry is considered, so these systems need not be uniform. Many of the systems in these considerations are actually unlikely to ever form, either as natural fault or fracture systems, or as chance numerical realisations. In Section 4.3.5, I consider uniform systems, and determine a threshold above which uniform systems cannot be connected, irrespective of their line density. In Section

4.3.7, I determine the line on the ternary *IYX* plot which represents the percolation threshold of random systems.

These sections take the form of lettered clauses, and conclusions from several clauses are used to make inferences about IYX system network properties. All systems are considered to be within the geometrical REV, and therefore boundary and scale effects are ignored. Many of the theoretical conclusions reached are tested numerically using the new network code in Section 4.4.

4.3.4 Non-uniform systems

This Section considers the characteristics of any conceivable network.

(A) Consider the three IX networks shown in Figure 4.7. If a cluster has $I{:}X > 2{:}1$, then that cluster cannot be the percolation cluster. A percolation cluster in an IX system has $I{:}X \leq 2{:}1$.

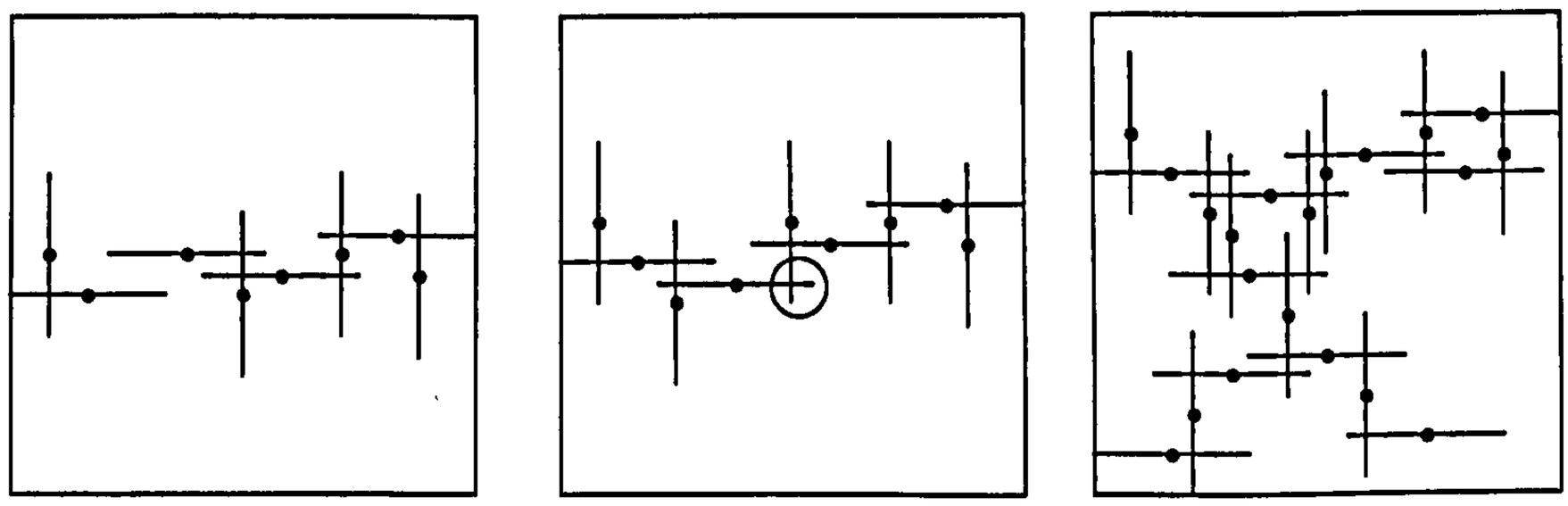

Figure 4.7. IX system. Each intersection in the percolation cluster (circle) involves one X and two I nodes. This is the critical, repeated structure.

(B) Consider the three IY networks (Figure 4.8). If a cluster has $I{:}Y > 1{:}1$, then that cluster cannot be the percolation cluster. A percolation cluster in an IY system has $I{:}Y \leq 1{:}1$.

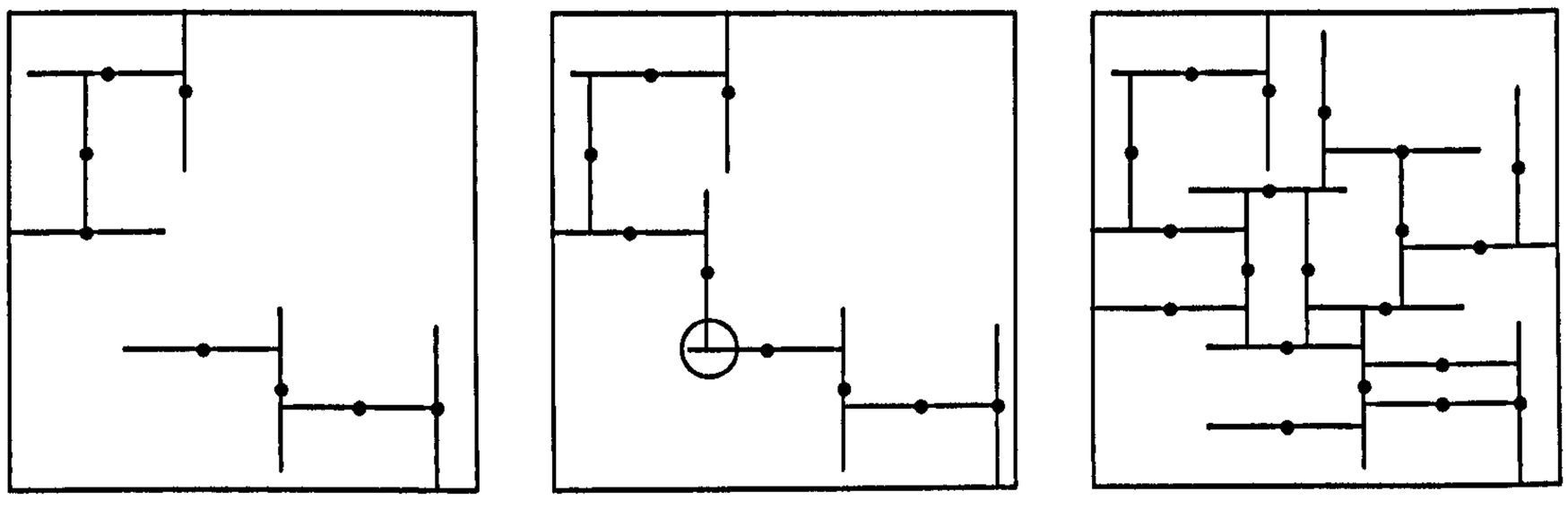

Figure 4.8. IY system. Each intersection in the percolation cluster (circle) involves one Y and one I node. This is the critical, repeated structure.

(C) Consider a finite area of an IX or IY system at the percolation threshold. In these clusters, $I:X \leq 2:1$ or $I:Y \leq 1:1$. The system may contain many lines which are not part of the percolation cluster, and which have $I:X > 2:1$ or $I:Y > 1:1$. In an extremely non-uniform system, all lines which are not part of the percolation cluster could have 2 I nodes and no X nodes (Figure 4.9a). There may be an infinite number of isolated lines in a system, but only a finite number of lines (and therefore X nodes) in the percolation cluster. A non-uniform system may therefore be connected even if $N_I \rightarrow \infty$. The only condition required for connectivity is that $I:(Y + X) < 1$.

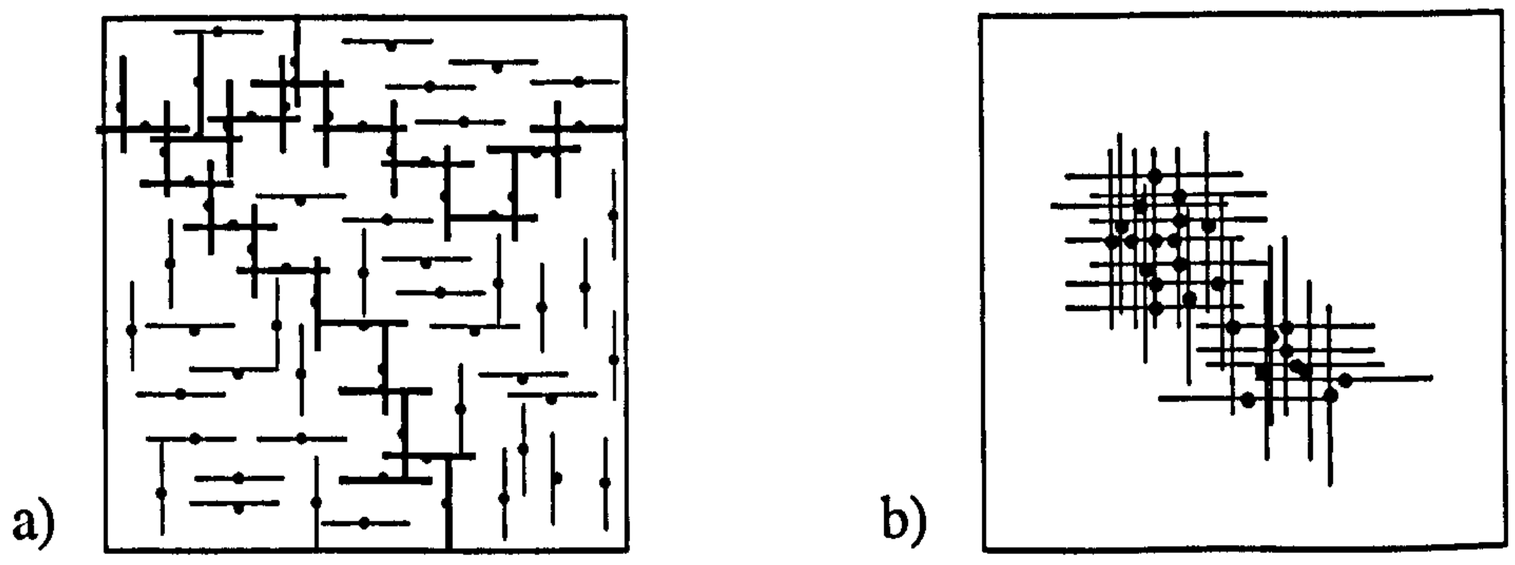

Figure 4.9. a) It is possible to form a percolating system with infinitely more isolated faults than faults in the percolation cluster (thicker lines). b) It is possible to form a non-percolating system with infinitely more intersections (Y or X nodes) than isolated tips (I nodes).

(D) Consider the IX network (Figure 4.9b). $I:X$ in this system is very low ($I:X << 2:1$), but the system is not connected. If N lines are present in the system, and the faults are equally divided between two populations, the maximum number of X

nodes possible (N_X) is $N^2 / 4$. The number of I nodes present (N_I) is always $2N$ for an IX system. Hence, for a system with a single, optimally connected cluster, $I{:}X = 8N{:}N^2$. As $N \to \infty$, $I{:}X \to 0$. Hence non-percolating systems are possible for any $I{:}X > 0$.

(E) Consider a system similar to that in Figure 4.9b, but in which Y nodes are also present. For such a system, $N_I < 2N$, as $N_I = 2N - N_Y$ (Equation 4.8). Therefore, in an extreme case, $I{:}(Y+X) < 8N{:}N^2$. As $N_F \to \infty$, $I{:}(Y+X) \to 0$. Therefore non-percolating systems are possible for any $I{:}(Y+X) > 0$.

(F) Summarising these clauses:

- Only if $I{:}(Y+X) = 1$ is a system definitely not connected.
- Only if $I{:}(Y+X) = 0$ is a system definitely connected.

In other words, a system with node proportions at any position within an IYX ternary diagram could be connected, provided it has <100% I nodes. Conversely, a system at any position within an IYX ternary diagram could be disconnected, provided it has >0% I nodes. The systems considered by these clauses are not necessarily uniform, so the connectivity properties of the percolation cluster may differ from those of the rest of the system. In the following section we consider uniform systems.

4.3.5 Uniform systems

In a uniform system, the node proportions in the percolating cluster must be similar to the node proportions in smaller clusters.

(G) Clauses (A) and (B) showed that, in a percolation cluster, $I{:}X \leq 2{:}1$ for an IX system, or $I{:}Y \leq 1{:}1$ for an IY system. Therefore, in a uniform system at the percolation threshold, all clusters must have $I{:}X \leq 2{:}1$ in an IX system, or $I{:}Y \leq 1{:}1$ in

an IY system. Hence, for uniform IX and IY systems to be connected, $I{:}X \leq 2{:}1$ and $I{:}Y \leq 1{:}1$.

(H) The systems considered in Clauses (D) and (E) contain only one fault cluster. Therefore these systems are uniform, because all the clusters have the same connectivity characteristics. This is, however, a trivial case.

(I) Consider an IX system with a particular number of clusters, each of which contains $M^2/4$ X nodes, where M is the number of lines in the cluster. This system is uniform, and if the number of clusters is small relative to M, $I{:}X$ will be very low. Following Clause (E), a similar reasoning also applies to IY systems.

(J) Summarising these clauses:

- Only if $I{:}(Y,X) = 0$ is a uniform system definitely connected.
- Only if $I{:}Y > 1{:}1$ is a uniform IY system definitely not connected.
- Only if $I{:}X > 2{:}1$ is a uniform IX system definitely not connected.

(K) The limits ($I{:}X = 2{:}1$, $I{:}Y = 1{:}1$) in clause (G) are extreme cases. Percolation within a uniform system can only be satisfied if the smallest cluster contains at least 4 lines in either an IX or an IY case (Figure 4.10). Most clusters will not have lines in ideal positions, so $I{:}X = 2{:}1$, $I{:}Y = 1{:}1$ is the threshold at which connectivity of a uniform system is theoretically possible, but the probability of connectivity at these node ratios is infinitesimally small. Therefore, the probability that a uniform system is connected ($p(\textit{connectivity})$) is zero at $I{:}X = 2{:}1$ and at $I{:}Y = 1{:}1$, and slowly increases as $I{:}(Y + X)$ decreases.

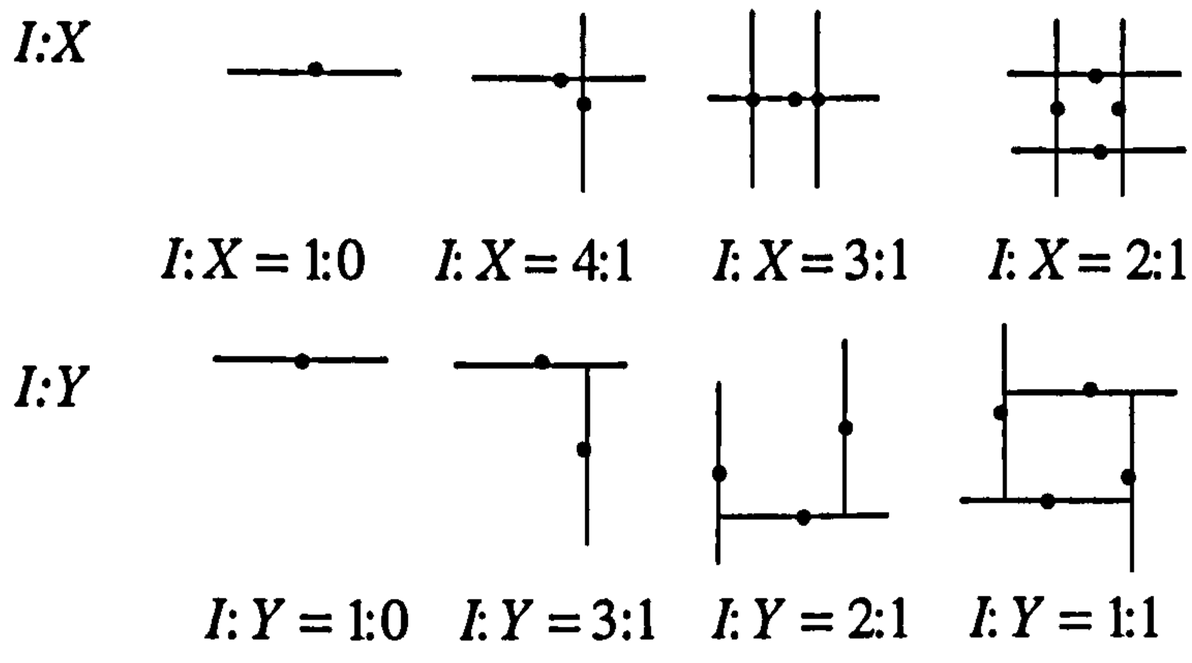

Figure 4.10. Clusters must contain at least four faults for the critical, repeated node ratio to be achieved.

(L) The systems considered in clauses (H) and (I) requires that all clusters in a system are identical. This is also theoretically possible, but infinitely unlikely. Therefore, for a uniform system, $p(connectivity) = 1$ at $I:(Y+X)=0$, and slowly decreases as $I:(Y+X)$ increases.

4.3.6 Characterisation of IYX space

Figure 4.11 shows an IYX ternary diagram, and summarises the points already made. The ternary diagram is split into three regions (A, B and C). Clause (J) states that if a uniform system lies in Region A, it is disconnected. Therefore (following Clause (F)) any system which falls in region A and is connected, is non-uniform.

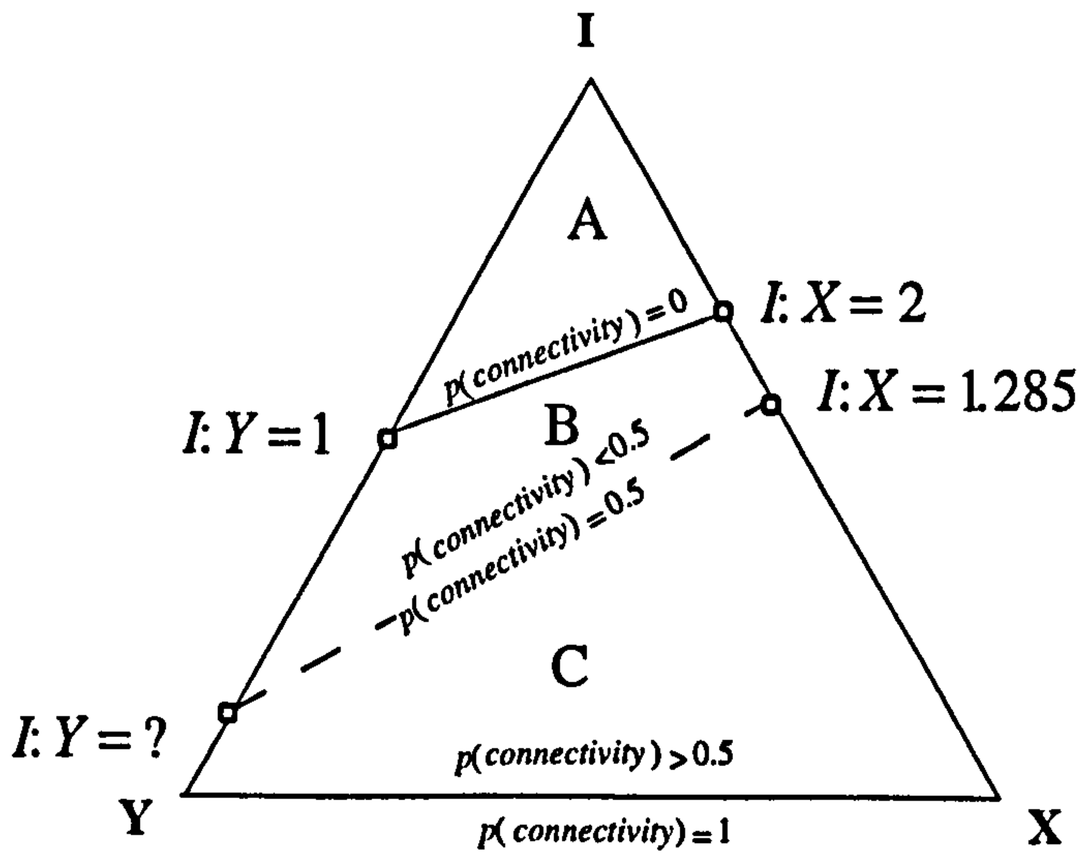

Figure 4.11. IYX ternary diagram showing the probability that a uniform system is connected.

Uniform systems may become connected only in regions B and C. *p(connectivity)* ranges from zero at the threshold between Regions A and B, to one on the YX axis. Between these limits there is a discrete probability that the system is connected, and the shape of the probability contours depend on the geometrical freedom the system has.

Geometrical freedom is considered in terms of how close to random the system is. Demanding that a system has a particular $Y{:}X$ ratio constitutes a diminution of geometrical freedom, however in a random IYX systems, this is the only reduction in freedom granted, and in every other way the system has maximum freedom (see Section 4.3.3). There is a particular $I{:}Y{:}X$ ratio which represents the percolation threshold of a random system at any $Y{:}X$. For a random system in region B, $p(connectivity) = 0$, and a random system in region C, $p(connectivity) = 1$. For a uniform system, the random percolation threshold represents $p(connectivity) = 0.5$ (Figure 4.11). In Section 4.3.7, the position of this line is calculated.

4.3.7 Determination of the random percolation threshold

In this section, two methods are described to determine the critical $I{:}Y$ ratio of a random IY system. Both methods are based on consideration of ζ_c for a random IX system, which is a known value. The first method (Clauses M to V) involves the random removal of lines from regular, topologically equivalent, IX and IY lattices at different levels of discretisation until ζ_c is reached, from which η_c is deduced. The second method is rather more abstract, and involves systematic replacement in a random system of Y nodes for X node and I nodes (Clause W). Both methods give identical values of η_c, allowing confidence in the prediction of the line separating regions B and C on Figure 4.11.

Random removal of lines from a regular lattice

(M) Consider Figure 4.12. This shows three discretisations of an IX system with $I{:}X = 1$. It is represented with periodic boundaries, and should be considered of infinite extent. Clearly it is a connected cluster, and clearly there are more lines present than necessary for this to be so.

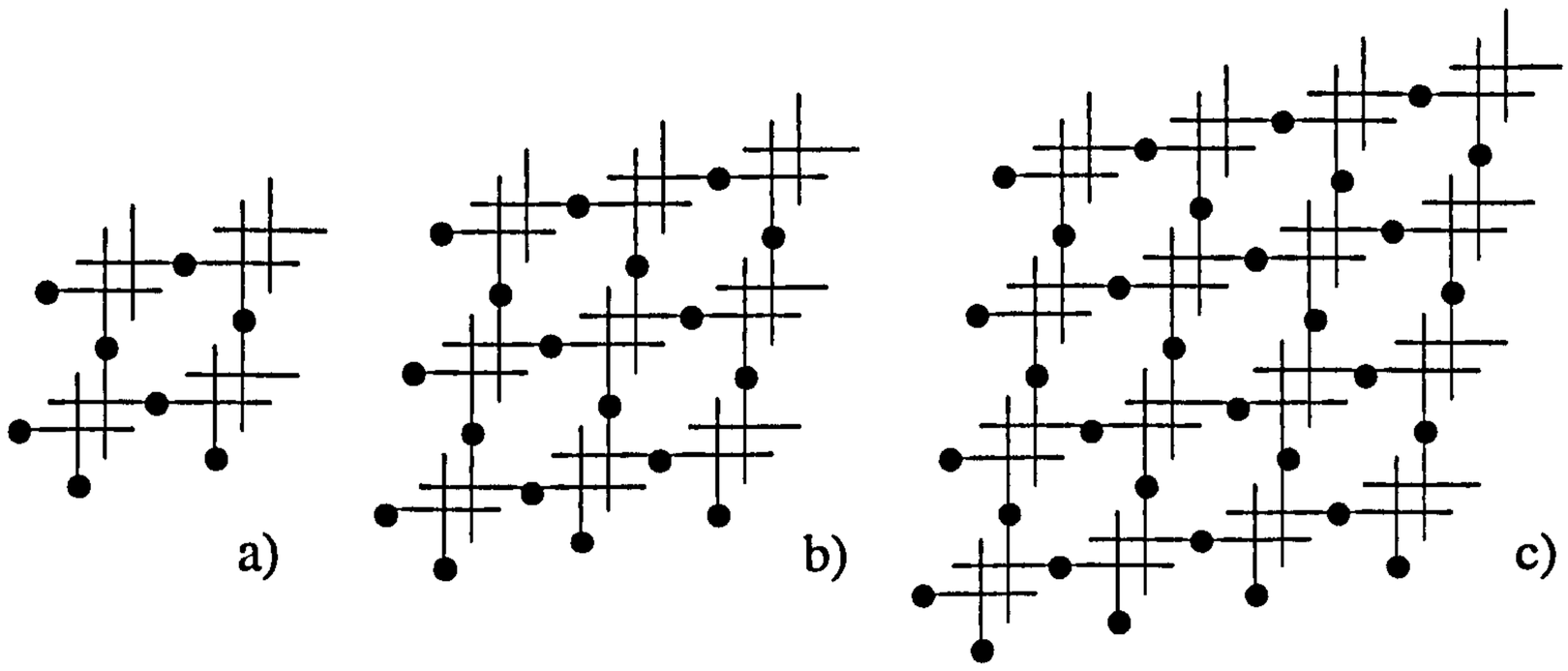

Figure 4.12. a) An IX system at different levels of discretisation. The systems represent infinite lattices of which a) 8, b) 18, and c) 32 lines are considered. The systems have periodic boundaries, and therefore half-lines have been drawn at the edges. The half-lines at the top and to the right should be considered as continuations of the half-lines at the bottom and to the left.

(N) The new modelling reproduces Robinson's result (1983), that an IX system in which lines are distributed at random has $I{:}X = 1.285$ at percolation (Figure 4.5). Therefore the system in Figure 4.12, as well as having more lines, must have a higher fraction of X nodes than necessary for percolation.

(O) If a line is removed from the system in Figure 4.12, the number of X nodes present (N_X) is lowered by 4, and the number of I nodes present (N_I) is lowered by 2. Therefore the network has $I{:}X > 1$.

(P) For each line that is removed, N_I is lowered by 2. For lines after the first one, N_X is lowered by < 4, as some lines which originally intersected this line may have already been removed. Therefore $I{:}X$ gradually increases as more lines are removed.

As there are fewer lines in the models with lower discretisation, $I{:}X$ will rise much more rapidly in these models.

(Q) For the three discretisations of the networks illustrated in Figure 4.12, probability trees of removal of the first three faults has been derived. The probability tree for the case involving 8 lines is shown on Figure 4.13. Results for all the cases are given on Table 4.1. From this table, N at ζ_c will be determined for each discretisation case (Clause T)

Table 4.1. $I{:}X$ ratio at three discretisations for the removal of the first three lines from the system in Figure 4.12.

N	N_I	N_X	$I{:}X$
8	16	16	1.000
7	14	12	1.167
6	12	8.571	1.400
5	10	5.714	1.750
18	36	36	1.000
17	34	32	1.063
16	32	28.235	1.133
15	30	24.706	1.214
32	64	64	1.000
31	62	60	1.033
30	60	56.129	1.069
29	58	52.396	1.107

(R) Consider Figure 4.14. This is a portion of an infinite IY system, represented with periodic boundaries. If every Y node is replaced with an I node and an X node, then the system is topologically identical to Figure 4.12. Therefore, it is reasonable to expect it to have the same N at percolation as the IX system considered above. Based on this assumption, η_c is calculated in the following few clauses.

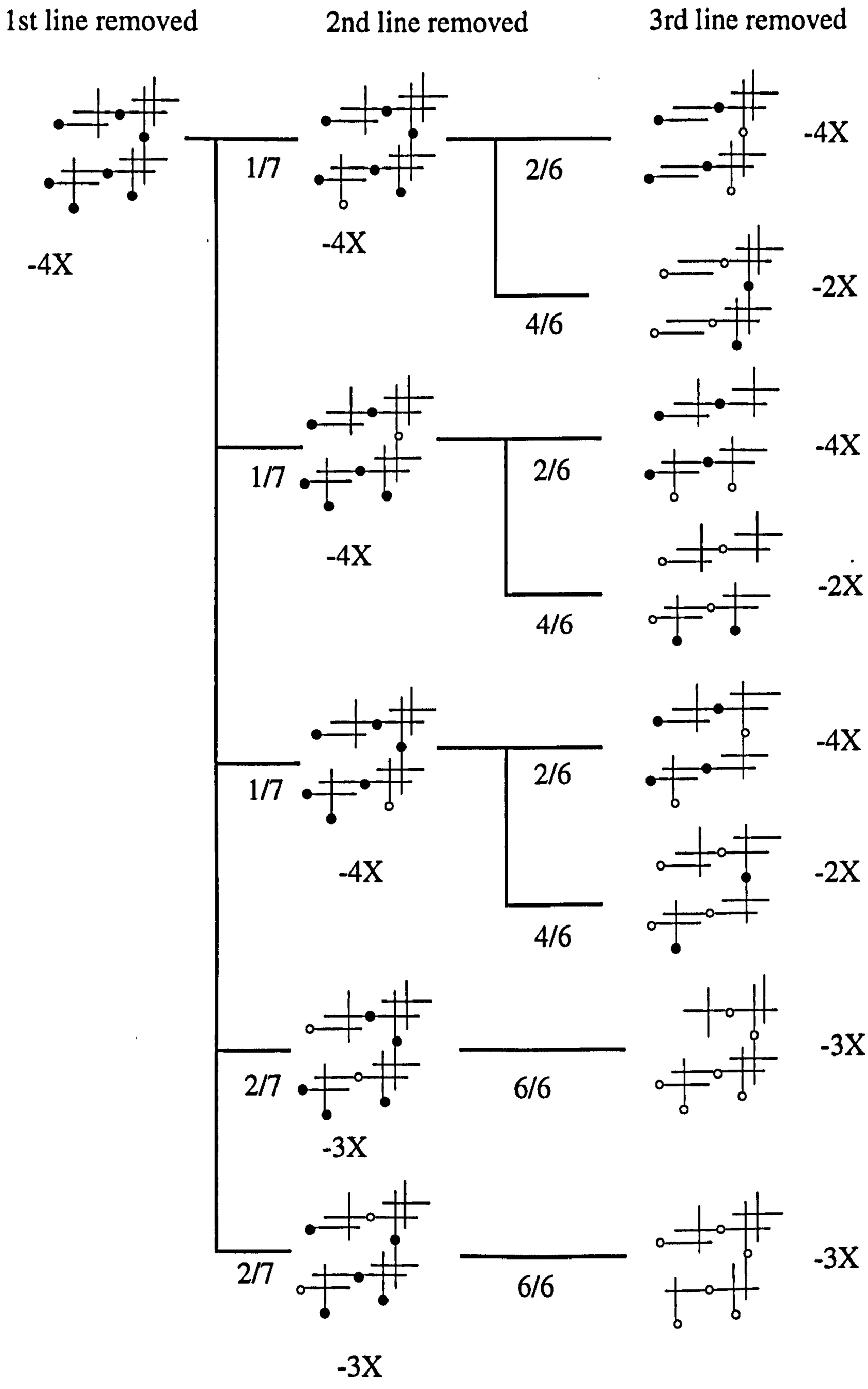

Figure 4.13. Probability tree for removal of the first three lines from the system containing 8 lines. Removal of the first line reduces the number of X nodes by 4. Removal of the second line reduces the number of X nodes by a further $4(3/7)+3(4/7)$. Removal of the third line further reduces the number of X nodes by $(3/7)(4(2/6)+2(4/6))+3(4/7)$. The lines with open circles represent those which could be removed to give the same result for each branch of the tree.

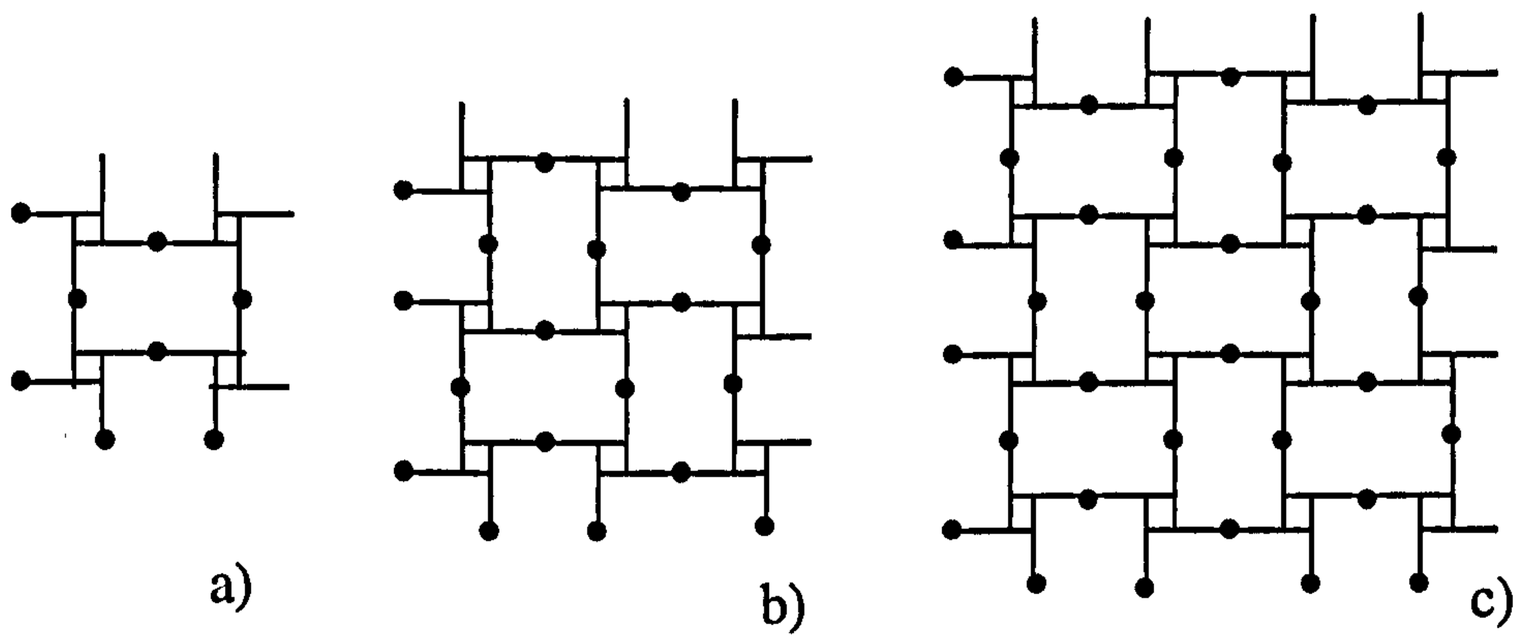

Figure 4.14. An IY system at the same three levels of discretisation as the IX systems in Figure 4.12. Each Y node replaces an I and an X node from the IX system. a) 8 lines. b) 18 lines. c) 32 lines.

(S) As lines are removed from the system in Figure 4.14, some Y nodes are eliminated altogether, and some are transformed into I nodes. The shape of the probability tree for this case is the same as for the IX case, except that:

- 4 X nodes removed becomes 4 Y nodes removed and 2 I nodes added,
- 3 X nodes removed becomes 3 Y nodes removed and 1 I node added, and
- 2 X nodes removed becomes 2 Y nodes removed.

The IY ratio during removal faults can therefore be derived from the probability trees for the IX system. The $I{:}Y$ ratio for the three discretisation levels is given on Table 4.2.

Table 4.2. $I{:}Y$ ratio during the removal of the first three lines from the IY system

N	N_I	N_Y	$I{:}Y$
8	0	16	0
7	2	12	0.167
6	3.429	8.571	0.400
5	4.296	5.714	0.750
18	0	36	0
17	2	32	0.063
16	3.765	28.235	0.133
15	5.294	24.706	0.214
32	0	64	0
31	2	60	0.033
30	3.871	56.129	0.069
29	5.604	52.396	0.107

(T) As ζ is inversely proportional to $I{:}X$ (equation 4.3), there is a linear relationship between N and $1/(I{:}X)$. Figure 4.15a shows the variation in N with respect to $1/(I{:}X)$ for the three levels of discretisation.

(U) Figure 4.15b shows variation in P_I with respect to N for the three levels of discretisation of the IY system. A linear correlation is found in each discretisation case.

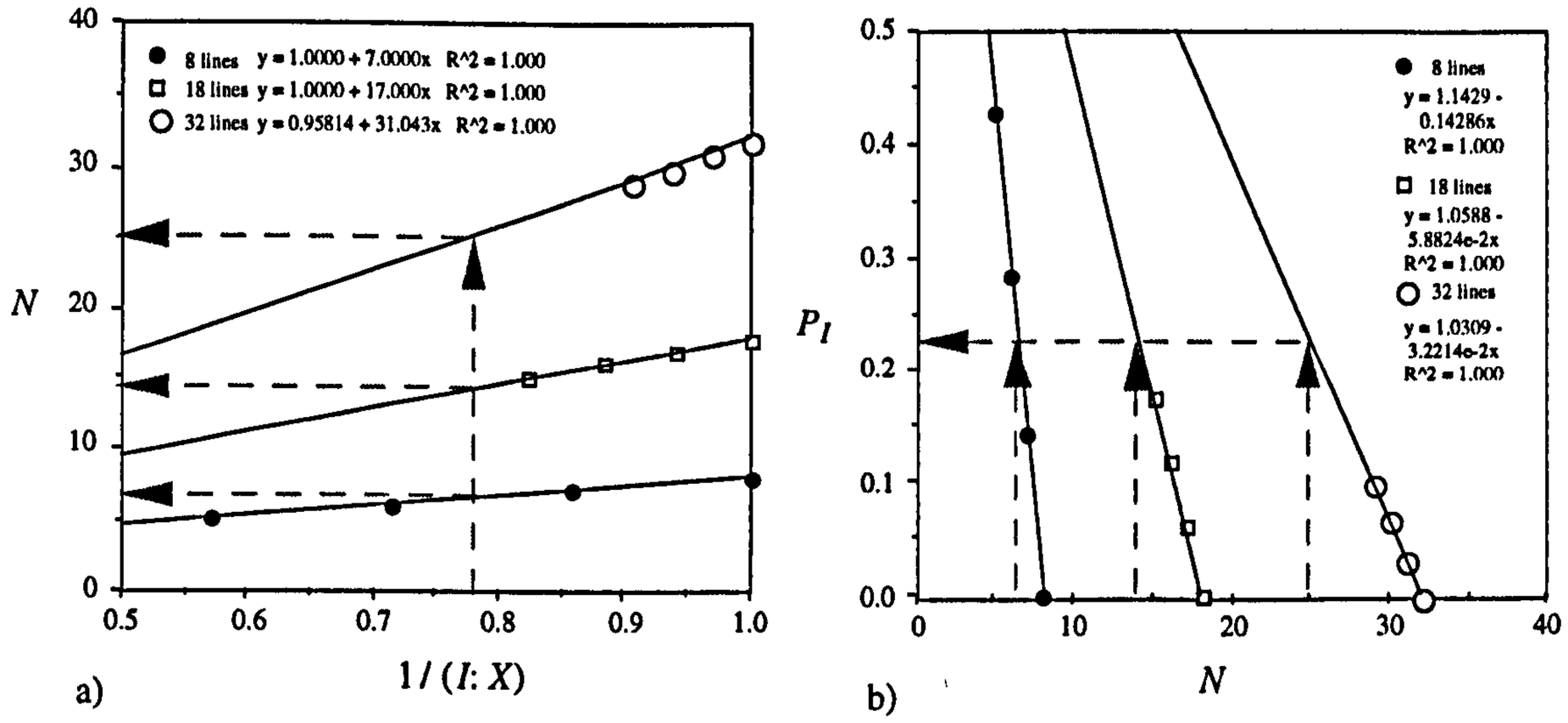

Figure 4.15. a) N vs. $1/(I{:}X)$ for the removal of the first three faults for each IX system. $(I{:}X)_c$ is known, so N_c can be calculated at each discretisation (arrows). b) P_I vs. N for removal of the first three faults for each IY system. N_c determined from (a) is input to determine P_{Ic} for the IY system at each discretisation level.

(V) The relationships on Figure 4.15a have been used to calculate the number of lines which should be removed from each of the discretisation levels to achieve the critical connectivity ($I{:}X = 1.285$). These values are input into the P_I vs. N relationship (Figure 4.15b), to determine P_{Ic} of an IY system. This two-step calculation is represented by the arrows on Figure 3.14. Each discretisation gives the critical P_I for an IY system at 0.222, and differ only in the fourth significant figure.

This is the first of two estimates of the percolation threshold of a random IY system. The second estimate is made below.

Systematic replacement of all X nodes from a random system

(W) A random IX system at percolation has $I{:}X = 1.285$. Therefore $N_X = 0.438N_N$, and $N_I = 0.562N_N$, where N_N is the total number of nodes present in the system. Assume that every X node in this system is converted into a Y node. For each X node in the system that is converted into a Y node, there is also an I node which is eliminated from the system (Figure 4.16). Hence, if a critical random IX system is converted to an IY system in this way, $N_Y = 0.438N_N$, and $N_I = (0.562 - 0.438)N_N$. Therefore $I{:}Y = 0.285$ for this IY system. $I{:}Y = 0.285$ corresponds to $P_I = 0.222$, a result identical to those obtained by the much more laborious method described above.

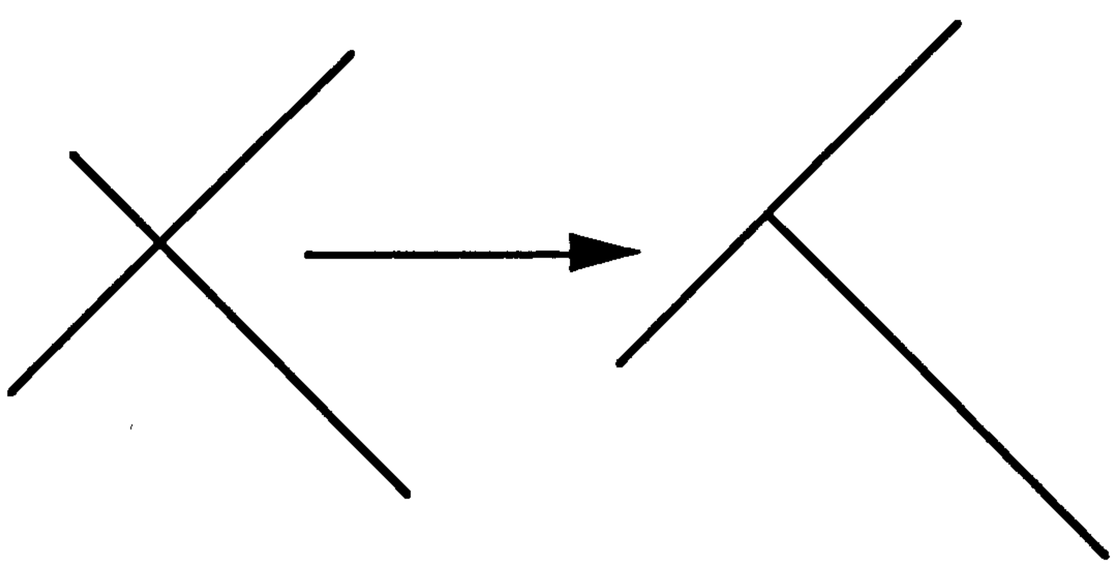

Figure 4.16. Replacing an X node in a system with a Y node implies that an I node is eliminated from the system.

The procedure described above involves sliding lines along their length until an X node becomes a Y node. During this process, the line could intersect another line it was previously unconnected to, creating an X node. Therefore the second line must be moved until this new X node is eliminated. This movement could create even more X nodes, so the process must be repeated, and many lines might have to be moved in order to transform a single X node. Eventually, a system (with a considerably lower line density) will be created which contains only I and Y nodes, and only as many Y nodes as there were originally X nodes. This system will have $I{:}Y = 0.285$. Creating a numerical algorithm to perform numerically this operation would be extremely difficult, and this discussion is intended purely as an abstraction. Significantly, however, both treatments described in this Section give the same critical connectivity for an IY system.

Another way to look at the problem is to consider that all the X nodes created are not necessary, and the system would be connected even without them. Consider, for example, that the two lines forming the new X node are slightly out of plane, so that although the 2D projection of the system contains X nodes, the 3D structure contains only the Y nodes created for the original X nodes.

4.3.8 Section summary

The conclusions of this theoretical discussion are summarised on Figure 4.17. For a system which has as many degrees of freedom as possible, the line separating regions B and C represents the percolation threshold of 2D line systems. If a random system has node proportions falling above this line (Region A or B) it is disconnected, and if it has proportions placing it in region C, it is connected. For system with fewer degrees of freedom, regions B and C are areas with some distinct probability that the system is connected. A system falling into region A can only be connected if the system incorporates explicit clustering systematics.

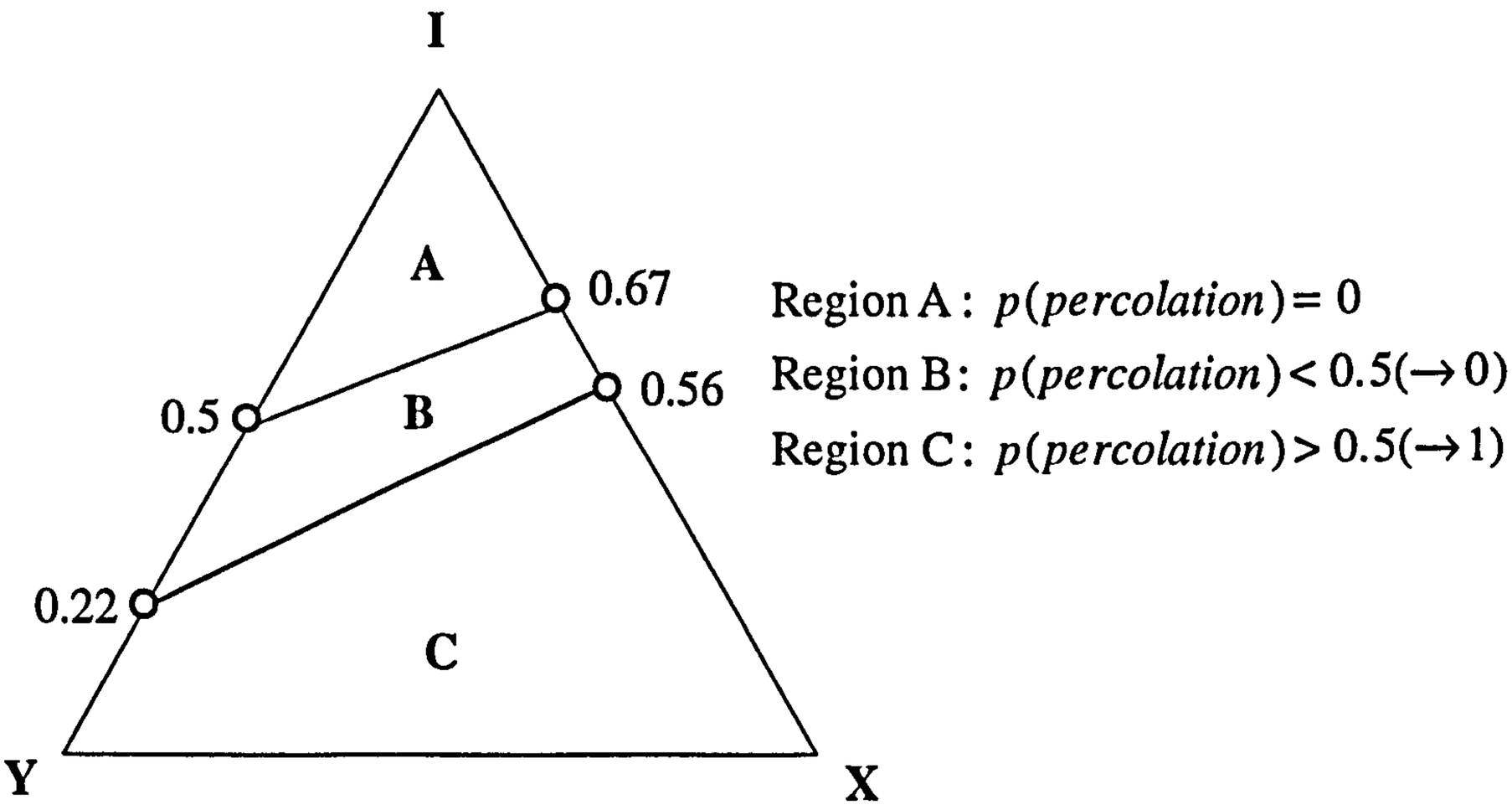

Figure 4.17. Theoretically derived percolation limits for an IYX system. The numbers on the vertices refer to the I-node proportions (P_I). Probability of connectivity for a uniform (and a random in parentheses) system are given for each region.

4.4 Network modelling results

A C++ code has been developed as part of this project to study continuum percolation of lines (programming by S. Schallenburger, D. Carruthers and M. Forrester). The code adopts a Boolean modelling approach (see Section 3.2.4). In its simplest state it hardly differs from the code used by Robinson (1983). Lines are placed randomly in an area (0,0) to (1,1), with their positions determined by their centre-point using a Poisson point process. In the models described in this thesis, lines are all the same length, and are equally divided between two orthogonal orientations. Modifications could allow lengths and orientations to be drawn from more variable PDFs, but this work considers only the simplest case.

Lines are added to the area sequentially, and after each line is added, a routine is run which checks for percolation. Run can be stopped and analysed at the percolation threshold, or any other line density. The length of the lines (L) is input as a fraction of the edge of the area. In a region at the edge of the area, portions of lines with their centres in the box pass outside it. No fault centres are placed outside the box, so there is no compensation for this loss of line density at the edge. To overcome this boundary effect, percolation is only checked to the edge of the inner area (Figure 4.18).

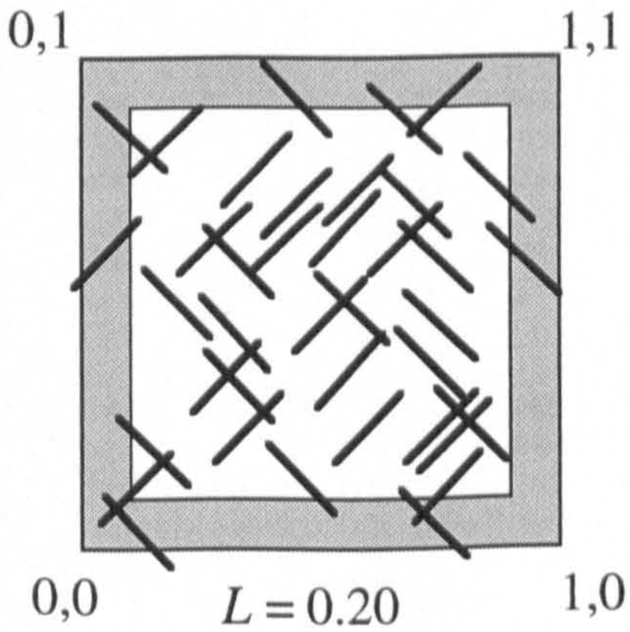

Figure 4.18. The length of the faults (L) is input as a fraction of the box edge. The shaded region is less dense due to boundary effects, and the size of the outer region is a function of the line length.

The width of the outer area is taken to be $L/2$, so the size of the inner area is $(1-L/2)^2$. If N lines are placed in the area $(0, 0)$ to $(1, 1)$, then the average number of line centres in the inner area is $N(1-L/2)^2$. Replacing $N(1-L/2)^2$ for N, and

$(1-L/2)^2$ for A in equation 4.1, gives d_L corrected for the boundary effect. This simplifies to:

$$d_L = NL^2 / 4. \qquad (4.12)$$

The line length is input as a fraction of the length of the edge of the area. If the length of the lines is small relative to the area, many more faults must be placed to attain the same d_L than if larger faults are modelled. If the program is to be used for determining percolation characteristics, then a small fault length must be used. For the analyses in this thesis, $L = 0.05$ has been chosen as a compromise between accuracy and computing time. This requires placement of about 2500 faults at percolation for a random system. Figure 4.3a showed a random IX system at percolation, and Figure 4.3b shows the percolation cluster of this system. This realisation percolated at $d_L = 1.565$, close to the value of $d_{Lc} \approx 1.556$ determined by Robinson. The mean d_{Lc} of 28 realisations is in agreement with Robinson's result to four significant figures, confirming that the code is operating correctly (see Figure 4.5).

4.4.1 Line placement rules

The code contains algorithms for the placement of lines according to nine different *placement Rules*. Each rule places lines according to different connectivity criteria within an overall Boolean scheme. The placement rules are summarised on Table 4.3. By combining lines placed according to different proportions of each placement rule, systems can be generated to occupy different portions of IYX node space at any particular line density, unlike any other fault placement scheme (see Section 3.2 and Figure 3.22).

Rule 1 places entirely random lines, and systems generated exclusively with Rule 1 are equivalent to the systems studied by Robinson (1983) and others. Placement Rules 4 and 7 place lines randomly as type 1, but any Rule 4 line which is placed is eliminated if

it produces an X node, while a Rule 7 line is eliminated if it does not produce an X node.

Table 4.3. Each line placement Rule produces a predetermined combination of I, Y and X nodes.

Placement Rule	I nodes	Y nodes	X nodes
1	2	0	≥0
2	1	1	≥0
3	0	2	≥0
4	2	0	0
5	1	1	0
6	0	2	0
7	2	0	≥1
8	1	1	≥1
9	0	2	≥1

Placement rules 2, 5 and 8 place lines at random, but then the line is moved parallel to its orientation until it forms a Y node with another line. This therefore produces one Y node and one I node. Apart from this, they are equivalent to Rules 1, 4 and 7: Rule 2 lines can contain any number of X nodes, Rule 5 lines do not form any X nodes, and Rule 8 lines form at least one X node.

Lines placed with placement rules 3, 6 and 9 form 2 Y nodes. A line is placed at random, then moved parallel to its orientation until it forms a Y node. It is then moved perpendicular to its orientation, within the length of the fault with which it forms a Y node, until it transforms an existing I node from another line into a Y node. Rule 3 lines can produce any number of X nodes, Rule 6 lines are allowed no X nodes, and Rule 9 lines must form at least one X node.

There is a problem with placement Rules 3, 6 and 9. In some cases the algorithm places a new fault in such a position that it does not simply add two Y nodes to the system, but instead adds 3 Y nodes and eliminates one I node (Figure 4.19). The code contains an algorithm which checks the system for fault intersections. These are recognised on the basis of the proximity of lines - if lines are within a certain distance of

each other, then the code considers them to be connected, and part of the same cluster. The additional Y node is recognised by this algorithm as an X node, and the I node which no longer exists is still considered present.

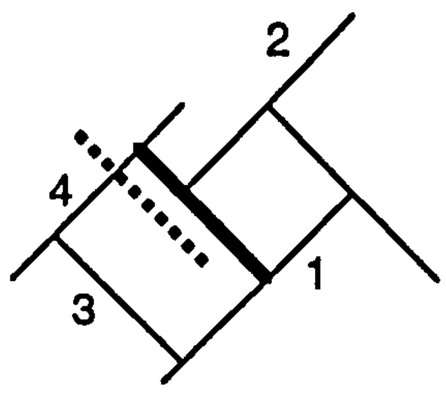

Figure 4.19. An error with the code, resulting in the calculation of X nodes for placement rules 3, 6 and 9. The dashed line has been placed according to Rule 3. First it is moved to form a Y node with line 1. Then it is moved until it forms a Y node with line 2. It is now the bold line. Due to the presence of the Y nodes connecting line 3 to lines 1 and 4, the bold line automatically forms a Y node with line 4. This extra Y node is recognised in the code , but is considered an X node. Therefore the bold line is still considered to have an I node at this end.

All placement rules except 1 and 4 require that the line being placed forms either a Y or an X node with a previously placed line. Therefore it is impossible to place lines of these types unless there is a background distribution of lines already placed. Hence a particular number of Rule 4 lines are placed in runs which require them, before any other lines are placed. Each of these background lines has 2 I nodes.

During the generation of a system, the first few line placed only form I nodes, so the system initially has $P_I = 1$. As line density increases so does connectivity, and the system follows a particular trajectory in IYX space. The position of this path depends on the placement rules used to generate the system. At a certain point the system will become connected, and both the IYX proportions and the line density at this point are recorded. In this way, the characteristics of system which become connected throughout IYX space may be determined. This is in contrast to existing methods for generating IYX systems, for which the systems are limited to only one path in IYX space (see Figure 3.22).

In Section 4.3.2 and 4.3.3, distinctions were made between random, uniform and non-uniform systems. A random IYX system was defined as one which has the same

clustering characteristics as a random IX system. Random systems at percolation can exist at any $Y{:}X$ ratio, and the percolation threshold of random system is represented as a line between the IX and the IY axis (Figure 4.6). The location of this line was determined theoretically in Section 4.3.7 (Figure 4.17). A uniform system has fewer degrees of freedom than a random system, and is either more or less clustered than a random system which becomes connected at the same $Y{:}X$ ratio. The clustering in uniform systems arises as a consequence of connectivity constrains, and no implicit clustering input are necessary to generate uniform systems. Section 4.3.5. determined the areas in IYX space in which uniform systems can become connected (Figure 4.17). Because there are only connectivity placement rules in the code, all systems generated are uniform. The following sections aim to confirm the results of the theoretical conceptualisations in Section 4.3, and also to determine critical line densities for random and uniform systems.

4.4.2 Connectivity thresholds for uniform systems

The upper threshold

In section 4.3.5, it was predicted that the upper I node proportion required for a uniform system to be connected lies on a line between $P_I = 0.5$ on the IY axis, and $P_I = 0.67$ on the IX axis (Figure 4.17). The location of this threshold has been evaluated with the code. Initially, 6400 Rule 4 faults are placed, corresponding to $d_L = 4$ (a much higher density to that needed for a random system to become connected). These lines each have 2 I nodes, and no X nodes, and therefore the system plots in the top corner of a ternary diagram. Then random lines are placed. Addition of Rule 1 lines increase the X node fraction very slowly, as each line adds another two I nodes to the system. Rule 3 lines increase the Y and X node fractions rather faster, as each line involves two Y nodes and any number of X nodes. The results for 10 realisations of each of these models are shown on Figure 4.20. Only when the I node fraction has been reduced to below the upper threshold do the systems become connected. Only if lines were placed with clustering criteria on the pre-existing

distribution of Rule 4 lines would it be possible to form a connected system with a higher P_I, and such a system would be non-uniform.

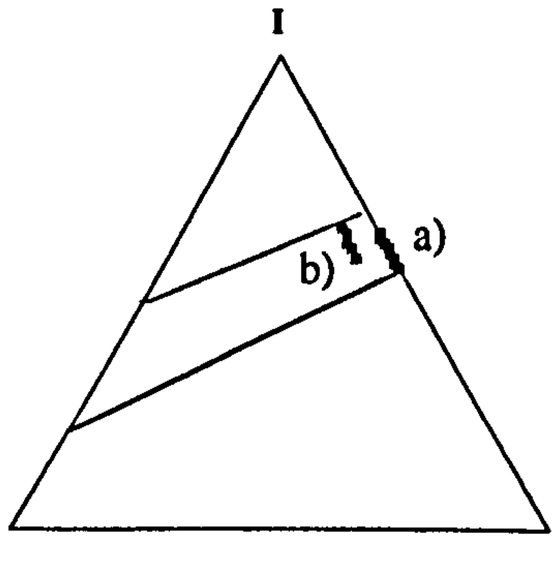

Figure 4.20. Confirmation of the upper connectivity threshold for uniform systems. Background $d_L = 4$ of line placed according to Rule 4. a) Addition lines added according to Rule 1. Average $d_{Lc} = 4.73$. 10 Realisations. b) Lines added according to Rule 3. Average $d_{Lc} = 4.38$. 10 realisations.

The lower threshold

In Section 4.3.5, it was predicted that it is possible to form a disconnected uniform system anywhere in IYX space. It is obviously possible to form disconnected uniform systems above the upper threshold - all uniform systems in this area will be disconnected. The lower threshold for uniform systems corresponds to the YX axis of the ternary diagram. 18 different combinations of placement Rules (Fields 0-17) have been run to determine the connectivity threshold at different IYX proportions. A summary of these results, and the placement rules used to generate each field are shown of Table 4.4. At least 20 realisations have been run for each field. Each datum on Figure 4.21 represents the position in IYX space at which each realisation became connected, and covers most of the area below the upper threshold. In the case of Field 3 (Figure 4.21), connectivity is achieved extremely close to the YX axis, confirming that uniform systems can remain disconnected at very low P_I.

Fields 1, 2 and 10 have been generated entirely with combinations of placement Rules 4, 5 and 6, and therefore should contain no X nodes (Table 4.3). The code, however, records X nodes for these systems (Table 4.4). This is due to the coding ambiguity, detailed in Section 4.4.1. The effect can be quantified for fields 1, 2 and 10, as no X nodes should be present. The error is not great, only between 3% and 6% of all nodes are affected in this way (Table 4.4). The locations of these fields on Figure 4.21 have

been corrected for this error. Any system containing placement Rules 3, 6 or 9 will have the same effect (Fields 3, 4, 6, 7, and 9 in addition to the three above), but for systems in which legitimate X nodes should exist, the effect cannot be quantified and corrected.

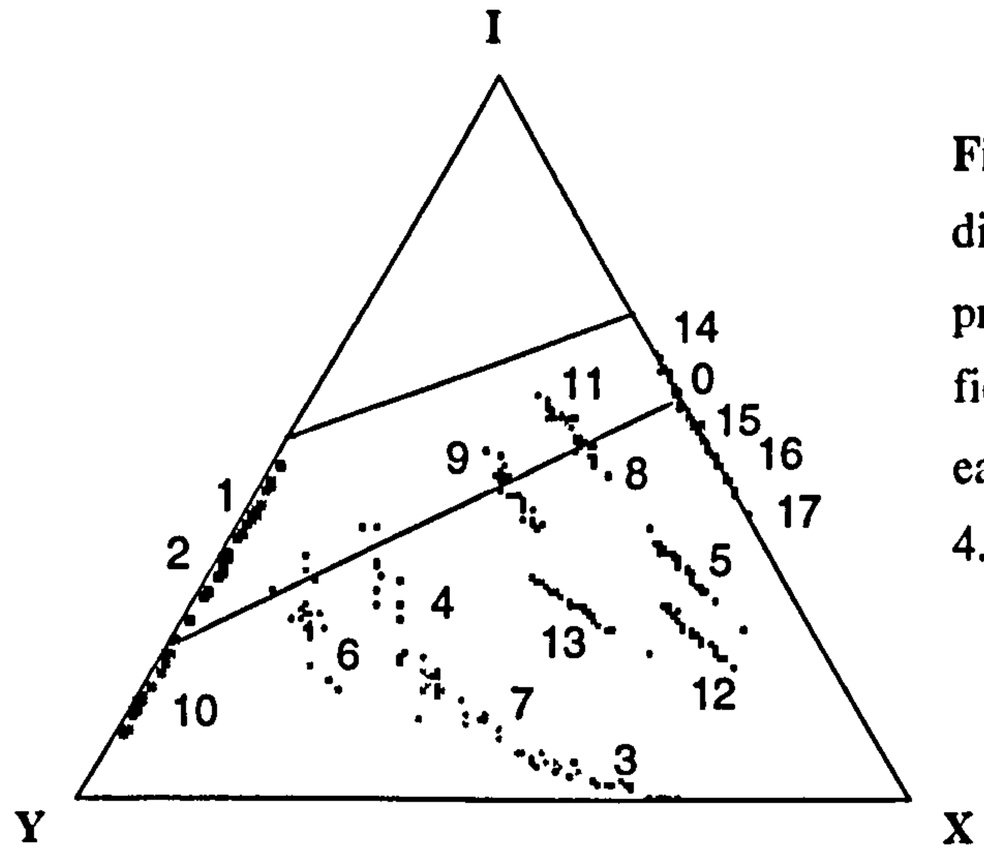

Figure 4.21. IYX ternary diagram showing the node proportions at percolation for 18 fields. The placement rules for each field are given on Table 4.4.

4.4.3 The characteristics of IYX systems

Figure 4.22 shows four transects through IYX space comprising 12 of the 18 data fields Transect A passes through three fields along the IX axis, and Transect B, through three fields on the IY axis. The three fields on Transect C have an approximately constant $Y{:}X$ ratio, but a variable P_I. Transect 4 follows the predicted percolation threshold for random systems. Realisations from these transects are illustrated on Figures 4.23 to 4.26, and each realisation has been stopped at the percolation threshold. Two realisations for each field are shown, so that the general characteristics of the fields can be appreciated - often there is no one realisation which is representative of the field.

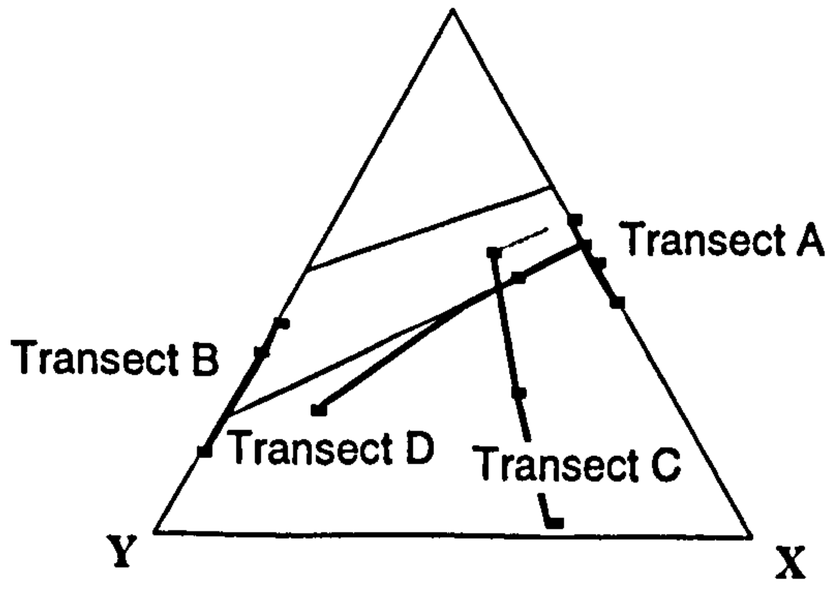

Figure 4.22. The locations in IYX space of the realisations in Figures 4.23 - 4.26 (Transects A - D respectively).

Table 4.4. Summary of results from the network modelling. All systems were generated with L=0.05. Percolation was checked every 20 lines, and therefore the d_L results are accurate to ± 0.01.

Field No.	Line placement Rules		Line density at percolation				Node proportions at percolation			Number of realisations
	Placement Types	Background Type 4	Maximum	Minimum	Mean	Coeficient of variation	X fraction	Y Fraction	I Fraction	
0	100% T1	0	1.83	1.36	1.56	0.07	0.43	0.00	0.57	28
1	50% T5, 50% T6	400	1.06	0.80	0.94	0.08	0.04	0.53	0.43	20
2	100% T6	400	0.80	0.51	0.65	0.11	0.03	0.60	0.37	20
3	100% T3	200	1.96	0.78	1.39	0.26	0.65	0.32	0.03	22
4	80%T3, 20% T6	400	1.00	0.54	0.78	0.20	0.29	0.47	0.23	23
5	50%T2, 50%T7	50	2.69	0.88	1.50	0.26	0.57	0.11	0.33	41
6	30% T3, 70% T6	300	0.88	0.49	0.63	0.15	0.15	0.60	0.25	23
7	90% T3, 10% T6	300	1.39	0.60	0.95	0.25	0.45	0.44	0.11	23
8	50% T1, 50% T2	200	1.44	1.00	1.17	0.09	0.35	0.15	0.50	21
9	50% T1, 50%T3	400	1.23	0.79	1.00	0.12	0.30	0.26	0.44	29
10	100% T6	200	0.68	0.44	0.54	0.13	0.06	0.72	0.22	22
11	50% T1, 50% T2	300	1.86	1.03	1.63	0.15	0.29	0.16	0.55	22
12	20% T7 80% T8	200	2.59	1.01	1.69	0.23	0.62	0.14	0.24	30
13	100% T2	50	1.84	0.66	1.04	0.23	0.46	0.26	0.28	30
14	70% T1, 30% T4	0	2.09	1.75	1.90	0.05	0.39	0.00	0.61	25
15	50% T1 50% T7	50	1.61	1.19	1.47	0.07	0.47	0.00	0.53	23
16	30% T1, 70%T7	50	1.74	1.30	1.50	0.09	0.49	0.00	0.51	25
17	10%T1, 90% T7	50	2.09	1.08	1.46	0.16	0.54	0.00	0.46	25

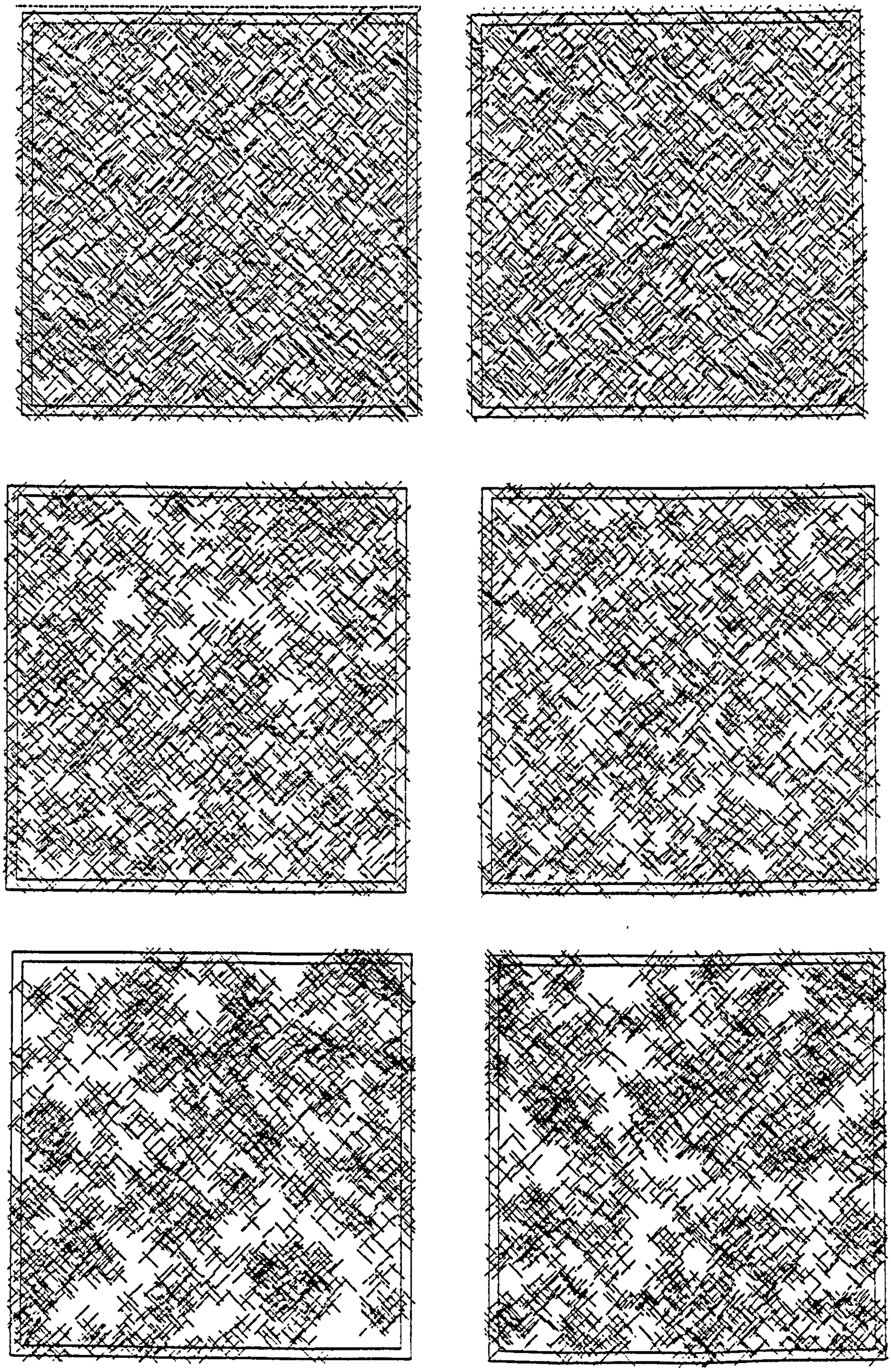

Figure 4.23. Two realisations each at percolation for IX systems. a) Field 14 (70% Rule 1, 30% Rule 4). b) Field 15 (50% Rule 1, 50% Rule 7, 50 Rule 4 in background). c) Field 17 (10% Rule 1, 90% Rule 7, 50 Rule 4 in background).

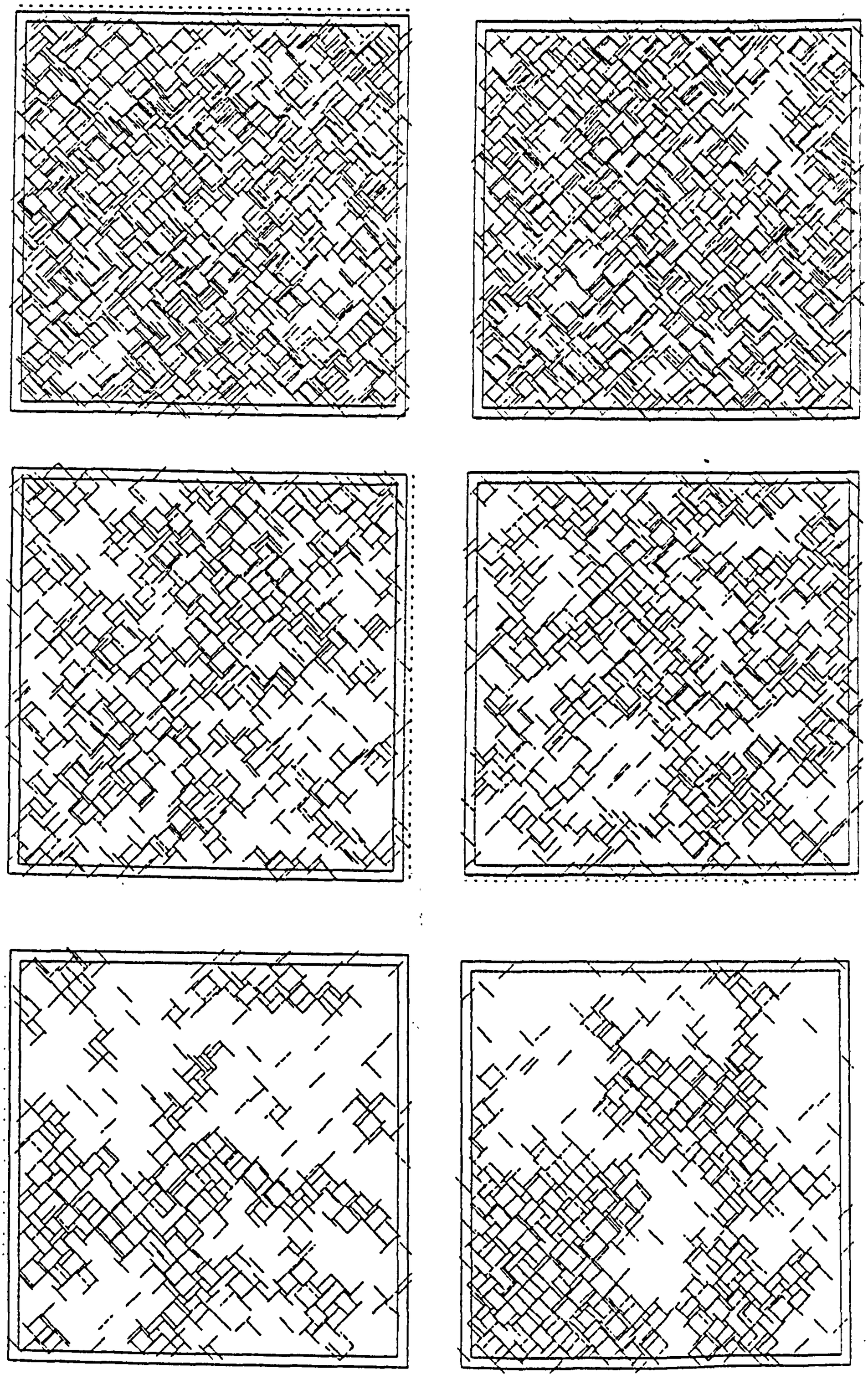

Figure 4.24. Two realisations each at percolation for IY systems. a) Field 1 (50% Rule 5, 50% Rule 6, 400 Rule 4 background). b) Field 2 (100% Rule 6, 400 Rule 4 in background). c) Field 10 (100% Rule 6, 200 Rule 4 in background).

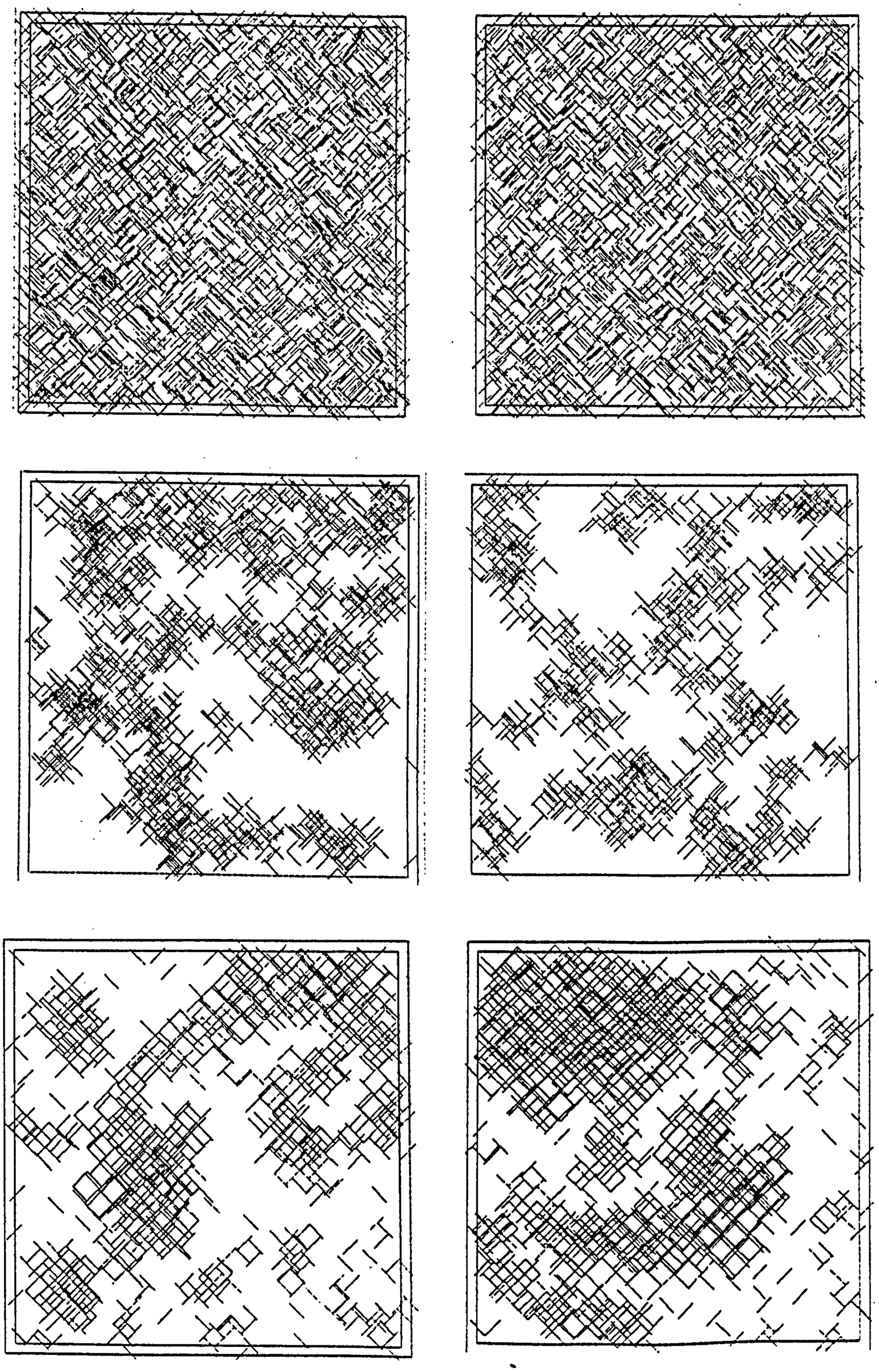

Figure 4.25. Two realisations each at percolation for systems at constant *Y:X*. a) Field 11 (50% Rule 1, 50% Rule 2, 300 Rule 4 in background) b) Field 13 (100% Rule 2, 50 Rule 4 in background). c) Field 3 (100% Rule 3, 200 Rule 4 in background).

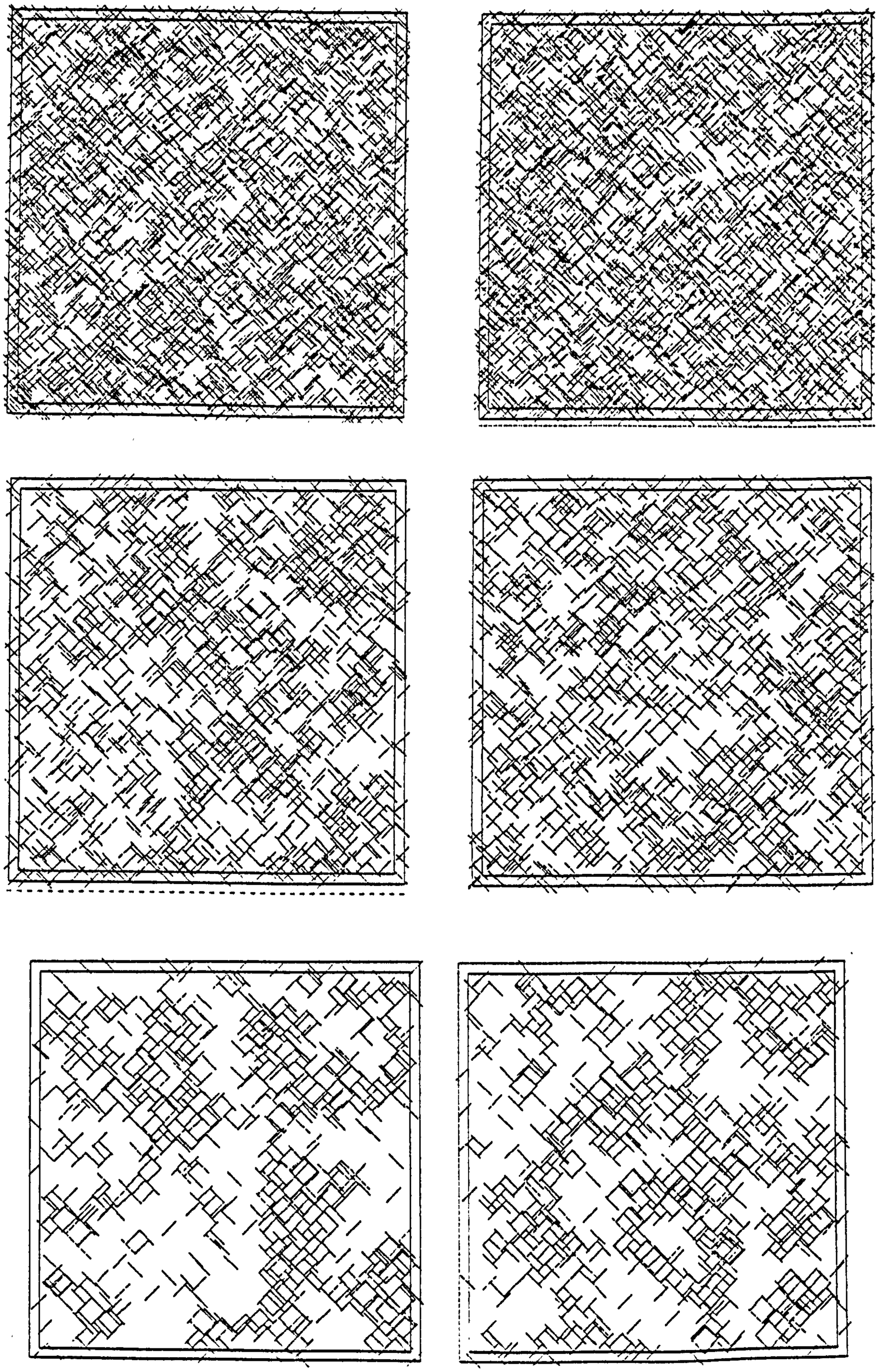

Figure 4.26. Two realisations each at percolation along the predicted percolation threshold of random systems. a) Field 0 (100% Rule 1). b) Field 8 (50% Rule 1, 50% Rule 2, 200 Rule 4 in background). c) Field 6 (30% Rule 3, 70% Rule 7, 300 Rule 4 in background).

4.4.4 The IX axis

Combinations of placement Rules 1, 4 and 7 produce systems with no Y nodes (Table 4.3), so these systems fall on the IX axis of an IYX ternary diagram. A line placed according to placement Rule 4 is not allowed to form an X node. Systems containing this sort of line are less connected at the same line density than random (Rule 1) systems, and therefore should percolate at a higher line density. A line generated by Rule 7 must form at least one X node upon being placed, and systems with a large number of Rule 7 lines form clustered systems, as lines are preferentially placed in areas which already have a large number of lines (Figure 4.23c).

In Section 4.3.2, a random system was distinguished from non-random systems in terms of clustering. All lines in a system generated with Rule 1 lines are completely uncorrelated, and so the system is neither clustered nor anti-clustered. Any system generated with Rule 1 lines is anti-clustered, and any system generated with Rule 7 lines is clustered. In an anti-clustered system (Field 14), the lines are self-repulsive, and therefore less connected than random, whilst in clustered systems (Fields 15, 16 and 17), the line density at percolation should be lower in a random system than either a clustered or anti-clustered system.

Figure 4.27 shows the line density and connectivity at percolation for five combinations of Rules 1, 4 and 7. While the system with Rule 4 faults clearly has a higher d_{Lc} than the random (100% Rule 1) systems, the three systems with Rule 7 lines actually have a lower d_{Lc} than the random system, contrary to expectation.

The systems with Rule 7 lines show a broader range in d_{Lc} (Figure 4.27). This can be attributed to spatial clustering (system heterogeneity). Heterogeneity increases when system become more connected with lower proportions of I nodes (Section 4.3.2). Clustered systems have a much larger uncertainty associated with attribution of both

d_{Lc} and ζ_c. In other words, this suggests that the REV of a heterogeneous (clustered) system is larger.

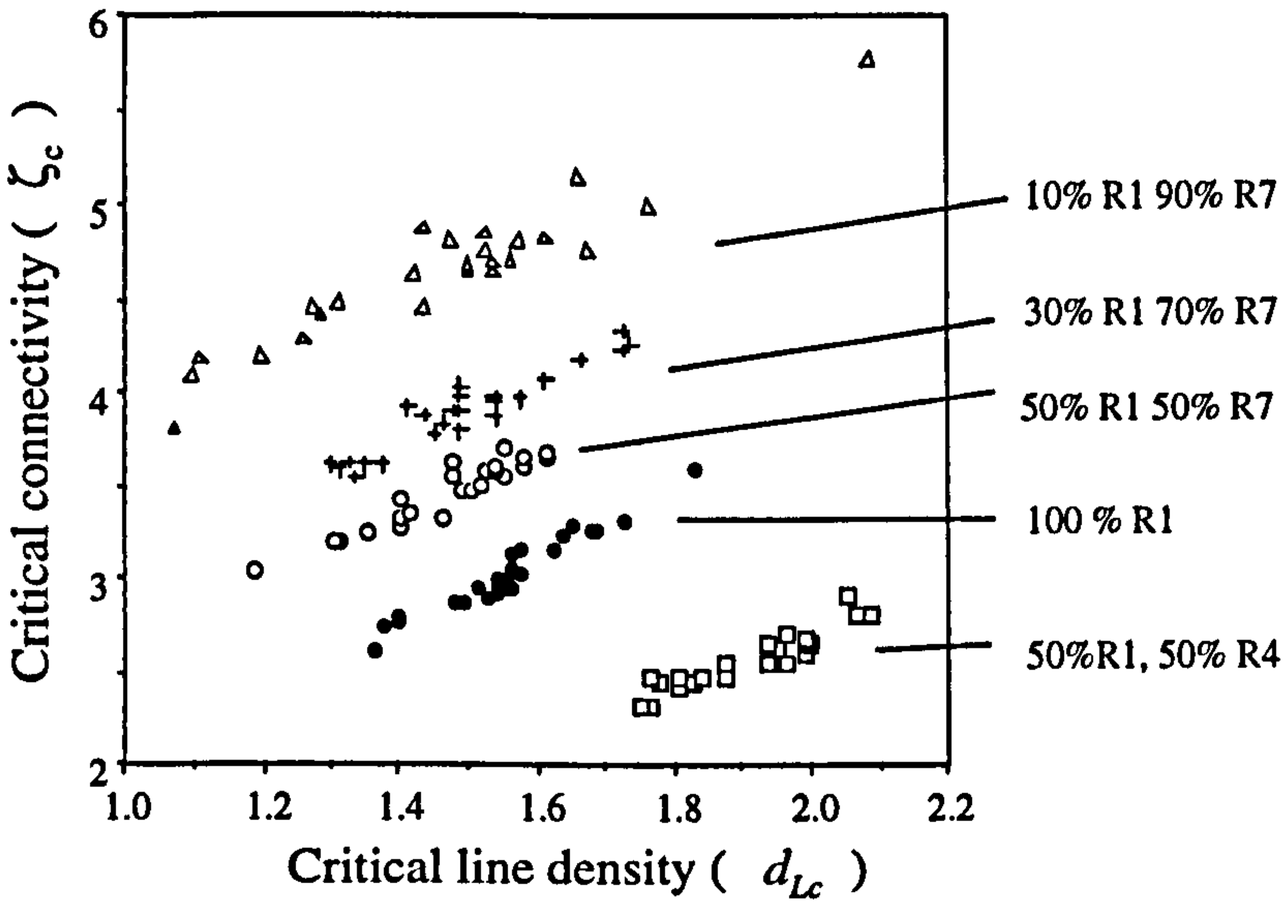

Figure 4.27 Critical connectivity vs. critical line density for realisations of five proportions of Rules 1, 4 and 7. (R1, R4 and R7 respectively)

In summary, on the IX axis of an IYX ternary diagram, there is a particular d_{Lc} and ζ_c for a random system. Non random systems, containing some form of deterministic line placement criteria, may percolate with either a higher or a lower ζ_c, but in either case should have a higher d_{Lc}, although this has not been demonstrated by these results. This is perhaps because the REV of clustered systems is larger, and sub-REV systems more sensitive to boundary effects have been generated.

4.4.5 The IY axis

Fields 1, 2 and 10 (Figure 4.24 and Table 4.3) should span the predicted percolation threshold of a random IY system. Figures 4.28 shows critical connectivty Vs. critical line density for IY systems, and the same general trends observed on the IX axis are present on the IY axis: as the I-node fraction decreases, the systems become more heterogeneous, and more regions are empty. The most obvious difference between these fields and the IX fields is that critical line density is lower on the IY axis. For the IY realisations, $0.44 < d_{Lc} < 0.94$, while for all IX fields, $1.08 < d_{Lc} < 2.09$.

Figure 4.28 shows a plot of critical connectivity η_c (see Section 4.3.1) vs. critical line density (d_{Lc}). The trend observed on the IX axis is repeated: for system which become connected at a low η_c, a small increase in η_c results in a large decrease in critical line density. At higher η_c, a large change in connectivity leads to a much smaller change in d_{Lc}. An η_c minimum, representing a random system, is not observed.

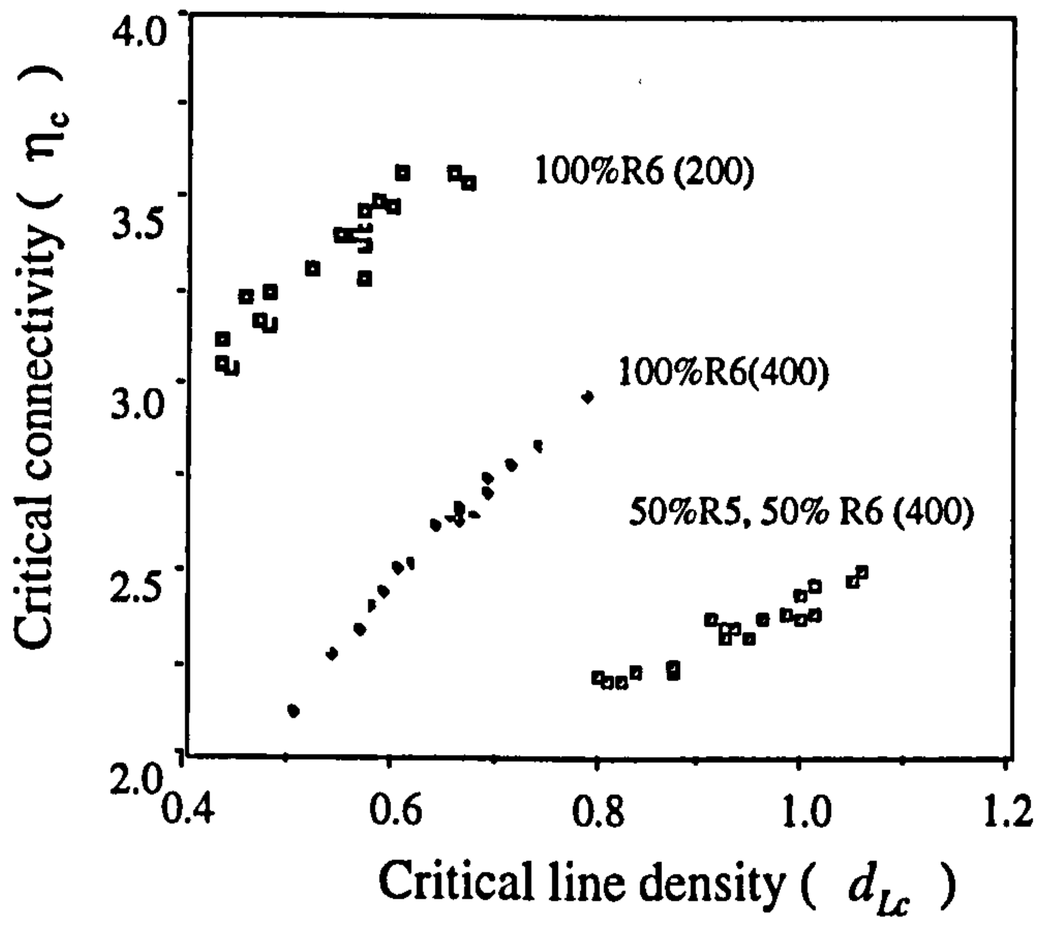

Figure 4.28. Critical connectivity vs. critical line density at percolation for realisations on the IY axis (combinations of placement rules 5 and 6). The number in brackets represents the number of background Type 4 lines placed.

4.4.6 Constant *Y:X* ratio

Two realisation each from fields 11, 13 and 3 are shown of Figure 4.25, and these realisation have an approximately constant *Y:X* ratio (Transect C in Figure 3.22). Fields 13 and 3 are a considerable distance below the predicted percolation threshold of a random system (Figure 4.21), and so, as expected, they form clustered systems. There is, however, a distinctly different character to their spatial clustering. Field 13 (Figure 3.24b) contains small (spatial) clusters which eventually link-up to form a connected system. Lines are placed according to placement Rule 2, so have one I node and one Y node. Therefore clusters grow outwards from a central core. Field 3 realisations (Figure 3.24c) consist of only a few clusters, which grow to much greater sizes, and often a vary large portion of the total area is taken up by the percolation cluster. These systems grow this way because many lines are placed according to placement Rule 3, in which they must form two Y nodes. In order to achieve this, lines

are preferentially placed in areas of existing high fault density, therefore clusters grow more slowly, and contain a greater fault density.

In the case of these realisations, the predicted change in d_{Lc} over the percolation threshold does occur. Field 11, which plots above the threshold of a random system, has a mean $d_{Lc} = 1.63$, field 13, which forms systems below the threshold has a mean $d_{Lc} = 1.04$, and the highly heterogeneous field 13 has mean $d_{Lc} = 1.39$.

4.4.7 Determination of the percolation threshold for random systems

It is impossible to determine η_c for a random IY system, because the code does not allow generation of IY systems with enough degrees of freedom for the system to be random. There are two reductions in degrees of freedom associated with numerical generation of IY systems, compared to only one associated with the analytical treatment in Section 4.3. The first involves the line placement rules. Line placement Rule 5 (One Y node) and to an even greater extent Rule 6 (2 Y nodes) require that lines must be moved deterministically once they have been placed initially at random. This loss in freedom is necessary if IY systems are to be modelled, and is accounted for within the definition of a random IY system (Section 4.3.2).

The second, more significant loss in freedom is due to the necessity for placing a background distribution of Rule 4 lines, before the lines with Y nodes can be placed. The characteristics of systems with identical placement proportions differs greatly when this initial background density is changed (Figure 4.28), and because of this, a random IY system cannot be generated. Therefore the line in IYX space which defines the percolation threshold of a random system (Figure 4.17) cannot be determined directly.

There are, however, three ways that the predicted percolation threshold of a random system can be validated with the numerical results. The first involves the supposition, made in Section 4.3.2 but not proven on either the IX or the IY axis, that systems

which become connected with either a higher of lower $I{:}(Y,X)$ than a random system with the same $Y{:}X$ should have a higher d_{Lc} than the random system. The second involves the supposition that random systems should show equal system heterogeneity. The third is based on the fact that random systems have fractal characteristics at the percolation threshold. The fourth concerns the distribution of lines on 1D sections through the models. These investigations are discussed in turn.

Mapping critical line density in IYX space

Figure 4.29 shows the numerical estimates of d_{Lc} contoured in IYX space. These contours has been made by simple triangulation of the averages of each of the 18 fields, so no subjectivity is introduced. There is a minima saddle, aligned closely with the predicted threshold throughout its length.

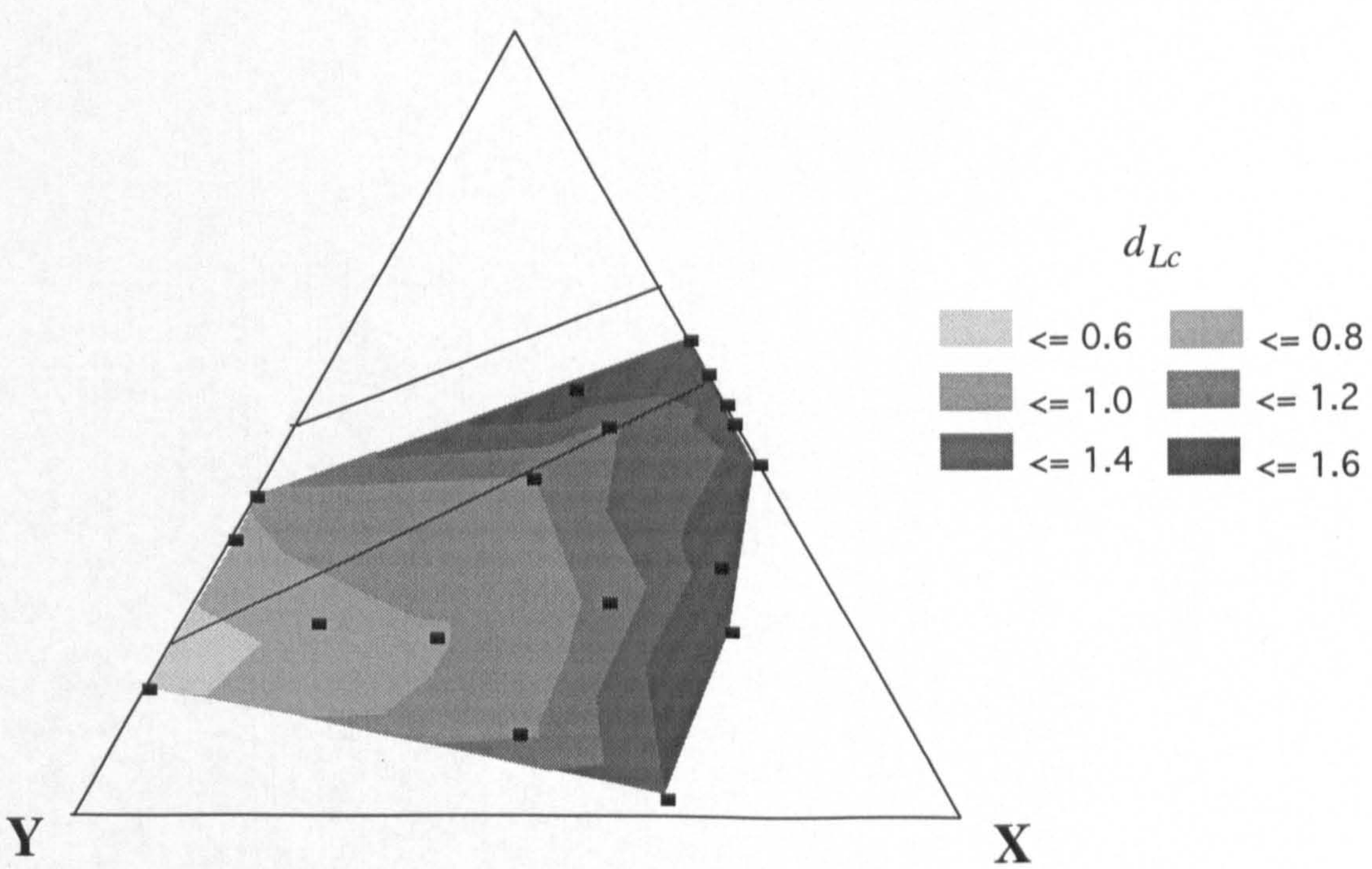

Figure 4.29. Critical line density as a function of critical connectivity in IYX space. Contours of the means of over 20 realisations of 18 placement rules.

Mapping critical heterogeneity in IYX space

Systems which become connected above the random percolation threshold should be more homogeneous than random systems, and system which plot below the threshold should be more heterogeneous. Representivity is a function of system homogeneity, and a homogenous system has a smaller REV than a heterogeneous one. Representivity can be measured as a function of the variability in d_{Lc} between different runs at the same level of discretisation, and so homogeneous systems should show less variability. The coefficient of variation (Cv) is given by normalising the standard deviation of a number of observations by their mean. Therefore, irrespective of the mean, a similar coefficient of variation indicates a similar homogeneity. Figure 4.30 shows Cv contoured in IYX space. The Cv contours are roughly parallel to the percolation threshold. As the position of the threshold on the IX axis is known, this implies that the threshold is in more or less the correct orientation, and the qualitative impression that realisations of the three fields along the percolation threshold (Figure 4.26) are similarly homogeneous is supported by the Cv contours.

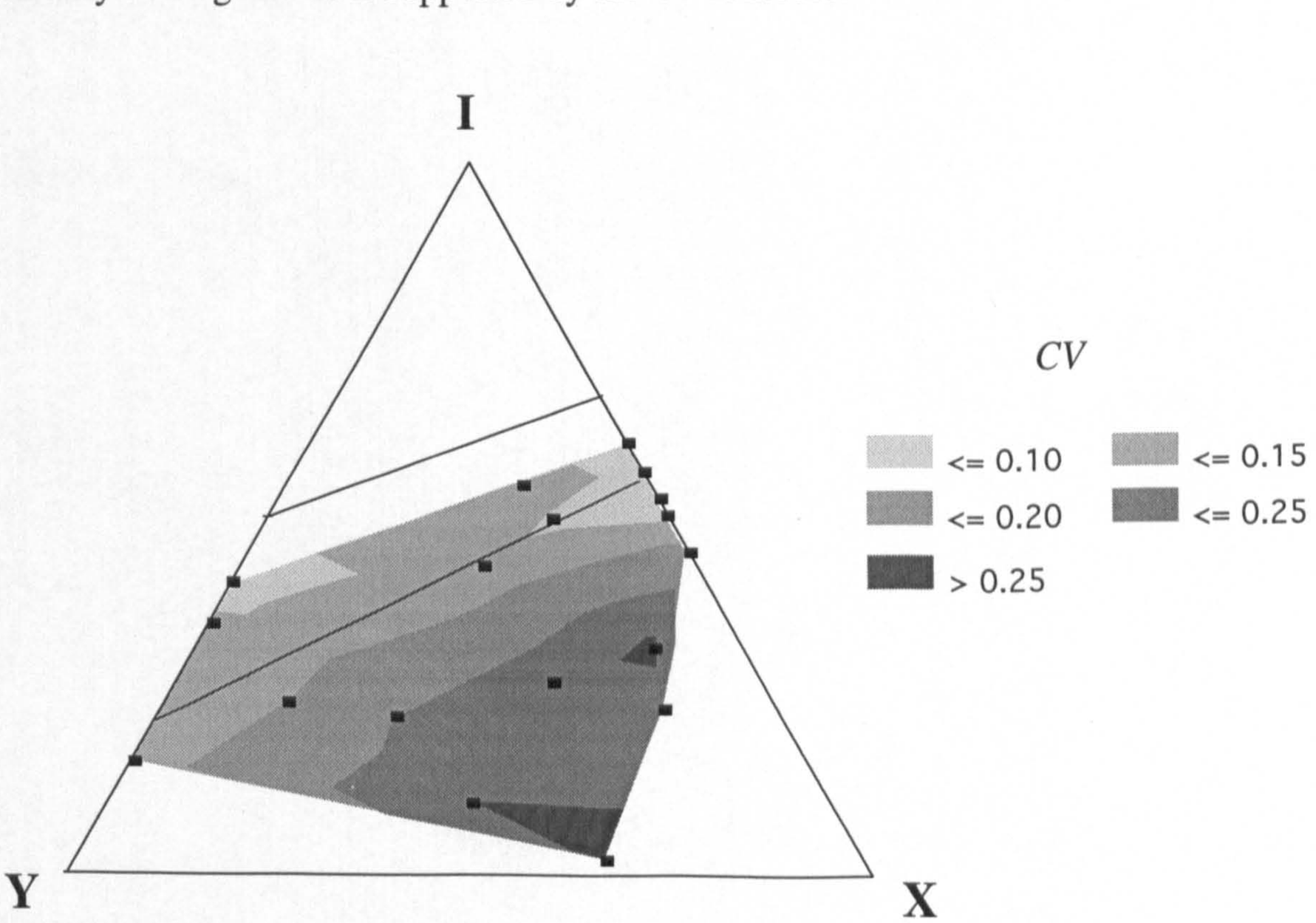

Figure 4.30. Coefficient of variation of critical line density as a function of critical connectivity in IYX space. Over 20 realisation of 18 placement Rules used to calculate Cv at each point.

Cumulative cluster mass distributions

The third method for determining the percolation threshold is based on an incontrovertible assertion: that random systems show fractal characteristics at their percolation threshold. This is a well established tenet of percolation theory, and has been studied specifically in continuum line systems by Balberg *et al.* (1991). One of these characteristics is that (connected) clusters have a fractal size distribution. Therefore:

$$N(cl) = aM^{-b}, \tag{4.13}$$

where M is the cluster mass (the number of lines in a cluster), $N(cl)$ is the number of clusters of mass $\geq M$, and a and b are constants. Relationships of this kind have been discussed in Section 2.4.

Figure 4.31 shows cumulative cluster mass frequency plots ($\log N(cl)$ vs. $\log M$) for eight of the fields. These plots contain data from each realisation in each field, and therefore show equivalent characteristics to cumulative displacement frequency plots for multi-line sampling of seismic displacement sections (Walsh *et al.*, 1994); i.e. a steep truncation bias at low $N(cl)$, then a ledge at slightly higher $N(cl)$ (see Section 2.3.1). For $N(cl)$ higher than this ledge a straight-line segment should be observed for systems which obey Equation 4.13. Also shown on each plot is the gradient of $\log N(cl)$ sampled over $\log M$ intervals of 0.2. The ledges have gradients close to zero, and for systems which obey Equation 4.13, the gradient should decrease to $-b$ over the range of cluster sizes which show fractal scaling.

The random IX system (Figure 4.31b) has a relatively constant gradient over 1.5 orders of magnitude of M, indicating that the cluster masses in these realisations have a fractal distribution. Two plots for non-random IX systems are also shown. The anti-clustered field (Figure 4.31a) has a gradient which gradually decreases and then increases again, indicating that there are too few medium sized clusters for it to be fractal, and the

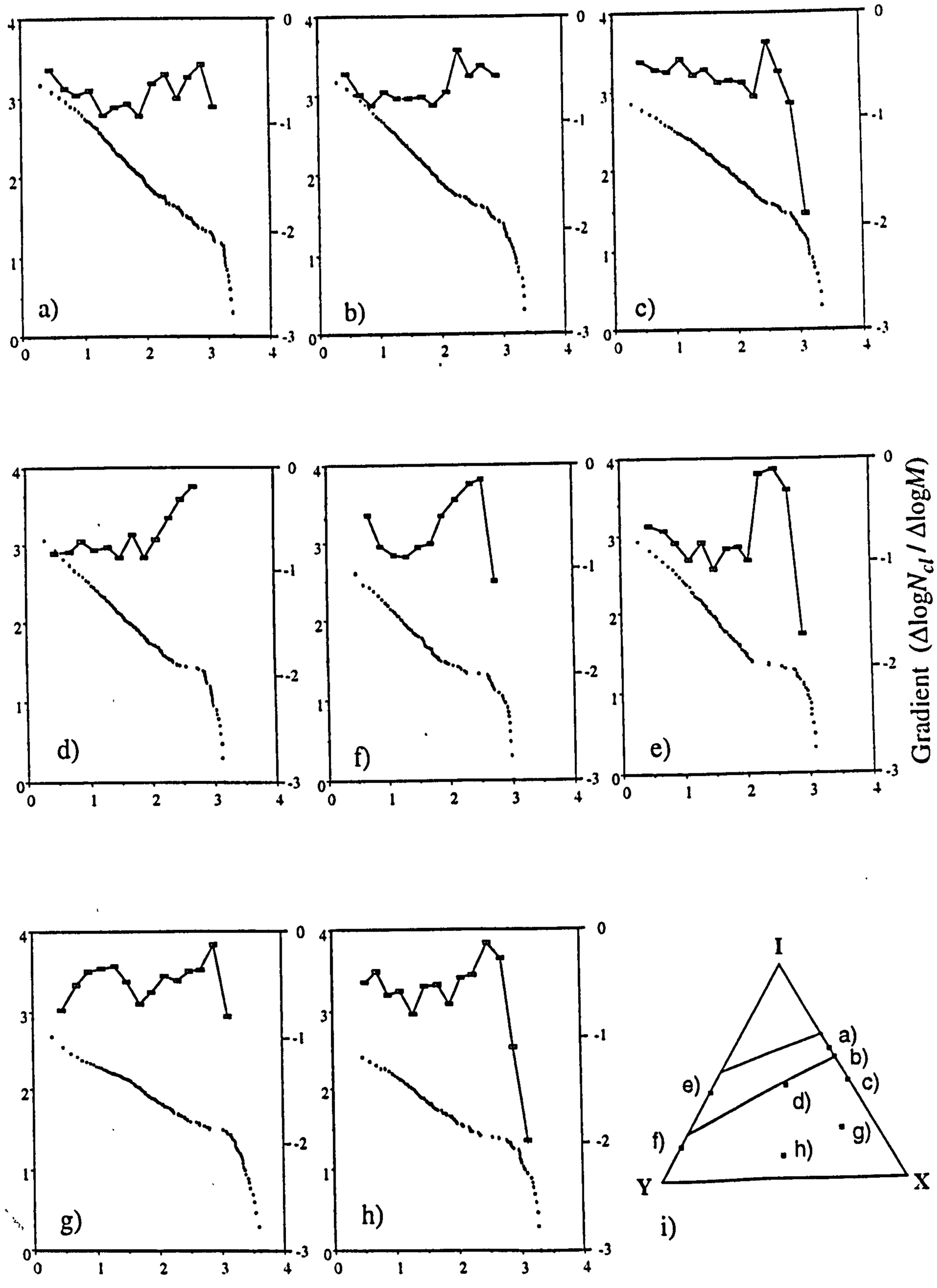

Figure 4.31. Cumulative cluster mass frequency plots for all realisations of particular fields in IYX space (dots). The squares show the gradient in cluster mass frequency sampled over a log(M) intervals of 0.2. a) Field 14. b) Field 0. C) Field 17. d) Field 9. e) Field 2. f) Field 10. g) Field 12. h) Field 7. i) Location of each field.

clustered field gradient (Figure 4.31c) decreases systematically as M increases (until the ledge is reached). Therefore random systems may be distinguished from non-random systems by recognising an invariant gradient. If these characteristics can be recognised from realisations throughout IYX space, then the predicted percolation threshold for a random system can be proven. Figure 4.31d, which lies more or less on the predicted threshold, has a reasonably constant gradient over more than one order of magnitude of M, and Figures 4.31g and h, which are highly clustered fields, have distinct non-fractal curves. The fields on the IY axis (Figures 4.31e and f) should be anti-clustered and clustered respectively, and hence should show characteristics similar to Figures 4.31a and b. Possibly they do, however these interpretations are speculative, as the changes in character are subtle. This analysis therefore supports the location of the random percolation threshold, however it is very difficult to characterise emphatically the trends on Figure 4.31.

Line spacing characteristics

In Section 3.3.1, semivariograms of fault spacing were presented (Figure 3.14), which proved problematic to interpret. These semivariograms indicated that some correlation of fault spacing was present in the datasets, and that the faults were, to some extent, clustered. Semivariograms constructed in the same way through 1D samples of an anti-clustered (Field 14), a random (Field 0) and a clustered (Field 17) IX system are shown on Figure 4.32a-c. Each semivariogram appears to display a pure nugget effect, indicating no correlation between line spacing. The clustered system does show a slight decrease in correlation over a lag of 7 line separations, but as the semivariance at 15 line separations is lower than the nugget, a range cannot be confidently interpreted for this system.

Jensen *et al.* (1996) have shown that semivariograms are extremely sensitive to details of the system being studied, and it would appear that none of the system contain sufficiently well-defined structure for semivariograms to be of used for determining the

clustered / anti-clustered transition. Nonetheless, there is a general increase in both the value and the amplitude of semivariance form Field 14 to 17, indicative of a general increase in system heterogeneity.

Although a random IX system cannot be recognised on the basis of clustering, the 1D surveys do contain the necessary information to do so. If points are distributed randomly on a line, then the separation between points follows an exponential distribution (*e.g.* Grady and Kipp, 1987). An exponential distribution follows the relationship:

$$N(S) = e^{-NS}, \tag{4.14}$$

where $N(S)$ is the cumulative fraction of separations > S, and N is the total number of separations in the sample. An exponential distributions forms a straight line on a plot of $\log N(S)$ Vs. S.

Figure 4.32d - f compares the characteristics of the three IX samples discussed above. Field 0 (random) shows a good exponential distribution of spacing. Field 14 (anti-clustered) has fewer large spacings, and Field 17 (clustered) more large spacings than an exponential distribution. On the IY axis, Fields 1 and 2 (Figures 4.32g and h, both predicted to be anti-clustered) show more or less exponential distributions, and Field 10 (Figure 4.32i) has the distribution characteristics of a clustered system, as expected. The other two fields plotted (Figure 4.32j and k) have clustered and random distributions, as expected from the IYX positions at which these systems percolate.

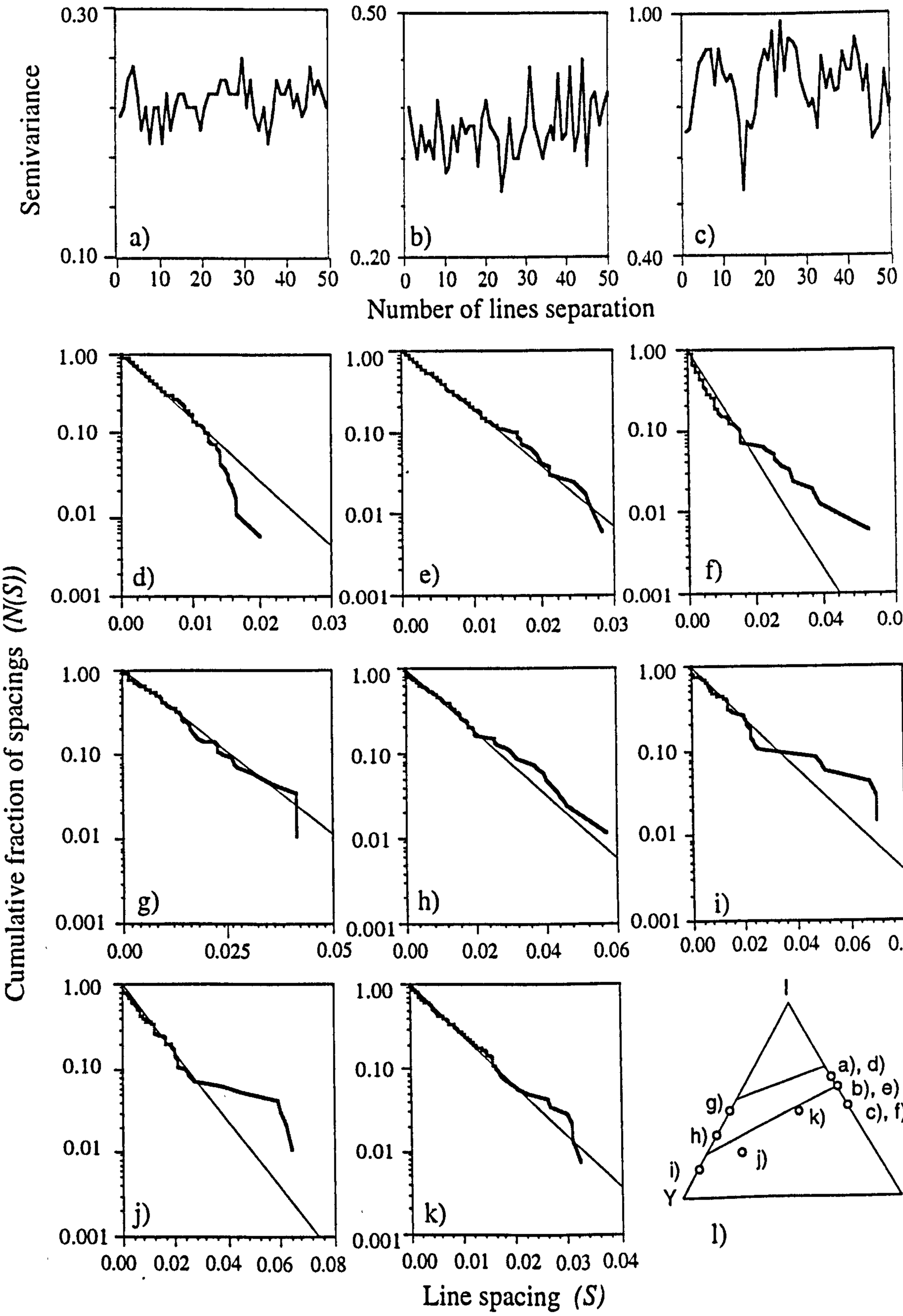

Figure 4.32. Analysis of line spacing. a) to c): Line spacing semivariograms for horizontal 1D samples of particular realisations of IX systems. (Semivariance is calculated as a function of $100S$.) d) to k): Cumulative fraction of spacing ($\log N(S)$) Vs. spacing (S) for fields in IYX space. Observed relationship (bold curves) and exponential distribution calculated based on the number of lines sampled (feint lines). All systems generated with $L = 0.025$. a), d) Field 14. b), e) Field 0. c), f) Field 17. g) Field 1. h) Field 2. i) Field 10. j) Field 6. k) Field 9. l) Location of each field.

Sub-section summary

No one method has proven the percolation threshold in IYX space of a random system, however four analyses (contoured trends in d_{Lc}, contoured trends in system heterogeneity, determination of the character of cluster mass distribution and determination of the line spacing distributions) have each strengthened the case, originally deduced analytically (with two methods in Section 4.3.6) that it lies on the line indicated on Figure 4.17. There remains little doubt that the percolation threshold in IYX space of a random system of lines of constant length distributed equally between two orientation populations has η_c very close to 0.285.

4.4.8 Section summary

Section 3.3 and 3.4 have considered systems of lines of a constant length, oriented at 90° to each other. Three kinds of systems have been defined; non-uniform, uniform and random systems. For each of these, the IYX characteristics at percolation have been determined, both theoretically (Section 4.3) and numerically (Section 4.4). The effects of considering greater system variability is discussed briefly in Section 4.5.1.

Random systems form connected systems on a specific line in IYX space, and the line density at which this occurs varies from $d_{Lc} \approx 0.6$ for a system with $P_X = 0$ to $d_{Lc} \approx 1.6$ for a system with $P_Y = 0$. As real fault and fracture systems have large proportions of Y nodes, the critical density of these systems is likely to be between one third and one half of previous accepted critical line densities (e.g. Berkowitz 1995), calculated with IX continuum percolation methods.

In the Section 4.3 it was deduced that uniform systems may become connected at any point within regions B and C of the IYX ternary diagram (Figure 4.20). Systems which become connected in region C are more heterogeneous, and systems which become connected in region B are more homogeneous, than random systems.

Importantly, non-random systems do not give fractal characteristics at percolation. The significance of this is addressed in Section 4.5.3.

Along the line of the percolation threshold of random systems, systems are equally heterogeneous, where equal heterogeneity is defined as equal coefficient of variation of d_{Lc} for different realisations at the same discretisation. As the coefficient of variation is given by normalising the standard deviation by the mean, a low mean d_{Lc} implies that the standard deviation of d_{Lc} is high. The REV is a function of the standard deviation, and therefore IY systems, although they are equally homogeneous as IX system, have a larger REV. The significance of the REV is addressed in Section 4.5.4.

4.5 Discussion

The previous sections have been theoretical in nature, and have considered certain properties of systems which contain Y nodes. In this section, some of the implications of these new results are discussed, with reference to flow in fault and fracture systems.

4.5.1 Effect of orientation and length variability

The 2D systems considered in this chapter are idealised: all lines are of identical length, equally distributed between two orthogonal orientations. However, there is an analytical solution for transforming an orthogonal to a non-orthogonal system. The area in which lines are placed has been considered square (Equation 4.1). For a system of parallel lines in two orientations at $\pm\alpha°$ from each other, line density can be reformulated for a rectangular area WJ:

$$d_L = NL^2 / 4WJ, \tag{4.15}$$

where $W = \sqrt{2}\sin\alpha$ and $J = \sqrt{2}\cos\alpha$ (Figure 4.33). The systems in Figure 4.33 are topologically identical, and, because the distance between opposite corners in both systems is $\sqrt{2}$, the line length is the same in both systems.

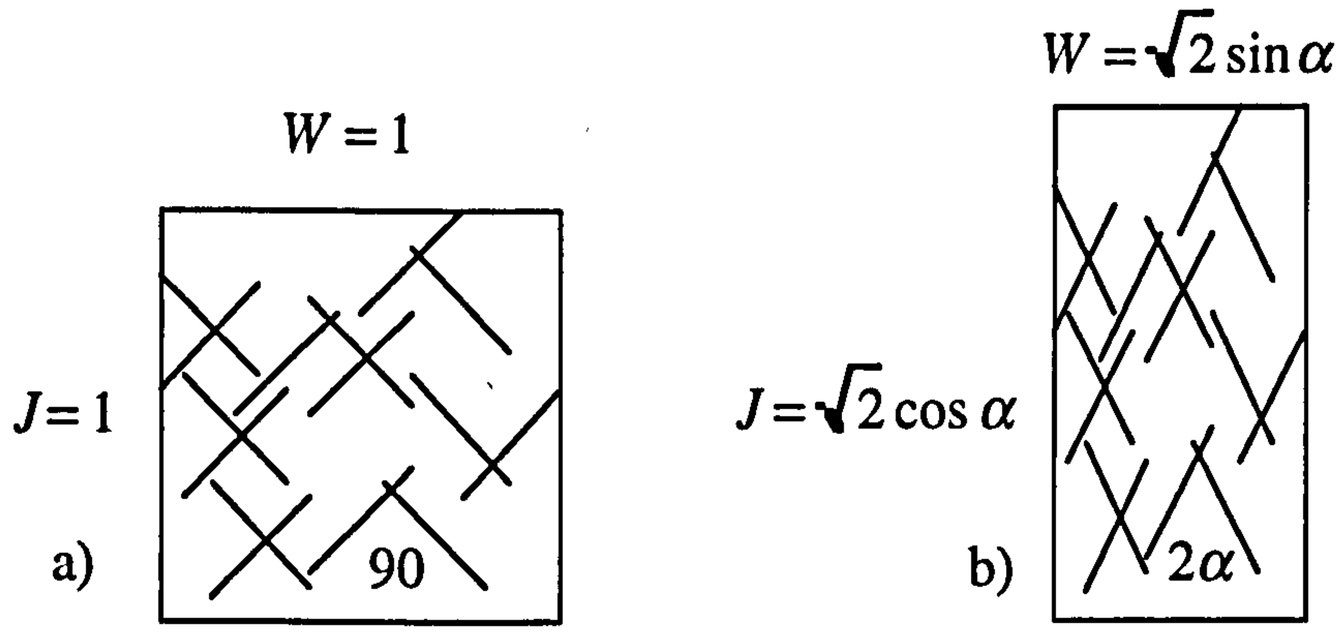

Figure 4.33. Reformulation of line density for a non-orthogonal system. a) an orthogonal system, and b) a topologically identical non-orthogonal system.

As α changes, the number of faults in WJ needed for percolation is constant, but the area changes, as $WJ = 2\cos\alpha\sin\alpha = \sin 2\alpha$. Therefore:

$$d_L = d_{L45} / \sin 2\alpha, \tag{4.16}$$

where d_L is line density of a system at any α, and d_{L45} is the equivalent orthogonal line density. It clear that for any $\alpha \neq 45°$, $d_{Lc} > 1.556$ for a random IX system, but ζ_c is independent of α.

The distribution of line lengths is very important for the determination of the critical line density. In a system incorporating large variations in lengths, the longer lines have a disproportionate influence on the critical line density. This can be considered analogous to a line of length $2L$ being composed of two connected lines of length L, etc. As the variance in L in a system increases, both d_{Lc} and ζ_c decrease, and d_{Lc} varies much more than ζ_c (Robinson, 1983; Berkowitz, 1995). The relationships between length distributions and critical line densities of IX systems are well-formulated (Berkowitz, 1995). Critical connectivity, more than critical line density, is relatively constant (in 2D) whatever the system orientation and length distribution.

4.5.2 Comparison of results with a natural fracture pattern

A study by Odling (1992a) compared the network properties of a natural joint pattern with 10 random realisations. These realisations honoured the length, density and orientation variation of fracture traces, but, being random, did not honour the presence of Y nodes. The main conclusion of the study are summarised as follows.

A) The natural system was above the percolation threshold, but the realisations were generally below it.

B) The natural system contained about half the number of clusters relative to the random realisations.

C) The largest cluster in the natural system contained about twice the cluster mass of the random realisations.

The modelling described in this chapter is in excellent qualitative agreement with Odling's observations, even though the models described here contain lines of a constant length and orientation, while those modelled by Odling have log-normal length distributions and a wide range in orientations (3 orientation populations, each containing non-parallel fractures).

The IYX node proportions of the natural system and of Odling's realisations are shown on Figure 4.34 (points 1 and 2 respectively). In the previous section it was shown that the critical connectivity characteristics are not very sensitive to either length or orientation variation, therefore the thresholds deduced in this chapter can be applied tentatively to more variable systems. The natural fracture system lies slightly below the random percolation threshold, while the realisations lie well above it. Thus, based only on node characteristics, the fracture system would be deduced to be connected, as it is. This inference can be made independently of the line density of the system, and only

depends on connectivity characteristics. Connectivity is a powerful system descriptor in its own right (see Sections 3.4.1, 4.2.3).

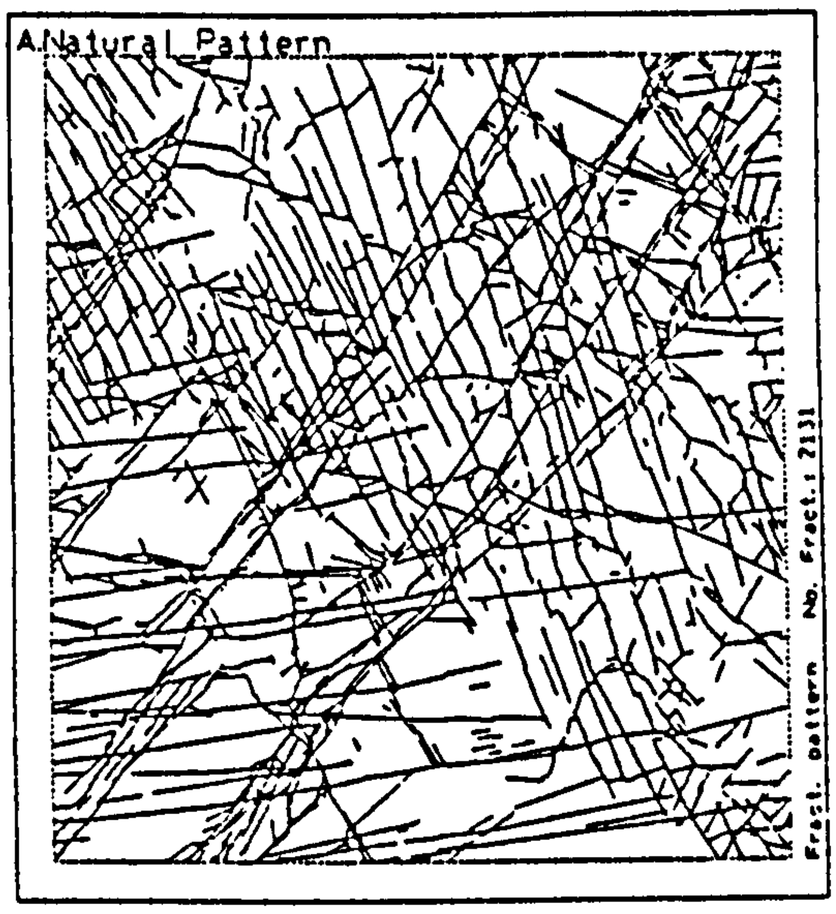

Figure 4.34. a) The fracture system studied by Odling (1992a). b) Comparison of results. 1 - The natural fracture system. 2 - The connectivity characteristics of Odling's random realisations. 3 - Field 6 at percolation ($d_{Lc} = 0.63$). 4 - The connectivity characteristics of a random IX system at $d_L = 0.63$.

The field closest to the distribution of the natural system from the modelling described in this chapter is Field 6 (point 3, Figure 4.34). Field 6 (shown on Figure 4.26c) has $d_{Lc} = 0.63$. A random IX system at this line density has $\zeta = 1.26$ (Equation 4.6), which corresponds to point 4 on figure 4.34. The average connectivity of Odling's realisations was $\zeta = 1.28$. The close proximity of both pairs of points on Figure 4.34 supports the supposition that connectivity characteristics are relatively insensitive to system geometry, and supports the conclusion that the thresholds on Figure 4.17 are valid for systems which are geometrically more variable that those on which they are based.

Table 4.5. Comparison between Odling (1992a) and the present study. $P(Cl_1)$ is the proportion of lines in the largest cluster, and N / N_{cl} is the average number of faults per cluster.

	$P(Cl_1)$	N / N_{cl}
Natural Pattern (Odling)	0.70	3.04
Realisations (Odling)	0.25	1.77
Field 6 at percolation	0.72	14.2
Random IX at 1008 lines	0.02	2.3

Odling's second and third conclusions relate to the distribution in cluster mass between the realisations and the natural system. Table 4.5 details the distribution of cluster mass for Odling's data, Field 6 at d_{Lc}, and the averages of 10 realisations of a random IX system at $d_L = 0.63$ (d_{Lc} of Field 6).

The proportion of cluster mass in the largest cluster ($P(Cl_1)$) is in excellent agreement between Field 6 and the natural system, but Odling's realisations contain a much greater cluster mass than the geometrically more simple models described here. This is because of the length variation in the natural system. Odling defined cluster mass as the sum of the lengths in each cluster, so long fractures contribute much more to the cluster mass than small ones. It is not surprising that Odling's disconnected realisations, which contain a log-normal length distribution, should have larger clusters than those which contain lines of a constant length - the longest line in the natural system probably contains more mass than the largest cluster in the random IYX realisations.

Data relating to the total numbers of clusters present in the system is affected also by the length distribution. Odling remarked that her realisations contained twice the number of clusters than the natural system. In the case of the IX realisations presented here, the random system contains six times as many clusters as the system which honours the IYX characteristics of the natural system. This is because Odling's realisations were closer to percolation than the IX realisations produced here, as d_{Lc} is lower when there is a large variation in line length (Section 4.5.1).

Odling's realisations contained all the geometrical variation of the natural system except the IYX proportions. Realisations presented here contain only the IYX proportions. It is not surprising, therefore, that we both fail to reproduce the quantitative results of the natural system. It is, however, clear, that were the IYX proportions honoured in addition to the orientation and length distributions, the realisations would be

significantly more representative of the natural system than either Odling's realisations or those reported here. However, even honouring only the IYX proportions leads to predicting a connected system as observed, whereas entirely random connectivity modelling of the correct length distributions fails to achieve this.

4.5.3 Random systems and self organised criticality

There is one further, rather profound, conclusion of Odling's (1992a) study. She found that the distribution in cluster masses followed similar scaling for both the natural system and the realisations. Because her realisations contained no spatial placement criteria whatsoever, they correspond to a system defined as random in this study. Therefore they should follow equation 4.13. If the natural system does, indeed, have the same scaling characteristics as the realisations, this means that it too is a random system.

Figure 4.35 shows plots of the distribution in length and cluster mass, for the natural system and the realisations. The data on these figures have been read off a graph of frequency vs. cluster mass (Odling, 1992a, Figure 3a), in which cluster masses have been distributed between different sized bins. Therefore this data has already been degraded during processing for another purpose, and so there only a few points on each curve.

Figure 4.35a shows the distribution in cluster mass over the entire range, and this is clearly not distributed fractally. The distribution of fracture lengths is log-normal, not power-law, so there are fewer short lines than would be present in a power-law length distribution. The log-normal distribution of lengths, is therefore responsible for the long, flat portion of the curves of both cluster mass distributions (Figure 4.35a). Only the central region of the distributions are plotted on Figure 4.35b, and it appears that the realisations and the natural system do display the same scaling characteristics - both have reasonably straight power-laws, and these gradients are parallel to each other.

This straight-line section covers slightly less than one order of magnitude of cluster mass, so is not conclusive, but the fact that the natural system is possibly random (in the sense of having a power-law distribution of cluster mass) is evidence in favour of considering fracture growth to be a self organised critical process.

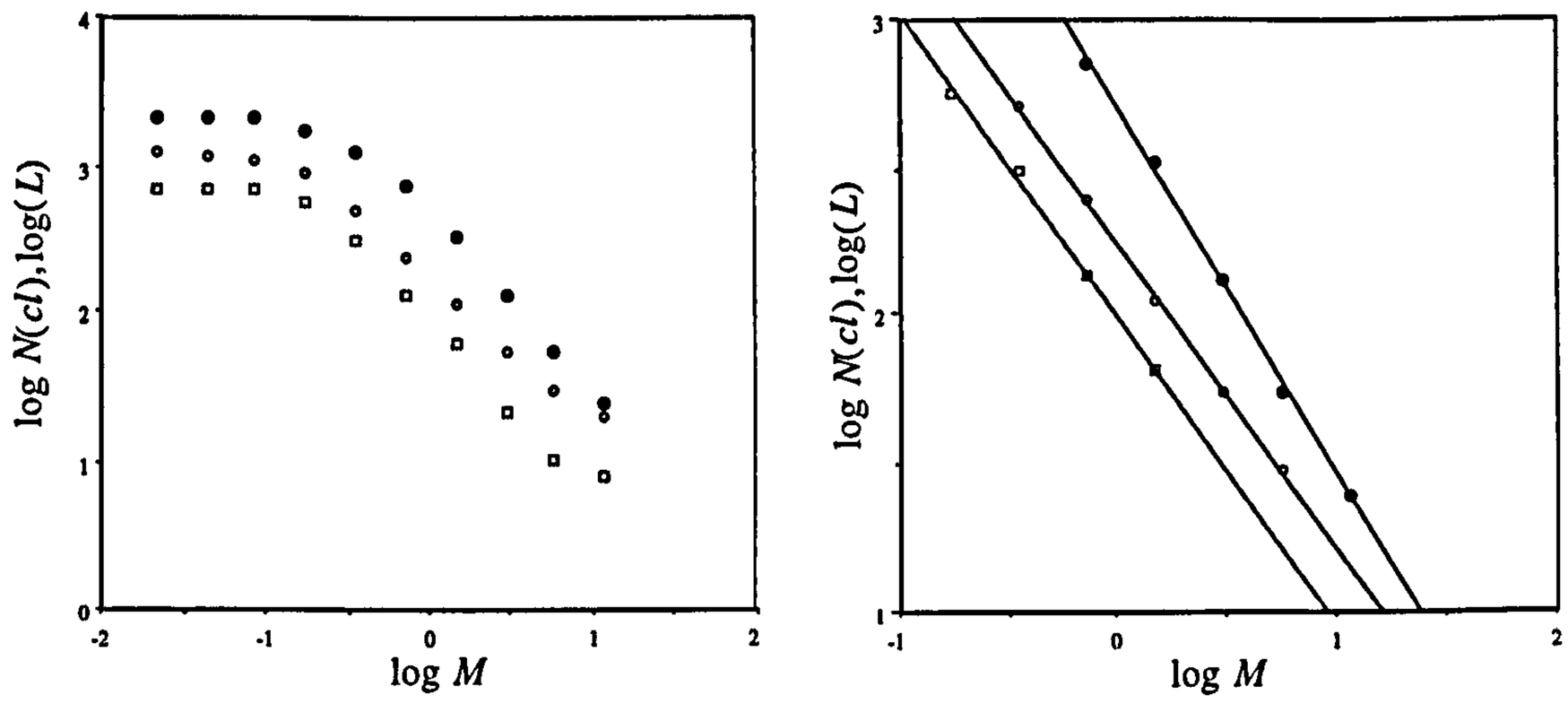

Figure 4.35. Log cumulative number of clusters (or fracture length) vs. log fracture length (filled circles), log cluster mass of the realisations (open circles) and log cluster mass for the natural system (open squares). a) For the entire mass range. b) For the central mass range, with best fit linear regressions. Data from Odling (1992a), Figure 3a.

Self organised criticality refers to the tendency of dynamic systems to grow towards a particular state. The theory (e.g. Bak and Tang, 1989) predicts that dynamic systems will tend towards an attractor which represents the meta-stable state of the system, no matter how far from equilibrium the system started, and in this state the system has no characteristic length scales or temporal periodicity. Self-organised critical systems are intrinsically self-similar, and need no system "tuning" to achieve this critical state.

The network models described in this chapter are, in fact, a handy example of self organised critical systems (albeit not dynamic ones). Recall that, through judicious choice of line placement Rules 1, 4, and 7, it is possible to create systems which reached percolation over a range of ζ values (Figure 4.27). Only one of these systems displayed self-similar scaling (Figure 4.31), and this was the system which required no tuning (100% Rule 1 lines). Indeed, model tuning was required to force the systems

away from this state (incorporation of placement Rules 4 and 7, both which represent a reduction in the freedom of the system). Therefore $d_{Lc} = 1.556$, $\zeta_c = 3.112$ represents the attractor for random IX systems of lines. Intriguingly, this attractor is the most energetically conservative state on the IX axis, as it is the point at which percolation can be achieved with the lowest line density (Figure 3.28).

This is not a good analogy for dynamic systems, as the addition of faults (driving the system to become connected) may be considered a form of tuning. In a dynamic self organised system, interactions within the system itself causes the formation of new faults, driven only by boundary conditions. After every change in the structure of a dynamic self organised critical system, the system responds in such a way as to drive it back towards the attractor. Sornette *et al.* (1990) have suggested that, for tectonic faulting, the lithosphere is in a state approaching failure everywhere and at every scale; and this is the attractor towards which faulting drives the system. Significantly, Madden (1983), in a study comparing the theoretical percolation threshold of random planes with the distribution of micro-fractures before and during failure in triaxial tests of crystalline rock, mentioned, with some surprise, that his results appeared to indicate that the distribution in micro-cracks was such that when the sample failed, it, also, was ready to fail everywhere.

Self-organised criticality is one of the few models of fault system growth which explains why self-similarity is so often observed in fault and earthquake systematics. If it is accepted, then a part of the growth model is that systems are random (as defined in Section 4.3.2), and tend towards an energetically favourable attractor. This attractor is the percolation threshold of the system. The percolation threshold is a line in IYX space, and the critical line density of the threshold is lowest, where the $Y{:}X$ ratio is high (Figure 4.29). Self organised criticality will therefore drive fault systems towards this energetically optimal edge of the percolation threshold.

4.5.4 The geometrical REV and probabilistic connectivity criteria

Fault system connectivity is of great importance to both fracture flow and flow in sealing fault systems; in the former case fracture connectivity is a prerequisite for an REV, and in the latter case, matrix connectivity is a prerequisite for an REV. This section describes an idealised system, in which both these flow situations operate, but in which, for geometrical reasons, no REV can be defined.

The following hypothetical scenario is loosely based on a field example at Bartlett canyon in SE Utah (Koestler *et al.*, 1994), where the Entrada Sandstone forms a wet aeolian system consisting of porous, permeable dune sandstones and impermeable silty claystone interdunes. The sequence is gently dipping, and there is no apparent stratigraphic communication between sandstones. The sequence has a large fault cutting through it, around which is a damage zone of faulting and fracturing. Suppose we wish to know if there is pressure communication between the large fault and the good quality reservoir sandstones (Figure 4.36). This situation is relevant to several situations. The fault could be a migration conduit, and the reservoir could only be charged if communication is possible. Alternatively, the fault could form a lateral seal to a reservoir, in which case the seal is integral only if flow is impossible between the fault and the sandstone. A third situation is that the fault could be an intra-reservoir fault, and production from the reservoir might be significantly different if this fault were able to transmit fluid and pressure between compartments.

Figure 4.37 shows two stick-plots of 1D samples measured perpendicular to the fault. On both transects fracturing and faulting is clustered around the main fault. We make the modelling simplification that the interdune sequences (Figure 4.37a) contain conductive fractures, while the sandstones (Figure 4.37b) contain sealing faults. There are two possible routes for flow between the fault and the sandstones. The simplest requires connectivity of the matrix in the sandstone. If the sealing faults in the

sandstone are connected, a second route involves fracture flow in the shales to a distance beyond the damage zone in the sandstones, and then flow directly from the fractures into the matrix. This is a very similar flow scenario to one envisioned for potential production of the structurally complex Clair field (Coney *et al.*, 1993).

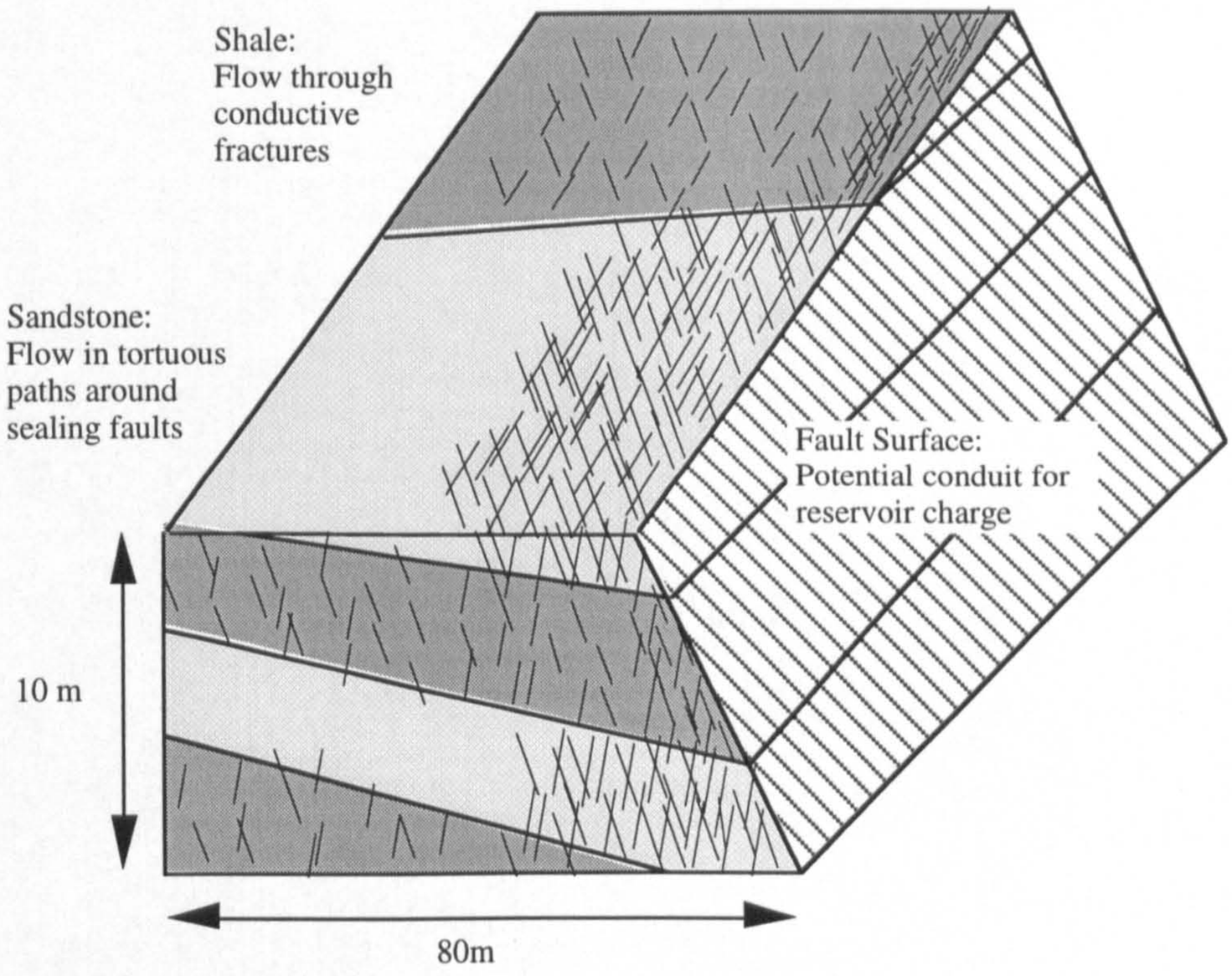

Figure 4.36. Scaled cartoon of the lithologically dependent faulting and fracturing at Bartlett Canyon, SE Utah.

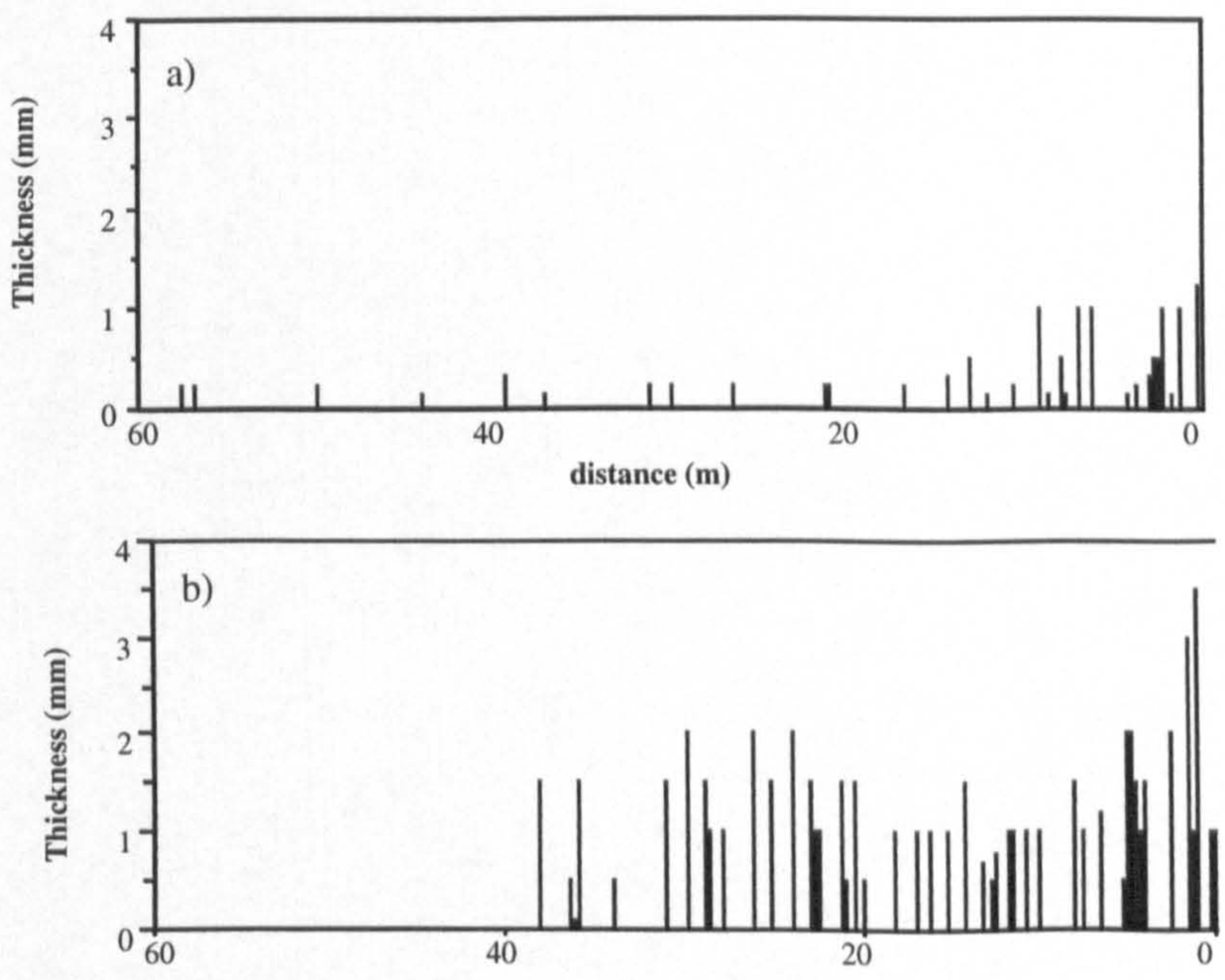

Figure 4.37. Thickness stick-plots measured perpendicular to the large fault of a) fractures in the interdune shales, and b) faults in the dune sandstones, from Bartlett Canyon, SE Utah.

The faults in the sandstone and the shale are markedly different due to the different mechanical properties of the two media. In the sandstone, the damage zone consisted of 60 faults distributed more or less evenly to a distance of 40m from the large fault. In the shales, 15 fractures are clustered tightly in the first 10 m from the large fault, and a further 50 fractures are sampled beyond this, to a total damage zone width of 60m. In both lithologies, the faults and fractures are distributed equally between two populations oriented at ±20° to the large fault. The faults in the sandstone are estimated to be 6 m long, while those in the shale are 5 m long.

Based on these data, representative orthogonal systems can be determined using the relationships discussed in Section 4.5.1. The line density of the system is determined as a function of the scan-line density (d_S, number of faults per metre). If the fractures are distributed randomly in the area, then the probability that a 1D line of length W will encounter any one fault is (Figure 4.38):

$$p = L\cos\alpha / J \tag{4.17}$$

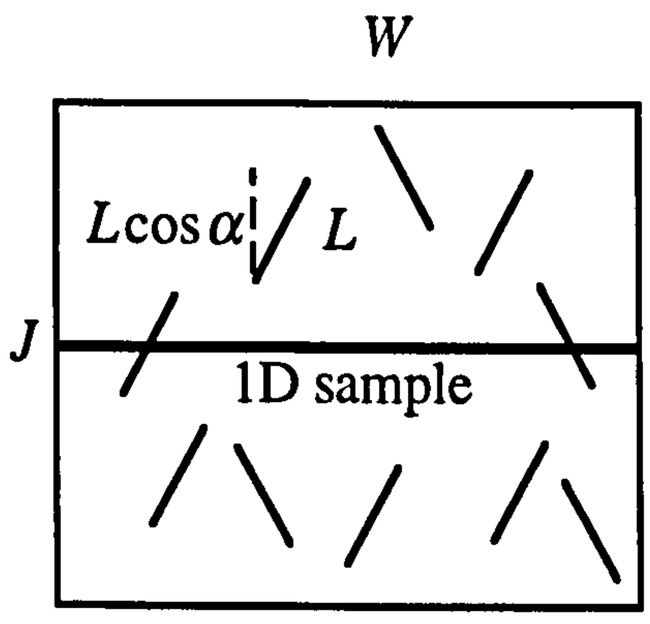

Figure 4.38. Conversion of a 1D scan-line density to a 2D line density

Equation 4.17 implies that if N faults are present in WJ, then the number that will be sampled by a random 1D section is $NL\cos\alpha / J$. Therefore:

$$N = d_S WJ / L\cos\alpha \tag{4.18}$$

Line density is defined in Equation 4.1 ($d_L = NL^2 / 4WJ$). From Equations 4.1 and 4.17, line density is determined as a function of scan-line density (d_S), fault length (L and orientation (α):

$$d_L = d_s L / 4\cos\alpha \tag{4.19}$$

From this, equivalent orthogonal line density is determined from Equation 4.16.

As the faults and fractures are long relative to the area containing them, no geometrical REV can be assumed, and discretisation effects must be considered. The discretisation of the system is given by normalising $\sqrt{2}L$ against the cross-sectional distance (Figure 4.33). These data are summarised on Table 4.6.

Table 4.6. Calculation of the equivalent orthogonal properties of the three systems modelled from Bartlett Canyon. Sealing faults in sandstone, and conductive fractures far from the fault (Shale A), and close to it (Shale B).

	Sandstone	Shale A	Shale B
L (m)	6	5	5
W (m)	40	50	15
d_S (m^{-1})	1.5	1.0	1.5
α (°)	20	20	20
d_L	2.4	1.3	2.0
d_{Lo}	1.53	0.83	1.28
Discretisation	0.072	0.048	0.24

Figure 4.39a show random IX realisations at percolation over a range of discretisations (L). As L increases, the system become geometrically less representative, and there is no single threshold at which the faults or fractures in the area become connected, but a discrete probability that they do over a range of line densities. Because the code checks for connectivity only between two sides of the model, the scatter on Figure 4.39a

become denser at line densities below the critical line density at large L. If a more rigorous percolation criterion demanding connectivity between all four sides is used, then, at large L, realisations tend to form connected systems at $d_L > d_{Lc}$ (Robinson 1984). For the purposes of this simple illustration, the probability contours have been drawn so that $p(connectivity) = 0.5$ lies on d_{Lc} (Figure 4.39b).

The possibility of flow is assessed in two situations; the first is a random IX system with $d_{Lc} = 1.56$, and the second is for an IYX system with $d_{Lc} = 1.0$. For this latter case (Figure 4.39c), the $p(connectivity)$ contours have been determined so that they reflect the larger REV of IYX systems (Section 4.4.7). The dots on Figures 4.39b and c represent the three areas into which the damage zone has been divided (Table 4.6).

The probability of having a connected flow path through the sandstone in about 0.5 for the IX system, and 0.1 for the IYX system. The probability of flow through the shale is close to zero for the IX system, and about 0.15 for the IYX system. There is therefore a chance that flow is possible through this damage zone however it is modelled. As the proportion of splays incorporated in the model is increased, the probability that flow may occur through the sandstone is reduced, but the chance of flow in the shales increases. The potential flow pathway is therefore crucially dependent on the geometrical fault system model. Random networks would predict a good chance of flow through the sandstone. Connectivity characteristics more representative of real systems would also predict the possibility of a flow path, but the path is now through the shale. A small difference in assumption about the connectivity characteristics of the system may therefore have a profound effect on the flow mechanism which should be modelled.

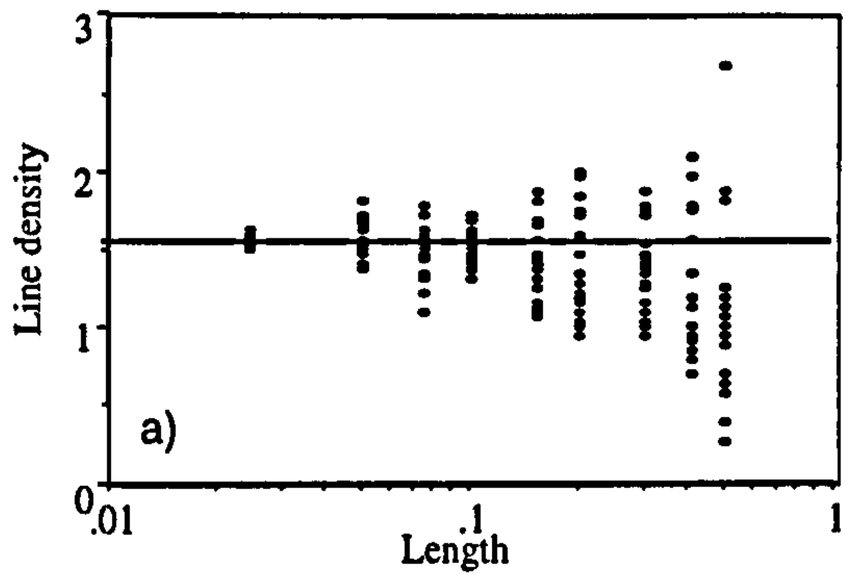

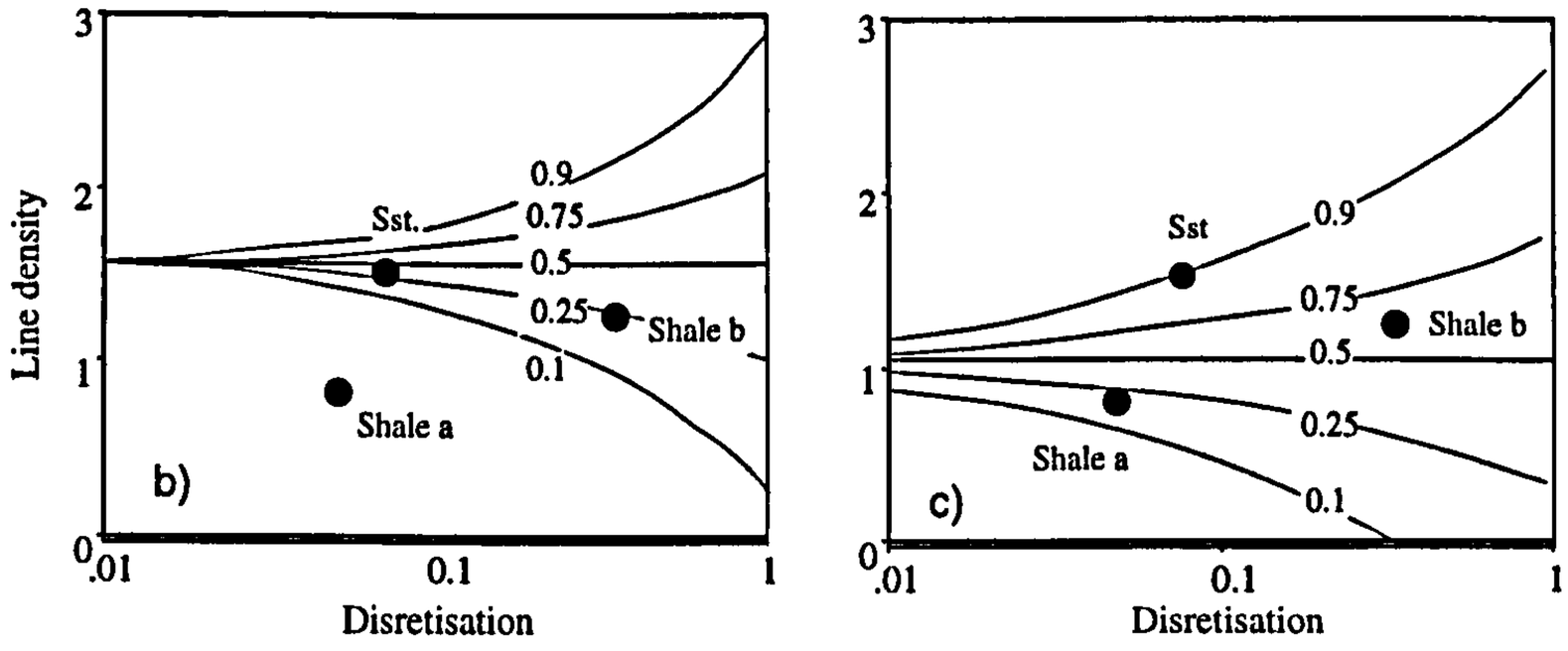

Figure 4.39. Critical line density as a function of system discretisation. a) Realisations of line density at percolation for a number of discretisations of random (100% Rule 1) orthogonal line systems. Contours of $p(connectivity)$ as a function of system discretisation for b), a random IX system, and c), an IYX system with $d_{Lc} = 1.0$. Spot vales represent the sealing faults in the sandstone (Sst), the fractures in the shale far from the fault (shale a), and the fractures in the shale close to the faults (shale b).

4.6 Summary and conclusions

The determination of fault and fracture system network connectivity characteristics are of paramount importance for both fracture flow and flow in sealing and partially sealing fault systems. Only through determination of system connectivity may an REV be defined for modelling approaches which require one. For partially-sealing faults, connectivity does not necessarily influence the REV determination, but is significant nonetheless, as it reflects the threshold at which the flow mechanism changes from tortuous flow around faults to flow through the faults.

Connectivity has been studied both analytically, and numerically using a continuum percolation code, for 2D systems of lines of a constant length equally distributed between two orientation populations. The main innovation in the modelling described in this thesis is the incorporation of spatial correlation between lines in the form of fault and fracture splaying systematics. In natural fault and fracture systems, the bulk of connectivity is achieved through splays, or Y-nodes, rather than through intersections, or X nodes. This is, however, the first time this characterisation has been incorporated in network models or analysed theoretically. Probably the most important conclusion of the analyses presented, is that the percolation threshold of a system which incorporates a high proportion of Y nodes occurs at between one half, and one third, of the line density of a traditional Boolean network model. This entirely new result is extremely significant to modelling and understanding fracture flow.

Nine line placement rules in the continuum code allow quasi-deterministic systems to be modelled, which may be more or less heterogeneous than random system depending on the connectivity systematics. A consideration of fault and fracture system growth as a self-organised critical process allows the assertion that there is a single line in IYX space which represents both the percolation threshold, and attractor, of a system. If a system plots above this line, irrespective of its line density it will be disconnected, and if it plots below it, irrespective of its line density, it will be connected.

A comparison with a natural fracture pattern (Odling 1992a) has confirmed that IYX node proportions are possibly the most diagnostic indicator of connectivity, and realisations which honoured nothing but the connectivity characteristics of the natural system correctly predicted it to be connected, while IX realisations which incorporated all other geometrical variability failed to do so.

Two conceptual connectivity models, one random and one containing a modest proportion of Y-nodes have been considered with respect to characterising possible flow across a large fault damage zone containing both sealing faults and conductive fractures. Although the probability that flow at any point be achieved is similar in this example, the probable flow paths calculated are different - in one case flow occurs thought the fracture system, and in the other case flow occurs in tortuous paths in the matrix around the sealing faults.

CHAPTER 5

EFFECTIVE PERMEABILITY OF A PARTIALLY-SEALING FAULT SYSTEM AT A SINGLE LENGTH-SCALE

5.1 Introduction

The effective permeability of a faulted medium is a product of the permeability structure. This Chapter details a method for determining the effective permeability through generic systems of identical faults in 2D. The method can be used to obtain an estimate of effective permeability for systems of any fault density, fault / matrix permeability contrast and fault orientation. The only constraint on the system geometry is the faults are distributed equally between two orientation populations. Two effective permeabilities may be determined in the directions bisecting these populations.

This model is a significant advance on the existing methods (see Section 1.3). The relative influences of system transmissibility and geometry have been isolated, and this has meant that the solutions can be applied to a much broader range of fault systems than other methods allow. The second significant factor in these models is that all systems have connectivities representative of the number of faults in the system. Connectivity is critical to flow behaviour when the fault / matrix transmissibility contrast is high, and has previously been treated only very superficially.

This Chapter deals with transmissibility and tortuosity through systems of fault baffles and barriers. These terms have been defined in Section 1.2.1. A baffle has a low permeability, while a barrier has zero permeability. Transmissibility concerns flow through baffles, while tortuosity concerns flow around barriers and baffles. The

modelling in this Chapter determines effective permeability (k_e) through a fault system as a function of five fundamental fault system parameters, listed below.

A) Line density (d_L) controls the connectivity, and hence tortuosity, of the system. Line density is determined as a function of N faults of length L contained in a area A.

B) Gouge density (d_G) is the area fraction of fault material contained in A, and is a function of N, L and the thickness (T) of the faults.

C) The matrix / fault permeability contrast (k_m / k_f).

D) Both d_G and k_m / k_f govern the transmissibility of the system, and are incorporated into a single transmissibility measure called Fault heterogeneity (H).

E) The final variable, which controls the anisotropy of the system, is a fault orientation term (α).

5.1.1 Permeability

Permeability is a proportionality constant in Darcy's law. Darcy's law derives from the empirical observation that the pressure drop observed over a length in a porous medium ($\Delta P / L$) is proportional to the volumetric flow rate (q; volume per unit time). Darcy's law for single phase flow is often expressed as:

$$q = \frac{kA\Delta P}{\mu L}, \tag{5.1}$$

where A is the cross-sectional area of a medium, μ is the fluid viscosity, and k is the permeability.

Muskat (1937) discussed how the validity of Darcy's law depends on the Reynolds number of the system. Reynolds number is given by $dv\gamma / \mu$, where d is a measure of the conduit size, v is the average fluid velocity, γ is the fluid density, and μ is the viscosity. With increasing Reynolds number, the flow regime in any medium changes from viscous flow, for which Darcy's law applies, to turbulent flow, for which $\Delta P / L$ is not linearly proportional to q, and therefore Darcy's law is not applicable. Muskat (1937) compiled experimental results to show that, for Reynolds numbers less than 1, Darcy's law is appropriate. Muskat showed that even at the high flow rates encountered in reservoirs close to wells, Reynolds number is unlikely to exceed 1 except locally, and therefore Darcy's law can be assumed valid for single phase flow under reservoir conditions.

5.1.2 Effective permeability and representative elementary volumes

The permeability of fault gouge is generally lower than the permeability of unfaulted sandstone. In the case of deformation bands, there are usually several orders of magnitude difference in permeability. A faulted sandstone contains a permeability structure, and this structure determines the bulk permeability of the system.

If a heterogeneous medium satisfies certain conditions, it may have an effective permeability. Effective permeability is defined as the permeability of a homogeneous volume, which, for the same pressure gradient in the same direction, gives the same flow rate as the heterogeneous volume it represents. A small sample of the reservoir may either consist of fault gouge or unfaulted matrix, and therefore the permeability of the system at this scale is either the permeability of the faults (k_f) or the permeability of the matrix (k_m). Larger domains contain both fault gouge and matrix, and the permeability of a domain depends on the specific quantities and geometrical arrangements of each. As a particular domain increases in size, its permeability will vary according to what is contains, and different domains of the same size may have

different permeabilities. Eventually, a domain may be sufficiently large to contain a representative volume of the system, in which case the permeability of the domain is independent of the size or position of the domain (provided it is larger than this representivity threshold). This permeability is the effective permeability of the system (Figure 5.1).

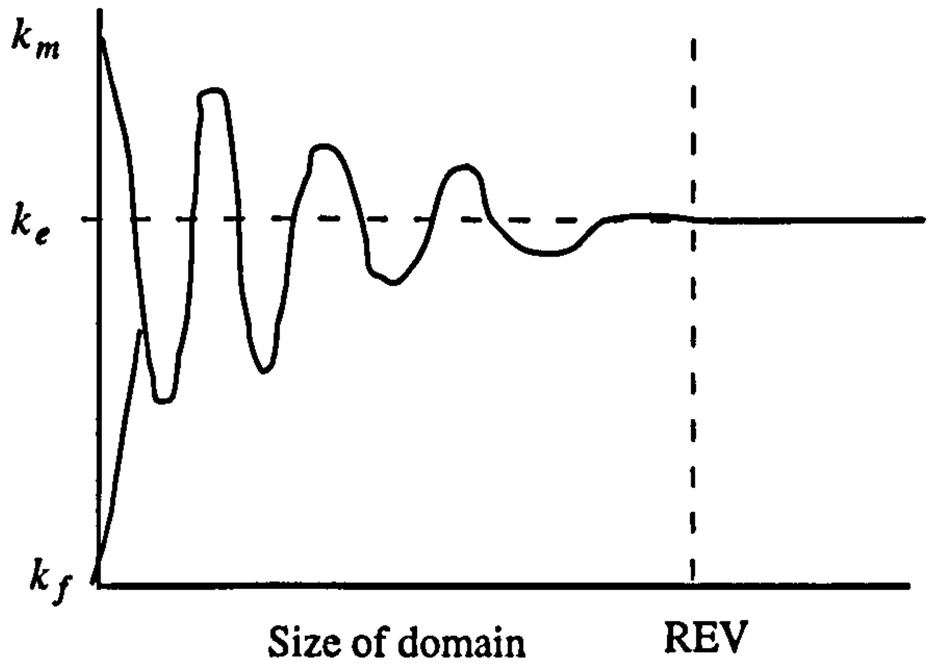

Figure 5.1 Permeability as a function of domain size. Only if an REV exists does the system have an effective permeability.

It is unlikely that fault systems generally satisfy the conditions necessary to define an effective permeability, as fault systems form continuous hierarchies. In a discrete hierarchy it is possible to have nested REVs, as there is a separation of scales within the hierarchy, and there may be REVs at each of these scale separations (Figure 5.2). In a continuous hierarchy there is no separation of scales, and therefore no REV at any scale.

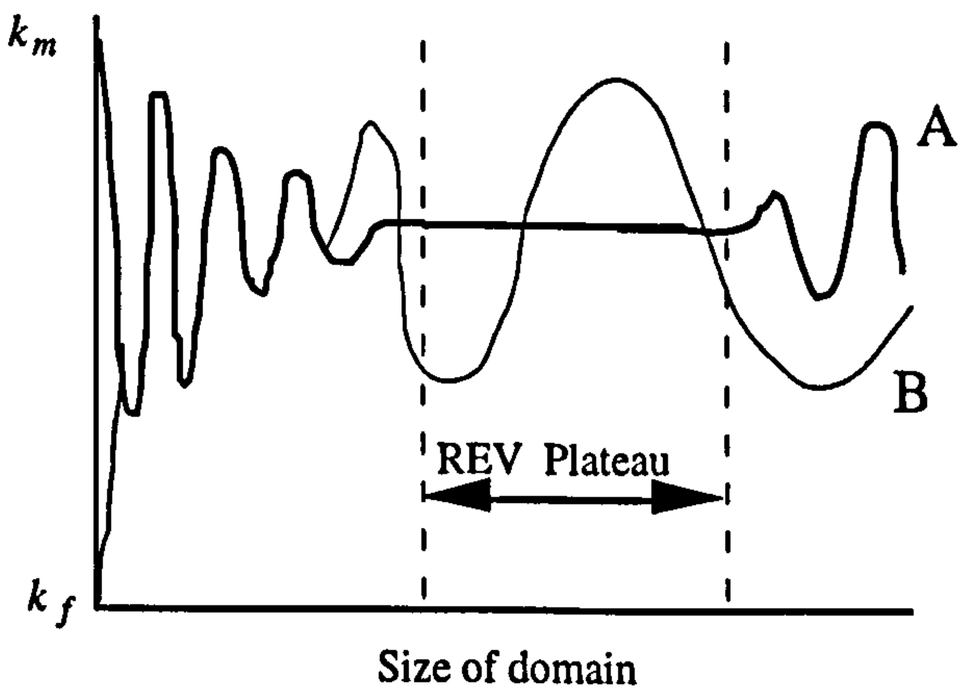

Figure 5.2 Comparison between discrete (A) and continuous (B) hierarchic porous media. In a discrete hierachic media there is separation of scales, potentially allowing nested REVs, but continuous hierachies do not form the plateau necessary for representivity.

Two important assumptions which are included in this work are addressed below. The first involves the transformation of the continuous scaling hierarchy into a discrete

approximation (See Section 2.2.3). The second concerns assuming an REV at each of these scale separations. Although these is some evidence for natural mechanical scaling transitions for fault systems in porous sandstones (see Section 2.4.7), these do not lead to separations of scales in the system. The transformation from a continuous to a discrete hierarchy (which is detailed in Chapter 6) allows the assumption of separation of scales to be made. As a consequence of this transformation, faulting in the entire sub-seismic scale-range is described by a series of models at progressive scales, each of which capture the density and geometrical characteristics of the faulting over the range. In each of these models, all faults are of identical length, thickness and permeability.

It is important to note that not all discrete hierarchies necessarily have REVs at each scale transition. Consider a system of lines of any single length. If the spatial distribution of the lines is heterogeneous at a scale of investigation smaller than the geometrical REV (which is a function of the length of the lines) there is no REV in the system. This aspect was discussed at length in the previous Chapter, and the fault system described in Section 4.5.4, although all faults were considered to be the same size, did not have an REV for this reason.

The approach used in this work, however, assumes an REV at each scale separation. The effective permeability of a system of faults is determined at each scale separation, as a function of the fundamental geometrical properties of the system contained in each scale range. The system is then reconstructed incorporating the permeability characteristics at each scale. This chapter concerns the determination of these permeability characteristics at any scale. Incorporation of the permeability of the entire system is discussed in Chapter 7, along with an assessment of the implications of assuming that fault systems can be transformed into discrete hierarchies with nested REVs. In the cases studied, the assumption that an REV exists does not compromise the permeability determination for reservoir grid-blocks (see Section 7.4).

5.1.3 Fault system permeability structure

The effective permeability of a faulted volume will vary, in general, as a function of four parameters:

A) the number of faults present,

B) the fault and matrix permeabilities,

C) the faults system geometry, and

D) the flow direction.

Effective permeability (k_e) can be easily solved analytically only in two flow directions for one specific geometrical arrangement: the case of infinitely long, parallel baffles (Figure 5.3). Perpendicular to these baffles, k_e is the thickness-weighted harmonic average permeability (k_h), and parallel to the faults k_e is the thickness-weighted arithmetic average permeability (k_a). In geometrically more complex situations, k_e must lie between these limits, and the value of k_e depends on the spatial arrangement of the baffles, as well as on permeability averages.

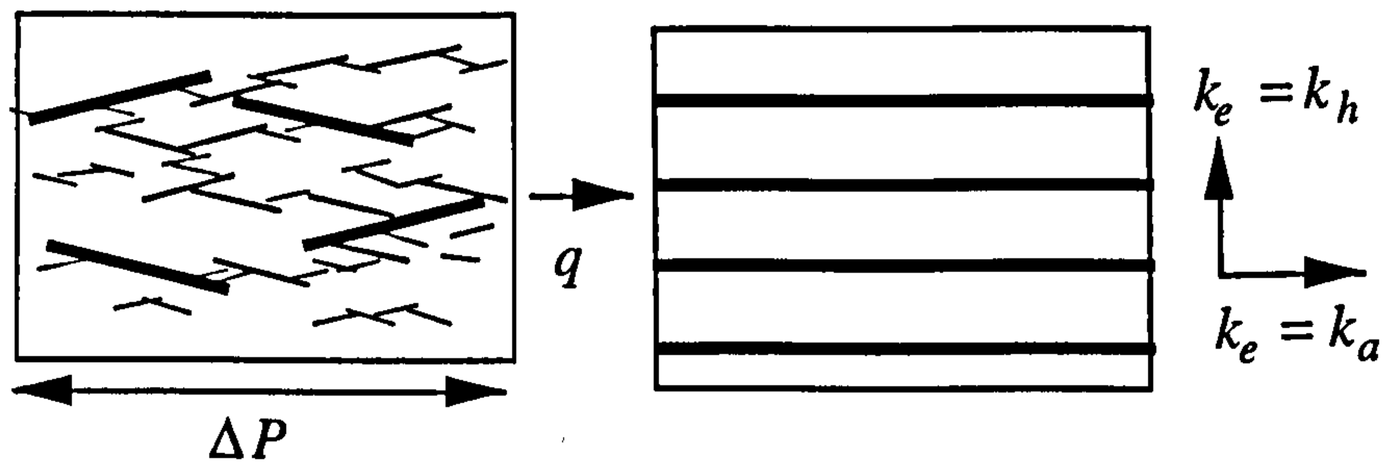

Figure 5.3. Effective permeability determination. Effective permeability (k_e) is the permeability of a homogeneous volume which, for a particular pressure drop in a particular direction (ΔP) gives the same flow rate, q, as the heterogeneous volume it represents. k_e lies between the harmonic (k_h) and arithmetic (k_a) average permeabilities, and depends on flow direction, the spatial arrangement of the faulting and the fault and matrix permeabilities (k_f and k_m).

All the systems considered here are 2D in a horizontal plane. The reason for considering only 2D systems is primarily one of simplicity: if a system cannot be understood in 2D, there is no chance that it can be in 3D. However reservoirs are generally layered horizontally or sub-horizontally over a large range of scales, resulting

in far greater permeability anisotropy vertically than horizontally. Faults, by contrast, are oriented sub-vertically (normal faults seldom have dips as low as 60°), and therefore the main permeability reduction is in the horizontal plane. Any baffle which dips at more than 45° will increase the overall vertical to horizontal permeability ratio, and horizontal permeability will show the greatest anisotropy due to faulting.

The systems considered are of the most general case possible: N faults of identical length, thickness and permeability (L,T,k_f respectively) contained in an area A, of constant matrix permeability (k_m). The faults are distributed equally between two orientation populations, and the flow direction bisects these populations. The angle between the populations (2α) has the range $0°<2\alpha<180°$. The connectivity of the system is representative of the particular line density and orientations present (see Figure 3.19). The aim is that the two principle components of the 2D effective permeability tensor may be calculated (using equations or look-up charts) as a function of these parameters.

This chapter is arranged as follows. In Section 5.2, orthogonal systems ($\alpha = 45°$) are considered. Numerical flow simulation of geometrically representative systems have been used to determine the effective permeability of any system, as a function of tortuosity and transmissibility components. This allows determination of k_e as a function of all the parameters in the previous paragraph with the exception of α, which is fixed at 45°.

Any non-orthogonal system is geometrically similar to a particular orthogonal system (see Section 4.5.2), for which the effective permeability can be determined (Section 5.2). Section 5.3 considers analytical methods for adapting the orthogonal permeability to fit the equivalent non-orthogonal system, and these methods are compared with flow simulation results of non-orthogonal systems.

The overall effective permeability model is presented in Section 5.4. While this method appears to be robust for $\alpha = 45°$, there are problems with anisotropic systems, due to difficulties in defining system tortuosity. These are problems summarised, and possible approaches are suggested to solve this hitherto neglected problem. Although the results for non-orthogonal systems are not very accurate, the method is still a significant advance on existing methods for determining the permeability of faults systems, which consider only entirely disconnected systems of parallel faults (e.g. Omre *et al.* 1994, Heath *et al.* 1994).

5.2 Effective permeability of an orthogonal system

This section is split into eight sections. In Section 5.2.1 the flow simulation scheme used is described. Section 5.2.2 discusses the twin issues of tortuosity and transmissibility, and in Section 5.2.3 a method is developed for combining all transmissibility terms into a single measure (called fault heterogeneity; H). This allows the development of effective permeability vs. transmissibility relationships which are specific to a particular case of system tortuosity (Sections 5.2.4 - 5.2.5). In Section 5.2.6 this method is applied to systems with connectivities representative of the range of line densities likely to be encountered in fault systems. Section 5.2.7 presents a generic method for determining the effective permeability of representative orthogonal systems as a function of line density and transmissibility. Section 5.2.8 summarises these treatments.

5.2.1 Flow simulation method

The numerical flow simulation scheme used to determine the effective permeability of a fault system has been devised so that the relative effects of transmissibility terms and geometrical terms may be evaluated separately (Figure 5.4). The commercial, finite difference, Eclipse 100 flow simulator is used. Arrays of injector and producer wells are placed at opposite ends of the model, giving a constant flow rate across the system. Faults are placed in discrete grid cells (rather than as transmissibility multipliers) oriented at 45° to the flow direction, according to a deterministic geometrical arrangement.

The models have a periodic geometrical arrangement: the faulting in each ninth of the model is identical to any other ninth, and k_e is calculated for the central ninth of the entire area. Grid-block pressures upstream and downstream of this central region are used to determine the average pressure drop across the region, and this pressure drop is used to determine k_e of the system according to Darcy's law (Equation 5.1). The

advantage of using this arrangement is that it reduces the influence of the no-flow boundaries at the top and bottom of the model.

The models are assumed to be representative, although this has not been tested by changing the size of the domain. Heath *et al.* (1994) determined that systems are representative, provided each barrier spans no more than 1/7 of the width of the entire model. In these models, the baffles span 1/12 of the width. Indirect evidence that the systems are representative is given in Section 5.3.4.

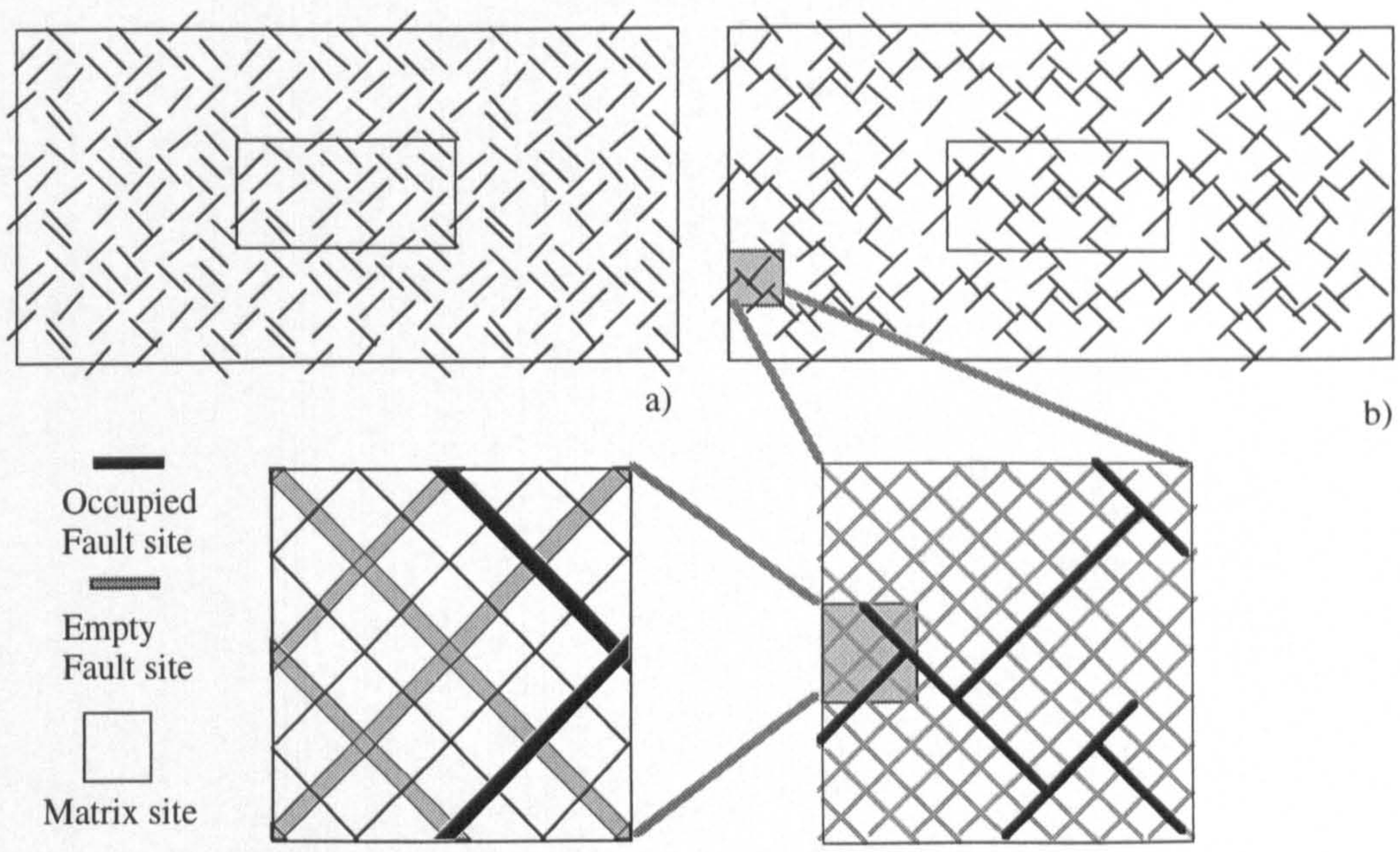

Figure 5.4 2D numerical flow simulation scheme. 97249 active grid-cells are distributed at 45° to the flow direction. Each potential fault site is separated by two matrix sites. The systems have a periodic geometrical arrangement, and effective permeability is calculated over the central ninth region. A) Disconnected system. b) Connected system. Both systems have the same line density ($d_L = 0.375$).

Numerical artefacts

Numerical artefacts are inevitable when finite difference methods are adopted, and this is particularly true for the flow models described in this Section, in which the grid orientation is at a 45° angle to the overall flow direction. There are two sources of numerical artefacts, firstly due to the orientation of the grid relative to the pressure gradient, and secondly due to grid discretisation.

The effect of grid orientation is summarised on Figure 5.5. The actual distance between two points parallel to the pressure gradient is L, but the simulator considers these two points to be $\sqrt{2}L$ apart, because flow can only occur between grid-blocks which share sides. This effect, which is entirely independent of discretisation, will tend to underestimate the effective permeability of the system, as $k_e \propto L / \Delta P$ (see Equation 5.1).

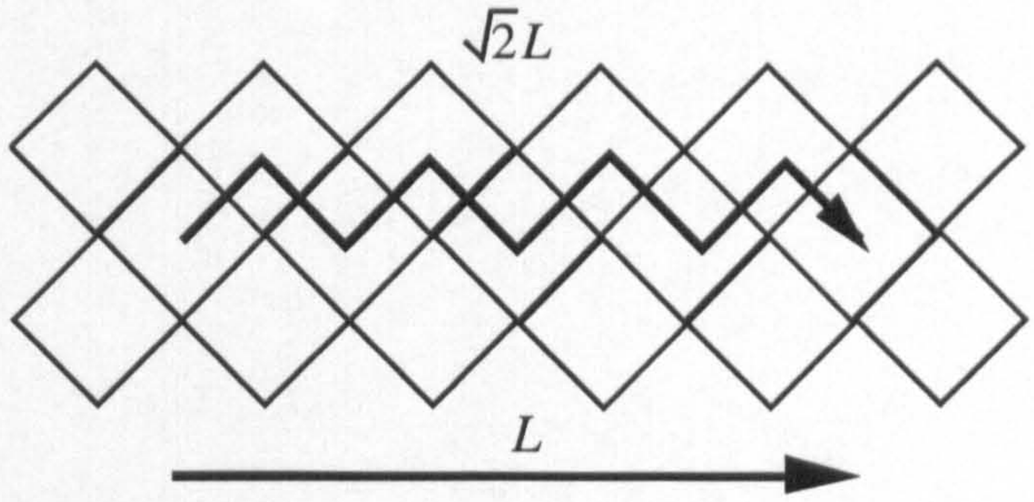

Figure 5.5 Effect of grid orientation. The distance between two points parallel to the pressure gradient is greater than it should be owing to the orientation of the grid.

There are two possible discretisation effects, temporal and spatial. Generally, the greater the discretisation for either of these, the more accurate the result, as the simulator solver is interpolating between smaller intervals. Effects of spatial discretisation are shown on Figure 5.6, from simulations performed on a small version

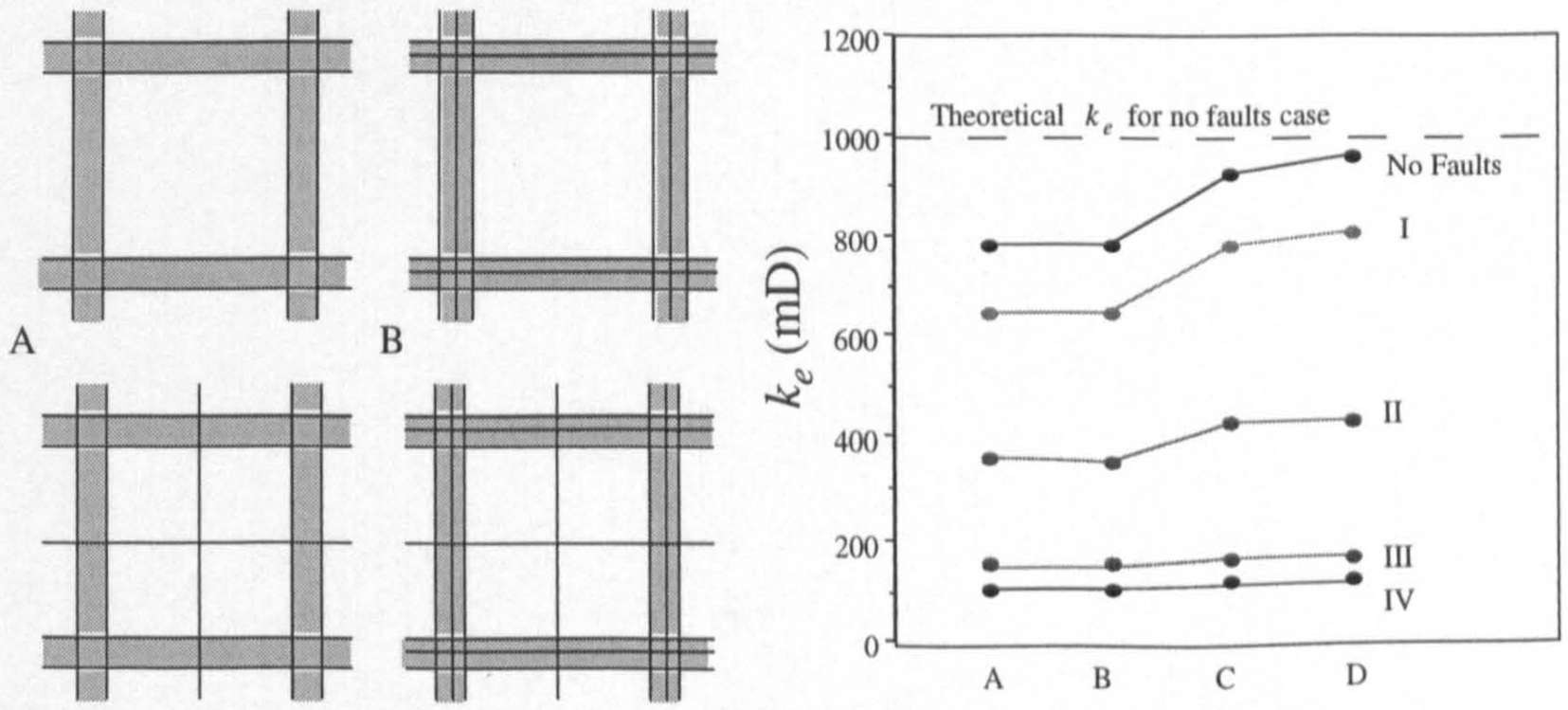

Figure 5.6 Effects of discretisation. a) Four discretisations of faults and matrix sites. The fault sites are shaded. b) Effective permeability for 1 mD faults in 1D matrix for four spatial arrangements of baffles (not shown) and an unfaulted case, at each discretisation level. Theoretical k_e for the unfaulted case is 1000 mD, but is unknown for the systems I to IV.

of the grid. Four discretisation cases have been tested over four arrangements of baffles, and for an unfaulted situation. It appears that it is more important to have a greater discretisation in the matrix sites than in the fault sites, and a reasonable result is achieved for the discretisation case used in this work (Case C in on Figure 5.6a).

5.2.2 Tortuosity and transmissibility

The two fault models illustrated in Figure 5.4 have the same number of faults, but different geometrical arrangements. In one model, all the faults are disconnected, and, were the faults impermeable, flow would still be possible in tortuous paths around them. In the second model the faults are well-connected, and form continuous barriers across the entire area. In this system, flow must pass through some of the faults, although tortuous paths are still possible around others. Effective permeability of the system is therefore a function of tortuosity and transmissibility components: the former determined by the system connectivity, and the latter by some form of bulk permeability average.

Permeability averages (harmonic or arithmetic) are independent of the spatial arrangement of the faults in the system, and depends exclusively on the amount of fault material which is present, which is termed gouge density. Consider an area A containing N rectangular faults, each of length L and thickness T. The gouge density (d_G) of this area is defined as the (dimensionless) fraction of fault material contained in the area. In other words,

$$d_G = NLT / A. \qquad (5.2)$$

Each fault in any simulation run has an identical thickness and permeability, but these values, and the matrix permeability, can be changed for different cases. This allows analysis of the changes in k_e as a function of given transmissibility values for each geometrical arrangement. The two systems in Figure 5.4 have been modelled with the

fault permeability held constant at 1 mD. For each of the templates, four fault thicknesses (T) were used, giving four different gouge densities. For each d_G, effective permeability was determined for four k_m values, to give a total of 16 simulation runs per template. The results are shown on Figure 5.7. The differences in character of the two curves at different gouge densities and fault / matrix permeability contrast are a function of the different geometrical arrangements.

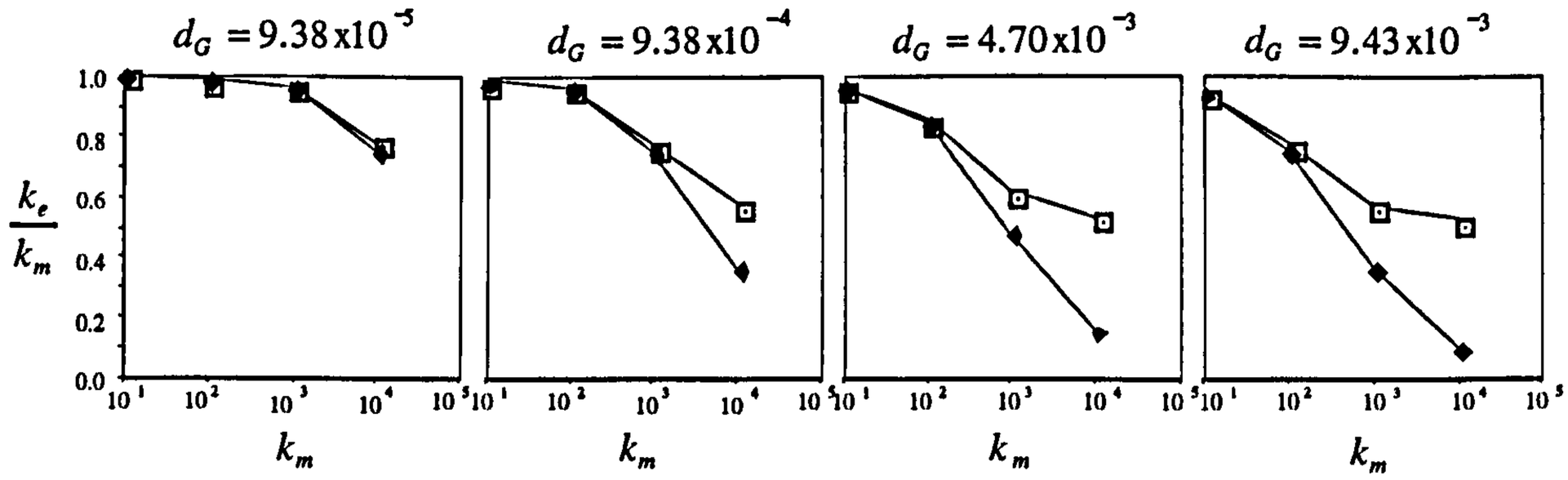

Figure 5.7. Fractional permeability (k_e / k_m) vs. matrix permeability (k_m) for the two fault systems illustrated in Figure 5.4, at four gouge densities (d_G). $k_f = 1$ mD throughout. k_m = 10, 100, 1000 and 10000 mD. Squares - disconnected system. Diamonds - connected system.

The differences in effective permeability between the connected and disconnected cases are greatest at high gouge density and high matrix permeability. Increasing either of these reduces the transmissibility of the systems. When the overall transmissibility of the system is lowered, tortuous flow becomes a more important mechanism, and the differences in effective permeability owing to differences in connectivity are greater. If the faults were barriers rather than baffles, then the connected system would be impermeable, as no tortuous paths exist through this system. In the disconnected system, flow would still be possible. Therefore the connected system k_e / k_m curves (Figure 5.7) tend to zero at low system transmissibility, while the disconnected system response plateaus at a particular value which represents the component of effective permeability governed by tortuous flow.

5.2.3 Fault heterogeneity

Three variables are being modelled in these runs; the gouge density, the fault and matrix permeabilities and the fault system geometry, and, because of this, it is difficult to isolate the effect of any one variable. To do this necessitates incorporation of all transmissibility terms (gouge density and the fault / matrix permeability contrast) into a single variable.

If each fault has a permeability k_f, and the unfaulted matrix has permeability k_m, the harmonic and arithmetic average permeabilities are given by:

$$k_h = \left[d_G / k_f + (1 - d_G) / k_m \right]^{-1}, \tag{5.3}$$

and

$$k_a = d_G k_f + (1 - d_G) k_m. \tag{5.4}$$

Permeability averages vary as a function of the bulk transmissibility properties of the system, but are independent of the geometrical arrangement of the faulting (fault orientations and spatial position). Figure 5.8a shows the relationship between arithmetic and harmonic average permeability, and gouge density for a 1 mD fault system in 1D matrix. The effective permeability of a fault system must plot between k_h and k_a, and the separation between the two averages is the maximum k_e range possible for a system with these permeabilities, at any particular gouge density.

As the matrix / fault permeability contrast (k_m / k_f) increases, the shape of the $k_a - k_h$ curve is similar but retains a higher value at lower fault densities. $k_a - k_h$ normalised against k_m to give $(k_a - k_h) / k_m$ is plotted against gouge density for three values of k_m / k_f (Figure 5.8b). The distance under each curve at a particular gouge density is a measure of the possible effective permeability range for each case of permeability contrast. Fault system geometrical variability can be significant only if the $(k_a - k_h) / k_m$ curve is high.

The term $(k_a - k_h)/k_m$ therefore reflects the overall permeability heterogeneity of the system, and if $(k_a - k_h)/k_m$ is high, then the geometrical distribution of the faulting is a significant factor in the effective permeability of the system. Because $(k_a - k_h)/k_m$ includes $(k_a - k_h)$, a particular value does not represent a unique case of fault heterogeneity. For instance, a value of $(k_a - k_h)/k_m = 0$ could imply either no faulting in the volume under consideration, or that it is composed entirely of fault gouge. To overcome this equivocality, a modified form in which the k_a term is replaced by k_m is used to represent fault system heterogeneity. Fault heterogeneity (H) is therefore given by:

$$H = 1 - k_h / k_m . \qquad (5.5)$$

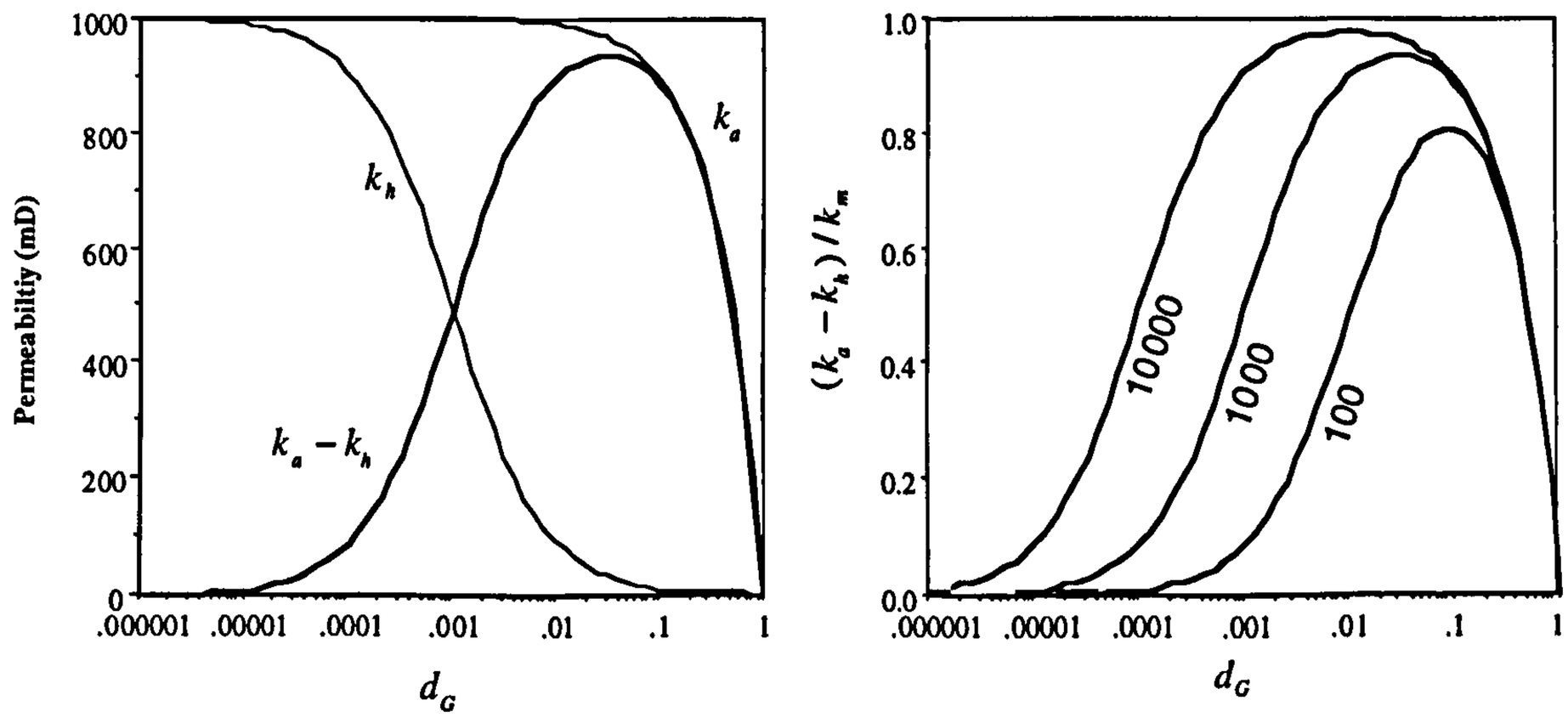

Figure 5.8. Permeability averages as a function of gouge density and permeability contrast. a) Average permeability vs. gouge density for 1 mD faults in 1 D matrix. k_a = arithmetic average k_h = harmonic average. The Effective permeability of the system must lie between these curves. $k_a - k_h$ is the total range in effective permeability which may be present in the system due to its geometrical architecture. b) $(k_a - k_h)/k_m$ vs. gouge density for 1 mD faults in 0.1, 1 and 10 D matrix.

This function is virtually identical to $(k_a - k_h)/k_m$ for gouge densities up to the values at which k_a is more variable than k_h (i.e. the turning points of the curves in Figure 5.8b), but rather than decreasing to 0 at a fault density of 1, it increases towards 1. H is similar in form to the Dykstra-Parsons heterogeneity measure (Dykstra and Parsons,

1950; Lake and Jensen, 1991); and ranges from $H = 0$ (for a case of $d_G = 0$ or $k_f = k_m$) to $H = 1$ (for a case of $k_f = 0$).

5.2.4 Geometry and Heterogeneity

Expanding Equation 5.5, using Equations 5.3 and 5.4 gives the matrix / fault permeability contrast as a function of H and d_G:

$$\frac{k_m}{k_f} = \frac{H}{d_G(1-H)} + 1. \qquad (5.6)$$

Contours at constant H derived from this relationship are drawn on the two plots in Figure 5.9. The 16 spot values on these plots are of k_e / k_m (termed fractional permeability) from the two geometrical cases discussed in Section 5.2.2. The fractional permeability spot values follow precisely the same trend as the H contours, except a very low k_m / k_f. This correlation means that the fault / matrix permeability contrast and gouge density may be combined into a single measure of fault system transmissibility (H), allowing geometrical variability to be considered in relation to

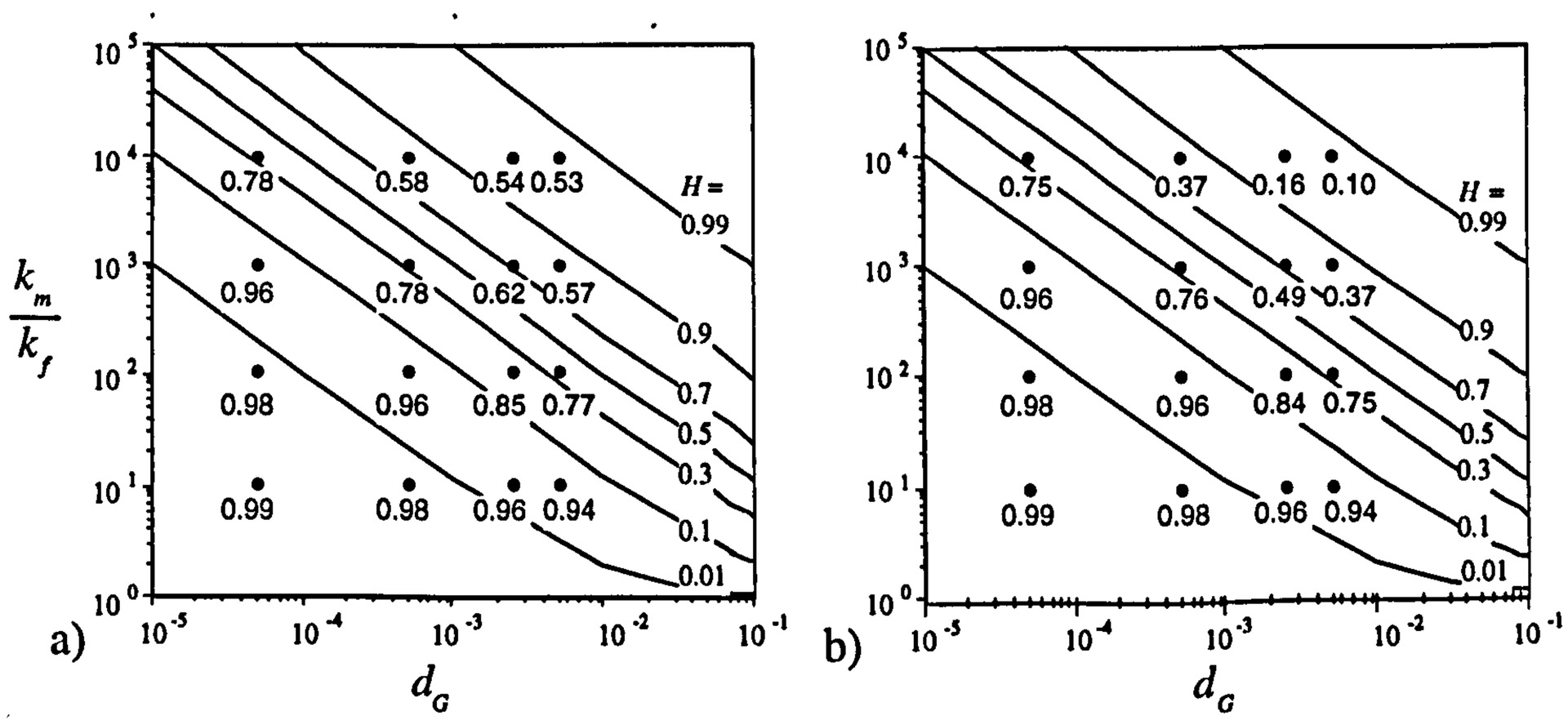

Figure 5.9. Matrix / fault permeability contrast (k_m / k_f) vs. gouge density (d_G), for a) the disconnected case and b), for the connected case. Spot values are fractional permeability (k_e / k_m) for the sixteen d_G, k_m / k_f pairs. Contours are of constant fault heterogeneity (H), calculated from Equation 5.6.

one, rather than two, other parameters. The problem is simplified to one of defining $(k_e / k_m) / H$ correlations as a function of fault system structure.

Figure 5.10 shows the k_e / k_m Vs. H relationships for the two geometrical cases. The two systems follow different trends lying somewhere between k_h and k_a, as expected from the discussion above, and the influences of the differences in system connectivity are immediately apparent.

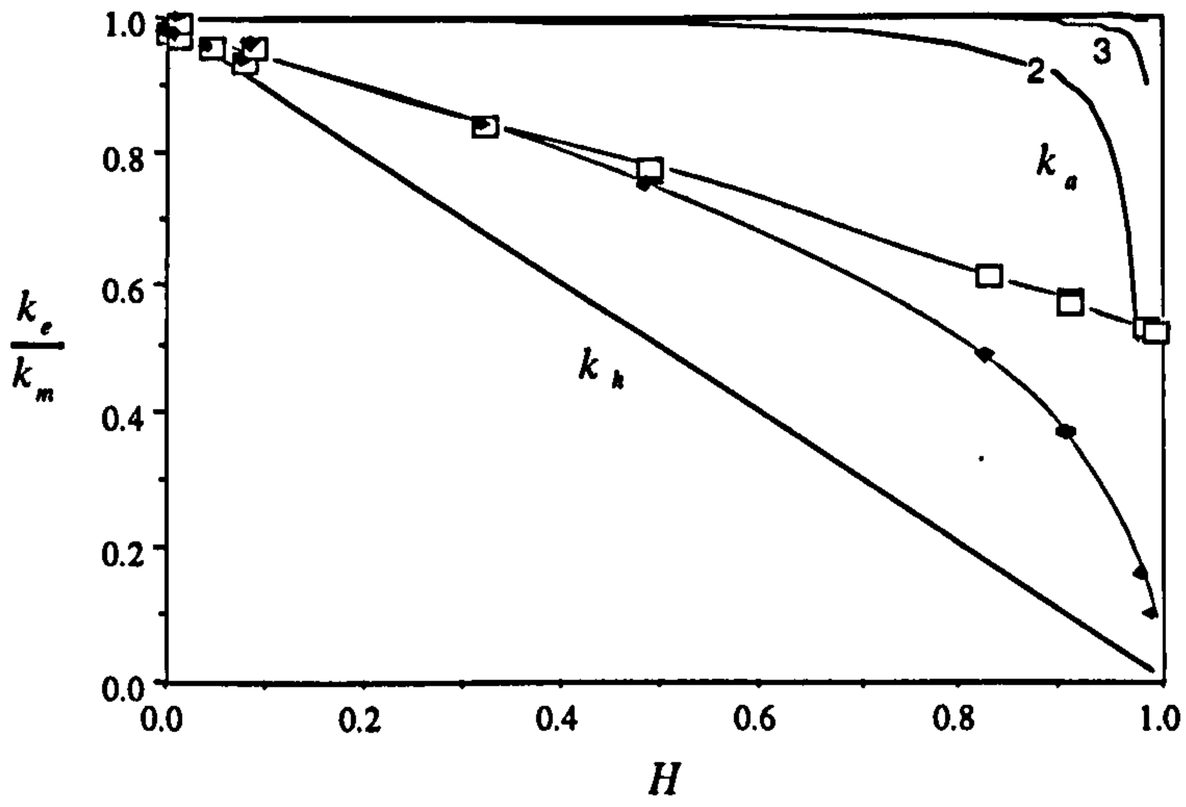

Figure 5.10. Fractional permeability (k_e / k_m) vs. Fault heterogeneity (H) for the disconnected and connected systems. Squares - disconnected case. Dots - connected case. Also shown are curves of k_h and k_a. Because H does not depend on k_a, the k_a curves are different for different k_m / k_f. The labels on the k_a curves relate to orders of magnitude difference in k_m and k_f.

At low H, the faults do not form appreciable baffles, as it is as easy to flow through the faults as it is to follow tortuous paths around them. Therefore the connected case gives only a slightly lower fractional permeability than the disconnected one. At high H, the faults form much more substantial baffles, and the two curves diverge. In the connected system, k_e / k_m rapidly descends to zero as the system transmissibility decreases, but in the disconnected system, tortuous flow is possible even when the faults are impermeable, and k_e is never less than about 50% of k_m. The curves follow a general trend with the form $k_e / k_m = (1 - aH)^{1/b}$, where a and b are system specific constants.

5.2.5 Summary and discussion

Fault system transmissibility terms can be incorporated into a single parameter (H). A high H implies a high gouge density or a low fault permeability, and, for the purposes of determining k_e, it is irrelevant which. Any geometrical case defines a unique curve of permeability reduction as a function of increasing H, which plots somewhere between the two theoretical limits of k_a and k_h. The curves for a disconnected and a connected system (Figure 5.4) are shown of Figure 5.10, and detrimental influence of connectivity at high H is clear.

There are potentially some problems at high H, due to the absence of k_a in the definition of H, resulting in no unique curve for k_a on a plot of k_e / k_m vs. H. At a high matrix / fault permeability contrast, the k_a curve lies very close to $k_e / k_m = 1$, and descends to zero sharply at high H. At a lower k_m / k_f, the k_a curve descends to zero much more gradually, and begins to descend at a lower H. This implies that, for fault systems which are structured such that their effective permeability tends towards k_a, a method of modelling k_e / k_m based on a correlation with H will not yield a consistent result at different k_m / k_f. This problem is only likely to be significant when k_m / k_f is low (< 2 orders of magnitude) and H is high.

A low k_m / k_f will tend to produce a low H, unless d_G is extremely high. As a result, this is not perceived as a significant problem, particularly considering that the effective permeability of deformation bands are, typically, about 3 orders of magnitude less permeable than the sandstone containing them, and d_G is very unlikely to be greater than about 0.01, assuming a suitably large area is being considered. Therefore a very high H is most likely to be calculated because of a very low k_f. A low k_f implies a high k_m / k_f, which produces a very sharp k_a drop. Therefore a (k_e / k_m) / H correlation is unlikely to produce spurious results even at very high H.

5.2.6 Effective permeability as a function of line density

The systems discussed above demonstrated the relative significance of fault system geometry and transmissibility. In Chapter 4, the connectivity of a fault system was shown to be a function of the line density of the system (Section 4.3), where line density is given by:

$$d_L = NL^2 / 4A, \tag{5.7}$$

where N is the number of faults of length L present in an area A. If d_L is low, occasional faults may be connected, but, on the whole, the system is disconnected and tortuous flow paths are possible. As d_L increases, the system becomes gradually more connected until, at a critical line density (the percolation threshold), a continuous connected fault cluster forms, requiring every possible flow path to pass through at least one fault. At higher line densities, the system becomes compartmentalised, and the availability of tortuous flow paths becomes increasingly scarce and virtually all flow is through faults. It was shown that systems with splaying characteristics representative of those observed in outcrops become connected at $d_L \approx 0.7$.

A modelling suite comprising six disconnected models ($0.09 \leq d_L \leq 0.625$) and eight connected models ($0.625 \leq d_L \leq 5.0$) have been constructed, each with connectivities (number of intersections per line) representative of their line density (Figure 5.11). These models have been used to determine the effective permeability variation as a function of H in the same manner as the two models discussed in the previous section (the results are shown later, on Figure 4.15).

The effective permeability results are tabulated in Appendix 2 (Tables A2.1 and A2.2). As in the previous runs, fault heterogeneity has been modelled by varying both gouge density and matrix / fault permeability contrast, and in each case there is a consistent trend between fractional permeability and H. The scope of these runs is to produce a

single empirical model from which the effective permeability of a system of orthogonal lines at any d_L, T, L, k_f and k_m may be determined. In order to do this, regression results from each of the fourteen systems are combined to give an over-all model, which differs below and above the percolation threshold.

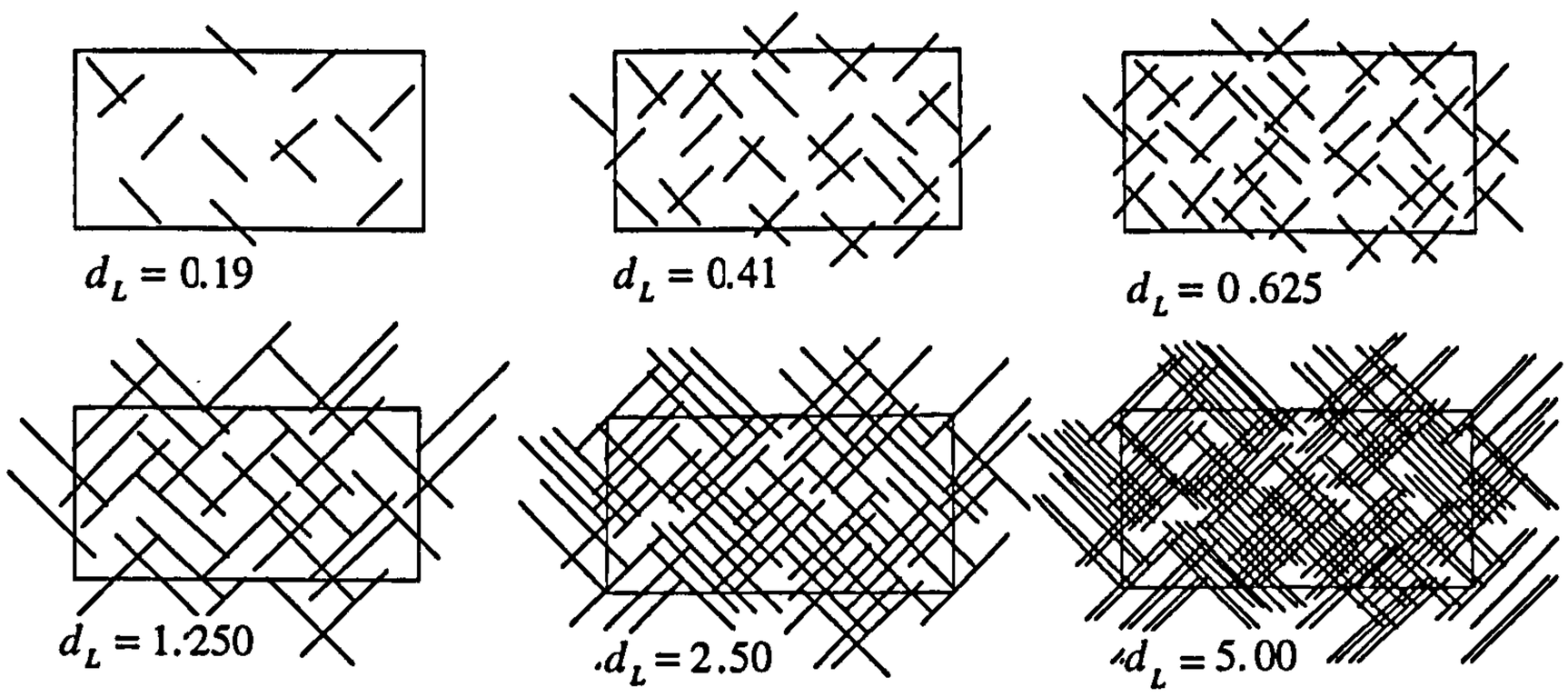

Figure 5.11. Six of fourteen models with variable line density and connectivity representative of systems which become connected at $d_L \approx 0.7$. Only the central ninth region of each model is shown.

Disconnected systems

The disconnected templates have the range $0.09 < d_L < 0.625$. For each of these, a k_e / k_m vs. H correlation with the form (See Section 5.2.4)

$$k_e / k_m = (1 - aH)^{1/2.26a} \tag{5.8}$$

was applied to the results, and values for a were calculated for each d_L. The parameter a may be viewed as a geometrical term for linking k_e / k_m to H, and varies as a function of the connectivity of the system. From these line density specific correlations, a general correlation between d_L and a was made (Figure 5.12). This relationship is given by:

$$a = 1.35 - 0.207 / d_L^{1.3816}, \tag{5.9}$$

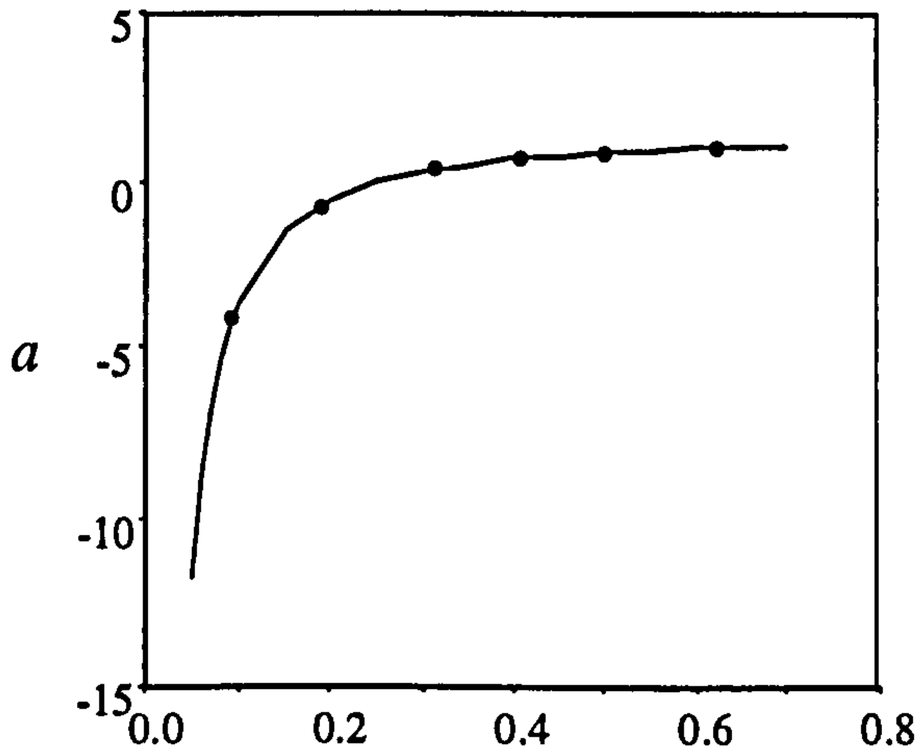

Figure 5.12. Determination of the variable a as a function of line density. a is calculated for each disconnected run (circles), and these data are used to determine the general correlation (Equation 5.9).

$$d_L$$

Connected systems

The connected runs have the range $0.625 < d_L < 5.00$. For connected systems, it is necessary that $k_e / k_m = 0$ at $H = 1$. To satisfy this, the correlation must contain the term $(1-H)$. If the correlation takes the simple form $k_e / k_m = (1-H)^{1/b}$, then k_e / k_m is consistently underestimated at low H and over-estimated at high H. A form which fits the results well is:

$$k_e / k_m = (1 - cH^5)(1-H)^{1/d}, \qquad (5.10)$$

where the power exponent of 5 present in the first term is included to achieve a closer fit. The relationships between d_L and c and d (Figure 5.13) are given by:

$$c = 0.282 + 0.0535 d_L, \qquad (5.11)$$

and

$$d = 1.867 + 0.188 / d_L. \qquad (5.12)$$

Some of the d_L cases produced spurious data, and for these cases, one or both of the coefficients have been omitted from the general regressions. These cases correspond to the runs with $d_L = 0.625$, $d_L = 1.25$, $d_L = 2.5$ and $d_L = 5$. Three of these four cases do not have a regular distribution of H in the range $0 < H < 1$ (Table A2.2). For these runs, the initial effective permeability results used to determine the correlations between c and d were skewed to either a high or a low H. The following Section shows that

$(k_e / k_m) / H$ correlations are much more sensitive to d_L for disconnected systems relative to connected ones. Because of this, it is easier to achieve a precise correlation between d_L and a (disconnected cases; Equation 5.10) than between d_L and c or d (connected cases Equations 5.11, 5.12). For connected systems, transmissibility effects (governed by H) are much more significant to k_e / k_m than tortuosity effects (governed by d_L, and incorporated in the terms c and d).

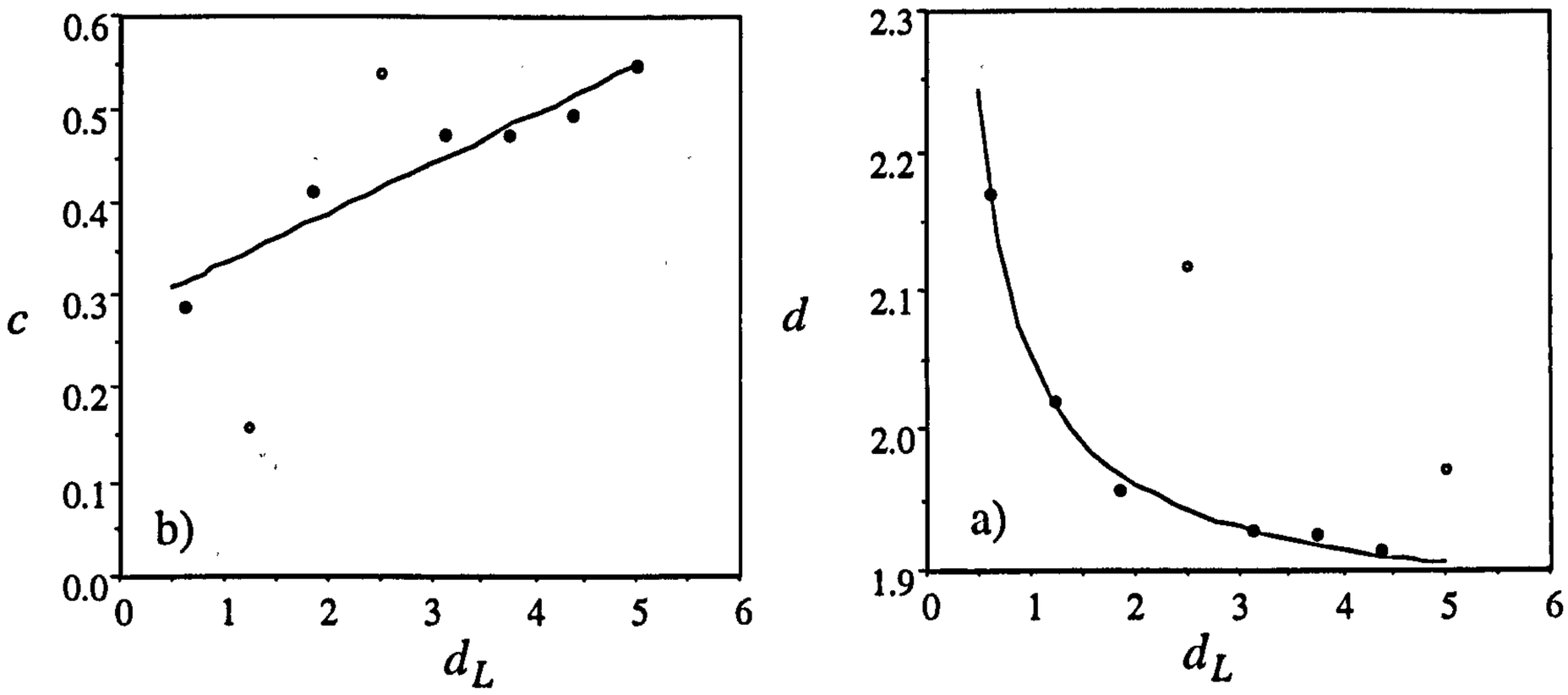

Figure 5.13. Determination of the variables c and d as a function of line density. The values are calculated from the 8 connected runs and these data are used to determine the overall correlation (Equations 5.11 and 5.12). The open circles represent data which were not used to determine the regression curves.

5.2.7 Effective permeability of generic, orthogonal systems

The results from all the disconnected runs and two of the connected runs are plotted on Figure 5.14, along with the k_e / k_m correlation for each d_L cases. Note that the curves are based on the overall model defined by Equations 5.8 to 5.12, rather than the correlations from the individual d_L case results. Both a connected and a disconnected template were used at $d_L = 0.625$, and both give a good match when the appropriate correlation is used. Indeed a consistently good match is given in all the runs.

These models have been constructed based on fault systems with the connectivity characteristics observed in faults systems in sandstones. In Section 4.3.1, the percolation threshold for such systems was shown to $d_{Lc} \approx 0.7$. Equation 5.8 gives a

result of $k_e / k_m = 0$ at $H = 1$ when $d_L = 0.68$. This is close to the calculated d_{Lc}, so the effective permeability model implicitly contains the correct connectivity characteristics of faults systems at any line density. Therefore, for an orthogonal system of faults, k_e / k_m is given as a function of H and d_L, using Equation 5.8 for $d_L < 0.68$ and Equation 5.10 for $d_L > 0.68$.

This empirical determination of k_e / k_m as a function of H and d_L is different below and above the percolation threshold of the system: in the disconnected runs ($d_L <$ 0.68), small changes in line density have a large effect on k_e, as the flow paths become gradually more tortuous. In the connected models, the transmissibility terms (combined in H) are more significant than line density, as tortuous flow is not possible, and the effective permeability through several narrow faults is the same as that through one thicker one. This is why only two of the eight connected results are plotted on Figure 5.14a, although all are used in determination of the connected regression model. It is because the k_e / k_m vs. H curve is not very sensitive to d_L for connected systems, that problems were encountered in trying to assign the variables c and d in Equation 5.10 (Figure 5.13). However these problems are not significant as there is little dependency of k_e on d_L for connected systems.

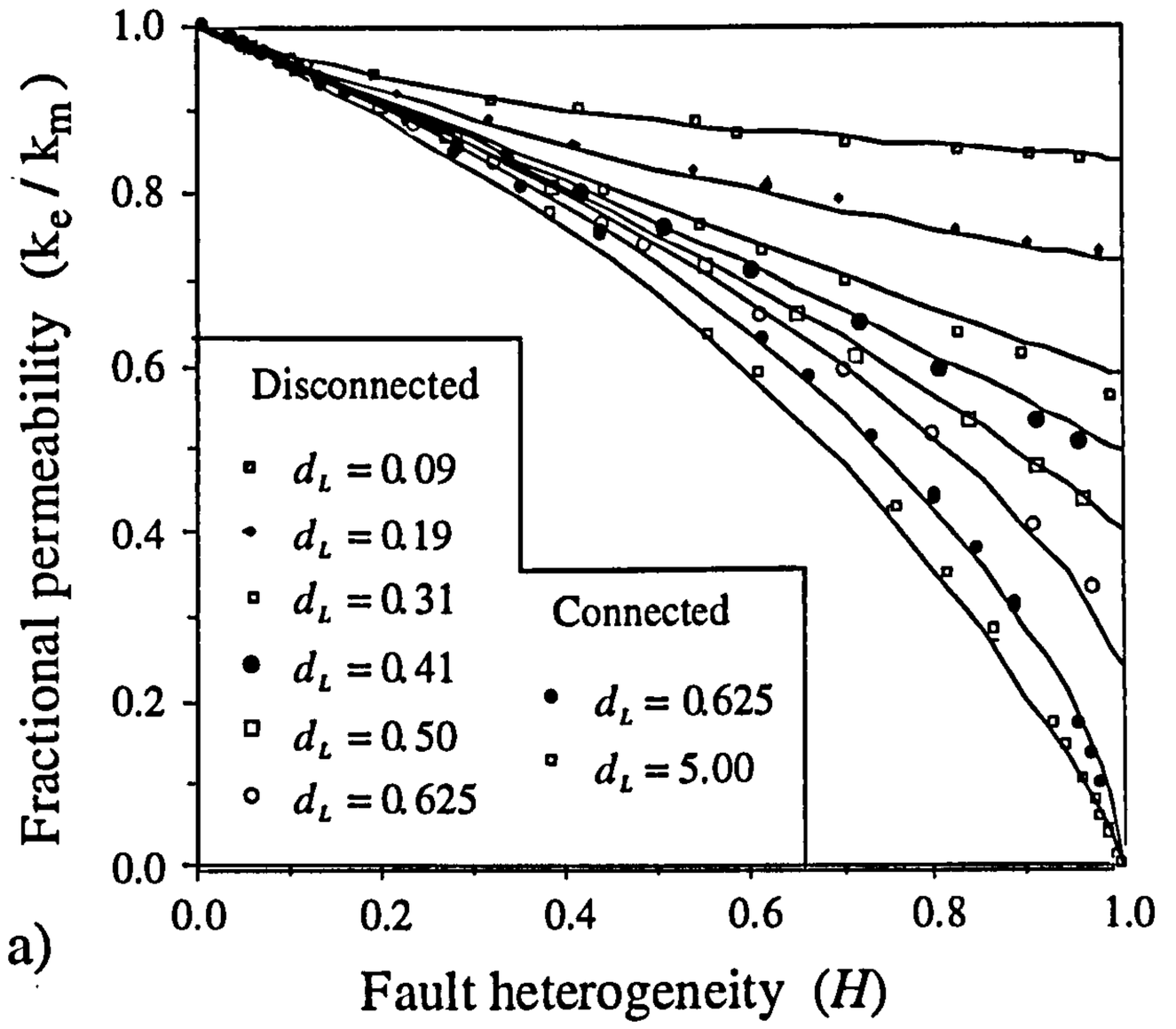

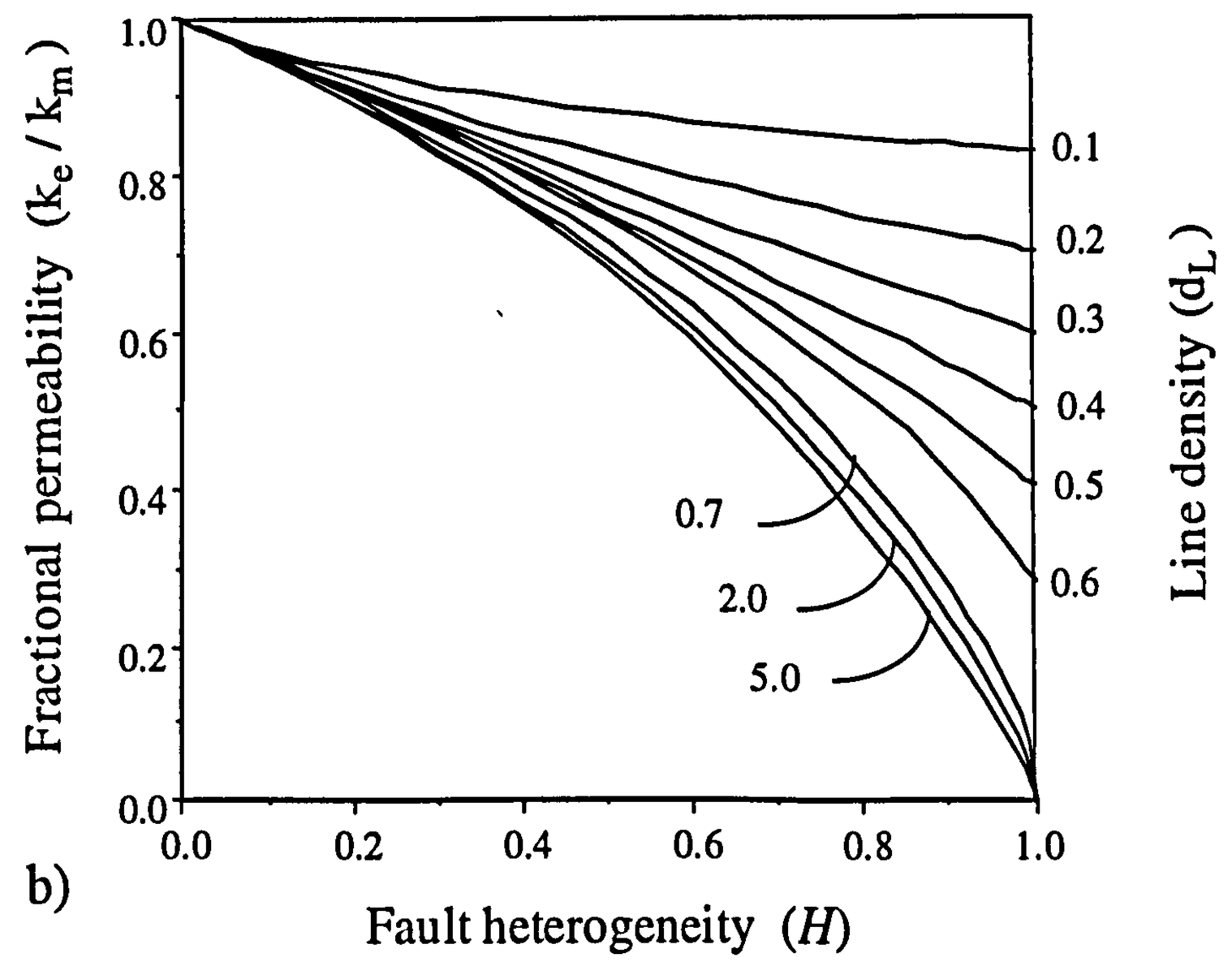

Figure 5.14. Simulation results for the systems shown on Figure 5.7. a) Fractional permeability (k_e / k_m) vs. fault heterogeneity (H). The curves represent the best overall fit to the entire dataset, rather than best fits to each d_L case. b) Mathematical model for normalised permeability as a function of fault heterogeneity (H) and line density (d_L).

5.2.8 Section summary

In this Section a series of flow simulation suites have been described to determine a model which allows inclusion of the fundamental geometrical and transmissibility terms of a fault system at a single length-scale. Figure 5.14b summarises the model. The curves are designed as a look-up chart for determination of effective permeability of an orthogonal system at a single scale as a function of both the bulk transmissibility terms of the system (k_f, k_m and d_G) and the geometrical terms (d_L). The former are used to determine the value of H for the system, and the latter determines the relevant k_e / k_m vs. H correlation. From these, k_e / k_m is read off the ordinate of the graph. All the faults in any system have identical length, thickness and permeability, and are distributed equally between two orthogonal orientation populations. k_e is determined in the direction bisecting these populations. The area over which effective permeability is calculated is assumed to be large enough for the faults to form systems with representative connectivities.

5.3 Effective permeability of non-orthogonal systems

In Section 5.2, a method was presented with which the effective permeability of a system of N identical faults of length L, thickness T and permeability k_f, contained in an area A of matrix permeability k_m, is determined in the direction bisecting the faults. In this Section the orientation variable (α) is incorporated into the model.

The aim of this work is to be able to apply the effective permeability solutions for orthogonal cases to any fault orientation, by modifying the line density and fault heterogeneity terms which reflect the flow impedance of an orthogonal system, to those which reflect the impedance of a geometrically equivalent, non-orthogonal system. Definitions and implications of geometric equivalence are given in Section 5.3.2. The orthogonal treatment in the previous section involved deriving a model from flow simulation results. In this section, attempts are made to formulate analytical expressions to incorporate fault orientation. These solutions are then compared to results obtained from three series of flow simulations. Each series measures the effective permeability of a particular arrangements of baffles, each with different connectivity characteristics, as a function of the orientation of the baffles, and of the bulk transmissibility of the system.

5.3.1 Flow simulation models

In order to vary the orientation between the faults, a rather different simulation scheme to the one used above is necessary. For orthogonal systems, the faults were distributed on a lattice of predetermined fault and matrix sites, and the pressure gradient was at an angle to the sites. In these runs there are no predetermined fault or matrix sites, and the pressure gradient is aligned with the grid. The faults in these models do not have realistic aspect ratios, nor are they distributed in realistic geometrical configurations. This is because the faults need to be several grid-blocks thick, which results in high gouge densities at low line density. That these systems are not representative of real system is not a problem: the aim of these simulations is to determine how orientation

variability might be combined with the geometrically more representative, but orthogonal, models presented above.

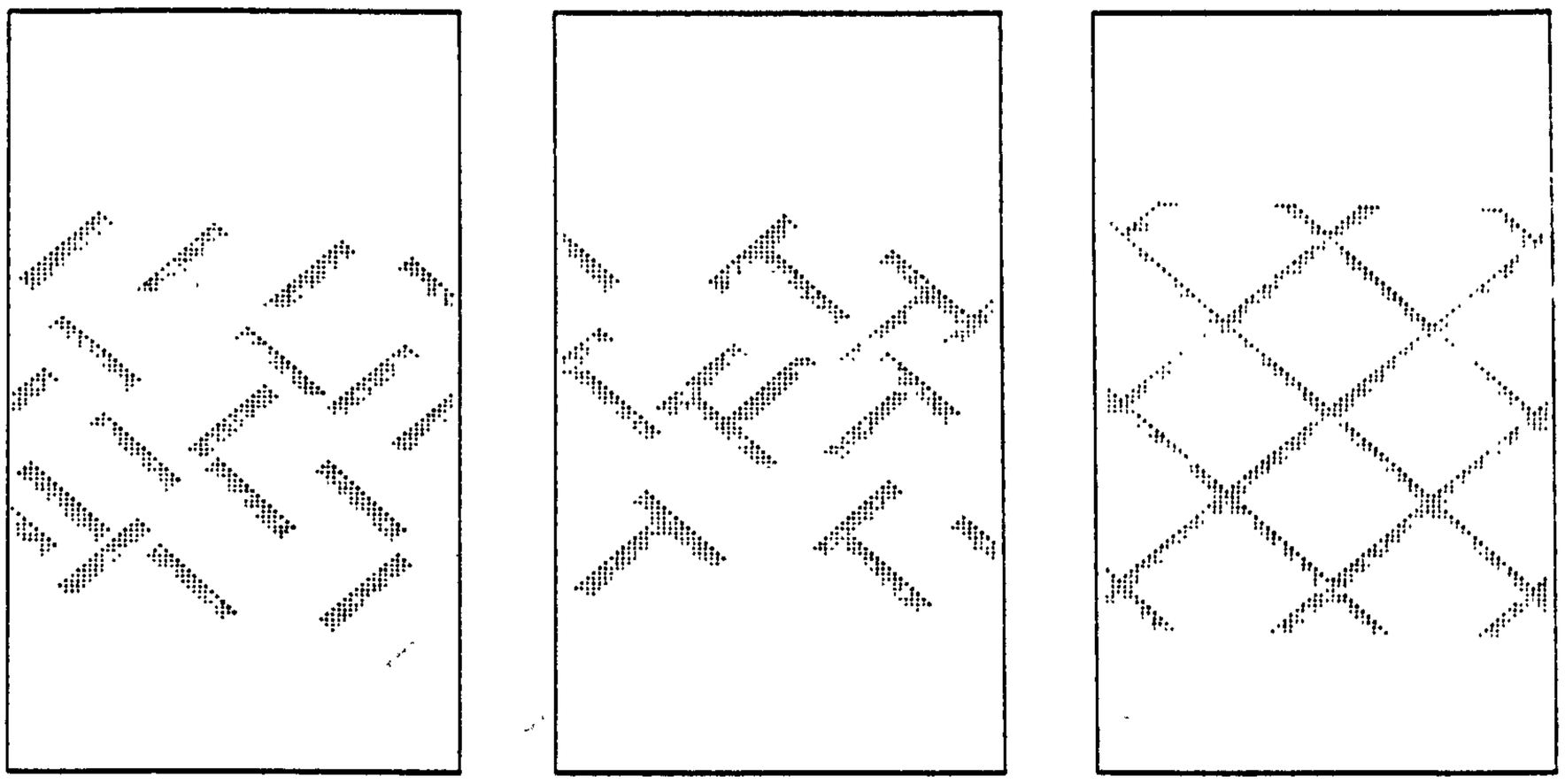

Figure 5.15. Simulation templates used to model the effect of orientation on effective permeability. a) Completely disconnected system. b). Partially connected system. c) Connected system. Flow direction is bottom to top, and the blank regions are buffer cells.

Three simulation templates are used (Figure 5.15). The angle between baffles is modified by changing the aspect ratio of the grid-blocks, and effective permeability results have been obtained for seven α cases in the range $10° \leq \alpha \leq 80°$, over a range of transmissibilities. Note that this scheme does not allow the thickness of the faults to be varied, therefore H has been changed only as a function of k_f / k_m. k_f is 1 mD for all cases except when $H = 0$, for which $k_f = 0$. k_m is in the range 5 mD to 200 mD. Tables A2.3 to A2.5 give the effective permeability results.

5.3.2 Geometrical representivity

Consider any system of orthogonal lines. In Section 4.5.1 it was shown that an orthogonal system of lines contained in square may be transformed into a non-orthogonal system contained in a rectangle, with the same connectivity characteristics as the orthogonal system (Figure 5.16). Let α be the angle between the faults and a line perpendicular to the pressure gradient. As α changes, the length of the diagonals in the area WJ (the dotted lines on Figure 5.16) remains constant. As all faults are parallel to

these lines, the length of the faults (L) is independent of α. The area WJ is not constant, and varies with respect to α by the relationship,

$$A = A_{45} \sin 2\alpha, \tag{5.13}$$

where A is the area of WJ at any α, and A_{45} is the area at $\alpha = 45°$.

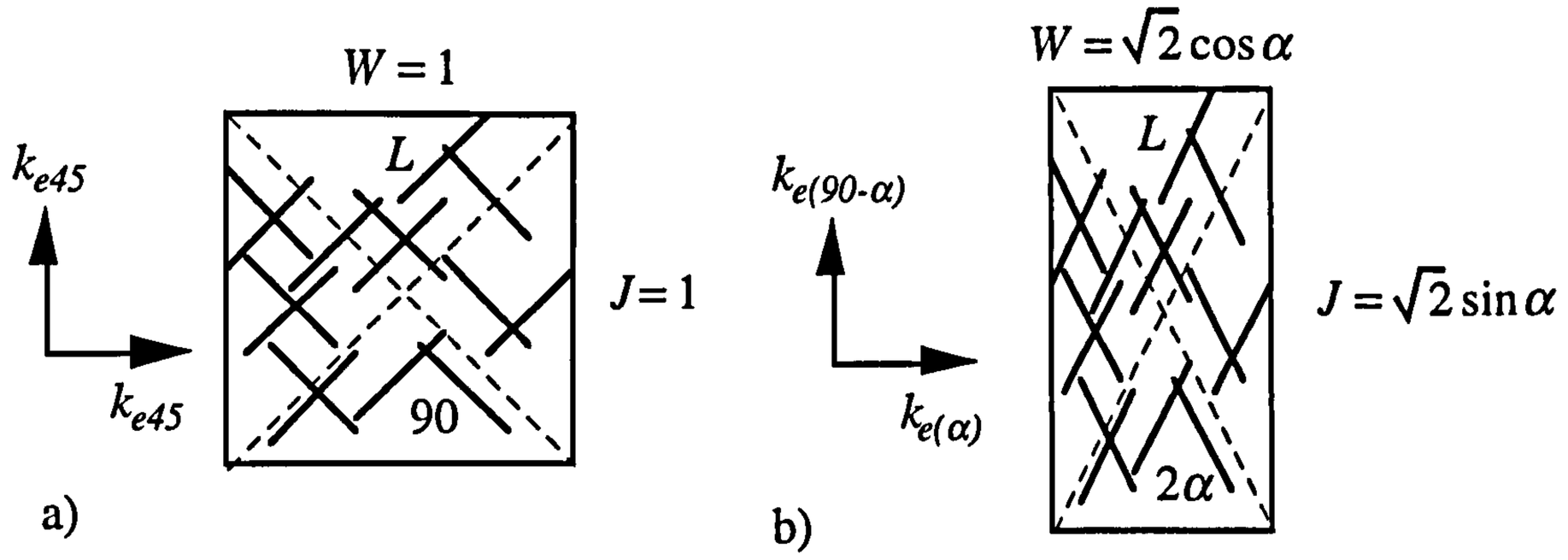

Figure 5.16. An orthogonal (a) and a geometrically equivalent non-orthogonal system (b). The length of each fault (L), and the connectivity characteristics are constant as α changes, but the area (WJ) changes.

Connectivity of the system is constant whatever α. Therefore the affinity for either tortuous flow around faults, or flow through faults is preserved. All that varies is the aspect ratio of the entire system. As for the orthogonal systems in the previous sections, the two issues of changes in tortuosity and transmissibility as a function of the aspect ratio must be considered separately.

Consider a system at $H = 1$. In this case, the faults are barriers, and the effective permeability of the system is reduced due to an increase in tortuosity of flow in the matrix. As α increases, the faults become aligned with the flow direction, and the tortuosity of the system is reduced. Therefore k_e is highest when α is greatest (Figure 5.17). In this case, flow is impossible if the system is connected, irrespective of α.

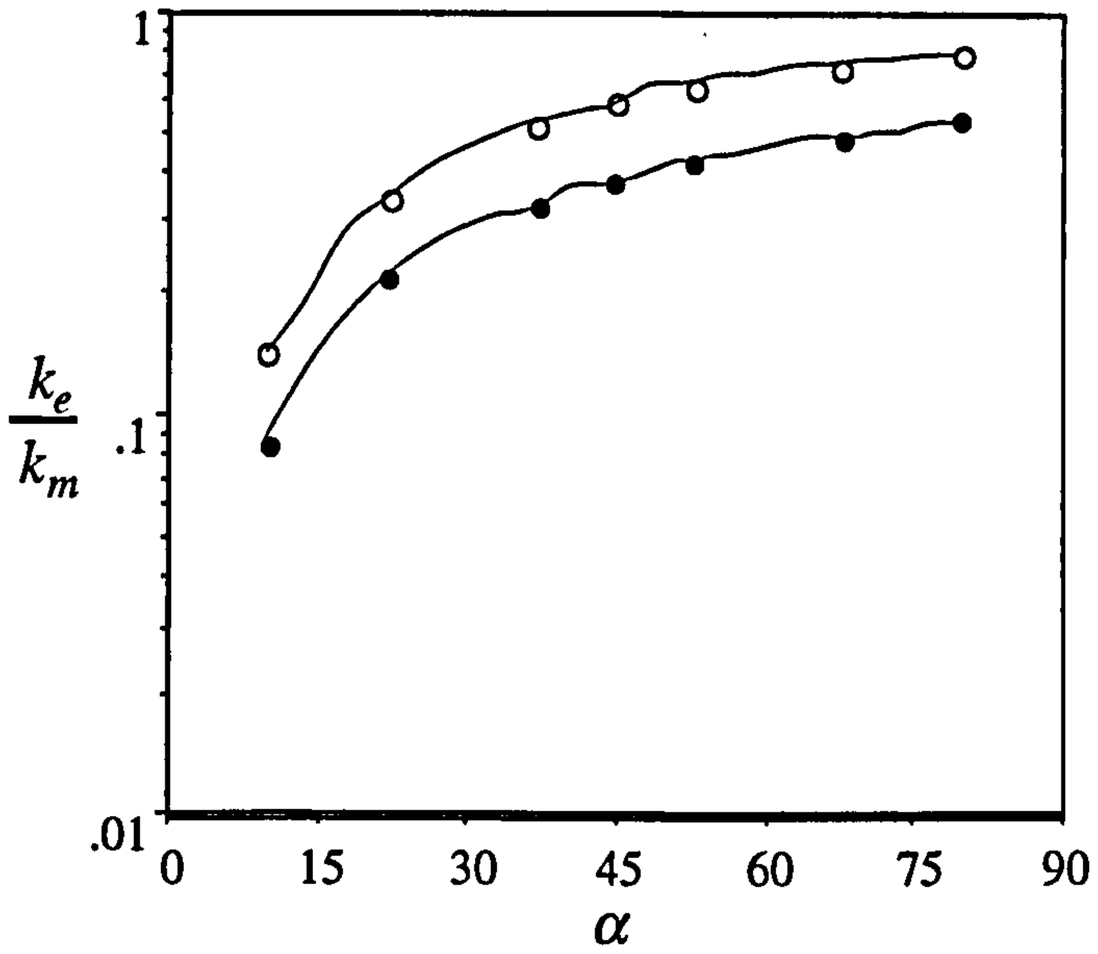

Figure 5.17. Fractional permeability vs. fault orientation at $H = 1$, for the disconnected (open circles, Figure 5.15a) and partially connected (filled circles, Figure 5.15b) systems. All simulation results are listed on Tables A2.3 and A2.4

Consider next an entirely connected system with $H < 1$. There is only a small tortuosity component associated with such a system, and the effective permeability is governed mainly by the low transmissibility of the faults. Flow through a baffle will follow the local pressure gradients present, and, if the baffle is relatively narrow, these gradients will be perpendicular to the baffle, rather than parallel to the overall pressure gradient. Therefore, as α increases, the matrix compartments become larger, but the effective thickness of the fault remains constant, so the effective permeability of a compartmentalised system is also highest when α is large (Figure 5.18).

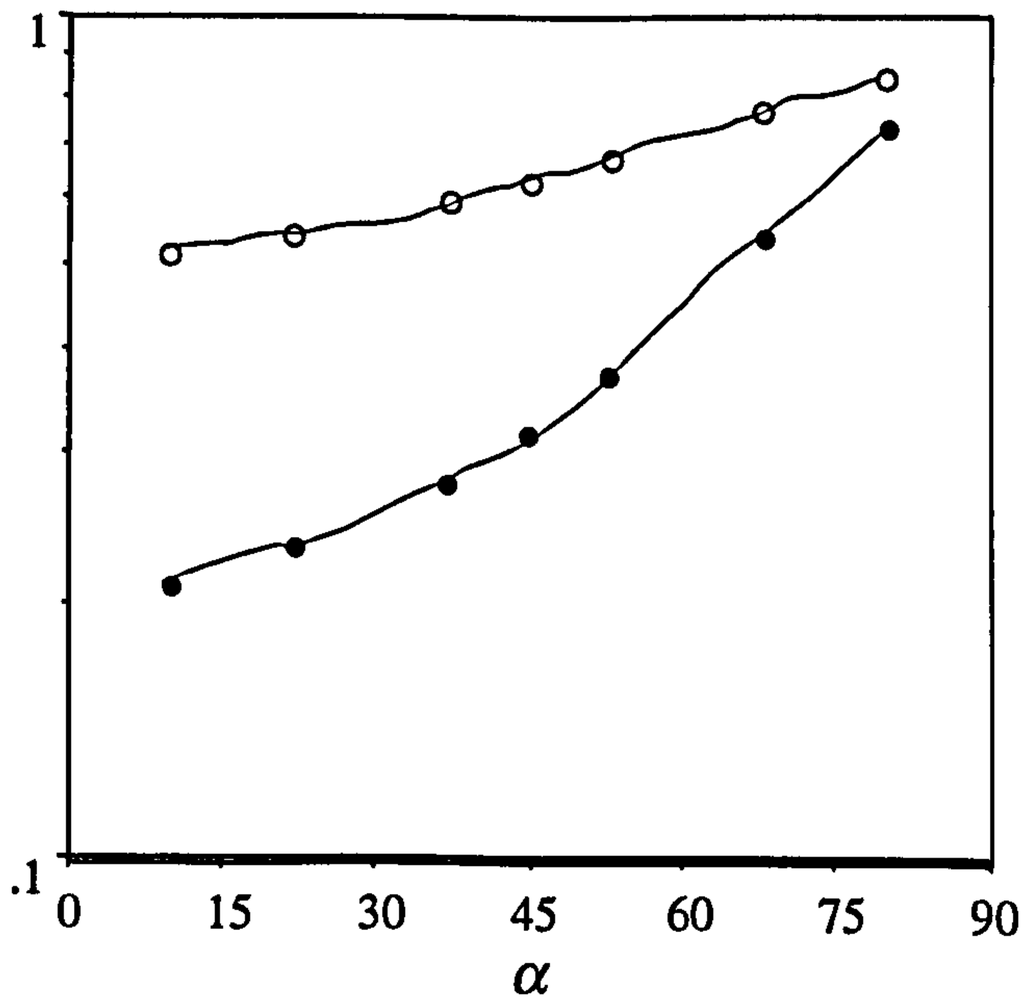

Figure 5.18. Fractional permeability vs. fault orientation for the connected system (Figure 5.15c), at $H = 0.45$ (open circles) and $H = 0.73$ (filled circles). All simulation results are listed on Table A2.5

Other methods to determine the effect of baffle orientation on effective permeability do not maintain connectivity, which is the most important geometrical property with respect to flow. For instance, Walsh *et al.* (in press), altered the angle between lines by rotating them around their centres and preserving the area containing them (see Section 1.3.4). This leads to different connectivity characteristics for different α (Figure 5.19), which therefore requires a completely new determination of the relative influences of tortuosity and transmissibility.

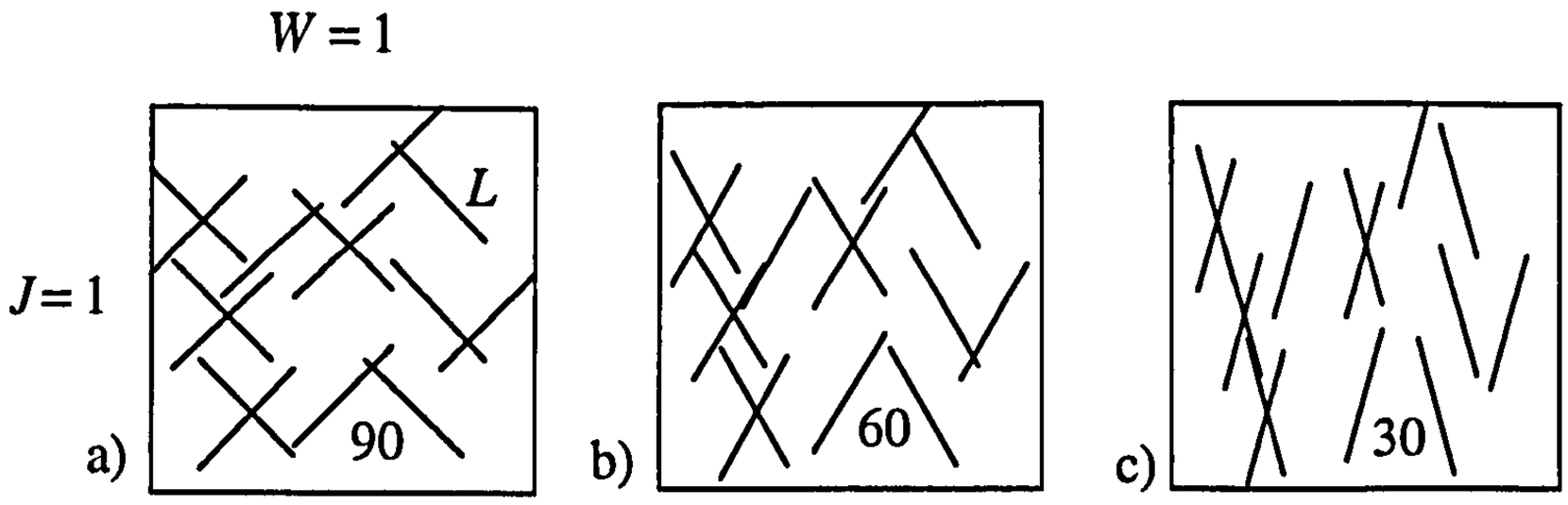

Figure 5.19. Rotating each fault in a constant area (WJ) does not preserve geometrical connectivity, and systems at a lower α are less connected.

5.3.3 Analytical streamline solutions for tortuosity effects

Analytical streamline methods have been used successfully to model the vertical permeability in sandstone / shale reservoirs (e.g. Begg *et al.* 1989). In these methods, the flux in the system is considered to occur in isolated streamlines of a particular length and variable width. Based on the assumption that all streamlines in the system are of similar length (i.e. the system is representative), the permeability of the system is characterised in terms of the length of the average streamline.

Begg and King (1985) and Begg *et al.* (1985) adapted a method from Haldorsen and Lake (1984) to determine the effective permeability of a permeable medium containing impermeable barriers oriented perpendicular to the over-all pressure gradient. They compared analytical and numerical results and concluded that, for a 2D system (Figure 5.20), k_e is given by:

$$k_e = k_m(1-F_s)(1+s\bar{L}/2)^{-2}, \qquad (5.14)$$

where F_S is the shale fraction (analogous to gouge density), s is the number of shale per meter, and $\bar{L}$ is the mean shale length.

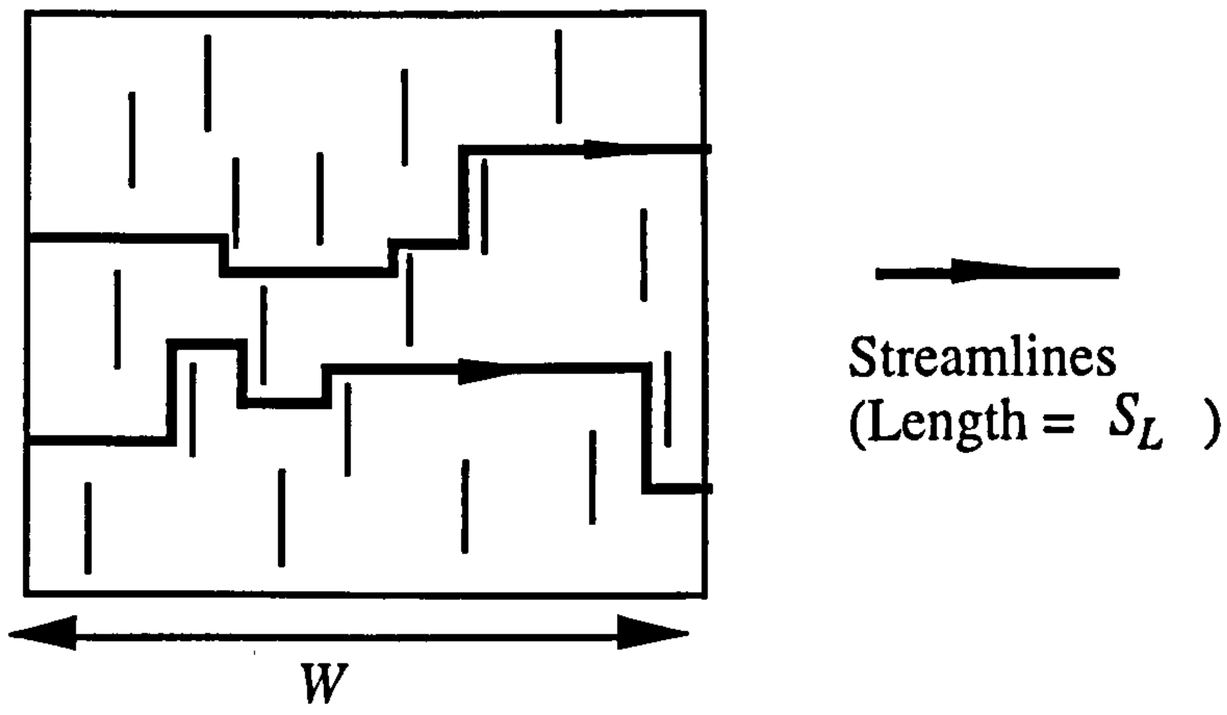

Figure 5.20. The statistical streamline technique of Begg and King (1985). A comparison of average streamline length (S_L) with the flow distance (W) allows approximation of k_e.

Heath *et al.* (1994) adopted this method to consider faults, and assumed that faults have sufficiently high aspect ratios as to make the effectively one dimensional (i.e. $F_s = 0$). They used a much greater variation in the length of the barriers (representing the power-law length distribution often observed for fault populations), and suggested variants to the $\bar{L}$ term in Equation 5.14, to account for the disproportionate effect of longer baffles.

These approaches have determined a permeability relationship of the form:

$$k_e = k_m(1-d_G)(1+t)^{-2}, \qquad (5.15)$$

for the effective permeability of a system of disconnected barriers oriented perpendicular to the pressure gradient, where t is a factor representing the extension of an average streamline, and is given by:

$$t = S_L / W. \tag{5.16}$$

For a system of equidimensional barriers, Begg and King (1985) and Heath et al. (1994) showed numerically that $t = d_S L / 2$ in 2D, and $t = d_S L / 3$ in 3D, where d_S is the scan-line density of the barriers.

Although Begg and King derived these t parameters analytically, they did so by using different formulations for S_L in 2D and in 3D. For the 2D case, a streamline extends its length by "*being forced to go to the end of the barrier closest to its home position*", whenever it encounters one. The home position is defined as the position closest to where it started, so the stream-line may be extended by anything up to L, and so, on average, will extend by $L/2$. In 3D this assumption is relaxed, and a streamtube is allowed to "*take the shortest path available to minimise kinetic energy*". Therefore in 3D, the streamtube is allowed to respond to local pressure gradients, while a streamline in 2D is not (Figure 5.21). If the assumption made in 3D is also made in 2D, then S_L would be $L/4$, and the solution would not fit the numerical results.

Analytical streamline methods therefore provide a simple estimation of the permeability reduction perpendicular to parallel barriers; however there are problems associated with the formulation of t, and Equation 5.14 can only be considered as an apparently robust, yet heuristic, relationship.

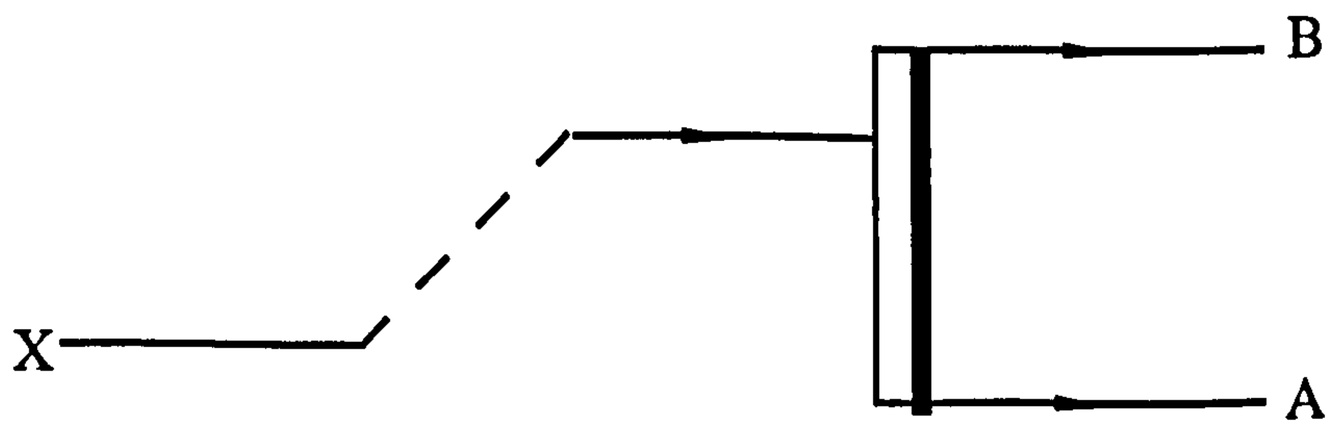

Figure 5.21. Different assumption in 2D and 3D in Begg and King (1985). In 2D a streamline always goes to the end of the barrier closest to its starting point (X), and therefore follows path A. In 3D a streamtube always goes to the end of the barrier closest to where it encountered it, and therefore follows path B.

5.3.4 Disconnected barriers

The solutions determined by Begg and King may be adapted to consider non-orthogonal barriers, within the framework of geometrical representivity (Section 5.3.2), by making some simple assumptions. Both Begg and King (1985) and Heath *et al.* (1994) confirmed numerically that Equation 5.15 works well for equidimensional baffles, if $t = d_S L / 2$. This streamtube extension geometry is illustrated in Figure 5.22a. If the barrier is rotated to an angle α relative the average flow direction, then the effective length of the baffle perpendicular to the pressure gradient is $L\cos\alpha$ (Figure 5.22b).

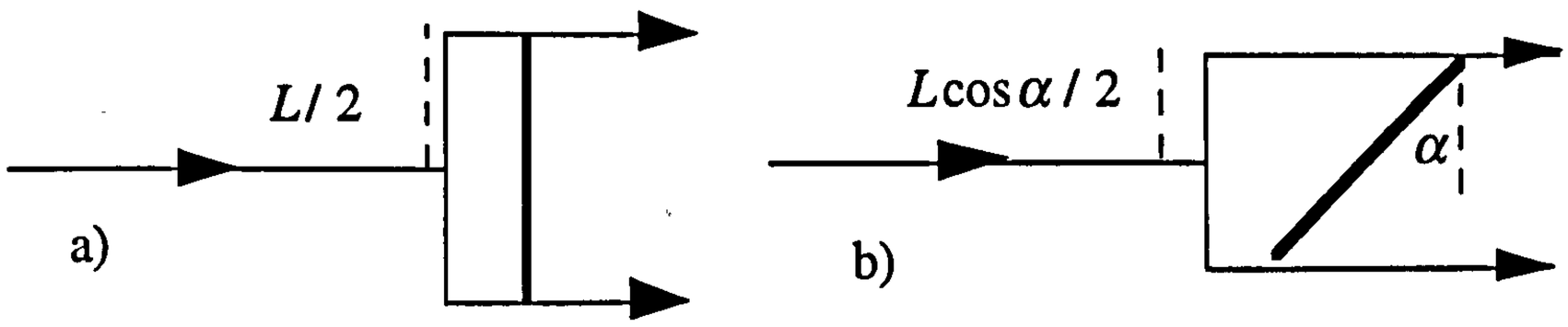

Figure 5.22. Streamline extension around a non-orthogonal barrier as a function of α.

Therefore, as suggested by Begg and King (1985),

$$S_L = d_S L\cos\alpha / 2. \qquad (5.17)$$

The other term affecting t is d_S, which represents the average scan-line density in the flow direction. If N lines are distributed in an area WJ then the scan-line density in the direction parallel to W is given by (See Section 4.5.4, Equation 4.18):

$$d_S = NL\cos\alpha / WJ. \qquad (5.18)$$

As α increases, so does W, the flow distance, and so the scan-line fault density decreases. Replacing Equation 5.17 and 5.18 in Equation 5.16 and then in 5.15, gives:

$$k_e = k_m(1-d_G)(1+NL^2\cos^2\alpha / 2WJ)^{-2} \qquad (5.19)$$

Since line density (d_L) is given by $NL^2 / 4WJ$, Equation 5.19 reduces to:

$$k_e = k_m(1-d_G)(1+2d_L\cos^2\alpha)^{-2}. \qquad (5.20)$$

Thus effective permeability for barriers with only I-node terminations may be determined analytically from geometrical parameters for all fault orientations, line densities and gouge densities. Below, Equation 5.20 is validated against simulation results. In Section 5.3.5, the solution is generalised to allow effective permeability determination for systems incorporating fault connectivity and transmissibility properties.

Comparison with simulation results

Figure 5.10 shows the k_e / k_m vs. H curve for an entirely disconnected system of baffles oriented at $\alpha = 45°$, for which $d_L = 0.375$. If we assume that $k_f = 0$, then $H = 1$ irrespective of d_G, so we may assume that d_G=0. This assumption does not cause the problems discussed in Section 5.2.5, as those problems were associated with a high H at a low k_m / k_f, whilst this assumption results in an infinite k_m / k_f. Inputting these values into equation 5.20 gives $k_e = 0.53k_m$. An extrapolation of the curve on Figure 5.10 gives $k_e \approx 0.52k_m$ at $H = 1$, confirming that Equation 5.20 is valid for this system, and also confirming that the systems considered in Section 5.2 are geometrically representative.

Figure 5.23 shows a comparison between k_e / k_m determined by Equation 5.20 and the simulation results for the disconnected system (Table A2.3). At any α, Equation 5.20 over-estimates k_e by about 7% of k_m. This is most likely to be because the system considered is too small to be representative. Also, the use of no-flow boundary conditions in these simulations implies that the baffles which encounter the edges of the model produce more flow impairment than the simple S_L term accounts for. In the case of the larger system discussed in the previous paragraph, an excellent match was

obtained at $\alpha = 45°$. That there is a consistent discrepancy between the numerical and analytical values over a range of α for the smaller systems tends to support the suitability of Equation 5.20 for determining the effective permeability of a representative, completely disconnected system for any α, at $H = 1$. However, the small model (Figure 5.15a) is more tortuous that a representative disconnected model at this line density.

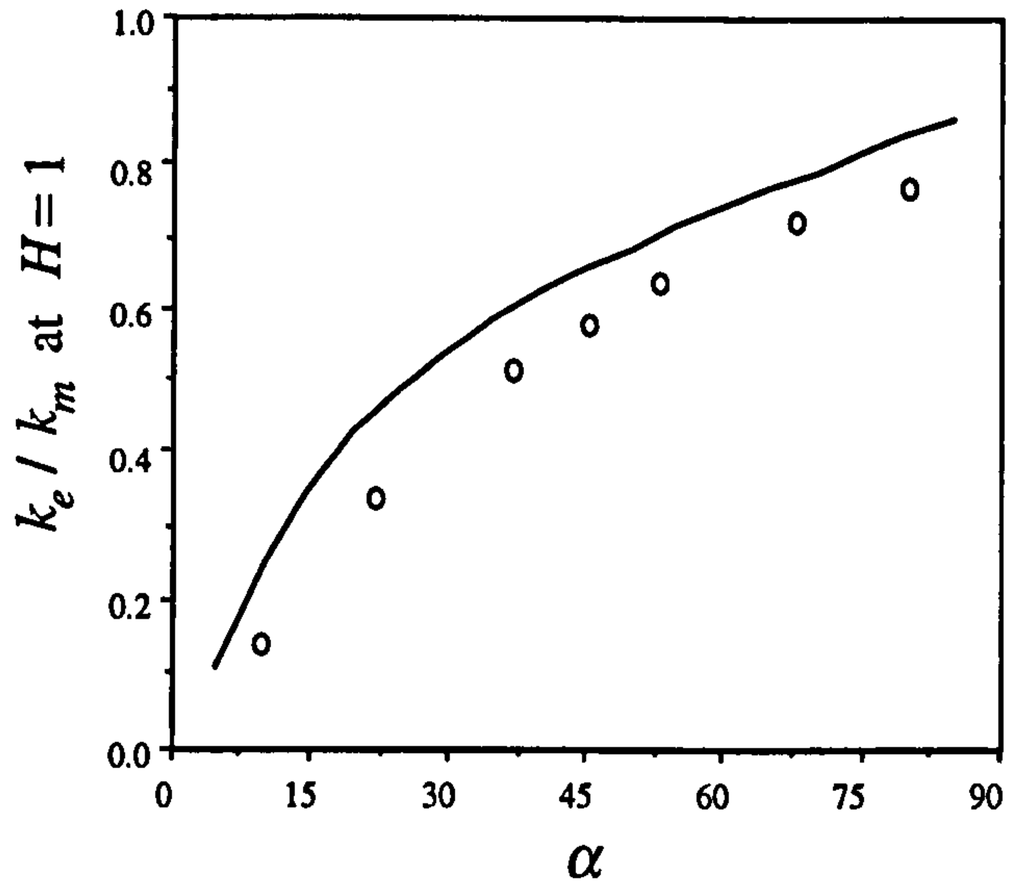

Figure 5.23. Comparison of simulation results for the disconnected system (dots) with the streamline equation (Equation 5.20, curve).

5.3.5 Partially connected barriers

Equation 5.20 gives the effective permeability of a representative, but entirely disconnected system as a function of k_m, d_G, d_L, and α, at $H = 1$. Such a system is not realistic, as any system of lines has a particular connectivity which is a function of the line density and orientation of the faults in the system. In this section we aim to generalise this solution to incorporate more realistic system geometry. Whilst still considering barriers (i.e. $H = 1$), the treatments below allow the barriers to be connected. Transmissibility effects (i.e. systems with $H < 1$) are considered later (Section 5.3.7).

Equation 5.15 can be reformulated with respect to t (the tortuosity factor in the streamline equation) as a quadratic equation by expanding the $(1+t)^{-2}$ term:

$$t^2 + 2t + \left[1 - (1 - d_G)(k_e / k_m)^{-1}\right] = 0, \qquad (5.21)$$

Assuming that k_e / k_m and d_G are known at $H = 1$, Equation 5.21 may be solved for t. Let t for an orthogonal system be denoted by t_{45}. For a geometrically similar, non-orthogonal system, t can be calculated as a function of t_{45}. Consider first an entirely disconnected system. Following equation 5.19, $t = NL^2 \cos^2 \alpha / 2WJ$. W varies linearly with $\sin\alpha$, J with $\cos\alpha$ and neither N nor L vary with respect to α. Therefore

$$t \propto 1 / \tan\alpha. \qquad (5.22)$$

Equation 5.22 can be used to determine t as a function of t_{45}. By considering that $t / t_{45} = \tan 45 / \tan\alpha$, then (as N and L are the same in both systems);

$$t = t_{45} / \tan\alpha. \qquad (5.23)$$

Replacing this in Equation 5.15 gives the fractional permeability for a system at any α and at $H = 1$ as a function of t_{45}:

$$k_e / k_m = (1 - d_G)(1 + t_{45} / \tan\alpha)^{-2}. \qquad (5.24)$$

This approach should apply to both disconnected and partially connected systems, as no attempt is made to calculate t from the structure of the system; it is simply derived from t_{45}, which can be determined from the orthogonal fractional permeability values at $H = 1$. Two assumptions, therefore, are used to generalise Equation 5.15 to considering tortuous flow effects in partially connected systems (i.e. systems with $0 < d_L < d_{Lc}$). First, that Equation 5.15 is correct in form; and second, that Equation 5.19, and hence Equation 5.22 is correct for partially connected systems as well as for disconnected systems. The latter can be easily shown (Figure 5.24).

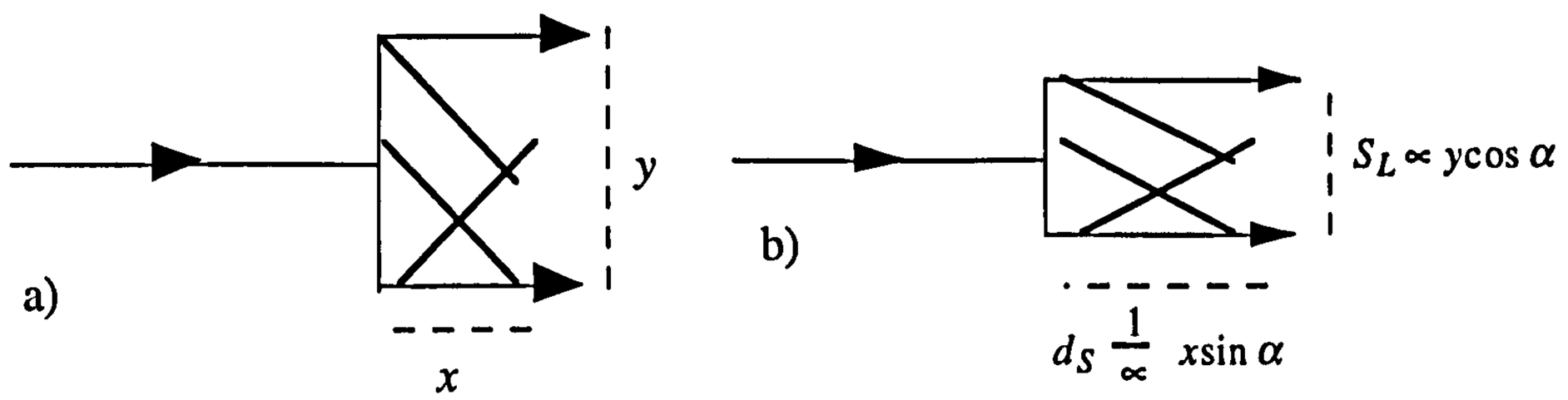

Figure 5.24. Tortuosity around a connected system of barriers. Extension of a streamline is proportional to $\cos\alpha$, and the scan-line density is inversely proportional to $\sin\alpha$. Therefore t is inversely proportional to $\tan\alpha$ (Equation 5.16).

Comparison with simulation results

In the case of the entirely disconnected system (Table A2.3), for which $d_G = 0.1157$ and $k_e / k_{m45} = 0.59$, Equation 5.21 gives $t_{45} = 0.224$. For the partially connected system (Table A2.4), $d_G = 0.1163$, k_e / k_{m45}=0.374, and $t_{45} = 0.537$.

Figure 5.25 shows fits from Equation 5.24 for the simulation results of the entirely disconnected and the partially connected simulation results (Figures 5.15a and b) at $H = 1$. While a good fit is achieved except at the largest α for the entirely disconnected case, the fit for the partially connected case is poor. There is no apparent reason why the assumptions used in this modelling should appear to work for the entirely disconnected runs but not for the partially connected one. The only assumptions made in deriving Equation 5.24, are that a) $t \propto d_S \cos\alpha$, which is

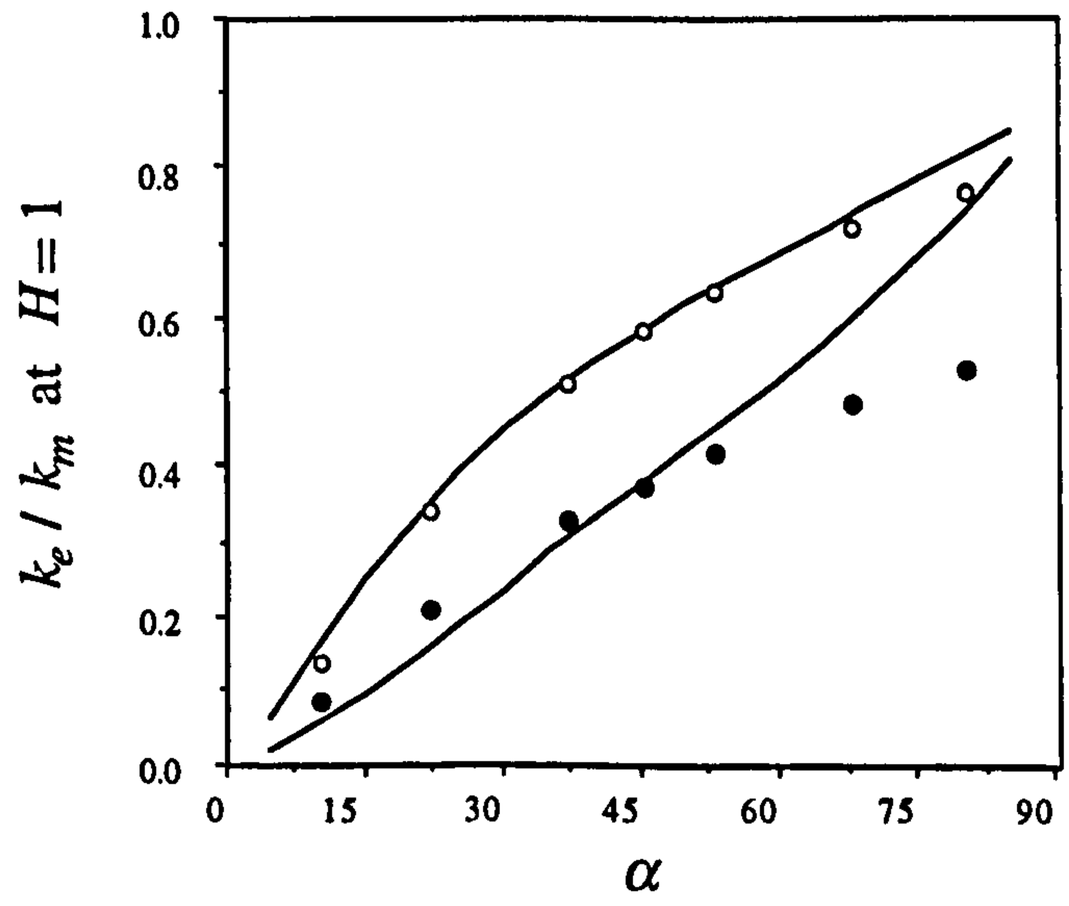

Figure 5.25. Comparison of simulation results for the disconnected (open circles) and partially connected (filled circles) systems with the modified streamline equation (Equation 4.24)

correct, and b), that Equation 5.15 is correct in form. Therefore one must conclude that this latter assumption is incorrect for partially connected systems. A clue as to why this might be is given by consideration of methods used to determine effective permeability as a function of pore geometry, by analogy to capillary bundles. This is discussed in the following Section.

5.3.6 Comparison of method with microscopic analogues

Attempts to solve permeability in a pore system as a function of the geometry of the pore system have much in common with the macroscopic methods discussed above. Amyx *et al.* (1960) redefine the Kozeny equation for such a purpose. The Kozeny equation conceptualises flow in a porous medium as occurring in a bundle of capillaries. A form of the equation is:

$$k = \phi / k_z S_p^2 \qquad (5.25)$$

where k is permeability, ϕ is porosity, S_p is the surface area/pore volume of the medium and k_z is the Kozeny constant. Many workers have expressed the Kozeny constant in terms of the tortuosity of the capillaries, and one such modification in that in the Carmen-Kozeny Equation:

$$k = \phi / k_o \tau S_p^2, \qquad (5.26)$$

where k_o is a shape factor, and τ is a tortuosity measure. τ is given by $\tau = (l_a / l)^2$, where l is the length across the porous medium, and l_a is the length of the actual capillary. This treatment of a porous medium at the pore scale as a series of disconnected capillaries is very similar to the treatment of a structured medium at a larger scale as a series of disconnected streamlines or streamtubes, and the form of the equations is witness to this. Equations 5.15 and 5.26 have a similar form, where ϕ and τ (Equation 5.26) are equivalent to $(1-d_G)$ and $(1+t)^2$ in Equation 5.15. The only

difference lies in two additional terms in the microscopic Carmen-Kozeny Equation which are absent from the macroscopic streamline equation; the specific surface area (S_P), and the shape factor (k_o).

Scheidegger (1974) presents a detailed discussion of the Kozeny and Carmen-Kozeny equations, and shows how S_P enters the equation due to the assumption that the fluid sticks to the walls of the conduits, which represent the pores. This adhesion effect is only relevant at the pore scale (e.g. Bear 1972). If the equation is conceptualised as describing the simulation of flow in streamlines around sealing faults, then the streamlines are not bounded by physical surfaces, but merely by other streamlines. Therefore the S_P term can be neglected in this situation. Even if S_P were used as a variable, it would vary as a function exclusively of α but any additional term in 5.15 must vary as a function of both α and t: Figure 5.25 shows that the disconnected system (low t) does not require as much correction as the partially connected system (higher t).

The shape factor (k_o) is a more likely candidate for incorporation into Equation 5.15. Scheidegger (1974) mentions that k_o varies as a function of the angle between the macroscopic flow direction and the average direction of the capillaries, which is given by $\cos^{-1}(S_L / W)$. This is a function of t. Definitions of k_o, and even detail of its original formulation, are invariably vague, (Scheidegger 1974, Amyx *et al.* 1960, Dullien 1979, Amaelfule *et al.* 1993), but a detailed perusal of the original work could allow the incorporation of this, or a similar parameter, into the streamline equation to gain a better estimation of k_e / k_m as a function of k_e / k_{m45}. This has not been undertaken, and the method discussed in Section 5.3.5 is applied to determine k_e for partially connected systems of barriers even though it is erroneous at high α. In the following Section, attention is shifted from the tortuosity effect to the transmissibility effect.

5.3.7 Connected, transmissible baffles

The previous sections were concerned with determining the effects on flow due to variable tortuosity, as a function of α, in the case where there is no transmissibility associated with the faults ($H = 1$). For $H < 1$, each fault has a transmissibility, and, in general, both transmissibility and tortuosity will vary as a function of α. This section considers a highly compartmentalised system, in which the tortuosity component to flow is very low and can be neglected, so all permeability reduction is due to transmissibility effects.

If the baffles are randomly distributed in the area, then 1D and 2D gouge density are the same. 1D gouge density can be given by:

$$d_G = x d_S, \tag{5.27}$$

where d_S is the scan-line density and x is the thickness of each baffle, measured parallel to the scan-line (Figure 5.26). If the assumption is made that the flow path will follow the local pressure gradient through the baffle, then it take the shortest route through the baffle, which is T. Therefore the effective gouge density (d_{Ge}) encountered by an average stream-line is given by:

$$d_{Ge} = x d_S \cos\alpha . \tag{5.28}$$

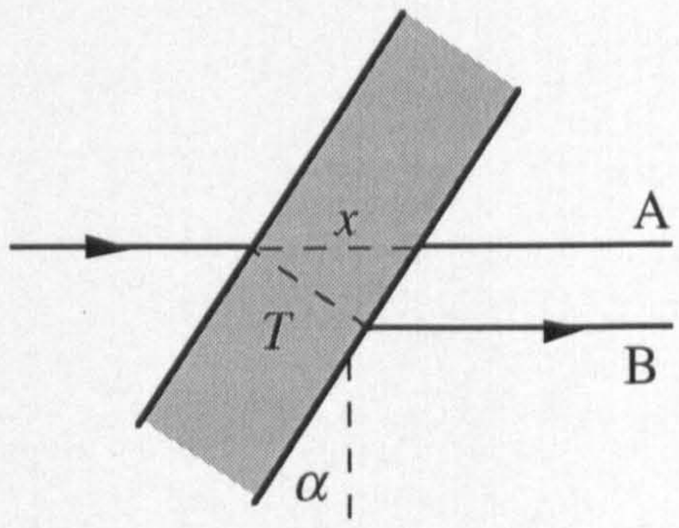

Figure 5.26. Flow geometry through an oblique baffle. A. Line parallel to the overall pressure gradient. B. Inferred flow path.

Gouge density is given by NLT / WJ, which can be reformulated with respect to x, as $T = x\cos\alpha$. Hence:

$$x = d_G WJ / NL\cos\alpha. \tag{2.29}$$

Replacing this in 5.28 gives:

$$d_{Ge} = d_G WJ d_S / NL. \tag{5.30}$$

Scan-line density is given by $d_S = NL\cos\alpha / WJ$, so 5.30 simplifies to:

$$d_{Ge} = d_G \cos\alpha. \tag{5.31}$$

Fault heterogeneity (H) is a function of k_f, k_m and d_G, but does not take into account the geometrical arrangement of the system. Let H_e be effective heterogeneity, which has the same form as H, but varies as a function of d_{Ge}, rather than d_G. In such a system, if the assumption is correct that the distance through a baffle of a flow path is T, rather than x, then there should be a consistent relationship between k_e / k_m and H_e, irrespective of α. This is because α is now included in the H_e term. For a system in which there is no tortuosity effect, this relationship should be $k_e / k_m = (1 - H_e)$, as it should follow the effective harmonic average permeability (i.e. k_h calculated as a function of d_{Ge}) of the system. Below, this treatment is tested against the flow simulation results from the connected systems (Figure 5.15c).

Comparison with simulation results

Figure 5.27a shows the relationship between k_e / k_m and H_e, for each α, for the compartmentalised simulation results (Table A2.5). If the tortuosity components are neglected, and the flow is assumed to be a function exclusively of d_{Ge}, then the effective permeability should be the effective harmonic average permeability, which is

the straight line drawn on Figure 5.27a. The cases with low α follow this trend reasonably, but the results at high α have higher permeabilities at any particular H_e than expected.

Figure 5.27b shows the errors in k_e / k_m, as a function of H_e that would occur if the orthogonal results were used to calculate effective permeabilities for the non-orthogonal systems. For $\alpha \leq 53°$, the error never exceeds ±5% of k_m, but for the most permeable case ($\alpha = 80°$), the error rises to about 25% of k_m. Two possible reasons for this error are discussed below.

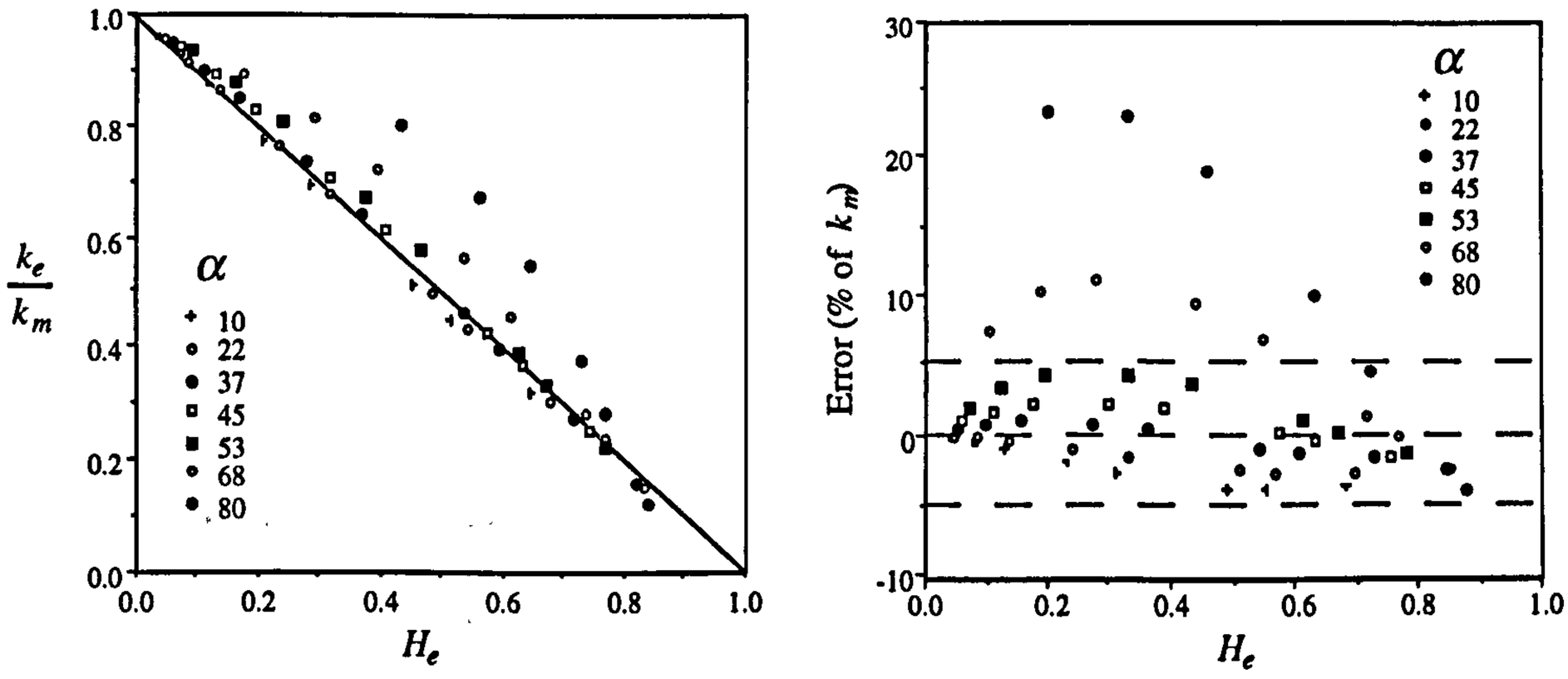

Figure 5.27. Simulation results of the compartmentalised case. Comparison of simulation results a) k_e / k_m vs. H_e, with the best fit correlation for the 45° case. B) error in k_e / k_m predicted from the 45° case as a percentage of k_m.

One reason for the discrepancy between observed and predicted effective permeability at high α involves neglecting tortuosity effects. It was shown in Section 5.3.5 that tortuous flow is most important in geometrically equivalent systems when α is highest. Therefore, if a system has a real, but sub-ordinate, tortuous flow component and this component is neglected, this neglect is most likely to be significant at high α. At high α, the tortuosity effect will result in systems being more permeable than a simple consideration of the transmissibility effect, compatible with the observed trends on Figure 5.27.

The discrepancy in effective permeability high α could also be an effect of the grid (Figure 5.28). The edges of the baffles are not parallel to the baffle itself, and, flow can only pass between grid-blocks which share edges. Therefore the flow through each baffle is able to follow a shorter path than it would do if it were to follow the net direction of T.

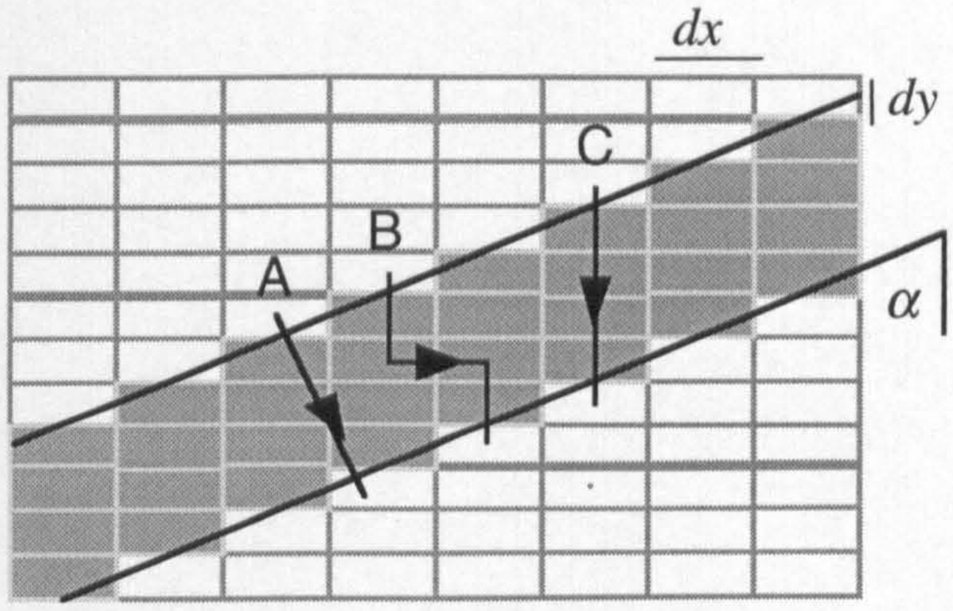

Figure 5.28. Effect of grid discretisation on the flow through a baffle. The flow path should follow the line A, which is the shortest distance through the baffle. On the grid, this would require the flux to follow path B, which is $3dy+dx$ long. A shorter path (Path C, length $4dy$) exists through the discretised baffle and the flux will follow this path, resulting in higher than expected effective permeabilities for $\alpha > 45°$.

5.3.8 Section summary

In Section 5.3, various analytical methods have been derived to estimate effective permeability at any α as a function of the permeability of an equivalent orthogonal system. Equations describing streamline tortuosity for entirely disconnected barriers have successfully been modified to take α into account (Section 5.3.3). In geometrically representative disconnected systems, the effective permeability can be calculated directly from consideration of the system geometry, but even for non-representative disconnected systems, if k_e / k_{m45} is known, then k_e / k_m at any other α may be determined.

Applying the modified streamline equation (Equation 5.24) to partially connected barriers, to calculate tortuosity as a function of orthogonal tortuosity has not produced accurate permeability results (Section 5.3.4). Consideration of analogous microscopic treatments shows the necessity for an additional term which varies as a function of the

line density of the system. For the partially connected system, Equation 5.24 slightly underestimated the effective permeability of the system at low α, and, more significantly, it overestimated k_e at high α. It therefore over-estimates the permeability anisotropy of the system.

These methods were concerned with tortuosity around impermeable barriers. A consideration of transmissibility through baffles in connected systems (Section 5.3.7) showed that effective permeability of the systems at any α may be calculated if the transmissibility term (H) is transformed into an effective transmissibility term (H_e). This assumption yielded a good match to the numerical results for $\alpha < 60°$. For α greater than this the match was poorer, but this could be due to a combination of tortuosity and discretisation effects.

These analytical treatments have not accurately reproduced the numerical results, and it is impossible, without extensive flow simulation modelling, to determine how much of this discrepancy is due to inaccuracies of the method, or to inaccuracies of the numerical results. Certainly, the only aspect of the treatment which definitely appears to be too simplistic is using Equation 5.24 to determine the effective flow properties as a function of the tortuosity of an equivalent orthogonal system.

5.4 Effective permeability at a single length-scale

This section describes a method to gain an estimate of the effective permeability of a system of baffles at a single length-scale, equally divided between two populations oriented at $\pm\alpha$ to the pressure gradient, for any N, L, T, k_f and k_m. This estimate is based on the treatments given above, so is not entirely proven. Nonetheless it still represents a significant advance from methods currently available, which are unable to produce permeability estimates for these kinds of system. The method, which is increasingly uncertain at high or low α, is based on the orthogonal effective permeability type curves (Figure 5.14), and involves calculating an effective line density (d_{Le}) and an effective heterogeneity (H_e) for the system.

The overall connectivity of the system is the critical variable, and is calculated from the line density. The line density at any α is given by $d_L = NL^2 / 4A$, and the line density of an equivalent orthogonal system by $d_{L45} = NL^2 \sin 2\alpha / 4A$. If $d_{L45} < 0.68$, the system is disconnected, and if $d_{L45} > 0.68$, then the system is connected. Disconnected and connected systems require different treatments.

5.4.1 Effective line density for disconnected systems

For a disconnected system, the first step is to calculate fractional permeability (k_e / k_m) for a equivalent orthogonal system, assuming that all faults are barriers. Equivalent orthogonal fractional permeability at $H = 1$ is termed k_e / k_{m45}. The value of k_e / k_{m45} is determined from Equations 5.8 and 5.9 (Section 5.2.6), using d_{L45}, and $H = 1$.

Next is the calculation of the tortuosity factor for the orthogonal system (t_{45}) using Equation 5.21. For this determination, the assumption that $d_G = 0$ must be made, but this does not produce errors (see the discussion in Section 5.3.4). Fractional permeability (k_e / k_m) at α is calculated from t_{45}, using Equation 5.24, again assuming that $d_G = 0$. Figure 5.29 shows how these parameters vary as a function of d_L. We now know one point (at $H = 1$) for the k_e / k_m vs. H curve specific to the particular α

and d_L of the system. This determination is where most of the error enters the eventual effective permeability estimation (See Figure 5.25), as Equation 5.23 is too simplistic for partially connected systems.

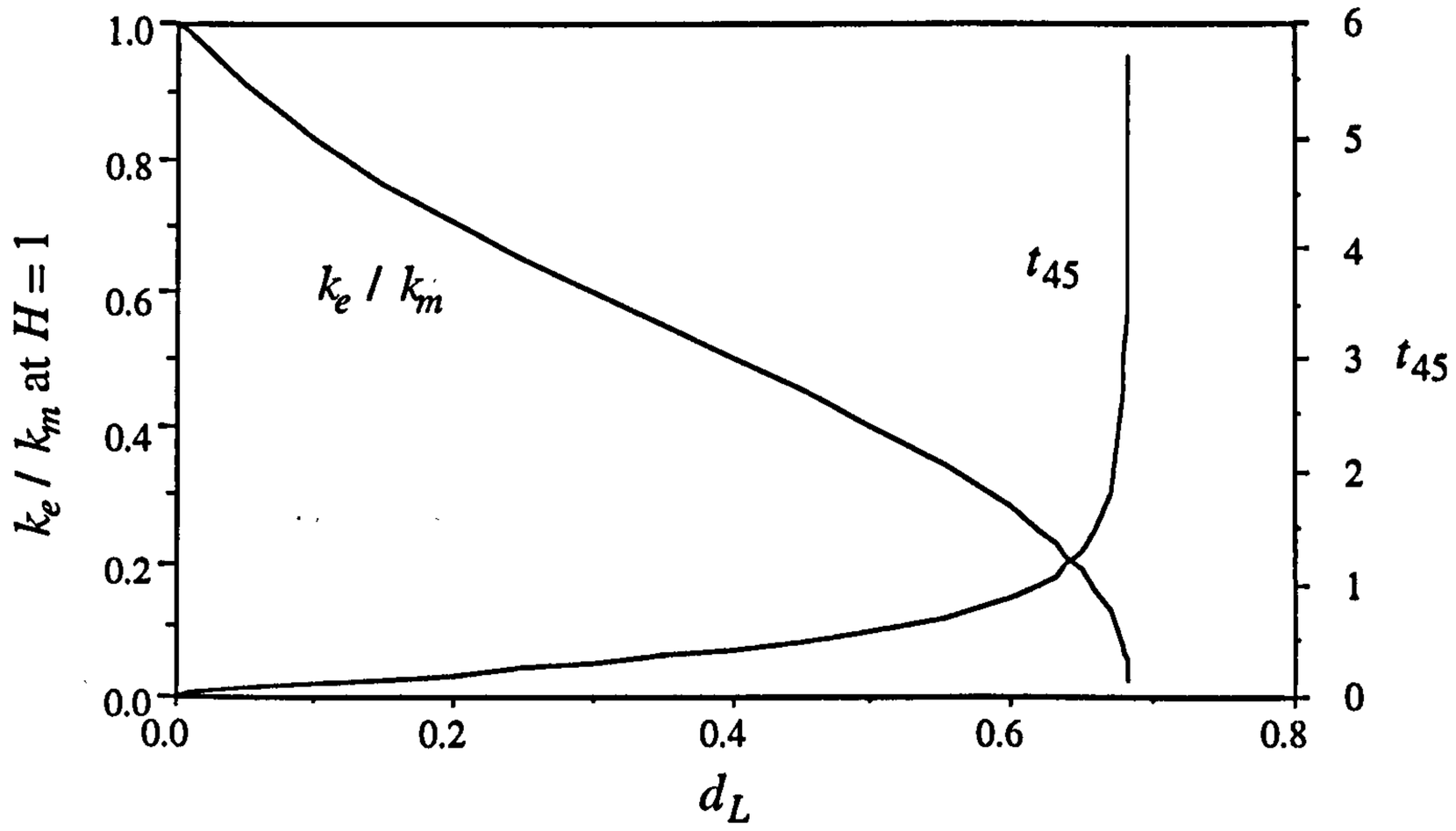

Figure 5.29. Fractional permeability and tortuosity as a function of line density for an orthogonal system. k_e / k_m at $H=1$ is a function of line density, and reflects the reduction in permeability in a system of orthogonal barriers as a function of tortuosity. This tortuosity effect is captured in the parameter t_{45}, which represents the increase in length of an average streamline through the system. Therefore $t_{45}=0$ when $d_L=0$, and rapidly increases as d_L approaches the percolation threshold of the system ($d_L=0.68$), above which there is no possibility for tortuous flow.

Once k_e / k_m at $H=1$ is known, then effective line density (d_{Le}) is obtained from Equations 5.8 and 5.9. Equation 5.8 cannot be reformulated directly with respect to the variable a, but a close approximation, based on trial and error, is given by:

$$a = 1 - 0.00679(10^{3.374 k_e/k_m}). \qquad (5.32)$$

Equation 5.9 may be reformulated to give:

$$d_{Le} = (0.207 / (1.35 - a))^{0.724} \qquad (5.33)$$

Once a has been determined from Equation 5.32, it can then be input into Equation 5.33 to give the effective line density (Figure 5.30).

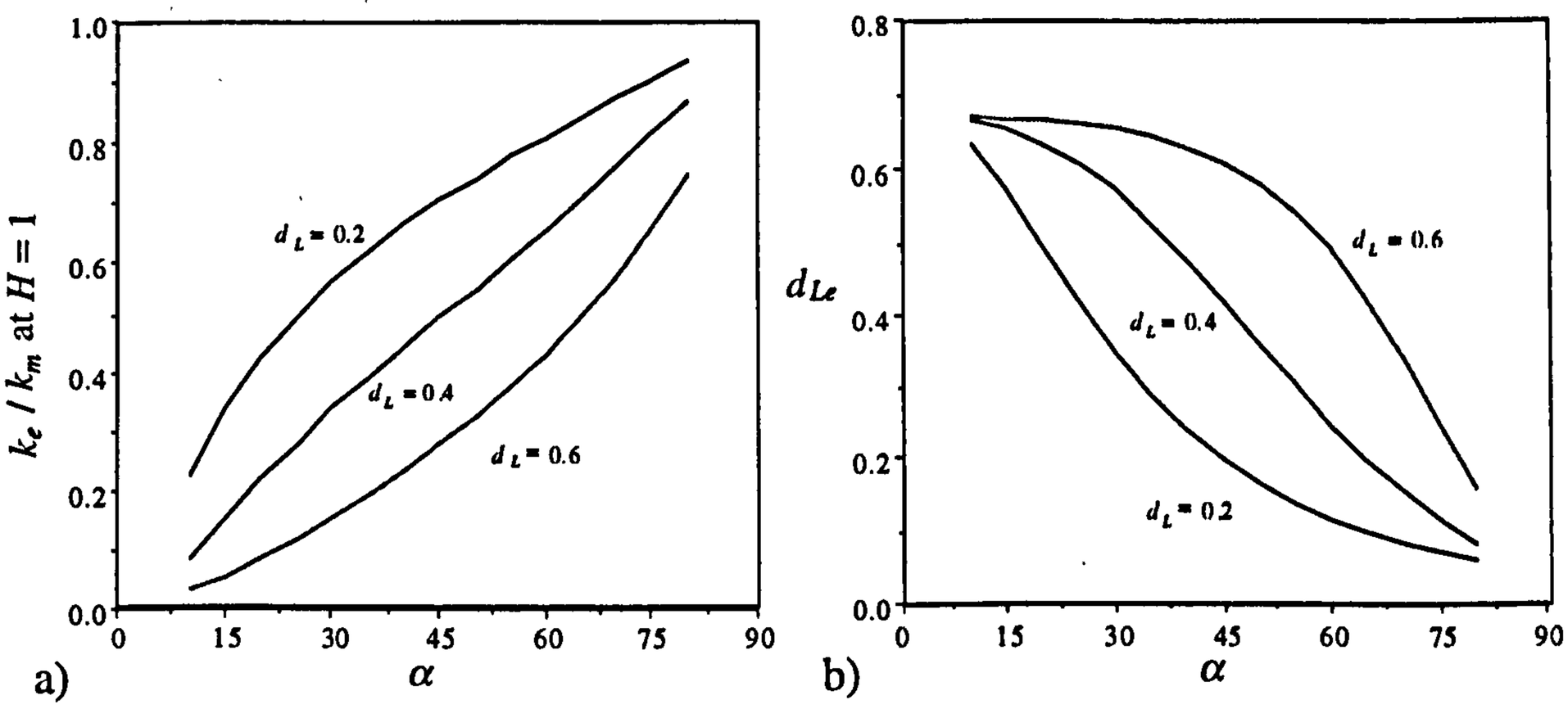

Figure 5.30. Effective line density as a function of alpha, for three line density cases. a). k_e / k_m at $H = 1$ vs. α. b) Effective line density (d_{Le}) vs. α.

Effective line density represents the line density of a system at $\alpha = 45°$, which give the same k_e / k_m at $H = 1$ as a system at any particular α and (disconnected) d_L. Note that $d_{Le} \neq d_{L45}$. This treatment isolates the tortuosity components of effective permeability. For $H < 1$, there is also a transmissibility component associated with the permeability determination. The k_e / k_m vs. H curves for disconnected orthogonal systems (Figure 5.14), incorporates the effects of both transmissibility and tortuosity. At $H = 1$, the tortuosity component of a non-orthogonal system of line density d_L is the same as the tortuosity component of an orthogonal system of line density d_{Le}. It is reasonable to assume that the tortuosity component of an orthogonal system of d_{Le} at H_e is the same as the tortuosity component of the non-orthogonal system of d_L at the same H_e.

5.4.2 Effective line density for connected systems

For connected systems ($d_{L45} > 0.68$), the actual line density of the system is of subordinate importance to the transmissibility of the system, but there is always a tortuosity component associated with the permeability of the system. In a connected

system, $k_e / k_m = 0$ at $H = 1$, irrespective of α, so a method to isolate the tortuosity component of the system similar to that used above is not possible. Because of the relative insensitivity to line density, and the absence of a method for isolating tortuosity, the effective line density of a connected system is simply assumed to be d_{L45}. This can be justified because the actual flow path for transmissible flow will tend to be perpendicular to the fault whatever the angle (Figure 5.26).

5.4.3 Effective heterogeneity

Effective heterogeneity (H_e) as a function of α was discussed in Section 5.3.7. H_e is calculated based on the effective gouge density (d_{Ge}) of the system. Applying the k_e / k_m vs. H correlations directly to a non-orthogonal system requires that d_{Ge} be normalised to that of an orthogonal system (d_{Ge45}), as the curves for the orthogonal system determined H as a function of d_G, not of d_{Ge}. This requires another gouge density term, which is termed normalised effective gouge density (d_{Geo}). The rationale behind these transformations is best explained with reference to Figure 5.31, which shows the variation of the gouge density terms with respect to α for a particular d_G case.

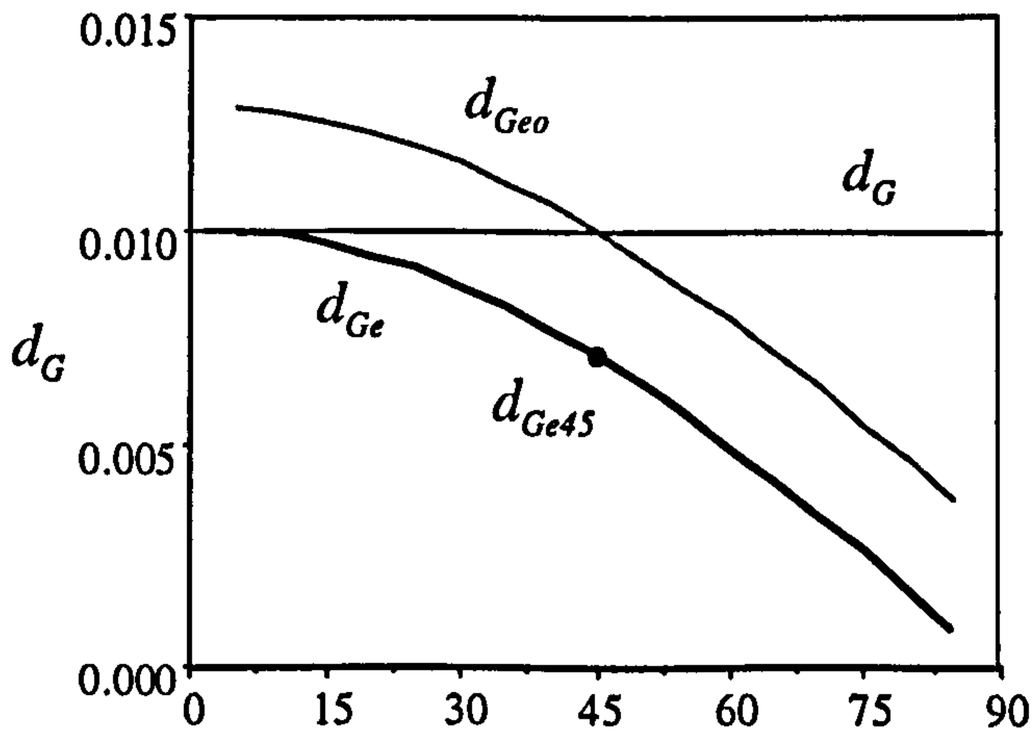

Figure 5.31. Effective gouge density terms as a function of orientation. See text for discussion.

Gouge density does not vary as a function of α, as it is simply given by $d_G = NLT / A$. Effective gouge density (d_{Ge}) is the term which reflects the transmissibility of the baffles at a particular angle, and is given by $d_{Ge} = d_G \cos\alpha$

(Equation 5.31). The k_e / k_m vs. H correlation for the orthogonal systems, however, are based on d_G, not d_{Ge45}. Therefore d_{Ge} must be transformed into d_{Geo}, for these correlations to be applicable to any α. d_{Geo} (normalised effective gouge density) is simply obtained by adding the difference in value between d_G and d_{Ge45} to the value of d_{Ge} (Figure 5.31). Therefore:

$$d_{Geo} = d_G + d_{Ge} - d_{Ge45}, \tag{5.34}$$

which is equivalent to:

$$d_{Geo} = d_G(1 + \cos\alpha - \cos 45). \tag{5.35}$$

Effective heterogeneity (H_e) can be calculated directly as a function of H and α. Equation 5.6 showed that $k_m / k_f = H / (d_G(1-H)) - 1$. Effective heterogeneity is given by $H_e = 1 - k_h / k_m$, where k_h is calculated as a function of d_{Geo}, not d_G. Therefore

$$k_m / k_f = H_e / (d_{Geo}(1 - H_e)) - 1. \tag{5.36}$$

Equating Equations 5.6 and 5.36, gives:

$$H_e = \frac{1 + \cos\alpha - \cos 45}{H^{-1} + \cos\alpha - \cos 45}. \tag{5.37}$$

5.4.4 Effective permeability

Effective permeability as a fraction of matrix permeability of a system of N faults of length L, thickness T, and permeability k_f, oriented at $\pm\alpha$ to the pressure gradient is determined as a function of effective line density (d_{Le}) and effective heterogeneity (H_e). These terms represent the line density and heterogeneity of a orthogonal system which gives has the same connectivity and transmissibility properties as the non-

orthogonal system in question. Therefore d_{Le} and H_e replace d_L and H in Equations 5.8 to 5.10, and the resultant k_e / k_m of the equivalent orthogonal system is also that of the non-orthogonal system for which d_{Le} and H_e were determined.

The model is summarised on Figure 5.32. At $\alpha = 45°$, the curves presented in Section 5.2.7 apply (Figure 5.32a). Consider a third axis (α) on this figure. Any system has a particular line density, heterogeneity and fault orientation, and its effective

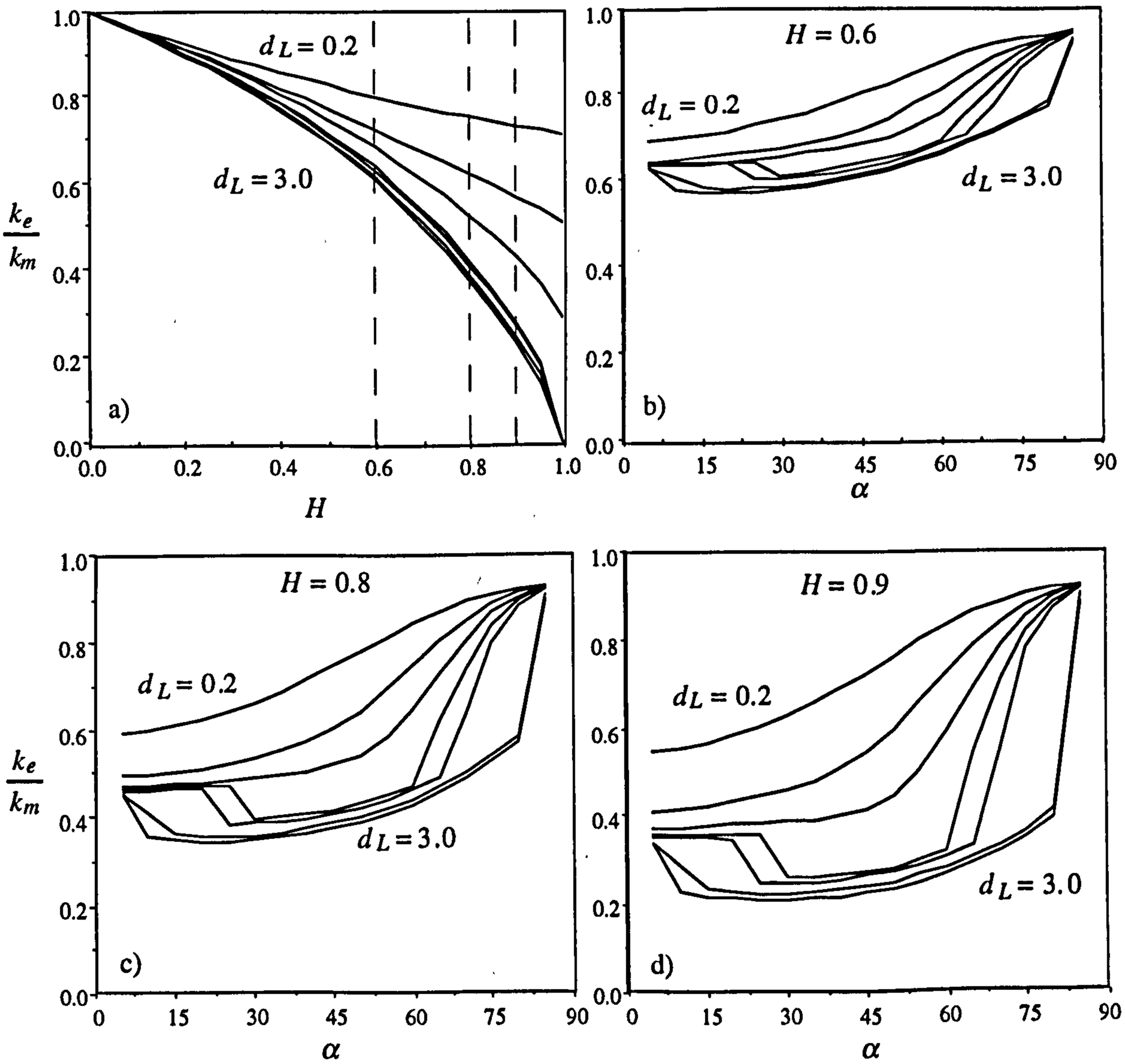

Figure 5.32. Effective permeability as a function of line density, fault heterogeneity and fault orientation. a) Fractional permeability vs. heterogeneity from $\alpha = 45°$. b), c), d). Fractional permeability vs. fault orientation at $H = 0.6$, $H = 0.8$, and $H = 0.9$. These are the dashed lines on a). All plots show curves for line density = 0.2, 0.4, 0.6, 0.8. 1.0, 2.0 and 3.0.

permeability would be given by a point on line density specific surfaces in k_e / k_m vs. H, α space. Figures 5.32b to 5.32d show graphs of the variation in k_e / k_m with respect to α, at three values of H. These curves are a function of the fundamental properties of the systems, and are determined as a function of N, L, T, A, k_f and k_m. Line density and Gouge density (and therefore heterogeneity) are independent of α.

The rapid increase in k_e / k_m at high α is a function of the systems becoming less connected. This is demonstrated on Figure 5.33, which is a plot of equivalent orthogonal line density (d_{L45}; Equation 4.16) against fault orientation, for the same line density cases as Figure 5.32. The effect is particularly marked when a system crosses the percolation threshold, for instance in the cases of $d_L = 2.0$ and $d_L = 3.0$ this occurs in the interval $80° < \alpha < 85°$. The counter-intuitive increase in k_e / k_m at low α for the systems with larger line densities is also a function of connectivity: at a low enough α any system, no matter how high its line density, will be disconnected, and this system will be more permeable than a system with the same line density at a higher α. This effect is particularly important at high H, and at $H = 1$ represents the threshold at which flow through the system becomes possible. The minimum line density at which a system at any α can be connected is 0.68, so all systems with $d_L > 0.68$ will show this phenomenon at low α.

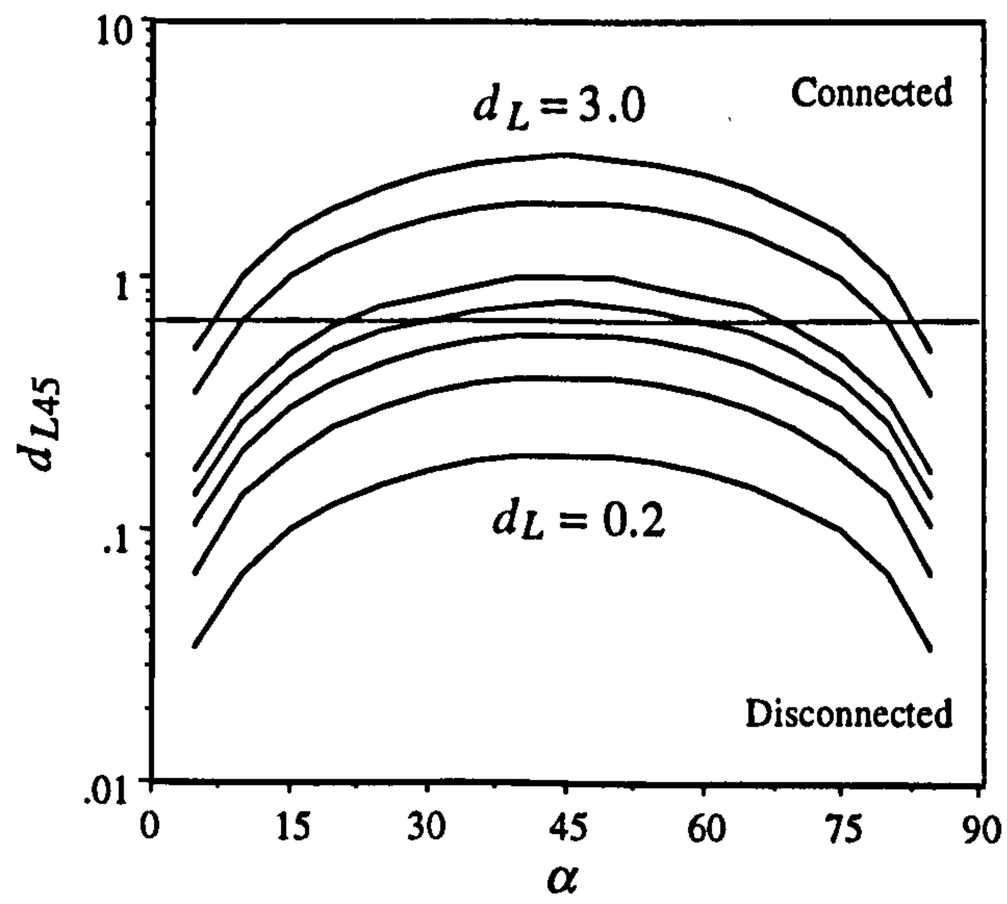

Figure 5.33. Equivalent orthogonal line density vs. α, for line density = 0.2, 0.4, 0.6, 0.8, 1.0, 2.0 and 3.0. The sysrems are connected when d_{L45} > 0.68, which is the horizontal line.

5.5 Summary

Throughout this Chapter, an analytical method has been derived with which the effective permeability of a 2D system of identical faults may be determined as a function of the characteristics of a representative volume of the system. The effective permeability calculated is in the direction bisecting the two orientation populations, which are assumed to contain the same number of faults. For the case where the populations are at 90° to each other, a suite of flow simulations at increasing line density have been used to determine an empirical model, with which the effective permeability of any system may be calculated. The model is presented both as look-up charts (Figure 5.14) and equations (Equations 5.8 to 5.12), allowing the determination of the effective permeability of the system as a function of a transmissibility term (H), incorporating fault frequency, thickness, length and fault and matrix permeabilities; and a geometrical term (d_L), which incorporates fault frequency, length and connectivity. Connectivity is a very important variable in determining the effective permeability through these system, and the model is based on systems which become connected at $d_L = 0.68$.

The second half of the Chapter has been concerned with determining the effective permeability of systems in which the two populations may be in any orientation, to determine the two principal components of the 2D effective permeability tensor. Analytical and geometrical treatments have been used to derive a method for adapting the tortuosity and transmissibility characteristics of an orthogonal system to these which describe the behaviour of a geometrically equivalent, non-orthogonal system. These methods have been backed up by results from numerical flow simulation, and have reproduced these results with variable success. The equation derived by modifying the statistical streamline equations to calculate effective permeability as a function of a tortuosity term works well for disconnected systems, but less well for partially connected systems. Further work is needed to determine another term which needs to be incorporated in this transformation. Apart from this, there appear to be no

significant inaccuracies in the overall method. A general set of graphs and equations have been developed for determining the effective permeability from the fundamental characteristics of the system (i.e. N faults of length L, thickness T and permeability k_f, oriented at an angle $\pm\alpha$ to flow direction, and contained in an area A of permeability k_m). These are summarised on Figure 5.32.

The fault system structure considered is an idealisation. Chapter 3 argued that provided the node proportions and gouge density of a system are reproduced in a flow model, then honouring the orientation and length characteristics of the system is of secondary importance. The models described in this Chapter have connectivities which are a function of line density, and the systems become connected at the percolation threshold of a random IY system of constant length ($d_{Lc} \approx 0.7$ for $\alpha = 45°$).

Natural systems are unlikely to have faults equally distributed between two populations, and the greater the distribution in orientation, the higher the critical line density (e.g. Hestir and Long, 1990). Also, the systems considered have random clustering. A clustered system becomes connected at a higher line density than a random one (Figure 4.29). Hence assumptions about orientation and clustering both result in the systems considered having optimum connectivity However, if a broader range of fault lengths were considered, then the system would connect at a lower line density (e.g. Robinson, 1983; Balberg and Binenbaum, 1983).

The effects of these simplifications therefore counter each other to some extent, but determining the actual degree to which the idealised scheme captures the true characteristics of a natural system is an area requiring further investigation. It is possible that system connectivity is underestimated when the method is applied to sub-surface and outcrop datasets in Chapter 7, as a power-law distribution in fault size covering four orders of magnitude is reduced to four systems of single-sized faults, with connectivity determined independently at each scale.

CHAPTER 6

CONSTRUCTION OF THE HIERARCHICAL FAULT MODEL

6.1 Introduction

This Chapter details the algebra associated with determining line density and gouge density at discrete length-scales from the 1D continuous fault scaling model. Figure 6.1 summarises the approach used. The manipulations presented in Sections 6.2 and 6.4 are well-established (e.g. Marrett and Allmendinger 1991, Westaway 1994), but are presented here to complete the framework of the thesis. New algebra is introduced in Section 6.5, in order to transform the continuous hierarchical scaling algebra into a discrete system for flow calculation. This chapter also contains a section comparing use of best-fit cumulative displacement frequency relationships from real datasets for determining fault density characteristics of fault systems (Section 6.3).

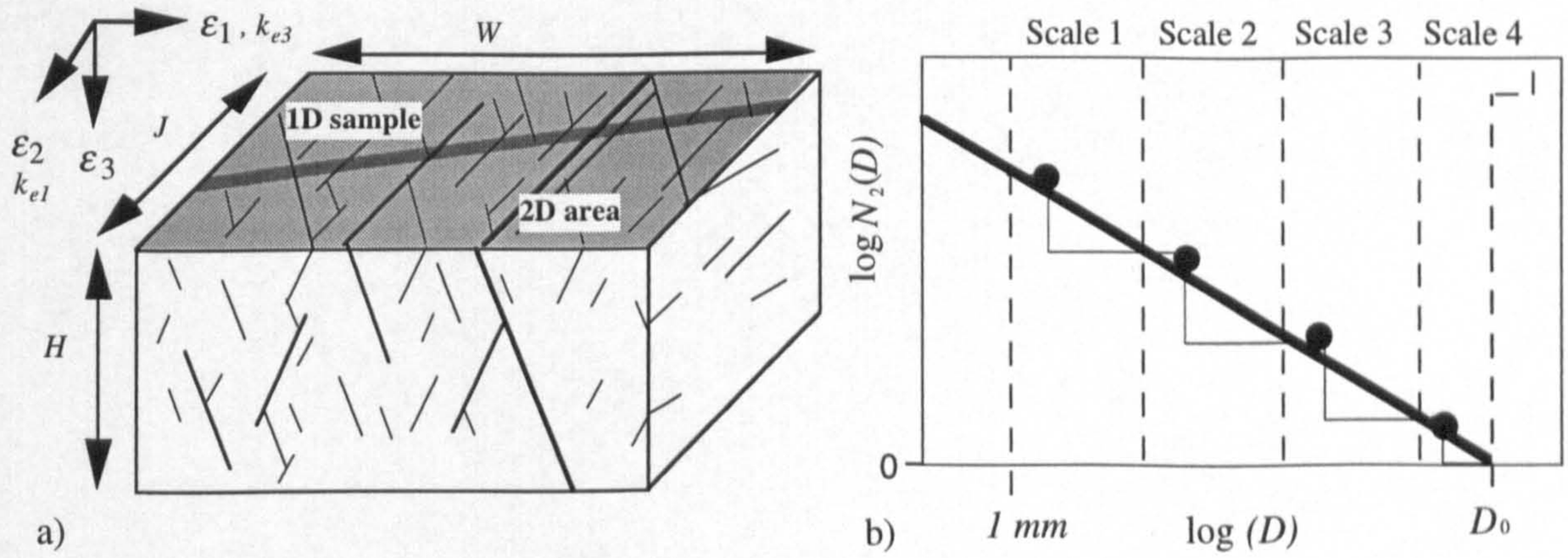

Figure 6.1. Conversion of a continuous 1D fault system description to a discrete 2D hierarchical model. A continuous 1D description of the faulting in an oriented sample is converted to a continuous 2D description of the faulting in the area *WJ* (a). This continuous 2D description is transformed to a discrete hierarchic model at specified displacement thresholds, and density terms are calculated in each scale-range (b). These are then used serially to determine the principal components of the effective permeability tensor (a). Reproduced from Figures 2.3 and 2.6.

6.1.1 Upscaling effective permeability

Chapter 2 and 3 describe the geological input to a mathematical model of sub-seismic faulting as a function of scaling and geometrical factors. In Chapter 4, these descriptions were used to determine the percolation threshold of a system incorporating the connectivity characteristics of faults in sandstones. This is a function of the line density and orientation of the faults. The significance of the percolation threshold on the effective permeability of the system was highlighted in Chapter 5 - solving effective permeability requires a different treatment either side of the threshold, owing to the competing influences of transmissibility and tortuosity. Chapter 5 presented a method for determining the effective permeability at a single length-scale in 2D, for a system as a function of line density, gouge density, orientation, and fault and matrix permeability. There are therefore two critical fault density parameters at any scale: line density and gouge density.

The mathematical model of fault system scaling describes the faulting as a continuous structural hierarchy (See Section 2.2.3). To apply the single length-scale flow models discussed in the previous chapter to faulting covering several length-scales, the model must be converted to one which retains the important geometrical features of the fault system, but in which the faulting is represented as a discrete hierarchy. The discrete hierarchical model is composed of several nested single scale systems in which the faults at any scale are all identical. These may then be used serially to determine the effective flow properties of the system at all length-scales (Figure 6.2).

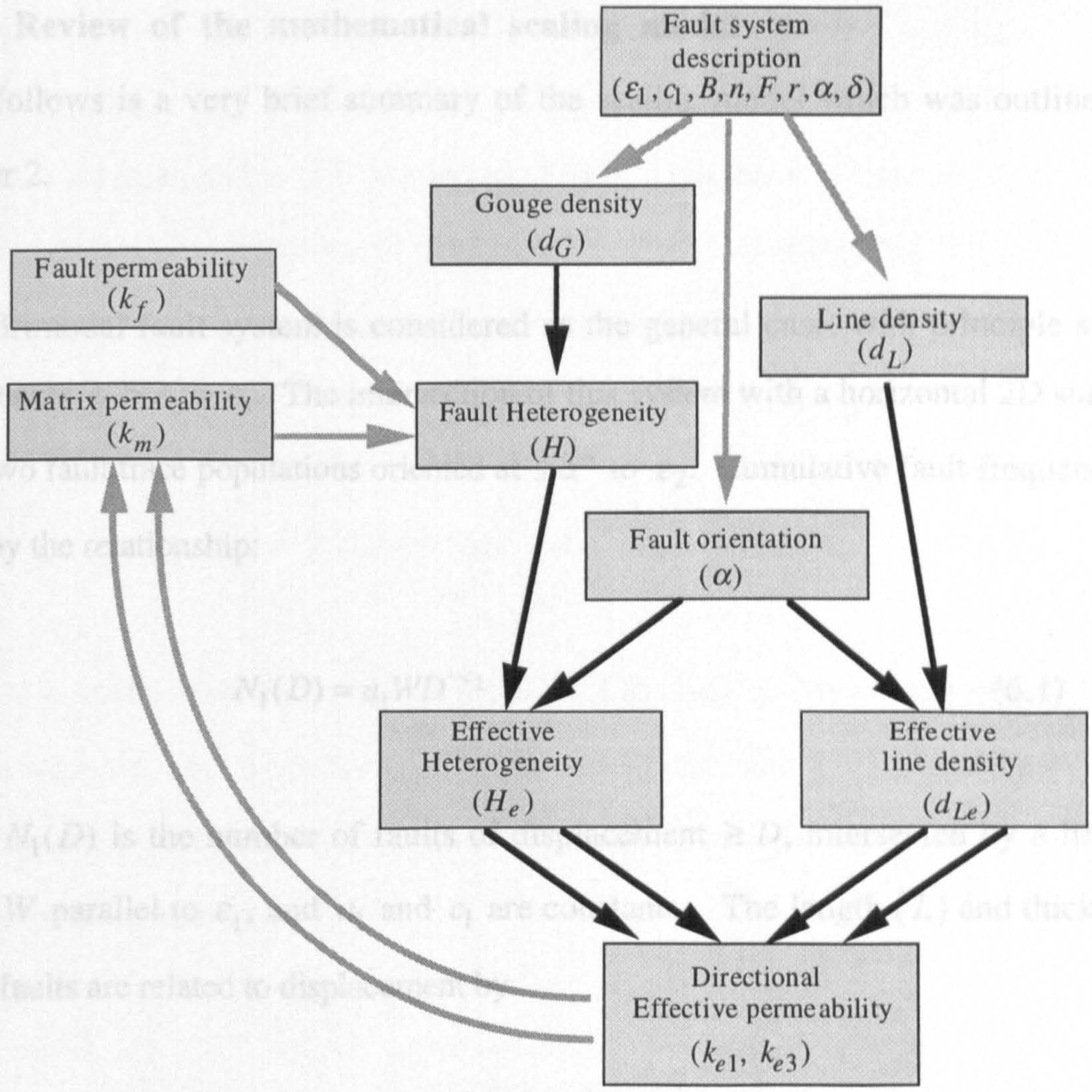

Figure 6.2. Flow diagram illustrating the method developed for determining the effective permeability of the discrete fault system model. The procedures annotated with black arrows are made independently at each scale, using the method detailed in Section 5.4. The procedures annotated with grey arrows determine the input required at each scale, and are determined either from the geological model, or from output at smaller scales.

The 2D effective permeability at a single scale is based on values of gouge density and line density. Fault and matrix permeabilities are incorporated to determine fault heterogeneity. The orientation of the faults is incorporated to determine the two directional effective permeabilities at each scale (These determinations are detailed in Chapter 5). The two directional effective permeabilities are input as directional matrix permeability values at the next scale in the discrete model, and the procedure repeated. This Chapter deals with the determination of line density and gouge density at each scale from the fault system description.

6.1.2 Review of the mathematical scaling model

What follows is a very brief summary of the scaling model which was outlined in Chapter 2.

A quadrimodal fault system is considered as the general case, with principle strain components $\varepsilon_1 > \varepsilon_2 > \varepsilon_3$. The intersection of this system with a horizontal 2D surface gives two fault trace populations oriented at $\pm\alpha°$ to ε_2. Cumulative fault frequency is given by the relationship:

$$N_1(D) = a_1 W D^{-c_1}, \tag{6.1}$$

where $N_1(D)$ is the number of faults of displacement $\geq D$, intersected by a line of length W parallel to ε_1, and a_1 and c_1 are constants. The length (L) and thickness (T) of faults are related to displacement by:

$$D = BL^n, \tag{6.2}$$

and

$$D = FT^r, \tag{6.3}$$

where B, F, n, and r are constants.

6.2 Analysis of 1D samples

6.2.1 1D strain

The following treatment is after Westaway (1994). Consider a 1D sample of length W taken perpendicular to the principle displacement. The extension parallel to ε_1 is given by e. This is given by $e = D\cos\alpha\cos\delta$ (Figure 6.3). ε_1 is given by $\varepsilon_1 = \sum D / W$. Therefore, provided that $\sum D << W$;

$$\varepsilon_1 = \sum D\cos\alpha\cos\delta / W, \qquad (6.4)$$

where ε_1 is extensional strain, $\sum D$ is the sum of the displacements sampled, δ is the average fault dip, and α is the angle between dip direction and the main extension axis. This is a simplification, as it ignores the slip obliquity of faults in quadrimodal systems (see Section 2.2.1).

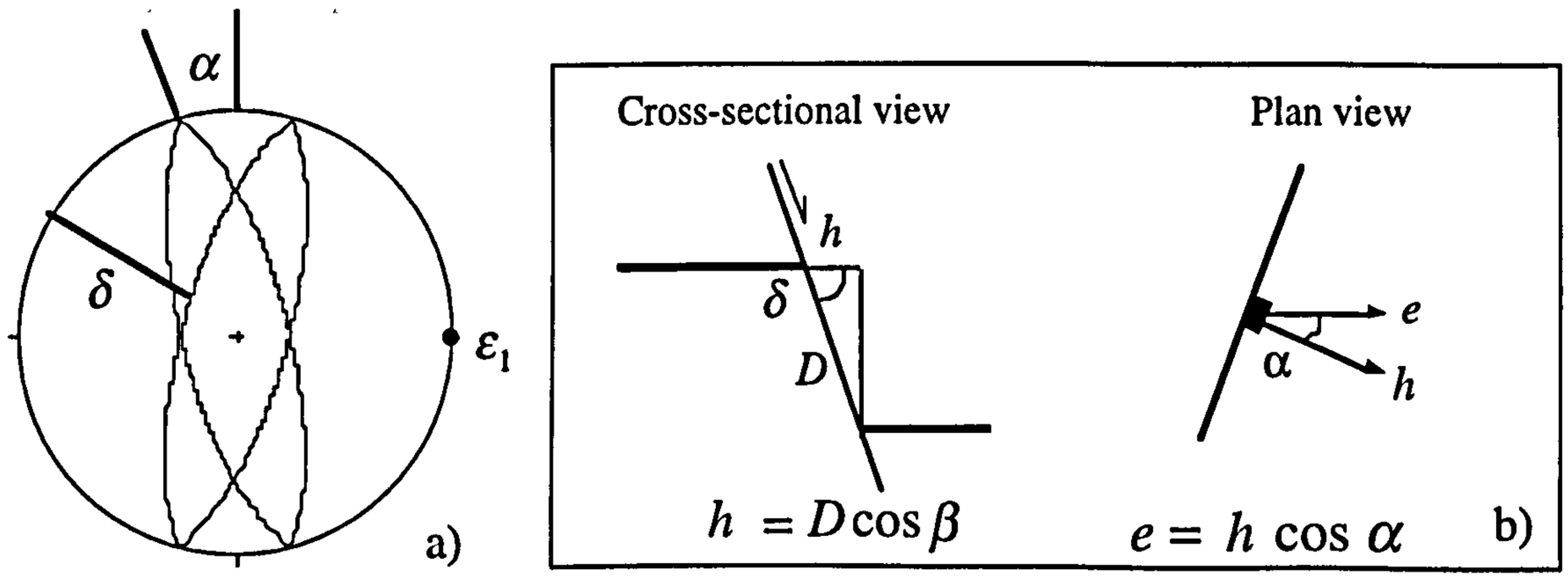

Figure 6.3. The average orientation of the faults relative to the sample line is used to calculate extension from the sample. a) Stereographic projection of quadrimodal faulting. α is the angle between dip direction and the intermediate strain axis, δ is the fault dip, ε_1 is the principle extension direction. b) Calculation of the extension component of each fault. D is displacement, h is fault heave and e is the extension component of each fault parallel to the sample line.

Following Equation 6.1, the total number of faults with individual displacements between two arbitrary values is $N_1(D_p) - N_1(D_q)$ (Figure 6.4). As $D_q - D_p$ tends to zero, $N_1(D_p) - N_1(D_q)$ tends to $-dN_1(D)$. The total number of faults of displacement

D is therefore $-dN_1(D)$, and the total displacement of faults with displacement D is $-dN_1(D)D$. Therefore the total displacement for the entire population is:

$$\sum D = -\int_{D_{\min}}^{D_0} dN_1(D)D, \tag{6.5}$$

where $D_{\min}$ and D_0 are the smallest and largest displacements sampled.

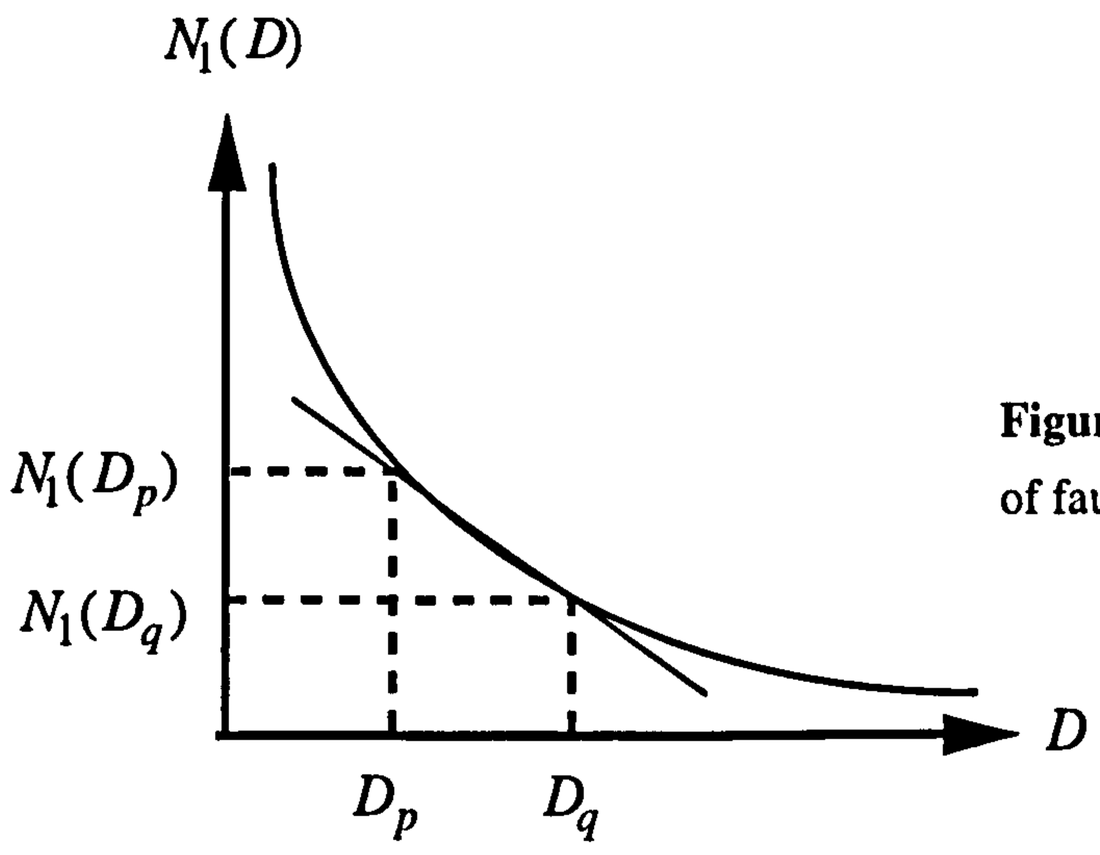

Figure 6.4. Determination of the number of faults present in a displacement range

Differentiating Equation 6.1 gives:

$$\frac{dN_1(D)}{dD} = -c_1 a_1 W D^{-(1+c_1)}, \tag{6.6}$$

and so:
$$\sum D = \int_{D_{\min}}^{D_0} c_1 a_1 W D^{(-c_1)} dD,$$

which gives:
$$\sum D = \frac{c_1 a_1 W}{1-c_1}\left[D_0^{(1-c_1)} - D_{\min}^{(1-c_1)}\right]. \tag{6.7}$$

Equating this with Equation 6.4 gives:

$$\varepsilon_1 = \frac{c_1 a_1}{(1-c_1)} \cos\alpha \cos\delta \left[D_0^{1-c_1} - D_{\min}^{1-c_1}\right], \tag{6.8}$$

which is the equation derived by Westaway (1994, his equation A17).

The displacement of the largest fault expected (D_0) can be calculated from Equation 6.1 because $D = D_0$ when $N_1(D) = 1$. Replacing these limits in 6.1 gives:

$$a_1 W D_0^{-c_1} = 1. \tag{6.9}$$

Therefore:

$$D_0 = (a_1 W)^{c_1}. \tag{6.10}$$

Equation 6.8 can therefore be reformulated to a version which explicitly shows the dependence on strain (ε_1) of the size of the sample (W):

$$\varepsilon_1 = \frac{c_1 a_1}{(1-c_1)} \cos\alpha \cos\delta \left[(a_1 W)^{1/c_1 - 1} - D_{\min}^{1-c_1} \right], \tag{6.11}$$

Equation 6.8 and 6.11 are both useful versions of the same relationship, and use of one or the other depends on the problem being considered.

6.2.2 Fault density measures

Equation 6.8 shows the dependence on strain (ε_1) of the fault scaling terms (a_1 and c_1), and the range in fault sizes which is being considered (D_0 and $D_{\min}$). a_1 relates to the overall fault frequency in the sample, and c_1 controls how this faulting is distributed between faults of various sizes. This is a 1D treatment, but 3D information about the system (intermediate and minimum strain components ε_2 and ε_3) is included through the fault orientation parameters (α and δ). Based on knowledge of any two of ε_1, a_1 and c_1, the third can be determined from Equation 6.8. The cumulative displacement frequency power-law gradient (c_1) is an important characteristic of a fault system, and it is unlikely that any sub-seismic fault frequency model will not contain an estimate of this variable. Whether to use ε_1 and a_1, as the second parameter is a matter

of choice. Often cumulative fault density(*CUMFD*, see Section 2.3.2) is used for mapping fault density.

As a starting point in the effective permeability determinations, maximum 1D strain (ε_1), is considered in preference to a_1 or *CUMFD* for several reasons, but principally because it is a more fundamental measure. As shown by Equation 6.4, ε_1 is a measure which relates to the macroscopic extension in the system, and is not necessarily associated with a fault system containing power-law cumulative frequency scaling. On the other hand, a_1 is intimately linked to c_1 (the dimensions of a_1 are m^{c_1-1}), and if c_1 changes, a_1 must change as well.

6.2.3 Interdependence of fault density parameters

Consider a layered sequence of high and low porosity reservoir sandstones in an extensional setting, in which the strain in both lithologies at any point in the reservoir is equal. Assume that the brittle strain in both lithologies is also equal (this is an over-simplification, as one medium would probably accommodate more ductile strain). The style of faulting, and therefore c_1, may not be the same in both lithologies, as discussed in Section 2.4.3. Because c_1 is different, a_1 must also change between lithologies to reflect this. ε_1, however, would remain constant.

The displacement frequency power-law exponent (c_1) reflects the ratio of small to large faults, and therefore has a physical significance. It varies as a function of structural position and mechanical properties of the system. ε_1 has physical significance, as it represents the maximum component of the brittle strain tensor. a_1, however, has no physical significance other than a connection with c_1 and ε_1. Therefore, if variation in fault system scaling as a function of lithology is incorporated in a reservoir model, it is much easier to vary only c_1, and model changes in a_1 as a function of a lithology-independent map of ε_1, rather than have to determine lithology dependent-maps of both c_1 and a_1.

Cumulative fault density (*CUMFD*) is more dependent on other variables than a_1, as it relates to a particular size of fault. In Section 2.3.2, *CUMFD* was defined as:

$$CUMFD_{D_P} = a_1 D_p^{-c_1}, \tag{6.12}$$

where D_p is a particular size of fault. Equation 6.12 shows that *CUMFD* varies as a function of c_1 partly through the a_1 term, as discussed in the previous paragraph, and also, explicitly, as a exponent to the D_p term. Therefore a map of *CUMFD* has even greater dependence on c_1 than a map of a_1. *CUMFD* maps made at different values of D_p might be significantly different in shape from each other. This effect is shown on Figure 6.5. a_1 has been calculated iteratively (using Equation 6.11) for a range of c_1 values and specific values of ε_1, $D_{\min}$, W, α and δ. The bold line on Figure 6.5 is a_1, and the other lines are *CUMFD* for a variety of D_p. At $D_p = 1$ m, $CUMFD = a_1$, but at different vales of D_p, the shape of the *CUMFD* curve are different.

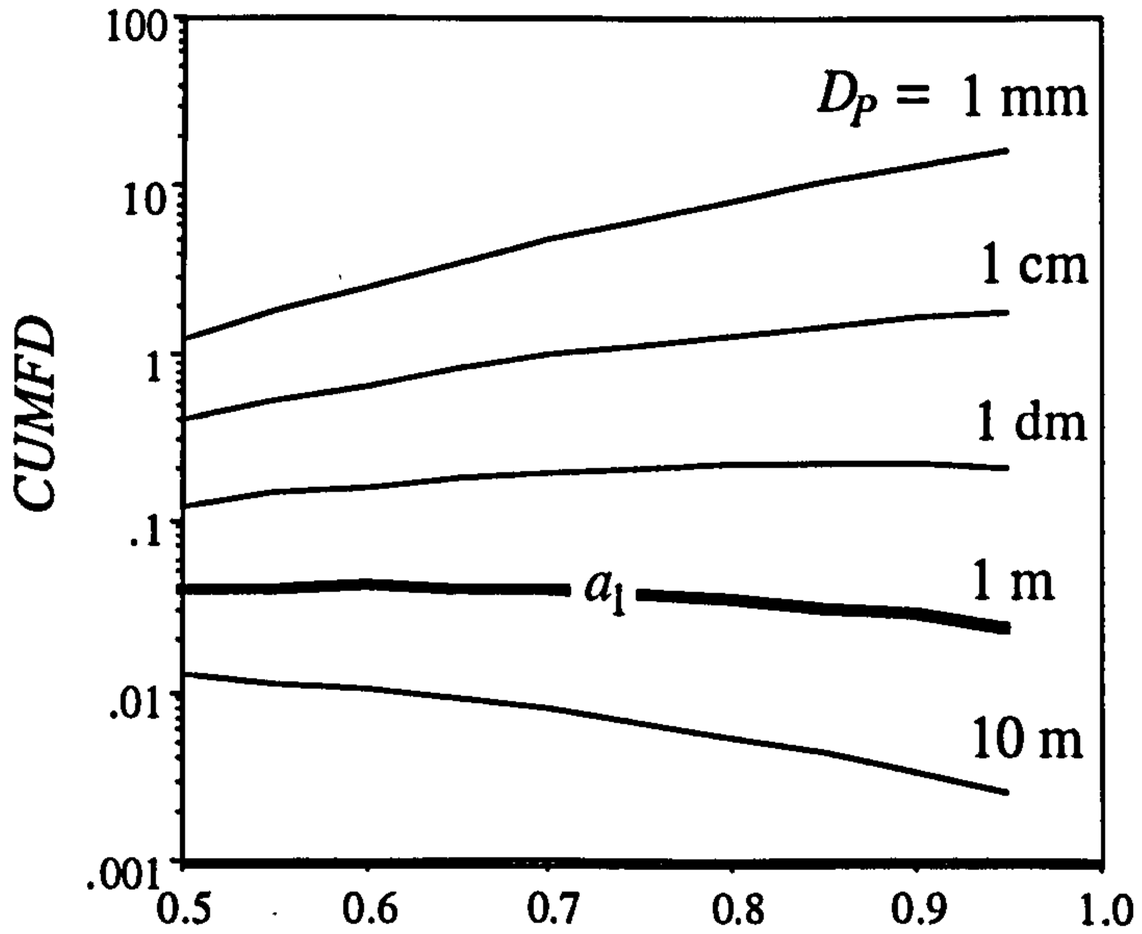

Figure 6.5. Cumulative fault density as a function of the fault displacement for which it is recorded (D_P) and the cumulative displacement frequency power-law exponent (c_1). See text for details.

($\varepsilon_1 = 0.05$, $D_{\min} = 1$ mm, $W = 100$ m, $\alpha = 15°, \delta = 70°$)

Therefore, general relationships between *CUMFD* and c_1 need not have a physical significance. Firstly, these relationships will vary depending on the value of D_p. Secondly, correlations are an expression of both population scaling terms responding in

tandem within a fairly homogeneous strain field (e.g. for the example quoted by Walsh *et al.*, 1994). In conclusion, ε_1 is the only independent measure with which the distribution of fault density can be determined. While fault scaling characteristics can vary locally, strain is homogeneous over much greater distances.

6.3 Analysis of 1D samples - Examples from the Vale of Eden.

Equation 6.11 equates 1D extension (ε_1) with c_1, a_1, W, $D_{\min}$, α and δ. Therefore, based on initial ε_1 and c_1 estimates, and knowing the fault system orientations, a full description of the 1D faulting may be obtained. This relationship is examined for two datasets from faulting in the Penrith Sandstone in the Vale of Eden. These datasets, from Belah Scar and George Gill, were discussed in Section 2.4.3.

6.3.1 Derivation of parameters

Fault orientation and displacement were measured along two 1D surveys (Tables A1.1 and A1.2). These surveys form the basis for this numerical illustration. Both systems consist of faults in two broad orientation populations (Figure 6.6). Faults from each orientation population have been used to derive the two population average orientations,

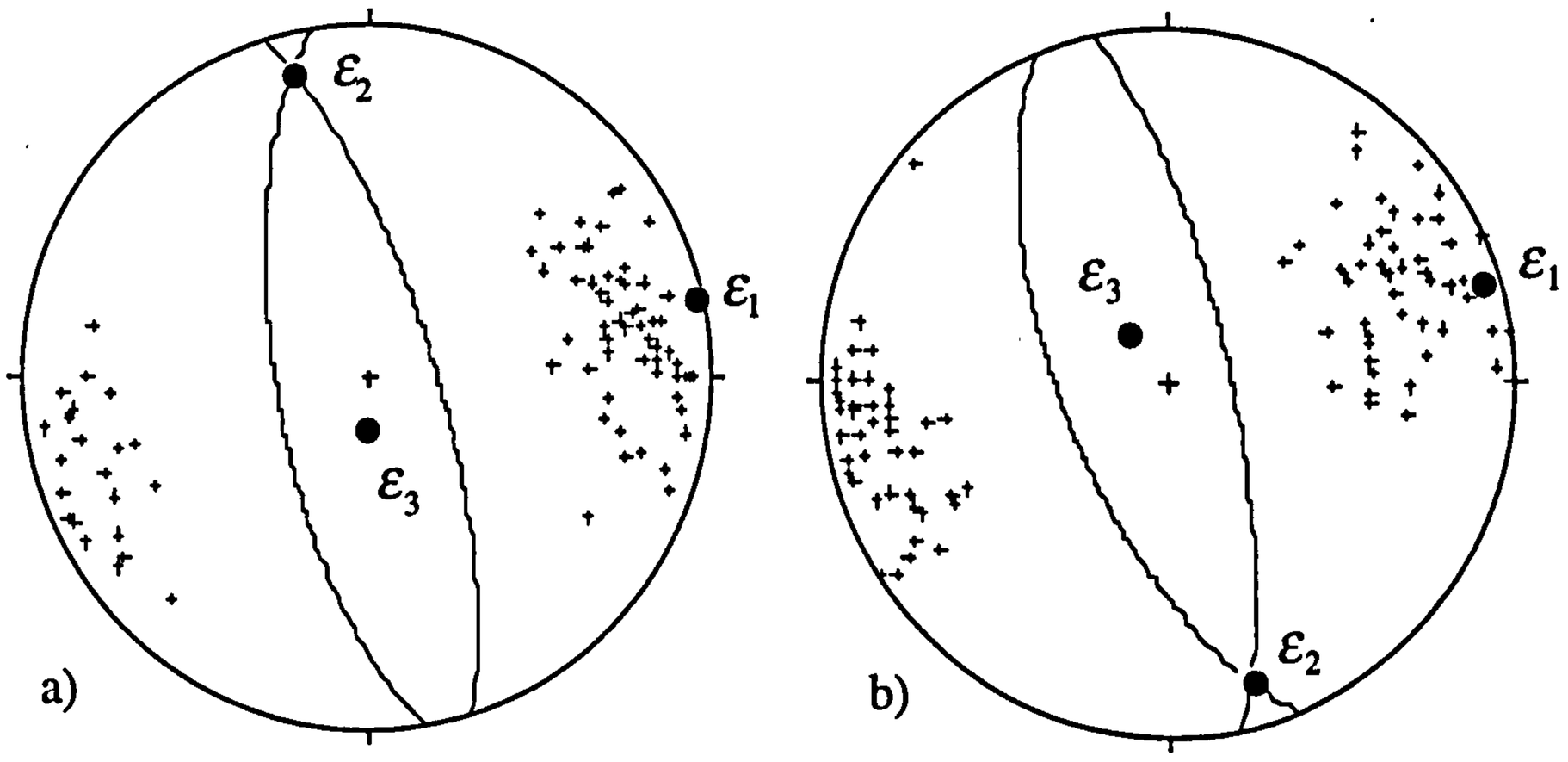

Figure 6.6. Equal angle stereographic projection of the faulting at Belah Scar (a) and George Gill (b), showing poles to individual faults (crosses), mean population orientations (great circles), and inferred principle strain axes ($\varepsilon_1, \varepsilon_2, \varepsilon_3$).

and these population averages are used to infer the principal strain orientations ($\varepsilon_1 > \varepsilon_2 > \varepsilon_3$). This method of determining the principle strain axes is not totally accurate, but is sufficient for this illustration. A more robust treatment which takes into account the relative displacements of each fault is given by Marrett and Allmendinger (1990).

In both cases, the orientation of the sample line is not parallel to the ε_1 orientation, and therefore W is obtained by multiplying the sample length by the cosine of the angle between ε_1 and the sample. The fault system is simplified by assuming that each fault is in the orientation of the population average, therefore α is zero, and δ is the average of the population dips. The magnitude of ε_1 is approximated by Equation 6.4.

The values of c_1 and a_1 are obtained from the cumulative displacement frequency plots (Figure 6.7). The equation of the regression line is:

$$\log N_1(D) = \log(a_1 W) - c_1 \log(D). \qquad (6.13)$$

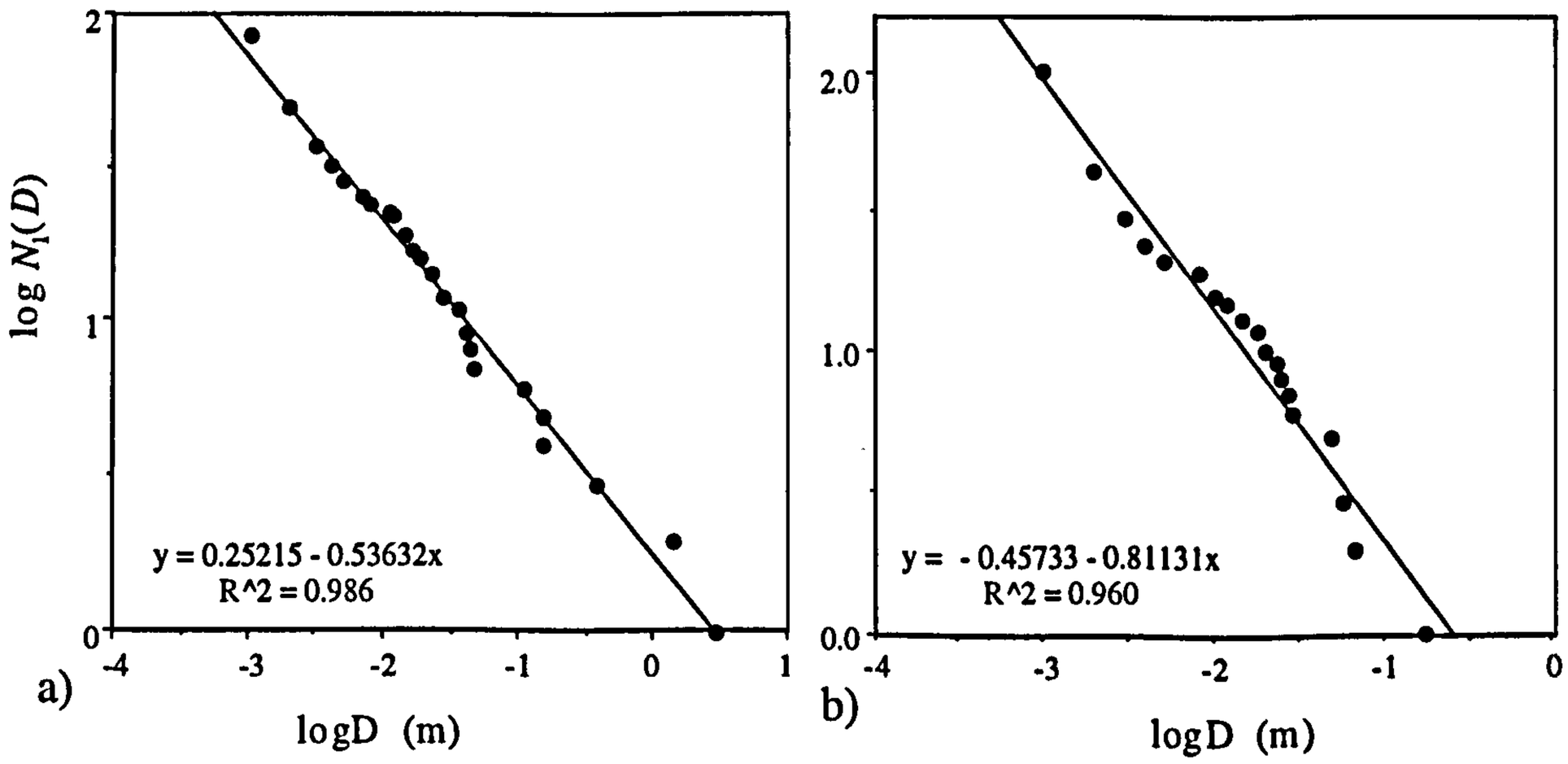

Figure 6.7. Cumulative displacement frequency plots from Belah Scar (a) and George Gill (b), including the best fit regressions.

Therefore all parameters in Equation 6.11 have been determined, either through a geometrical analysis of the orientation and displacement data, or through a regression of

the 1D cumulative displacement frequency plot (Table 6.1). For reservoir fault prediction it is unlikely that all these parameters may be determined, and Equation 6.11 must be used iteratively to determine the variables which are not known. Below is an examination of how closely the parameters derived from the equation fit the real data they estimate.

6.3.2 Algebraic modelling

Based on any two of ε_1, c_1 and a_1, the third can be derived, if W, D_{min}, α and δ are held constant. Three methods are considered.

In Method 1, ε_1 is calculated directly from the values of c_1 and a_1 derived from the regression. The other methods apply the geometrical estimate of ε_1 to Equation 6.11 , to iteratively solve a_1 based on the known c_1 (Method 2); and c_1 based on regression a_1 (Method 3). For the three methods, $\sum D$ and D_0 have been derived from Equations. 6.7 and 6.11. These results are tabulated below (Table 6.2).

The number of faults in a displacement range $D_p < D < D_q$ is derived from Equation 6.1:

$$\sum_{D_p}^{D_q} D = a_1 W\left(D_p^{-c_1} - D_q^{-c_1}\right). \qquad (6.14)$$

The number of faults in four displacement ranges for the two datasets for each of the three methods are compared to the actual number of faults sampled in these ranges, by comparison of two histograms (Figure 6.8). In the following Section, Table 6.2 and Figure 6.8 are used to examine the robustness of the algebra in reproducing the fault density characteristics of these real, and therefore imperfect, datasets.

Table 6.1. Summary of the fault system data from Belah Scar and George Gill .

		Belah Scar	George Gill
Measured	Sample length (m)	73.8	13.38
	Sample Orientation (°)	247	125
	Total number of faults	87	101
	D_0 (m)	3.00	0.180
	$\sum D$ (m)	5.71	0.750
Derived geometrically	Average population orientations	162 / 74 E 170 / 68 W	168 / 75 E 158 / 65 W
	ε_1 orientation	3 / 77	5 / 73
	W (m)	72.7	8.24
	α (°)	0	0
	δ (°)	71	70
	ε_1	0.0256	0.0311
Derived from regression	c_1	0.536	0.811
	a_1	0.0246	0.0424

Table 6.2. Comparison of scaling parameters for three algebraic models of ε_1, c_1 and a_1, for faulting observed at Belah Scar and George Gill. The measured values are those on Table 6.1. The bold values indicate parameters derived from the other two parameters using Equation 6.11.

	Belah scar				George Gill			
	Measured	Method 1	Method 2	Method 3	Measured	Method 1	Method 2	Method 3
a_1	0.0246	0.0246	**0.0316**	0.0246	0.0424	0.0424	**0.0417**	0.0424
c_1	0.536	0.536	0.536	**0.702**	0.811	0.811	0.811	**0.754**
ε_1	0.0256	**0.0149**	0.0256	0.0256	0.0311	**0.0318**	0.0311	0.0311
$\sum D$	5.71	3.33	5.36	4.85	0.750	0.767	0.750	0.563
D_0	3.00	2.95	4.72	2.29	0.180	0.273	0.268	0.247

6.3.3 Discussion

For the Belah Scar faulting, none of the three algebraic methods provide particularly accurate estimates of the derived variable (the bold values in Table 6.2). Method 1 provides a good estimate of D_0, because the largest measured fault lies on the regression line, but $\sum D$, and therefore ε_1, are underestimated by about 60%. Method 1 underestimates the number of faults present in three out of four size ranges (Figure 6.8a).

Method 2 matches the observed ε_1 and the regression c_1, and provides the closest estimate of $\sum D$. This is at the expense of over-predicting D_0. In order to match ε_1, an a_1 value higher than that measured is calculated. As the units of measurement used throughout are the metre, a_1 is proportional to the number of faults of $D \geq 1$ m. Therefore a higher a_1 implies a higher D_0 (see Equation 6.11). The number of faults in the range $D \geq 1$ m in the dataset is small, so that although a_1 is too high, the estimate of faults in this range is close to that recorded (Figure 6.8a). Method 2 provides the best estimate of the number of faults in three of the four size ranges, as well as the closest estimate of the overall number of faults present.

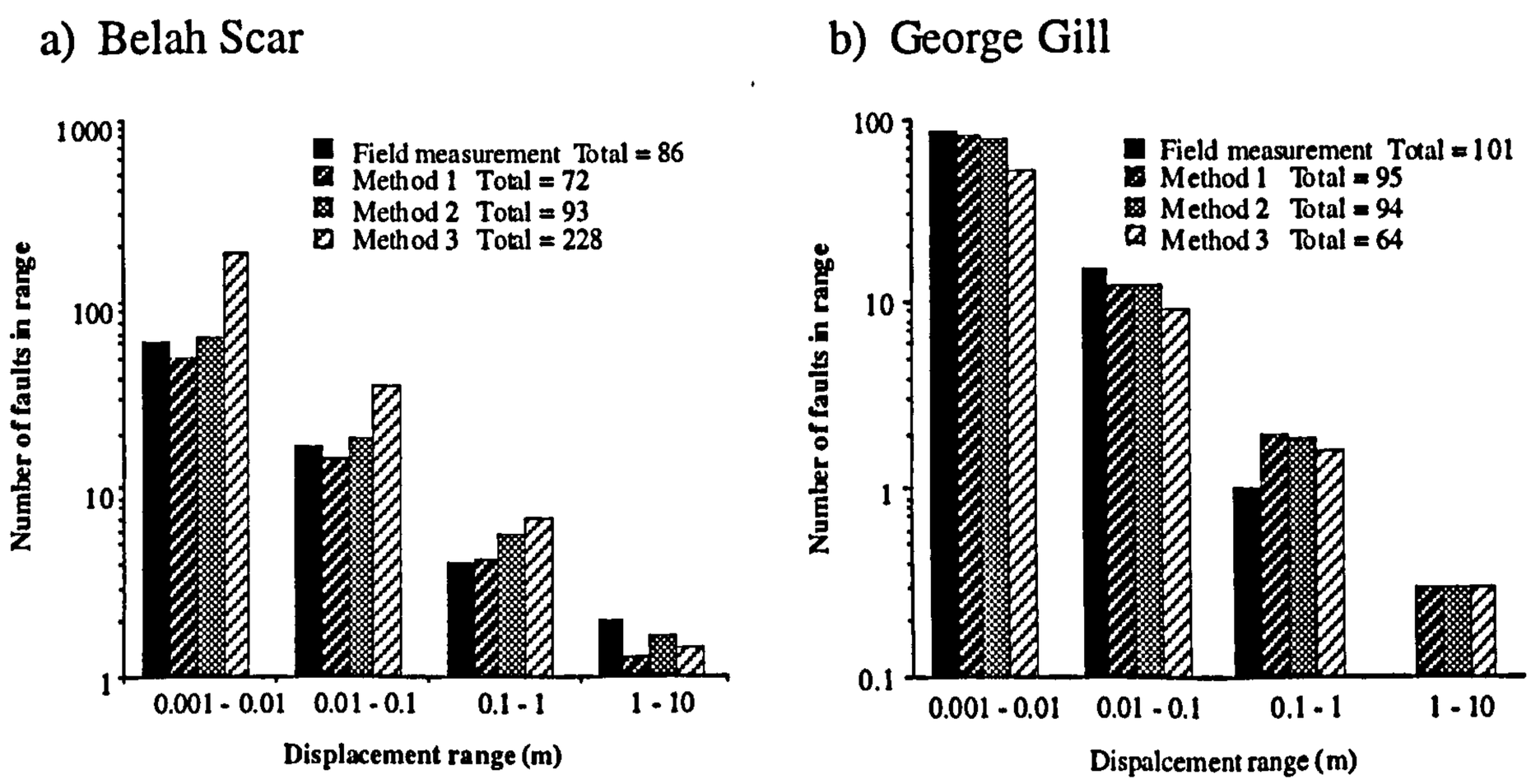

Figure 6.8. Histograms comparing the actual number of faults in four displacement ranges for 1D samples with those predicted for three algebraic methods (see text for details)

Method 3 matches ε_1 and a_1, and calculates values of $\sum D$ and D_0 which are reasonably close: $\sum D$ is better than for Method 1, and D_0 is better than for Method 2. However Method 3 calculates c_1 much greater than recorded. c_1 represents the ratio of small to large faults, and a high c_1 implies that there are many more small faults present. This is demonstrated on Figure 6.8a; Method 3 predicts over 180 faults in the range $0.001 < D < 0.01$, as opposed to 63 that exist in this range. Method 3 overestimates the number of faults present in all but the largest length-scale.

For the George Gill dataset, Methods 1 and 2 provide close estimates of ε_1 and a_1 respectively, but the c_1 estimate (Method 3) is poorer. All three methods over-estimate D_0, because the largest faults in the dataset lie below the regression line (Figure 2.12a). Method 3 provides the best estimate of D_0 but the worst estimate of $\sum D$, and Method 2 estimates $\sum D$ correctly to three significant figures. Unlike the Belah Scar dataset, for which Method 3 over-estimated c_1, in the George Gill dataset c_1 is underestimated, though not so markedly. Therefore Method 3 under-estimates the total number of faults present (64 vs. 101), particularly in the smallest displacement range (Figure 6.7b). There is very little difference between Methods 1 and 2, as they both calculate virtually the same estimates of the number of faults in each displacement range. Method 1 provides a slightly closer estimate of the total number of faults present. These estimates are not as close as those for Method 2 at Belah Scar, reflecting the poorer power-law fit to the original data (Belah Scar $R^2 = 0.986$ vs. George Gill $R^2 = 0.960$). Overall, Method 2 gives the best set of estimates.

Thus, the analysis of the George Gill and Belah Scar datasets has served several purposes. First, it has confirmed that the algebra derived in the previous section can be applied to field datasets to get a reasonable estimate of the frequency of faulting observed. The analysis of 1D fault samples in the form of cumulative displacement frequency plots provides values of a_1 and c_1, which give estimates of total extension close to that calculated geometrically from the discrete fault data (Equation 6.11; Method 1). By considering the extension as a function of the actual faults present (Equation 6.7), along with c_1 calculated from a plot of $\log N_1(D)$ vs. $\log D$, a_1 may be derived (Method 2). This gives a better approximation of the fault population characteristics. Calculating c_1 from the geometrical extension and regression a_1 provides a very poor match to real data. This is because the population power-law gradient (c_1) is the most critical population characteristic, and a value which is not extremely close to the

measured value may give spurious results, particularly if many length-scales are considered by the same relationship.

For any 1D dataset, running Methods 1 and 2 and comparing the results is a method of checking the robustness of the population power-law scaling relationship. It is not critical that the two independent determinations of ε_1 are close, it is more important for the purposes of flow analysis that the actual number of faults in each displacement range is similar. This study assumes initial maps of ε_1 and c_1 for flow analysis, as detailed in section 6.1. From these, Method 2 is used to determine fault densities in displacement ranges. This is the preferred method, because in the subsurface away from wells it simpler to estimate ε_1 than a_1. The analysis has not only demonstrated that this produces robust results, but has also indicated that this method may be preferable even when an estimate of a_1 is available, for instance at a well.

6.4 Conversion to a 2D scaling model

Faulting in an area WJ follows the power-law:

$$N_2(D) = a_2 WJD^{-c_2}, \tag{6.15}$$

and the number of faults of displacement D in the area is $-dN_2(D)$. The length of these faults, calculated from Equation 6.2, is $(D/B)^{1/n}$. If the faults are randomly distributed throughout the area, then the probability that a 1D sample W encounters any fault of length L (See section 4.5.4, Equation 4.17) is:

$$p_1(L) = L\cos\alpha / J. \tag{6.16}$$

Expressing this in terms of displacement gives:

$$p_1(D) = \frac{D^{1/n}\cos\alpha}{JB^{1/n}}. \tag{6.17}$$

The total number of faults of displacement D in an area WJ which are encountered by the 1D sample is:

$$-dN_1(D) = -dN_2(D)p_1(D).$$

which can be manipulated to give:

$$\frac{dN_2(D)}{dD} = \frac{dN_1(D)}{p_1(D)dD} \tag{6.18}$$

Replacing Equations 6.6 and 6.17 into the right hand side of Equation 6.18 gives:

$$dN_2(D) = \frac{-c_1 a_1 WJB^{1/n}}{\cos\alpha} D^{-(1+c_1+1/n)} dD \tag{6.19}$$

Integrating both sides of Equation 6.19 gives $N_2(D)$:

$$N_2(D) = \frac{c_1 a_1 WJB^{1/n}}{\cos\alpha(c_1 + 1/n)} D^{-(c_1+1/n)}. \tag{6.20}$$

Equating this with 6.15 gives the 2D cumulative displacement frequency constants:

$$c_2 = c_1 + 1/n, \tag{6.21}$$

and

$$a_2 = \frac{c_1 a_1 B^{1/n}}{\cos\alpha(c_1 + 1/n)}. \tag{6.22}$$

Hence based on a 1D sample estimate of extension and c_1, the two dimensional scaling parameters which define the continuous faulting in the area WJ may be determined. Westaway (1994) pointed out that this reasoning is only appropriate when $L\cos\alpha \leq J$.

If this condition is not satisfied, Equation 6.16 calculates a meaningless probability > 1. This is overcome by changing WJ at each scale (Section 6.5.3).

6.5 Transformation to discrete length-scales

The fault scaling algebra derived in Sections 6.2.1 and 6.3 is concerned with correctly manipulating the scaling terms so that the extension and the 1D sample characteristics are preserved in a 2D description. These manipulations are well established and may be found (with the exception of Equation 6.11) in the excellent appendices by Westaway (1994). These presents a coherent mathematical model of faulting as a continuous hierarchy in which there are no specific length-scales and faults may be of any size up to D_0. As discussed in Section 6.1.1, the method used in applying fault scaling to flow calculation requires representation of continuous faulting as a discrete hierarchy. This section details this transformation, which is concerned with retaining the fault system parameters which are important to flow, namely line density and gouge density.

6.5.1 Determination of the average displacement

The number of faults in WJ with displacements in the range $D_p \leq D < D_q$ is given by applying limits to Equation 6.15:

$$N_2(D_{pq}) = a_2 WJ\left[D_p^{-c_2} - D_q^{-c_2}\right] \tag{6.23}$$

The total displacement of the faults in this range (see Section 6.2.1 for a detailed 1D treatment of this problem) is given by :

$$\sum_{D_p}^{D_q} D = -\int_{D_q}^{D_p} \frac{dN_2(D)}{dD} DdD. \tag{6.24}$$

Differentiating Equation 6.15 gives:

$$\frac{dN_2(D)}{dD} = -c_2 a_2 WJD^{-c_2-1}; \tag{6.25}$$

and so:
$$\sum_{D_p}^{D_q} D = \frac{c_2 a_2 WJ}{c_2 - 1}\left[D_p{}^{1-c_2} - D_q{}^{1-c_2}\right]. \tag{6.26}$$

The continuous faulting in the displacement range $D_p \le D < D_q$ is represented by $N_2(D_{pq})$ faults, each of displacement $\overline{D}_{pq}$, where $\overline{D}_{pq}$ is the average displacement in the range, and is given by dividing the total fault displacement (Equation 6.26) by the total number of faults (Equation 6.23):

$$\overline{D}_{pq} = \frac{c_2\left[D_p{}^{1-c_2} - D_q{}^{1-c_2}\right]}{(c_2 - 1)\left[D_p{}^{-c_2} - D_q{}^{-c_2}\right]}. \tag{6.27}$$

6.5.2 Determination of the average length and thickness

According to Equation 6.2, the length of a fault of displacement $\overline{D}_{pq}$ should be $\left(\overline{D}_{pq} / B\right)^{1/n}$. As will be shown below, this is an incorrect method for the discrete hierarchy if $n \neq 1$, because the faulting in the discrete model does not follow the same power-law relationships that make up the continuous model. The correct method for determining $\overline{L}_{pq}$ is to sum the length of all faults in the displacement range, and divide this by the number of faults present.

Replacing the displacement terms in Equation 6.15 with the length terms in Equation 6.2 gives the 2D length frequency relationship:

$$N_2(L) = a_2 WJB^{-c_2} L^{-nc_2}, \tag{6.28}$$

and the total length of the faults with displacements $D_p \le D < D_q$ is given by:

$$\sum_{L_p}^{L_q} L = -\int_{L_p}^{L_q} \frac{dN_2(L)}{dL} L dL, \tag{6.29}$$

where L_p and L_q are the lengths of faults with displacements D_p and D_q respectively.

Differentiating Equation 6.28 gives:

$$\frac{dN_2(L)}{dL} = -nc_2a_2WJB^{-c_2}L^{-nc_2-1}. \quad (6.30)$$

Replacing this in Equation 6.29, and integrating, gives:

$$\sum_{L_p}^{L_q} L = \frac{nc_2a_2WJB^{-c_2}}{nc_2-1}\left[L_q^{1-nc_2} - L_p^{1-nc_2}\right]. \quad (6.31)$$

This may be expressed in terms of displacement, as (from Equation 6.2), $L_p = B^{-1/n}D_p^{1/n}$ and $L_q = B^{-1/n}D_q^{1/n}$. Replacing these in Equation 6.31 gives:

$$\sum_{D_p}^{D_q} L = \frac{nc_2a_2WJB^{-1/n}}{nc_2-1}\left[D_q^{(n^{-1}-c_2)} - D_p^{(n^{-1}-c_2)}\right]. \quad (6.32)$$

This equation gives the total length of faults in an area WJ which have displacements in the range $D_p \le D < D_q$. $\overline{L}_{pq}$ is given by $\overline{L}_{pq} = \sum_{D_p}^{D_q} L / N_2(D_{pq})$, which, when determined from Equations 6.32 and 6.23, will give:

$$\overline{L}_{pq} = \frac{nc_2B^{-n^{-1}}}{nc_2-1}\left(\frac{D_p^{(n^{-1}-c_2)} - D_q^{(n^{-1}-c_2)}}{D_p^{-c_2} - D_q^{-c_2}}\right). \quad (6.33)$$

If the assumption is made that the mean displacement in the range follows the power-law for the continuous hierarchy (i.e. that $\overline{D}_{pq} = B\overline{L}_{pq}^{n}$), then $\overline{L}_{pq}$ can be calculated directly from Equation 6.27. This gives:

$$\overline{L}_{pq} = \left(\frac{c_2 B^{-1}}{c_2 - 1} \left(\frac{D_p^{1-c_2} - D_q^{1-c_2}}{D_p^{-c_2} - D_q^{-c_2}} \right) \right)^{1/n}, \qquad (6.34)$$

which differs from Equation 6.33. Only if $n = 1$ (i.e. when length increases in direct proportion to displacement) are the two calculations of $\overline{L}_{pq}$ the same. The reason the two equations give different quantities for $\overline{L}_{pq}$ is that, for $n \neq 1$, $D_q / D_p \neq L_q / L_p$. In other words, the system scaling is not strictly self-similar (see Section 1.4.3). For $n > 1$, the displacement / length ratio of large faults is greater than for small faults. The reasoning in Equation 6.34 is only appropriate for self-similar systems in which this ratio is constant, and Equation 6.33 needs to be for the general case.

The fact that Equations 6.33 and 6.34 are different for $n \neq 1$ implies that the displacement / length ratio of the faults which form the discrete model do not lie on the displacement / length relationship which defines the continuous model (Equation 6.2). This is not a problem - what is important is that fault density is preserved in the numerical model. Fault density is preserved by summing the length of faults present in the continuous mathematical model within the displacement range of the discrete model, and distributing this length between the single sized faults present in the discrete model (Equation 6.33). This procedure was conceptualised on Figure 3.19. If the assumption that $\overline{D}_{pq} = B\overline{L}_{pq}^{\,n}$ is made, then the faults in the discrete model would fit the same scaling characteristics as in the continuous model, but fault density would not be preserved (Equation 6.34).

Following the procedure of Equations 6.28 to 6.33, but considering fault thickness (Equation 6.3) instead of length (Equation 6.2) permits the calculation of the average thickness ($\overline{T}_{pq}$) of the faults in the displacement range $D_p < D < D_q$. This is:

$$\overline{T}_{pq} = \frac{r c_2 F^{-r^{-1}}}{r c_2 - 1} \left(\frac{D_p^{(r^{-1}-c_2)} - D_q^{(r^{-1}-c_2)}}{D_p^{-c_2} - D_q^{-c_2}} \right). \qquad (6.35)$$

6.5.3 Determination of the fault density measures

The two fault density measures used in the flow calculation are gouge density and line density. Line density (d_L) is the number of faults present in an area determined as a function of the length of the faults. Line density is given by:

$$d_L = \frac{N_2(D_{pq})\overline{L}_{pq}^{\,2}}{4WJ}. \tag{6.36}$$

Gouge density (d_G) is the fault area fraction and is given by:

$$d_G = \frac{N_2(D_{pq})\overline{L}_{pq}\overline{T}_{pq}}{WJ}. \tag{6.37}$$

$N_2(D_{pq})$is directly proportional to WJ (Equation 6.23), therefore WJ cancels out in both these calculations. J is not involved in any other equations: neither $\overline{L}_{pq}$ or $\overline{T}_{pq}$ are functions of J, and nor are any of the parameters they depend on. For the transformation of the mathematical model from 1D to 2D, it is necessary that $L\cos\alpha \leq J$, as discussed in Section 6.4. In the calculations, J is varied at each length-scale. For faulting in the range $D_p < D < D_q$, J is given the arbitrary value of L_q, which is the length of the largest fault present in this range. In this way the condition above is always satisfied. Both gouge density and line density are functions of the number of faults in an area, and the width of the area being considered (J) is irrelevant.

The length of the area being considered (W) is much more important. $N_2(D_{pq})$ is a function of a_2, which is a function of a_1, which is a function of W (Equation 6.11). The significance of W is paramount, and is discussed in the following chapter. This chapter deals with manipulation of the mathematical and numerical models, and as W is

an initial input into the mathematical model, its effect is retained in the final density calculations, but its significance will be discussed elsewhere (Section 7.4.3).

Figure 6.9 shows maps of d_G and d_L as a function of c_1 vs. ε_1 , for faulting in the displacement ranges 1 mm < D < 1 cm, 1 cm < D < 10 cm, 10 cm < D < 1 m and 1m < D < D_0. Note that, in some of the individual length-scales, c_1 has almost as much influence over the fault density measures as ε_1. At each length-scale, the shape of the contours for both density measures are the same, because both d_G and d_L, are linear functions of $N_2(D_{pq})$. The magnitudes of d_G and d_L, however do not follow the same pattern. At low c_1 and ε_1 in the smallest length-scale, d_G is smaller compared to larger length-scales, but d_L is greater than it is at larger length-scales. These differences are due to the displacement / length and the displacement / thickness scaling parameters selected. In the cases illustrated ($D = 0.01L$ and $D = 100T^{1.5}$), faults get relatively narrower as they get larger, so the greatest gouge density values are for the smallest faults. Because line density is independent of fault thickness, and because the displacement / length scaling power-law gradient is 1, line density is greatest where there are most faults present; i.e. at high c_1 for small length-scales and at low c_1 for large length-scales. A comparison of these two sets of graphs illustrates that the systems considered are generally not strictly self-similar, as illustrated conceptually on Figure 1.9.

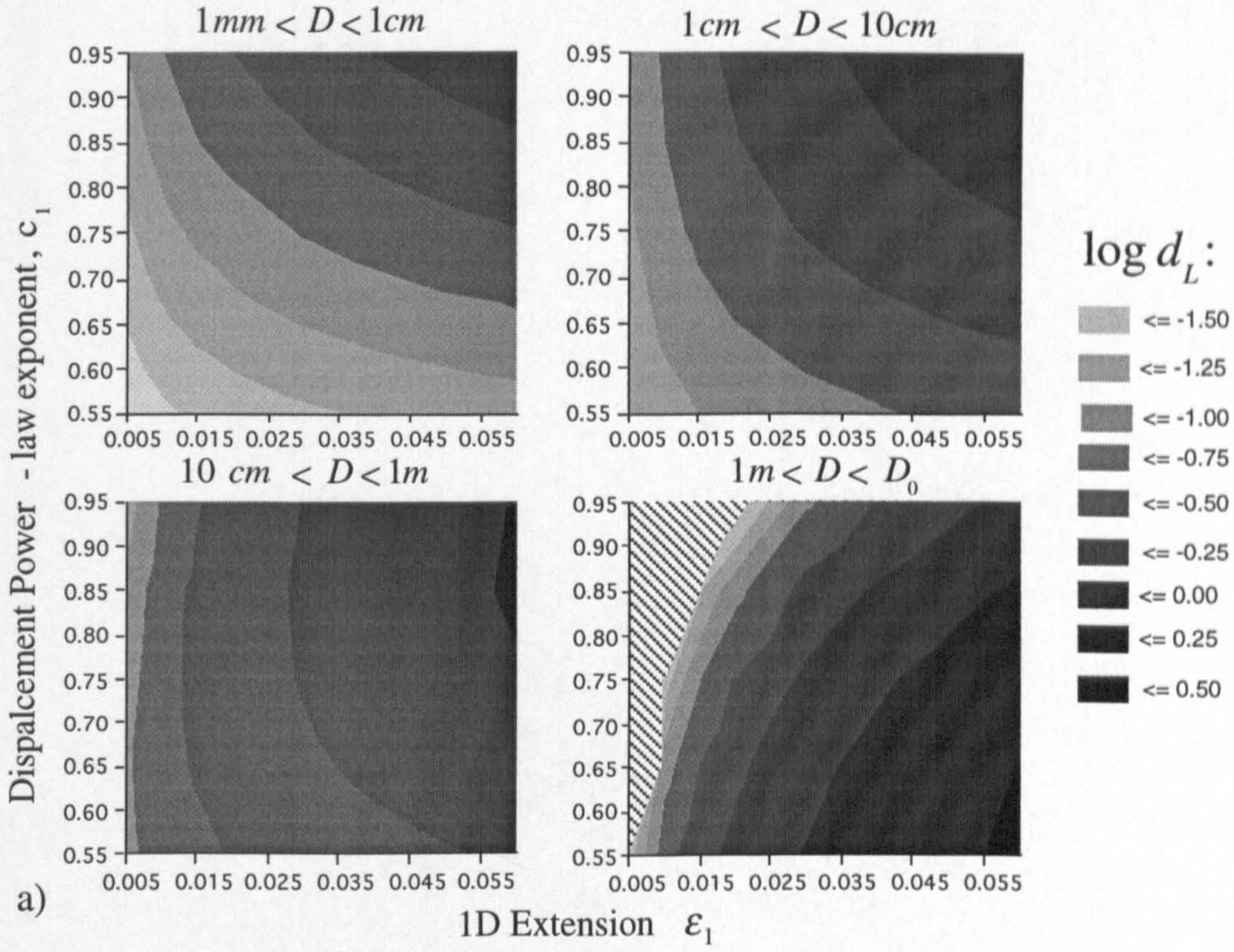

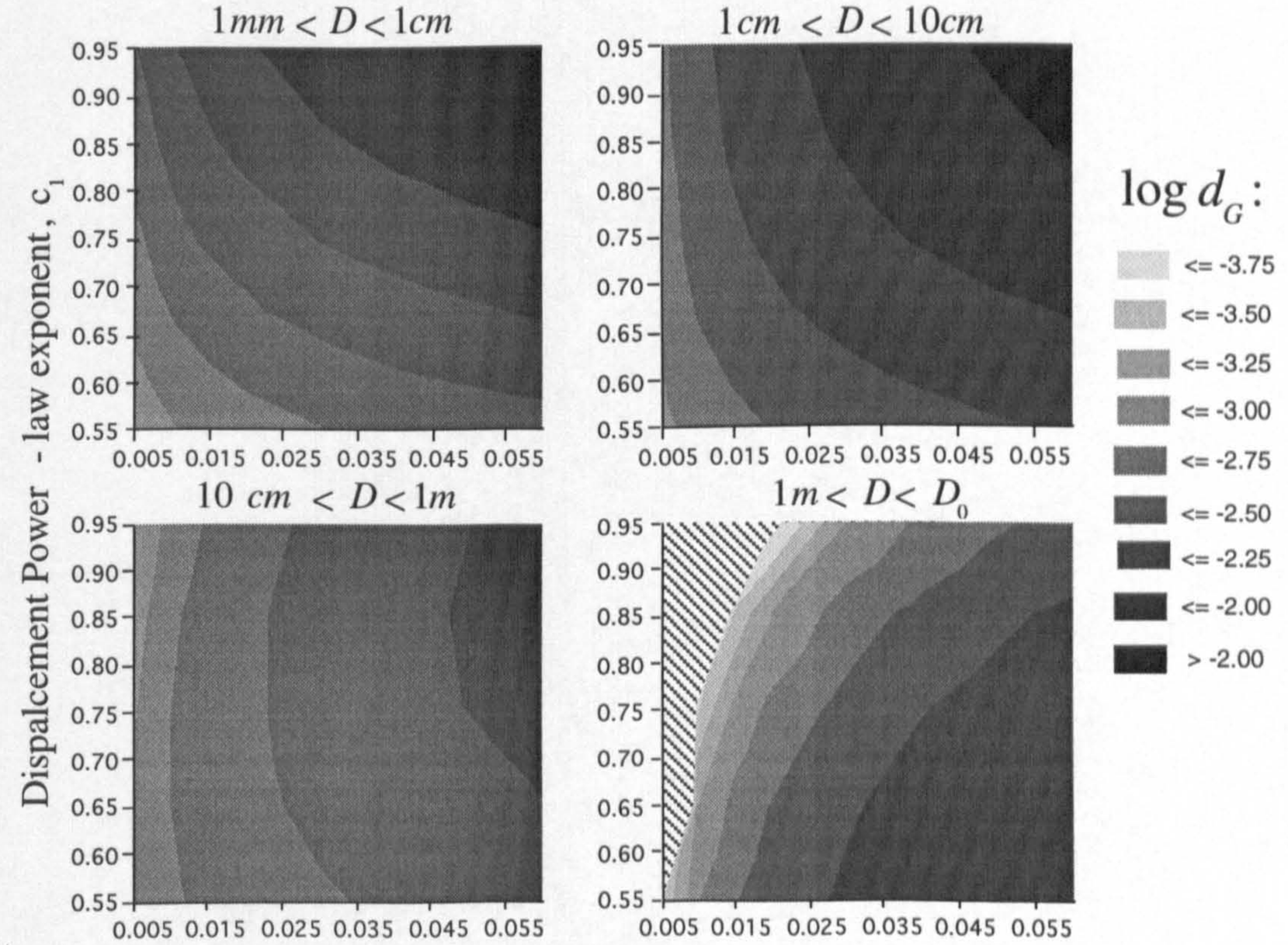

Figure 6.9. (a) Line density (d_L), and (b) gouge density (d_G), as a function of 1D cumulative displacement frequency power-law exponent (c_1) and extension (ε_1), for faulting in four displacement ranges. The patterned areas are regions which contain less than one fault at that scale. Other parameters are $D_{\min} = 0.001$ m, $W = 100$ m, $\alpha = 15°$, $\delta = 70°$, $B = 0.01$, $n = 1.0$, $F = 100$, and $r = 1.5$.

6.6 Summary

This Chapter has dealt with the transformation of the continuous mathematical fault model to a discrete numerical model in which faults exist only at particular length-scales. Fault gouge density and line density (d_G and d_L) representative of particular length ranges in the system are calculated based on values of 1D maximum extension (ε_1), 1D displacement frequency power-law gradient (c_1), displacement / length scaling parameters (B, n), displacement / thickness scaling parameters (F, r), 1D sample length (W) and fault orientation parameters (α, δ).

The overall fault density of the system is a function of a_1. Often the term *CUMFD* is used to model fault density (e.g. Yielding *et al.*, 1992; Walsh *et al.* 1994). *CUMFD* is a function of a_1, and c_1 (Equation 6.12), but a much more fundamental indicator of the amount of faulting present is the magnitude of the maximum strain, ε_1. In Section 6.2, the relationships between these three terms was derived.

Section 6.3 investigated the differences in fault frequencies which are calculated as a function of assuming an initial estimate of a_1 or ε_1. For two Vale of Eden fault datasets, each gave a sturdy fault system description. Such comparison are a useful method for assessing the robustness the cumulative displacement frequency relationship derived for a specific dataset.

Section 6.4. details the algebra involved in the transformation of the system description from 1D to 2D. This transformation is well-established (e.g. Marrett and Allmendinger, 1991; Westaway, 1994). Section 6.5 introduces new algebra for the transformation from a continuous 2D hierarchy to the discrete one from which line density and gouge density are calculated.

CHAPTER 7

EFFECTIVE FLOW PROPERTIES IN FAULTED SANDSTONE RESERVOIRS

7.1 Introduction

This Chapter concerns the application of the methods developed throughout this thesis. The thesis has dealt with determining an effective permeability estimate as a function of a geological description of sub-seismic faulting. Terms which describe the fault system quantitatively have been defined (Chapters 2 and 3). Based on the (continuous hierarchical) scaling characteristics of a fault system, gouge density (d_G) and line density (d_L) at a series of (discrete) nested length-scales can be determined (Chapter 6). Gouge density and fault and matrix permeabilities are combined into a parameter called fault heterogeneity (H). Fault heterogeneity defines the overall transmissibility of the system, and line density defines the overall tortuosity (Chapter 5). These factors determine the effective permeability at each length-scale in the hierarchical model. This chapter combines the fault scaling model with the analytical effective permeability determination method, to calculate effective permeabilities of sub-seismic fault systems for incorporation in reservoir simulation models.

In Section 7.2, the basic permeability scaleup method is described in detail. This is then applied to determine effective permeability based on outcrop samples of fault systems. Even with detailed scaling models which may be obtained from outcrop, significant uncertainty is associated with the final effective permeability determination. The relative influences of various aspects of the fault system model on this uncertainty are discussed in Section 7.3. Section 7.3 calculates effective permeability from extrapolations of fault scaling from basin -scale stretching factors. This procedure considers sub-seismic fault systems about which there is absolutely no hard data:

i.e. all parameters in the model must be assumed. In Section 7.4, the method is applied to an example of a reservoir dataset, for which aspects of the spatial distribution of fault scaling parameters have been published. Stochastic maps of effective permeability for the reservoir are presented. Section 7.4 also evaluates the assumptions inherent in determining these maps, and concludes that the scales over which faults system parameters vary are sufficiently large to mean that the lack of an REV in a fault systems is not a problem except close to wells. In Section 7.5, two-phase flow is discussed, focusing on the differences in fault system models which must be considered due to the differences in flow processes. The results and conclusions from the modelling in this Chapter are summarised in Section 7.6.

7.1.1 Effective permeability determination: input

The effective permeability of an area of a reservoir containing a sub-seismic system of low permeability faults is calculated based on six criteria, detailed below.

A) The sub-seismic fault density. This may be represented by any one of three parameters (Section 6.2.2). These are: the 1D cumulative displacement frequency constant a_1 (Equation 2.2); the cumulative fault density term *CUMFD* (Equation 2.7); or in terms of the maximum component of the brittle strain tensor (ε_1) (Equation 6.4). a_1 and ε_1 are linked by Equation 6.8, and a_1 and *CUMFD* are linked by Equation 6.12.

B) The cumulative displacement frequency power-law gradient; c_1 (Equation 6.2). This represents the relative frequencies of small to large faults present in a system. If c_1 is high, there is a greater relative frequency of small faults (Section 2.2.1).

C) Displacement / length scaling parameters (constant B and power-law exponent n, Sections 2.2.2, 2.4.2).

D) Displacement / thickness scaling parameters (constant F and power-law exponent r, Sections 2.2.2, 2.4.3).

E) Fault orientation parameters (strike parameter α and dip parameter δ). These are defined on Figure 6.3. See also Sections 4.5.1 and 5.3.2 for discussed regarding α.

F) Fault and matrix permeabilities k_f and k_m (Section 2.2.5).

7.1.2 Effective permeability determination: output

Details of the permeability upscaling method discussed in Chapters 5 and 6 are summarised conceptually on Figure 6.2. This method allows a rapid estimation of the principal permeability components (k_{e1} and k_{e3}) using no more than a spreadsheet. The output from any single combination of input parameters are two permeabilities k_{e1} and k_{e3}. These are the minimum and maximum components of the second order, diagonal, 2D effective permeability tensor $\begin{bmatrix} k_{e1} & 0 \\ 0 & k_{e3} \end{bmatrix}$. k_{e1} is the permeability in the ε_3 direction, and k_{e3} is the permeability in the ε_1 direction (See Figures 5.16 and 6.1). The tensor is diagonal, as the total faulting is equally divided between two orientation populations (oriented at $\pm\alpha$ to k_{e1}). In this chapter, $\begin{bmatrix} k_{e1} & 0 \\ 0 & k_{e3} \end{bmatrix}$ is rendered as $[k_{e1}\ ,\ k_{e3}]$.

7.2 Effective permeability for outcrop samples

In this Section, three outcrops which were discussed in Chapter 2 are revisited. Pertinent differences in system scaling at these outcrops are summarised. Section 7.2.2. details the effective permeability scaleup method. Four models are used to define system aspects about which little is known (Section 7.2.3). Permeability is calculated for each model at each outcrop, and these results are discussed in Section 7.2.4.

7.2.1 Summary of the outcrops

Figure 7.1 shows displacement stick-plots for 1D samples of faults from three sandstone outcrops. Both Belah Scar and George Gill are cliff outcrops of Penrith Sandstone in the Vale of Eden. Molly's Castle is a pavement of Entrada Sandstone on the San Rafael Swell. These datasets were discussed in Section 2.4, where lithological dependency on the population scaling systematics was highlighted. Of the outcrops studied, Belah Scar has the highest values of displacement frequency power-law exponent (c_1) and displacement / thickness scaling exponent (r), and George Gill the lowest.

In Chapter 6, the 1D maximum extension (ε_1) was determined by a variety of methods for the Belah Scar and George Gill outcrops. These systems exhibited similar values of maximum extension (ε_1 = 0.026 at Belah Scar and 0.031 at George Gill). Owing to the differences in scaling characteristics, the scan-line density, d_S (the number of faults per meter) at George Gill is an order of magnitude greater than at Belah Scar (Figure 7.1). The fault scaling at Molly's Castle is intermediate between Belah Scar and George Gill, but the system has a much lower extension (ε_1 = 0.0081). Belah Scar and Molly's Castle have similar scan-line fault densities; a function of the relative proportions of small and large faulting (controlled by c_1).

The data measured at these outcrops necessary for determination of the effective permeability are shown on Figure 7.1. In the following sections, details are given of the k_e upscaling method. Discussion in the subsequent section is focused on the influence of uncertainties in the input parameters on permeability, as well as on the general influences of lithologically controlled fault scaling variations on effective permeability.

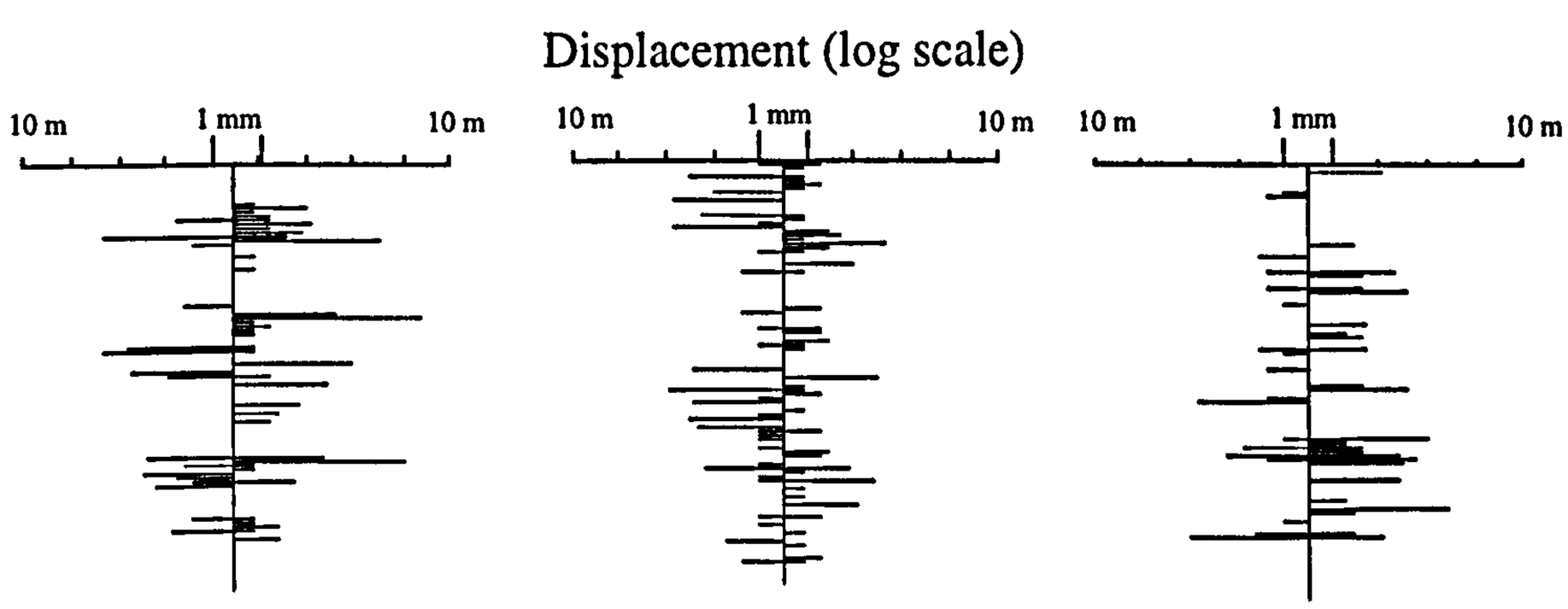

Figure 7.1. Fault displacement stick-plots for the faulting at (a) Belah Scar (b) George Gill (c) and Molly's Castle. The faulting at each outcrop is separated into two dip direction populations.

7.2.2 Effective permeability scaleup

In this Section, maximum and minimum effective permeabilities [k_{e1}, k_{e3}] are determined based on the fault scaling systematics observed at George Gill. k_{e3} is determined as a function of $(90-\alpha)$, and all other input parameters are the same for determination of each permeability component.

Fault density information (a_1), cumulative displacement frequency power-law exponent (c_1) and displacement / thickness scaling parameters (F and r) have been determined

from the outcrop data (Section 2.4.4). No data is available about displacement / length scaling at the outcrops, yet this scaling relationship is an important aspect of the fault model. This relationship must therefore be assumed. Fault orientation needs to be incorporated to determine the directional values of effective permeability. At each outcrop, fault orientations are scattered around two dip population averages (differentiated as two dip populations on each stick-plots on the Figure 7.1), resulting in one trace orientation population. The scatter around this population is approximated to two orientation populations separated by 30° (i.e. $\alpha = 15°$). Fault dip (δ) is taken as 70°. Matrix permeability (k_m) is taken as 1 D throughout, and various cases of fault permeability (k_f) are considered.

Table 7.1 shows the full permeability determination for the George Gill dataset based on a fault permeability of 1 mD irrespective of fault displacement, and a displacement / length relationship $D = 0.001L^{1.5}$. The determination of a_1 is based on the data obtained from the cumulative displacement frequency plots, rather than from the geometrical determination of ε_1 (i.e. using Method 1 of the three cases discussed in Section 6.3). The full set of input requirements are listed at the head of Table 7.1. Every step in the upscaling method (Chapter 5 and 6) is shown on the rest of the table, which also lists the equations used at each stage in the procedure. Note that different routines are necessary depending on whether the faulting at any length-scales forms a connected or a disconnected system (Section 5.5). For the particular set of input used on Table 7.1, k_e = [73, 33] mD.

Table 7.1. Effective permeability scaleup details for one model of the faulting at George Gill.

INPUT DATA

		COMMENTS
α (°)	15	Assumed
W (m)	8.238	Measured
a_1	0.0424	Measured
c_1	0.81	Measured
F	1.44	Eqn. 2.10
r	1.06	Eqn. 2.11
B	0.001	Assumed
n	1.5	Assumed
D_0 (m)	0.273	Eqn. 6.10
c_2	1.478	Eqn. 6.21
a_2	0.000241	Eqn. 6.22
k_f (mD)	1	Assumed
k_m (mD)	1000	Assumed

PERMEABILITY SCALEUP

	SCALE 1	SCALE 2	SCALE 3	COMMENTS	
D_p (m)	0.001	0.01	0.1		
D_q (m)	0.01	0.1	0.273	D_0 defines the largest scale	
$\overline{D}_{pq}$ (m)	0.0021	0.0213	0.1525	Eqn. 6.27	
$\overline{L}_{pq}$ (m)	1.593	7.396	28.284	Eqn. 6.33	
$\overline{T}_{pq}$ (m)	0.0021	0.0188	0.1205	Eqn. 6.35	
d_L	4.011	2.875	1.119	Eqn. 6.36	
d_G	0.0216	0.0292	0.0191	Eqn. 6.37	
k_{m3} (mD)	1000	123.0	45.6	From previous scale	
k_{m1} (mD)	1000	200.7	88.6	From previous scale	
H_3	0.956	0.781	0.460	Eqn. 5.5	
H_1	0.956	0.854	0.626	Eqn. 5.5	
d_{L45}	2.006	1.438	0.560	Eqn. 4.15	
Connected?	Yes	Yes	No	Criterion is $d_{L45} > 0.68$	
				Connected	Disconnected
k_e / k_{m45}			0.336		Eqn. 5.8, 5.9
t_{45}			0.726		Eqn. 5.21
k_e / k_{m3} @ $H = 1$			0.071		Eqn. 5.24
k_e / k_{m1} @ $H = 1$			0.687		Eqn. 5.24
d_{Le3}	2.006	1.438	0.667	Equals d_{L45}	Eqn 5.32, 5.33
d_{Le1}	2.006	1.438	0.212	Equals d_{L45}	Eqn 5.32, 5.33
H_{e3}	0.965	0.818	0.517	Eqn. 5.37	Eqn. 5.37
H_{e1}	0.923	0.763	0.480	Eqn. 5.37	Eqn. 5.37
k_e / k_{m3}	0.123	0.371	0.726	Eqn 5.10-5.13	Eqn 5.8, 5.9
k_e / k_{m1}	0.201	0.442	0.824	Eqn 5.10-5.13	Eqn. 5.8, 5.9
k_{e3} (mD)	123.0	45.6	**33.1**		
k_{e1} (mD)	200.7	88.6	**73.0**		

7.2.3 Effective permeability modelling

Sixteen effective permeabilities have been calculated for each outcrop according to four fault models, detailed below. The results are given on Table 7.2. For each model, four displacement / length scaling model are used. These are the four lines on Figure 2.10.

Model A: k_f = 1 mD irrespective of D. The displacement thickness scaling terms are those determined from the cumulative frequency plots in Section 2.4.7.

Model B. k_f = 1 mD irrespective of D. The displacement / thickness scaling constant F is five times greater than in Case 1, in an attempt to capture the effect of scatter in the displacement / thickness data at each outcrop, as discussed in Section 2.4.8.

Models C and D. These follow cases A and B respectively in terms of displacement / thickness scaling, but in these cases, k_f varies as a function of fault displacement. Fault permeabilities are k_f = 10 mD for $D < 0.01$m , k_f = 1 mD for $D < 0.1$m , k_f = 0.1 mD for $D < 1$ m, and k_f = 0.01 mD for $D \geq 1$ m.

7.2.4 Discussion

Firstly, note that are much larger differences in k_e as a function of the displacement / length scaling than as a function of the displacement / thickness cases. This is particularly the case for the models with variable fault permeability (see for example George Gill, Model C, for which the k_e extremes are [621, 84] mD and [23, 11] mD). Relatively small modifications to any parameter for which data is available (e.g. displacement / thickness scaling) have a much smaller impact on k_e than uncertainty about the aspects of the system for which no information is available.

Secondly, it is clear that it is the *details* of the fault system model which determine the effective permeability, rather than general descriptions of system properties. For

instance, although generally the effective permeabilities calculated at George Gill are considerably lower than those at Belah Scar, this is not inevitably the case. In one case (Model D with displacement / length scaling $D=0.001L$) George Gill actually has a higher permeability. This is because Belah Scar is the only outcrop which contains faults with $D>1$ m. Usually, the greater density of smaller faults at George Gill means the effective permeability is greater at Belah Scar. In this one case, however, a connected system at the largest scale is calculated at Belah Scar, resulting in a huge k_e reduction at the scale with the least transmissible faults. This k_e result can therefore be *understood* in terms of the fault system model, but there is no way it could be *predicted* from the geological model alone: it is only with a rigorous upscaling method that k_e can be determined.

Table 7.2. Effective permeability determinations for various fault system models at the three outcrops

	Belah Scar		George Gill		Molly's Castle	
D/L scaling	k_{e1} (mD)	k_{e3} (mD)	k_{e1} (mD)	k_{e3} (mD)	k_{e1} (mD)	k_{e3} (mD)
Model A. D/T scaling as measured, $k_f=1$ mD						
$D=0.01L$	728.50	351.43	585.44	68.41	806.69	490.30
$D=0.01L^{1.5}$	760.21	413.20	581.31	63.34	810.37	548.98
$D=0.001L^{1.5}$	672.25	262.32	73.03	33.10	754.75	307.42
$D=0.001L$	460.21	242.43	63.08	30.57	564.26	292.59
Model B. D/T scaling modified, $k_f=1$ mD						
$D=0.01L$	756.09	416.54	634.92	146.92	865.26	649.54
$D=0.01L^{1.5}$	781.94	460.92	631.06	142.22	865.43	670.12
$D=0.001L^{1.5}$	706.32	331.22	195.09	93.31	834.17	547.48
$D=0.001L$	542.20	313.71	174.47	89.63	763.40	546.75
Model C. D/T scaling as measured, k_f varies as a function of D						
$D=0.01L$	691.08	88.25	602.89	50.49	820.83	431.03
$D=0.01L^{1.5}$	752.85	344.03	620.78	83.70	830.37	594.39
$D=0.001L^{1.5}$	637.85	67.97	105.01	22.90	779.80	246.12
$D=0.001L$	35.84	16.95	23.18	10.82	216.08	114.82
Model D. D/T scaling modified, k_f varies as a function of D						
$D=0.01L$	702.21	101.52	659.44	102.24	858.36	519.16
$D=0.01L^{1.5}$	763.90	362.29	694.12	154.26	866.96	674.63
$D=0.001L^{1.5}$	652.73	84.49	242.29	63.29	829.92	388.75
$D=0.001L$	50.41	24.10	69.86	33.50	427.92	260.37

Figure 7.2 shows all k_{e3} determinations as a function of 1D characteristics of the system. k_{e3} does not vary systematically as a function of scan-line density (d_S) or cumulative displacement frequency power-law exponent (c_1). The lack of a relationship between effective permeability and scan-line density is particularly important, as scan-line density is the most common fault density reported for wells. There is a general permeability correlation with both ε_1 and a_1, the parameters which are most representative of the over-all fault density of a system, but the huge range at each outcrop as a function of displacement / length scaling and fault permeability models completely outweigh these crude trends.

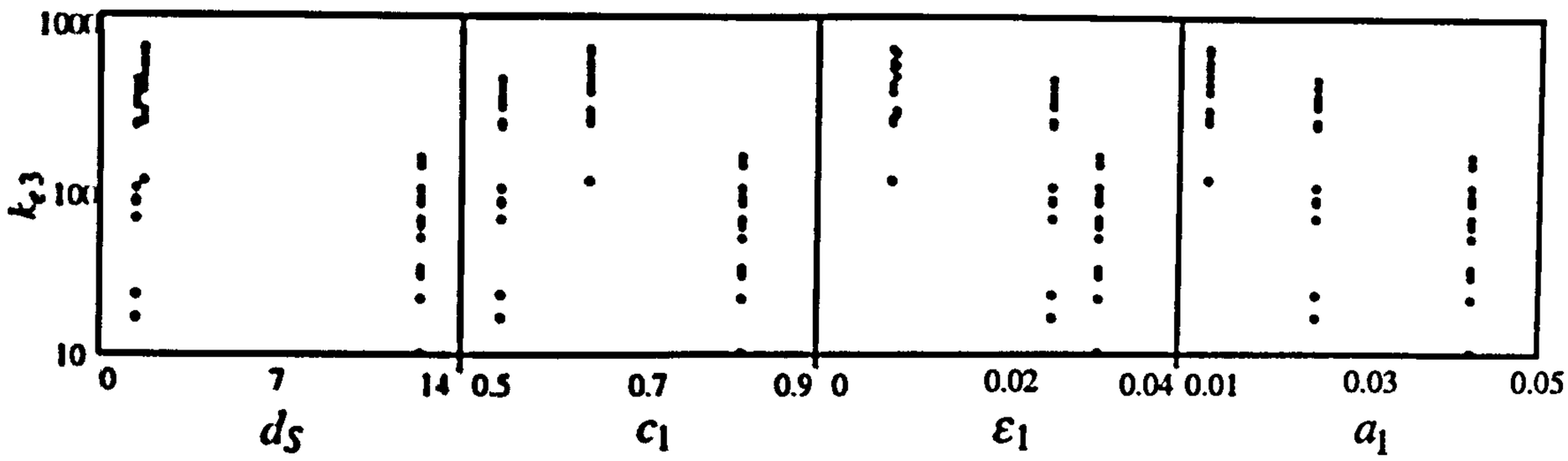

Figure 7.2. Outcrop minimum effective permeability as a function of scan-line density (d_S), cumulative displacement frequency power-law exponent (c_1), maximum extension (ε_1) and displacement frequency coefficient (a_1) for the cases on Table 7.2.

The mean effective permeability at for each model are [606, 243] mD at Belah Scar, [372, 74] mD at George Gill, and [743, 455] mD at Molly's Castle. From Table 7.2 it is clear that considerable uncertainty is associated with any of the permeability determinations; especially regarding the fault permeabilities. Effective permeability can be calculated rapidly for many sensitivity cases, and this uncertainty could be incorporated stochastically in reservoir flow models, as will be discussed in the following Sections.

7.2.5 Section summary

In summary, the scaleup method can be used to gain a quick estimate of the principal directional effective permeabilities based on descriptions of the scaling, density and permeability properties of the fault system. Effective permeability is extremely sensitive to differences in fault scaling. Even from well characterised outcrops, it is impossible to determine a single effective permeability value, due to uncertainties in the description of the faulting. In general, the scaling characteristics of deformation band systems (i.e. low c_1 and low r) results in a greater permeability reduction than would be observed in other lithologies with the same fault and matrix permeability and brittle strain.

7.3 Effective permeability determination from seismic extrapolation

In this section, results from published fault analyses on the North Viking Graben are used to estimate the effective permeability incorporating sub-seismic faulting. These fault system analyses have highlighted the degree of uncertainty in fault scaling parameters as a consequence of different interpretations within the same area (Walsh *et al.*, 1991; Marrett and Allmendinger, 1992; Roberts *et al.*, 1993; Westaway, 1994). These differences are discussed in Section 7.3.1. Subsequent Sections contain an assessment of the influence on this uncertainty on the ranges in effective permeability calculated.

7.3.1 Introduction

Roberts *et al.* (1993) estimate that the total Jurassic extension between the East Shetland Platform and the Fenno-Scandian High (an area comprising, from west to east, the East Shetland Basin, the Tampen Spur, the main axis of the Viking Graben, and the Horda Platform) is 0.15, rising to about 0.3 in the main axis of the graben, and falling to about 0.05 on the Horda Platform. Estimates for the sub-seismic contribution to this strain vary. Roberts *et al.* (1993) estimate that about 35% of the extension is sub-seismic, while Westaway (1994) calculates that sub-seismic faulting accounts for only 25% of the total extension. Walsh *et al.* (1991) suggest a sub-seismic contribution of about 40%, while the largest estimate (Marrett and Allmendinger, 1992) is that up to 60% of the extension could be sub-seismic. The average extensional value of Roberts *et al.* (1993) of 0.15 includes a 35% sub-seismic contribution, and therefore implies that the seismically visible extension is about 0.1.

Estimates for the effective permeability of idealised faulted formations in this area have been calculated, for a variety of fault models. Four parameters are modelled; the sub-seismic contribution to extension (ε_1), the cumulative displacement frequency power-law exponent (c_1), displacement / length scaling (B and n) and displacement / thickness scaling (F and r). Fault orientation parameters are taken as $\alpha = 15°$ and

$\delta = 70°$. Sub-seismic extension values taken are 20% or 40% of total extension. Two values of the exponent c_1 are modelled; 0.6 and 0.8 (the latter being the value reported by Walsh *et al.*, 1991; for the seismic faulting in this area). The same four cases of displacement / length scaling are used as in the previous section. Displacement / thickness scaling is also an unknown, so four plausible relationships are used (illustrated on Figure 2.11). Sub-seismic extension is assumed to be accommodated by faults with displacements in the range 1 mm $\leq D <$ 20 m.

7.3.2 Effects of uncertainty in system scaling

Based on combinations of maximum extension (ε_1), fault orientation (α and δ) and displacement frequency power-law exponent (c_1), a_1 is calculated from Equation 6.8. From this value of a_1, W can be calculated from Equation 6.9. For the sub-seismic fault population to be coherent with the seismic faulting, W should correspond to the average spacing of faults with $D \geq 20$ m. This length should be obtainable from the analysis of the seismic data, however different datasets give different values of W (e.g. Walsh *et al.*, 1991; Figure 2b implies $W \approx 1200$ m. Roberts *et al.*, 1993; Figure 9b implies $W \approx 600$ m). For the cases considered, W varies between 150 m ($\varepsilon_1 = 40\%$, $c_1 = 0.6$) to $W = 935$ m ($\varepsilon_1 = 20\%$, $c_1 = 0.8$).

Combinations of all four variables give a total of 64 fault system models, and in each case, effective permeability has been calculated assuming 1 mD faults in 1 D matrix (Appendix 3, Table A3.1). The data are considered in terms of the range of effective permeability results. If all cases are considered equally probable, then the minimum, most likely, and maximum effective permeability can be determined. Minimum k_e is defined as the values for which 10% of the cases give a lower k_e (p_{10}), most likely k_e is the value for which 50% of the cases give a lower k_e (p_{50}), and maximum k_e is the value for which 90% of cases give a lower k_e (p_{90}) (Figure 7.3).

Cumulative probability density functions (CDF) for [k_{e1}, k_{e3}] are shown on Figure 7.3. The uneven nature of the CDFs are due to incorporation of several sets of scaling parameters. All the displacement / length and displacement / thickness scaling cases considered are rather separate from each other (see Figures 2.10 and 2.11), and therefore the permeabilities calculated can change abruptly when sorted into a CDF. This effect is most apparent when fewer cases are considered for each CDF, or when sharp changes in fault permeability with scale are modelled (see Figures 7.4 and 7.5).

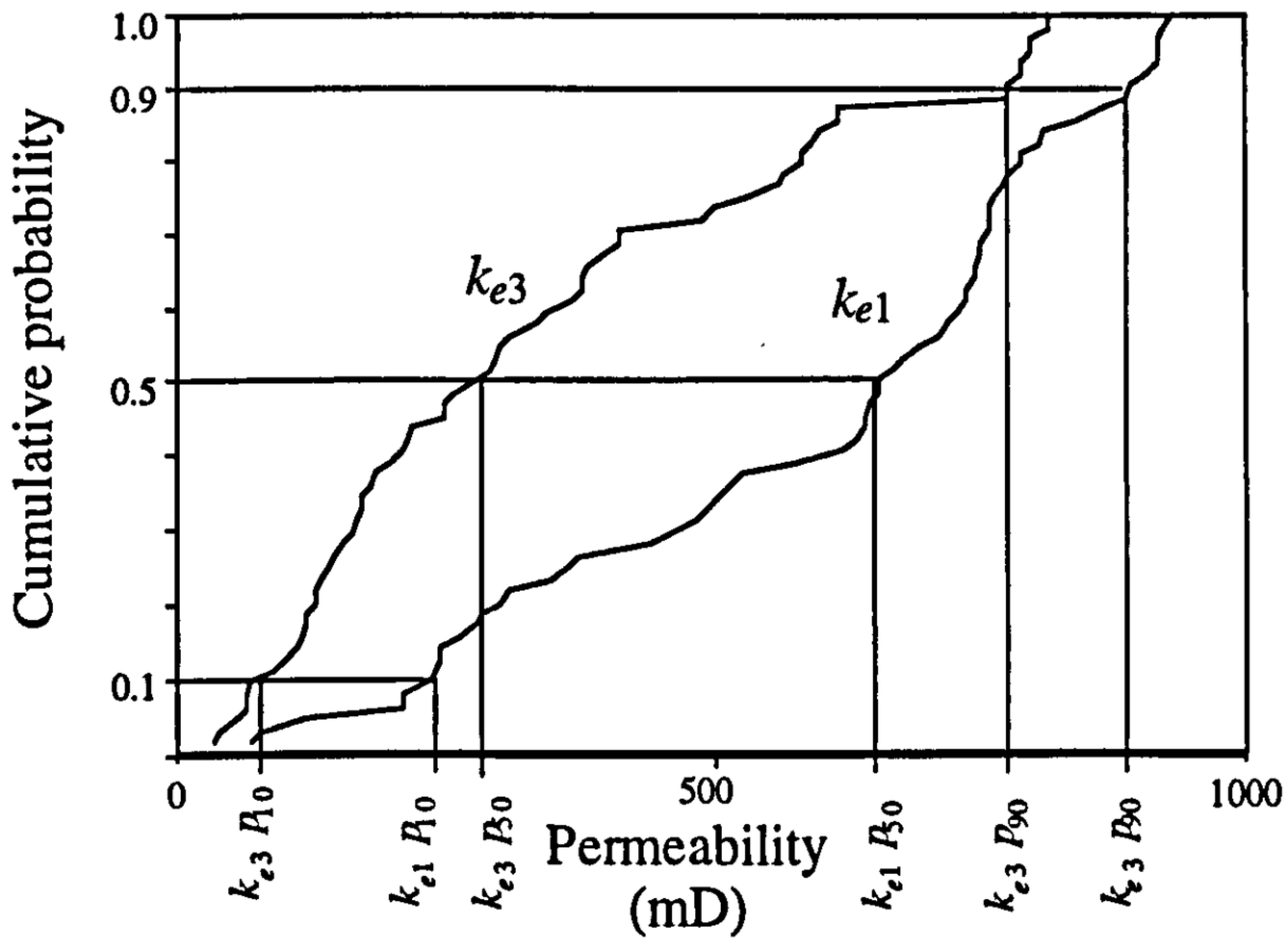

Figure 7.3. Cumulative probability density function (CDF) of effective permeability showing determination of minimum (p_{10}), most likely (p_{50}), and maximum (p_{90}) effective permeabilities

The 64 results yield a p_{10} of [234, 66] mD, a p_{50} of [654, 277] mD and a p_{90} of [893, 777] mD. This range, which is greater than one order of magnitude, indicates once more that effective permeability is extremely sensitive to the initial scaling assumptions, and not simply to the fault and matrix permeabilities. Below, the relative significance of this variability is addressed with respect to individual input parameters.

On Figure 7.4, the results are presented as CDFs of k_{e3} for each variable. On each of these plots, all the k_{e3} results are split between the selected values for each of the four variables. A comparison of the p_{50} values indicates the relative significance of each variable. By far the most important variable is the displacement / thickness scaling. p_{50} for this variable range from k_{e3} = 97 mD for $F = 10$, $r = 1.5$; to k_{e3} = 617 mD for $F = 100$, $r = 1$, a difference of 520 mD. The difference in k_{e3} is only 213 mD due

to the two values of sub-seismic extension; 77 mD due to displacement frequency power-law exponent, 77 mD; and 174 mD due to displacement / length scaling.

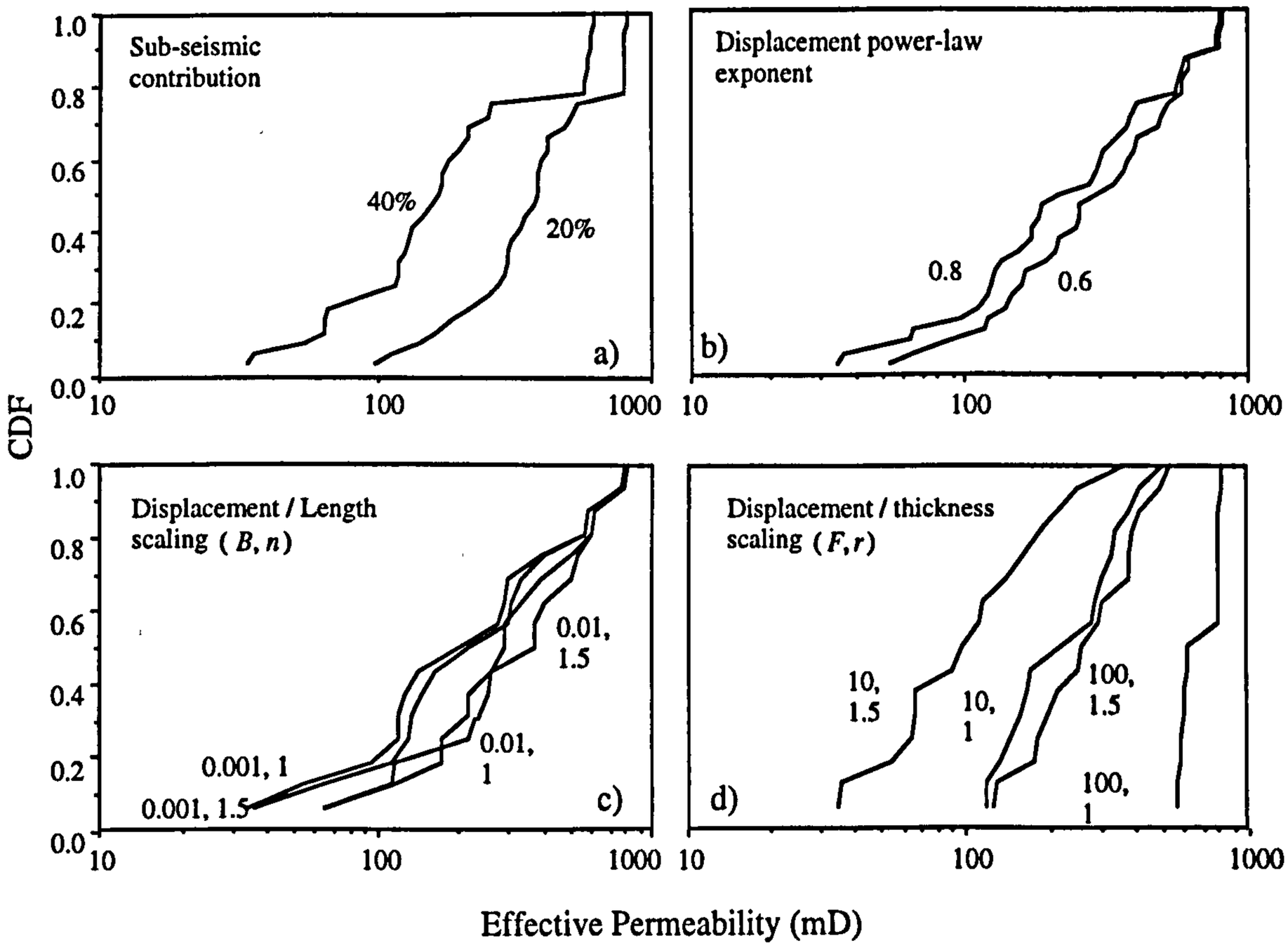

Figure 7.4. Cumulative probability density functions for the minimum effective permeability for the Northern North Sea calculations, assuming fault permeability of 1D and a matrix permeability of 1 mD for all scales of faulting. a) Sub-seismic contribution to total extension. b) Cumulative 1D displacement frequency power-law exponent. c) Displacement / length scaling. d) Displacement thickness scaling. In each case, effective permeability is determined as a function of combinations of the other three variables, assuming any combination to be equally probable.

The dependence on sub-seismic contribution is not surprising - this is the factor that determines the absolute fault density. The displacement frequency power-law gradient (c_1) determines the relative proportions of faults at different length-scales, and is not significant, because the maximum fault size is 20 m. Although a high c_1 indicates more small scale faulting, and therefore a greater reduction in effective permeability due to small faults, this is compensated by a lower frequency of large faults. The most important variable is displacement / thickness scaling, which controls the

transmissibility of each fault. Displacement / length scaling has only limited influence on the overall effective permeability value calculated. These relative influences are not constant, and their variation as a function of over-all system transmissibility is discussed below.

7.3.3 Tortuosity and transmissibility effects

In this Section, the same fault models considered in the previous section are utilised, but the fault permeability is modified to either k_f = 100 mD, or k_f = 0.01 mD. Results are given in Appendix 3 (Tables A3.2 and A3.3). For a case with a small fault / matrix permeability contrast (Figure 7.5 a, b), the modest permeability reduction is governed entirely by displacement / thickness scaling and therefore by changes in system transmissibility. In the case where there are five orders of magnitude between the permeability of the matrix and of the faults (Figure 7.5 c, d), small changes in the line density of the system have a profound effect on the connectivity, and because the transmissibility of the faults is so low, tortuous flow is a much more important mechanism. In this case, displacement / length scaling is the critical scaling parameter.

These tortuosity and transmissibility effects are manifest clearly on Figure 7.6. This shows the effective permeability estimations split into classes according to how many length-scales the systems are connected at. Each displacement / length scaling case can result in either a connected or a disconnected system at any of the four length-scales in the discrete hierarchy (see Table 7.1). Figure 7.6 shows plots of k_{e3}, vs. the number of connected length-scales for each system model. For k_f = 0.01 mD, there is a clear trend towards increased permeability reduction with increased connectivity. This trend is reduced for 1 mD faults, and for k_f = 100 mD, there is no trend. Tortuosity is most important at low k_f, but at high k_f transmissibility effects are paramount.

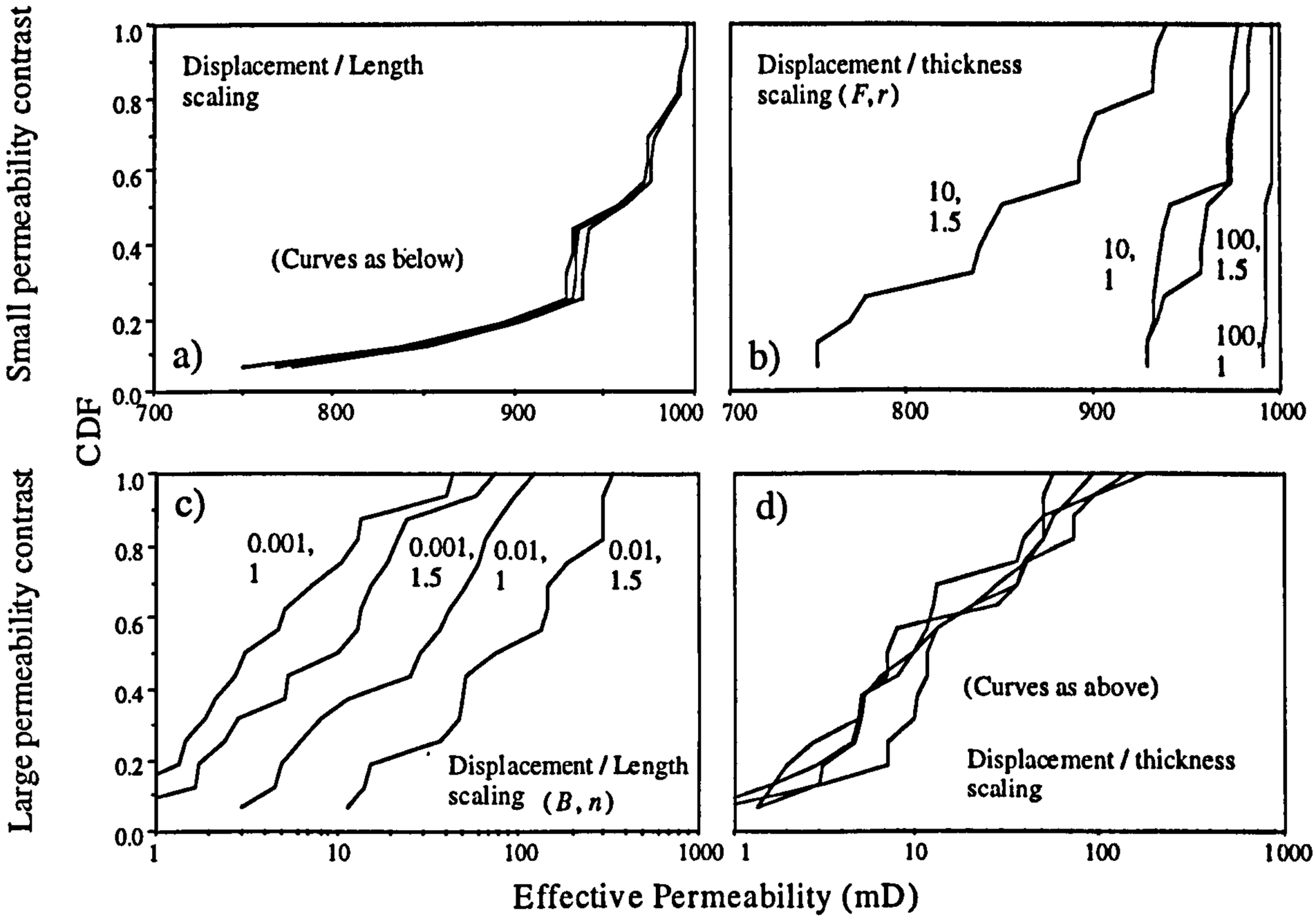

Figure 7.5. CDFs of minimum effective permeability for different displacement / length scaling and displacement / thickness scaling cases, for 100 mD faults (a, b) and 0.01 mD faults (c, d) in 1D matrix.

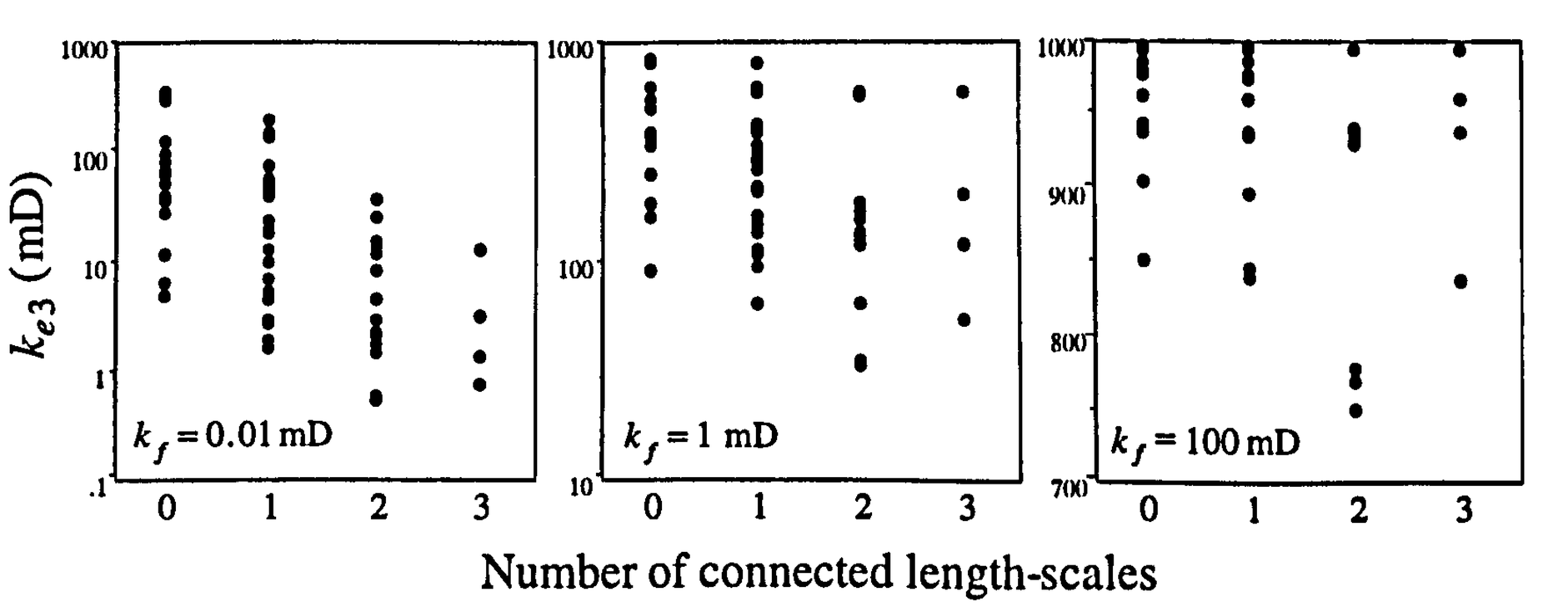

Figure 7.6. Minimum effective permeability as a function of the number of length-scales at which the hierarchical faults system is connected and the fault permeability. Plots for each case of fault permeability. Matrix permeability is 1 D.

Determining the effective permeability through a fault system is a complex function of transmissibility and tortuosity terms at a variety of length-scales. There are no hard-and-fast rules as to which variables are the most important. For very low permeability faults, connectivity (governed by displacement / length scaling) is critical. This parameter becomes less important for more transmissible faults, when the actual

transmissibility (governed by displacement / thickness scaling and fault permeability) is the most important variable. The value of sub-seismic extension (ε_1) is always critical as it determines overall fault density. The scaling frequency term (c_1) governs the relative fault density at different scales, and does not have a major influence over effective permeability *per se*. It is nonetheless highly significant as it is the parameter on which displacement / thickness and displacement / length correlations are based.

7.3.4 Section summary

The method developed allows a rapid calculation of the principal components of the 2D effective permeability tensor based on six input criteria: the sub-seismic strain in any block, the displacement frequency power-law gradient (c_1), displacement / length scaling (B and n), displacement / thickness scaling (F and r), fault orientation parameters (α and δ), and the fault and matrix permeabilities (k_f and k_m).

None of these parameters can possibly be known accurately for any particular position in any specific reservoir, and establishing probability distributions of the variables, coupled with analytical permeability prediction, allows assessment not only of the most likely effective permeability in any particular grid block, but also the confidence with which this value can be applied. It is considered that the uncertainty in effective permeability owing to the unpredictable nature of fault systems outweighs the inaccuracies caused by the simplified scheme used in this work.

7.4 Assigning effective permeability to faulted reservoirs

The determination of effective permeability incorporating all scales of sub-seismic faulting developed in this thesis can be considered as a *far-field* method. The differences between near-field and far-field modelling approaches were discussed in Section 4.1. In a far field method, precise details of the system, such as the locations of individual faults, are irrelevant, as flow is calculated over the representative elementary volume (REV) of the system. This section addresses whether the method

developed in this thesis is appropriate, by evaluating the assumption that an REV exists for sub-seismic fault systems. This assumption is fundamental to all far-field methods.

In Section 7.4.1, an effective permeability map is produced from published fault parameter maps of a North Sea reservoir. In Section 7.4.2 and 7.4.3, the spatial variability in these fault parameters is examined. Results indicate that the rate at which these parameters vary, are sufficiently low to allow REVs in the reservoir to be assumed. Therefore, effective permeability maps of the reservoir are appropriate, and sub-seismic faulting does not need to be modelled discretely - far-field approaches are reasonably accurate. Section 7.4.4 focuses on determining effective permeability in the vicinity of a well. For this situation, the REV is much too large for the permeability result to be applied. A near-field method is necessary for the near-well regions of a reservoir (e.g. for well test interpretations).

7.4.1 Effective permeability distribution

Two maps reproduced from Walsh *et al.* (1994) were presented in Section 2.3.2. These maps show the spatial distribution of two fault system parameters, *CUMFD* and c_1, determined from interpretation of the 3D seismic in the area. The maps are reproduced on Figure 7.7. The third map in Figure 7.7 is of k_{e3}, calculated from the other two maps, using the methods developed in this thesis. The k_{e3} map (Figure 7.7c) has been produced by assuming one set of displacement / length, displacement / thickness, orientation and permeability parameters. None of these are reported by Walsh *et al.* (1994). Therefore the variation in k_{e3} is the simple product of variations in *CUMFD* and c_1.

As shown in Chapter 2, large uncertainty is associated with determining scaling relationships for any fault system, and (as shown in Section 7.3), very large differences in effective permeability can be calculated as a function of assuming subtly different fault system scaling parameters. Therefore Figure 7.7c is no more than an example of

how the method can be applied to gain a permeability estimate from a sub-surface dataset. The values on Figure 7.7c are based on data about which no information is available. The map is not intended as a best model of the effective permeability in this region of the North Sea, it simply shows a possible map of permeability based on the scant data available. It displays, as have all the examples discussed in this chapter, that it is difficult to predict even broad trends in effective permeability distribution (i.e. the contours on Figure 7.7c) from trends in the various parameters which define the system: effective permeability is a complex function of all of these.

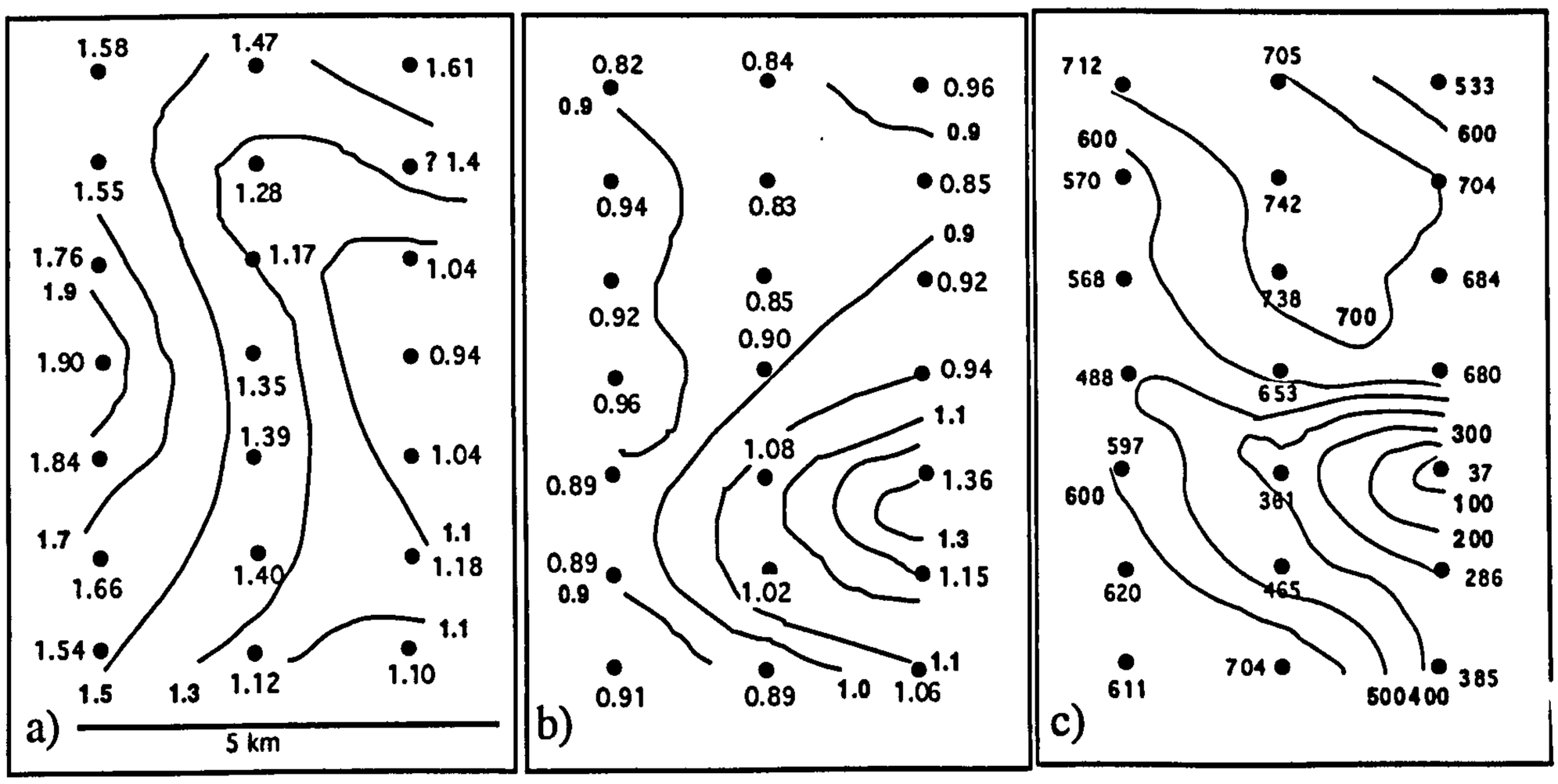

Figure 7.7. Maps of cumulative fault density (a) and displacement frequency power-law exponent (b), from Walsh *et al.* (1994), and minimum effective permeability, calculated from these maps (c). The *CUMFD* is based on 10 ms travel time, which is assumed equivalent to 20m displacement. Fault permeability is taken as 1 mD irrespective of fault size, and matrix permeability is 1 D. α is taken as 15°, displacement / length scaling $D = 0.01L$ and displacement / thickness scaling is $D = 100T$

Figure 7.8 demonstrates how the upscaling method can be used to generate stochastic reservoir permeability maps. In these examples, all geometrical and scaling terms are the same as in Figure 7.7c, but in each case the fault permeability has been determined stochastically at each control point and at each of the four scales in the discrete hierarchy. Fault permeability is the greatest source of uncertainty in any sub-seismic flow model, and these realisations capture this uncertainty. In these examples, fault permeability takes the range $0.1\,\text{mD} < k_f < 10\,\text{mD}$, by randomly sampling a rectangular PDF of the $\log(k_f)$. Even though the range in k_f in these maps is $\pm$ one order of magnitude, the main permeability trends observed on Figure 7.7c are reproduced in each realisation. Hence the fault scaling and geometrical characteristics of the system control the broad trends in permeability, notwithstanding the large uncertainty incorporated in the fault permeabilities.

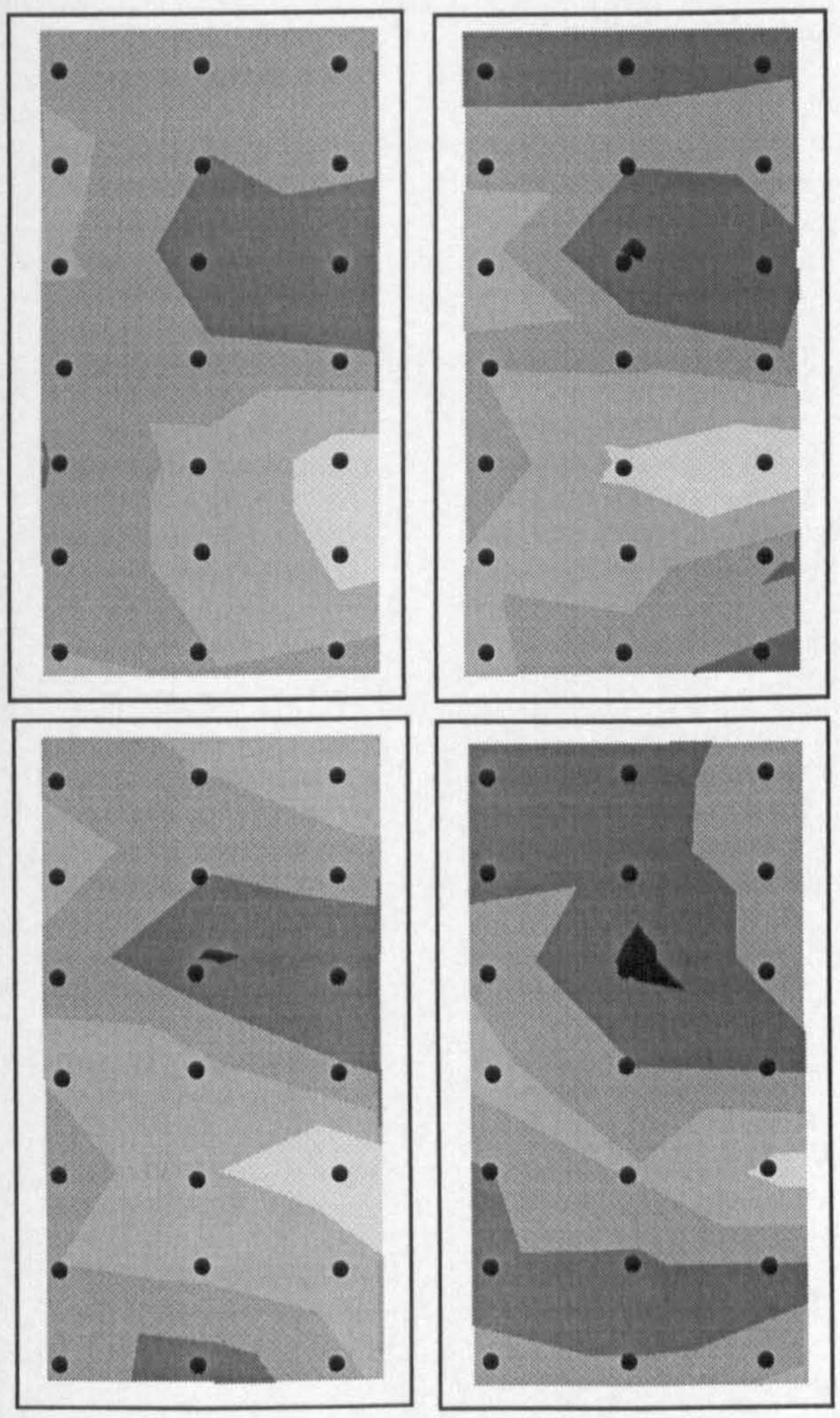

Figure 7.8. Four Equiprobable stochastic realisations of minimum effective permeability (k_{e3}) for the area in Figure 7.7. All scaling terms are deterministic, but the fault permeability is randomly selected in the range $0.1\,\text{mD} < k_f < 10\,\text{mD}$, independently at each control point and each level in the hierarchy. Matrix permeability is 1 D.

7.4.2 Effective permeability at the scale of the largest REV

In the example given above, each permeability value is calculated from a 10.5 km^2 region (Walsh *et al.*, 1994). The dimensions of a typical reservoir grid-block are about 100 x 100 m. Consider Figure 7.9a. This shows the *CUMFD* map used in the previous section, and the highlighted square (1 km^2) contains 100 grid-blocks. This region is enlarged on Figure 7.9b. On this figure, the square in the middle is one grid-block. Based on the maps of *CUMFD* and c_1, values of k_{e1} and k_{e3} may be calculated for this grid-block.

In determining a k_e value for this grid-block, the fault system is assumed to have an identifiable REV at each scale (see Section 5.1.2). Several steps are taken to determine the properties of the system within this volume. First, the parameter W is calculated. W represents the length of a representative sample of sub-seismic faulting, and enters the model through the displacement scaling relationship (Equation 2.1; $N_1(D) = a_1 W D^{-c_1}$). W is calculated from Equation 6.10 ($D_0 = (a_1 W)^{1/c_1}$), and D_0 is known as it is the seismic resolution (in these examples assumed to be 20 m). W therefore represents the average spacing of faults with displacements $\geq$ 20 m, and is the length within which sub-seismic faulting is determined. For the grid-block on Figure 7.9b, W is about 800 m. Therefore the total area over which fault density is homogeneous must be at least 800 m x 800 m, or 64 grid-blocks. This is large shaded box on Figure 7.9b. (in this discussion α is taken as 45° for the sake of simplicity). The effective permeability value calculated for this grid-block (568 mD), is therefore based on faulting in the entire shaded region.

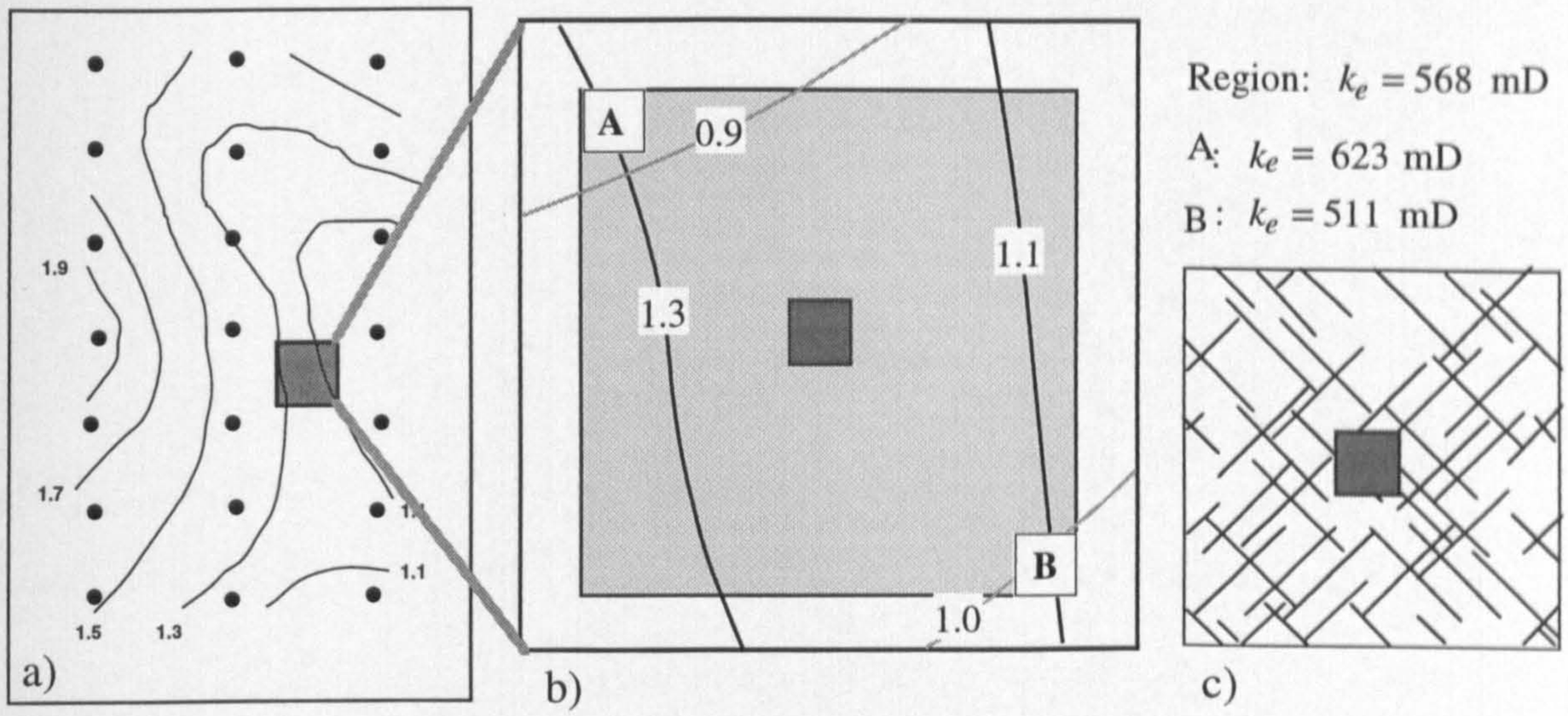

Figure 7.9. The representative elementary volume (REV) of the largest scale of sub-seismic faulting. a) Map of cumulative fault density, from Walsh et al. (1994) b) 100 grid-block region showing a single grid-block (dense pattern) and the REV defined with respect to W. Contours of *CUMFD* (black lines) and c_1 (grey lines). c) Map of the largest scale of the hierarchical fault model, at the same scale as b). This map shows a single grid-block and has a line density representative of the central grid-block in b). The area of this map is the REV for the effective permeability calculation (Figure 5.4), and its size depends strongly on the displacement / length scaling of the system.

It is clear from Figure 7.9b, that the assumption that the fault system within this region is homogeneous is wrong, as the area contains two fault density contours at a *CUMFD* interval of 0.2, and two displacement power-law exponent contours at a c_1 interval of 0.1. Effective permeabilities based on *CUMFD* and c_1 values at opposite corners of this area (A and B, figure 7.9b) have been calculated (apart from orientation, the same assumptions were used as in the previous section). Although both *CUMFD* and c_1 are different at A and B, they are not sufficient different to have a marked impact on the effective permeability calculated over this area. For this system, therefore, the strictly incorrect assumption that a fault system is homogeneous over the area necessary for an REV has not significantly compromised the result. Thus, the REV assumption appears to hold as long as regional gradients in scaling parameters are not too great, as in this sub-surface example. Another independent aspect of representivity needing consideration is addressed in the following section.

7.4.3 Effective permeability at the grid-block scale

The effective permeability calculated for the central grid-block on Figure 7.9b, is based on a sample of faulting within the larger shaded area, which is the area which contains a geologically representative sample of faults of the largest sub-seismic scale. The largest length-scale of the discontinuous model represents all faults in the displacement range 1 m < D < 20 m. All faults in this range are converted to a single length $\overline{L}_{pq}$ (see Section 6.5). Effective permeability of these faults is then determined as a function of the line density of the faults in this system, within a representative area. This representative area is a function of the length $\overline{L}_{pq}$. For the flow simulation models, this representative area is taken as being four times the width of each fault (i.e. the widths of the systems in Figure 5.11, Section 5.2).

$\overline{L}_{pq}$ is a function of the displacement frequency and displacement / length scaling terms (Equation 6.31). Figure 7.9c shows the representative area for faults in the largest sub-seismic scale-range 1 m < D < 20 m, for the central grid-block in Figure 7.9b, based on a displacement / length relationship $D = 0.01L$. This map, which is at the same scale as Figure 7.9b, shows that this area is slightly smaller than the area which must be considered as a function of W (i.e. the area shown on Figure 7.8b). Therefore, this assumption does not compromise the permeability calculated for the grid-block, as the system can be assumed more or less homogeneous over this region. Extreme cases of displacement / length scaling can result in needing a much larger REV. In this example, were $D = 0.001L$ used instead of $D = 0.01L$, the area in Figure 7.9c would be about 10 times larger than the area in Figure 7.9b. Clearly, in this case, the assumption that the system variability occurs over length-scales larger than that needed for a flow determination to be made, is incorrect and a method relying on an REV is impossible.

7.4.4 Summary and discussion

Sections 7.2 and 7.3 have considered the implications of assuming an REV at the largest sub-seismic length-scale. This discussion has shown that the assumption does not jeopardise far-field effective permeability estimations, so long as:

A) The area over which the scaling and density characteristics of the system vary significantly, is larger than the area needed to define a representative sample of sub-seismic faulting. This area is related to the length W.

B) The area over which the scaling and density characteristics of the system vary significantly, is larger than the area needed to define a geometrically representative sample of the fault system for flow analysis. This is approximately four times the length of the faults at each scale in the discrete nested model.

The significance of variations in these parameters depends on the overall properties of the system (fault density, fault permeability, etc.) In the case studied, a change in c_1 of 0.1, and in *CUMFD* of 0.2 (cumulative faults per kilometre, calibrated to seismic resolution) do not produce significant differences in effective permeability. Stratigraphically, the area considered overlies a salt dome (Walsh *et al.*, 1994). Therefore the rate of change of fault system scaling parameters in this example are likely to be higher than normal. Notwithstanding this, both the conditions listed above were satisfied (figure 7.9).

These issues address the assumption that an REV can be defined at the largest sub-seismic scale, in the discrete model, but did not consider smaller scales. If faults system are considered to be fractal, then variability in them should be more or less self-similar. In other words, the areas over which fault systems characteristics vary is in direct proportion to the size of fault being considered. Therefore, if a geometrical REV

can be assumed at the largest scale, a (smaller) REV can also be assumed at every smaller scale in the discrete hierarchy.

One final point remains to be made from Figure 7.9, in part also discussed (in a different context) by Begg *et al.* (1989). The effective permeability calculated is an average value over the entire, geometrically representative area (figure 7.9c). Therefore the effective permeability calculated is appropriate for this region of the reservoir (the shaded area on Figure 7.9b), and can be assigned to each grid-block in this region in a reservoir simulation model. The representative area, however is much larger than a grid-block. Indeed, each fault in Figure 7.9c is larger than a grid-block. The permeability calculated, therefore, is not appropriate to any sub-REV scale, as it is an effective permeability at the REV scale. The actual local permeability in a smaller region of a reservoir might become important at the grid-block (or smaller) scale, for instance at a well. In this context, the global (REV) effective permeability is irrelevant, and more local aspects of the system must be considered. This is discussed in the following Section.

7.4.5 Effective permeability at the well scale

The permeability determinations in this thesis apply a far-field approach, in which the area of interest is assumed to be larger than the REV. This approach cannot be applied close to wells, as particular details of the fault system structure have a great influence on the flow responses observed. The determination of the outcrop permeabilities given in Section 7.1 explicitly included the W term from each outcrop. Therefore the outcrop determinations of k_e are based on the faulting up to the largest fault observed at outcrop, rather than all sub-seismic faulting.

Figure 7.10a shows the variation in D_0 expected as a function of the length of the sample being considered, based on the fault system scaling systematics at each outcrop (Equation 6.10). From pairs of values of D_0 and W, effective permeability at each W

can be calculated, based on the D_0 at each scale. (Figure 7.10b). Note that the slight inflections in the curves in Figure 7.10b occur as a consequence of introducing a new scale-range into the discrete hierarchical model (the number of scale-ranges is determined as a function of D_0). The subtlety of these inflections implies that introducing a new length-scale into the hierarchy does not cause significance changes in effective permeability.

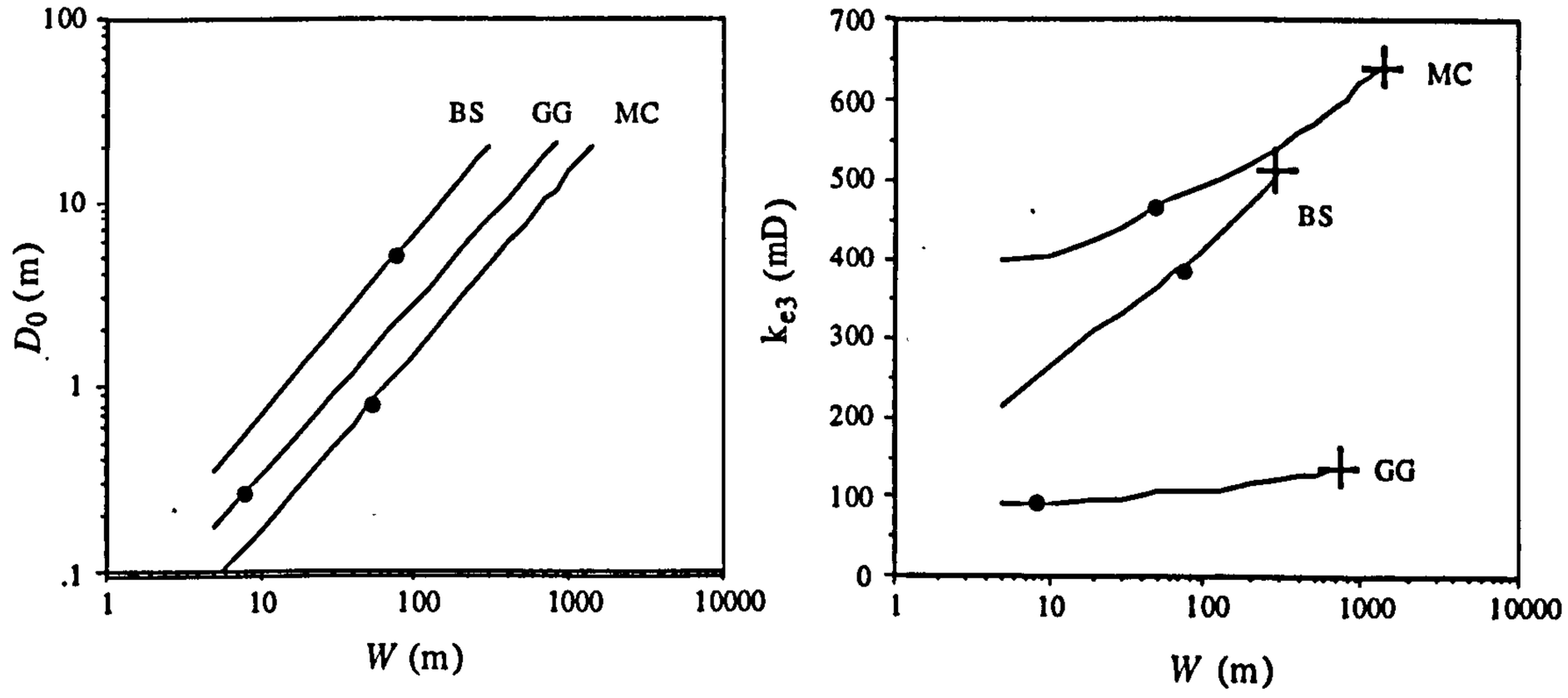

Figure 7.10. a) The largest fault expected (D_0) in a sample as a function of the length of the sample (W). b) Minimum local permeability (k_{e3}) as a function of sample length, for D_0 up to 20 m. Dots are the scales observed at outcrop. Crosses are the REV effective permeabilities. BS: Belah Scar. GG: George Gill. MC Molly's Castle. k_{e3} calculation based on k_f = 1 mD, k_m = 1 D, α = 15°, $D = 0.001L^{1.5}$, displacement / thickness scaling as Case B (Table 7.2).

At D_0= 20 m, the system is considered to be representative of all sub-seismic faulting, and so this value of k_e is considered the regional, REV scale, effective permeability (*c.f.* Figure 7.9). At the scale of a well, however, the regional permeability is of secondary significance compared to the local effects. Therefore the most appropriate permeability determination is one which considers W as a function of the length of the well, and D_0 as the largest fault observed in the well (i.e. using the methods discussed in Section 7.1, the results of which are the dots on Figure 7.10b). This permeability can be significantly different to the regional effective permeability (the crosses on Figure 7.10b).

Whilst the approach used in Section 7.1 avoids the problems associated with the size of W (e.g. Figure 7.9b), there method still includes the assumption that permeability may be averaged over the geometrical REV at each scale (e.g. Figure 7.9c). This is not a valid assumption for considering the flow response during a well test, as over the duration of a well-test it is unlikely that flow within the REV is sampled. Modelling fault permeability close to wells requires a near-field method: discrete modelling of individual faults. Approaches for determining k_e close to wells using the methods discussed in Section 7.2 are incorrect, as they assume an REV. These approaches may, however, use the data obtained at a well to determine likely REV k_e in other (undrilled) portions of the reservoir believed to have similar fault systematics (e.g. Figure 7.10).

7.4.6 Section summary

Section 7.4 has shown that the far-field effective permeability scaleup method developed in this thesis may be applied to a reservoir model of fault distribution with comparatively few problems related to assuming separation of scales and an REV at each scale separation. For the example considered here (the maps of Walsh *et al.*, 1994), the spatial variability of the fault population systematics at the largest sub-seismic scale occur over similar distances to those required for the system to have a geometrical REV. The differences in fault system structure in the REV are not large, and therefore the lack of an REV is unlikely to cause problems. The REV however is much too large for this approach to be used at the scale of a well, and in such cases, near-field modelling methods should be used.

7.5 Discussion

This thesis is concerned with effective permeability, but production from most oil reservoirs involves interaction of two immiscible phases. Section 7.5.1 addresses briefly some of the differences in modelling approach which should be made to determine effective two phase flow properties in sub-seismic faults systems. Section 7.5.2 focuses on damage zones. General conclusions arising from this Chapter are contained in Section 7.6.

7.5.1 Two phase flow

As shown in Chapter 5, the effective permeability through a fault system depends on tortuosity and transmissibility terms. Provided the system is representative it is independent of boundary conditions and scale. Two phase flow, on the other hand, is governed by dynamic, saturation dependent, relative permeability and capillary pressure functions. Waterflooding of sandstones is usually considered an imbibition process, in which a wetting phase (water) displaces a non-wetting phase (oil). During a waterflood, recovery is determined by the interplay of viscous, capillary and gravity forces. Capillary forces are most significant at smaller length-scales or lower flow rates (e.g. Ringrose *et al.*, 1993). The capillary entry pressures of low permeability baffles may result in high residual oil saturations in high permeability matrix, a phenomenon observed in experimental waterflooding of heterogeneous slabs (Huang *et al.*, 1995). At larger scales or higher flow rates, viscous forces dominate two phase flow processes, resulting in less capillary trapping. This effect results in preferential inhibition of oil recovery at smaller length-scales (Figure 7.11).

The four systems in Figure 7.11 have an identical geometrical arrangement (controlling tortuosity) and gouge density and fault permeability (governing transmissibility. Therefore they have identical effective permeabilities. The systems, however, are at different scales. In the smallest model, the faults are 0.1 cm thick and the matrix grid-

cells 4.95 cm. These are increased by an order of magnitude in each simulation run, and the largest has 1 m thick faults and 49.5 m thick matrix cells.

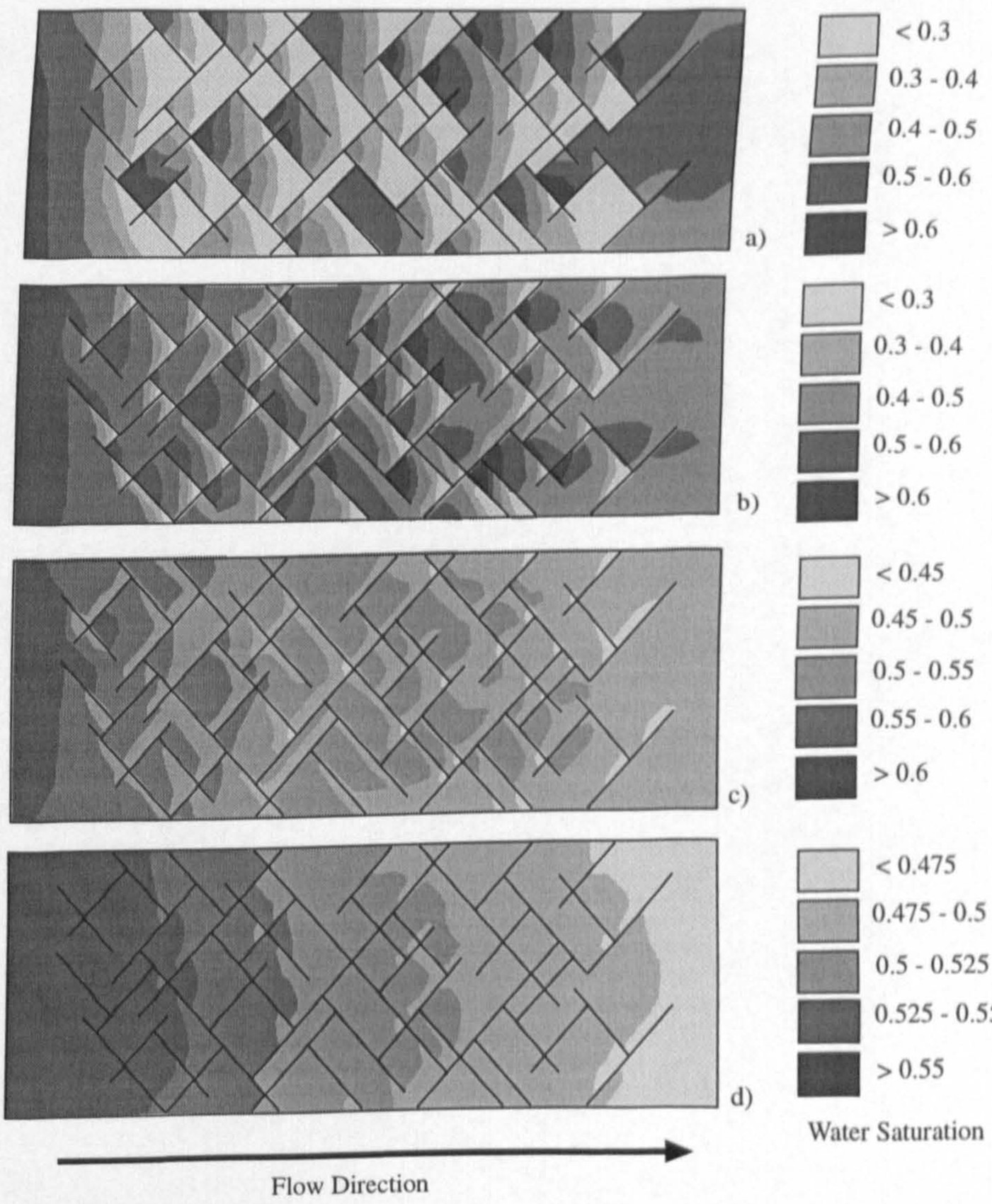

Figure 7.11. Results from waterflooding a geometrically similar fault system at different scales. Maps of water saturation after 2 pore volumes (2PV) of water injected at a Darcy velocity of 1 ft / day. Model length is 3 m (a), 30 m (b), 300 m (c) and 3 km (d), The faults are 1 mm , 1 cm, 10 cm and 1m thick. k_m = 1 D, k_f = 10 mD. The capillary pressure and relative permeability curves used in these models are determined from the empirical relationships given by Ringrose and Corbett (1994). Total recovery in the largest model is about twice that in the smallest model, due to capillary trapping in small compartments.

A set of dimensionless ratios (scaling groups) incorporate the fundamental physical processes active in two phase flow (e.g. Rapoport, 1955; Shook *et al.*, 1992). Gravitational forces can be ignored in this example, as the models are horizontal and two dimensional, with a constant thickness. The relevant scaling group relates viscous to capillary forces.

A 1D form of the viscous / capillary ratio is:

$$uL\mu_o / k(dPc / dS), \qquad (7.1)$$

where u is the Darcy velocity (distance / time), L is a length term (e.g. the distance between fault baffles), μ_o is the oil viscosity, k is average permeability and (dPc / dS) is the gradient of capillary pressure with respect to phase saturation. When the viscous / capillary ratio is high, the system tends towards viscous dominated flow, and recovery is enhanced. The only parameter in 7.1 which varies in Figure 7.11 is L. As the viscous / capillary ratio is directly proportional to L, the ratio increases as a function of length-scale, and the flow regime for the larger length-scales tends towards viscous dominated flow with increased recovery.

Unlike effective permeability, waterflood recovery also depends on fault clustering (Figure 7.12). These six 1D models each contain fourteen 10 mD faults in 1 D matrix. The effective permeability of each model is the harmonic average of the system (723 mD). This is a static quantity, and does not vary as a function of clustering. In a waterflood simulation, the models originally contain oil and irreducible water, then water is injected into one end of the model and oil is produced at the other. The flow of oil through each fault is controlled by its relative permeability. At low water saturation, the faults are more permeable to oil than water, and the converse is true at high water saturation. As the waterflood approaches a fault, some oil will be trapped behind it, as the water saturation in the fault rises to a value at which it is no longer permeable to oil,

even though oil is still the more mobile phase in the matrix. The amount of oil flushed from each compartment is a function of the compartment size. In large compartments, the amount of trapped oil is small, and some distance upstream of the fault, the water saturation after waterflooding is the lowest residual water saturation possible for the matrix, under the particular pressure conditions operative. In smaller compartments, there is insufficient distance upstream of the fault for this endpoint saturation to be reached, and so a greater proportion of oil is trapped.

In a 1D case, the recovery from any compartment is a function of the size of that compartment, and is independent of the sizes of the surrounding compartments. In an homogeneous system, all compartments are of a similar size, and therefore all have a similar recovery. In an heterogeneous case, there are many small compartments with low recoveries and a few large ones from which recovery is much greater. As the large compartments contain the bulk of the original reserves, the total recovery from a clustered system is greater.

Oil recovery is therefore dependent on the scale of the system, as at smaller length-scales the capillary forces in the system become more significant. The fault system

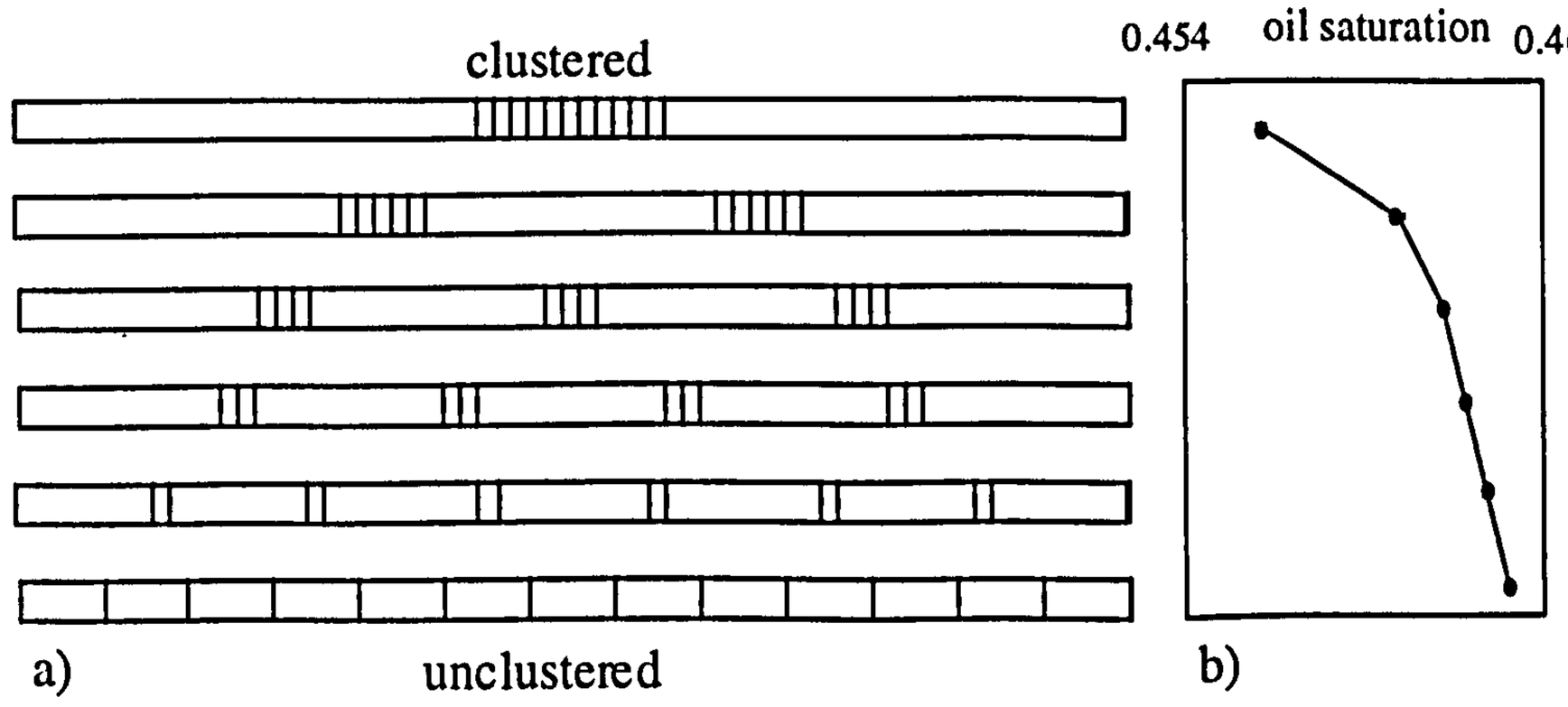

Figure 7.12. 1D simulation models with identical fault density. Two faults are maintained at each end of the model, and the other twelve show variable clustering. k_m = 1 D, k_f = 10 mD . Model length is 17 m , and all faults are 4 mm thick. b) Oil saturation at 10 PV

structure determines the distribution of high capillary pressure regions, and therefore oil recovery is most sensitive to the structure of the fault system at capillary dominated length-scales.

In summary, single phase permeability in a sub-seismic fault system requires determination only of effective permeability, while two phase scaleup requires both effective permeability and pseudo relative permeability and capillary pressure functions. Both the scale of the model, and details of the geometry (particularly the degree of compartmentalisation and clustering) are more important in two phase flow. Because two phase flow is dynamic, there is no unique solution for any particular fault model - different fluid properties and different pressure conditions for the same volume give different effective two-phase flow properties even if the volume is geometrically representative. Determining effective two phase flow properties as a function of sub-seismic faulting requires both a more complex fault model (incorporating clustering) and a more complex flow determination procedure than effective permeability.

7.5.2 Fault clustering and damage zones

In the method developed in this thesis, faults are assumed to be distributed uniformly within the area being considered. Introducing fault clustering into the model results in a larger geometrical REV (Figure 4.29), however (as argued in Sections 1.3 and 3.4), effective permeability does not vary as a function of clustering within a system at a single length-scale, provided that connectivity is honoured, and that a geometrically representative system is considered. Clustering between faults of different length-scales (damage zones) is likely to be much more significant, with the bulk of permeability reduction at any scale occurring primarily very close to faults at the larger scale, and little reduction elsewhere. Damage zones need to be better understood geologically before they can be incorporated in quantitative models (see Section 1.4.2).

Although scaling methods, incorporating some form of clustering systematics could be used to predict the frequency of sub-seismic clusters, there is no way of determining their locations, and there will always be a distinct probability that any well drilled into a faulted reservoir may encounter such a cluster, and be unable to attain sustainable flow rates. For example, the George Gill outcrop represents a fault cluster which would be seismically invisible. The very low effective permeability calculated from the George Gill dataset makes it unlikely that a well drilled on one side of the cluster could produce hydrocarbon from the other side of it. If sub-seismic clusters of this scale are connected, they may have a significant effect on reservoir production, and portions of the reservoir bounded by clusters of this type, which do not contain a producer and injector pair might have extremely low recoveries.

Methods for the determination of the effective flow properties due to sub-seismic faulting depend on the flow process and scales being considered. In the case of effective permeability, all sub-seismic scales contribute to permeability reduction, and geometrically similar systems at different scales give identical effective permeabilities. Geometrical variability for the same fault density may have a significant influence on effective permeability. It is particularly important that the correct connectivity characteristics are incorporated into a the flow model, as shown in Chapters 4 and 5. Two phase flow is sensitive to scale, and capillary trapping at small length-scales implies that scaleup of effective two phase properties is most significant when the smallest length-scales are considered. It is impossible to make deterministic inferences about likely sub-seismic fault systematics at any position in a reservoir, but small changes in assumptions regarding fault system scaling can have severe influences on the effective permeability determination.

At the scale of any geometrical REV, fault clustering within the volume is not a significant control on effective permeability, but would have a major influence on multiphase oil recovery. Determination of any effective flow property depends

fundamentally on the estimate of the fault density and connectivity at all scales in the grid-block, and for determination of the distribution of density throughout the reservoir, the model of clustering used is of great importance. In most siliciclastic reservoirs, realistic fault placement models should be based on the recognition that damage zones occur around faults at all scales. This means that the effective permeability in most of the reservoir will not be significantly reduced due to sub-seismic faulting, but there will be sub-seismic clusters throughout the reservoir, and these clusters may have a severe impact on recoverable reserves, particularly if they are connected.

Compartmentalisation of the reservoir by sub-seismic fault clusters can only be modelled probabilistically, based on as yet undefined fault placement and scaling criteria. The effective permeabilities of the compartment-bounding clusters as well as the likely sizes of the compartments themselves should be considered when making reserves estimates and determining development plans for structurally complex fields. For a geological variable about which there is such inherent uncertainty, and one for which small differences in modelling assumptions can lead to such significantly different results, probabilistic methods are a necessity. The topic of uncertainty management is fraught with complications (e.g. Øvreberg *et al.* 1992, Beliveau 1995, Patricelli and McMichael 1995, Laherrère 1995), but is the only realistic way of managing the likely impact of sub-seismic faulting in reservoirs.

Any reservoir containing seismically resolved faults *must* contain sub-seismic faulting. Most of these sub-seismic faults will occur in discrete clusters around larger faults, and in these clusters, k_e might be low. In the bulk of the reservoir, however, fault density will not be sufficiently high to influence flow. If a well drilled in a modestly faulted reservoir intersects a cluster, sidetracking a few hundred meters perpendicular to the regional structural grain should be sufficient to achieve respectable well deliverabilities.

7.6 Summary and conclusions

In this Chapter, the new effective permeability upscaling method developed in this thesis has been applied to a variety of real outcrop and sub-surface examples. This technique allows a rapid and simple estimation of effective permeability based on a quantitative geological description. The method incorporates a much more realistic geological model than has previously been used to assess the influence of sub-seismic faulting on flow (e.g. Omre *et al.*, 1994, Heath *et al.*, 1994; Walsh *et al.*, in press). In particular, the new method allows the simultaneous incorporation of all sub-seismic scales of faulting (> 4 orders of magnitude), and the fault systems have connectivity (incorporating fault splays) representative of the particular fault density at each scale. The models used by previous workers have been limited to a maximum of one order of magnitude of parallel (i.e. disconnected) faults.

The main conclusions of this Chapter are:

A) The scaling characteristics of small-scale faults in high porosity sandstones are such that they give a much greater permeability reduction for the same strain than faults in more competent lithologies (Table 7.2, Figure 7.10b).

B) Fault density (strain) must be extremely high for effective permeability to be severely reduced. On Figure 7.8, the effective permeability is, on average, about half the matrix permeability. These examples are for real sub-surface scaling and density parameters, and a fault permeability which is, on average, three orders of magnitude less than the matrix permeability.

C) Determination of an effective permeability in a region of a reservoir using a far-field approach is tenable. The area this effective permeability relates to, however, is large. In most of the reservoir, local permeabilities will be much

higher that the effective permeability, and only if a well encounters a fault cluster will it be lower (Section 7.5.2).

D) Tortuous flow becomes a significant mechanism only when k_f is at least four orders of magnitude less than k_m (Figures 7.4, 7.5). Tortuous flow is therefore relatively insignificant in deformation band and zone systems ($D < 1$ m) in which $k_f / k_m \approx 10^{-3} - 10^{-2}$, but very significant for slip surfaces (k_f / k_m as low as 10^{-7}).

E) There is no general rule as to whether small or large sub-seismic faults are most significant to flow. For effective permeability determination, the relative importance of length-scale is dictated by specific scaling and permeability characteristics of the system. Unlike effective permeability, two phase flow is scale dependent and oil recovery is preferentially inhibited at smaller length-scales in a self-similar system. Therefore small-scale faults are more important in two-phase flow than they are in single phase flow.

F) There is great uncertainty associated with assigning effective flow properties to faulted reservoirs. Simple, yet robust tools are needed to determine input into any uncertainty management program. The permeability upscaling method developed in this work allows, for the first time, effective permeability input to be determined directly from a set of explicitly defined fault scaling and geometry parameters.

CHAPTER 8

CONCLUSIONS AND RECOMMENDATIONS

This study was prompted by the lack of consensus as to the significance of deformation bands on flow in sandstone reservoirs. Deformation bands systems can be described quantitatively with the same techniques as other styles of faulting and fracturing. Therefore, while some of the conclusions arising from this work are specific to deformation band systems, many are significant to modelling flow in diverse fault and fracture systems. Conclusions from the study are drawn in the following sections, which also contain recommendations for future research in each topic.

8.1 Upscaling permeability in fault systems

The main theme of this thesis has been the presentation of a method to determine the contribution of sub-seismic faults to the effective permeability of undrilled regions of a reservoir. In order for such a method to be of practical use, it must satisfy certain conditions:

A) Determination of the geological input to the model must be possible from available reservoir data.

B) The method must be computationally expedient.

C) The characteristics of fault systems which are most significant to flow must be included.

To this end, the main features of the method developed are:

A) The input comprises three fault scaling relationships (cumulative displacement frequency, displacement / thickness scaling and displacement / length scaling), two fault orientation descriptors (related to strike and dip) and fault and matrix permeability values.

B) The output are minimum and maximum horizontal effective permeability components, comprising effects of all scales of sub-seismic faulting. These can be calculated on a simple spread-sheet.

C) The continuous fault system is simplified to a discrete hierarchy at particular scale transitions, and effective permeability at each level in the hierarchy is determined separately. Results from smaller scales determine the permeability input to larger scales. Effective permeability at each length is governed by transmissibility and tortuosity components. Both are honoured in the scheme used.

The method represents a significant advance towards the incorporating the effects of sub-seismic faults in reservoir simulation, however considerable work is still needed in order to extend this sort of treatment to considering 3D systems and two phase flow.

8.2 Fault system scaling

A theoretical consideration of the mechanics of deformation band, zone of deformation band and slip surface growth has focused on a scaling transition between zones of deformation bands and slip surfaces. A comparison of scaling characteristics at three outcrops shows:

A) Cumulative displacement frequency power-law exponent (c_1) increases as a function of increased sandstone porosity. This is a manifestation of deformation bands strain hardening.

B) The displacement / thickness power-law exponent is greater for small-scale faults in less porous sandstones. This is a consequence of the zone of deformation bands / slip surface threshold being at a lower displacement in higher strength (less porous) sandstones.

Displacement / length and displacement / thickness cross-plots from any single source rarely contain more than about two orders of magnitude of data, yet the data is usually scattered over more than one order of magnitude. This scatter is not a product of sampling methods, but is a real property of fault systems, and should be incorporated in flow models. A method for determining cross-plot correlations based on the more robust single parameter cumulative size frequency plots has been proposed. Additionally, weighting schemes must be incorporated to honour the significance on flow of the data scatter.

A) Displacement / thickness scaling should be weighted towards thin faults.

B) Displacement / length scaling should be weighted towards longer faults.

C) Displacement / permeability data should be weighted towards permeability highs.

Precise details of optimum transformations have not been studied. The natural variability in fault data is an area requiring further study, as are methods for incorporating this variability in flow models.

8.3 Fault connectivity

A quantitative method to describe fault connectivity has been introduced. The connectivity of any fault or fracture system can be represented as a point on a ternary diagram of isolated fault tips (I nodes), fault splays (Y nodes) and fault intersections (X nodes; Figure 8.1).

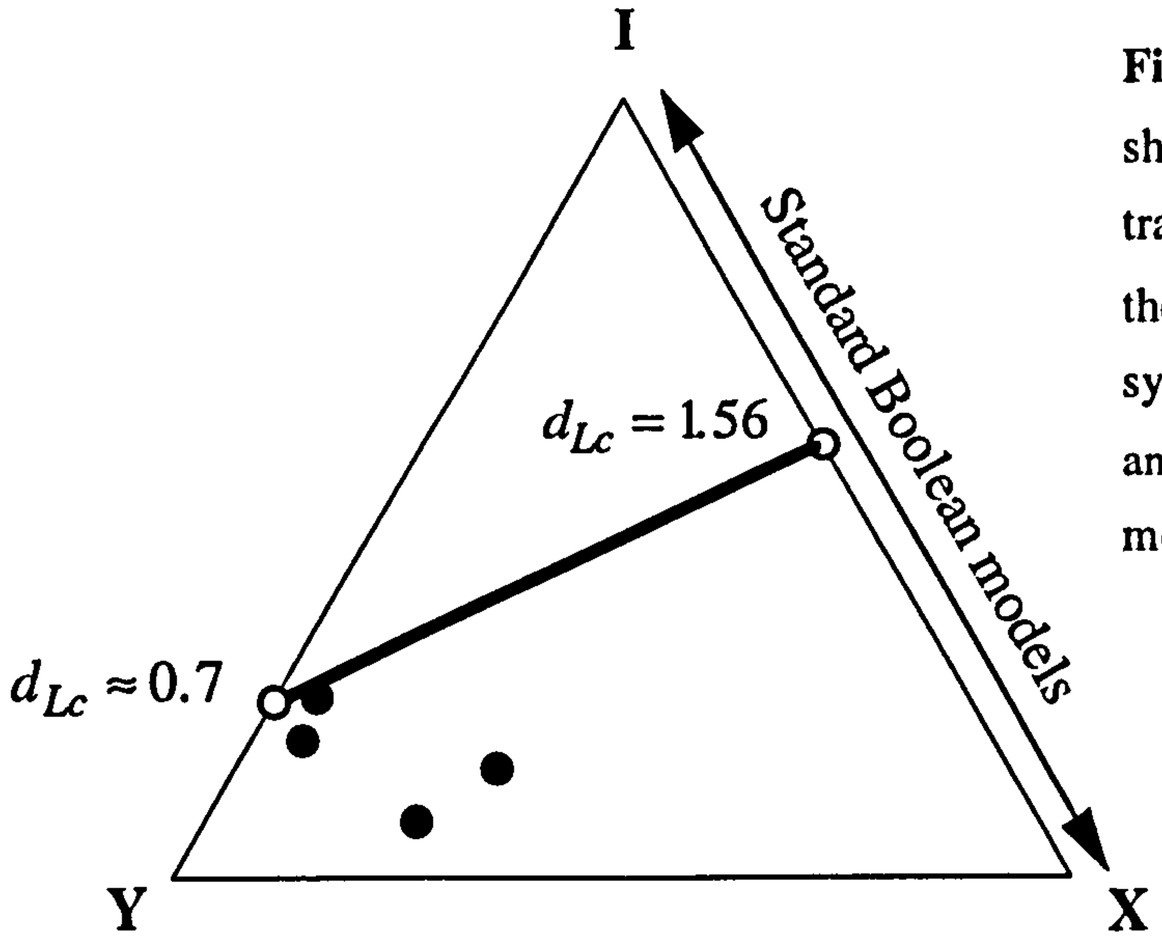

Figure 8.1. IYX ternary diagram showing the connectivities of of outcrop trace maps of deformation band systems, the percolation threshold of random systems and the critical line density of IX and IY systems. Conventional Boolean models cannot honour these node ratios.

A modification to conventional Boolean network modelling methods has been developed which allows the generation of networks in which the connectivity characteristics are determined as input. The systems formed can be clustered or anti-clustered. However, the novelty of the code is that clustering is a consequence of connectivity, and not vice versa. This subtle distinction is actually rather important, as connectivity in a fault or fracture system can be easily quantified, but it is difficult to quantify clustering. Therefore, the code can be used to generate networks which are more representative of natural systems than has previously been possible.

The main application of this code has been to deduce the percolation threshold of a system containing the high proportions of Y nodes observed in natural fault and fracture systems. The critical line density of a random orthogonal system of lines of constant length in which all connections are Y nodes is $d_{Lc} \approx 0.7$. This is less that half the critical line density for a conventional continuum system, in which all connections are X

nodes ($d_{Lc} = 1.56$). This entirely new result has profound implications, particularly on fracture flow, as it implies that flow is possible in system which might previously have been considered disconnected.

The percolation threshold has also been determined in terms of connectivity, and is represented as a line on an IYX ternary diagram. Irrespective of the fault density and orientation, the overall connectivity of a system may be judged purely based the node proportions.

One of the most exciting conclusions of this modelling is a purely geological one. Critical connectivity can be understood from the perspective of *self-organised criticality*, and the percolation threshold of an IY system is the optimum system attractor. Outcrop trace maps studied had connectivities close to this point (Figure 8.1). This analysis therefore provides evidence supporting the conjecture that faulting is a self-organised critical phenomenon. More systems need to be studied to strengthen this case.

Quantification and analysis of connectivity on IYX ternary diagrams is entirely new; previously, connectivity in geological systems has only been discussed qualitatively. Rather than extending this study to 3D, much is yet to be learned from 2D systems. With the incorporation of fault scaling systematics, the code could form the basis for a fault system modelling algorithm incorporating realistic connectivities. Due to these connectivities, geologically plausible clustering will emerge naturally in the models.

8.4 Flow in fault systems at a single scale

The geometrical controls on flow in a representative system of partially sealing faults of the same length has been simplified to:

A) A system transmissibility term, which is a function of the number, length and thickness of the faults, and of the fault and matrix permeability.

B) A system tortuosity term, which is a function of the number, length and connectivity of the faults.

C) A system anisotropy term.

The first important result arising from this work is the determination of a single transmissibility term. The parameter is termed fault heterogeneity (H), and is given by $H = 1 - k_h / k_m$, where k_h is the harmonic average permeability, and k_m is the matrix permeability. This new term is invaluable, as it reduces the number of independent variables to a manageable quantity. Any particular geometrical arrangement of baffles has been shown to have a single curve of fractional permeability vs. H, and from this curve, the effective permeability for any fault and matrix permeability and fault thickness can be determined (Figure 8.2). Tortuous flow is significant in systems in which fault heterogeneity is greater than about 0.5.

The second main innovation in the method lies in considering fault connectivity in a quantitative manner. This means that fault orientation only controls the anisotropy of the system, and that fault clustering has no effect whatsoever, and can therefore be neglected. Previous approaches relied on achieving connectivity through variations in orientation and clustering. Connectivity is the most important geometrical control on tortuous flow in either this kind of system or in fracture systems, and should therefore be incorporated as a fundamental variable.

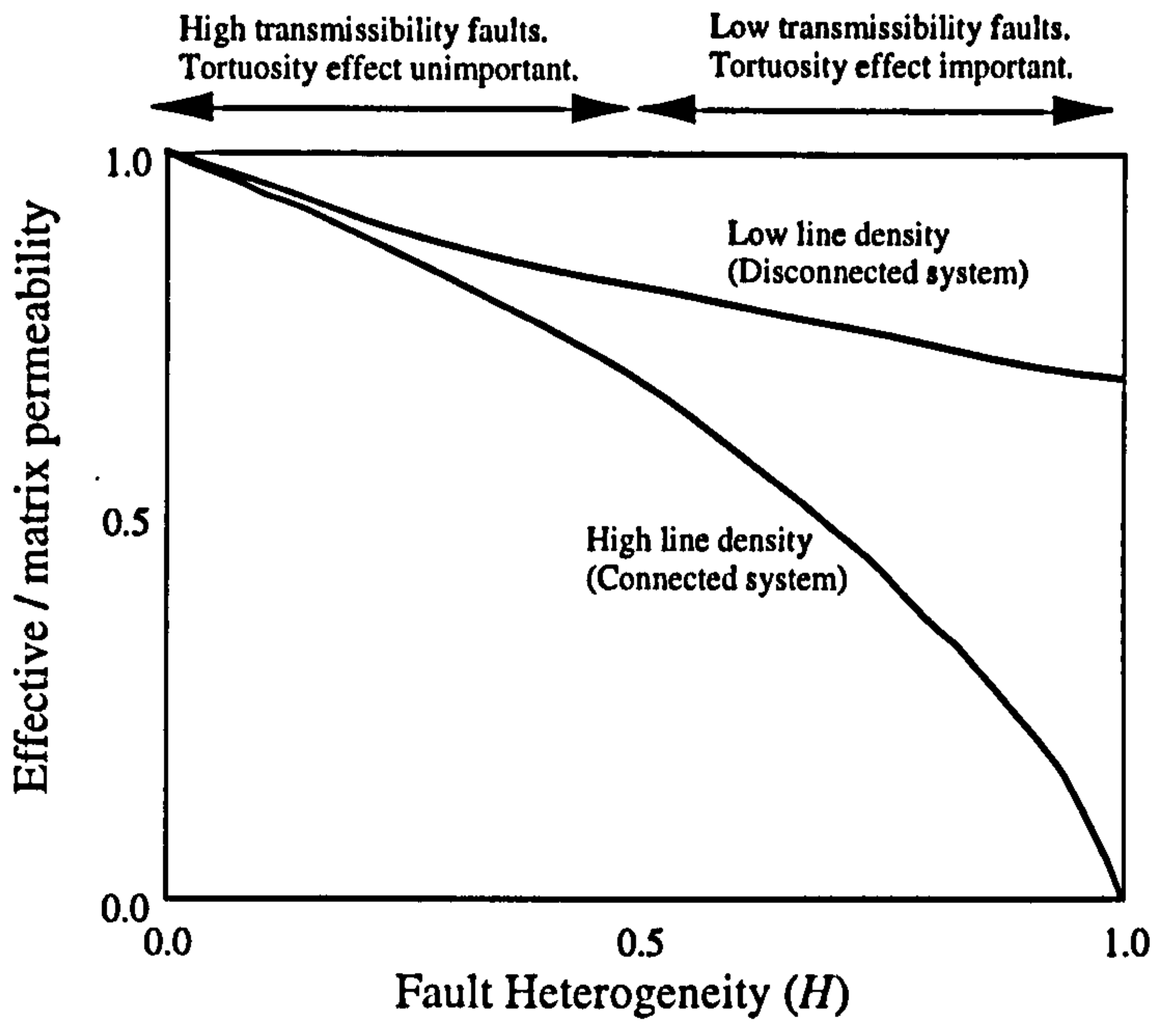

Figure 8.2. Effective permeability as a function of fault heterogeneity and line density.

Fault connectivity is incorporated through the line density term (d_L). For orthogonal systems, curves and equations relating effective permeability to H and d_L have been determined numerically. Based around geometrical relationships linking connectivity to orientation and line density, these empirical effective permeability results have been generalised to any orientation.

Type curves and equations are presented, from which the effective permeability of a system of baffles at a single length-scale, equally divided between two orientation populations at any angle, for any gouge density, line density and fault and matrix permeability can be determined. The method is increasingly uncertain if the angle between the two orientations is large, as the relationship deduced for comparing tortuosity of systems with the same connectivity but different anisotropy is over-simplistic and an additional term is needed. This is a topic for further study, and affects mainly the maximum directional effective permeability. The most significant effective permeability is the minimum one.

The strength of the method lies in reducing the number of variables to the minimum number required: a transmissibility term, a tortuosity term and an anisotropy term. The approach could easily be extended to considering the effective permeability of a

conductive fracture network in a sealing or low permeability matrix. Additionally, analytical rather than empirical solutions might be gained by combining the approach more closely with methods from percolation theory.

8.5 The effect of sub-seismic faulting in reservoirs

Application of the effective permeability upscaling method to a variety of outcrop and sub-surface datasets has shown that effective permeability may, meaningfully, be assigned to undrilled regions of the reservoir. With care, a representative elementary volume can be defined for sub-seismic systems. In the example considered, the representative elementary volume of the sub-seismic fault system is about 16 km^2. Within this distance of a well, a homogenised effective permeability is inappropriate, as flow will be governed by specific details of the fault system. Paradoxically, the geological REV is larger if fault density is lower.

The most important variable is fault permeability, however considerable sensitivity is also attached to the scaling parameters. The relative significance of length scaling and thickness scaling depends on the particular balance of tortuous to transmissible flow operative at any scale in the system, whilst displacement frequency scaling determines the relative proportions of large to small faults. No single input parameter is critical, as effective permeability is a complex function of them all.

None of the input parameters can possibly be known accurately for any particular grid-block, and in the light of this uncertainty, probabilistic methods are necessary. Establishing probability distributions of the input variables, coupled with the proposed permeability up-scaling method, would allow assessment not only of the most likely effective permeability in any particular grid block, but also the confidence with which this value can be applied.

In general, fault density needs to be high for sub-seismic faulting to have a significant influence on effective permeability. In such cases, the methods developed in this thesis could usefully be applied to determining the likely permeability in the seismic fault compartments. Application of these methods to tangible reservoir development problems will be the only true test of their worth.

REFERENCES

Acuna, J. A. and Yortsos, Y. C. 1991. Numerical construction and flow simulation in networks of fractures using fractal geometry. *SPE annual technical conference and exhibition.*

Acuna, J. A. and Yortsos, Y. C. 1995. Application of fractal geometry to the study of networks of fractures and their pressure transient. *Water Resources Research*, 31 (3). p 527-540.

Amaefule, J. O., Altunbay, M., Tiab, D., Kersey, D. G. and Keelan, D. K. 1993. Enhanced reservoir description: using core and log data to identify hydraulic (flow) units and predict permeability in uncored intervals/wells (SPE 26436). *68 th. SPE annual technical conference and exhibition*, Houston, Texas, p. 205-220.

Amyx, J. W., Bass, D. M. and Whiting, R. L. 1960. *Petroleum Reservoir Engineering - Physical Properties.* McGraw-Hill, 610 pp.

Anderson, E. M. 1951. *The Dynamics of Faulting and Dyke Formation with Applications to Britain.* Oliver & Boyd, Edinburgh.

Antonellini, M. and Aydin, A. 1994. Effect of faulting on Fluid Flow in Porous Sandstones: Petrophysical Properties. *The American Association of Petroleum Geologists Bulletin*, 78 (3). p 355-377.

Antonellini, M. and Aydin, A. 1995. Effect of Faulting on Fluid Flow in Porous Sandstones: Geometry and Spatial Distribution. *The American Association of Petroleum Geologists Bulletin*, 79 (5). p 642-671.

Antonellini, M., Aydin, A. and Pollard, D. D. 1994. Microstructure of deformation bands in porous sandstones at Arches National Park, Utah. *Journal of Structural Geology*, 16 (7). p 941-959.

Arboleya, M. L. and Engelder, T. 1995. Concentrated slip zones with subsidiary shears: their development on three scales in the Cerro Brass fault zone, Appalachian valley and ridge. *Journal of Structural Geology*, 17 (4). p 519-532.

Aydin, A. 1978. Small Faults Formed as Deformation Bands in Sandstone. *Pure and Applied Geophysics*, 116. p 913 - 930.

Aydin, A. and Johnson, A. M. 1978. Development of Faults as Zones of Deformation Bands and as Slip Surfaces in Sandstone. *Pure and Applied Geophysics*, 116. p 931-942.

Aydin, A. and Johnson, A. M. 1983. Analysis of faulting in porous sandstones. *Journal of Structural Geology*, 5 (1). p 19-31.

Aydin, A. and Reches, Z. 1982. Number and orientation of fault sets in the field and in experiments. *Geology*, 10. p 107-112.

Bak, P. and Tang, C. 1989. Earthquakes as Self-Organised Critical Phenomenon. *Journal of Geophysical Research*, 94 (B11). p 15635-15637.

Balberg, I. and Binenbaum, N. 1983. Computer study of the percolation threshold in a two-dimensional system of conducting sticks. *Physical Review B*, 28 (7). p 3799-3812.

Balberg, I. 1986. Connectivity and conductivity in 2D and 3D fracture systems. *Annals Israel Physical Society*, 8. p 89-100.

Balberg, I., Berkowitz, B. and Drachsler, G. E. 1991. Application of a percolation model to flow in fractured hard rocks. *Journal of Geophysical Research*, 96 (B6). p 10015-10021.

Barnsley, M. F. 1988. *Fractals everywhere.* Academic Press, San Diego, California. 394pp.

Barton, C. C. and Larsen, E. 1985. Fractal geometry of two-dimensional fracture networks at Yucca Mountain, southwestern Nevada. *Proceeding of the International Symposium on Fundamentals of Rock Joints*, Bjorkliden, p. 77-84.

Barton, C. C. and Hsieh, P. A. 1989. Physical and hydrologic-flow properties of fractures. *In*: *"28th International geological congress: Environmental, Engineering and Urban geology in the United Sates"*, Volume 2, American Geophysical Union, p T385:1-T385:36.

Bear, J. 1972. *Dynamics of fluids in porous media.* Elsevier, New York. 764 pp.

Bear, J. 1993. Modelling flow and contaminant transport in fractured rocks. *In*: Bear, J. (ed.) *Flow and contaminant transport in fractured rock.* Academic Press, London. p 1-37.

Bear, J. and Berkowitz, B. 1987. Groundwater flow and Pollution in Fractured Rock Aquifers. *In*: Norvak, P. (ed.) *Developments in Hydraulic Engineering*. Elsevier Applied Sciences Publication 4., p 175-238.

Begg, S. H., Carter, R. R. and Dranfield, P. 1989. Assigning effective values to simulator gridblock parameters for heterogeneous reservoirs. *SPE Reservoir Engineering*, November 1989. p 455-463.

Begg, S. H., Chang, D. M. and Haldorsen, H. H. 1985. A simple statistical method for calculating the effective vertical permeability of a reservoir containing discontinuous shales. *60th SPE annual conference and exhibition*, Las Vegas, Nevada, September 22-25, 1985.

Begg, S. H. and King, P. R. 1985. Modelling the Effects of Shale on Reservoir Performance: Calculation of Effective Vertical Permeabilities (SPE 13529). *SPE reservoir simulation symposium, February 10-13*, Dallas, Texas, p. 331-338.

Belfield, W. C. 1992. Simulation of Subseismic Faults Using Fractal and Multifractal Geometry. *SPE Annual Technical Conference and Exhibition*, Washington DC, SPE 24751.

Beliveau, D. 1995. Heterogeneity, Geostatistics, Horizontal Wells and Blackjack Poker. *Journal of Petroleum Technology*, (December 1995). p 1068-1074.

Berkowitz, B. 1995. Analysis of Fracture Connectivity Using Percolation Theory. *Mathematical Geology*, 27 (4). p 467-483.

Berkowitz, B. and Balberg, I. 1993. Percolation Theory and Its Application to Groundwater Hydrology. *Water Resources Research*, 29 (4). p 775-794.

British Geological Survey. 1982. *Lake District 1:250,000, Sheet 54°N-04°W, Solid.* Institute of Geological Sciences, Southampton.

Bu, T. and Damsleth, E. 1996. Errors and uncertainties in Reservoir Performance Predictions. *SPE Formation Evaluation*, September 1996. p 194-200.

Burgmann, R., Pollard, D. D. and Martel, S. J. 1994. Slip distributions on faults: effects of stress gradients, inelastic deformation, heterogeneous host-rock stiffness, and fault interaction. *Journal of Structural Geology*, 16. p 1675-1690.

Cartwright, J. and Lonergan, L. 1996. Polygonal fault systems in shale sequences: implications for top seal integrity and reservoir compartmentalisation (Abstract). *Faulting, fault seal and fluid flow in hydrocarbon reservoirs*, Leeds, September 23-25.

Cartwright, J. A., Mansfield, C. and Trudgill, B. 1996. The growth of normal faults by segment linkage. *In*: Buchanan, P. G. and Nieuwland, D. A. (eds.) *Modern Developments in Structural Interpretation, Validation and Modelling*. London. p 163-177.

Childs, C., Walsh, J. J. and Watterson, J. 1990. A method for Estimation of the Density of Fault Displacements below the Limits of Seismic Resolution in Reservoir Formations. *In*: Buller, A. T. *et al.* (eds.) *North Sea oil and Gas Reservoirs II*. Graham and Trotman, London, London. p 309-318.

Childs, C., Watterson, J. and Walsh, J. J. 1996. A model for the structure and development of fault zones. *Journal of the Geological Society, London*, 153. p 337-340.

Chilés, J.-P. and de Marsily, G. 1993. Stochastic models of fracture systems and their use in flow and transport modelling. *In*: Bear, J. (ed.) *Flow and contaminant transport in fractured rock*. Academic Press, London. p 169-236.

Ciammetti, G., Ringrose, P. S., Good, T. R., Lewis, J. M. L. and Sorbie, K. S. 1995. Waterflood Recovery and Fluid Flow Upscaling in a shallow Marine and Fluvial Sandstone Sequence (SPE 30783). *SPE Annual Technical conference and Exhibition,* Dallas, U.S.A, 22-25 October 1995.

Cladouhos, T. T. and Marrett, R. 1996. Are fault growth and linkage models consistent with power-law distributions of fault lengths? *Journal of structural geology*, 18 (2/3). p 281-294.

Coney, D., Fyfe, T. B., Retail, P. and Smith, P. J. 1993. Clair appraisal: the benefits of a co-operative approach. *In*: Parker, J. R. (ed.) *Petroleum Geology of North West Europe: Proceedings of the 4th conference*. The Geological Society, London. p 1409-1420.

Conybeare, D., Buck, S., Tribe, I., McKeever, M., Aplin, G. 1996. Microstructure and permeability variations associated with deformation bands in North Sea Jurassic sandstone reservoirs (Abstract). *Faulting, fault seal and fluid flow in hydrocarbon reservoirs*, Leeds, September 25-25.

Corbett, P. W. M. (1993) Reservoir characterisation of a laminated sediment. PhD. thesis, Heriot-Watt University, Edinburgh.

Corrigan, A. F. 1993. Estimation of recoverable reserves: the geologist's job. *In*: Parker, J. R. (eds.) *Petroleum Geology of North West Europe: Proceedings of the 4th conference*. The Geological Society, London. p 1473-1481.

Cowie, P. A., Knipe, R. J. and Main, I. G. 1996. Introduction to the special issue. *Journal of structural geology*, 18 (2/3). p v-xi.

Cowie, P. A. and Scholz, C. H. 1992a. Displacement-length scaling relationship data for faults: data synthesis and discussion. *Journal of Structural Geology*, 14 (10). p 1149-1156.

Cowie, P. A. and Scholz, C. H. 1992b. Physical explanation for the displacement-length relationship of faults using a post-yield fracture mechanics model. *Journal of Structural Geology*, 14 (10). p 1133-1148.

Cowie, P. A., Sornette, D. and Vanneste, C. 1995. Multifractal scaling properties of a growing fault population. *Geophys. J. Int*, 122 (457-469).

Cowie, P. A., Vanneste, C. and Sornette, D. 1993. Statistical physics model for the spatio-temporal evolution of faults. *Journal of geophysical research*, 98. p 21809-21821.

Cox, S. J. D. a. and Scholz, C. H. 1988. On the formation and growth of faults: an experimental study. *Journal of Structural Geology*, 10. p 413-430.

Crawford, B. R. in Press. Experimental fault sealing: shear band permeability dependency on cataclastic fault gouge characteristics. *In*: Coward, M. P. *et al.* (eds.) *Structural Geology in Reservoir Characterisation and Field Development.* Geological Society (London) Special Publication.

Cruikshank, K. M., Zhao, G. and Johnson, A. M. 1991. Duplex structures connecting fault segments in Entrada sandstone. *Journal of Structural Geology*, 13 (10). p 1185-1196.

Cushman, J. H. 1990. An Introduction to Hierarchical Porous Media. *In*: Cushman, J. H. (ed.) *Dynamics of Fluids in Hierarchical Porous Media.* Academic Press, London. p 1-6.

Davidson, I. 1994. Linked Fault Systems; Extensional Strike-Slip and Contractional. *In*: Hancock, P. L. (ed.) *Continental Deformation.* Permagon Press, Oxford. p 121-142.

Dawers, N. H. and Anders, M. H. 1995. Displacement-length scaling and fault linkage. *Journal of structural geology*, 17 (5). p 607-614.

Dawers, N. H., Anders, M. H. and Scholz, C. H. 1993. Fault length and displacement: Scaling laws. *Geology*, 21. p 1107-1110.

de Marsily, G. 1985. Flow and transport in fractured rock: connectivity and scale effect. *17th international symposium on the hydrogeology of rocks of low permeability*, Tuscon, Arizona, 17 Pt 2, p 267-277.

Dershowitz, W. S. and Einstein, H. H. 1988. Characterizing Rock Joint Geometry with Joint System Models. *Rock Mechanics and Rock Engineering*, 21. p 21-51.

Deutsch, C. V. 1989. Calculating Effective Absolute Permeability in Sandstone/Shale Sequences (SPE 17264). *SPE Formation Evaluation.* p 343-348.

Doelling, H. H. 1985. Geology of Arches National Park. Notes to accompany Map 74, Utah Geological Survey.

Doelling, H. H. 1993. Interim geologic map, Moab 30' x 60' quadrangle, Grand County, Utah and Mesa County, Colorado. Utah Geological Survey, Open-File Report 287.

Dullien, F. A. L. 1979. *Porous media - fluid transport and pore structure.* Academic press, New York. 396 pp.

Dunn, D. E., La Fountain, L. J. and Jackson, R. E. 1973. Porosity dependence and Mechanism of Brittle Fracture in Sandstones. *Journal of Geophysical Research*, 78 (14). p 2403-2417.

Dykstra, H. and Parsons, R. L. 1950. The prediction of oil recovery by waterflood. *In*: *Secondary recovery of oil in the United States, Principles and practice. 2nd ed.* American Petroleum Institute, p 160-174.

Edwards, H. E., Becker, A. D. and Howell, J. A. 1993. Compartmentalisation of an aeolian sandstone by structural heterogeneity: Permo-Triassic Hopeman Sandstone, Moray Firth, Scotland. *In:* North, C. P. and Prosser D. J. (eds.) *Characterisation of Fluvial and Aeolian Reservoirs, Geological society special publication*, 73. p 339-365.

Engelder, T. 1974. Cataclasis and the generation of fault gouge. *Geological Society of America Bulletin*, 85. p 1515-1522.

Engelder, T. 1987. Joints and shear fractures in rock. *In*: Atkinson, B. K. (ed.) "*Fracture mechanics of rock.*" Academic press, London. p 27-69.

Evans, J. P. 1990. Thickness-displacement relationships for fault zones. *Journal of Structural Geology*, 12 (8). p 1061-1065.

Fisher, Q. J. and Knipe, R. 1996. Microstructural controls on the petrophysical properties of deformation features (Abstract). *Faulting, fault seal and fluid flow in hydrocarbon reservoirs*, Leeds, September 23-25.

Fowles, J. and Burley, S. 1994. Textural and permeability characteristics of faulted, high porosity sandstones. *Marine and Petroleum Geology*, 11 (5). p 608-623.

Foxford, K. A., Garden, I. R., Guscott, S. C., Burley, S. D., Lewis, J. J. M. 1996. The field geology of the Moab fault. *In*: Huffman, A. C., *et al.* (eds.) *Geology and resources of the Paradox Basin.* Utah Geological Association, Salt Lake City. p 265-283.

Foxford, K. A., Walsh, J. J., Watterson, J., Garden, I. R., Guscott, S. C. in review. Structure and content of the Moab Fault zone, Utah, U. S. A. In: *Faulting fault seal and fluid flow*. Special Issue of the Geological Society, London (In review),

Gauthier, B. D. M. and Lake, S. D. 1993. Probabilistic modelling of Faults Below the Limit of Seismic Resolution in the Pelican Field, North Sea, Offshore United Kingdom. *The American Association of Petroleum Geologists Bulletin*, 77 (5). p 761-777.

Gillespie, P. A., Howard, C. B., Walsh, J. J. and Watterson, J. 1993. Measurement and characterisation of spatial distribution of fractures. *Tectonophysics*, 226. p 113-141.

Gillespie, P. A., Walsh, J. J. and Watterson, J. 1992. Limitations of dimension and displacement data from single faults and the consequences for data analysis and interpretation. *Journal of Structural Geology*, 14 (10). p 1157-1172.

Golf-Racht, T. D. 1982. *Fundamentals of fractured reservoir engineering.* Elsevier.

Gomez, J. B., Pacheco, A. F. and Segui-Santonja, A. J. 1995. A Model for Crack Connectivity in Rocks, a Discussion. *Mathematical Geology*, 27 (1). p 23-39.

Grady, D. E. and Kipp, M. E. 1987. Dynamic rock fragmentation. *In*: Atkinson, B. K. (ed.) *Fracture mechanics of rock.* Academic press, London. p 429-476.

Gutenberg, B. and Richter, C. F. 1944. Frequency of earthquakes in California. *Bull. Seism. Soc. Am.*, 34. p 185-188.

Haldorsen, H. H. and Lake, L. W. 1984. A new approach to shale management in field-scale models. *Society of Petroleum Engineers journal*, August 1984. p 447-457.

Hatton, C. G., Main, I. G. and Meredith, P. G. 1994. Non-universal scaling of fracture length and opening displacement. *Nature*, 367. p 160-162.

Heath, A. E., Walsh, J. J. and Watterson, J. 1994. Estimation of the Effect of Sub-seismic Sealing Faults on Effective Permeabilities in Sandstone Reservoirs. *In*: Aasen, J. O., *et al.* (eds.) *North Sea Oil and Gas Reservoirs III.* Kluwer Academic Publishers, Dordrecht. p 173-183.

Heffer, K. J. and Bevan, T. G. 1990. Scaling relationships in Natural Fractures: Data, Theory and Application. *Society of Petroleum Engineers, Paper No. 209819.*

Hestir, K. and Long, J. C. S. 1990. Analytical expressions for the permeability of random two-dimensional Poisson fracture networks based on regular lattice percolation and equivalent media theories. *Journal of Geophysical Research*, 95 (B13), p 21565-21581.

Hewett, T. A. 1994. Fractal Methods for Fracture Characterization. *In*: Yarus, J. M. and Chambers, R. L. (eds.) *Computer Applications in Geology No. 3. Stochastic Modeling and Geostatistics.* AAPG, Tulsa, Oklahoma. p 249-260.

Hirata, T. 1989. Fractal Dimension of Fault Systems in Japan: Fractal Structure in Rock Fracture Geometry at Various Scales. *Pure and Applied Geophysics*, 131 (1/2). p 157-170.

Hobbs, B. E. 1993. The significance of structural Geology in Rock Mechanics. *In*: Hudson, J. A. (ed.) *Comprehensive Rock Engineering Principles, Practice and Projects, Volume 1. Fundamentals.* Permagon Press, Oxford. p 25 - 62.

Homann, H. and Gaulthier, B. D. M. 1995. Sampling Fracture Parameters in Borehole Imaging Logs and Cores: an Integrated Approach Applied to the Dutch Offshore (Abstract). *The American Association of Petroleum Geologists Bulletin*, 78 (8). p 1222.

Huang, Y., Ringrose, P. S. and Sorbie, K. S. 1995. Capillary Trapping Mechanisms in Water-Wet Laminated Rocks. *SPE Reservoir Engineering*, November 1995. p 287-292.

Hull, J. 1988. Thickness-displacement relationships for deformation zones. *Journal of Structural Geology*, 10 (4). p 431-435.

Jamison, W. R. and Stearns, D. W. 1982. Tectonic Deformation of Wingate Sandstone, Colorado National Monument. *The American Association of Petroleum Geologists Bulletin*, 66 (12). p 2584-2608.

Jensen, J. L., Corbett, P. W. M., Pickup, G. E., and Ringrose, P. S. 1996. Permeability semivariograms, geological structure and flow performance. *Mathematical Geology*, 28 (4), p. 419-435.

Jensen, J. L., Lake, L. W., Corbett, P. W. M. and Goggin, D. J. 1997. *Statistics for petroleum engineers and geoscientists.* Prentice Hall, Upper Saddle River, New Jersey. 390 pp.

Kakimi, T. 1980. Magnitude-Frequency Relation for Displacement of Minor Faults and Its Significance in Crustal Deformation. *Bulletin of the Geological Survey of Japan*, 31 (10). p 467-487.

Kazemi, H. 1969. Pressure transient analysis of naturally fractured reservoirs with uniform fracture distribution. *SPE Journal* . p 451-462.

Knott, S. D. 1994. Fault zone thickness versus displacement in the Permo-Triassic sandstones of NW England. *Journal of the Geological Society, London*, 151. p 17-25.

Knott, S. D., Beach. A., Brockband, P. J., Brown, J. L., McCallum, J. E. 1996. Spatial and mechanical controls on normal fault populations. *Journal of Structural Geology*, 18 (2/3). p 359-372.

Koestler, A. G., Milnes A. G., Olsen T. S. and Buller A. T. 1994. A Structural Simulation Tool for Faulted Sandstone Reservoirs: Exploratory Study Using Data From Utah and the Gullfaks Field. *In*: Aasen, J. O., *et al.* (eds.) *North Sea Oil and Gas Reservoirs III*. Kluwer Academic Publishers, Dordrecht. p 157-165.

Koestler, A. G. and Reksten, K. 1995. Fracture-Network 3D Characterisation in a Deformed Chalk Reservoir Analogue - the Lagerdork Case. *SPE Formation Evaluation.* p 148-152.

Krantz, R. W. 1988. Multiple fault sets and three-dimensional strain: theory and application. *Journal of Structural Geology*, 10 (3). p 225-237.

Kulander, B. R., Dean, S. L. and Ward, B. J. 1990. *Fractured Core analysis: Interpretation, Logging and Use of Natural and Induced Fractures in core.* American Association of Petroleum Geologists, Tulsa. 88 pp.

La Pointe, P. R. and Hudson, J. A. 1985. *Characterisation and Interpretation of Rock Mass Joint Patterns.* The geological Society of America Special Paper 199, 37 pp.

Ladeira, F. L. and Price, N. J. 1981. Relationship between fracture spacing and bed thickness. *Journal of Structural Geology*, 3 (2). p 179-183.

Laherrere, J. H. 1995. Discussion of An Integrated Deterministic / Probabilistic Approach to Reserves Estimations. *Journal of Petroleum Technology*, (December 1995). p 1082-1083.

Lake, L. W. and Jensen, J. L. 1991. A review of heterogeneity measures used in reservoir characterisation. *In Situ*, 15 (4). p 409-437.

Lisle, R. J. 1994. Detection of Zones of Abnormal Strains in Structures Using Gaussian Curvature Analysis. *The American Association of Petroleum Geologists Bulletin*, 78 (12). p 1811 - 1819.

Long, J. C. S. and Billaux, D. M. 1987. From Field Data to Fracture Network Modelling: An Example Incorporating Spatial Structure. *Water Resources Research*, 23 (7). p 1201-1216.

Ma, X. Q. and Kusznir, N. J. 1992. 3-D subsurface displacement and strain field for faults and fault arrays in a layered elastic half-space. *Geophys. J. Int.*, 111. p 542-558.

Ma, X. Q. and Kusznir, N. J. 1993. Modelling of near-field subsurface displacements for generalised faults and fault arrays. *Journal of Structural Geology*, 15 (12). p 1471-1484.

Madden, T. R. 1983. Microcrack Connectivity in rocks: A renormalization group approach to the critical phenomena of conduction and failure in crystalline rocks. *Journal of the Geophysical Research*, 88 (B1). p 585-592.

Manzocchi, T., Ringrose, P. S. and Underhill, J. R. in press. Flow through fault systems in high porosity sandstones. *In*: Coward, M. P. *et al.* (eds.) *Structural geology in reservoir characterisation.* Geological Society, London.

Marrett, R. 1996. Aggregate properties of fracture populations. *Journal of Structural Geology*, 18 (2/3). p 169-178.

Marrett, R. and Allmendinger, R. W. 1990. Kinematic analysis of fault slip data. *Journal of structural geology*, 12 (8). p 973-986.

Marrett, R. and Allmendinger, R. W. 1991. Estimation of strain due to brittle faulting. *Journal of Structural Geology*, 13 (6). p 735-738.

Marrett, R. and Allmendinger, R. W. 1992. Amount of extension on "small" faults: an example from the Viking Graben. *Geology*, 20. p 47-50.

McGrath, A. (1992) Fault propagation and growth; a study of Triassic and Jurassic faults from Watchet and Kilve, North Somerset. MSc Thesis, Royal Holloway, London University.

Munthe, K., Holden, L., Mostad, P. and Townsend, C. 1994. Modelling Sub-seismic Fault Patterns Using a Marked Point Process. *Proceedings 4th Conference on the Mathematics of Oil Recovery, Røros, Norway, 7-10 June 1994.*

Muroka, H. and Kamata, H. 1983. Displacement distribution along normal fault traces. *Journal of Structural Geology*, 5 (5). p 483-495.

Muskat, M. 1937. *Flow of homogeneous fluids.* McGraw-Hill, New York.

Naylor, M. A., Mandl, G. and Sijpesteijn, C. H. K. 1986. Fault geometries in basin-induced wrench faulting under different initial stress states. *Journal of Structural Geology*, 8. p 737-752.

Needham, T., Yielding, G. and Fox, R. 1996. Fault population description and prediction using examples from offshore U.K. *Journal of Structural Geology*, 18 (2/3). p 155-168.

Nelson, R. A. 1987. Fractured Reservoirs: Turning Knowledge into Practice. *Journal of Petroleum Technology*, p 407-414.

Nicol, A., Walsh, J. J., Watterson, J. and Bretan, P. G. 1995. Three-dimensional geometry and growth of conjugate normal faults. *Journal of Structural Geology*, 17 (6). p 847-862.

Nicol, A., Walsh, J. J., Watterson, J. and Gillespie, P. A. 1996. Fault size distributions - are they really power-law? *Journal of Structural Geology*, 18 (2/3). p 191-198.

Odling, N., E. 1992a. Network Properties of a Two- Dimensional Natural Fracture Pattern. *Pure and Applied Geophysics*, 138 (1). p 95 - 114.

Odling, N. E. 1992b. Permeability of natural and simulated fracture patterns. *In*: Larsen, R. M., *et al.* (eds.) *Structural and Tectonic Modelling and Its application to Petroleum Geology*. Elsevier, Amsterdam. p 365-380.

Odling, N. E. 1993. The development of network properties in natural fracture patterns. *In*: Proceedings of the XXIVth congress of the international association of Hydrogeologists, Ås, Norway.

Odling, N. E. 1997. Dataset from Hornelen, Western Norway. In: E. S. Aarseth *et al.* (eds.) *Interim guide to fracture interpretation and flow modelling in fractured reservoirs.* Office for the publication of the European Communities, Luxembourg. p 117-133.

Omre, H., Knut, S., Dhal, N. and Tørudbakken, B. 1994. Impact of Fault Heterogeneity in Fault Zones on Fluid Flow. *In*: Aasen, J. O., Berg, E., Buller, A. T., Hjelmeland, O., Holt, R. M., Kleppe, J., Torsæter. (eds.) *North Sea Oil and gas Reservoirs III*. Kluwer Academic Publishers, Dordrecht. p 285 - 200.

Oudmayer, B. C. and de Jager, J. 1993. Fault reactivation and oblique-slip in the Southern North Sea. In: Parker, J. R. (ed) *Petroleum Geology of North West Europe: Proceedings of the 4th conference*, London, The Geological Society, 2, p 1281-1290.

Øvreberg, O., Damsleth, E. and Haldorsen, H. H. 1992. Putting Error Bars on Reservoir Engineering Forecasts. *Journal of Petroleum Technology*, June 1992. p 732-738.

Patricelli, J. A. and McMichael, C. L. 1995. An Integrated Deterministic / Probabilistic Approach to Reserves Estimations. *Journal of Petroleum Technology*, (January 1995). p 49-53.

Peacock, D. C. P. and Sanderson, D. 1991. Displacement, segment linkage and relay ramps in normal fault zones. *Journal of Structural Geology*, 13 (6). p 721-733.

Peacock, D. C. P. and Sanderson, D. J. 1996. Effect of propagation rate on displacement variations along faults. *Journal of Structural Geology*, 18 (2/3). p 311-320.

Pickering, G., Bull, J. M. and Sanderson, D. J. 1996. Scaling of fault displacements and implications for the estimation of sub-seismic strain. *In*: Buchanan, P. G. and Nieuwland, D. A. (eds.) *Modern Developments in Structural Interpretation, Validation and Modelling*. The Geological Society, London, Special Publication, London. p 11-26.

Pickering, G., Peacock, D. C. P., Sanderson, D. J. and Bull, J. M. 1997. Modelling tip zones to predict the throw and length characteristics of faults. *AAPG Bulletin*, 81 (1). p 82-99.

Pittman, E. D. 1981. Effect of Fault-Related Granulation on Porosity and Permeability of Quartz Sandstones, Simpson Group (Ordovician), Oklahoma. *The American Association of Petroleum Geologists Bulletin*, 65 (11). p 2381-2387.

Ramsay, J. G. and Huber, M. I. 1983. *The techniques of modern structural geology. Volume 1: strain analysis.* Academic Press, London. 307 pp.

Rapoport, L. A. 1955. Scaling Laws for Use in Design and Operation of Water-Oil Flow Models. *Petroleum Transactions, AIME*, 204. p 143-150.

Reches, Z. 1977. Analysis of faulting in three-dimensional strain field. *Tectonophysics*, 47. p 109-129.

Reches, Z. 1983. Faulting of rocks in three-dimensional strain fields II. Theoretical analysis. *Tectonophysics*, 95. p 133-156.

Reiss, L. H. 1980. *The reservoir engineering aspects of fractured formations.* Gulf Publishing Company, Houston.

Ringrose, P. S., Sorbie, K. S., Corbett, P. W. M. and Jensen, J. L. 1993. Immiscible flow behaviour in laminated and cross-bedded sandstones. *Journal of Petroleum Science and Engineering*, 9. p 103-124.

Ringrose, P. S. and Corbett, P. W. M. 1994. Controls on two-phase flow in heterogeneous sandstones. *In*: Parnell, J. (ed.)*: Origin, Migration and Evolution of Fluids in Sedimentary Basins.* Geological Society, London, Special Publications, 78, p 141-150.

Roberts, A. M., Yielding, G., Kusznir, N. J., Walker, I. and Dorn-Lopez, D. 1993. Mesozoic extension in the North Sea: constraints from flexural backstripping, forward modelling and fault populations. *In*: Parker, J. R. (ed.) *Petroleum Geology of North West Europe: Proceedings of the 4th conference.* The Geological Society, London. p 1123-1136.

Robertson, E. C. 1983. Relationship of fault displacement to gouge and breccia thicknesses. *Institute of Mining Engineers*, 35. p 1426-1432.

Robinson, P. C. 1983. Connectivity of fracture systems - a percolation theory approach. *Journal of Physics A: Mathematical and General*, 16. p 605-614.

Robinson, P. C. 1984. Numerical calculations of critical densities for lines and planes. *Journal of Physics A: Mathematical and General*, 17. p 2823-2830.

Rudnicki, J. W. 1977. The inception of faulting in a rock-mass with a weakened zone. *Journal of Geophysical Research*, 82. p 844-854.

Rudnicki, J. W. and Rice, J. R. 1975. Conditions for the localisation of deformation in pressure-sensitive dilatent materials. *Journal of the Mechanics and Physics of Solids*, 23. p 371-394.

Rutter, E. H. 1986. On the nomenclature of mode of failure transitions in rocks. *Tectonophysics*, 122. p 381-387.

Schiedegger, A. E. 1974. *The physics of flow through porous media (3rd edition).* University of Toronto Press, 313 pp.

Schlische, R. W.; Young, S. S., Ackermann, R. V. and Gupta, A. 1996. Geometry and scaling relations of a population of very small rift-related normal faults. *Geology*, 24 (8). p 683-686.

Scholz, C. H. 1987. Wear and gouge formation in brittle fracturing. *Geology*, 15. p 493-495.

Scholz, C. H. 1990. *Mechanics of Earthquakes and Faulting.* Cambridge University Press, Cambridge. 439 pp.

Scholz, C. H. and Cowie, P. A. 1990. Determination of total strain from faulting using slip measurements. *Nature*, 346. p 837-838.

Segal and Pollard, D. D. 1987. Theoretical displacements and stresses near fractures in rock: with application to faults, joints, dykes, veins and solution surfaces. *In*: Atkinson, B. K. (ed.) *Fracture mechanics of rock.* Academic Press, London. p 277-349.

Shook, M., Li, D. and Lake, L. W. 1992. Scaling immiscible flow through permeable media by inspectional analysis. *In Situ*, 16 (4). p 311-349.

Sibson, R. H. 1996. Structural permeability of fluid-driven fault-fracture meshes. *Journal of Structural Geology*, 18 (8). p 1031-1042.

Smalley, P. C. and Hale, N. A. 1996. Early Identification of Reservoir Compartmentalisation by combining a Range of Conventional and Novel Data Types. *SPE Formation Evaluation*, September 1996. p 163-169.

Smith, L. and Schwartz, F. W. 1993. Solute transport through fracture networks. *In*: Bear, J., *et al.* (eds.) *Flow and contaminant transport in fractured rock.* Academic Press, London. p 129-167.

Sornette, D., Davy, P. and Sornette, A. 1990. Structuration of the Lithosphere in Plate Tectonics as a Self-Organized Critical Phenomenon. *Journal of Geophysical Research*, 95 (B11). p 17353-17361.

Sornette, D., Vanneste, C. and Knopoff, L. 1992. Statistical model of earthquake foreshock. *Phys. Rev. A*, 45. p 8351-8357.

Stauffer, D. 1985. *Introduction to Percolation Theory.* Taylor & Francis, London. 124 pp.

Stokes, W. L. 1986. *Geology of Utah.* Utah Geological and mineral survey, Salt Lake City.

Sylvester, I. F., Carruthers, D., Ringrose, P. S., Bratvold, R. B. and Lia, O. 1996. Gas/Water Flow Upscaling in a Stochastic Mixed Fluvial-Aeolian Reservoir Simulation Model (SPE 35492). *SPE/NFP European 3D Reservoir Modelling Conference*, Stavanger, Norway, April 16-17 1996.

Tchalenko, J. S. 1970. Similarities between Shear Zones of Different Magnitudes. *Geological Society of America Bulletin*, 81. p 1625-1640.

Turcotte, D. L. 1992. *Fractals and chaos in geology and geophysics.* Cambridge University Press, Cambridge. 221 pp

Turing, A. M. 1952. The chemical basis of morphogenesis. *Transactions of the Royal Society B*, 237. p 37-72.

Underhill, J. R. and Woodcock, N. H. 1987. Faulting mechanisms in high-porosity sandstones; New Red Sandstone, Arran, Scotland. *In*: Jones, M. E. and Preston, R. M. F. (eds.) *Deformation of Sediments and Sedimentary Rocks*. Geological Society, London, Special Publication, London. p 91-105.

Van Wagoner, J. C., Mitchum, R. M., Campion, K. M. and Rahmanian, V. D. 1990. *Siliciclastic sequence stratigraphy in Well Logs, Cores and Outcrops.* AAPG, Tulsa, Oklahoma. 55 pp.

Voss, R. F. and Wyatt, J. C. Y. 1993. Multifractals and the Local Connected Fractal Dimension: Classification of Early Chinese Landscape Painting. *In*: Crilly, A. J. and al, e. (eds.) *Application of fractals and chaos: the shape of things*. Springer, p 171-184.

Walsh, J. J. and Watterson, J. 1987. Distributions of cumulative displacement gradients on a single normal fault surface. *Journal of Structural Geology*, 9 (8). p 1039-1046.

Walsh, J. J. and Watterson, J. 1988. Analysis of the relationship between displacements and dimension of faults. *Journal of Structural Geology*, 10 (3). p 239-247.

Walsh, J. J. and Watterson, J. 1991. Geometric and kinematic coherence and scale effects in normal fault systems. *In*: Roberts, A. M., *et al.* (eds.) *The Geometry of Normal Faults*. Geological Society, London, Special Publication, London. p 193-203.

Walsh, J. J. and Watterson, J. 1993. Fractal analysis of fracture patterns using the standard box-counting techniques: valid and invalid methodologies. *Journal of Structural Geology*, 15 (12). p 1509-1512.

Walsh, J. J., Watterson, J., Heath, A., Gillespie, P. A. G. and Childs, C. In press. Assessment of the effects of sub-seismic faults on bulk permeabilities of reservoir sequences. *In*: Coward, M. P., *et al.* (*eds.*) *Structural geology in reservoir characterisation*. Geological Society, London.

Walsh, J.J., Watterson, J. and Yielding, G. 1991. The importance in small-scale faulting in regional extension. *Nature*, 351 (6325). p 391-393.

Walsh, J. J., Watterson, J. and Yielding, G. 1994. Determination and Interpretation of Fault Size Populations: Processes and Problems. *In*: Aasen, J. O., Berg, E., Buller, A. T., Hjelmeland, O., Holt, R. M., Kleppe, J., Torsæter. (eds.) *North Sea Oil and Gas Reservoirs III*. Kluwer Academic Publishers, Dordrecht. p 141 - 155.

Warren, J. E. and Root, P. J. 1962. The behaviour of naturally fractured reservoirs. *SPE Journal (September 1962)*, p 245-255.

Watterson, J. 1986. Fault Dimension, Displacement and Growth. *Pure and Applied Geophysics*, 124. p 365-373.

Watterson, J., Walsh, J. J., Gillespie, P. A. and Easton, S. 1996. Scaling systematics on fault sizes on a large-scale range fault map. *Journal of Structural Geology*, 18 (2/3). p 199-216.

Welbon, A. I., Beach, A., Brockbank, P. J., Brown, L. J., Knott, S. D. 1996. Damage zone geometry: outcrop examples from Western Sinai and the United Kingdom (Abstract). *Faulting, Fault seal and fluid flow in hydrocarbon reservoirs, Leeds, September 23-25.*

Westaway, R. 1992. Evidence for anomalous earthquake size distribution in regions of minimal strain. *Geophysical Research Letters*, 19. p 1499-1502.

Westaway, R. 1994. Quantitative analysis of populations of small faults. *Journal of Structural Geology*, 16 (9). p 1259-1273.

Yielding, G., Needham, T. and Jones, H. 1996. Sampling of fault populations using sub-seismic data: a review. *Journal of Structural Geology*, 18 (2/3). p 135-146.

Yielding, G., Walsh, J. and Watterson, J. J. 1992. The prediction of small-scale faulting in reservoirs. *First Break*, 10 (12). p 449-460.

Zhao, G. and Johnson, A. M. 1991. Sequential and incremental formation of conjugate sets of rocks. *Journal of Structural Geology*, 13 (8). p 887-895.

APPENDIX 1 - 1D OUTCROP SURVEY DATA

Table A1.1 Discontinuity Survey data for George Gill
Distance represents Cumulative distance from the start of the survey. *D* is displacement, *T* is thickness.

Distance (m)	Strike	Dip		D (mm)	T (mm)
0	146	60	W	180.0	50
0.1	156	70	E	0.0	1
0.12	162	75	W	0.5	1
0.145	140	70	W	2.0	1
0.175	178	70	E	0.0	1
0.185	148	75	W	0.0	1
0.2	160	70	W	2.0	1
0.26	134	60	W	0.0	1
0.53	170	60	E	25.0	15
0.54	175	65	W	0.0	1
0.74	150	80	W	1.0	1
0.84	155	80	W	2.0	1
0.94	8	60	W	0.0	1
0.99	0	85	E	8.0	2
1.05	172	70	E	1.0	1
1.09	164	65	E	1.0	1
1.13	158	75	E	5.0	1
1.32	148	75	E	60.0	10
1.355	0	75	E	4.0	2
1.825	158	80	E	15.0	2
1.835	146	85	W	1.0	1
1.975	165	85	W	0.0	1
2.105	40	85	E	0.0	2
2.205	0	80	E	0.0	1
2.325	170	55	E	60.0	40
2.385	2	60	W	3.0	2
2.465	158	70	W	3.0	2
2.485	144	70	W	5.0	3
2.625	130	75	W	1.0	2
2.725	140	85	W	3.0	3
2.775	150	50	W	50.0	70
2.935	155	65	W	3.0	2
3.015	10	80	E	0.0	1
3.105	150	55	W	1.0	1
3.435	155	70	W	10.0	5
3.475	155	60	W	4.0	3
3.755	164	85	E	2.0	3
3.885	0	90	W	0.0	2
4.905	178	85	W	0.0	1
4.925	140	85	W	2.0	2
5.095	175	85	E	2.0	3
5.715	165	85	W	2.0	3
5.735	146	80	E	0.0	1
5.785	150	65	W	2.0	3
6.035	146	65	W	3.0	3
6.155	176	85	E	0.0	1
6.205	172	90	W	0.0	1
6.295	160	70	W	1.0	1
6.905	166	80	E	0.0	1
6.965	175	70	E	20.0	30
7.235	165	50	W	8.0	4
7.305	154	60	W	30.0	60
7.495	168	65	W	0.0	1
7.595	165	70	E	70.0	50
7.665	174	80	E	0.0	2
7.695	160	60	W	1.0	2
7.745	6	50	W	2.0	4
7.815	165	80	W	0.0	20
7.895	178	85	E	0.0	1
7.925	170	70	E	0.0	1
7.965	2	85	E	0.0	1
7.985	0	75	E	1.0	1
8.085	5	75	E	20.0	30
8.365	162	80	W	0.0	1
8.445	152	70	E	0.0	1
8.565	162	85	E	24.0	20
8.865	175	75	E	18.0	25
8.935	5	80	E	1.0	2
8.965	148	50	W	2.0	10
9.065	170	70	W	1.0	2
9.135	152	55	E	1.0	1
9.305	154	70	E	0.0	1
9.535	170	80	E	1.0	1
9.595	170	50	W	3.0	2
9.645	152	50	W	1.0	1
9.825	164	40	W	2.0	1
10.115	150	60	E	1.0	3
10.195	146	60	W	2.0	2
10.225	135	40	W	8.0	5
10.265	144	70	E	12.0	18
10.345	2	40	W	1.0	1
10.365	4	50	W	0.0	1
10.515	172	75	E	0.0	3
10.555	166	85	E	0.0	1
10.585	165	60	W	28.0	25
10.655	170	85	E	0.5	1
10.805	135	45	W	1.0	1
11.155	172	85	W	1.0	2
11.335	178	50	W	12.0	10
11.755	146	85	W	2.0	1
11.825	158	80	E	0.0	1
12.075	146	90	E	0.0	1
12.105	145	85	E	0.0	1
12.385	168	50	W	1.0	2
12.565	175	80	E	4.0	5
12.765	156	90	W	0.0	2
13.085	152	60	W	2.0	3
13.165	175	50	W	0.0	1
13.215	128	80	W	1.0	1
13.255	152	60	E	2.0	2
13.385	146	60	W	1.0	2

Table A1.2 Discontinuity Survey data for Belah Scar

Distance (m)	Strike	Dip		D (mm)	T (mm)
7.45	168	70	W	1	2
8.55	10	76	W	12	40
9.91	164	78	W	1	1
10.21	2	74	W	1	1
10.41	7	70	W	2	1
11.22	168	74	E	4	9
11.56	172	82	W	2	2
11.78	165	65	W	14	8
12.04	176	57	W	2	2
12.07	170	63	W	4	5
12.71	26	82	W	1	1
12.88	6	80	W	2	0.5
12.91	163	79	E	1	1
13.81	52	65	W	11	9
13.87	30	60	W	1	1
14.01	18	55	W	1	3
14.25	25	60	W	5	15
14.36	167	56	E	150	22
14.4	15	60	W	1	0.5
14.43	10	66	W	1	1
14.46	170	62	W	1	1
14.54	178	60	W	2	1
14.81	20	84	W	1	1
14.83	18	80	W	1	1
14.84	20	80	W	1	1
14.99	7	68	W	380	28
15.34	5	82	E	2	1
18.39	10	50	W	1	3
18.43	17	45	W	1	3
18.49	170	50	W	1	2
20.21	11	60	W	1	2
20.27	175	70	E	1	1
27.36	14	75	E	3	2
28.49	178	70	W	1	2
28.6	3	62	W	1	1
29.12	1	62	W	46	2
29.39	163	50	W	3000	165
30.33	14	74	W	1	3
31.43	17	70	W	2	3
32.3	10	50	W	1	2
32.88	0	68	W	1	2
32.98	175	85	W	1	1
33.14	20	70	E	1	1
34.29	4	64	E	1	1
34.82	179	84	E	42	7
35.33	164	76	E	147	18
35.65	10	74	W	1	2
37.99	17	74	W	111	14
38.14	24	80	W	40	4
38.18	16	78	W	18	1
38.25	32	65	W	16	1
39.46	4	60	E	35	17
40.56	20	85	W	2	2
40.68	16	64	E	7	3
41.89	1	68	W	35	4
45.71	13	72	W	8	3
47.51	37	68	W	3	2
47.56	20	80	W	2	1
48.66	40	84	W	1	3
48.98	20	83	W	2	3
54.98	10	70	W	14	12
55.02	164	80	W	27	4
55.25	157	58	W	23	5
55.37	8	74	E	18	3
55.77	9	60	W	12	4
56.12	178	65	W	1400	96
56.94	37	80	W	1	2
57.14	175	86	E	3	2
57.22	170	84	E	1	1
58.07	20	80	W	1	1
58.08	12	76	E	1	1
58.7	30	70	E	23	1
59.01	152	74	E	5	2
59.43	20	70	E	4	2
60.05	13	76	E	2	5
60.51	35	72	W	7	3
60.85	17	78	E	12	3
67	0	70	E	2	4
67.42	19	74	W	1	1
67.54	11	84	E	1	4
68.34	10	70	W	1	1
68.47	8	64	W	3	2
68.99	174	84	E	5	2
69.37	173	58	E	4	1
69.62	0	70	E	1	2
71.57	30	84	W	3	4

Table A1.3 Discontinuity Survey data for Molly's Castle

Distance (m)	Strike	Dip		D (mm)	T (mm)
0.12	135	68	N	2	3
0.24	140	70	N	2	2
0.42	134	68	S	12	1
0.64	141	56	N	80	42
1.06	127	61	S	3	2
1.37	100	55	S	2	1
1.42	100	54	N	4	2
2.89	125	64	N	1	2
4.35	130	65	S	3	3
4.47	117	60	S	290	110
6.08	91	66	S	2	1
6.11	107	61	S	1	1
6.29	109	67	S	1	2
9.09	123	68	S	30	6
12.04	138	61	S	32	8
12.57	100	72	S	63	7
12.64	116	76	S	1	1
12.69	118	74	S	1	1
12.99	113	56	N	2	2
13.00	127	63	S	2	1
13.03	122	69	S	1	3
13.10	127	73	S	2	2
13.26	117	62	N	14	8
13.44	120	50	S	3	3
13.46	113	70	S	1	1
13.61	117	69	S	30	16
13.85	108	70	S	3	5
14.13	109	67	S	1	3
14.21	115	70	S	1	2
14.31	127	78	S	4	4
14.61	125	69	N	6	8
14.63	131	72	S	4	2
14.70	111	67	S	2	3
14.79	96	74	S	2	2
14.91	119	70	S	1	2
15.11	107	62	S	1	2
15.27	110	60	S	2	1
15.51	114	77	S	2	2
15.59	132	74	S	2	1
15.86	113	72	S	1	2
16.38	130	74	S	2	2
16.42	132	56	N	1	1
16.59	125	67	S	104	58
21.63	135	52	N	56	14
22.53	122	58	N	2	1
22.60	113	52	N	1	1
24.25	130	67	S	36	12
24.29	139	63	S	4	15
24.59	116	68	S	4	2
26.72	152	64	N	2	2
26.84	137	70	N	1	1
30.14	138	69	N	1	1
30.72	127	61	S	6	8
30.96	138	63	N	3	1
32.82	106	67	S	4	3
32.95	101	68	S	1	1
33.17	110	63	S	3	1
33.48	120	66	S	2	1
33.88	135	69	S	2	1
34.38	119	52	S	5	4
37.80	137	60	N	1	2
40.30	137	65	S	40	11
40.35	140	76	S	1	2
40.66	123	61	N	1	1
40.96	130	63	S	4	8
41.04	124	61	N	2	2
42.74	128	67	S	4	4
42.86	132	62	N	2	3
42.96	118	56	S	20	9
43.11	120	48	S	2	3
45.75	132	64	N	2	2
45.77	134	71	N	3	1
47.80	131	64	S	3	2
55.60	137	61	N	2	2
56.61	138	66	N	1	2
59.51	134	61	S	1	2
59.66	131	53	S	12	5

On Tables A1.4 to A1.7 (all from Seven Mile Canyon), "Type" indicates the characteristics of each structure. B = Deformation band. ZB = Zone of deformation bands (estimates of number of bands contained in the zone is sometimes given). SS = Slip surface. OF = Open Fracture with no evidence of cataclasis. FJ = Faulted joint (*sensu* Zhao and Johnson, 1991).

Table A1.4 Discontinuity Survey data from Seven Mile Canyon, Transect 1 (Figure 3.9).

Distance (m)	T (mm)	Type
0		
0.29	0.2	B
0.4	0.2	B
0.63	0.2	B
0.69	0.2	B
0.88	1	B
1.04	0.5	B
1.59	0.2	FJ
1.62	0.5	FJ
2.16	0.1	FJ
2.837	0.1	OF
2.93	0.1	OF
3.4	0.1	OF
3.85	4	ZB+SS
3.8505	5	ZBOF
4.17	0.5	B
4.22	1	B
4.24	0.5	B
4.6	20	ZB3OF
4.611	0.5	B
4.615	0.5	B
4.637	1	B
4.645	1	B
4.657	1	B
4.667	8	ZB5
4.683	0.5	B
4.685	0.5	B
4.696	1	B
4.704	1	B
4.753	1	B
4.777	0.5	B
4.78	0.5	B
4.79	0.2	B
4.88	0.6	B
5.004	0.2	B
5.016	1	B
5.019	1	B
5.0195	4	ZB
5.0225	0.8	B
5.73	0.2	B
5.85	0.1	FJ
6.29	0.5	B
6.298	0.5	B
6.334	1	B
6.342	1.5	ZB
6.378	0.2	B
6.56	0.6	B+FJ
7.524	0.5	B
7.526	1	B
7.8	0.1	B
7.95	0.1	B
8.16	0.1	OF
8.295	0.6	B
8.31	1	B
9.12	0.4	B
9.158	1	B
9.256	1	B
9.272	0.5	B
9.83	0.5	ZB
9.836	1	ZB
9.9	0.5	B
9.99	1	B
10		

Table A1.5 Discontinuity Survey data from Seven Mile Canyon Transect 2 (Figure 3.9).

Distance (m)	T (mm)	Type
0.42	6	ZB
0.423	1.5	ZB
0.427	5	ZB
0.43	4	ZB
0.432	1.5	ZB
0.433	2	ZB
0.437	3	ZB
0.442	2.5	ZB
1.25	1.5	ZB
1.44	1	B
1.94	1	ZB
1.945	1	B
1.963	1	B
1.973	1.5	B
1.976	1	B
1.982	2.5	ZB
2.021	1.5	ZB
2.049	1	B
2.053	1	B
2.068	1	B
2.21	3	ZB
2.226	6	ZB
2.228	3	ZB
2.229	1	B
2.23	6	ZB
2.2305	15	ZB
2.2335	4	ZB
2.234	20	ZB+SS
2.235	0.5	OF
2.2355	7	ZB
2.2475	1.5	B
2.2495	1	B
2.2515	2	ZB
2.2665	1	ZB
2.2735	0.8	ZB
2.2895	1	B
2.3035	0.5	B
2.3075	0.5	ZB
2.309	0.5	B
2.315	0.5	B
2.338	0.8	B
2.354	0.5	B
2.378	0.5	B
2.394	0.5	B
2.397	0.5	B
2.449	0.3	B
2.462	0.5	B
2.487	1	B
2.62	0.3	B
2.65	0.5	B
2.661	14	ZB
2.6611	3	ZB
2.6641	1.5	B
2.6681	11	ZB6
2.6741	0.8	B
2.6961	0.5	B
2.7031	0.5	B
2.7081	0.5	B
2.7201	1.5	B
2.7221	0.8	ZB
2.7261	0.5	B
2.7301	1	B
2.7351	0.5	B
2.7551	0.5	B
2.7801	0.5	B
2.7921	0.5	B
2.8021	0.5	B
3.11	13	ZB4
3.325	1	B
3.328	1	B
3.332	2	B
3.35	0.5	B
3.37	1.5	ZB
3.445	0.5	B
3.63	0.5	B
3.69	0.2	B
3.696	1.5	ZB
3.698	1	ZB
3.699	1.1	ZBOF
3.77	0.5	ZB
3.771	0.5	ZB
3.801	0.2	B
3.83	1	B
3.99	0.2	B
4.1	0.6	B
4.11	4	ZB
4.1101	0.5	OF
4.1106	6	ZB
4.1186	4	ZB
4.1216	1	B
4.1226	0.5	B
4.1246	0.5	B
4.1247	0.1	OF
4.1747	3	ZB3
4.28	0.2	B
4.53	0.1	OF
4.82	8	ZB6
4.91	1	OF
4.96	1.5	ZB
5	0.5	B
5.04	1	ZB
5.07	2	ZB
5.079	1	B
5.081	0.5	B
5.082	0.2	B
5.083	0.2	B
5.085	1	B
5.153	0.1	OF
5.65	0.1	ZB
5.745	0.2	B
6.15	0.1	OF
6.53	0.2	OF
6.94	0.1	OF
7.16	0.1	OF
7.34	0.1	OF
7.62	0.1	OF
7.66	0.2	OF
7.875	0.2	B
7.883	0.3	B
8.23	1	B
8.46	0.1	OF
8.615	0.1	OF
8.83	0.5	B
9.28	0.1	OF

Table A1.6 Discontinuity Survey data from Seven Mile Canyon Transect 3 (Figure 3.9).

Distance (m)	T (mm)	Type	Distance (m)	T (mm)	Type
0.26	3	zb	3.576	1.5	zb(2)
0.43	0.7	b	3.581	2	zb(6)
0.46	0.7	b	3.6	6	zb
1.3	0.5	b	3.614	1	ss
1.317	1	b	3.618	1.5	zb(2)
1.325	1.2	b	3.62	0.7	b
1.327	1	b	3.628	1	b
1.337	1	zb(2)	3.63	0.5	b
1.341	1	b	3.641	1	b
1.371	0.5	b	3.649	2.5	zb(4)
1.401	1	zb(2)	3.653	1.3	zb
1.56	2	zb(2)	3.662	0.5	b
1.567	0.5	b	3.664	0.7	b
1.571	0.7	b	3.678	1.5	zb(3)
1.592	1	b	3.718	1	OF
1.598	4	zb(5)	3.89	1	b
1.604	0.5	b	3.97	0.7	b
1.614	1	b	4.09	0.7	b
1.619	0.5	b	4.25	0.3	OF
1.62	1.5	zb(2)	4.32	1	zb(2)
1.622	1.5	b	4.38	0.2	OF
1.627	0.5	b	4.39	0.5	b + ss
1.6275	3.7	zb(2) + ss	4.435	0.3	b
1.6295	2	zb(2)	4.46	0.3	b
1.6355	0.5	b	4.55	1.3	zb(3)
1.6375	0.5	b	4.557	2	b
1.6405	0.2	OF	4.564	3	zb
1.71	1	b	4.615	0.7	b
1.79	1.5	b	4.68	7	zb
1.794	0.5	b	4.682	1	zb
1.798	0.4	b	4.683	1	zb
1.835	0.7	b	4.688	0.6	b
1.84	1.5	zb(3)	4.711	1.2	b
1.858	0.7	b	4.715	4	zb
1.861	0.7	b	4.72	0.5	b
1.865	2.5	zb(3)	4.845	1.5	zb(2)
1.878	0.5	b	4.848	1	b
1.905	1.5	zb(2)	4.858	0.7	b
1.959	0.5	b	5.75	0.2	OF
2.008	2.5	zb(3)	5.91	0.2	OF
2.011	0.5	b	5.925	0.2	OF
2.04	2.7	zb20+ + of	6.32	0.1	OF
2.063	0.5	b	6.47	0.1	OF
2.0655	1	b	6.5	0.5	b + OF
2.0705	1.5	zb(2)	6.567	0.4	OF
2.1465	0.7	b	7.025	0.3	OF
2.38	0.5	b	7.2	1.5	zb(2)
2.433	2	zb(4)	7.4	0.5	zb
2.445	1	b	7.46	0.3	OF
2.45	8	zb + ss.s	7.53	0.2	OF
2.458	6	zb + ss	7.79	0.5	b
2.472	10	zb(12+)	7.888	0.7	b
2.562	0.3	ss	8.09	0.5	b
2.57	0.1	OF	8.095	1	zb(2)
2.576	3	zb + 2 ss	9.5	0.3	OF
2.616	1	b	9.84	1	b
3.01	2	zb(4)	10		
3.038	0.4	OF			
3.103	0.2	OF			
3.108	0.2	OF			
3.111	0.8	b			
3.124	1.8	zb(3)			
3.144	4	zb(7)			
3.564	0.5	b			

Table A1.7 Discontinuity Survey data from Seven Mile Canyon Transect 4 (Figure 3.9).

Distance (m)	T (mm)	Type	Distance (m)	T (mm)	Type	Distance (m)	T (mm)	Type
0.31	1.5	ZB(2)	1.9441	3	B	4.19	21	ZB
0.35	0.1	OF	1.9461	1.5	B	4.194	1	ZB
0.66	1	B	1.9511	0.5	B	4.209	2	ZB
0.74	0.1	OF	1.9551	0.5	ZB	4.219	1.1	ZB
0.97	0.4	OF	1.9631	1.2	B	4.223	0.5	B
1.01	0.5	B	1.9761	3.2	ZB+SS	4.273	0.5	ZB
1.04	3	ZB(4)	1.9781	0.5	B	4.298	0.5	ZB
1.11	0.5	B	1.9801	0.5	B	4.318	1	ZB
1.2	0.5	B	1.9831	0.7	B	4.43	0.1	OF
1.26	3	ZB	1.9861	1	B	4.5	0.2	OF
1.34	0.5	B	2.0111	0.3	B	4.515	0.3	OF
1.37	0.7	B	2.0211	1	ZB	4.89	0.7	B
1.39	0.7	B	2.0291	0.7	ZB	4.95	0.5	B
1.45	0.4	B	2.0294	4	ZB	4.975	1	B
1.52	0.5	B	2.1244	0.3	B	4.983	7	ZB
1.54	1	B	2.1394	0.5	B	5.043	0.1	FJ
1.55	0.5	B	2.1444	0.3	B	5.48	0.2	OF
1.57	0.5	B	2.2144	0.7	B	5.488	0.1	OF
1.6	1	B	2.2294	4	ZB+SS	5.498	0.2	OF
1.605	8	B + 2SS	2.2494	0.6	B	5.538	0.2	OF
1.608	0.3	B	2.2844	1	B	6.33	0.5	B
1.611	0.5	B	2.2994	0.2	B	6.42	1.5	ZB
1.615	0.5	B	2.3094	1	B	6.44	0.5	B
1.616	1	B	2.3104	1.5	ZB+SS	6.61	0.5	B
1.617	1	B	2.3254	0.3	B	6.612	1	B
1.618	0.7	B	2.3354	1	B	8	2.5	B
1.71	0.8	B	2.3504	1	B	8.29	0.3	FJ
1.72	0.5	B	2.3604	0.5	B	8.3	0.1	FJ
1.754	0.3	B	2.3724	1.3	ZB(3)+ SS	9	0.7	B
1.759	0.8	B	2.3764	1	B	9.485	0.3	FJ
1.76	0.1	OF	2.3824	1	B	9.49	1	fj
1.761	1	B	2.3844	0.2	OF	9.55	0.1	FJ
1.762	0.2	B	2.4044	0.3	B	9.93	0.2	FJ
1.763	0.3	B	2.4124	0.3	B			
1.765	6	ZB	2.4164	2.5	ZB(5)			
1.769	0.8	ZB	2.4324	0.7	B			
1.783	0.8	B	2.4374	0.5	OF			
1.785	0.6	B	2.99	14	ZB			
1.799	1.5	ZB+SS	3.005	0.8	B			
1.804	0.3	B	3.11	1	B			
1.805	0.2	B	3.23	0.5	B			
1.819	0.3	B	3.28	1.8	B			
1.824	0.8	B	3.29	0.8	B			
1.848	24	ZB(3)	3.3	0.5	B			
1.856	0.7	B	3.304	0.5	B			
1.86	0.3	B	3.309	0.4	B			
1.861	0.3	B	3.3097	0.6	B			
1.868	1	B	3.3547	0.1	OF			
1.878	2.2	ZB	3.3777	0.1	OF			
1.883	0.2	B	3.4177	0.1	OF			
1.895	0.2	B	3.4577	0.7	B			
1.897	0.5	B	3.4578	0.1	OF			
1.898	0.5	B	3.4618	0.1	OF			
1.903	1.2	ZB	3.4658	0.1	OF			
1.909	0.3	B	3.55	0.2	OF			
1.912	0.2	B	3.62	0.1	OF			
1.913	0.1	OF	3.64	0.1	OF			
1.915	0.5	B	3.74	0.3	OF			
1.918	1	B	3.783	0.2	B			
1.921	1	B	3.793	0.7	B			
1.923	5	ZB	3.809	0.8	B			
1.9231	0.2	OF+SS	3.859	0.3	OF			
1.9251	1.5	B	3.93	0.3	OF			
1.9271	0.4	B	4.025	0.3	B			
1.9281	0.5	B	4.045	1	B			
1.9301	0.4	B	4.08	3.5	ZB			
1.9331	1	B	4.09	1	ZB			

APPENDIX 2 - EFFECTIVE PERMEABILITY MODELLING RESULTS

Table A2.1 Results from the disconnected orthogonal cases (Figure 5.11)

d_L	d_G	k_m / k_f	H	k_e / k_m
0.094	0.00023	300	0.0655	0.9775
0.094	0.00118	100	0.1042	0.9623
0.094	0.00023	1000	0.1898	0.9417
0.094	0.00475	100	0.3197	0.9093
0.094	0.00118	600	0.4132	0.8998
0.094	0.00118	1000	0.5401	0.8839
0.094	0.00475	300	0.5866	0.8736
0.094	0.00475	500	0.7031	0.8623
0.094	0.00475	1000	0.8258	0.8521
0.094	0.00475	2000	0.9046	0.8463
0.094	0.00475	5000	0.9596	0.8426
0.188	0.00047	100	0.0444	0.9824
0.188	0.00047	300	0.1230	0.9508
0.188	0.00047	600	0.2193	0.9161
0.188	0.00047	1000	0.3191	0.8846
0.188	0.00235	300	0.4128	0.8561
0.188	0.00235	500	0.5398	0.8242
0.188	0.00235	700	0.6217	0.8055
0.188	0.00235	1000	0.7014	0.7885
0.188	0.00949	500	0.8257	0.7553
0.188	0.00949	1000	0.9046	0.7404
0.188	0.00949	5000	0.9794	0.7269
0.313	0.00078	100	0.0718	0.9684
0.313	0.00078	200	0.1346	0.9404
0.313	0.00078	400	0.2378	0.8951
0.313	0.00078	500	0.2806	0.8768
0.313	0.00078	1000	0.4385	0.8111
0.313	0.00392	300	0.5395	0.7674
0.313	0.00392	400	0.6099	0.7391
0.313	0.00392	600	0.7012	0.7022
0.313	0.01582	300	0.8255	0.6398
0.313	0.01582	500	0.8876	0.6129
0.313	0.01582	5000	0.9875	0.5671
0.406	0.00051	100	0.0479	0.9797
0.406	0.00102	100	0.0914	0.9581
0.406	0.00102	300	0.2330	0.8913
0.406	0.00102	500	0.3365	0.8421
0.406	0.00102	700	0.4153	0.8044
0.406	0.00102	1000	0.5038	0.7617
0.406	0.00509	300	0.6037	0.7095
0.406	0.00509	500	0.7177	0.6515
0.406	0.02057	200	0.8036	0.5943
0.406	0.02057	500	0.9112	0.5324
0.406	0.02057	1000	0.9536	0.5061
0.500	0.00063	100	0.0583	0.9743
0.500	0.00125	100	0.1102	0.9481
0.500	0.00125	200	0.1993	0.9046
0.500	0.00125	300	0.2722	0.8681
0.500	0.00627	100	0.3830	0.8070
0.500	0.00627	200	0.5551	0.7154
0.500	0.00627	300	0.6521	0.6604
0.500	0.02531	100	0.7148	0.6111
0.500	0.02531	200	0.8344	0.5345
0.500	0.02531	400	0.9099	0.4808
0.500	0.02531	1000	0.9620	0.4402
0.625	0.00078	100	0.0718	0.9673
0.625	0.00078	200	0.1346	0.9364
0.625	0.00156	200	0.2373	0.8822
0.625	0.00156	300	0.3186	0.8383
0.625	0.00156	500	0.4383	0.7702
0.625	0.00156	600	0.4836	0.7431
0.625	0.00156	1000	0.6097	0.6629
0.625	0.00784	300	0.7009	0.5958
0.625	0.00784	500	0.7964	0.5219
0.625	0.03164	300	0.9044	0.4105
0.625	0.03164	1000	0.9693	0.3323

Table A2.2 Results from the connected orthogonal cases (Figure 5.11).

d_L	d_G	k_m / k_f	H	k_e / k_m
0.625	0.00008	100	0.0077	0.9999
0.625	0.00039	100	0.0372	0.9849
0.625	0.00008	500	0.0375	0.9867
0.625	0.00078	100	0.0718	0.9671
0.625	0.00008	1000	0.0724	0.9692
0.625	0.00156	100	0.1340	0.9344
0.625	0.00039	500	0.1631	0.9214
0.625	0.00391	100	0.2792	0.8537
0.625	0.00078	500	0.2806	0.8561
0.625	0.00039	1000	0.2807	0.8564
0.625	0.00008	5000	0.2809	0.8567
0.625	0.00548	100	0.3517	0.8100
0.625	0.00784	100	0.4369	0.7550
0.625	0.00156	500	0.4383	0.7585
0.625	0.00078	1000	0.4384	0.7589
0.625	0.00156	1000	0.6097	0.6326
0.625	0.00391	500	0.6613	0.5871
0.625	0.00039	5000	0.6614	0.5887
0.625	0.00548	500	0.7323	0.5179
0.625	0.00078	5000	0.7962	0.4472
0.625	0.00391	1000	0.7963	0.4460
0.625	0.00784	500	0.7964	0.4446
0.625	0.00548	1000	0.8456	0.3791
0.625	0.00156	5000	0.8866	0.3141
0.625	0.00784	1000	0.8867	0.3124
0.625	0.00391	5000	0.9514	0.1731
0.625	0.00548	5000	0.9648	0.1342
0.625	0.00784	5000	0.9751	0.1005
1.250	0.00078	100	0.0543	0.9671
1.250	0.00078	150	0.1043	0.9509
1.250	0.00156	150	0.1889	0.9046
1.250	0.00156	300	0.3186	0.8290
1.250	0.00156	500	0.4383	0.7507
1.250	0.00784	150	0.5387	0.6739
1.250	0.00784	200	0.6093	0.6171
1.250	0.00784	400	0.7577	0.4762
1.250	0.00784	600	0.8244	0.3983
1.250	0.00784	1000	0.8867	0.3103
1.875	0.00117	50	0.0543	0.9733
1.875	0.00117	100	0.1040	0.9494
1.875	0.00235	100	0.1884	0.9018
1.875	0.00235	200	0.3182	0.8232
1.875	0.00235	400	0.4834	0.7053
1.875	0.01176	100	0.5378	0.6563
1.875	0.01176	200	0.7005	0.5026
1.875	0.01176	400	0.8243	0.3513
1.875	0.01176	600	0.8756	0.2740
1.875	0.01176	1000	0.9215	0.1932
2.500	0.00039	100	0.0372	0.9896
2.500	0.00195	100	0.1621	0.9372
2.500	0.00039	500	0.1631	0.9391
2.500	0.00313	100	0.2363	0.8801
2.500	0.00625	100	0.3824	0.7868
2.500	0.01565	100	0.6077	0.6038
2.500	0.00313	500	0.6094	0.6075
2.500	0.02192	100	0.6846	0.5255
2.500	0.03135	100	0.7563	0.4419
2.500	0.00625	500	0.7573	0.4474
2.500	0.00313	1000	0.7574	0.4481
2.500	0.00625	1000	0.8620	0.3012
2.500	0.01565	500	0.8865	0.2593
2.500	0.02192	500	0.9162	0.2049
2.500	0.01565	1000	0.9399	0.1583
2.500	0.03135	500	0.9399	0.1569
2.500	0.02192	1000	0.9563	0.1215
2.500	0.03135	1000	0.9691	0.0904
3.125	0.00195	50	0.0874	0.9553
3.125	0.00195	100	0.1621	0.9161
3.125	0.00391	100	0.2790	0.8444
3.125	0.00391	150	0.3680	0.7853
3.125	0.00391	200	0.4375	0.7347
3.125	0.00391	300	0.5389	0.6526
3.125	0.01959	100	0.6598	0.5328
3.125	0.00391	1000	0.7961	0.3791
3.125	0.02351	300	0.8542	0.2941
3.125	0.01959	1000	0.9514	0.1229
3.750	0.00234	50	0.1030	0.9468
3.750	0.00234	100	0.1884	0.9008
3.750	0.00469	100	0.3171	0.8193
3.750	0.00469	150	0.4114	0.7538
3.750	0.00469	200	0.4828	0.6989
3.750	0.00469	300	0.5838	0.6121
3.750	0.02351	100	0.6995	0.4895
3.750	0.00469	1000	0.8241	0.3403
3.750	0.02351	300	0.8755	0.2601
3.750	0.02351	1000	0.9592	0.1056
4.375	0.00274	50	0.1182	0.9382
4.375	0.00274	100	0.2131	0.8856
4.375	0.00547	100	0.3514	0.7949
4.375	0.00547	150	0.4491	0.7236
4.375	0.00547	200	0.5213	0.6650
4.375	0.00547	300	0.6207	0.5743
4.375	0.02743	100	0.7309	0.4498
4.375	0.00547	1000	0.8454	0.3048
4.375	0.02743	300	0.8913	0.2292
4.375	0.02743	1000	0.9648	0.0897
5.000	0.00063	100	0.0583	0.9747
5.000	0.00313	100	0.2363	0.8750
5.000	0.00063	500	0.2377	0.8770
5.000	0.00625	100	0.3823	0.7781
5.000	0.00063	1000	0.3844	0.7807
5.000	0.01251	100	0.5532	0.6403
5.000	0.00313	500	0.6093	0.5929
5.000	0.03130	100	0.7560	0.4245
5.000	0.00625	500	0.7573	0.4297
5.000	0.00313	1000	0.7574	0.4304
5.000	0.00063	5000	0.7575	0.4309
5.000	0.04385	100	0.8128	0.3484
5.000	0.06270	100	0.8612	0.2753
5.000	0.01251	500	0.8619	0.2824
5.000	0.00625	1000	0.8620	0.2833
5.000	0.01251	1000	0.9259	0.1721
5.000	0.03130	500	0.9398	0.1433
5.000	0.00313	5000	0.9398	0.1456
5.000	0.04385	500	0.9563	0.1087
5.000	0.00625	5000	0.9690	0.0824
5.000	0.03130	1000	0.9690	0.0813
5.000	0.06270	500	0.9690	0.0799
5.000	0.04385	1000	0.9777	0.0604
5.000	0.01251	5000	0.9843	0.0448
5.000	0.06270	1000	0.9843	0.0436
5.000	0.03130	5000	0.9936	0.0010
5.000	0.04385	5000	0.9955	0.0137
5.000	0.06270	5000	0.9968	0.0096

Table A2.3 Results from the entirely disconnected non-orthogonal cases (Figure 5.15a).

α (°)	k_m (mD)	k_f (mD)	d_L	H	k_e / k_m
10.0	5	1	0.473	0.3165	0.7184
10.0	8	1	0.473	0.4476	0.6063
10.0	10	1	0.473	0.5102	0.5538
10.0	20	1	0.473	0.6874	0.4072
10.0	30	1	0.473	0.7705	0.3386
10.0	60	1	0.473	0.8723	0.2535
10.0	100	1	0.473	0.9197	0.2126
10.0	200	1	0.473	0.9584	0.1783
10.0	200	0	0.473	1.0000	0.1391
22.0	5	1	0.233	0.3165	0.7601
22.0	8	1	0.233	0.4476	0.6703
22.0	10	1	0.233	0.5102	0.6296
22.0	20	1	0.233	0.6874	0.5204
22.0	30	1	0.233	0.7705	0.4715
22.0	60	1	0.233	0.8723	0.4128
22.0	100	1	0.233	0.9197	0.3857
22.0	200	1	0.233	0.9584	0.3637
22.0	200	0	0.233	1.0000	0.3399
37.0	5	1	0.168	0.3165	0.8043
37.0	8	1	0.168	0.4476	0.7372
37.0	10	1	0.168	0.5102	0.7078
37.0	20	1	0.168	0.6874	0.6311
37.0	30	1	0.168	0.7705	0.5979
37.0	60	1	0.168	0.8723	0.5589
37.0	100	1	0.168	0.9197	0.5413
37.0	200	1	0.168	0.9584	0.5272
37.0	200	0	0.168	1.0000	0.5122
45.0	5	1	0.161	0.3165	0.8258
45.0	8	1	0.161	0.4476	0.7685
45.0	10	1	0.161	0.5102	0.7437
45.0	20	1	0.161	0.6874	0.6793
45.0	30	1	0.161	0.7705	0.6515
45.0	60	1	0.161	0.8723	0.6188
45.0	100	1	0.161	0.9197	0.6041
45.0	200	1	0.161	0.9584	0.5922
45.0	200	0	0.161	1.0000	0.5797
53.0	5	1	0.168	0.3165	0.8460
53.0	8	1	0.168	0.4476	0.7975
53.0	10	1	0.168	0.5102	0.7765
53.0	20	1	0.168	0.6874	0.7222
53.0	30	1	0.168	0.7705	0.6984
53.0	60	1	0.168	0.8723	0.6702
53.0	100	1	0.168	0.9197	0.6574
53.0	200	1	0.168	0.9584	0.6469
53.0	200	0	0.168	1.0000	0.6359
68.0	5	1	0.233	0.3165	0.8816
68.0	8	1	0.233	0.4476	0.8471
68.0	10	1	0.233	0.5102	0.8323
68.0	20	1	0.233	0.6874	0.7930
68.0	30	1	0.233	0.7705	0.7746
68.0	60	1	0.233	0.8723	0.7511
68.0	100	1	0.233	0.9197	0.7396
68.0	200	1	0.233	0.9584	0.7297
68.0	200	0	0.233	1.0000	0.7187
80.0	5	1	0.473	0.3165	1.1658
80.0	8	1	0.473	0.4476	0.8842
80.0	10	1	0.473	0.5102	0.8738
80.0	20	1	0.473	0.6874	0.8465
80.0	30	1	0.473	0.7705	0.8327
80.0	60	1	0.473	0.8723	0.8118
80.0	100	1	0.473	0.9197	0.7989
80.0	200	1	0.473	0.9584	0.7855
80.0	200	0	0.473	1.0000	0.7660

Table A2.4 Results from the partially connected non-orthogonal cases (Figure 5.15b).

α (°)	k_m (mD)	k_f (mD)	d_L	H	k_e / k_m
10.0	5	1	0.473	0.3174	0.7196
10.0	8	1	0.473	0.4487	0.6073
10.0	10	1	0.473	0.5113	0.5542
10.0	20	1	0.473	0.6884	0.4030
10.0	30	1	0.473	0.7713	0.3300
10.0	60	1	0.473	0.8728	0.2352
10.0	100	1	0.473	0.9201	0.1866
10.0	200	1	0.473	0.9586	0.1424
10.0	200	0	0.473	1.0000	0.0828
22.0	5	1	0.233	0.3174	0.7574
22.0	8	1	0.233	0.4487	0.6625
22.0	10	1	0.233	0.5113	0.6182
22.0	20	1	0.233	0.6884	0.4924
22.0	30	1	0.233	0.7713	0.4308
22.0	60	1	0.233	0.8728	0.3484
22.0	100	1	0.233	0.9201	0.3048
22.0	200	1	0.233	0.9586	0.2643
22.0	200	0	0.233	1.0000	0.2111
37.0	5	1	0.168	0.3174	0.7962
37.0	8	1	0.168	0.4487	0.7193
37.0	10	1	0.168	0.5113	0.6835
37.0	20	1	0.168	0.6884	0.5800
37.0	30	1	0.168	0.7713	0.5277
37.0	60	1	0.168	0.8728	0.4550
37.0	100	1	0.168	0.9201	0.4148
37.0	200	1	0.168	0.9586	0.3768
37.0	200	0	0.168	1.0000	0.3265
45.0	5	1	0.161	0.3174	0.8157
45.0	8	1	0.161	0.4487	0.7474
45.0	10	1	0.161	0.5113	0.7154
45.0	20	1	0.161	0.6884	0.6217
45.0	30	1	0.161	0.7713	0.5730
45.0	60	1	0.161	0.8728	0.5035
45.0	100	1	0.161	0.9201	0.4641
45.0	200	1	0.161	0.9586	0.4259
45.0	200	0	0.161	1.0000	0.3742
53.0	5	1	0.168	0.3174	0.8350
53.0	8	1	0.168	0.4487	0.7751
53.0	10	1	0.168	0.5113	0.7469
53.0	20	1	0.168	0.6884	0.6625
53.0	30	1	0.168	0.7713	0.6173
53.0	60	1	0.168	0.8728	0.5504
53.0	100	1	0.168	0.9201	0.5109
53.0	200	1	0.168	0.9586	0.4715
53.0	200	0	0.168	1.0000	0.4158
68.0	5	1	0.233	0.3174	0.8715
68.0	8	1	0.233	0.4487	0.8280
68.0	10	1	0.233	0.5113	0.8076
68.0	20	1	0.233	0.6884	0.7437
68.0	30	1	0.233	0.7713	0.7064
68.0	60	1	0.233	0.8728	0.6453
68.0	100	1	0.233	0.9201	0.6048
68.0	200	1	0.233	0.9586	0.5596
68.0	200	0	0.233	1.0000	0.4826
80.0	5	1	0.473	0.3174	1.1658
80.0	8	1	0.473	0.4487	0.8734
80.0	10	1	0.473	0.5113	0.8603
80.0	20	1	0.473	0.6884	0.8209
80.0	30	1	0.473	0.7713	0.7969
80.0	60	1	0.473	0.8728	0.7520
80.0	100	1	0.473	0.9201	0.7161
80.0	200	1	0.473	0.9586	0.6669
80.0	200	0	0.473	1.0000	0.5269

Table A2.5 Results from the connected non-orthogonal cases (Figure 5.15c).

α (°)	k_m (mD)	k_f (mD)	H	k_e / k_m
10.0	5	1	0.3197	0.6474
10.0	8	1	0.4513	0.5139
10.0	10	1	0.5140	0.4526
10.0	20	1	0.6906	0.2857
10.0	30	1	0.7731	0.2100
10.0	60	1	0.8739	0.1183
10.0	100	1	0.9208	0.0753
10.0	200	1	0.9590	0.0398
22.0	5	1	0.3197	0.6716
22.0	8	1	0.4513	0.5419
22.0	10	1	0.5140	0.4813
22.0	20	1	0.6906	0.3120
22.0	30	1	0.7731	0.2324
22.0	60	1	0.8739	0.1327
22.0	100	1	0.9208	0.0847
22.0	200	1	0.9590	0.0446
37.0	5	1	0.3197	0.7109
37.0	8	1	0.4513	0.5924
37.0	10	1	0.5140	0.5349
37.0	20	1	0.6906	0.3645
37.0	30	1	0.7731	0.2783
37.0	60	1	0.8739	0.1638
37.0	100	1	0.9208	0.1061
37.0	200	1	0.9590	0.0565
45.0	5	1	0.3197	0.7373
45.0	8	1	0.4513	0.6284
45.0	10	1	0.5140	0.5742
45.0	20	1	0.6906	0.4067
45.0	30	1	0.7731	0.3171
45.0	60	1	0.8739	0.1922
45.0	100	1	0.9208	0.1264
45.0	200	1	0.9590	0.0682
53.0	5	1	0.3197	0.7670
53.0	8	1	0.4513	0.6709
53.0	10	1	0.5140	0.6220
53.0	20	1	0.6906	0.4628
53.0	30	1	0.7731	0.3714
53.0	60	1	0.8739	0.2351
53.0	100	1	0.9208	0.1584
53.0	200	1	0.9590	0.0874
68.0	5	1	0.3197	0.8273
68.0	8	1	0.4513	0.7640
68.0	10	1	0.5140	0.7313
68.0	20	1	0.6906	0.6145
68.0	30	1	0.7731	0.5355
68.0	60	1	0.8739	0.3912
68.0	100	1	0.9208	0.2895
68.0	200	1	0.9590	0.1761
80.0	5	1	0.3197	1.1658
80.0	8	1	0.4513	0.8370
80.0	10	1	0.5140	0.8206
80.0	20	1	0.6906	0.7665
80.0	30	1	0.7731	0.7283
80.0	60	1	0.8739	0.6434
80.0	100	1	0.9208	0.5622
80.0	200	1	0.9590	0.4313

APPENDIX 3 - EFFECTIVE PERMEABILITY UPSCALING RESULTS

Table A3.1 Summary of the North Sea effective permeability upscaling results, for $\alpha = 15°$, $k_f = 1$ mD, $k_m = 1$ D.

		B	n	F	r	k_e3(mD)	k_e1(mD)
ε_1	0.024355	0.01	1	100	1	814.6	923.8
c_1	0.6			100	1.5	486.6	777.1
a_1	0.0151			10	1.5	248.9	670.3
W	399.2			10	1	379.1	757.4
		0.01	1.5	100	1	815.0	931.3
				100	1.5	530.7	807.1
				10	1.5	369.6	728.5
				10	1	500.7	809.8
		0.001	1.5	100	1	790.6	917.0
				100	1.5	410.0	752.7
				10	1.5	161.2	635.1
				10	1	334.6	744.3
		0.001	1	100	1	789.8	893.3
				100	1.5	396.0	622.1
				10	1.5	139.3	308.9
				10	1	292.4	484.2
ε_1	0.024355	0.01	1	100	1	799.3	917.9
c_1	0.8			100	1.5	382.6	747.9
a_1	0.0117			10	1.5	185.0	654.4
W	935.4			10	1	341.7	739.4
		0.01	1.5	100	1	797.11	920.0
				100	1.5	377.11	765.0
				10	1.5	214.6	693.2
				10	1	411.0	773.0
		0.001	1.5	100	1	777.4	906.3
				100	1.5	307.3	642.4
				10	1.5	110.9	507.1
				10	1	301.0	676.7
		0.001	1	100	1	775.4	885.4
				100	1.5	294.9	492.3
				10	1.5	96.8	208.3
				10	1	277.3	459.3
ε_1	0.065	0.01	1	100	1	617.0	790.2
c_1	0.6			100	1.5	251.0	525.8
a_1	0.0403			10	1.5	91.2	262.0
W	149.6			10	1	164.8	347.11
		0.01	1.5	100	1	616.7	867.11
				100	1.5	258.1	714.2
				10	1.5	115.6	647.3
				10	1	215.4	719.5
		0.001	1.5	100	1	585.6	759.4
				100	1.5	211.8	444.4
				10	1.5	65.5	212.5
				10	1	145.1	297.8
		0.001	1	100	1	583.7	757.4
				100	1.5	195.2	362.8
				10	1.5	53.7	119.7
				10	1	119.9	241.5
ε_1	0.065	0.01	1	100	1	599.7	787.8
c_1	0.8			100	1.5	181.6	513.2
a_1	0.0313			10	1.5	66.1	279.6
W	350.5			10	1	155.0	374.0
		0.01	1.5	100	1	590.1	841.9
				100	1.5	172.2	643.6
				10	1.5	63.9	574.7
				10	1	171.5	656.0
		0.001	1.5	100	1	567.2	750.5
				100	1.5	129.0	246.1
				10	1.5	36.2	74.1
				10	1	133.4	280.4
		0.001	1	100	1	561.6	739.3
				100	1.5	125.4	238.7
				10	1.5	34.2	69.3
				10	1	119.6	234.3

Table A3.2 Summary of the North Sea effective permeability upscaling results, for $\alpha = 15°$, $k_f = 100$ mD, $k_m = 1$ D.

		B	n	F	r	k_e3(mD)	k_e1(mD)
ε_1	0.024355	0.01	1	100	1	997.10	999.0
c_1	0.6			100	1.5	986.0	993.9
a_1	0.0151			10	1.5	939.6	973.6
W	399.2			10	1	978.5	990.7
		0.01	1.5	100	1	997.4	998.9
				100	1.5	984.8	993.4
				10	1.5	935.7	972.5
				10	1	975.4	989.6
		0.001	1.5	100	1	997.4	998.9
				100	1.5	984.7	993.3
				10	1.5	933.5	971.1
				10	1	975.0	989.2
		0.001	1	100	1	997.9	998.9
				100	1.5	984.6	993.2
				10	1.5	933.1	969.6
				10	1	975.5	989.1
ε_1	0.024355	0.01	1	100	1	997.8	999.0
c_1	0.8			100	1.5	976.5	989.8
a_1	0.0117			10	1.5	902.7	959.0
W	935.4			10	1	976.7	989.9
		0.01	1.5	100	1	997.3	998.8
				100	1.5	974.8	989.1
				10	1.5	896.5	956.9
				10	1	973.9	988.8
		0.001	1.5	100	1	997.3	998.8
				100	1.5	974.7	988.9
				10	1.5	894.4	952.6
				10	1	973.6	988.5
		0.001	1	100	1	997.3	998.8
				100	1.5	974.5	988.6
				10	1.5	893.4	950.0
				10	1	973.7	988.3
ε_1	0.065	0.01	1	100	1	993.8	997.3
c_1	0.6			100	1.5	962.3	983.4
a_1	0.0403			10	1.5	850.7	932.1
W	149.6			10	1	941.9	973.6
		0.01	1.5	100	1	993.2	997.0
				100	1.5	960.5	983.0
				10	1.5	844.7	935.4
				10	1	937.1	974.2
		0.001	1.5	100	1	992.8	996.8
				100	1.5	959.4	981.8
				10	1.5	839.5	923.3
				10	1	933.8	969.6
		0.001	1	100	1	993.1	997.0
				100	1.5	958.5	981.3
				10	1.5	836.0	920.0
				10	1	935.9	970.6
ε_1	0.065	0.01	1	100	1	993.4	997.1
c_1	0.8			100	1.5	939.3	973.5
a_1	0.0313			10	1.5	777.9	901.3
W	350.5			10	1	938.8	972.4
		0.01	1.5	100	1	992.8	996.8
				100	1.5	935.9	972.2
				10	1.5	768.0	899.8
				10	1	933.4	971.9
		0.001	1.5	100	1	992.3	996.6
				100	1.5	930.1	967.11
				10	1.5	749.7	869.0
				10	1	928.9	967.3
		0.001	1	100	1	992.5	996.7
				100	1.5	930.5	968.1
				10	1.5	750.1	869.5
				10	1	930.5	965.0

Table A3.3 Summary of the North Sea effective permeability upscaling results for α=15°, k_f = 0.01 mD, k_m = 1 D.

		B	n	F	r	k_e3(mD)	k_e1(mD)
ε_1	0.024355	0.01	1	100	1	124.3	646.7
c_1	0.6			100	1.5	78.4	616.4
a_1	0.0151			10	1.5	61.4	609.8
W	399.2			10	1	65.7	616.2
		0.01	1.5	100	1	334.6	719.9
				100	1.5	299.9	691.9
				10	1.5	293.4	686.1
				10	1	299.4	692.5
		0.001	1.5	100	1	75.1	615.1
				100	1.5	24.4	576.2
				10	1.5	13.5	568.9
				10	1	18.7	576.8
		0.001	1	100	1	43.2	97.4
				100	1.5	10.5	29.3
				10	1.5	2.8	8.1
				10	1	5.2	13.6
ε_1	0.024355	0.01	1	100	1	95.4	635.7
c_1	0.8			100	1.5	51.4	614.7
a_1	0.0117			10	1.5	36.7	606.4
W	935.4			10	1	41.5	614.2
		0.01	1.5	100	1	188.6	687.9
				100	1.5	142.8	668.8
				10	1.5	136.2	660.8
				10	1	143.7	669.1
		0.001	1.5	100	1	57.8	495.1
				100	1.5	12.7	450.0
				10	1.5	5.2	440.2
				10	1	10.1	451.8
		0.001	1	100	1	40.6	88.7
				100	1.5	7.2	18.2
				10	1.5	1.9	4.8
				10	1	4.8	11.2
ε_1	0.065	0.01	1	100	1	28.8	94.3
c_1	0.6			100	1.5	11.6	49.7
a_1	0.0403			10	1.5	4.9	23.1
W	149.6			10	1	6.5	28.9
		0.01	1.5	100	1	74.3	652.3
				100	1.5	52.0	635.5
				10	1.5	46.8	623.5
				10	1	50.1	633.8
		0.001	1.5	100	1	21.0	75.2
				100	1.5	5.3	40.1
				10	1.5	1.7	18.7
				10	1	2.9	22.8
		0.001	1	100	1	13.2	30.0
				100	1.5	3.1	7.9
				10	1.5	0.7	1.8
				10	1	1.4	3.1
ε_1	0.065	0.01	1	100	1	25.1	107.9
c_1	0.8			100	1.5	8.1	56.1
a_1	0.0313			10	1.5	3.0	26.2
W	350.5			10	1	4.5	33.6
		0.01	1.5	100	1	37.4	589.5
				100	1.5	15.3	574.4
				10	1.5	11.5	554.5
				10	1	14.2	574.7
		0.001	1.5	100	1	15.4	33.3
				100	1.5	2.4	5.0
				10	1.5	0.6	1.3
				10	1	1.8	3.8
		0.001	1	100	1	13.8	30.4
				100	1.5	2.1	4.5
				10	1.5	0.5	1.1
				10	1	1.5	3.3